The influence of the spectrum of jet turbulence on the stability, NO_x emissions and heat release profile of pulverised coal flames

Ph.D. Thesis

Neil Lincoln Smith

The University of Adelaide

Departments of Mechanical and Chemical Engineering

October 2000

Table of contents

Chapter 1. Introduction

Chapter 2. Experimental Design and Scaling Criteria

Chapter 3. Turbulent structure in single phase non-reacting annular flows

Chapter 4. The influence of large scale jet oscillations on particle motion

Chapter 5. The influence of precession on small-scale PF flames

Chapter 7 Assessment of the dominant mechanisms by which precession influences ignition and combustion using sensitivity analyses

Chapter 8 Conclusions and Future Work

Appendices

Abstract

The hypothesis investigated in the current study is that, *increasing the scale of, and energy contained in, the larger scales of jet turbulence can beneficially influence the stability of pulverised fuel (PF) flames, their heat release profiles, and NO_x emissions*. The hypothesis is investigated using precessing jet nozzles to enlarge the largest scales of turbulence and shift the energy in the spectrum of turbulence away from the fine scales. These effects are referred to as "enhanced large scale mixing" in the text.

Experiments were conducted to measure and compare the effects of a number of types of central jet, located within a co-annular stream, on the turbulent structure of the combined flow. Modelling was performed in water using a planar laser induced fluorescence visualisation technique, and limited to a region corresponding to the pre-ignition region of flames, where reasonable similarity exists. Individual fluid structures were tracked on successive video images. The effects of precession on jet half angles, convection velocities and characteristic strain rates were measured and compared with those of steady jets.

In a separate experiment, glass beads with particle size distributions similar to that of pulverised coal, were visualised in non-reacting air jets at ambient temperature, using a planar laser technique. The effects of large-scale structures, generated by centrally located precessing air flows, on particle motion and preferential concentration of particles in an annular jet were measured. Only the region corresponding to the pre-combustion region of flames was investigated since combustion is known to dramatically alter particle motion.

The effects of enhanced large scale mixing and particle clustering on PF flames were measured in two refractory lined kilns operated at 130 kW and 2.5 MW, respectively. A scaling parameter, which relates the effects of the dominant mechanisms on flame ignition distance was developed, and used to estimate the influence of enhanced large scale mixing at full scale. The dominant mechanisms, by which enhanced large scale mixing and particle clustering influences combustion, were assessed using sensitivity analyses.

It was demonstrated that large-scale particle clustering results from the promotion of the large scales of turbulence. These changes are shown to have potential to provide a means to simultaneously control NO_x emissions, and improve heat release and stability of PF flames in rotary kiln applications.

Statement of Originality

This work contains no material which has been accepted for the award of any other degree or diploma in any university or other tertiary institution and, to the best of my knowledge and belief, contains no material previously published or written by another person, except where due reference has been made in the text.

Neil L. Smith

Permission to Copy

I give consent to this copy of my thesis, when deposited in the University Library, being available for loan and photocopying.

Neil L. Smith

Acknowledgement

My thanks go to Dr. Gus Nathan, for his guidance, support and meticulous supervision of this work, and to Prof. Dong-ke Zhang for his additional supervision and many considered suggestions. The following people have all assisted with my understanding of the thesis, and were generous with their time and expertise: Steven Hill, Emeritus Prof. R.E. Luxton, Dr. Greg Newbold, Dr. David Nobes, Dr. John Smart, Dr. Gerald Schneider and Jordan Parham.

The work owes much to Graham Perry, Graham Kelly, Ron Jager, Anthony Sherry, Craig Price, Silvio DeIeso and George Osborne who all contributed technically to the experiments or the development of them. I would also like to thank Dr. Nik Megalos who assisted in the experiments detailed in Chapter 5 and analysed solid samples, and prepared Figures 5.15-5.20, and Jordan Parham for his assistance with the techniques detailed in Chapter 3. Image processing was performed with help from Dr. Richard Kelso, Jordan Parham and Philip Cutler. Dr. Z Alwahabi assisted with the LDA measurements reported in Appendix 3.

My thanks also go to the staff of the University of Wales, Cardiff and in particular to Dr. Ben Evans and Dr. Wolfgang Fick, who assisted with the laser sheet visualisation work detailed in Chapter 4. The staff of the International Flame Research Foundation also contributed to this work, especially Dr. Paul Dacombe, who managed the campaign from which the results detailed in Chapter 6 were drawn, and Ad Verlan who helped develop the LSV technique used in Chapter 6.

The research was funded by the Australian Government, through an Australian Post-graduate Award (Industry) scholarship, in conjunction with Fuel and Combustion Technology Ltd. I would also like to thank Con Manias, Dr. Barrie Jenkins and Dr. Peter Mullinger for their provision of the furnace used for the experiments detailed in Chapter 5, and for their interest in the work, and the Departments of Mechanical and Chemical Engineering at the University of Adelaide for their support.

I have been fortunate to have been blessed with support, love and understanding from my wife Stacey throughout the course of this research.

Terminology

Primary fluid	The primary stream is the pulverised fuel transport air stream, usually co-annular with a mixing nozzle. When modelled in water no particles were used.
Secondary fluid	In combusting cases, this is the bulk of the combustion air.
Mixing fluid	The fluid stream provided through a nozzle or jets to create a mixing effect between the primary (and PF) and secondary streams.

Notation

Abbreviations and Constants

A	Constant in Equation 7-9
C	Constant in Spalding's eddy break-up model (Equation 7-8)
C_{pl}	Plank's constant $= 1.44 \times 10^{-2}$ (m.K)
FPJ	Fluidic precessing jet (nozzle)
g	Gravitational acceleration (ms^{-2})
k, K	constant of proportionality, rate constant
K	Saffman lift force coefficient = 6.46
LIF	Laser induced fluorescence
MPJ	Mechanical precessing jet (nozzle)
NBZ	Near burner zone
PF	pulverised fuel
PJ	Precessing Jet

Variable Quantities

A	Furnace surface area (m^2)
A	Frequency factor (s^{-1})
A_c	Cluster projected area (m^2)
A_p	Particle projected surface area (m^2)
a	Particle surface area = πd_p^2
c	Speed of sound (ms^{-1})
c	Fluid concentration
c	Particle number concentration ($number.m^{-3}$)
C	Particle mass concentration ($kg.m^{-3}$)
C_a	Concentration of species "a"
C_g	Cluster gas specific heat ($kJ.kg^{-1}.K^{-1}$)
C_p	Specific heat ($kJ.kg^{-1}.K^{-1}$)
C_v	Volume fraction of soot particles
d	Jet diameter (m)
d	MPJ nozzle diameter (m)
d	Mixing nozzle jet diameter (m)
d.a.f.	dry, ash free
d_{eq}	Equivalent nozzle diameter (m) – Equation 7-2
d_p	Particle diameter (m)
d_t	FPJ nozzle inlet (throat) diameter (m)
$\bar{d}$	Particle diameter for which $R = 100/e$. (m)

D	FPJ nozzle chamber internal diameter - The characteristic FPJ nozzle dimension (m)
D	Laminar diffusivity or diffusion coefficient (m^2s^{-1}),
$D_{A,1}$	Internal diameter of the annular PF stream (m)
$D_{A,2}$	External diameter of the annular PF stream (m)
D_2	Characteristic diameter of the secondary air channel (m)
D_q	Quarl throat diameter (m)
E	Activation energy ($kJ.gmol^{-1}$)
E	Ratio of entrained air to burner air, Equations 7-3, 7-4.
E_i	Emissive power at temperature, T_i (Wm^{-2})
E_τ	Eddy diffusivity
F	View factor
f	Frequency (Hz)
f_p	Frequency of precessional motion (Hz)
G	Axial momentum flux (N or $kg.m.s^{-2}$), typically calculated at the exit plane
G_{PJe}	FPJ axial momentum flux (N or $kg.m.s^{-2}$), estimated at the nozzle exit plane, using one-third of the cross-sectional area between the nozzle centre-body and internal wall, and assuming that the entire PJ flow is directed axially (see Equation 2-6)
G_{PJt}	FPJ axial momentum flux (N or $kg.m.s^{-2}$) at the nozzle inlet (throat)
h	Step height of the sudden expansion at the inlet to the FPJ chamber (m)
h	Convective heat transfer coefficent ($Wm^{-2}K^{-1}$)
k	Number of particles in given cell in the Poisson distribution
k	Ratio of specific heats = 1.4 for air
k	Kinetic energy
k_{gi}	Radiation absorption coefficient of gas species i
k_g	Gas thermal conductivity ($Wm^{-1}K^{-1}$)
k_p	Particle thermal conductivity ($Wm^{-1}K^{-1}$)
l	Characteristic large-scale structure length scale (m)
L	FPJ nozzle chamber length (m)
L	Duct radius (m) in Thring-Newby parameter, Equations 7-6 and 7-7
L_b	Mean radiation beam length (m)
L_c	Cluster radiation beam length ~ cluster diameter
L_q	Length of the quarl (m)
m_p	Particle mass (kg)
$\dot{m}$	Mass flow rate ($kg.s^{-1}$)
$\dot{m}'''_{fu}$	Mass rate of consumption of fuel, per unit time and volume ($kg.m^{-3}s^{-1}$)
N	Number of particles in a cluster
N_a	Molar flow rate of species "a" ($mol.s^{-1}$)
M_p	Single particle mass (kg)
M_g	Cluster gas mass (kg)
p_{gi}	Partial pressure of species i
p_k	Fraction of cells containing k particles in the Poisson distribution
Q	Rate of energy transfer (W)
Q	Volumetric flow rate (m^3s^{-1})
Q_c	Convective heating rate (W)
Qc_{cg}	Convective heat transfer - surface of cluster and surrounding gases (W)
Q_d	Heat of devolatilisation (W)
Q_p	Rate of heat release by solid particle combustion (W)
Q_{pg}	Rate of convective heat transfer - particles and gas within a cluster (W)
Qr_{cg}	Radiative transfer between the cluster gas and surrounding gases (W)
Qr_{wp}	Radiative transfer between the furnace walls and particles in the cluster (W)
Qr_{wg}	Radiative transfer between the furnace walls and cluster gas (W)
Qr_{fp}	Radiative transfer between the flame and particles in the cluster (W)
Qr_{ep}	Radiative transfer between the cluster particles and the entrained flow (W)

Q_v Rate of heat release by volatile matter combustion (W)
r Radial coordinate (m)
r' Devolatilisation kinetic rate (s^{-1})
$r_{1/2}$ Jet half width (m)
R Rosin-Rammler size distribution
R Ideal gas constant = 287 $J.kg^{-1}K^{-1}$
R Reaction rate in Chapter 7 only ($kg.m^{-3}s^{-1}$)
RR Reaction rate
S Structure celerity or convection velocity (ms^{-1})
S_c Cluster surface area (m^2)
S_L Laminar flame speed (ms^{-1})
$\overline{S_1 S_2}$ Effective total interchange area between grey bodies 1 and 2 (m^2)
t Time (s)
$t_{1/2}$ Half life of reaction (s)
t' Time fluctuation in Basset history force formulation (s)
T Temperature (K)
T_1 Temperature at "position 1"
u Fluid axial velocity (ms^{-1})
u^* Characteristic velocity of fine structures (ms^{-1})
U Characteristic nozzle fluid velocity (ms^{-1})
U_{rel} Oscillating slip velocity (ms^{-1})
v Fluid transverse velocity (ms^{-1})
V Volume (m^3)
V Transient volatile yield
V_o MPJ nozzle exit velocity (ms^{-1})
V_p Characteristic particle velocity (ms^{-1})
V^* Ultimate volatile yield
w z component of fluid velocity (ms^{-1})
W_k Mass fraction of ash in raw coal
W_x Mass fraction of ash in burnt coal
x Stream-wise (axial) coordinate
x_{ign} Ignition distance (m)
$x_{ign.q}$ Ignition distance downstream from the quarl exit plane (m)
x_{door} Apparent width of a furnace slot door on a video screen in Chapter 6 (m)
$x_{ign,s}$ Raw ignition distance measured on a video screen in Chapter 6 (m)
X Mole fraction
X_C Axial position of the core of external recirculation eddy (m)
X_N Axial position where all secondary air is entrained into an enclosed jet (m)
X_P Axial position where an enclosed jet meets the wall (m)
ΔX Flame tip fluctuation length (m)
y Cross-stream coordinate – in the image plane
y_p Mean particle spread in Chapter 4 (m)
Y_{vol} Volatile matter yield
$Y_{vol,ht}$ High temperature yield, ie. for $T_p > 1000$ °C.
z Cross-stream coordinate – out of the image plane

Greek

α Thermal diffusivity = $\dfrac{\lambda}{\rho C_p}$ (m^2s^{-1})

α Radiant absorptivity

α Fraction of coal converted to volatiles
χ Fraction of fine structures which may react
Δ Difference
ε Emissivity
ε Kinetic energy dissipation rate per unit mass (m^2s^{-3})
ε_c cluster emissivity = $(1- e^{-caLc/4})$
ϕ MPJ exit angle (Figure 1.4)
ϕ Mechanism factor (Equation 5-24)
γ Mass fraction of fluid in fine structures
λ Thermal conductivity ($Wm^{-1}K^{-1}$)
η Kolmogorov (length) micro-scale
μ Fluid viscosity ($kg.m^{-1}.s^{-1}$)
μ Mean number of particles per cell in the Poisson distribution
θ Thring-Newby parameter, Equations 7-6 and 7-7
$\theta_{1/2}$ Jet half angle (degrees)
ρ Density ($kg.m^{-3}$)
ρ_p Particle density
σ Standard deviation or r.m.s.
τ Time-scale (s)
τ Reactedness – in Equation 7-20
υ Fluid kinematic viscosity (m^2s^{-1})
ω Frequency of particle oscillation in Equation 5-31 (s^{-1})
ξ Scalar mixture fraction (concentration)
ξ Ratio of oscillating slip velocity to steady slip velocity

Non-dimensional Parameters

Bi Biot number
Da Damköhler number - ratio of mixing time to reaction time
Fr Froude number
Le Lewis number
M Mach number
Nu Nusselt number
Nu_t Time and space averaged Nusselt number due to fluid fluctuations
Pr Prandtl number
Re Reynolds number = ud/ν
Sc Schmidt number = ν /D
S Strouhal number of precession of the MPJ nozzle = $f_p d/u$
S_h Strouhal number of precession for the FPJ nozzle based on step height, h = $f_p h/u$
S_M Strouhal number of precession for the FPJ nozzle based on jet source momentum, = $f_p D^2 \sqrt{(\rho/G_{PJ,t})}$
St Stokes number
η Entrainment factor (in Equation 5-19)

Subscripts and Superscripts

1 primary fluid (including PF)
2 secondary fluid
1,2 numbering used variously for species, surfaces, reactions
a air or secondary air
c convection
c carbon dioxide

cl	cluster, cloud
e	entrained
eq	equivalent
f	flame, fluid
fu	fuel
g	gas
hc	convective heating
lam	laminar
m	maximum
max	maximum
min	minimum
MIX	Mixing fluid
i	i^{th} component (eg. of velocity)
ign	ignition
o	nozzle flow
o	original or datum value
p	particle
PJ	Precessing Jet
q	quarl
r	radiation
r	refractory
rel	relative
s	solid
s	secondary or entrained air
t	total
w	wall
w	water
x,y,z	geometric positions
~	phase-averaged component
′	fluctuating component
—	time mean value

Chapter 1. Introduction

1.1 Introduction

1.1.1 Objectives and scope

The combustion of coal provides the major source of energy for the industrialised world and its use will continue in the foreseeable future. However there is a growing awareness of the need to minimise adverse environmental impacts associated with its use. The motivation for the present study arises from the desire for a means to improve heat release profiles from pulverised fuel (PF) flames without compromising flame stability, while also reducing polluting emissions from industrial kilns. The objective of the present study is to measure and explain the extent of changes in PF flame properties that can be produced by manipulation of the structure of turbulence. A novel means for manipulation of large turbulent structures, which predominantly control the ignition and chemical reaction rates of PF flames, is used. The scope of the study is directed toward rotary kiln type flames since existing technologies, which have been developed for improving boiler flames, have only been partially successful when applied to rotary kilns. However the results of the present study are not limited to rotary kilns and may have wider applications, including in boilers, in the longer term.

Although large scale mixing is known to control the stability, heat release rate and NO_x emissions from a range of flames, there appear to have been no specific attempts to enhance the large-scale structure of turbulence as a means of improving PF flames. The present work details the results from combustion trials at both 130 kW and 2.5 MW scales, in which precessing air flows were used as a means of altering the structure of two phase turbulent jets. The results and supporting analysis reveal mechanisms for improved flame performance that can also be applied to full-scale industrial flames.

1.1.2 Thesis outline

Chapter 1 discusses issues that impact on the continued use of pulverised coal flames and the successes and limitations of current practices for flame stabilisation, control of NO_x emissions and heat release in industrial pulverised coal flames. The controlling role played by the largest scales of turbulent mixing is highlighted. Recent advances in understanding of the effects of large-scale structures on particle motion are reviewed and four hypotheses are presented, which postulate how the enhancement of large-scale turbulence can be used as a means of improving the current practice of PF combustion.

Chapter 2 details some of the issues related to the use of small-scale experimental data to predict full scale PF flame performance. A rationale is presented for the selection of the non-reacting and reacting experiments conducted in the current work. In Chapters 3 to 6 the four hypotheses are investigated experimentally. Each chapter (except Chapter 6) commences with a review of the physical and chemical processes that underlie the hypotheses investigated in that chapter. In each chapter, a description of the techniques and procedures used is given. This is followed by presentation and discussion of the experimental results, in the context of the hypotheses. In Chapter 7, the hypotheses are tested further by sensitivity analyses, which are used to clarify the dominant mechanisms by which flame properties are altered. Chapter 8 draws the conclusions of the study and provides suggestions for future work.

1.2 Issues pertaining to the continued use of pulverised fuel

1.2.1 Current usage of pulverised fuel and future outlook

In comparison to other fossil fuels, huge reserves of coal exist worldwide. The world's known reserves of coal are sufficient for 200 years at 1988 consumption rates, while undiscovered reserves are estimated to be sufficient for 1500 years compared to 60 years for oil and 120 years for natural gas (Fulkerston *et al.*, 1990). Pulverised fuels are used chiefly for power generation and in process industries. The availability and low cost of pulverised fuels together with practical, political and economic issues related to the use of nuclear and renewable energy and other fossil fuels mean that pulverised fuel firing will continue to be important in the industrial sector for the foreseeable future. Furthermore PF flames are often preferred to gas flames because of their higher emissivity, and hence heat transfer, and their ability to produce higher flame temperatures (Hottel and Sarofim, 1967).

Pulverised fuel combustion is the dominant technique used in utility boilers installed through the 1960's to 1980's. More recently, technologies such as circulating fluidised bed combustion (CFBC) and pressurised fluidised bed combustion (PFBC) have been developed for power plants to improve thermodynamic efficiency and reduce pollution from oxides of nitrogen and sulphur. Thus while the use of PF may reduce in the power generation sector, it is likely to expand in the process industries, where alternative means of providing heat are often impractical.

1.2.2 Pollutants

The role of NO_x pollution in the production of photochemical smog, acid rain and stratospheric ozone depletion is well known. Transportation and power generation account for most of the 10 million tonnes (as nitrogen equivalent) of annual global NO_x emissions (Bowman, 1992). Industry contributes only 15% of global NO_x emissions, but individual plants produce high local NO_x emissions, normally within the range of 500 – 3000 ppm (Mullinger and Jenkins, 1994), prompting increased efforts to reduce industrial NO_x emissions over the past decade. Technologies for NO_x reduction from power stations burning pulverised fuel are well established and include such techniques as air staging, fuel staging (reburn), flue gas recirculation and post combustion NO_x removal (eg. ammonia or urea injection). As a result NO_x emissions from boilers can be controlled to 200 ppm, much lower than the 500 – 3000 ppm from rotary kilns, where flame temperatures are higher and these techniques are generally not applicable. In a wide range of semi-industrial scale rotary kiln flames, NO_x emissions were shown to reduce with the quantity of air in the flame at the point of ignition (van de Kamp and Smart, 1992). However reductions in air entrainment rates generally correlate with a reduction in the mixing intensity and heat release rates (Mullinger, 1994a).

Changes in sea level, ocean and terrestrial eco-systems and impacts on agricultural practices are predicted to result from anthropogenic greenhouse gas emissions (Tegart *et al.*, 1990). These predictions are based on an observed increase in atmospheric CO_2 concentration from 280 at the start of the industrial revolution to its present value of 358 ppm (Bolin *et al.*, 1995). Combustion contributes an estimated 80% of anthropogenic sources of CO_2 (Bolin *et al.*, 1995). Improvements in the fuel efficiency of rotary kiln operation have a significant long term role to play in reducing CO_2 emissions. Although still relatively minor in percentage terms, the relative contributions of process industries towards pollutant generation is bound to rise as newer and alternative technologies are progressively introduced into the power and transport sectors. Any improvements that can be realised in specific fuel consumption have additional economic benefits for the industry.

1.2.3 Process operation

In addition to the control of pollutants, research in pulverised fuel utility boiler applications has been directed at improving flame stability, turn-down ratio, fuel efficiency and combustion intensity (energy release / combustor volume), and reduction in ash slagging (Smoot and Smith, 1985). In rotary kilns, the flame heat release profile is also required to match process requirements in order to maximise production and ensure product quality. For example, production rates of cement clinker are highest when the peak heat release occurs near the burner, a factor which also improves clinker quality by allowing rapid cooling on leaving the flame zone (Ono, 1980). Rotary kiln flame heat flux profiles are affected by both the nature of large-scale mixing and ignition distances (van de Kamp and Smart, 1992). Consequently, burners for rotary kilns are often designed with a number of separate air channels. The flow rate of air through each channel, in addition to the coal flow rate, can be varied to optimise the heat release profile for a given kiln, fuel and product combination (Nobis, 1991). Burners are also designed to provide airflow patterns that prevent flame impingement onto the clinker which causes reducing conditions and thus poorer product quality (Lowes and Evans, 1989).

1.2.4 Summary

Pulverised fuels are appropriate for rotary kiln applications and are likely to be used ever more heavily in this sector. There is a need for research to simultaneously improve heat release profiles (and hence fuel efficiency) and the reduction of NO_x emissions for long term sustainability of process industries.

1.3 Flame stabilisation

1.3.1 Physical and chemical requirements for flame stability

The most basic requirement of any burner is that it produces a stable flame. Stable flames are necessary to provide good utilisation and safety (ie. to prevent or reduce the frequency of flame-outs and the extent of damage and injury caused). Furthermore, as discussed above, a reduction in the ignition distance (between the burner and flame front) of rotary kiln flames (see Figure 1.1) improves heat flux. An effect of reduced ignition distance is an increase in local gas temperature close to the burner resulting in earlier char ignition and increased coal burnout (Wall, 1987). The stabilisation process can also be influential in NO_x formation (van de Kamp and Smart, 1992). For these reasons, more details on flame stabilisation are provided below.

Numerous investigations have shown that pulverised fuel flame stability relies on the following factors:

1) Heating of particles is required to liberate volatile matter, which provides a homogeneous volatile matter ignition source (Wolanski and Wojcicki, 1974).
2) Adequate mixing of fuel and air is required to provide a flammable mixture of volatile matter and oxidant (Beer and Chigier, 1969, Schefer *et al.*, 1994).
3) Sufficient residence time is required to allow devolatilisation to proceed. Flame stabilisation is enhanced by promoting the decay in the velocity of particles and volatile matter (Costa *et al.*, 1990a). Recent whole-field concentration and velocity studies of gas diffusion flames have found that stabilisation occurs in regions where the local velocity drops to the order of the laminar flame speed (Schefer and Goix, 1998, Muniz and Mungal, 1997). By analogy, regions of low velocity in the volatile matter – air mixture in a PF flame can be deduced to promote flame stability.
4) Liberation of sufficient heat of reaction to balance convective and radiant heat losses (Godoy *et al.*, 1986).

Large scale mixing has a dominant role in all of the above processes. Consequently, the flame stabilisation position depends heavily on the mixing characteristics of the burner.

1.3.2 Historical development of technologies used to provide flame stability

In the nineteenth century coal was coarsely crushed and combusted in open hearth and grate furnaces. A major advance was made by reducing the size of particles which allows the time-scales of the processes required for stabilisation, namely particle heating, devolatilisation and ignition, to be reduced dramatically, thereby increasing the heat generation rate and combustor capacity. The first industrial application of pulverised coal, introduced because of these benefits, was in a cement kiln in 1895 (Essenhigh, 1962). However the high combustion intensities possible with pulverised fuel required high air flow rates and transport velocities which introduced a flame stabilisation problem, summarised by Thring (1962) as, "*flame stabilisation is essentially a problem of overcoming high velocity*".

To provide increase the rate of decay in PF jet velocity, and to meet the other conditions necessary for stable combustion, burners were altered from single pipe to single annular arrangements. Some improvements due to greater entrainment were realised by this change (Essenhigh, 1962). Double concentric burners were then developed and were used in both cement kilns and boilers. In double concentric flows, when the momentum of the outer stream dominates over the inner, an internal recirculation zone (IRZ) is produced. If coal is introduced with the central air, and if the particles are fine enough, the stability of the flame can be improved due to the increased residence time of particles influenced by the IRZ (Beer, 1964).

A great step forward in the development of highly stable PF flames, for example in wall-fired boiler designs, came with the introduction of swirl to the outer air stream, which can be used to produce a dominant internal recirculation zone. Beer and Chigier (1969) showed that the IRZ promotes rapid devolatilisation, and a rapid rise in flame temperature with axial distance downstream from the burner, even for low volatile pulverised coal flames. The rapid devolatilisation and improved stability of swirled PF flames allows greater combustion intensity and improved coal burnout relative to unswirled flames. Beer and Chigier (1969) also showed that high velocity impinging jets of secondary air (which was pre-heated to 500°C) reduced ignition distances compared to a double concentric burner. The design strategy of pulverised coal burners to promote stability has, since these developments, been based on the generation and control of "zones" with characteristic time-averaged mixing conditions. Examples are internal recirculation zones produced by swirl or bluff body effects, regions of high entrainment into a jet and external recirculation zones.

While the significance of a recirculation zone in promoting flame stability was recognised early, the mechanisms by which it enhances stability have been less clear. Claypole and Syred, 1982) demonstrated that the increased rates of mixing, or turbulence levels, associated with the swirl, in these "zones", is at least as important as the recirculation of combustion products in the stabilisation of gas flames. A similar result has been found in pulverised coal flames (Weber *et al.*, 1992b). The significance of rapid mixing (together with fuel - air mixture fraction) for stabilisation, was recognised as early as 1922 by deGrey (cited in Essenhigh, 1962) even in non-swirled flames. This finding influenced burner designers to seek to achieve high rates of initial mixing of secondary air with the primary stream with a view to maximise "turbulent flame speed" close to the burner exit. Aerodynamic stabilisation, achieved through rapid mixing, is used in modern furnaces in which re-radiation from water tube walls is very low and contributes little to particle heating (Beer, 1962). High secondary air pre-heat temperatures are also used to aid stabilisation. However rapid mixing can also promote high NO_x emissions, an issue that was not a relevant consideration during most of the historical development of burners, but is important now.

More recent laboratory studies have confirmed the effectiveness of the creation of "zones" with high characteristic time-averaged mixing rates as a means of flame stabilisation in model PF boiler flames. Wolanski and Wojcicki (1974) demonstrated the effectiveness of an IRZ produced by bluff body effects. Smart and Weber (1989), Abbas *et al.* (1993a) and Truelove and Holcombe (1990) have shown that stabilisation can be achieved by introducing all of the secondary air through the burner quarl to produce an internal recirculation zone. In these flames, stability depends on both the level of swirl used and the particle trajectories – sufficient particles must enter the IRZ where volatiles can be liberated and combusted.

1.3.3 Stabilisation in rotary kilns

In boilers, the high momentum secondary air stream can be swirled where it enters the furnace, subsequently passing through a large expansion into the furnace chamber. In rotary kilns the secondary air is introduced through the entire kiln cross-section, at a lower momentum than in boilers, and as such is not conducive to the application of swirl (Figure 1.2). Consequently, an internal recirculation zone is difficult to achieve in rotary kilns. The difficulty is exacerbated by the high confinement. As a result, stabilisation is traditionally achieved by entrainment of hot secondary air and externally recirculated gases. A smaller contribution to particle heating is provided by radiation from the clinker, the kiln walls and the flame (Lowes and Evans, 1989).

"Direct fired" rotary kiln flames, in which the PF is transported directly from the pulverising mill, rely on the high momentum of the fuel transport stream to ensure "good" mixing between the fuel and secondary air. Such systems utilise 15 - 45% of the total air as transport air at velocities up to 60 m/s (Nobis, 1991). In contrast, "indirect fired" kilns decouple the transport air supply from the mill so that the transport air flow-rate can be reduced to typically 3 – 10% of the total air flow-rate, at a velocity of approximately 20 ms^{-1} as it exits the burner. These "indirect" fired kilns generally use multi-channel burners in which a separate mixing air stream, supplied from a fan, is used to ensure "good" mixing (Lowes and Evans, 1989). Nobis (1991) classifies three generations of commercially available rotary kiln pulverised coal burners, as follows:

1) **Annular mono-channel burners** in direct fired kilns. The disadvantages associated with using large quantities of non-preheated transport air, aside from the thermodynamic penalties, are listed by Nobis (1991) as poor stability during start-up, poor turndown ratio, lack of flame shaping capability and high NO_x emissions.

2) **Multi-channel burners** in indirect fired kilns, produce stable flames with lower primary air rates than annular mono-channel burners. Typically 5% of the total air is used to transport the coal and another 5 % is used as high velocity swirled and/or axial air injected through separate burner channels. Shorter, more divergent flames with good stability are produced, although the air flows must be adjusted for flame shaping which can also limit NO_x control benefits (Nobis, 1991).

3) **Low divergence multi-channel burners** in indirect fired kilns; differ from standard multi-channel burners in that they produce "more dense", less divergent flames. Reduced flame spread may be useful in preventing flame impingement on the walls. Flame divergence is reduced by either eliminating swirl and instead using natural gas or bluff body techniques for stabilisation, or by using a non-diverging swirling air stream (Nobis, 1991).

The International Flame Research Foundation, IFRF, compared 2 MW flames from scaled down commercial multi-channel burners in the "Cemflame 1" trials (van de Kamp and Smart, 1992). These flames were compared with those from a generic multi-channel burner and a number of mono-channel burners. The multi-channel burner flames that incorporated either swirl or high momentum axial jets demonstrated improved stability (reduced ignition distance) compared to mono-channel burners due to creation of "zones" with increased mixing rates near the burner. However the existence of internal recirculation zones in the multi-channel flames was not confirmed.

1.3.4 Summary

Mixing can be manipulated to improve flame stability. The use of swirled air to improve flame stability is not as effective in rotary kilns as in boilers since only a small fraction of the air is swirled. Improvements in stabilisation, which rely on high mixing rates, have often been achieved at the expense of increases in NO_x emissions. The next section deals with some of the means currently used to minimise NO_x emissions without compromising stabilisation, and how they relate to rotary kilns.

1.4 Nitrogen oxides

1.4.1 A review of fundamental research on NO_X formation in PF flames

Nitrogen oxides are predominantly formed by thermal and fuel routes. Thermal NO_X is formed by the oxidation of atmospheric nitrogen by reactions which can be simplified to the scheme formulated by Zeldovich (Glassman, 1987).

$$O + N_2 \leftrightarrows NO + N \qquad 1 - 1$$

$$N + O_2 \leftrightarrows NO + H \qquad 1 - 2$$

The rate limiting step in the Zeldovich reaction scheme is controlled by temperature, with a weaker dependence on oxygen concentration and residence time. As a result, thermal NO_X formation rates increase dramatically with temperature, and less significantly with increases in oxygen concentration (Westenberg, 1971).

"Prompt" NO_x, assumed to result from the reaction of hydrocarbon radicals with nitrogen (Fenimore, 1971), is considered to contribute only 5% of the total NO_X in most practical high temperature diffusion flames (van de Kamp and Smart, 1992), and so are of minor importance for primary control strategies.

Fuel NO_x is formed by the reaction of fuel bound nitrogen with atmospheric oxygen. In PF fired boiler applications the fuel route is traditionally the major source of NO_x emissions. Nitrogen is bound in coal in a number of different forms, which release N to form NO_x precursors at different temperatures. However, it appears that the total quantity of NO_x precursors formed does not depend on coal type or nitrogen content (Nelson, *et al.*, 1992). Up to 80 % of fuel nitrogen is liberated with the volatiles (Blair *et al.*, 1977) and, of this, over 60 % is converted to NO_x if the oxygen availability is high in the region of volatile matter evolution. In contrast, only 13 % of the nitrogen remaining in the char is converted to NO_x under the same conditions (Pershing and Wendt, 1977). Consequently volatile NO_x emissions are far more significant than char NO_x emissions and are the focus of NO_x reduction techniques such as staging used in boilers. However, in the cement industry, thermal NO_x is typically of greater significance due to the higher temperatures and control of NO_x emissions is more difficult (van de Kamp and Smart, 1992).

1.4.2 Existing NO_x reduction strategies

Control of fuel NO_x is usually achieved by creating zones of characteristic fuel rich chemistry into which coal is injected. Combustion staging involves limiting the availability of oxygen in the early stages of the flame where volatiles are liberated. Factors which can result in high fuel NO_x emissions under un-staged conditions include high mixing rates, small particle size and high temperatures. However, under fuel rich conditions, these factors result in reduced NO_x emissions due to the increased rates of volatile matter evolution and subsequent NO_x destruction (Glass and Wendt, 1983). The gas phase NO_x destruction reactions are far more rapid than those of char or soot particles (Bose *et al.*, 1988). This fact allows gas phase staging to be carried out within "zones" of characteristic time-averaged mixing conditions and stoichiometry, within the practical space constraints imposed by the combustor geometry. The optimal stoichiometric fraction in the first stage of combustion for maximum NO_x destruction is 0.6 to 0.7, which, if applied can reduce NO_x emissions from approximately 1000 ppm in un-staged boiler flames to less than 200 ppm (Glass and Wendt, 1983).

Air staging in power station boilers can be achieved by segregation of the air into separate streams to create a "primary" stage where volatiles are liberated in a fuel rich environment followed by a "secondary" stage where combustion is completed. The air for the second stage can be introduced through ports, separate from the burner. More recently, aerodynamic air staging has been developed, in which all the secondary air is introduced through the burner (Smart and Weber, 1989) and (Abbas *et al.*, 1993a). The injection of particles is controlled so that heating and volatile release occurs in the fuel rich IRZ. Chen and Niksa (1992) have shown that, as fuel volatility decreases, lower percentages of fuel nitrogen are released in the IRZ, so reducing the effectiveness of staging for low volatile fuels.

The reduction in NO_x emissions, which has been achieved in boilers, has not been observed in rotary kilns for a number of reasons. Firstly the advances in boiler staging techniques are difficult to apply to rotary kilns. In addition staging techniques are only partially effective in controlling NO_x emissions in rotary cement kilns since the thermal route to NO_x production is usually dominant due to the higher temperatures. Thermal NO_x can also be controlled by flue gas recirculation in boiler applications, which reduces the peak flame temperature (Offen *et al.*, 1987). However, the duct work required for flue gas recirculation would be costly in rotary kilns and its effectiveness would be reduced due to sealing problems. Any reduction in flame temperature would also down-rate the kiln capacity. Dust losses from the

kiln would also increase due to higher exit velocities since the mass flow of kiln gases would increase.

Multi-channel rotary cement kiln burner designs attempt to achieve staging by the use of swirled air (eg. Bauer, 1990 and Rosenmann and Kunne, 1990), but with less effect than in boilers, since only a small fraction of the combustion air can be swirled and there is no quarl to assist in the formation of an adverse pressure gradient (Figure 1.2). Consequently, NO_x emission reduction in cement kilns is normally achieved by reducing the mixing intensity as a means of reducing temperatures, which as noted earlier, carries with it the cost of reduced heat transfer and reduced combustion efficiency (Mullinger, 1994a). Research into NO_x reduction from cement kilns lags far behind that in the transportation and power industries.

In the IFRF Cemflame 1 research program (van de Kamp and Smart, 1992), high NO_x levels were found to occur when high burner axial momentum is used, causing increased quantities of oxygen to be entrained into the flame before ignition. Other findings of Cemflame 1 (van de Kamp and Smart, 1992) can be summarised as follows:

- Increasing the tangential momentum of the swirl air also increases oxygen levels at ignition, resulting in higher NO_x emissions, unless some of the coal is entrained into the centre of the flame where oxygen concentration is lower.
- Injection of the pulverised fuel from the inside of the swirl air channel aids the entrainment of particles into the centre of the flame, thereby reducing NO_x emissions. By contrast, NO_x levels are high if high momentum air jets are used to increase the entrainment of combustion air and the mixing rates with coal.
- There is a strong relationship between fuel type and NO_x emissions. High volatile fuel ignites rapidly, at a point where relatively low quantities of oxygen are mixed into the flame, resulting in lower NO_x. In contrast, petroleum coke was found to ignite much later, in a higher oxygen environment, resulting in higher NO_x emissions.

The IFRF work shows that the formation of "zones" of low oxygen concentration, be they in the centre of the flame or by promotion of early ignition, can produce some reductions in NO_x emissions via both fuel and thermal routes. However, due to the geometry of rotary kilns and the low quantities of swirl air used, aerodynamic means of providing fuel rich stabilisation and control of thermal and fuel NO_x emissions remains more difficult to achieve than in boilers. The IFRF tests also showed that none of the kiln burners tested optimised both heat transfer and NO_x together under the same operating conditions. Low NO_x flames

from multi-channel burners also tend to produce poorer burnout than do flames with higher levels of oxygen entrained into the flame at the point of ignition.

1.4.3 Summary: Some shortcomings of existing rotary kiln burner technologies

In boilers, the staging of the combustion process to reduce fuel NO_x emissions can also "delay" complete mixing and so reduce the combustion intensity and fuel efficiency. Flue gas recirculation can be used in boilers to reduce thermal NO_x emissions but it also reduces combustion intensity and fuel efficiency. In rotary kilns the use of staging is only partially successful in reducing fuel NO_x emissions, whilst thermal NO_x emissions, which are more significant, remain high. Furthermore, the use of flue gas recirculation is inappropriate in kilns. The requirement for early heat release is not conducive to minimisation of NO_x formation when using existing burners. Hence there is a significant need for an alternative technology for NO_x reduction in kilns.

1.5 The impact of large scale turbulence on PF flames

1.5.1 Large scale turbulent structures

It has been demonstrated above that flame stability, heat release profiles and the quantity of fuel- NO_x and thermal-NO_x emissions are greatly influenced by the nature of the mixing of fuel with air. It has also been widely demonstrated (as detailed below) that the large-scale fluid structures in a turbulent shear flow dramatically influence the local particle concentrations (eg Longmire and Eaton, 1992). However, manipulation of the mixing in PF flames through the management of these structures does not yet appear to have been attempted.

Winnant and Brownand (1974) identified organised, coherent large-scale structures in two dimensional plane single phase mixing layers. Formation of structures was attributed to repeated pairing of the vortices. Brown and Roshko (1974) showed that the coherent structures dominate mixing and entrainment by "entanglement" of fluids at the scale of the large structures as they make "incursions" into each other. Hussain (1986) defined a "coherent" structure as a connected turbulent fluid mass which possesses phase correlated vorticity. Robinson (1991) broadened the definition of coherent structures, suggesting that they occupy regions in which only one flow property need show significant correlation with itself or another parameter. The latter definition is implied in the present study, reference being made to techniques in which significant correlation of fluid concentrations are used to determine the extent of coherent structures (Chapter 2).

Large-scale structures have been found to dominate the mixing in jet flows (Crow and Champagne, 1971). The large structures are embedded within local turbulent flow instabilities and scale with the jet diameter and distance from the nozzle. Non-vortical fluid is engulfed by the large vortical structures and is sheared into thin layers so that the fluids are not intimately mixed initially (Hussain, 1986). Consequently, jets contain regions with high concentrations of nozzle fluid and other regions of predominantly entrained fluid. Subsequent diffusion occurs both in the finer scales of turbulence, principally in the "braids" between the large structures, and by molecular diffusion (Dahm and Dimotakis, 1987). The dominance of large-scale structures in the mixing process has also been shown in gas jet flames. Subbarao and Cantwell (1992) demonstrated that, although fine scale turbulence increases with Reynolds number in gas jet flames, it is superimposed on the prevailing large-scale structure.

Single point measurement techniques have allowed great advancement in classical statistical analyses of turbulence, but has often concealed the significance of large-scale turbulent structures in flames. Whole field imaging of velocity and/or concentration has allowed the influence of turbulent structure to be more effectively assessed (Muniz and Mungal, 1997). These methods have allowed greater understanding of gas jet flame stabilisation and have also allowed the influence of large structures on particle motion to be assessed, as will be discussed in the next section.

1.5.2 Effects of large turbulent structures on particle motions.

Measurements of particle dispersion, concentration and velocity in flows have been dominated by statistical approaches, (Wall *et al.*, 1982). In swirl stabilised flames coal particle motion has been characterised by mean trajectories from laser Doppler velocimetry measurements (Schnell *et al.*, 1993), in relation to the position of "zones" of characteristic time-averaged mixing conditions. Likewise the effects of turbulence on heat transfer to particles has been measured as a function of statistical measures of turbulence intensity. Bellan and Harstad (1988) modelled spray evaporation and combustion and showed that turbulence causes increased droplet evaporation rates. Hanby (1967) found an increase of over 100% in the convective heat transfer coefficient between gas and coal particles due to gaseous oscillations and the resultant oscillating slip velocity produced in a pulsating combustor. However none of these approaches offers any understanding of the effects of individual turbulent structures on particles in PF flames.

Preferential concentration of particles by large scale turbulent structures has been investigated in non-reacting free shear layers. A greater rate of dispersion of particles than of the fluid in the shear layer itself has been attributed to the action of the large vortices. Particles have been observed to be flung outwards from the centre of vortices by centrifugal forces (Crowe *et al.*, 1985). Likewise, Lazaro and Lasheras (1992) showed that water droplets with a typical diameter of 20 μm, when introduced into one side of a laboratory scale (acoustically excited) plane mixing layer are concentrated in the braid regions between the large structures and are dispersed away from vortex cores.

Crowe *et al.* (1985) showed that particle dispersion is controlled by the Stokes number, $St = \frac{\tau_p}{\tau_f}$. Here, the particle time-scale, $\tau_p = \frac{\rho_p d_p^{\,2}}{18\mu}$ is defined as the ratio of particle inertia to fluid drag, by assuming that the particle is a sphere, the particle density is much greater than the fluid density, and that creeping flow (Re_p <1) prevails. The fluid time-scale, $\tau_f = \frac{L_f}{U_f}$, is the ratio of fluid structure length and velocity scales. The characterisation of structure length and velocity scales will be addressed in Chapter 3. Although the definition of *St* assumes creeping flow, its application has been widely and successfully used to classify particle response to turbulence in flows outside the creeping flow regime. Small particles (*St* <<1) are found to concentrate within structures, intermediate sized particles (*St* ~ 1) are

found to concentrate in the braid regions between structures where vorticity is low and strain is high, whilst large particles (St >>1) are unaffected by the flow structures (Eaton and Fessler, 1994). Consideration of forces on particles other than drag and inertia is presented in Chapter 3.

Longmire and Eaton (1992) have also demonstrated preferential concentration of particles in a non-reacting, acoustically forced round jet. Their study confirmed particle clustering in the regions of high strain "braids" between the large-scale structures and the general trends with St described in the previous paragraph. Droplet clusters in an experimental, simple jet, oil flame have been observed, and their size and concentration measured, leading to the conclusion that clusters of larger sizes burn as a group from the outside inwards (Wark, *et al.*, 2000). Extrapolation of these concepts to PF flames suggests that it should be possible to generate conditions which favour particle clustering, at least in the pre-ignition and ignition regions of a flame, upstream from the effects of combustion on particle motion. Promotion of such clusters can be expected to alter the instantaneous reaction environment by producing local fuel rich conditions within the clusters. This in turn suggests the possibility of influencing flame stability and emissions through the control of particle clustering effects, which occur to some extent in all two-phase shear flows, rather than through the creation of zones of time-averaged characteristic stoichiometry.

1.5.3 Turbulence scales

As already outlined, it is predominantly the largest scales of turbulence which are responsible for particle clustering effects due to their large time-scales. The present study seeks to enhance clustering effects by increasing the energy associated with the larger scales of turbulence at the expense of that associated with the smaller scales, to determine whether heat release and stability can be improved and NO_x emissions reduced in PF flames. In order to proceed, some of the statistical measures of turbulence, and their application to the measurement of the influence of turbulence scales on combustion are reviewed.

Tennekes (1968) proposed a model to describe the structure of turbulence and energy transfer from large scales to smaller scales. It was suggested that large eddies stretch smaller scale eddies and transfer mass and energy in the process. Viscous dissipation occurs down to the smallest structures, the Kolmogorov micro-scale η, beyond which only molecular diffusion can occur. Hence the Kolmogorov scale determines reaction rates. Physically, the small scales of turbulence can be observed as wrinkles on the boundaries of large structures (Ballal and Lefebvre, 1975).

The motion of a fluid volume element can be expressed in vector form (Foust *et al.*, 1980, pg 218) as a function of shear stress, pressure and gravity forces, ie.

$$-\rho\frac{Dv}{Dt}=\nabla\cdot\tau+\nabla P-\rho g \qquad 1\text{-}3$$

In diffusion flames pressure and gravity forces are generally insignificant and can be ignored. The shear stress term is dominated by turbulent eddy, or Reynolds stresses, (expressed here as a mean value assuming that the x, y and z component velocity fluctuations, u', v' and w', are of equal magnitude),

$$\tau_{turb}=-\rho\overline{u'^2}. \qquad 1\text{-}4$$

The Reynolds stresses are commonly estimated by the use of the Prandtl eddy mixing length, by analogy to the mean free path of gas molecules (Foust *et al.*, 1980). The eddies are assumed to maintain their form over a transverse distance l, gaining axial (x component) velocity from the surrounding fluid, equal to the velocity fluctuation u' (Tennekes and Lumley, 1972). As such, the axial velocity gain is,

$$u'=l\frac{du}{dy}. \qquad 1\text{-}5$$

Thus if u' and v' are of similar magnitude, the eddy stress is given by,

$$\tau_{turb} = -\rho l^2 (du/dy)^2 . \qquad 1\text{-}6$$

The eddy diffusivity, E_τ, is defined by Boussinesq by analogy to kinematic viscosity (Foust *et al.*, 1980), as a function of shear stress,

$$\tau_{turb} = -\rho E_\tau \frac{du}{dy}, \qquad 1\text{-}7$$

and hence by comparison with 1-5,

$$E_\tau = u' l . \qquad 1\text{-}8$$

Despite the simplicity of the Prandtl analogy, and the difficulty in defining and estimating a meaningful length scale, the eddy diffusivity concept is commonly used in turbulence modelling.

The largest diffusive length scale, which transfers momentum in a transverse direction to the bulk flow and so is responsible for entrainment and jet spreading, can be assumed equal to the scale of the largest eddies, l (Tennekes and Lumley, 1972). This length scale is effectively the same as the Prandtl mixing length. Diffusive time-scales are thus typically designated, l/u', on a statistical basis. The dissipation rate per unit mass, ε, is set by the kinetic energy transferred from the large structures, u'^2, and the time-scale of the large structures. Hence, Taylor's approximation for the mean energy dissipation rate, ε, (Tennekes and Lumley, 1972),

$$\varepsilon \sim u'^3 / l . \qquad 1\text{-}9$$

The Kolmogorov length scale is defined in terms of ε, and the kinematic viscosity, υ, and can be estimated from the local Re and large-scale length scale, Monin and Yaglom (1975).

$$\eta = (\varepsilon/\upsilon^3)^{-0.25} \approx \mathrm{Re}^{-0.75} l_x \qquad 1\text{-}10$$

The Kolmogrov time and velocity scales are given by Tennekes and Lumley (1972):

$$\tau_K = (\upsilon/\varepsilon)^{0.5} \qquad 1\text{-}11$$

and,

$$v_K = (\upsilon\varepsilon)^{0.25} . \qquad 1\text{-}12$$

Ballal and Lefebvre (1974 and 1975) investigated the influence of turbulence intensity and scale on transverse turbulent propagation velocity of premixed propane/air flames. From hot wire measurements, they calculated an integral length scale, L, the mean rate of dissipation, ε, and the Kolmogorov velocity and length scales. The key finding was that an increase in interfacial surface area between fuel and air eddies increased the mixing rate and so the

turbulent flame speed, although the mechanism varied depending on the strength of turbulence. In strong turbulence, $u' > 90$ cms^{-1}, the Kolmogorov length scale was smaller than the laminar flame thickness, so that a reduction in the Kolmogorov length scale increased the flame speed by increasing the surface area of eddies within the flame region. In weak turbulence, $u' < 90$ cms^{-1}, eddies were larger than the laminar flame thickness and an increase in Kolmogorov scale caused an increased wrinkling of the flame surface, and increased flame speed. These results demonstrate that statistical descriptions such as dissipation rates, without an accompanying understanding of fluid structure, can not fully describe combustion phenomenon.

1.5.4 Influence of the scale of turbulence on PF combustion

The mixing rate of large-scale turbulent structures limits the rate of many of the other processes occurring in PF flames. Some indicative time-scales for particle heating and reactions in PF flames are:

1) heating time for volatile matter evolution ~ 4 ms for a 50 μm particle (Wall, 1987),
2) volatile matter reaction to CO – a few ms (Smart, 1992),
3) thermal NO_x formation ~ 1 second at 2000K (Smart, 1992),
4) fuel NO_x formation, ~ 2 ms at 1600K (Smart, 1992).

In comparison, the convective macro-mixing time-scale in a typical industrial mono-channel flame with convection velocity of 5 ms^{-1} and structure diameter of 200 mm, is 40 ms. Hence, for such a structure, the large scale mixing process limits the stabilisation, fuel NO_x formation and heat release processes. Large scale mixing also has an indirect effect on thermal NO_x formation, although not obvious from the comparison of time-scales, by influencing local temperatures and oxygen concentrations. Although the large-scale structures greatly influence the major flame processes, no research specifically directed at controlling these structures in rotary kiln flames has been attempted. The objective of the current research is to attempt to advance burner design techniques by assessing the role of large scale mixing and its control in burners designed primarily for rotary kilns.

1.5.5 Summary

Statistical descriptions of turbulence do not provide a full description of individual large scale structures and their influence on particle motion, but can be used to estimate the effects. Particles with intermediate Stokes numbers (St ~1) are preferentially concentrated between large scale turbulent structures, whilst those with St <<1 conform to the fluid structures. Large scale mixing also limits the rates of most of the reactions involved in flame stabilisation and NO_x formation, suggesting that management of large scale turbulence may provide a tool for NO_x control. The effects of enhancing the large scales of turbulence on local particle clustering and PF flame performance will be investigated in the present work.

1.6 Means of varying turbulent structure in annular jet flows

The transport channel used in most multi-channel burners is annular. Consequently a means of increasing the scale of structures in annular jets and the energy contained in them, relative to that contained in the small structures, is required. Free annular jets exhibit similar characteristics to round turbulent jets, which demonstrate a linear growth in jet diameter (and hence structure size), with axial distance, x, downstream from the nozzle (Abramovich, 1963). Brown and Roshko (1974) showed that spreading rates of the 2-D mixing layer are closely related to the scale of the largest structures in the flow. The same is true for round jets. Round jet spreading half angles are approximately 6^{o} (Becker *et al.*, 1967), providing a baseline for assessing growth rate of large structures.

A number of techniques have been described in the literature to alter the mixing characteristics of simple and annular jets. Co-axial gas phase jets have been studied largely because they produce less noise than simple jets due to altered near field vortex dynamics. Co-axial jets also demonstrate a range of structural characteristics depending on their absolute velocity and the velocity ratio between the co-axial streams (Dahm *et al.*, 1992). If the velocity of the inner stream is sufficiently high, small structures that dominate the outer stream are produced. Such a combined jet has smaller structures than the outer stream alone would produce. If the velocity of the outer stream is increased above that of the inner, vortices produced at the shear layer between the inner and outer streams adopt opposite spin and lock together breaking up the inner potential core and producing structures approximately of the scale of the outer stream (Dahm *et al.*, 1992). If the velocity ratio of the outer to inner stream is increased beyond 5, the outer stream can truncate the inner potential core and produce an unsteady low frequency recirculating bubble. However the scale of structures produced is not significantly altered from that of the outer annular stream alone (Rehab *et al.*, 1997).

Another means of stimulating large-scale turbulent structure in turbulent flows, which could be applied to annular flows, is by periodic boundary layer shedding from bluff bodies. Examples researched include the torus (Leweke and Provansal, 1995), discs and spheres (Achenbach, 1974, Berger *et al.*, 1990). However, the scale of the periodic structures is comparable with the diameter of the bluff body, and does not provide a dramatic increase in size for realistic burner designs. In addition, bluff bodies are subjected to both very high erosion and temperatures in PF applications. Another possible means of stimulating large-scale turbulent structure is the use of non-standard nozzle outlets which introduce three

dimensional perturbations into the near field jet vortex rings. Longmire *et al.* (1992) investigated jets emanating from elliptical and triangular nozzles, nozzles with tabs, and crown shaped nozzles. All these nozzles produce changes in three dimensional structure of turbulence, but do not dramatically alter the scale of the largest turbulent structures.

Acoustic excitation has also been used to control large structures. Longmire and Eaton (1994) added energy to a simple jet using a loud speaker at frequencies that stabilised the vortex ring structures of the jet. This enlarged the vortex cores and allowed them to persist further downstream than in a simple jet, where pairing occurs rapidly. Effects on particle motion were also measured. Despite the effectiveness of the technique for research, problems with reliability could be expected in the harsh and abrasive environment of an industrial pulverised fuel combustion system. An alternative to acoustic excitation of jets, which does not suffer from the same practical problems, is precessing jets, to which the next section in devoted.

1.7 Precessing jets

1.7.1 The Phenomenon of Precession produced by a Stationary Nozzle

A means of creating a precessing jet of fluid from an axi-symmetric nozzle which has no moving parts, utilising a naturally occurring flow instability was first described by Nathan (1988) and patented by Luxton *et al.* (1988). The nozzle, which generates a single jet that rotates about the geometric axis of the nozzle in such a manner that the jet axis sweeps out a cone, has been termed a precessing jet nozzle (Nathan, *et al.*, 1998). The flow generated when the precessing jet breaks down has been shown to increase the energy contained in large structures at the expense of that contained in the small structures. A summary of the mechanism by which precession is generated (Luxton, 1993) is provided below, and is illustrated in Fig. 1.3.

The Fluidic Precessing Jet (FPJ) nozzle consists of an inlet throat of diameter, d_t, expanding to an axi-symmetric chamber with diameter, D, terminating in an outlet orifice (lip). When used as a burner, combustion occurs outside of this chamber. After passing through the sudden expansion, small variations in local entrainment within the entering jet produces a fluctuating pressure which is amplified by the chamber to produce an asymmetric pressure field. A positive feedback effect causes the jet to reattach asymmetrically to the inside of the nozzle. Asymmetries in azimuthal entrainment produce a rotating pressure field that causes the position of reattachment of the jet within the chamber to precess (Nathan, *et al.*, 1998). Precession of the jet exiting the throat occurs optimally when the geometric ratios conform to those used in commercial gas burners (Nathan, *et al.,* 1998, Hill, 2000), and when the throat Re > 20,000. The flow can intermittently fall into an "axial" non-precessing, mode in which fluid passes directly through the nozzle. The inclusion of the centre-body shown in Figure 1.3 minimises the occurrence of this mode (Nathan, *et al.,* 1998, Hill, 2000).

1.7.2 The exiting precessing jet

The jet that emerges from the nozzle chamber does so asymmetrically, so that it is instantaneously directed at 45 – 60° to the nozzle axis (Figure 1.3). The emerging jet precesses (or gyrates) about the nozzle axis at a frequency characterised by the Strouhal number of precession, S_p (Nathan, *et al.*, 1998), based on the velocity at the inlet to the chamber, U_t and the step height, $h = \frac{(D - d_t)}{2}$ ie,

$$S_p = \frac{f_p h}{U_t} = 5x10^{-3} \qquad 1\text{-}13$$

A more recent characterisation, has proven to apply to a wider range of expansion ratios (Hill *et al.*, 1995, Nathan, *et al.*, 1998). In this case the Strouhal number is based on the momentum flux at the inlet to the expansion, G_{PJt} and the chamber diameter, D, ie.,

$$S_M = \frac{f_p D^2}{\sqrt{G_{PJt}/\rho}} \approx 0.08 \qquad 1\text{-}14$$

In FPJ flows at axial locations downstream from the nozzle exit plane, $\frac{x}{D} \geq 2$, the dominant turbulent structures are many times larger than the nozzle chamber diameter. The mean flow spreads rapidly and the mean axial velocity has been estimated to decay by two orders of magnitude relative to that at the inlet to the nozzle (Newbold *et al.*, 1995). An experiment using the shroud technique of Ricou and Spalding (1961) showed increased entrainment by a factor of seven in the region $0 \leq \frac{x}{D} \leq 5$ (Nathan and Luxton, 1991).

The mixing characteristics of FPJ flows in the region immediately downstream from the nozzle, $\frac{x}{D} \leq 2$, are difficult to visualise and more difficult to quantify. A mechanical analogue of the precessing jet, the Mechanical Precessing Jet (MPJ), has been used to provide greater understanding of the fluid mechanics of precession (Schneider *et al.*, 1993, 1997, Schneider, 1996, Nobes, 1998). The MPJ nozzle and its flow field are depicted in Fig 1.4. in which the jet is shown to exit from the centre-line of the nozzle at 45° to the nozzle axis. The nozzle is rotated mechanically to generate a precessing jet. The use of the MPJ has allowed phase averaged visualisation, concentration and turbulence data to be obtained, by sampling data with reference to the phase of the precession cycle (Nobes, 1998, Schneider *et al.*, 1993, 1997, Schneider, 1996).

Nobes (1998) found that for an MPJ with Strouhal number, $S_p = \frac{f_p d}{V_o} = 0.005$, where d and V_o are the jet exit diameter and velocity respectively, the phase averaged trajectory of the emerging jet forms a helix which persists for 2π radians, covering an axial distance, $\frac{x}{d} \leq 7 \pm 2$. In the centre of this helical region a small central reverse flow zone (Schneider *et al.*, 1997) and a low pressure core (Schneider *et al.*, 1993) are present. It should be noted that the diameter of the MPJ, *d*, does not correspond to the FPJ nozzle diameter, since the FPJ does not fill the exit plane of the FPJ nozzle. The helical region of the MPJ flows scales with the region of the FPJ flow $\frac{x}{D} \leq 2$, although the cross-section of the emerging FPJ is probably more kidney shaped than circular and the jet origin is eccentric relative to the axis of the nozzle, unlike the MPJ. In contrast to MPJ flows, FPJ flows do not appear to exhibit any recirculation outside the nozzle (Newbold, 1997), but the low pressure core and large scale motion are present (Newbold, *et al.*, 1995). For $\frac{x}{d} \geq 7 \pm 2$ in the MPJ flow, the helix "collapses" to form large-scale structures broadly comparable with those produced by the FPJ.

Despite some differences between MPJ and FPJ flows, gas flames produced by them are similar (Nathan *et al.*, 1996) and the MPJ can be used to estimate characteristic flow properties of the FPJ, such as turbulence intensity. When phase averaged sampling is used turbulence fluctuations in the region of the MPJ flow, $x/d \leq 5$, are indicative of structures smaller than the helix. Schneider (1996) measured phase averaged turbulence intensities in an MPJ flow with $St_p = 0.015$ and $Re = 26{,}600$ using 3-D laser Doppler anemometry. Axial turbulence intensities, of $5\% < \frac{\sqrt{u_x'}}{\tilde{u}_x} < 10\%$ were measured, where u_x' = local axial fluctuating velocity and $\tilde{u}_x$ = the local mean axial velocity. These values are of the order of 5 times the maximum reported in the near field of simple jets. For example, in the shear layer of a simple jet (where turbulence intensity is greatest), the local axial turbulence intensity is 1.6% at $\frac{x}{d} = 0.1$ (calculated from data reported by Husain and Hussain, 1979). The high turbulence intensities in MPJ flows in the region $\frac{x}{d} \leq 5$ are responsible for the high entrainment rates observed. Nobes (1998) proposed an additional strain created by the

precessional translation of the jet, which partially accounts for the increased turbulence intensity and entrainment in this region. The additional strain is equal to $f.\sin\phi$, where ϕ is the angle between the jet and nozzle axes.

1.7.3 The region of large scale turbulence

The region where large-scale structures occur ($\frac{x}{D} \geq 2$ for FPJ flows) is of most interest because it is where combustion occurs in gas flames (Nathan *et al.,* 1997) and is expected to do so in coal flames. Instantaneous and statistical jet fluid concentration data in the non-reacting FPJ flow field, obtained by use of a planar laser Mie scattering technique in air, showed that the FPJ produces larger structures and engulfs more ambient fluid than does a simple jet (Newbold, 1997). The engulfment of ambient fluid was observed to result in pockets of predominantly nozzle fluid being interspersed with predominantly ambient fluid (Newbold, 1997).

The enlargement of the large scales of turbulence in FPJ flows is demonstrated by the magnitude of jet half angles, which are proportional to the large scales in single phase jets. The half angle is approximately 40° in the region $(x-L)/d < 60$ (Newbold, 1997). Beyond this region the jet expands more modestly, with a half angle of 11° compared to 6.6° for a simple jet (Newbold, 1997). A two-dimensional measure of the relative size of local macro scales of turbulence was obtained from the 50% contour of two point spatial correlations of concentration fluctuations (Newbold, 1997). (The technique relies on the assumption that if reasonable correlations exist between two points they are likely to be in the same structure). The magnitude of the integral scale (a Taylor scale) in the FPJ flow was found to be twice that in a simple jet (Newbold, 1997).

1.7.4 The energy associated with different scales of turbulence

As well as amplifying the largest scales of turbulence, the FPJ acts to "*shift energy in the spectrum of turbulence toward these large scales and away from the fine scales. The absolute energy in the fine scales is reduced.... by an order of magnitude*", (Nathan *et al.*, 1997). Evidence for reduced energy in the small scales in the downstream region of FPJ flows was inferred from the shape of the 50% contours of two point spatial correlations of fluid concentration (Newbold, 1997). Away from the central axis, fluid structures, and consequently the 50% concentration contours, are stretched to an elliptical shape in the direction of strain. In a simple jet the 50% contours have an aspect ratio of 1.7:1, whereas FPJ 50% contours are more circular, having an aspect ratio of 1.4:1. The more circular shape of the FPJ contours is indicative of reduced mean local strain rate, dU/dy, which correlates with reduced energy associated with small scales. Newbold (1997) also measured broadened concentration distributions of nozzle and entrained fluid, and a far field unmixedness (concentration r.m.s. / concentration mean) of 0.5 for the FPJ compared to 0.3 for a simple jet. These measurements reflect the observations made by flow visualisation, that precession increases the large-scale engulfment of ambient fluid and reduces fine scale mixing.

The stabilisation region of MPJ methane flames has been shown to be adequately represented by non-reacting MPJ flows as described below. The instantaneous reaction zone in a methane MPJ flame was observed using planar laser induced fluorescence of OH radicals, and was shown to correspond to the boundaries of large scale structures observed in cold flow (Nathan, *et al.*, 1997). Comparison of methane MPJ flames using cold non-reacting concentration measurements showed that reaction occurs in regions where stoichiometric mixtures are generated (Nathan, *et al.*, 1997). Sufficiently low phase mean velocities of less than 10 ms^{-1} (obtained by 3D-laser Doppler velicometer) and phase mean concentrations within the flammability limits of methane (obtained by planar Mie scattering) were also measured in the stabilisation region of the methane MPJ flame (Nathan, *et al.*, 1997).

The above correlations between reacting and non-reacting techniques provided a rationale for the use of non-reacting measurements of turbulence intensity and turbulence spectra to compare an MPJ flow with a simple jet (Nathan, *et al.*, 1997). Non-reacting turbulence spectra measurements were taken (by hot wire anemometry) at two points in an MPJ and 2 points in a simple axial jet (AJ) flow, labelled PJ3, PJ4, AJ5 and AJ2 in Figure 1.5. The turbulence intensity data at the same points are also shown in Figure 1.5 (Nathan, *et al.*, 1997).

The frequency of turbulence shown in Figure 1.5. was normalised by the axial distance from the nozzle, x, and the maximum velocity in the appropriate x plane, ie. $f' = \frac{fx}{U_{max}}$. Away from the jet axis (where reaction occurs) in both precessing and simple axial jets "*a greater proportion of energy resides in the larger scales, at the expense of that in the smaller scales, than occurs nearer the axis*" (Nathan, *et al.*, 1997). However, the effect is far more pronounced in precessing jets. The simple jet spectra on the centre-line (AJ2) is shown as a reference.

Local phase averaged axial turbulence intensities of ~1 were found throughout the region in the MPJ flow where large-scale structures are found ($x/d \geq 5$, Schneider, 1996). However turbulence intensities are of the order 0.5 at two points near the boundary of the flow where conditions conducive to stabilisation occur (positions PJ3 and PJ4 in Figure 1.5.). These conditions represent a reduction in axial velocity to 3% of the exit velocity and considerable dilution of the nozzle fluid by entrainment has occurred, so that if the nozzle fluid was a gaseous fuel, the lean limit is achieved. In a simple jet, these same mean velocity and concentration conditions occur at $\frac{x}{d} = 30$ (AJ5 in Figure 1.5) where turbulence intensity is higher, approximately 1.0.

These measurements taken together, show that precession acts to augment large scale engulfment of ambient fluid while reducing the energy available for fine scale straining (which controls the reaction rates of species) in the region where reaction occurs. It is also consistent with conservation of energy, since the nozzle chamber does not add any energy to the flow (in fact it removes energy due to pressure losses), so an increase in large scale energy occurs with a reduction in fine scale mixing. The term "enhanced large scale mixing" will be used to refer to these combined effects in the region x/D > 1 of FPJ flows.

1.7.5 Gas FPJ flames

When the FPJ nozzle is used as a gaseous fuel burner, the initial high mixing rates and rapid velocity decay result in a reduction in flame lift-off height by an order of magnitude compared to a simple jet (Nathan *et al.*, 1996 and Newbold *et al.*, 1997). Nathan and Luxton (1989) showed that an unconfined gas flame, from an FPJ nozzle with $d_t = 2.4$ mm, could not be blown off by increasing the gas velocity at the throat of the nozzle to choked conditions and further increasing the pressure drop across the nozzle to 800 kPa. Precessing jet gas burners have been successfully applied in cement kilns where other NO_x reduction techniques developed for gas fired boilers are not applicable. FPJ flames generate high heat release rates in the region immediately downstream from the burner, allowing improvements in cement clinker quality due to rapid cooling of clinker once it leaves the flame zone (Manias and Nathan, 1994). Evidence, which suggests that the enhanced large scale mixing characteristics of PJ flows are responsible for these improvements, was provided in laboratory investigations, and is summarised below.

Newbold (1997) found that flame tip strain rates, $S/\Delta X$, in free vertical gas FPJ flames, are an order of magnitude lower than those of simple turbulent jet flames. The flame tip strain rate is considered characteristic of the flame, since the fluctuation length is governed by the burnout of individual large structures (Newbold, 1997). The low strain rates of FPJ gas flames are due to both low celerity (convection speed) of structures, which become buoyancy-dominated due to the dramatic increase in initial growth of the jet, and to increases in fluctuation lengths. Kent and Bastian (1984) showed that low strain rates in gas flames correlate with high soot production levels, due to mixing limitation of soot oxidation. Turns and Myhr (1991) showed that reduced thermal NO_x emissions occur in gas flames with high radiant fractions due to flame cooling. Atreya *et al.* (1996) found soot oxidation also reduces the availability of OH radicals for NO formation in low strain rate gas diffusion flames. Nathan *et al.* (1996) postulated that sooting is responsible for the high radiant fractions, low flame temperatures and reduced NO_x emissions observed in free vertical gas MPJ flames. It can be postulated that a similar mechanism operates in horizontally fired FPJ flames in industrial cement kilns, in which the PJ momentum is sufficient to dominate over that of the combustion air. In such a situation buoyancy effects are generally not significant, but a reduction in strain rate due the enhancement of large scale mixing can be expected to occur.

1.7.6 Summary

Precessing jets rapidly entrain ambient fluid in the near nozzle region due to high levels of turbulence. Further downstream, in the region $\frac{x}{D} \geq 2$ FPJ's generate larger structures than simple jets with a greater fraction of the total energy contained in the large structures. These characteristics of FPJ flows have been shown to be responsible for high heat flux and low thermal NO_x emissions from methane FPJ flames.

1.8 Hypotheses

The key question to be tested in the present research program is whether altering the structure of turbulence by enhancing large scale mixing at the expense of small scale mixing can beneficially influence pulverised fuel combustion, and in particular whether it can improve flame stability, heat release and/or reduce NO_x emissions. FPJ flows are used as a tool in the current study to promote the large scales of turbulence. It is expected, based on the research of others reviewed above and in Chapter 4, that particle motions can be affected, resulting in altered ignition and combustion characteristics. In addition, the potential for making use of the reduced strain rates, which occur slightly downstream from a FPJ nozzle, to control the local rates of the dominant reactions in PF combustion will be assessed.

The key research question is addressed as an investigation of four hypotheses. Turbulence and particle motion in non-reacting FPJ flows are considered before considering the influence of precession on PF flames. This approach is adopted to avoid difficulties associated with quantifying the structure of turbulence and particle motion in PF flames (Weber *et al.*, 1992a). Such difficulties are due to high particle loading and high radiant emission. The hypotheses are examined in a nozzle configuration that generates a central FPJ flow and a surrounding annular flow. The annular flow models the primary coal transport stream of PF flames.

The 4 key hypotheses to be tested are:

1) *That the structure of the turbulence in an annular jet used to transport coal particles can be altered, here by a centrally located precessing jet flow, to enhance large scale turbulence at the expense of small scale turbulence.*
2) *That clustering of pulverised coal particles within jet flows can be significantly increased by enhanced large-scale turbulence and reduced small-scale turbulence, here generated by precession.*
3) *That control of the structure of jet turbulence, and hence particle clustering, can be used to improve flame stability and increase early heat release rates.*
4) *That control of the structure of jet turbulence, and hence particle clustering, can be used to control NO_x emissions.*

The first two hypotheses will be treated in turn in Chapters 3 and 4, while hypotheses 3 and 4 will be treated together in Chapters 5 and 6 which detail combustion experiments at two different scales.

1.9 Summary

Pulverised fuel will continue to be a major fuel source in the power and process industries in the foreseeable future. The major operational issues in industry are the provision of flame stability to allow stable operation and wide turndown ratio, and a means of matching the heat release profile from the flame to the process requirements, or in the case of power stations to provide high combustion intensity per unit volume. These objectives need to be met within the context of more stringent controls on NO_X emissions and concerns about global warming. Wall fired swirl burners in power boilers achieve stability by the provision of a reverse flow zone of combustion products into which particles are injected, thereby providing a heating source and long residence times for the ignition of volatile matter. Fuel staging for NO_x reduction can be achieved by injecting particles into the internal recirculation zone. In rotary kilns the usefulness of swirl is limited since only a small fraction of the total air can be swirled, and there is high confinement resulting in lifted flames that are more difficult to stabilise. As such, there is a need to investigate improved burner designs for rotary kilns, although the concepts may also have applicability to boilers.

Recent research, using full field planar laser techniques, has shown that particles of a size typical of pulverised fuel can be influenced by large scale turbulence to concentrate within fluid structures or in regions between structures. It is hypothesised that such particle concentration effects can be accentuated by enhancing the large scales of turbulence at the expense of the small, and that the combined effects of particle concentration and turbulence modification can have beneficial effects on stability, heat release and NO_X emissions. In particular attempts will be made to apply the principle developed in staged combustion, of using for time averaged zones of characteristic conditions, such as the generation of fuel rich ignition for the reduction of NO_x emissions, to the local turbulence structure. Precessing jet nozzles have been selected to explore the influence of clustering effects because they have been shown to be effective in enhancing large-scale turbulence and because they are more robust than acoustic excitation.

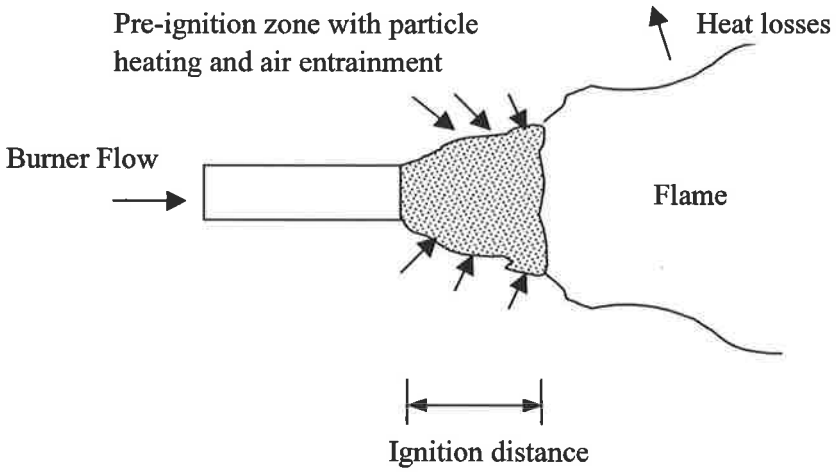

Figure 1.1. A schematic diagram of a "lifted" pulverised coal flame typical of a cement kiln and non-swirled burner designs

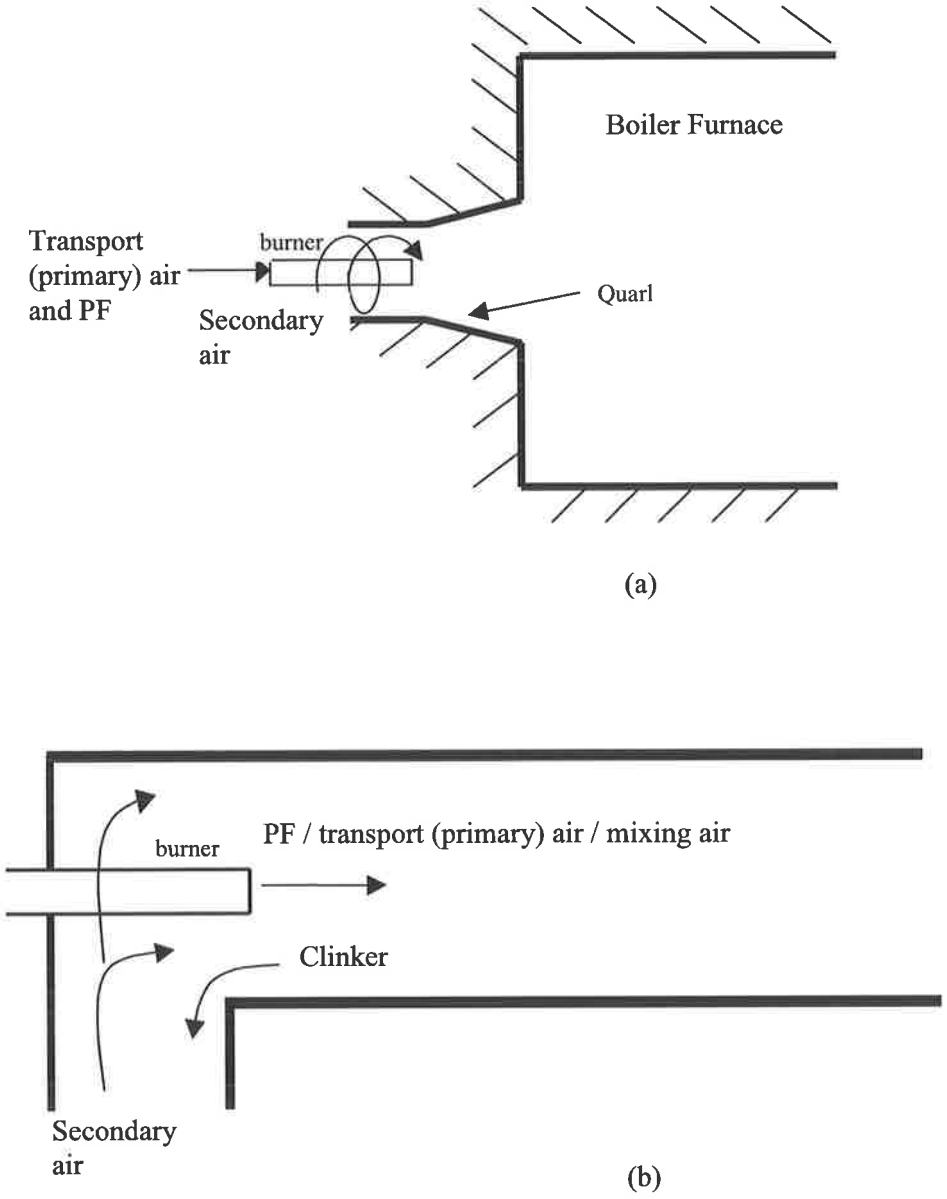

Figure 1.2. Schematic diagrams of typical firing arrangements in:
(a) a wall fired boiler, where the furnace diameter is much greater than the burner diameter – low confinement
(b) a cement kiln, where the kiln diameter is less than an order of magnitude greater than the burner diameter – high confinement.

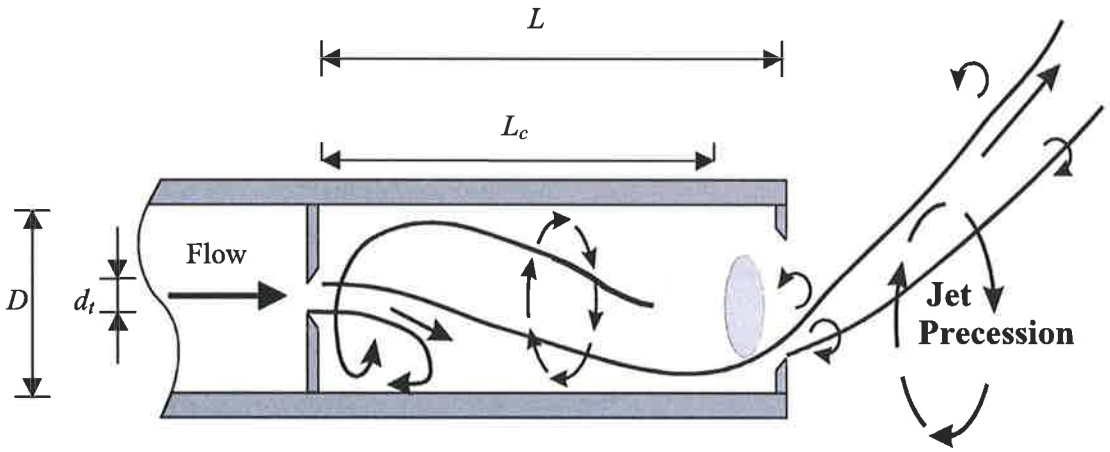

Figure 1.3. A schematic diagram of the Fluidic Precessing Jet (FPJ) nozzle and the mechanism of precession. Optimum dimensions are d_t/D = 0.20, d_2/D = 0.88, L/D = 2.75, L_c/D =2.30, d_c/D =0.79, w_c/D =0.20, where d_t is the inlet throat diameter, d_2 is the exit diameter, d_c is the centre-body diameter, and w_c is the centre-body width.

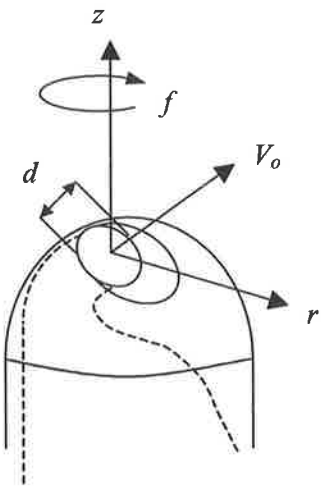

Figure 1.4 A schematic diagram of the rotating tip of the Mechanical Precessing Jet (MPJ) nozzle (Nobes, 1998) showing the nozzle diameter, d, nozzle exit velocity, V_o, nozzle rotation frequency , f, and spatial coordinates, z and r.

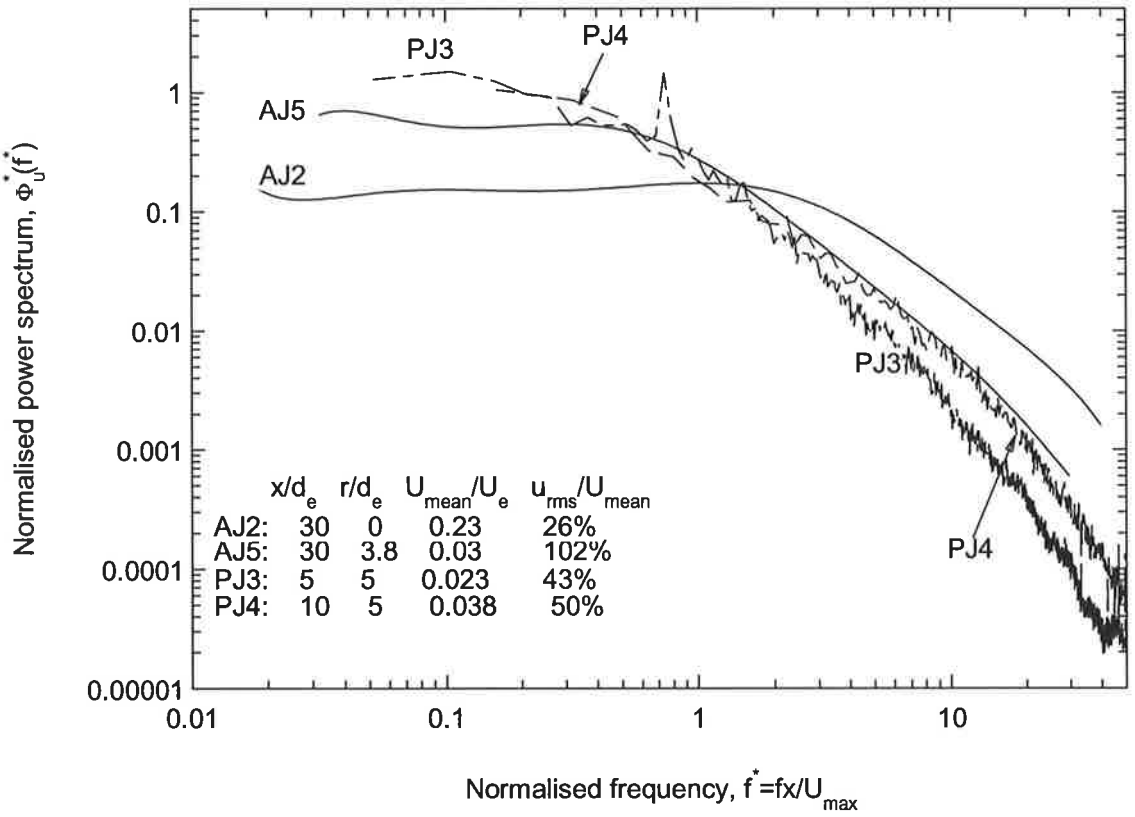

Figure 1.5. Turbulence spectra at selected points in a simple axial jet flow (AJ) and a MPJ flow (PJ) determined by hot wire measurements (Nathan *et al.*, 1997). Position AJ2 is located on the simple jet axis, AJ5 is located at a position where the simple jet velocity has decayed to 3% of its initial value. Likewise the two points in the MPJ flow are located at positions where the jet velocity has decayed to 3% of its initial value. The plot shows the higher energy levels at low frequencies, and lower energy levels at high frequencies for the MPJ.

Chapter 2. Experimental Design and Scaling Criteria

2.1 Introduction

A range of small-scale experimental methods are used in the present work to assess different aspects of the physics and chemistry occurring in PF flames employing PJ flows. In Chapters 3 and 4 non-reacting techniques are used to assess the influence of enhanced large scale mixing on the scale of turbulence in an annular flow, and on particle clustering, respectively. In Chapters 5 and 6 the effects of enhanced large scale mixing on PF flame properties are investigated at 130 kW and 2.5 MW scales.

The current chapter develops a rationale for the modelling approach adopted in each set of experiments. That approach is to use experimental methods to determine the dominant mechanisms operating in PJ flames, and to thereby assess scaling. Subsequently, general design principles for full-scale burners are developed, rather than for the design of a specific full-scale rotary kiln burner. The performance characteristics of two hypothetical full scale burners are assessed in Chapter 6. These burners are sized at nominal capacities of 35 MW and 105 MW, which are representative of a typical small and large industrial kiln respectively.

2.2 Modelling PF flames

Modelling of pulverised fuel flames is complicated by the fact that many of the physical and chemical processes that influence flame stability, heat release and NO_x emissions do not scale in the same way. Spalding, (1963) introduced the concept of partial combustion modelling, in which only the dominant processes are simulated in a simplified system, whilst the need for similarity of the other processes is relaxed. Smart (1992) lists some of the similarity requirements which can be relaxed in PF flames under the assumption that the large scale turbulent mixing processes largely control the physical and chemical processes in these flames. If molecular transport processes are of secondary importance, similarity of Pr, Sc and Le can be relaxed. Likewise, if inertial forces dominate over buoyancy forces, similarity in Fr can also be relaxed. In contrast, geometric similarity, kinematic similarity (fluid flow and mass transfer), thermal similarity (which strongly influences chemical reaction rates) should ideally be maintained for adequate modelling (Smart, 1992).

The two most common practical scaling approaches, which have been developed to allow similarity of the dominant processes to be maintained in PF flames, are constant inlet velocity and constant residence time scaling (Smart, 1992). Constant Re scaling, often used in aerodynamic modelling, requires that velocities in the model be increased to account for reduced physical scale. Consequently constant Re scaling becomes impossible when the model is significantly smaller than the full-scale burner, and will not be considered further. Conversely, constant residence time scaling requires a reduction in velocity in proportion to the reduction in physical length scale. If the scaling ratio is sufficiently large, this requirement results in particle settling within the particle transport pipe due to lower transport velocities at small scale. Particle sizes can be reduced to prevent settling, but doing so causes the time-scales of the fundamental processes involved in stability, heat release and NO_x emissions to be altered. Consequently, the constant residence time approach is less suitable than constant velocity scaling when the physical size of the model burner is significantly smaller than the full-scale burner.

2.3 A comparison of constant velocity and constant residence time scaling

To maintain kinematic similarity it is necessary to hold constant both the momentum ratio and inlet velocity ratio of the fuel relative to all coaxial air streams. These ratios control entrainment and mixing rates (Smart, 1992). Smart (1992) shows that if these requirements are met, the fractional degree of mixing between streams at any axial location, $\frac{x}{D}$, is proportional to axial position and is independent of scale and scaling criteria used, ie. the fractional degree of mixing is proportional to the product of residence time $\frac{x}{U}$ and mixing rate $\frac{U}{D}$.

Fractional degree of mixing $\alpha \quad (x/U)\cdot(U/D)=(x/D)$ 2 - 1

If constant residence time scaling is used, then both the residence time and mixing rate are constant ensuring constant specific mixing rates and so similarity in fractional degree of reaction (Smart, 1992). For constant velocity scaling the mixing rate increases with reduced scale. However, a constant fractional degree of reaction at constant *x/D* can be assumed if the reactions are mixing limited (Smart, 1992).

To maintain true thermal similarity identical flame temperatures, heat release rates and time-scales of all temperature dependent processes are required. Pulverised coal flame temperatures are influenced both by reaction rates (dominated by mixing rates) and heat release rates (dominated by radiation). If flame emissivity is assumed to be constant between flames, then the spatial variations in in-flame temperature, are inversely proportional to local velocities, which can be assumed to scale with the characteristic inlet velocity, U (Smart, 1992):

$$\frac{dT_f}{d(x/D)} \quad \alpha \quad \frac{1}{U}. \qquad 2 - 2$$

Hence the heat release profiles, as a function of *x/D*, of constant velocity scaled flames should be relatively similar at all scales. However, any reduction in velocity relative to full scale, such as would occur in small scale constant residence time flames, will result in shorter relative flame temperature and heat release profiles.

The emissivity of PF flames is likely to depend on scale. Flame emissivity can be estimated from the individual contributions of combustion gases, ε_g, soot, ε_s, and particles, ε_p, by the relation, (Sarofim and Wall, 1980):

$$\varepsilon_f = 1-(1-\varepsilon_g)(1-\varepsilon_s)(1-\varepsilon_p) \qquad 2-3$$

Ash and soot particles can make a significant contribution to flame radiation. If soot emissivity dominates, the following relation can be used to estimate flame emissivity (Sarofim and Wall, 1980):

$$\varepsilon_{soot} = 1-\exp\left(-1.24x10^{-3}(C/\rho)TL\right) \qquad 2-4$$

where C is the mass concentration of soot (kgm^{-3}), ρ is soot density (kgm^{-3}) and the mean radiation beam length, L, is expressed in microns. A reduction in scale causes a reduction in mean radiation beam length, and may produce a significant reduction in emissivity, and hence in heat release, to the furnace walls. However such a reduction is independent of the scaling criterion used. In summary, constant velocity scaling can provide better thermal similarity than constant residence time scaling, but the scaling criterion chosen may have less impact than differences in furnace and flame temperatures between scales, and the effect of reduced emissivity at small scale.

An additional criterion, which is particularly relevant in the current context, is the need to maintain similarity in particle - turbulence interactions between scales. As outlined in Section 1.5.2. Stokes number is the main parameter used to characterise these interactions. If fluid properties are constant between large and small scale, then St is a function of residence time and particle diameter,

$$St \;\alpha\; \frac{U}{D}\cdot d_p^{\,2} \qquad 2-5$$

Hence one way to preserve St similarity as the scale of the facility is reduced is to maintain a constant particle size and use constant residence time scaling. Alternatively if constant velocity scaling is used, inspection of equation 2-5 shows that St similarity can be maintained by varying particle size with the square root of the burner diameter. However, as noted above, reductions in particle size lead to increased rates of devolatilisation and consequently increased temperatures and altered NO_x emissions and radiation characteristics, so that thermal similarity is lost (Smart, 1992). For this reason (along with practical issues related to milling) particle size is generally not used as an experimental variable in coal flames. This is also the case in the current study.

The above analysis shows that constant residence time scaling theoretically provides superior similarity in St between scales. However, Smart *et al.* (1996), using 2.5 MW flames scaled down from a 12 MW flame, showed that neither scaling criterion models exactly the interactions between particles and the IRZ of swirl stabilised boiler flames. Smart *et al.* (1996) inferred dominant mean particle trajectories from flue NO_x emissions and in-flame temperature and gas concentration measurements. Reasonable similarity in both

particle trajectories and flame properties was observed using constant velocity scaling at 2.5 MW (Smart, *et al.*, 1996). Consequently, 2.5 MW flames employing standard industrial particle size distributions and constant velocity scaling, relative to hypothetical full scale burners, are investigated in Chapter 6. These investigations serve as an adjunct to smaller scale PF flame experiments in which neither constant velocity nor constant residence time scaling was strictly observed (Chapter 5).

In summary, no single scaling parameter is capable of maintaining complete similarity between different scale facilities. However, kinematic similarity, or similarity in the fractional degree of mixing between scales, can be modelled by both constant residence time and constant velocity scaling. Thermal similarity is best modelled by constant velocity scaling but requires a model furnace capable of operating at the same temperatures as encountered in full-scale furnaces. Reasonable similarity in two-phase interactions can be achieved using constant velocity scaling at 2.5 MW or larger scale. Practical constraints dictate that "partial scaling" principles, in which only the processes which are judged to have the greatest influence on flame output, are applied in the current work .

2.4 "Partial scaling" in experimental design

The partial scaling approach is used to explore the hypotheses detailed in section 1.8. Two combustion experiments and two non-reacting experiments have been performed. Each experiment investigates a different aspect of the dominant physics or chemistry of PF flames, while relaxing the need for full similarity. The bulk of the combustion experiments were conducted at 130 kW scale for reasons of cost and availability (Chapter 5). These 130 kW experiments were conducted to assess the impact of enhanced large scale mixing and particle clustering on flame properties. The requirement for geometric, thermal and kinematic similarity with hypothetical full-scale kilns was relaxed in order to examine the issues of most interest without requiring a more expensive facility. Due to the use of the partial scaling approach, scale up of the trends (rather than absolute values) in flame properties is possible.

Two non-reacting techniques were used to measure the influence of PJ mixing on (a) the structure of an annular flow and (b) on the motion of particles transported in the annular flow. The use of non-reacting techniques allows these aspects of the "dominant physics" to be assessed with far greater precision, and in a simpler manner than is possible in PF flames. It is therefore also possible to investigate a wider range of conditions than is possible in flames. The non-reacting experiments were designed to allow use of the same nozzles and ratios of PJ to annular momentum as those used in the 130 kW flames. The experiments are detailed in Chapters 3 and 4 respectively.

Care must be taken when relating results from isothermal studies to combusting flows. Variation in fluid density and viscosity with temperature are not the only issues which alter particle response to turbulence. For example, McCreath and Makepeace (1971) compared isothermal and burning oil sprays emanating from a bluff body nozzle, and found that the droplet spread and velocities were substantially greater for the combusting case than for the cold case. The effects were attributed to a reduction in the drag on the surface of the burning oil droplets due to evaporation. Similar observations in coal flames suggest that the release of volatiles reduces the drag coefficient of burning particles (Mullinger, 1994b). Despite such differences between combusting and cold flows, reasonable similarity can be expected in the pre-ignition region of a lifted flame, ie. between the burner exit and the location of the flame front. Consequently, the non-reacting experiments (Chapters 3 and 4) focus on the region corresponding to the pre-ignition region of the 130 kW flames.

Finally a set of combustion experiments at 2.5 MW scale, where clustering effects are more representative of full scale, was performed in a boiler simulator (Chapter 6). The 2.5 MW experiments ratify the validity of the trends produced at the 130 kW scale. As was the case for the 130 kW experiments, those conducted at 2.5 MW focussed on investigating the impact of changes in the dominant two-phase physics on flame properties, rather than strictly adhering to geometric, kinematic and thermal similarity with hypothetical full-scale flames.

2.5 Burner design and the range of conditions studied

A burner design has been developed to provide a simple practical means of incorporating a PJ flow into a PF stream. This burner employs an annular primary "transport" air flow to convey the coal particles. A central PJ nozzle can be located within the annular channel (Figure 2.1a), or alternatively, a central bluff body can be used so that the annular channel functions as an annular mono-channel burner (Figure 2.1b).

Practical constraints have influenced the approach taken to scaling the 130 kW flames. The annular width of the channel used to convey the particles was designed to be large enough to prevent slugging of particles, and to avoid back-pressuring the feed system. The outer dimension of the annular channel was determined by the internal diameter of readily available high temperature stainless steel pipe. The inner dimension can be varied by using inter-changeable machined components corresponding to the outer surface of the central PJ nozzle or bluff body. To allow meaningful comparisons between air and water studies, the PJ axial momentum flux, G_{PJ}, is calculated at the PJ exit plane, where it is denoted G_{PJe}. It is calculated by assuming that the jet exit area occupies one third of the annular area between the centre-body and the internal chamber wall, and that the jet is directed axially, ie.

$$G_{PJe} = \frac{12\dot{m}_{PJ}^{\ 2}}{\pi\rho_e(D^2 - (0.79D)^2)} \qquad 2\text{-}6$$

The chosen dimensions are shown in Table 2.1, which also shows the range of conditions tested in Chapters 3 - 6.

Table 2.1. Summary of nozzle dimensions and range of operating conditions – all experiments

Experiment	*Ch.*	*Annular Fluid*	*PJ fluid*	$D_{A,2}$ *(mm)*	$D_{A,1}$ *(mm)*	D *(mm)*	*Primary velocity* (ms^{-1})	G_{PJe}/G_1
Fluid turbulence	3	Water	Water	32.5	24.0	10 or 19	0.12– 0.65	0 – 18
Particle motion	4	Air	Air	32.5	24.0	10 or 19	2.4 or 9.8	0 – 51
130 kW	5	Air	Air	32.5	24.0	10 or 19	9.8 – 13.5	0 – 7
2.5 MW	6	Air	Air	135.8	88.5	55 or 80	20	0 – 3.6

Note: $D_{A,1}$ is internal diameter of the annular stream, $D_{A,2}$ is the external diameter of the annular stream, D is the internal diameter of the FPJ nozzle. The primary axial momentum flux, G_1, includes the contribution of particles.

Standard PF size distributions were used in the 130 kW experiments. Consequently, constant residence time scaling from hypothetical full-scale burners was not attempted since particle settling in the transport channel would ensue. For example, scaling down a 100 MW

burner with a transport velocity of 20 ms^{-1} to 130 kW would require a transport velocity of 2 ms^{-1}. Constant velocity scaling of the transport stream using the industrial standard velocity of 20 ms^{-1} was attempted. However, it was found that baseline mono-channel flames could not be stabilised using a transport velocity of 20 ms^{-1}, and that a reduced velocity of 9.8 - 13.5 ms^{-1} (7 - 10 % of total air) was necessary for good stability (see Chapter 5). Consistent transport of PF, without slugging, was achieved at these velocities. Consequently, transport air velocities in the range of 9.8 - 13.5 ms^{-1} are used in most of the 130 kW flames investigated. The quantities of primary air are intermediate between those used in direct fired (15 – 40 % of total air) and indirect fired (3 – 5% of total air) rotary kilns. Consequently, performance trends are applicable to both types of firing system. In summary, the 130 kW experiments were designed to provide indicative trends of the influence of enhanced large scale mixing on PF flame properties, rather than to strictly adhere to the desirable similarity criteria outlined in section 2.2. This approach allows the dominant mechanisms that control flame properties to be determined.

As noted in section 2.3 the non-reacting visualisation experiments (Chapters 3 and 4) maintain exact geometric similarity with respect to burner dimensions used in the 130 kW experiments. The momentum ratios of PJ fluid to "transport" fluid are varied over a wider range than in the combustion experiments (Table 2.1). In the 2.5 MW combustion experiments (Chapter 6), the transport air channel was sized to provide 20 % of the total air flow at a velocity of 20 ms^{-1} (at 70°C). Two inter-changeable central PJ nozzles were designed to be placed within the annular transport channel, and be capable of operating over a similar range of PJ to transport momentum ratios to those used in the 130 kW experiments. Details are provided in Table 2.1. An additional turbulence similarity criteria for fluidic precessing nozzles, which is maintained in all experiments, is that the FPJ throat Re be greater than 20,000 (Nathan *et al.*, 1997) to ensure that a precessing flow is consistently generated.

2.6. Summary

The experiments detailed in the current work can be expected to allow a good assessment of the effect of enhanced large scale mixing on flame properties, and an investigation of the hypotheses. The assessment is aided by the ability to investigate a wider range of velocity and momentum ratios, and consequently a wider range of near field mixing conditions than will be encountered in full-scale rotary kilns. The investigations are conducted using both reacting and non-reacting techniques, each of which models a particular aspect of the dominant physics or chemistry rather than providing full geometric, kinematic and thermal similarity. The chosen techniques allow the dominant mechanisms that control flame properties to be determined. These mechanisms are used to indicate the likely effects of precession at full scale rather than to scale a particular full-scale burner.

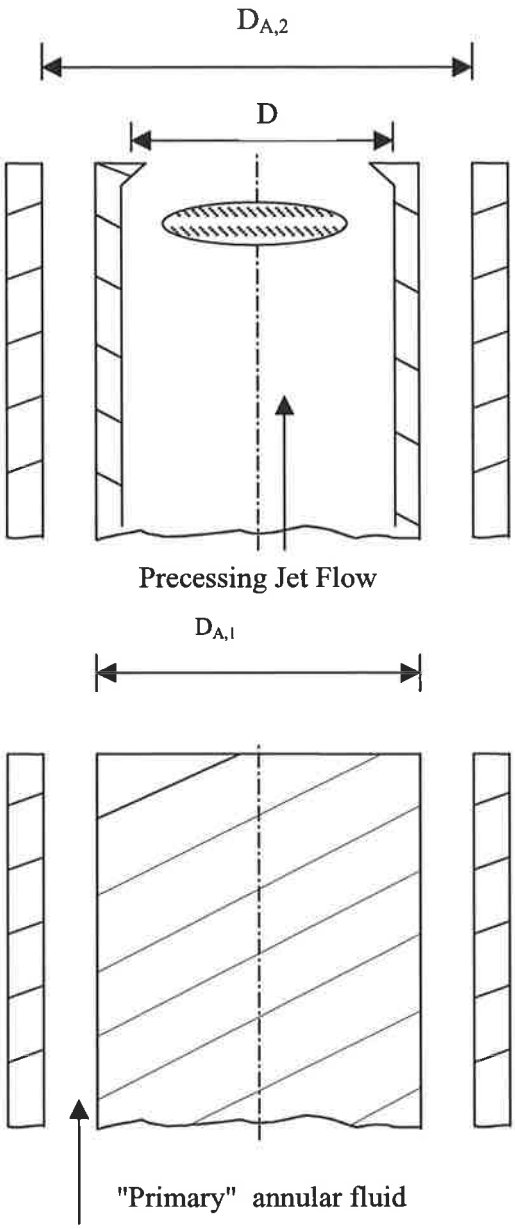

(a)

(b)

Figure 2.1. Schematic diagrams of the exit regions of the two major types of nozzle used in all experiments, showing the standard annular channel used for "primary" fluid, with inner dimension $D_{A,1}$, outer dimension $D_{A,2}$.
(a) PJ nozzle (with chamber internal diameter, D) located centrally within the annular primary "transport" channel
(b) The annular channel with central bluff body used as a mono-channel annular nozzle.

Chapter 3. Turbulent structure in single phase non-reacting annular flows

3.1 Introduction

The first hypothesis is developed here, namely that "the structure of turbulence in an annular jet used to transport coal particles can be beneficially altered, by a centrally located precessing jet flow, to enhance large scale turbulence at the expense of small scale turbulence". The hypothesis is explored using a single phase non-reacting flow visualisation technique. Despite the differences between combusting and non-reacting flows, reasonable similarity can be expected in the pre-ignition region of a lifted flame, ie. between the burner exit and the flame front. Consequently, this region is explored in the current chapter by isothermal modelling.

3.2 Rationale for use of a single phase water flow technique

A non-reacting single phase water flow visualisation technique is used in the current chapter. The size of individual large-scale turbulent structures is assessed by qualitative analysis of video records of the visualisations. A semi-quantitative planar laser induced fluorescence technique, which images the jet fluid concentration, allows determination of the jet half width, $r_{1/2}$. The half width is a measure of the scale of the largest flow structures, and hence the characteristic length scale of the jet, assuming that large-scale coherent structures span the width of the jet (Tennekes and Lumley, 1972). Mean local strain rates are estimated from measurements of structure convection velocity and characteristic length scale, $r_{1/2}$. To assess the effect of precession by comparison, a range of alternative mixing nozzles is also assessed. These are interchangeable with the PJ nozzle and are also located centrally within the annular jet. The half width measurement technique is used to determine the influence of each jet on the scale of turbulent structures. These measurements are also used in subsequent chapters to estimate conditions in reacting flows, and so to assess mechanisms involved in flame stability, heat release and NO_x emissions.

High resolution quantitative measurements of fluid concentrations require a uniform light sheet of thickness less than that of the smallest scales of turbulence. Other requirements include, high signal to noise ratio (eg. high laser power), flat camera response or correction for light intensity measured from every pixel, correction for laser pulse variation if a pulsed laser is used, and correction for background illumination (Nobes, 1998). Apparatus which allow all of these requirements to be met were not available for the current study, but Newbold (1997) has shown the validity of a semi-quantitative LIF technique for the calculation of structure sizes, based on jet half widths, which can be correlated with other turbulence parameters. The technique has been successfully used previously in water by Schneider (1996), Newbold (1997) and Parham (1998), and the identical facilities have been chosen for the present investigation.

LIF techniques for flow visualisation and for quantitative measurement of scalar concentration utilise fluorescence, by which a photon is absorbed, causing excitation of the species and emission of a photon of a different wavelength as the species drops back to the ground energy state (Guilbault, 1973). LIF techniques in water have been used to demonstrate the controlling role played by large scale structures in mixing and entrainment processes (Dahm and Dimotakis, 1987). Fluorescent dyes with different emission

wavelengths can be used to mark different fluids and so to visualise the interaction between them (Dahm *et al.*, 1992).

Koochesfahani and Dimotakis (1985) showed that there are benefits to be gained by using water to visualise turbulent transport processes since the Schmidt No, Sc (the ratio of turbulent to molecular diffusivity, υ/D), for water is approximately 600 compared to approximately 0.8 for air. Using water capitalises on the low molecular diffusivity of water to highlight the turbulent transport processes. The use of water also allows a reduction in velocity of ~ 15 times compared to air and, in the present investigation, a reduction in FPJ precession frequency by an order of magnitude relative to that in air, so that a standard video camera can be used to capture the motion of the precessing flow. For example, a typical case in the current experiments used a nozzle of dimension, D = 19 mm, with a water flow rate of 250 l/hr through it to produce an inlet throat velocity of 6.12 $m.s^{-1}$. Using equation 1-14, f_p = 4.6 Hz. By using a video camera with a framing rate of 25 $f.s^{-1}$, approximately 5 images are captured for each precession cycle. Use of the video technique can cause blurring of the mixture field if the shutter speed is slower than the time-scales of the Kolmogorov scale of structures (Koochesfahani and Dimotakis, 1985). However, the calculation of jet half widths, which are much larger, is not affected by such blurring.

3.3 Apparatus and experimental procedures

3.3.1 Nozzles investigated by the water LIF technique

The nozzles used in the LIF experiments, together with their characteristic dimensions, are illustrated in Figure 3.1. Figure 3.1.(a) shows the baseline annular channel used to supply primary "transport" fluid. The central bluff body is interchangeable with all of the mixing nozzles shown in Figures 3.1(b) – (e). In all cases, the outside diameter of the central nozzle serves as the inside diameter of the annular spacing, ie. $D_{A,I}$ = 24 mm. Two FPJ nozzles with dimensions D =19 mm (and d_t = 3.8 mm), and D = 10 mm (and d_t = 1.75 mm) respectively were assessed (Figure 3.1b). They are denoted 19PJ and 10PJ respectively. The annulus and FPJ nozzles used in the LIF experiments are the identical nozzles also used in the 130 kW combustion experiments (Chapter 5), providing exact geometric similarity.

The other mixing nozzles (Figure 3.1c-e) are designed to provide comparisons to the unsteady PJ flow by producing various "steady analogues" of the PJ flow. Each steady jet nozzle was designed to have a cross-sectional exit area equal to that of the jet emerging from the 19PJ nozzle. The cross-sectional area of the emerging 19mm FPJ has been estimated to be 35.53 mm^2, following the method of Nathan *et al.* (1995) based on one third of the area between the nozzle wall and the centre-body (Figure 3.1b). In this way, equal flow rates of mixing and primary fluid have been maintained for each configuration, providing constant initial momentum and velocity ratios, to aid in the evaluation of hypothesis 1. The only exception is the 10PJ nozzle, which has a smaller cross-sectional exit area. Nevertheless, it allows the ratio of PJ nozzle diameter to annular diameter to be investigated.

The "conically diverging" jet (Figure 3.1c) provides the same total momentum as the exiting FPJ and simulates the mean flow of the exiting FPJ, without the unsteady effects, ie. simulating precession at frequency = ∞. The central cone is attached to the body of the nozzle by three support legs, each tapering to a width of 1 mm at their narrowest point. Preliminary visualisation tests showed that these support legs create a local disturbance in the conically diverging flow. Consequently, the nozzle was positioned relative to the laser sheet, in the manner sketched in the plan view in Figure 3.1(c). This arrangement was designed to illuminate a portion of the jet (the right side) in which minimum interference from the support legs occurred. Consequently the right side of the jet can be taken to be representative of jet as a whole. The left side of the jet (as imaged) suffers considerable interference, and can be considered to be non-representative of the jet as a whole. By rotating the nozzle 30^o clockwise from the position shown in Figure 3.1(c), a minor degree

of interference from the nearest support leg on both sides of the jet was observed in preliminary tests. Consequently the original position of the nozzle was used. The annular channel, Figure 3.1a, and the PJ centre-body, Figure 3.1b, were also supported with three support legs, but interference from these legs was not observed in preliminary tests. This was presumably because the support legs are located further upstream and, in the case of the PJ, because of the high levels of turbulence generated by the unsteady PJ flow at the exit plane.

The "co-axial" jet (Figure 3.1d) provides the same total momentum as the FPJ in the form of a steady axial jet without the initial large-scale oscillations in jet direction. The "45° directed" jet (Figure 3.1.e) provides the same momentum, in approximately the same direction as the instantaneous exiting FPJ, but as a steady jet, ie. it simulates the PJ flow at precession frequency = 0.

3.3.2 Experimental Technique

The LIF technique (Newbold, 1997) is illustrated schematically in Fig 3.2. The experiments were conducted in water in a perspex tank, 750 x 750 mm square and 1500 mm high. The width of the tank is more than twenty times greater than the diameter of the largest nozzle, so that wall and confinement effects are negligible. Prior to each experiment the tank was filled with clean water, after which no further ambient fluid was added. The "mixing" and annular streams are marked with fluorescent dyes while the ambient fluid is unmarked. Fluorescein, which fluoresces in the yellow/green part of the spectrum, was used to mark the annular fluid (representing transport air and PF), while Rhodamine B, which fluoresces in the red part of the spectrum, was used to mark the flow through the central "mixing" nozzle. The dyes were diluted to 0.05 $mg.l^{-1}$ in accordance with recommendations in Arcoumanis *et al.* (1990) and stored in separate 200 litre tanks. A Fischer and Porter rotameter (½-27-G-10 tube and ½-GSVT- 44A float) was used to meter the central "mixing" flow. A second Fischer and Porter rotameter (1-27-G-10 tube and GNSVT64 float) was used to meter the annular flow. The nozzle arrangement is mounted centrally on vertical pipes, fixed externally and oriented vertically downwards with the exit plane located approximately 500 mm below the top of the tank. Fluid exits from the top of the tank, over weirs on all sides which ensure even overflow and limit interference with the mixing patterns in the tank.

The beam from a 5W Ar-ion laser (Spectra Physics) was focussed with a 1 m focal length spherical lens and spread with a cylindrical lens to create a thin, slightly divergent light sheet. The focal line of the light sheet was aligned with the nozzle centre-line. Images of a region from the nozzle exit plane to approximately 200 mm downstream from the nozzle were recorded at 1/1000 second shutter speed on Hi-8 digital video tape using a Panasonic lipstick camera with a Sony zoom lens. Photographs, also with shutter speeds of 1/1000 second, were taken on 800 ASA Fuji print film using a Pentax SLR camera with an 80 – 200 mm zoom lens. The cameras were not fitted with filters, to minimise loss of signal intensity and contrast between the two colours. As a result, scattered light from solid particles and air bubbles is evident in some images.

3.3.3 Experimental Procedures

The effects of varying the type of mixing nozzle (Figure 3.1b-e) on the "primary" annular flow are assessed at a single momentum ratio. In a second experiment, the effects of varying the momentum ratio of the FPJ to the "primary" annular flow, and varying the FPJ nozzle diameter are investigated. Flow visualisation and measurement of jet half widths and mean characteristics strain rates are used to assess these effects. Flow visualisation was performed with either both streams marked, or, with only one stream marked. The marked flows were video-recorded for approximately one minute for each condition. The images cover the axial region $0 \leq x/D_{A,2} \leq 5.25$, where $D_{A,2}$ is the outer diameter of the exiting annular stream (32.5 mm).

In the first series of experiments, the constant momentum ratio of mixing to primary fluids was $G_{MIX}/G_1 = 2.56$. This corresponds to the standard momentum ratio used with the 19PJ in the 130 kW combustion experiments (Chapter 5). All the nozzles shown in Figure 3.1, except the 10PJ were selected. The mixing fluid flow rate was 250 l.hr^{-1} (u = 1.95 ms^{-1}, Re = 13,150) and the primary fluid flow rate was 592 litres/hr (u = 0.44 ms^{-1}, Re = 14,170). The 19PJ throat Reynolds number was 23,300, which is sufficient to ensure consistent precession. Calculation of combined jet half widths was performed using images in which only the "primary" annular stream was marked, enabling the effect of the mixing jet on the primary stream to be determined.

In the second series of experiments the effect of varying the ratios of 19PJ and 10PJ exit momentum to primary momentum, G_{PJe}/G_1, on the scale of the large structures was investigated by varying the primary flow rate at fixed PJ flow rate. In this second series of experiments, combined jet half widths were calculated from video images in which only the PJ fluid was marked, to assess the effect of varying the annular momentum on the large scale structures emerging from the FPJ nozzle. By marking the PJ fluid rather than the annular fluid, the data signal to noise ratio at low annular flow rates was also improved. The full range of experimental conditions is given in Table 3.1.

Table 3.1. Experimental conditions - Water Flow LIF

Nozzle Name	*Central Mixing Flow ($l.hr^{-1}$)*	*Mixing jet exit velocity (ms^{-1})*	*Annular Flow ($l.hr^{-1}$)*	*Annular velocity (ms^{-1})*	G_{MIX}/G_1*
Annular	0	0	592	0.44	N/A
19PJ	250	1.95	592	0.44	2.56
Co-axial	250	1.95	592	0.44	2.56
Conically diverging	250	1.95	592	0.44	2.56
45° angled	250	1.95	592	0.44	2.56

Nozzle Name	*Central Mixing Flow ($l.hr^{-1}$)*	*Mixing jet exit velocity (ms^{-1})*	*Annular Flow ($l.hr^{-1}$)*	*Annular velocity (ms^{-1})*	G_{MIX}/G_1*
19PJ	250	1.95	262	0.19	10
	250	1.95	346	0.25	5.6
	250	1.95	487	0.36	2.9
	250	1.95	888	0.65	0.83

Nozzle Name	*Central Mixing Flow ($l.hr^{-1}$)*	*Mixing jet exit velocity (ms^{-1})*	*Annular Flow ($l.hr^{-1}$)*	*Annular velocity (ms^{-1})*	G_{MIX}/G_1*
10PJ	113	3.19	162	0.12	18
	113	3.19	346	0.25	4.2
	113	3.19	487	0.36	2.1
	113	3.19	888	0.65	0.62

* $G_{MIX} = G_{PJe}$ for FPJ nozzles, and is calculated at the nozzle exit.

3.3.4 Methods of data analysis

For a simple jet, the half width, $r_{1/2}$ is the radial position at which the average concentration is half the centre-line concentration. More generally $r_{1/2}$ is determined relative to the maximum local concentration which may occur away from the centre-line (Newbold, 1997). By using the half-width analysis to characterise large-scale structure within jets, and with relatively minor assumptions as discussed below, the need to correct for beam profile can be avoided (Newbold, 1997). The half width analysis also does not require high resolution of low concentration fluid, requiring only mean data, so that it is not sensitive to compromises in temporal resolution (slight blurring) or spatial resolution (not resolving the Batchelor scale). Not correcting for beam profile requires that beam divergence is minimal and results only in axial variation in beam intensity, and negligible attenuation. This technique is sufficiently accurate to quantify large differences in flow features, and so is adequate for the present requirements, which are primarily comparative. The validity of the current technique was proven by Newbold (1997) who measured the half angle of a simple round jet as 6.6°, similar to the value of 6° obtained by Becker *et al.*, (1967).

The present video images were digitised and converted to still images with a frame grabber, then adjusted for brightness and contrast and converted to 8 bit greyscale 640x480 pixel images. Commercial software, "Transform" from Fortner Research Ltd. is used for image processing following the method of Parham (1998). Using Transform, 40 digital images are summed and averaged to provide a mean flow field. Since the flow is directed from the top of the image downwards, each row of the mean digital image is oriented to represent positions of equal *x/D*. The background concentration is measured in the mean image, in a region well away from the jet. The maximum concentration in the jet is also identified, and a correction to the original concentration in each pixel, ξ_o, is performed using the relation,

$$\xi = \frac{\xi_o - \xi_{\min}}{\xi_{\max} - \xi_{\min}} \qquad 3\text{-}1$$

to create a corrected average image. Each pixel in the corrected average image is then divided by the maximum value in its own row rather than the centre-line value, as the maximum may occur away from the centre-line. The final image is thus a normalised mean image in which the concentration of marked fluid in each pixel is expressed as a fraction of the maximum value at the corresponding axial position, *x/D*. This equates to a normalised mixture fraction, $\frac{\overline{\xi}}{\overline{\xi}_{\max}}$.

3.4 Flow visualisation

Figure 3.3 shows typical images of each of the jets acting alone. Large structures are evident in each flow, in quantitative agreement with many previous investigations (eg. Crow and Champagne, 1971, Dahm *et al.*, 1992) The images are 0.001 s exposure photographs, except for the 45° angled and conically diverging jets which are 1/25 s video images, and consequently show some blurring. The right side of the conically diverging jet (Figure 3.3.f) appears to be more dominant than the left due to the location of the laser sheet relative to the cone support legs, as discussed earlier, and illustrated in Figure 1.3(c). The images in Figure 3.3 show that precession of the emerging jet generates significantly larger structures than any of the other jets. Note that in contrast to the other images, Figure 3.3(e) shows the 19PJ flow dominating a small annular flow. This image is presented due to the lack of availability of an image for the FPJ acting alone. The momentum ratio in this case was $G_{PJe}/G_1 = 10$.

Figure 3.4 presents instantaneous PLIF images (0.001 s exposure photographs) of each of the combined jets, examined for the condition $G_{MIX}/G_1 = 2.56$. In cases (a) – (c) the green fluid represents the co-annular flow and the red colour represents the central mixing jet flow. (The central mixing jet is unmarked in (c), which highlights its effect on the annular flow.) In cases (d) and (e) the yellow colour represents the PJ flow, and the red colour, the co-annular flow. In each case there is interaction between the annular flow and the mixing jet, but the FPJ flows, in contrast to the other flows, produce large discrete structures without bias away from the central axis. The 19PJ produces the largest structures of all.

The instantaneous images of the 19PJ-annular and 10-PJ annular flows presented in Figure 3.4(d) and (e) show that the emerging precessing jets entrain annular fluid from all directions. Consequently, it can be deduced that similarity in the interaction between precessing and annular jets relies on the momentum ratio between streams, which controls entrainment rates, rather than on the instantaneous position of the emerging PJ flow. Likewise, similarity does not rely on maintenance of a constant ratio of precession cycle time-scale ($1/f_p$) to annular fluid residence time in the NBZ, i.e.

$$\frac{\tau_{prec}}{\tau_1} = \frac{U_1}{f_p D} \neq \text{constant} \qquad 3\text{-}2$$

These deductions further strengthen the validity of the water technique, since maintenance of similarity in $\frac{\tau_{prec}}{\tau_1}$ between water and air cases is not feasible.

3.5 The effect of nozzle type on jet half angles and half widths

The minimum ignition distance observed in the 130 kW flames (reported in Chapter 5) using the current annular channel, is in the region of 100 mm, or $x/D_{A,2} \sim 3$. Since modelling using the current non-reacting technique is only valid in the region corresponding to the pre-ignition region of the flames, the following discussion will focus on measurements in the region $0 \leq x / D_{A,2} \leq 3$.

Figure 3.5 shows the locally normalised mean concentration map of the flow issuing from the baseline annular nozzle acting alone. Pseudo colours mark regions with different concentrations. The red pseudo colour is used for values of $\frac{\overline{\xi}}{\overline{\xi}_{max}} > 0.5$, blue for $\frac{\overline{\xi}}{\overline{\xi}_{max}} < 0.5$ and white for the transition at $\frac{\overline{\xi}}{\overline{\xi}_{max}} = 0.5$. This colour scheme is useful for identifying the 0.5 concentration contour. The 0.5 locally normalised concentration contour is overlaid on the colour scheme to increase clarity. The technique used to determine jet half angles and half widths is illustrated in Figure 3.5. The initial jet half angle, $\theta_{1/2}$, is calculated by drawing a straight line along the 0.5 concentration contour (following the roots rather than the tips of any protrusions) in the initial region of the jet and measuring its angle to an axial line. In order to minimise attenuation errors, the side of the image closest to the light source (the left side) is used for calculation of the jet half angle of the annular jet. The measured value of $\theta_{1/2}$ of the annular jet shown in Figure 3.5 is 5.6°. This compares well with the half angle of a simple round jet, measured at 6° by Becker *et al.*, (1967), and 6.6° by Newbold (1997), using the current technique.

The jet half width can be calculated from the jet half angle, at any axial position, x, using the relationship,

$$r_{1/2} = x \tan \theta_{1/2} + 0.5(D_{A,2}) \qquad 3\text{-}3$$

Using this method, the half width of the annular jet at $x/D_{A,2} = 3$, is $r_{1/2} = 0.79D_{A,2}$. Alternatively, the half width can be calculated by using the 50% contours on both sides of the jet. Use of the right side of the flow, relies on the assumption that attenuation errors, produced as the beam is partially absorbed by the marking fluid, are small. The good axial symmetry of the 50% contour in Figure 3.5 verifies that attenuation errors are small. The annular jet half width measured directly from Figure 3.5, using 50% contours on both sides of the flow is also $0.79D_{A,2}$. This latter method of determining the jet half width is the most

appropriate method for the conically diverging and 45° directed combined jets for reasons outlined below, and to be consistent, was adopted for all the combined jets.

Figure 3.6 shows locally normalised mean concentration plots for combined flows with $G_{MIX}/G_1 = 2.56$. Only the "primary" annular stream was marked, enabling the effect of the mixing jet on the primary stream to be determined. Figure 3.6(a) demonstrates the dramatic influence which the 19PJ flow has on the annular flow. Initially in the region, $0 \le x/D_{A,2} \le 2$ the combined flow spreads rapidly at a mean half angle of 29°. The rate of spread then reduces, so that over the larger region, $0 \le x/D_{A,2} \le 3$, the mean half angle is 23°, still a dramatic increase over that of the annular jet alone (5.6°). The jet half width, calculated from 50% contours on both sides of the jet at $x/D_{A,2} = 3$, is $1.23D_{A,2}$. In contrast to the PJ flow, the half angle of the co-axial jet (Figure 3.6b) is consistent throughout the region, $0 \le x/D_{A,2} \le 3$, and at 3.4°, is less than that of the annular jet alone, presumably because the central jet entrains the annular jet into it. The half width of the co-axial jet at $x/D_{A,2} = 3$, is $0.50D_{A,2}$.

The conically diverging jet interacts with the annular jet to produce a conical jet with a central region with low annular fluid concentration (Figure 3.6c). It can be expected that a central reverse flow zone is established by the bluff body, which can provide benefits to combustion (Beer and Chigier, 1972). However the present images suggest that such a phenomenon is not dominant and does not produce large structures which span the entire flow. Since the combined jet spreads as a conical fan without filling the central region, the most accurate representation of the scale of the dominant structures can be obtained by considering each side of the fan separately. The right fan of the jet is taken to be representative of the entire jet, as discussed earlier. Since the right fan of the jet is not symmetric about the nozzle axis, the total angle between straight lines drawn along the 50 % contours on each side of the fan is measured and halved to give a half angle, $\theta_{1/2}$, of 8.6°. The half width determined from the same straight lines at $x/D_{A,2} = 3$, is $0.52D_{A,2}$.

The "45° directed jet" was aligned with the plane of the light sheet, so that its structure could be observed. Figure 3.6(d) shows that when combined with the annular jet, the 45° directed jet, produces a non-symmetric jet. The bulk of the annular fluid maintains a generally axial trajectory, whilst only a relatively small fraction is entrained into the directed jet, thus adopting its trajectory. A lower concentration of annular fluid can be found in the region

between the two jets. The large scale structures in the flow are thus best characterised by the half angles of the two separate sections of the jet. The right side of the jet is more dominant than the left and is taken to be representative of the entire jet. The procedure described above for the conical jet was used to calculate a jet half angle of 8.3° and half width of $0.69D_{A,2}$ at $x/D_{A,2} = 3$. In contrast, to the conically diverging and 45° directed jets, the combined 19PJ - annular jet is three dimensional and symmetric so the measured half width genuinely represent the scale of the dominant structures, which are substantially greater than all other mixing nozzles tested. Normalised jet half widths at $x/D_{A,2} = 3$, are summarised in Table 3.2. The data summarised in Table 3.2 demonstrates that the 19PJ flow enhances large scale structure in the annular flow relative to all other nozzles.

Table 3.2 Half widths of combined jet flows with $G_{MIX}/G_1 = 2.56$*

Jet	$r_{1/2}/D_{A,2}$ $(at\ x/D_{A,2} = 3)$
19PJ	1.23
Co-axial	0.50
Conically diverging	0.52
45° directed	0.69
Annular*	0.74

*The annular jet is included for comparison

3.6 Strain rates of flows with $G_{MIX}/G_1 = 2.56$

A quantitative measure of the effect of precession on the scale of large structures has been demonstrated in the half width measurements above. Time series of visualisation images, collected on videotape, can also be used to measure the celerity or convection velocity, S, of the large structures. They can also be used to estimate the characteristic residence times of structures within the pre-ignition region (where the isothermal technique is relevant) of analogous combusting cases, by scaling differences in velocity and allowing for expansion of gases when heated. As noted earlier, the minimum ignition distance observed in the 130 kW flames is $\frac{x}{D_{A,2}} \sim 3$, but the pre-ignition region is typically $\frac{x}{D_{A,2}} < 5$. Consequently, the convection velocity of the large structures is obtained by manually tracking their axial position, X_{LS}, from frame to frame on video tape, and plotting it as a function of time, in the region $\frac{x}{D_{A,2}} < 5$.

Figure 3.7(a) shows a sequence of consecutive video images for the annular flow alone. Figure 3.7(b-e) show the combined flows with $G_{MIX}/G_1 = 2.56$. In each case only the annular fluid was marked with dye. The convection velocities of structures in the annular, 45° directed and conically diverging flows are relatively consistent, as can be observed by examination of successive frames in Figure 3.7. These flows all have a steady source of momentum behind (upstream of) structures. In contrast, the momentum source emanating from a PJ nozzle continuously moves as the jet precesses. Consequently, the convection velocities of the large structures in PJ flows are lower and considerably more variable than those in the other flows (Figure 3.7e). Structures on the outer boundaries of the PJ flow tend to have very low convection velocities whilst those closer to the centre-line have convection velocities more comparable with those of the other flows studied. The visualisation also highlights the presence of some structures that penetrate through the annular flow and become "isolated". From close observation of many such video sequences it can be hypothesised that these isolated structures result from variations in cycle to cycle precessional motion (an effect observed only in FPJ flows, and not in MPJ flows). Further work may clarify this point. The structures that become isolated have a much lower convection velocity than average and may be important in aiding flame stability, particularly if they trap particles and so increase their residence times.

The co-axial jet, like the PJ, generates structures with very low velocities near to the boundary of the flow. Such structures are ejected from the annular stream during the entrainment process, punching through the momentum driven flow in a manner akin to structures in the PJ flow. However, they are much smaller (~ 2 mm) than those in PJ flows (~ 30 mm), and represent a much less significant proportion of the structures.

Figure 3.8 presents the measured values of X_{LS} as a function of time based on visual tracking of the edge of large structures. Values of X_{LS} were measured for all of the combined flows with $G_{MIX}/G_1 = 2.56$. The structures tracked were chosen at random. In the PJ and co-axial cases, the trajectory of one isolated structure, with a convection velocity considerably lower than average, is presented and is plotted with diamonds in Figure 3.8 (b and e).

Figure 3.9 shows the local mean convection velocities, calculated from the data plotted in Figure 3.8, as a function of X_{LS}. A general trend of reduced convection velocity with increased axial distance is evident as expected. (The slowest structure in the 19PJ and co-axial cases, as identified earlier, were ignored when calculating convection velocities). Figure 3.10 summarises the mean and standard deviation (σ) axial structure convection velocities of the flows. The PJ flow causes a reduction in S relative to the annular stream despite an increase in mean exit velocity, caused by the additional PJ flow. The other jets cause increases in S, with the greatest increases produced by flows with least spread. In some cases it was not possible to track structures in the region $X_{LS} < 60$ mm, due to the high velocities there. Consequently, the mean convection velocities shown in Figure 3.10 were calculated from the time taken for the structure to move through the remainder of the region, $\frac{x}{D_{A,2}} < 5$, ie. through the region 60 mm $< X_{LS} <$ 160 mm. The measured standard deviations (Figure 3.10) illustrate the level of random variation in S.

A characteristic local strain rate, defined here as $S/r_{1/2}$, can also be calculated from the above data. These local strain rates are shown later to be important in determining gas phase reaction rates within the ignition region. Figure 3.11 shows the characteristic local strain rates of the combined flows with $G_{MIX}/G_1 = 2.56$ at $x/D_{A,2} = 3$. The PJ flow causes a two fold **reduction** in the local strain rate relative to the annular jet alone, whereas the 45° directed and conically diverging jets cause a 60% **increase** in the annular jet local strain rate by over 60%, and the co-axial jet increases the local strain rate by 200%.

3.7 The effect of PJ nozzle size and momentum ratio on jet half widths

The mean locally normalised concentration maps obtained when varying the ratio of precessing jet to annular momentum, G_{PJe}/G_1, are shown in Figures 3.12 and 3.13 for the 19PJ and 10PJ flows respectively. In these cases the PJ flow, rather than the annular flow, was marked with dye and the figures therefore show the effect of the variable annular momentum on the PJ flow. The four 19PJ flows (Figure 3.12a-d) have similar initial jet half angles. However, the axial distance over which the jet maintains its initial angle reduces with decreasing G_{PJe}/G_1. A similar trend is observed for the 10PJ flows (Figure 3.13a-d). Consequently, in these flows, the initial half angle is not as effective a measure of the characteristic length scale as the half width.

Figure 3.14 shows the measured jet half widths at $x/D_{A,2}$ = 3 for the two PJ nozzles. Normalised jet half widths of 19PJ flows, $r_{1/2}/D_{A,2}$ increase from 0.74 to 1.22 as the momentum ratio G_{PJe}/G_1 is increased from 0 (annular flow only) to 10. In contrast, only the highest value of G_{PJe}/G_1 tested with the 10 mm PJ nozzle produces an increase in $r_{1/2}$ compared to the annular jet, despite the clear differences in structure between the annular flow and 10PJ flows (eg. comparing Figure 3.4a with Figure 3.4d). In Figure 3.15, the half-width data are presented, normalised relative to the PJ nozzle diameter, rather than the annular channel diameter. This plot indicates that the 10PJ flows have a greater relative spread than the 19 PJ flows, demonstrating the effects of both the annular and PJ flows on the half width of the combined flow. Consequently, the use of D as a length scale for normalisation is inappropriate and the low half widths of the 10PJ flows shown in Figure 3.14 are deduced to be the result of the small PJ nozzle to annular channel diameter, $D/D_{A,2}$. A conclusion, which may be drawn, is that most of the 10PJ flows, while altering the nature of mixing in manner characteristic of precessing jets, do not alter the characteristic length scale of the annular jet because of the small PJ nozzle to annular channel diameter, $D/D_{A,2}$. In summary, jet half widths of the PJ-annular flows generally increase with the momentum ratio G_{PJe}/G_1, with the exception of the 10PJ flows with $G_{PJe}/G_1 < 5$, for which the jet half width is similar to that of the annular jet alone.

3.8 The effect of G_{PJe}/G_1 on strain rates

Characteristic convection velocities were determined for a series of flows in which the momentum ratio of PJ and annular flows was varied at a constant PJ flow rate. The raw structure axial position and residence time data is plotted in Figure 3.16 for the 19PJ and in Figure 3.17 for the 10PJ. Measurements were performed for a small number of structures to provide indicative results. Again, the structures were chosen at random. The mean convection velocities are summarised in Figure 3.18, and the standard deviations in S are shown in Figure 3.19. The data suggests that within the level of accuracy of the data, S is relatively constant over the range of momentum ratios tested for the 19PJ, whilst showing an exponential decay with increasing G_{PJe}/G_1 for the 10PJ flows.

Figure 3.20 shows the characteristic local strain rates of the PJ-annular flows, with $r_{1/2}$ calculated at $x/D_{A,2} = 3$. The data needs to be interpreted bearing in mind its level of accuracy. Since the PJ flow was marked with dye, it is the PJ structures that are being followed. In all cases the PJ exit velocity is greater than the annular exit velocity. For example the 19PJ exit velocity is 1.95 ms^{-1} and the 10PJ exit velocity is 3.19 ms^{-1}, compared to a maximum annular exit velocity of 0.66 ms^{-1}. Consequently, the mean structure velocity is a measure of the extent to which the annular flow modifies the PJ structure velocity, rather than a measure of the mean convection velocity of the entire combined flow. Hence, correcting the convection velocity data to account for the variable total flow-rates used, is not informative.

The PJ structure convection velocities in the 19PJ flows (Figure 3.18), have values only slightly higher than that observed for the 19PJ flow alone (0.118 ms^{-1}). It can be deduced from this similarity in convection velocities, that PJ structures are able to penetrate through, and remain relatively unaffected by, the annular flow, even at the lowest values of G_{PJe}/G_1 tested. The relatively small change in 19PJ half widths for $G_{PJe}/G_1 > 1$ (Figure 3.14) also support this conclusion. Structure convection velocities in most of the 10 PJ flows also show a degree of consistency. The major exception is the case where G_{PJe}/G_1 is decreased to 0.62. In this case the mean structure convection velocity increased dramatically, to 0.33ms^{-1}. This value is similar to that which would be obtained by scaling the structure convection velocity observed for the baseline annular case (0.25 ms^{-1}) by the ratio of annular flow rates used in the two cases (592 $kg.hr^{-1}$ in the baseline case, compared to 888 $kg.hr^{-1}$ in the current case). Consequently, the structure convection velocity is deduced to be controlled by the

annular flow in this case, indicating that structures are confined within the annular flow and that the momentum of the annular flow dominates.

The local strain rates plotted in Figure 3.20 reflect the points made in the above discussion. They are the characteristic strain rates of the large structures that emanate from the PJ nozzle, rather than being representative of the entire flow field or the annular flow. The low structure strain rates for the 19 PJ flows demonstrate that structures characteristic of PJ flows persist, whereas for the 10PJ at low values of G_{PJe}/G_1, the structures take on characteristics of the annular flow. The higher strain rates of the 10PJ flows at low values of G_{PJe}/G_1 are influenced by the small diameter ratio, $D/D_{A,2}$.

3.9 Conclusions

The effect of a range of alternative central mixing jets; all with equal exit cross-sectional areas, on the structure of a surrounding annular jet were examined. The alternative central mixing nozzles were designed as steady analogues of the 19 mm PJ nozzle, and were operated to provide the same ratio of mixing jet exit momentum to annular jet momentum, $G_{MIX}/G_1 = 2.56$. Flow visualisation using the LIF technique demonstrated that:

- The FPJ flows, in contrast to the other flows, produce large discrete structures without bias away from the central axis. Some structures penetrate through the annular flow and become "isolated" from the bulk flow. The 19PJ produces larger structures than the other mixing jets. These findings highlight the importance of large-scale unsteadiness in the emerging jet.

The jet half widths, $r_{1/2}$, determined at $x/D_{A,2} = 3$, corresponding to a position in the pre-ignition region of the flames, confirm that the 19PJ increases the scale of structures in the annular jet. The other mixing jets reduced the characteristic size of structures in the annular flow. The 45° directed, and the conically diverging nozzles simulate the initial trajectory of the PJ flow at frequencies of zero and infinity respectively. The failure of these nozzles to enlarge the structure of turbulence in the annular jet illustrates that it is the unsteady nature of the PJ flow, rather than the initial spread of the PJ flow, that is responsible for enlarging the structure of turbulence. The specific findings are:

- Annular jet alone, $r_{1/2} = 0.79D_{A,2}$.
- 19PJ – annular jet, $r_{1/2} = 1.23D_{A,2}$.
- Co-axial jet, $r_{1/2} = 0.50D_{A,2}$.
- 45° directed jet, $r_{1/2} = 0.69D_{A,2}$
- Conically diverging jet, $r_{1/2} = 0.52D_{A,2}$

Convection velocities of structures were obtained by tracking structures on consecutive video tape frames. The key findings are:

- Combined PJ - annular flows produced the widest range of convection velocities.
- "Isolated" large structures (~30 mm in diameter) located beyond the mean half width of the 19PJ flow were observed to move with the slowest convection velocities of any structures in any of the flows. It is hypothesised that these structures may result from variability in cycle to cycle precession, and can provide the conditions required to reduce

the ignition distance in flames, ie. extended residence time, which aids particle heating, and low local velocities.

- The mean convection velocity of structures in the annular flow alone were 0.24 ms^{-1}.
- In the combined 19PJ-annular flow, with $G_{PJe}/G_1 = 2.56$, the mean convection velocity is reduced to 0.21 ms^{-1} despite an increase in total flow-rate relative to the annular flow.
- In contrast, the steady jets all caused increases the mean convection velocity of the combined mixing jet - annular flow to levels in the range from 0.34 to 0.54 ms^{-1}.

Combining measurements of convection velocity and half width, allows a characteristic strain rate to be obtained for each flow. The key findings are:

- The 19PJ flow reduces the characteristic strain of the annular flow from 10 s^{-1} to 5 s^{-1}.
- Steady jet flows increase the strain rate from 10 s^{-1} to values in the range 17 to 32 s^{-1}.

The effects of variations in the physical size of the central PJ nozzle and the exit momentum ratio G_{PJe}/G_1 were investigated. The key findings are:

- Structures produced by the 19 mm PJ nozzle, with a nozzle to annular channel outer diameter ratio of 0.58, produced mean half widths in the range $1.12D_{A,2}$ to $1.22D_{A,2}$ over the entire range of momentum ratios tested ($0.8 < G_{PJe}/G_1 < 10$). These half widths were considerably larger than those of the annular jet alone ($0.74D_{A,2}$). The characteristic strain rates of the 19PJ-annular flows were all in the region of 4 s^{-1}, compared to $10s^{-1}$ for the annular jet alone, showing that even the condition with the lowest PJ momentum flux produced a significant impact on the scale of mixing.
- Structures produced by the 10 mm PJ nozzle, with a nozzle to annular channel outer diameter ratio of 0.31, produce mean half widths similar to those of the annular jet, except when G_{PJe}/G_1 is increased to 18, when the half width increases to $0.93D_{A,2}$. The strain rates of 10PJ flows were also similar to those of the annular jets at low values of G_{PJe}/G_1, but an increase in momentum to $G_{PJe}/G_1 = 2$ was sufficient to reduce the strain rate to a level similar to that of the 19PJ flows. Therefore higher levels of G_{PJe}/G_1 are required to significantly enhance large scale mixing when the PJ to annular diameter ratio is small.

The evidence presented here confirms the first hypothesis presented in section 1.8, that "*the structure of turbulence in an annular jet used to transport coal particles can be beneficially altered by PJ flows, to enhance large scale turbulence at the expense of small scale turbulence*". As such PJ nozzles are viable tools for investigating hypotheses 2 – 4.

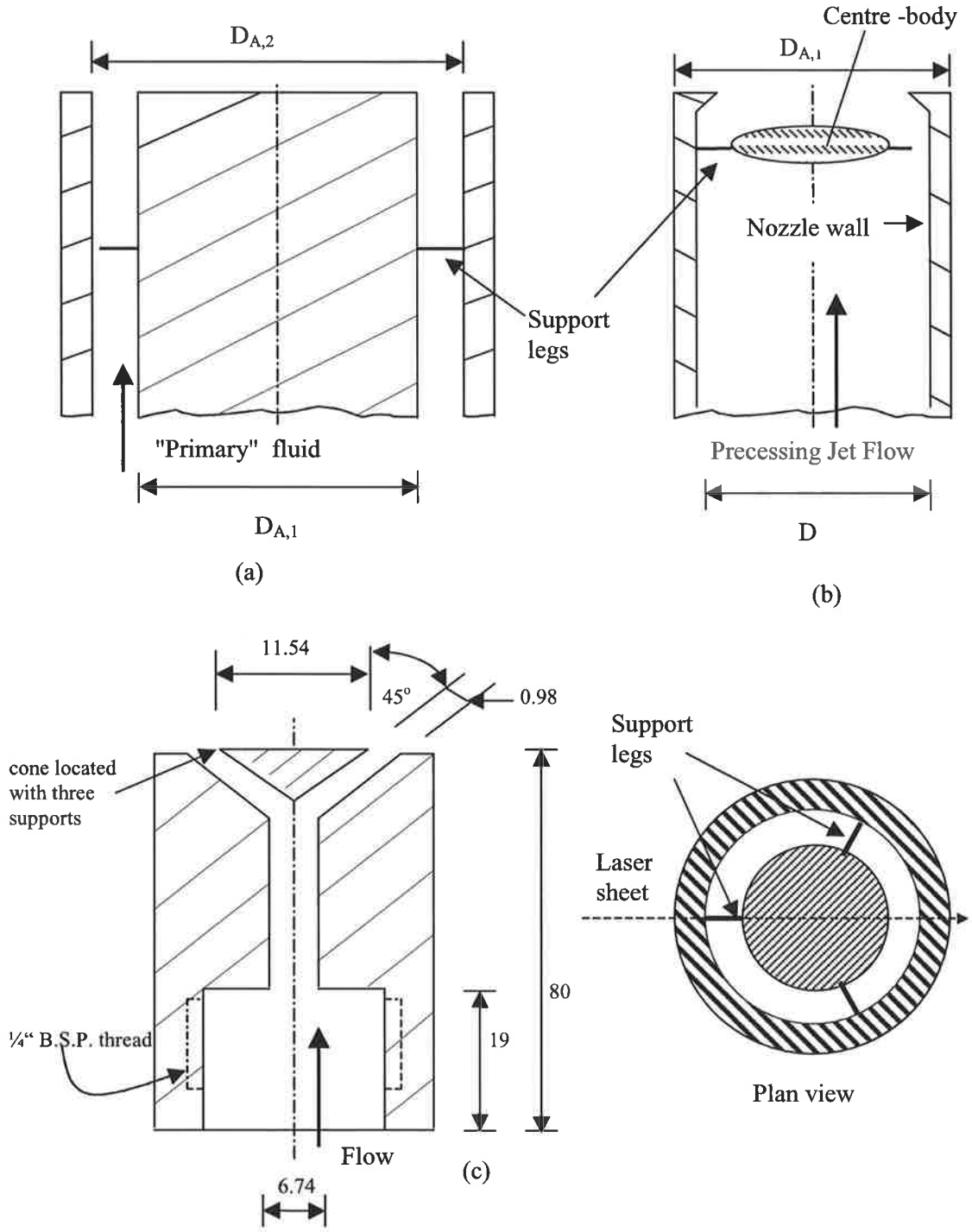

Figure 3.1 Schematic diagrams of nozzles used in water LIF experiments.
(a) Mono-channel annular, showing the baseline annular channel used for "primary" fluid, $D_{A,1}$ = 24.0 mm, $D_{A,2}$ = 32.5 mm. The remaining parts show the central mixing nozzles that can be fitted inside the annular channel in place of the bluff body.
(b) PJ nozzle, two nozzles with D = 10 and 19 mm, respectively, and $D_{A,1}$ = 24 mm
(c) Conically diverging jet, with 3 support legs for central cone (each 1.2 mm in diameter, which reduced the jet cross-section to equal other jets). This nozzle models a precession frequency = ∞.

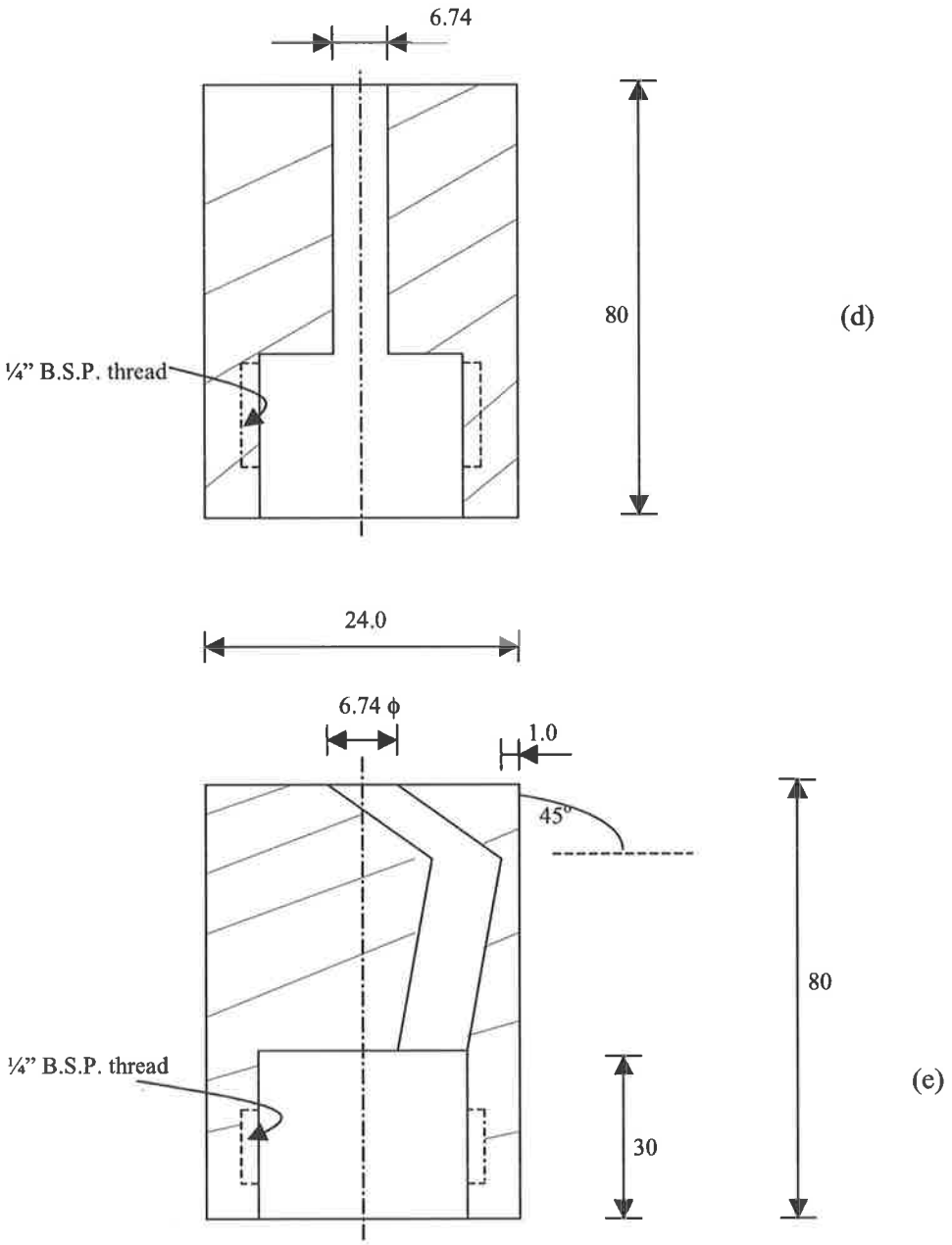

Figure 3.1 (cont.) Schematic diagrams of central nozzles used in LIF experiments.
(d) Simple (co-axial), $d = 6.74$ mm (steady jet, not deflected at exit)
(e) 45° angled jet, $d = 6.74$ mm (jet deflected at exit with $f_p = 0$)

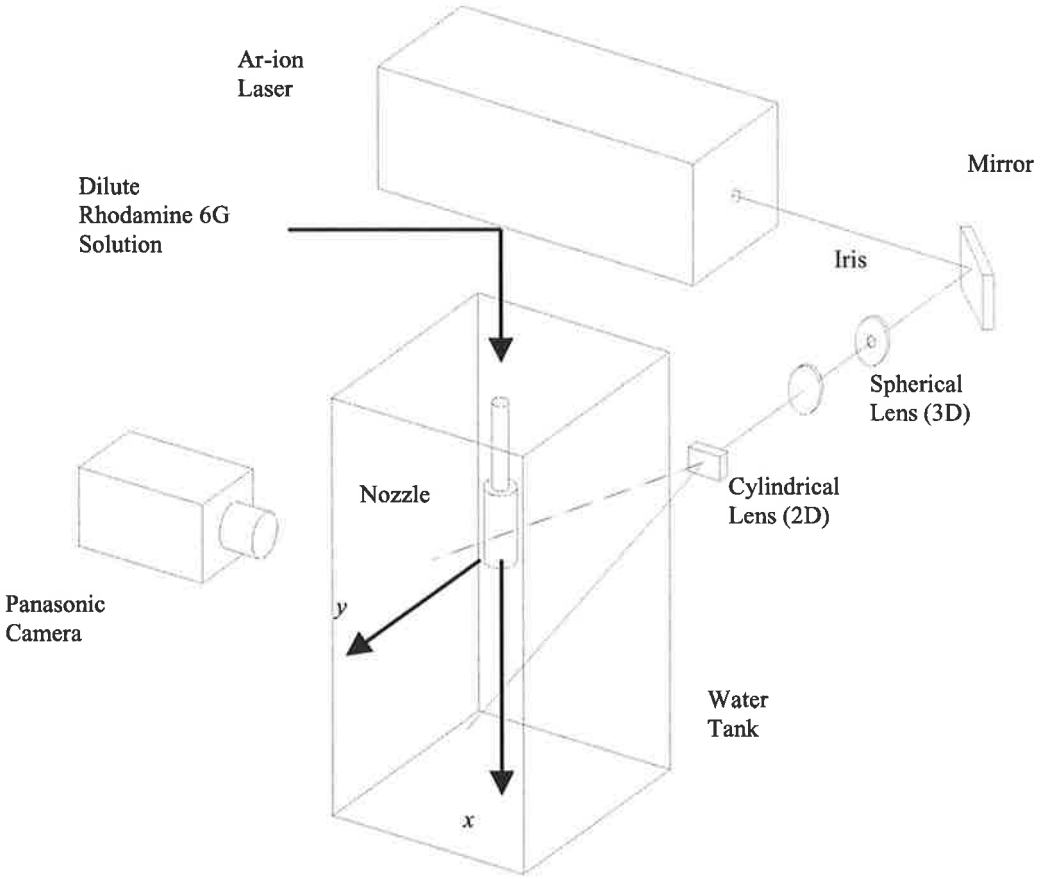

Figure 3.2. A schematic diagram of the optical experimental arrangement used for planar laser-induced fluorescence (PLIF) experiments in the water tank facility for flow visualisation (Newbold, 1997).

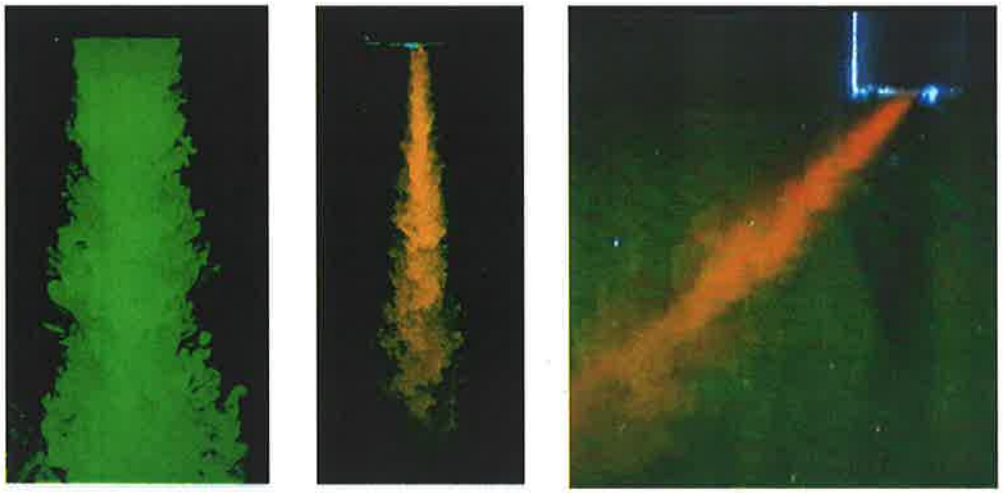

(a) (b) (c)

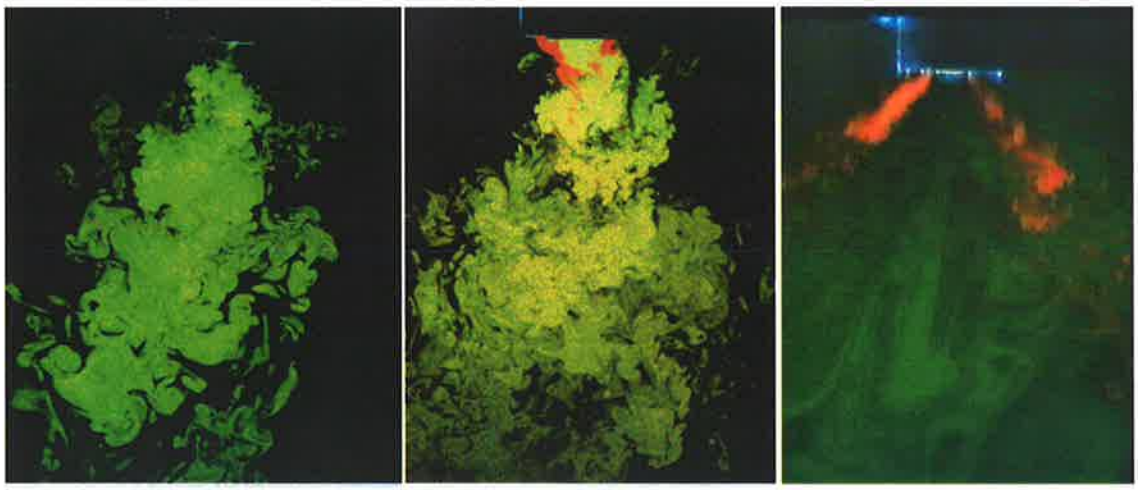

(d) (e) (f)

Figure 3.3 Planar Laser Induced Fluorescence (PLIF) images of each of the jets issuing alone into an unconfined environment. In turn they are: (a) annular jet (0.44 ms^{-1}), (b) axial jet (1.95 ms^{-1}), (c) 45° angled jet (1.95 ms^{-1}), (d) 10PJ (3.19 ms^{-1}), (e) 19PJ (1.95 ms^{-1}), (f) conically diverging (1.95 ms^{-1}).

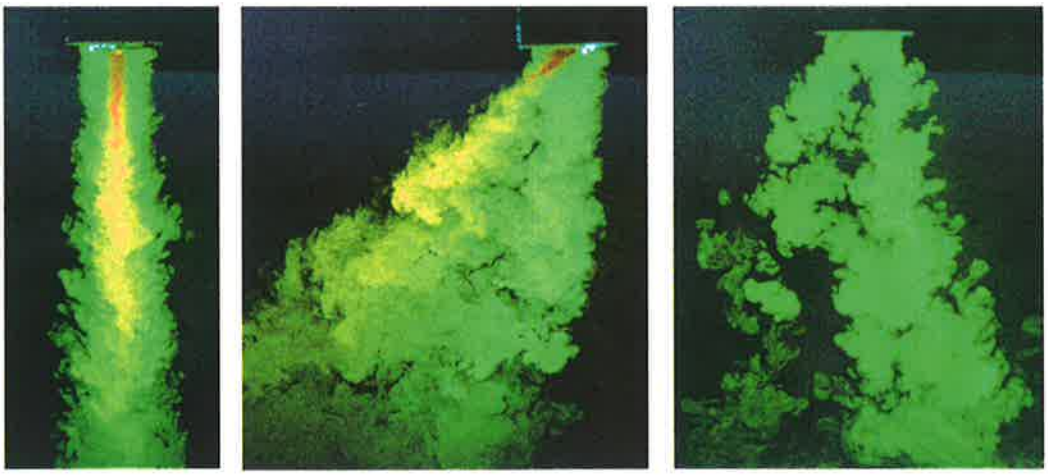

(a) (b) (c)

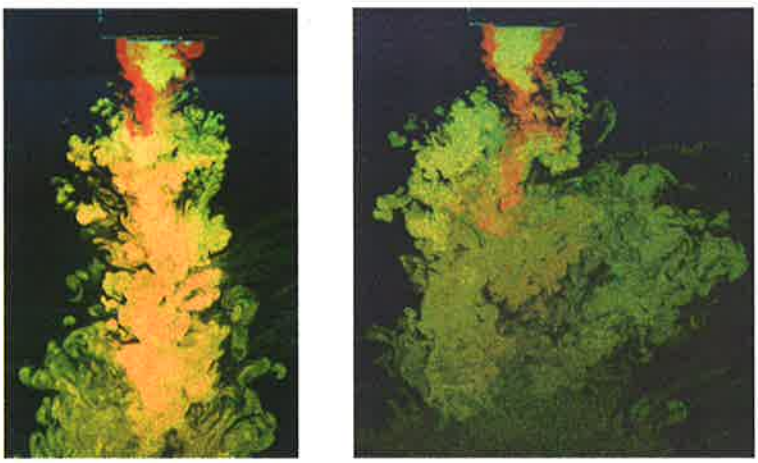

(d) (e)

Figure 3.4 Instantaneous PLIF images (0.001 s exposure) of the combined jets with $G_{MIX}/G_1 = 2.56$, in an unconfined environment. The jets are:
(a) co-axial jet (b) 45° angled jet (c) conically diverging jet (d) 10PJ (e) 19PJ.
In cases (a) – (c) the green fluid represents the co-annular flow and the red colour represents the central mixing jet flow. The central mixing jet is unmarked in (c), which highlights its effect on the annular flow. In cases (d) and (e) the yellow colour represents the PJ flow and the red colour the co- annular flow.

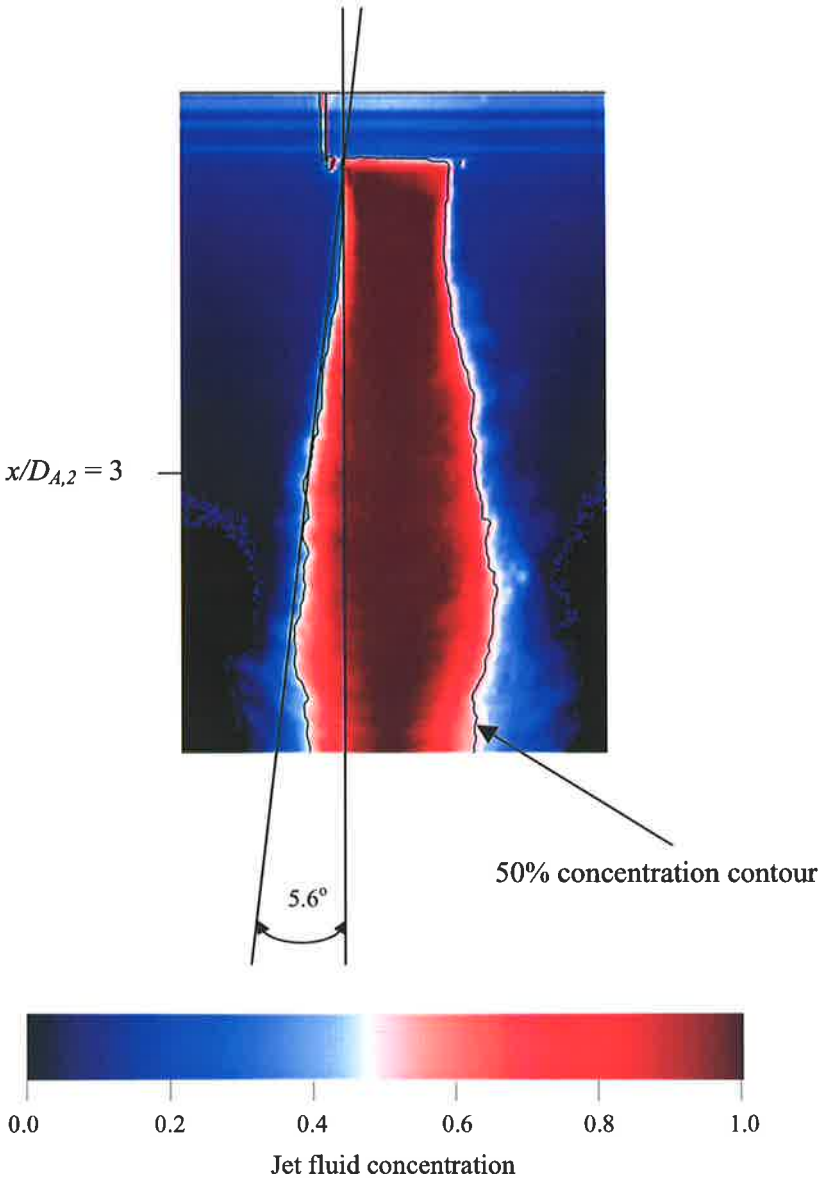

Figure 3.5 Normalised mean jet fluid concentration map of the annular jet (0.44 ms^{-1}), showing method for measuring jet half angle, $\theta_{1/2}$, and the axial location $x/D_{A,2} = 3$, at which the half width, $r_{1/2}$, is measured.

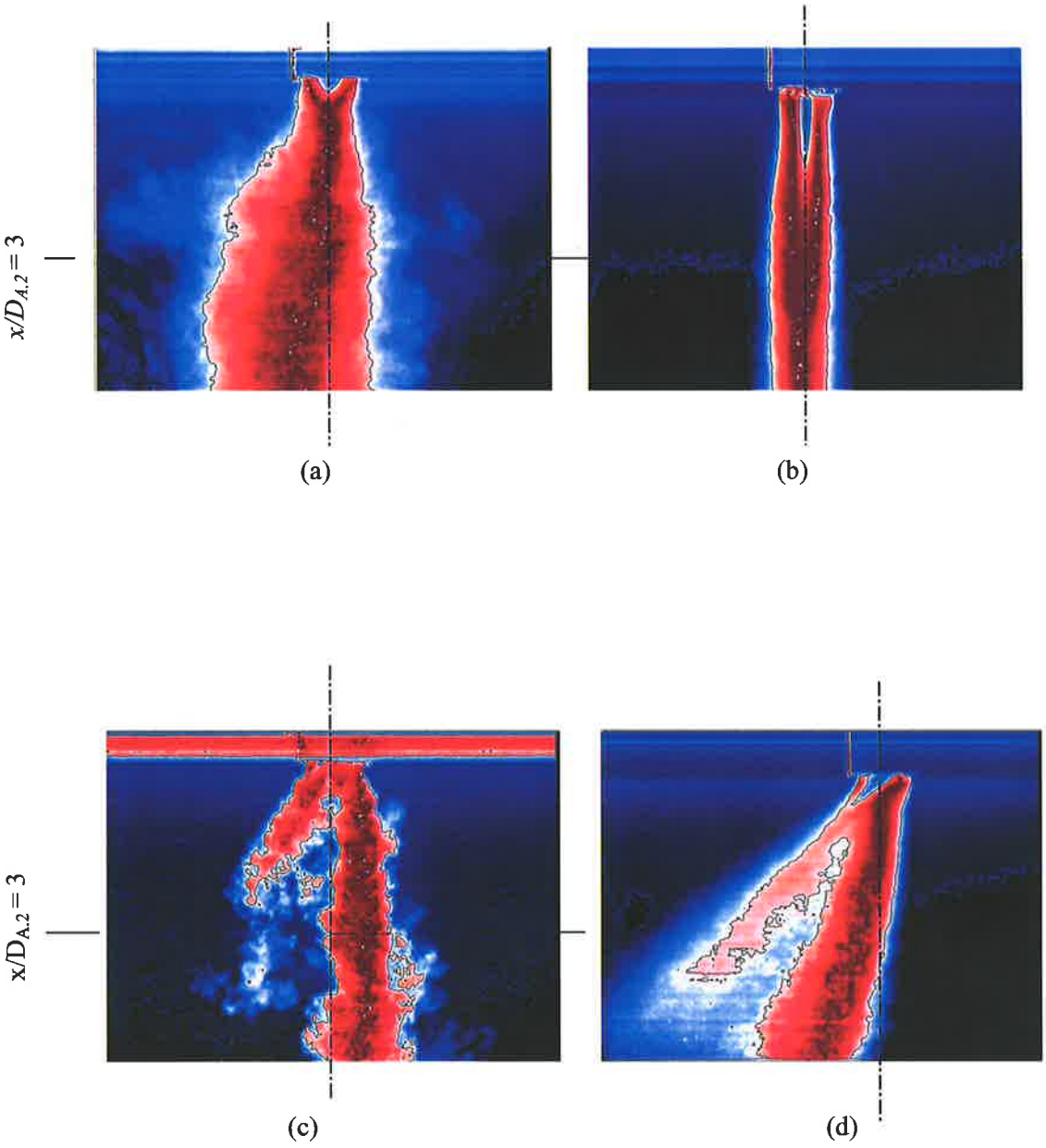

Figure 3.6 Normalised mean concentration of annular fluid in combined mixing – annular flows with $G_{MIX}/G_1 = 2.56$.
(a) 19PJ, (b) 6.74 mm simple co-axial jet, (c) conically diverging jet, (d) 6.74 mm simple 45° directed jet

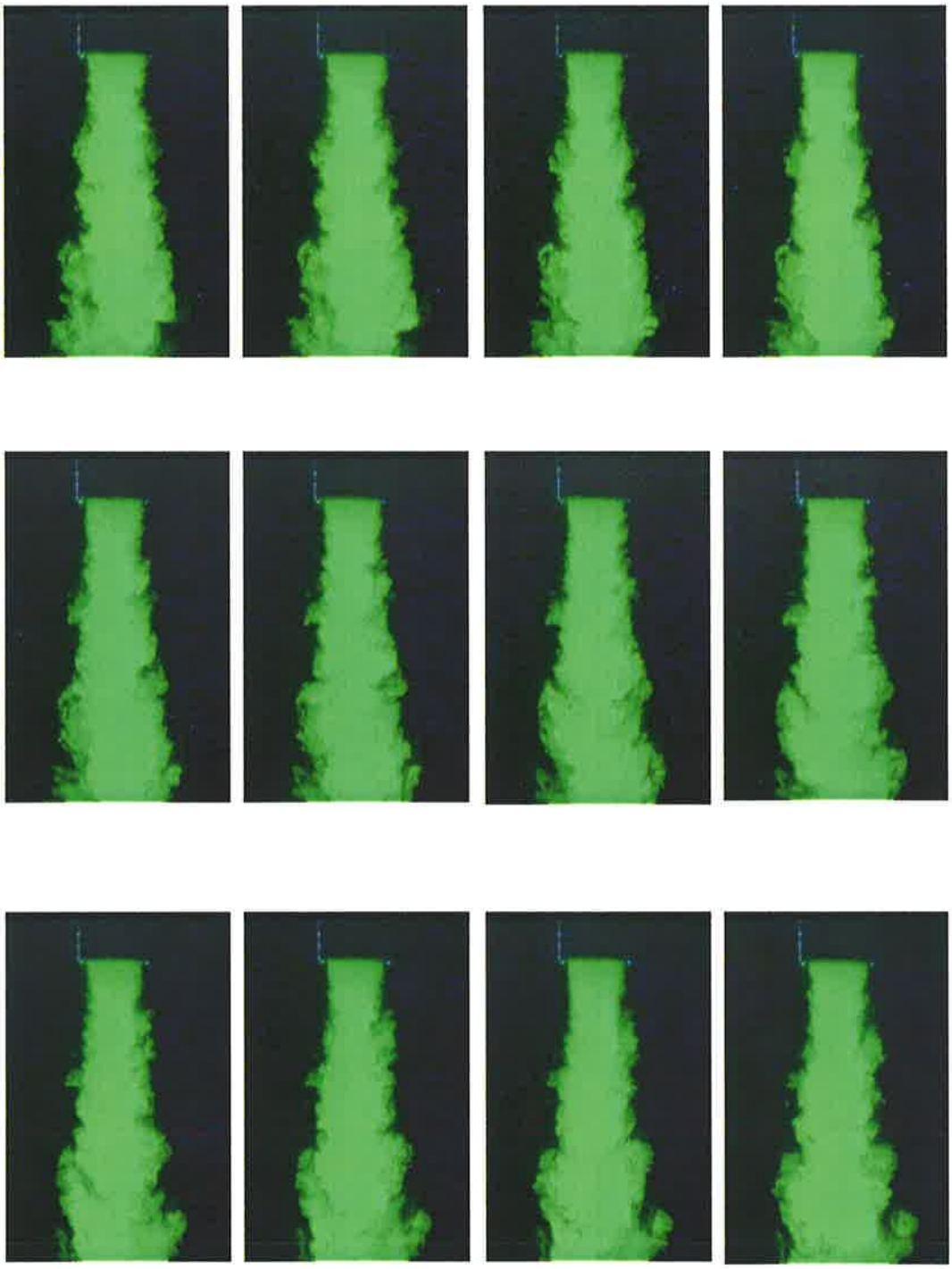

Figure 3.7 (a) 12 consecutive LIF video images of the centre-line cross-section of the annular flow alone, marked with fluorescein and discharging into quiescent surroundings. Annular exit velocity = 0.44 ms^{-1}. Video framing rate 25 frames per second. Image sequence follows rows from left to right starting at top left.

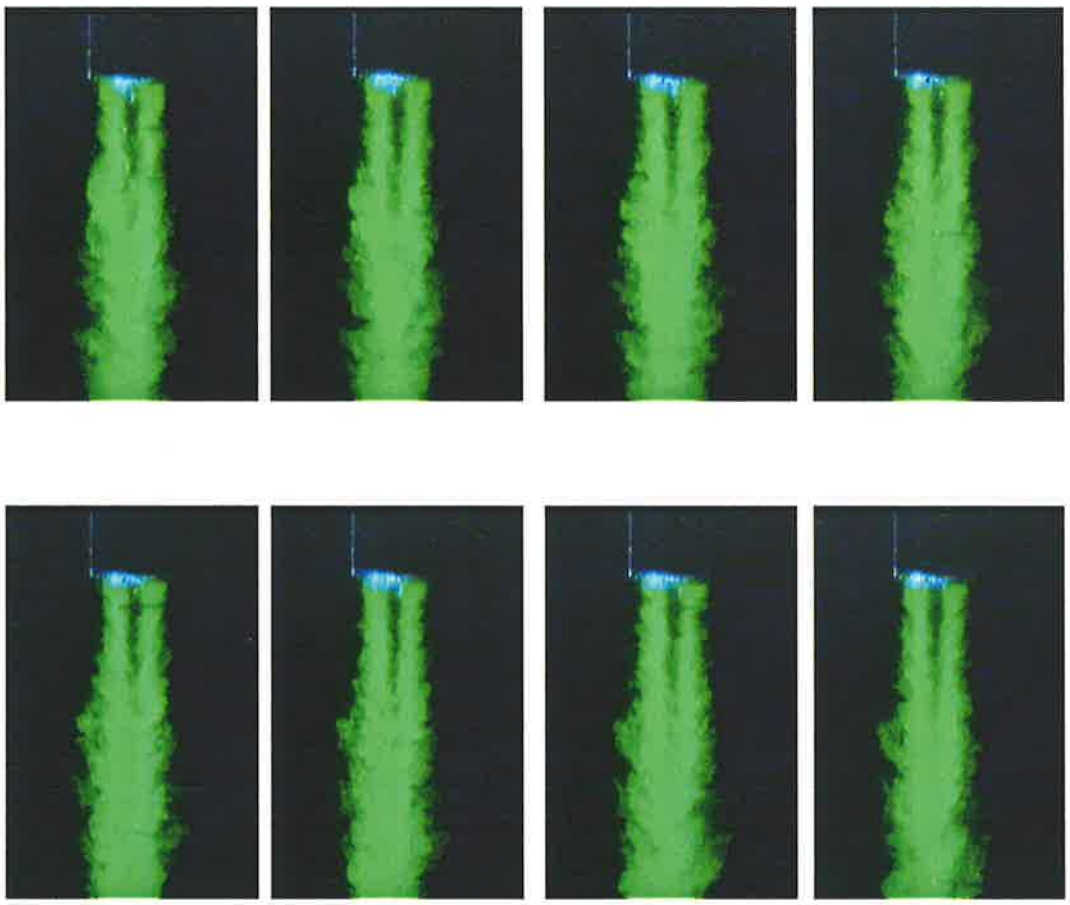

Figure 3.7 (b) A sequence of eight consecutive LIF images of the co-axial jet with $G_{MIX}/G_1 = 2.56$. Only the annular fluid was marked with dye. Annular exit velocity = 0.44 ms^{-1}. Axial jet exit velocity = 1.95 ms^{-1}. Video framing rate 25 fps. Image sequence follows rows from left to right starting at top left.

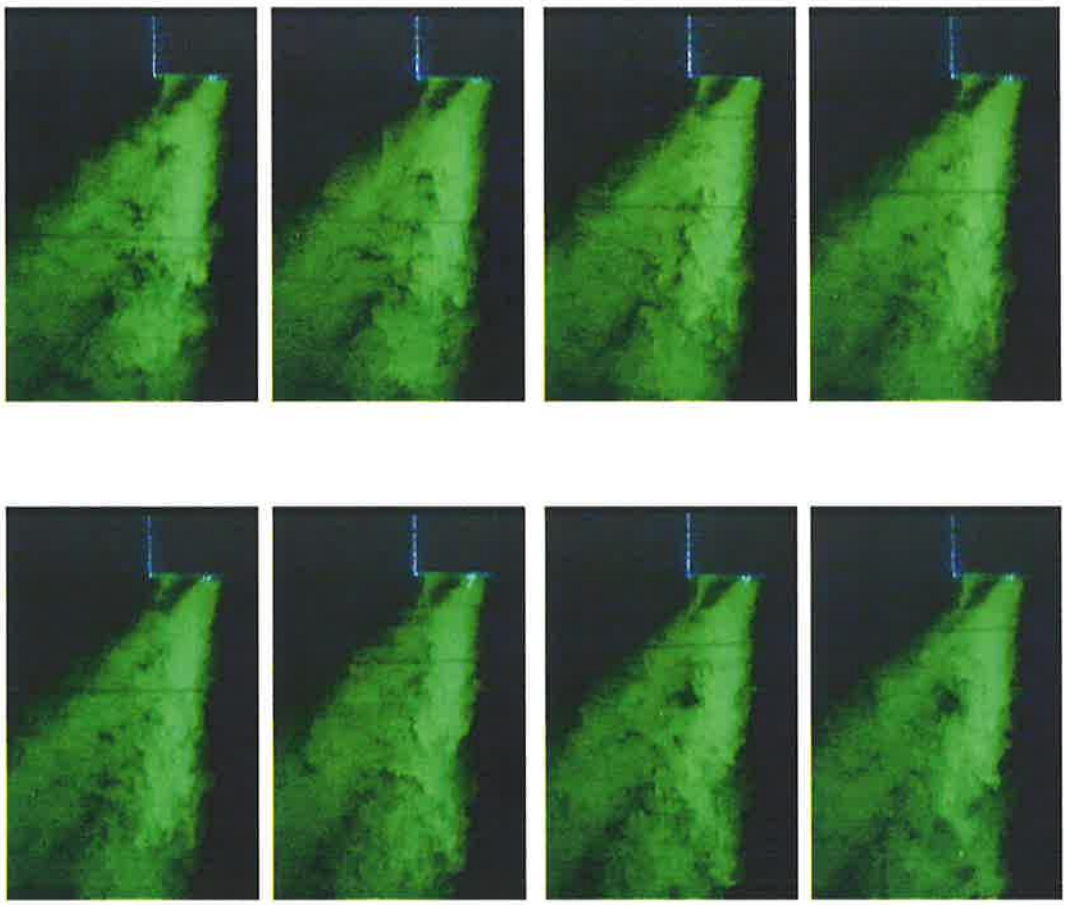

Figure 3.7 (c) A sequence of eight consecutive LIF images of the the 45° directed jet with $G_{MIX}/G_1 = 2.56$. Only the annular fluid was marked with dye. Annular exit velocity = 0.44 ms^{-1}, 45° directed jet exit velocity = 1.95 ms^{-1}. Video framing rate 25 fps. Image sequence follows rows from left to right starting at top left.

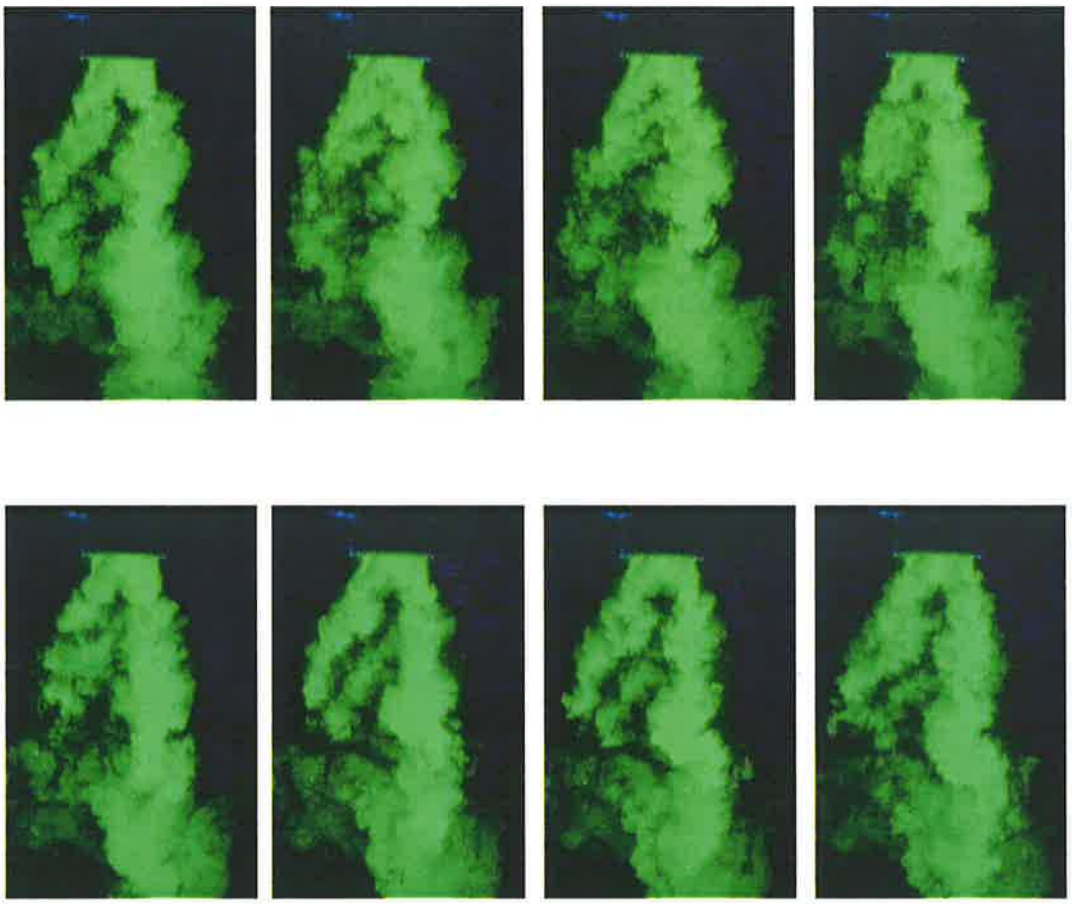

Figure 3.7 (d) A sequence of eight consecutive LIF images of the conically diverging jet with $G_{MIX}/G_1 = 2.56$. Only the annular fluid was marked with dye. Annular jet exit velocity = 0.44 ms^{-1}. Conically diverging jet exit velocity = 1.95 ms^{-1}. Video framing rate 25 fps. Image sequence follows rows from left to right starting at top left.

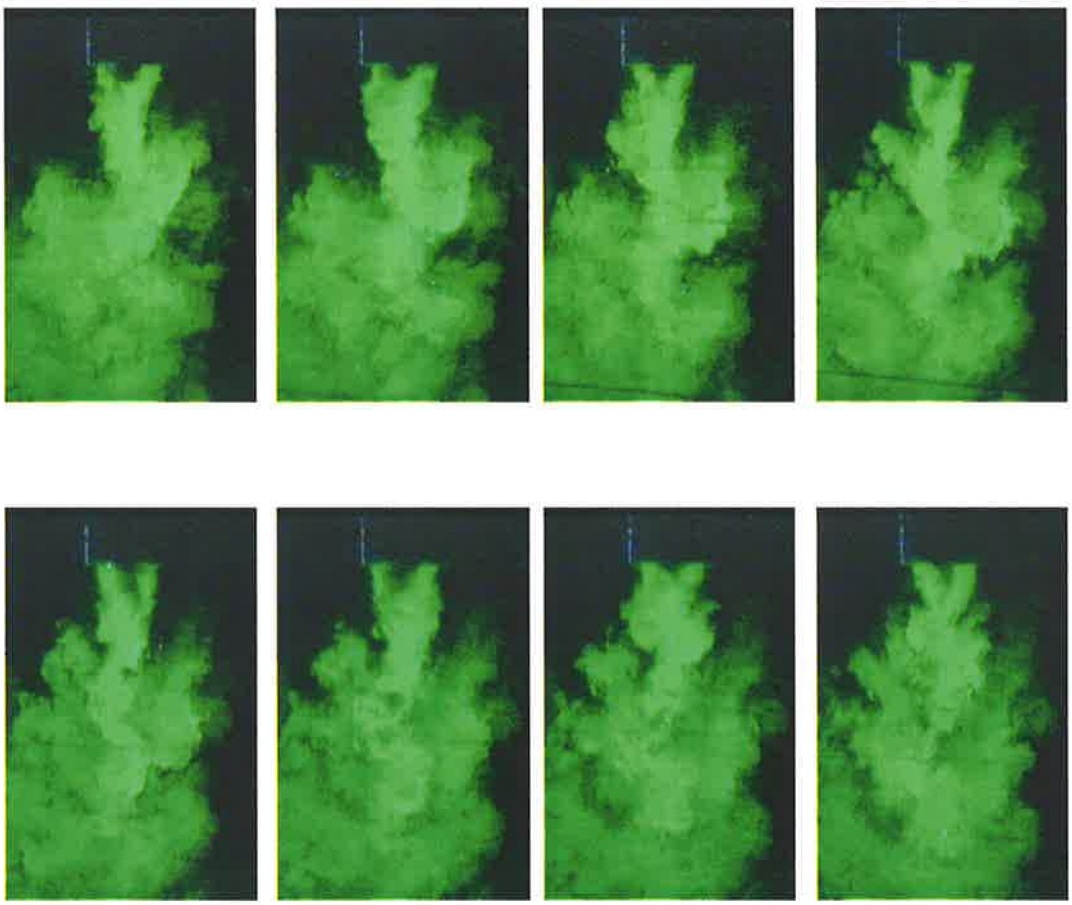

Figure 3.7 (e) A sequence of eight consecutive LIF images of the 19PJ – annular jet with $G_{MIX}/G_1 = 2.56$. Only the annular fluid was marked with dye. Annular exit velocity = 0.44 ms^{-1}. PJ exit velocity = 1.95 ms^{-1}. Video framing rate 25 fps. Image sequence follows rows from left to right starting at top left.

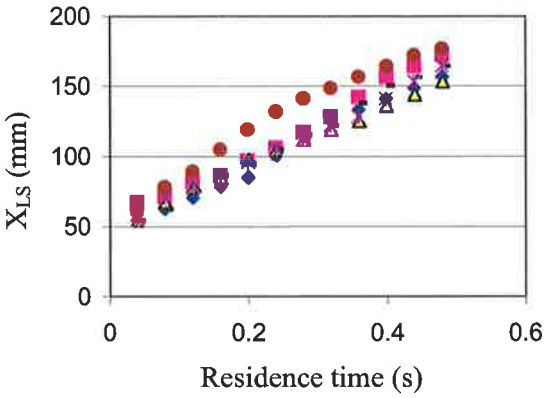

(a) Annular alone marked

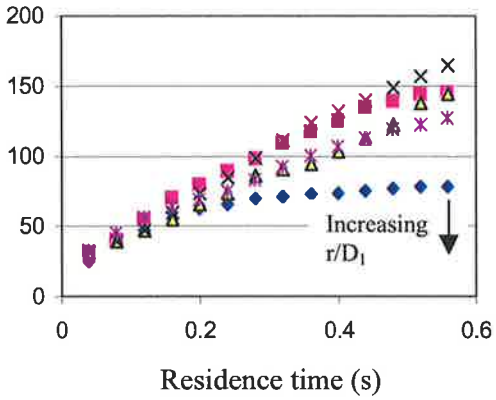

(b) 19PJ with annular fluid

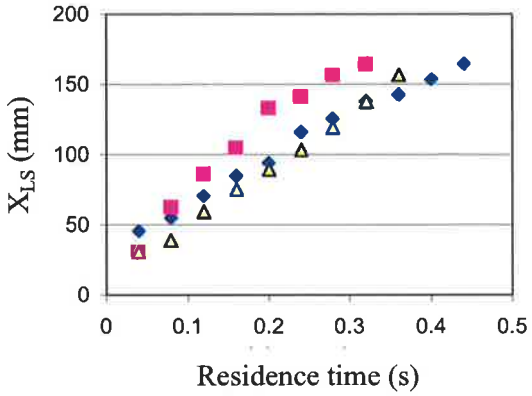

(c) Conically diverging jet

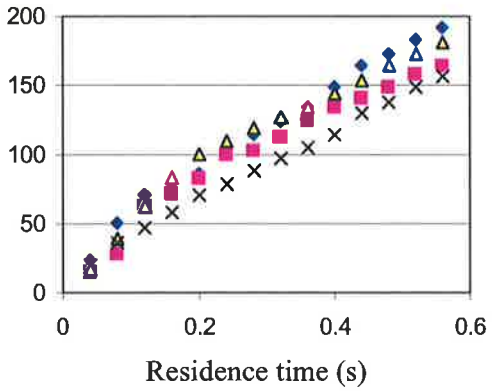

(d) 45 degree directed jet

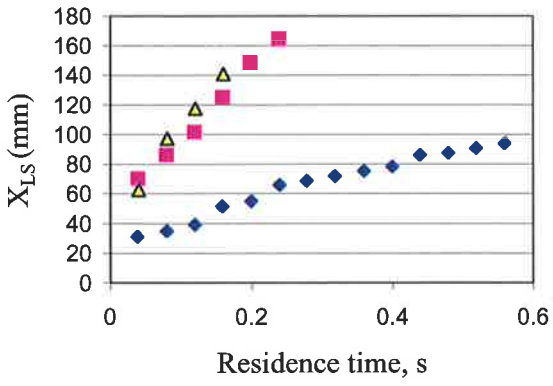

(e) Co-axial

Figure 3.8 Axial positions of the edge of structures, X_{LS}, as a function of time, as measured visually by tracking of structures in successive video images in which only the annular fluid was marked with dye. All combined non-reacting jets have $G_{MIX}/G_1 = 2.56$.

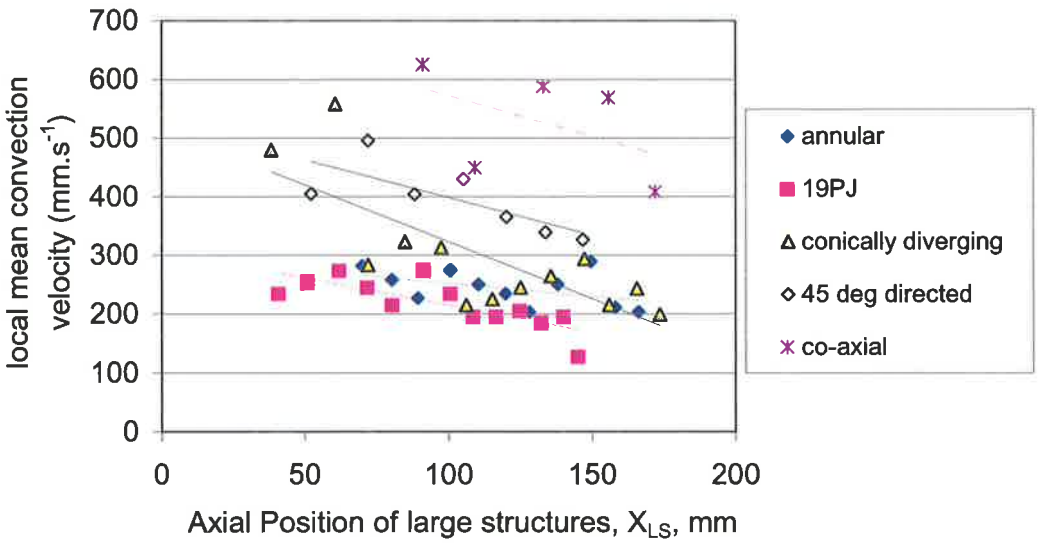

Figure 3.9 Mean local structure convection velocities as a function of X_{LS} for the combined flows, $G_{MIX}/G_1 = 2.56$.

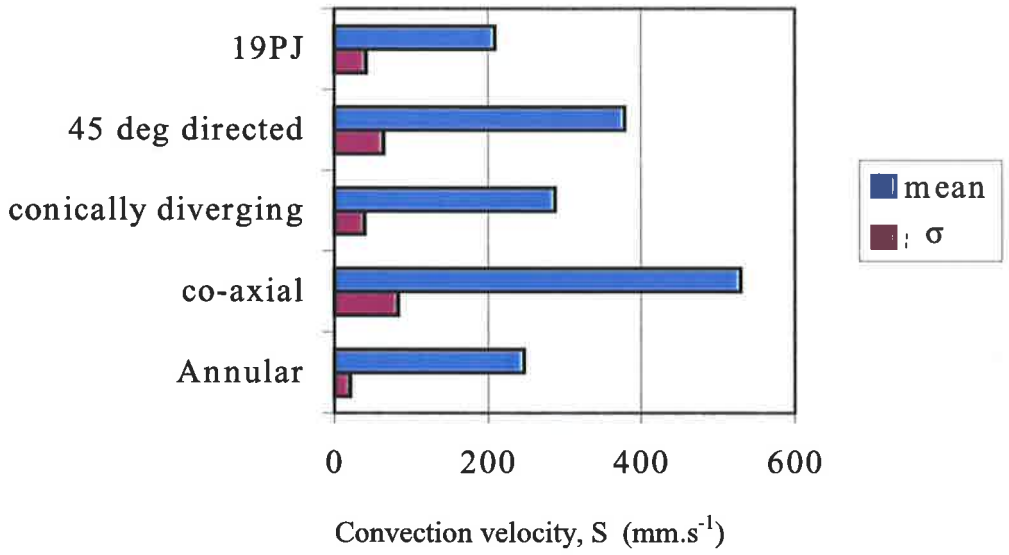

Figure 3.10 Mean and standard deviation (σ), structure convection velocities, S, for the combined flows with $G_{MIX}/G_1 = 2.56$.

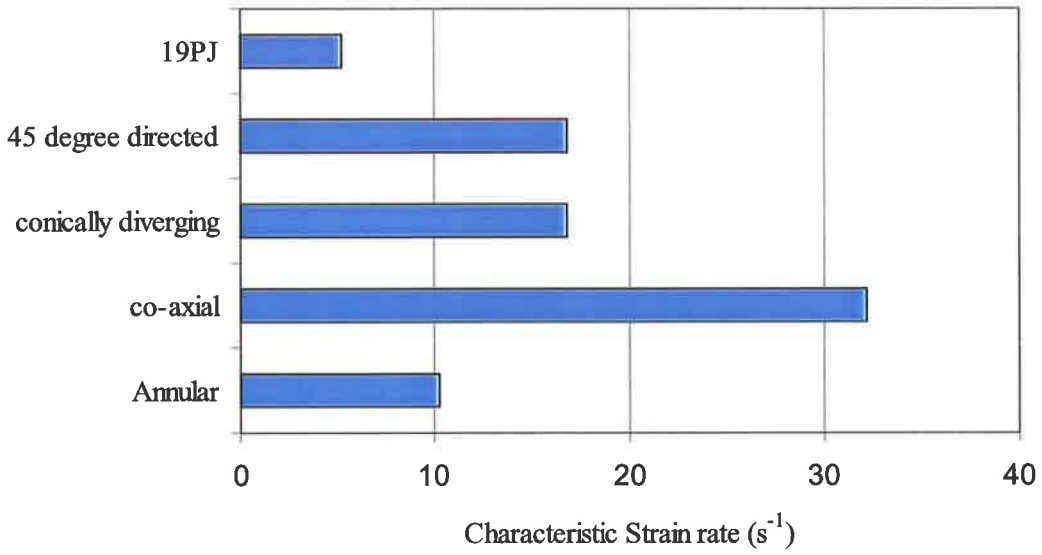

Figure 3.11 Characteristic mean local strain rate, $S/r_{1/2}$ in combined jet flows with G_{MIX}/G_1 = 2.56, determined at $x/D_{A,2}$ = 3.

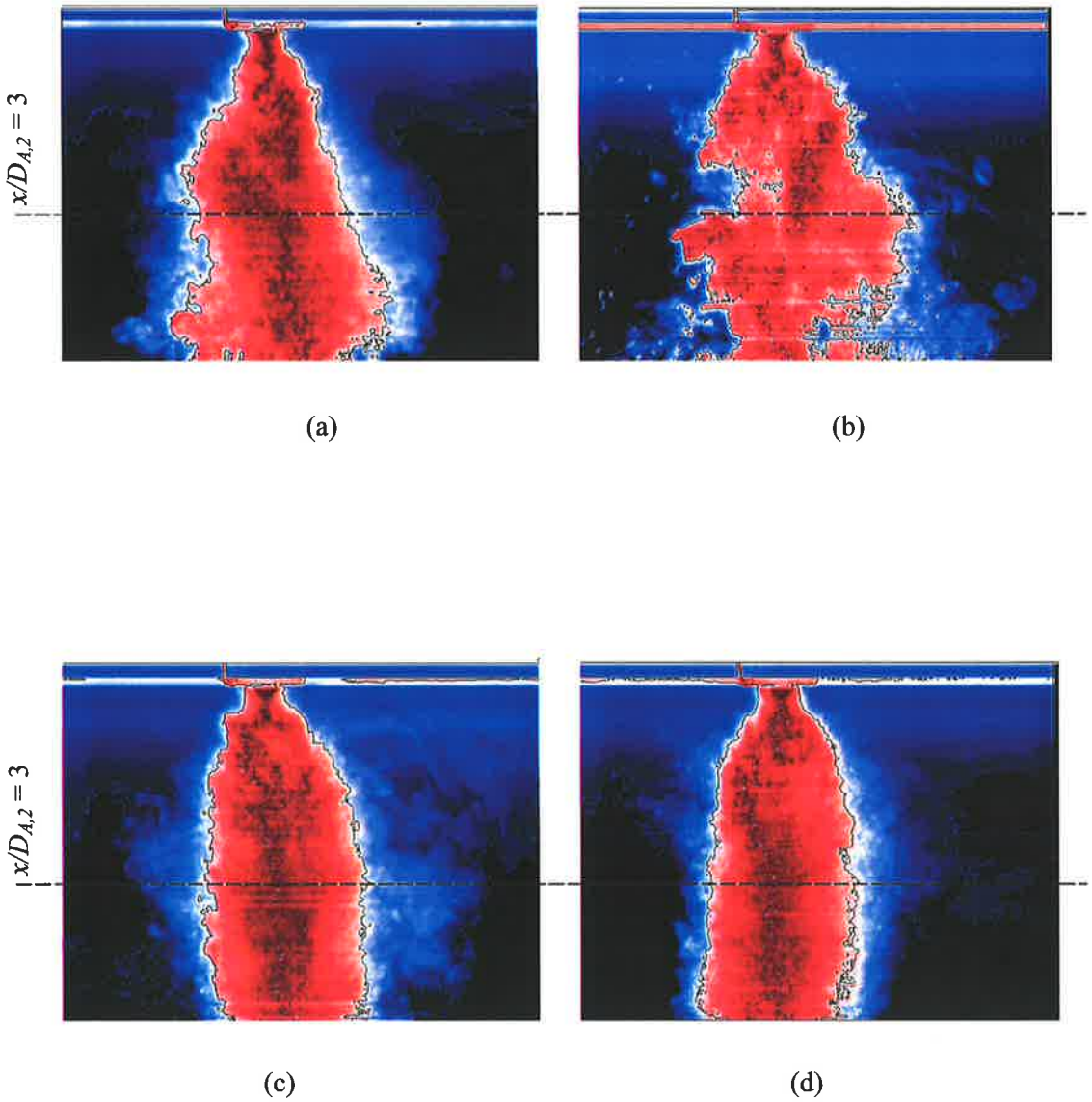

Figure 3.12. Normalised concentration plots, showing the local 0.5 concentration contour, of 19PJ-annular flows with momentum ratios, G_{PJe}/G_1 of (a) 10, (b) 5.6 (c) 2.8, (d) 0.83.

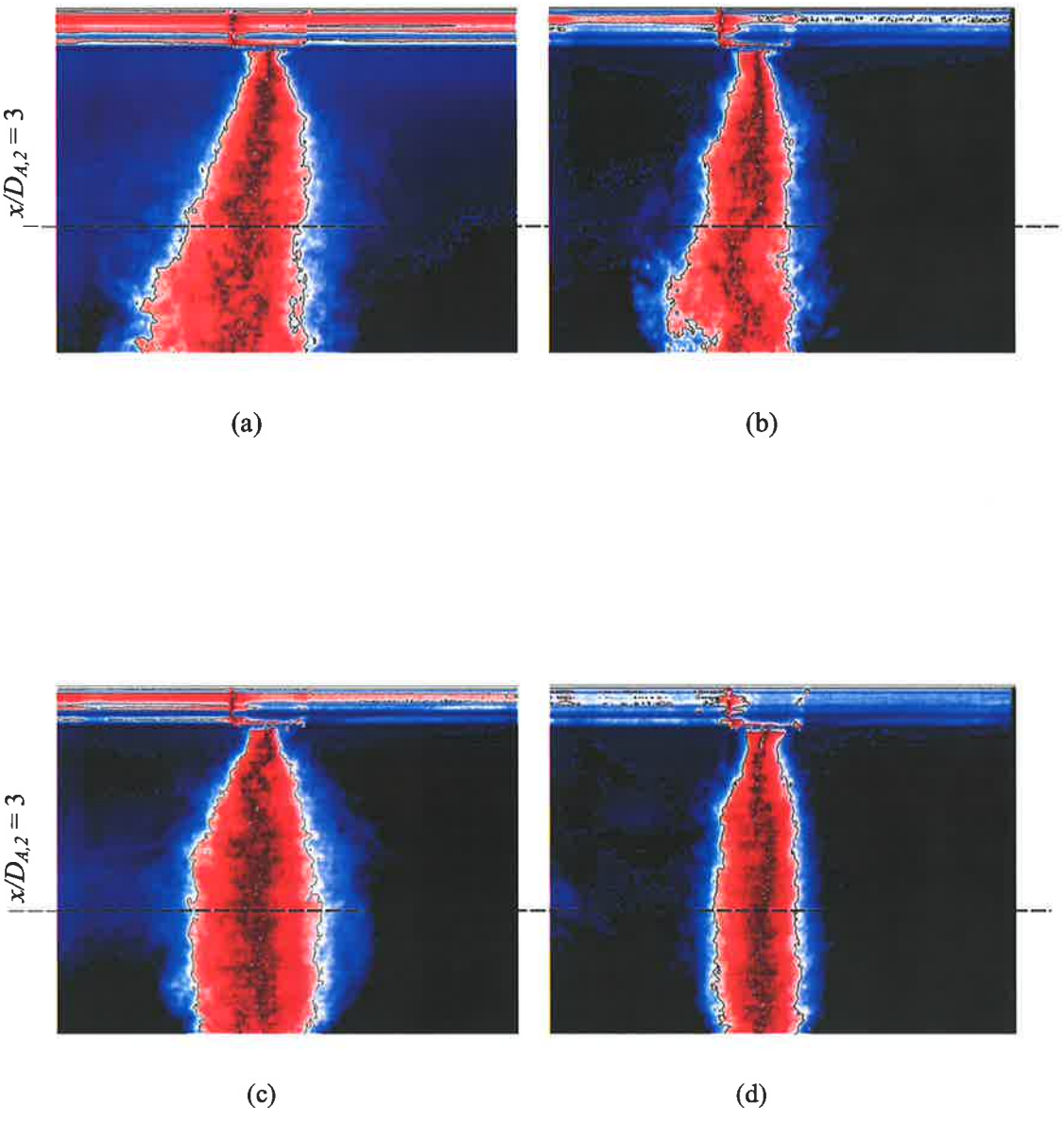

Figure 3.13. Normalised concentration plots, showing the local 0.5 concentration contour, of 10PJ-annular flows with momentum ratios, G_{PJe}/G_1 of (a) 18.4, (b) 4.1 (c) 2.1, (d) 0.62.

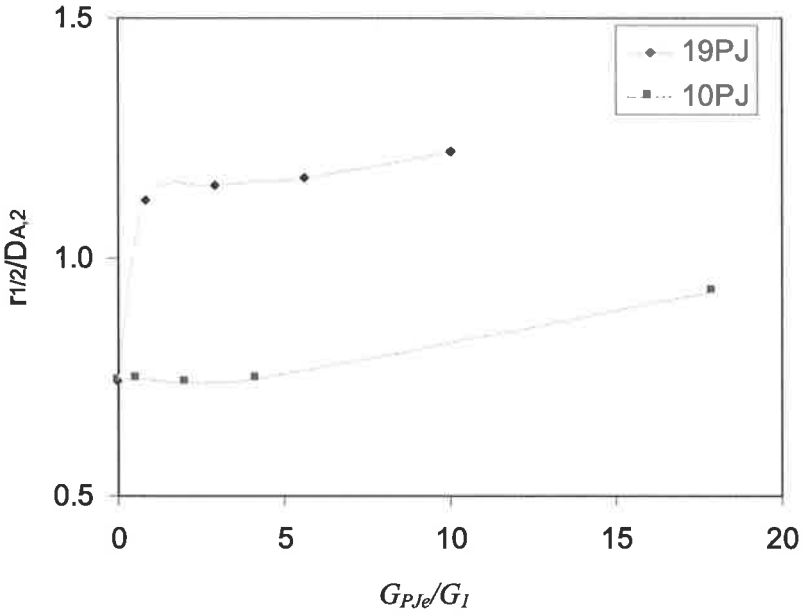

Figure 3.14 The effect of momentum ratio, G_{PJe}/G_1, on the half widths of combined PJ-annular flows at $x/D_{A,2} = 3$.

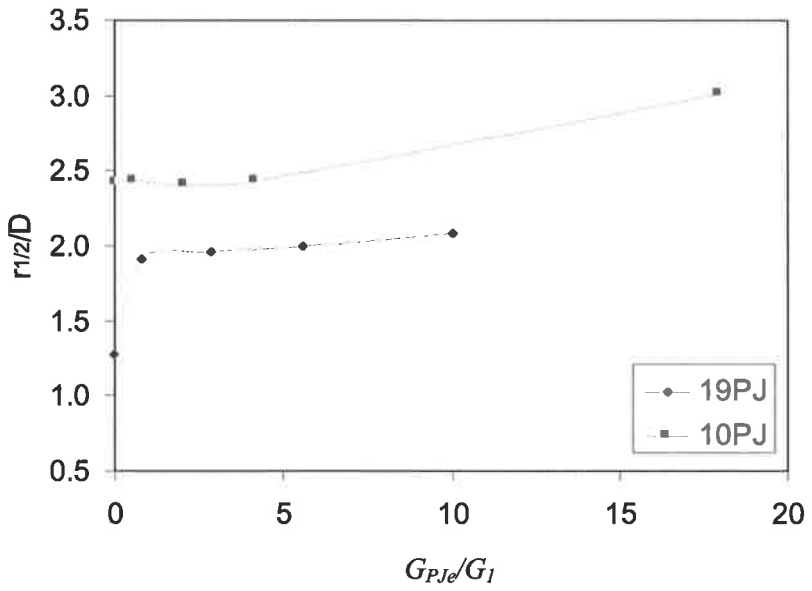

Figure 3.15 The effect of momentum ratio, G_{PJe}/G_1, on the half widths, normalised against the PJ nozzle diameter, D, of combined PJ-annular flows at $x/D_{A,2} = 3$.

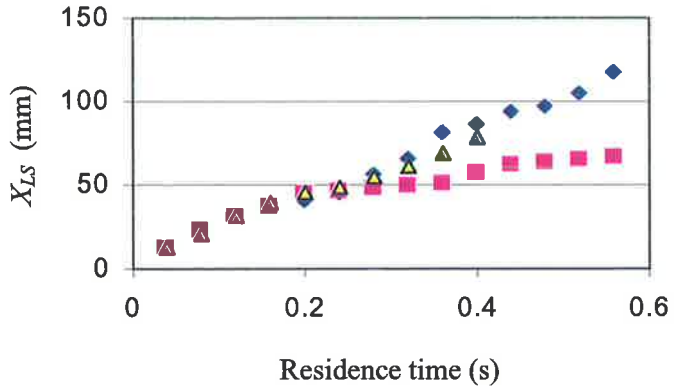

(a)

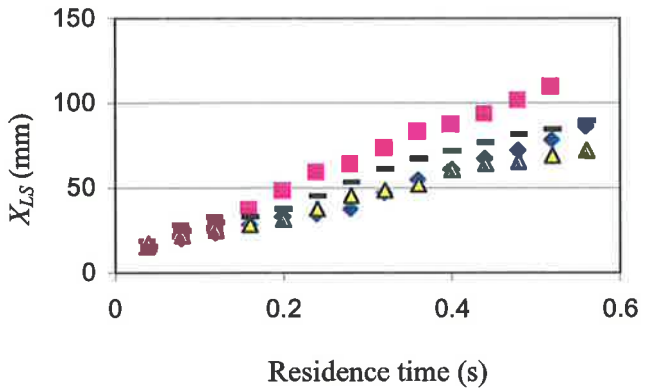

(b)

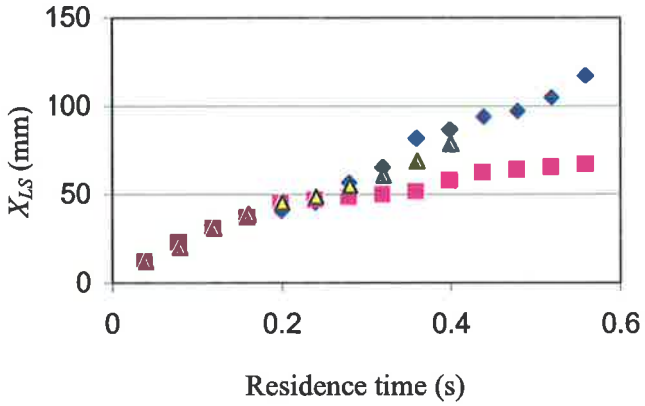

(c)

Figure 3.16 Axial positions of structures, X_{LS}, as a function of residence time for combined 19PJ-annular non-reacting jets with varying G_{PJe}/G_1. G_{PJe}/G_1 = (a) 9.7, (b) 2.8, (c) 0.83.

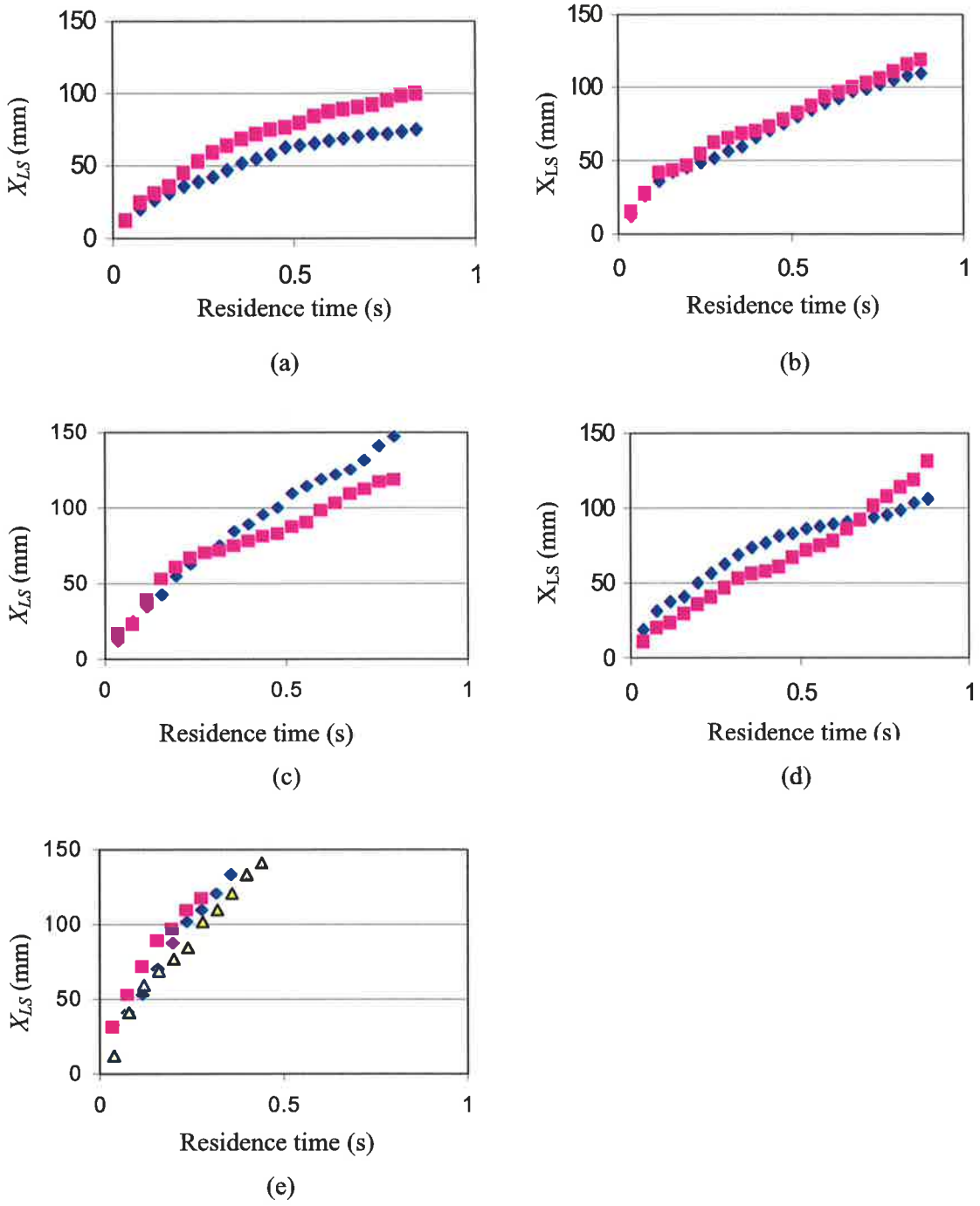

Figure 3.17 Axial positions of structures, X_{LS}, as a function of residence time for combined 10PJ-annular non-reacting jets with varying G_{PJe}/G_1. G_{PJe}/G_1 = (a) 18.4, (b) 4.1, (c) 2.1 (d) 0.62.

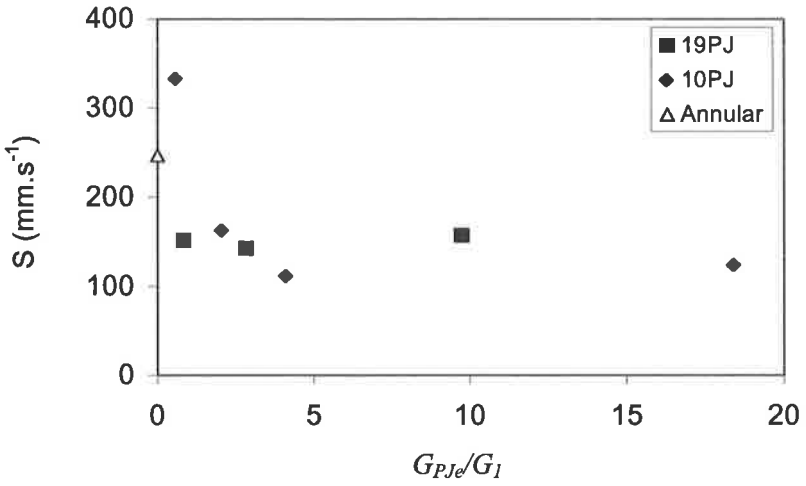

Figure 3.18 Mean structure convection velocities, S, for the combined PJ-annular flows with varying G_{PJe}/G_1

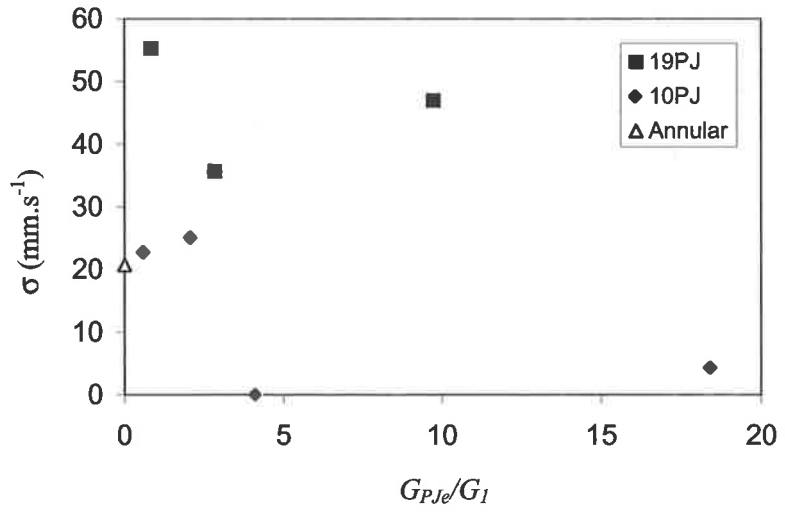

Figure 3.19 Standard deviation (σ) in structure convection velocities, S, for the combined PJ-annular flows with varying G_{PJe}/G_1

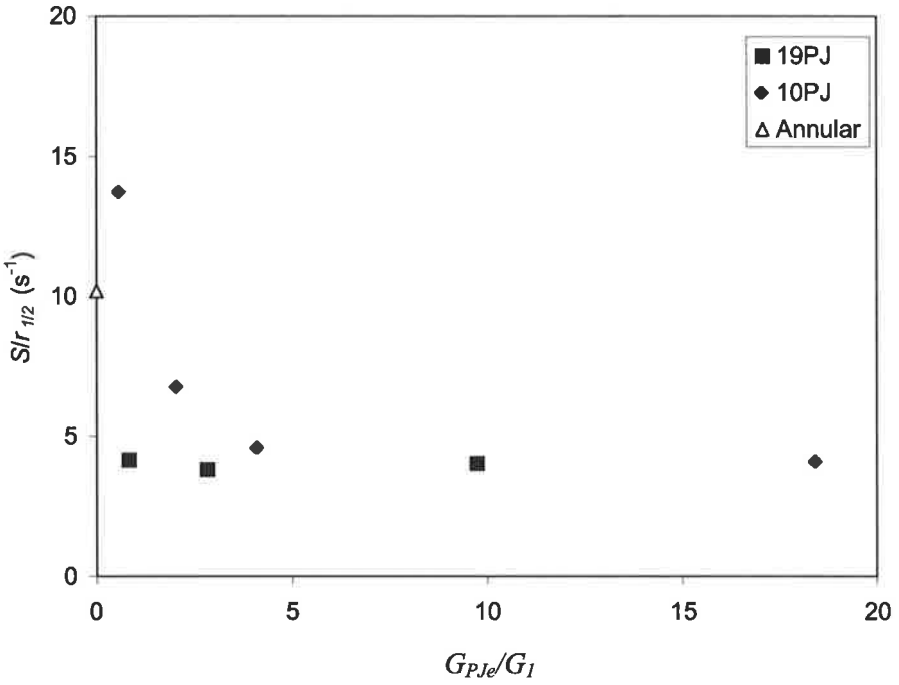

Figure 3.20 Characteristic mean local strain rate, $S/r_{1/2}$ of PJ structures in PJ-annular flows, calculated at $x/D_{A,2} = 3$, as a function of the momentum ratio, G_{PJe}/G_1.

Chapter 4. The influence of large scale jet oscillations on particle motion

4.1 Introduction

Chapter 3 demonstrated that precessing jet flows can dramatically increase the scale of the dominant turbulent structures in the near field of annular jets used to transport PF, and can simultaneously reduce the characteristic jet local strain rate and the convection velocity associated with the largest structures. In the present chapter, the second hypothesis introduced in Section 1.8 is tested, namely, that the large scale oscillations of the emerging PJ flow, which amplify the large scales of turbulence and suppress the fine scales, cause a significant increase in clustering of pulverised coal particles within jet flows. In Section 4.1 previous mathematical, numerical and experimental investigations of the mechanisms by which individual turbulent structures affect particle motion are reviewed. In the remainder of the Chapter, results are presented from a range of experiments, in which the influence of enhanced large scale mixing on the "clustering" or "preferential concentration" of particles in the pre-ignition region of PF flames is investigated. "Preferential concentration" occurs when *"the instantaneous particle concentration field is correlated to the turbulent motions"* (Eaton and Fessler, 1994). The current investigations are carried out in ambient temperature air flows using non-reacting particles to simulate coal particles, and to mark the flow.

4.2 Preferential concentration of particles by turbulence

4.2.1 The significance of the Stokes number in determining the influence of turbulence on particle motion

The motion of a spherical particle under the influence of turbulence can be described by Equation 4-1. This form of the equation of motion, cited by Rogers and Eaton (1989), is due to Tchen. The terms are defined in the notation section.

$$\frac{\pi}{6}d_p^3\rho_p\frac{dVi}{dt} = \frac{\pi}{6}d_p^3(\rho_p-\rho_f)g_i - 3\pi d_p\mu(V_i-U_i) + \frac{\pi}{6}d_p^3\rho_f\left(\frac{\partial U_i}{\partial t}+V_i\frac{\partial U_i}{\partial x_i}\right) - \frac{\pi}{12}d_p^3\rho_f\left\{\frac{dVi}{dt}-\left(\frac{\partial U_i}{\partial t}+V_i\frac{\partial U_i}{\partial x_i}\right)\right\} - \frac{3}{2}\pi d_p^2\mu\int dt'\left\{\frac{\frac{dVi}{dt'}-\left(\frac{\partial U_i}{\partial t'}+V_i\frac{\partial U_i}{\partial x_i}\right)}{\sqrt{\pi\nu(t-t')}}\right\} \quad 4\text{-}1$$

Particle inertia is represented by the term on the left-hand-side of Equation 4-1. It is balanced by the forces on the right hand side, which are in turn: gravity (or buoyancy), viscous (Stokes) drag, fluid pressure gradient, added mass (i.e. acceleration of displaced fluid) and finally the Basset history force (increased drag due to unsteady flow). Tchen's formulation assumes that particles follow the flow and that flow unsteadiness only affects the Basset history force term. The equation of motion of a spherical particle is the focus of continual modification and verification. A more recent form of the equation incorporates improvements including allowances for flow unsteadiness and relaxation of the requirement that particles follow the flow (Maxey, 1993). However Tchen's formulation is adequate to illustrate the relative significance of the various forces. Equation 4-1 can be rearranged so that the left-hand side is the particle acceleration resulting from the action of forces. If, in addition, it is assumed that $\rho_p \gg \rho_f$ (ie. considering gas - particle flows), and with Saffman and Magnus lift force terms included (Rogers and Eaton, 1989) as the last two terms, the equation becomes:

$$\frac{dV_i}{dt} = g_i - \frac{18\mu}{d_p^2\rho_p}(V_i-U_i) + \frac{\rho_f}{\rho_p}\left(\frac{\partial U_i}{\partial t}+V_i\frac{\partial U_i}{\partial x_i}\right) - \frac{1}{2}\frac{\rho_f}{\rho_p}\left\{\frac{dV_i}{dt}-\left(\frac{\partial U_i}{\partial t}+V_i\frac{\partial U_i}{\partial x_i}\right)\right\} - \frac{9\sqrt{\mu\rho_f}}{d_p\rho_p\sqrt{\pi}}\int dt'\left\{\frac{\frac{dVi}{dt'}-\left(\frac{\partial U_i}{\partial t'}+V_i\frac{\partial U_i}{\partial x_i}\right)}{\sqrt{(t-t')}}\right\} + \frac{6K\sqrt{\mu\rho_f}}{\pi d_p\rho_p}(V_i-U_i)\sqrt{\frac{\partial U_i}{\partial x_i}} + \frac{3}{4}\frac{\rho_f}{\rho_p}(V_i-U_i)\frac{\partial U_i}{\partial x_i} \quad 4\text{-}2$$

The Saffman lift term includes an analytically derived constant, K = 6.46. If d_p is small, and $\rho_p \gg \rho_f$, and ignoring gravity, inspection of the non-time dependent parts of each term suggests that the Stokes drag force has the greatest magnitude. The Saffman lift force is the next most dominant term but only for relatively large particles i.e. d_p > 300 μm, and in regions of high strain. Furthermore, the expression for Saffman lift in Equation 4-2 is for

$Re_p < 10$. For higher Re_p (eg. for a 70 μm PF particle in ambient air with a relative velocity of 2 ms^{-1}), McLaughlin (1991) has shown that the magnitude of Saffman lift is significantly lower than that given by the term in Equation 4-2. Further discussion of the influence of the Saffman lift force in PJ flows is provided later in this Chapter. Consequently, the equation of particle motion, for spherical particles and $Re_p < 0.1$, i.e. "creeping flow", can be simplified, following Stokes (cited by Rogers and Eaton, 1989) to:

$$\frac{dV_i}{dt} = -\frac{1}{\tau_p}(V_i - U_i) \qquad 4\text{-}3$$

where

$$Re_p = \frac{\rho_f |V_i - U_i|}{\mu}. \qquad 4\text{-}4$$

Integrating Equation 4-3 yields,

$$\frac{V_i}{U_i} = 1 - e^{-\frac{t}{\tau_p}}. \qquad 4\text{-}5$$

The particle time-scale, or relaxation time, is given by:

$$\tau_p = \rho_p d_p^2 / 18\mu \qquad 4\text{-}6$$

showing that τ_p equals the time required for the particle to adopt a velocity, $V_i = (1-1/e)U_i = 0.63U_i$.

Coal particles are non-spherical, and often experience $Re_p > 0.1$ in turbulent jets, so the conditions for Stokes drag may not apply. Experimentally determined correlations between the drag coefficient, C_d, and Re_p can be used to estimate the drag force for higher Re_p. However the Stokes equation has proven adequate to correlate the effect of drag with experimental particle concentration and dispersion data (Eaton and Fessler, 1994), and as such will be used here. The particle response to Stokes drag is incorporated into the Stokes number, *St*, which is the ratio of particle to fluid time-scales:

$$St = \frac{\tau_p}{\tau_f}. \qquad 4\text{-}7$$

The most difficult issue in defining *St* is the selection of the fluid time-scale of the dominant turbulent structures especially in complex flows (Eaton and Fessler, 1994). Aggarwal (1994) suggested that the fluid time-scale could be equated to the inverse of the frequency of production of the most dominant structures of jet fluid, and validated this definition against experimental data. However, while the frequency of production of large-scale structures in FPJ flows may scale with the precession frequency, it is lower by approximately an order of

magnitude. A number of characteristic fluid time-scales have been reviewed by Eaton and Fessler (1994) which include the lifetime of a dominant eddy, and the time taken for a particle to traverse an eddy. Measurement of τ_f using any of the above definitions is difficult in complex 3-D flows such as FPJ flows. Likewise the more conventional definition of τ_f in jets as the ratio of characteristic length and velocity scales, l/U, at the jet exit plane, is not appropriate here because of the rapid velocity decay exhibited by PJ flows.

Most means of determining τ_f ignore the relative velocity between particles and fluid, and are based on a fixed Eulerian reference frame that overestimates the actual frequency of structures passing a particle if the particle is moving with the fluid. Ideally, a fluid time-scale based on the relative velocity, ie, $\tau_f = l/(S-V)$, and using a frame of reference fixed on the particle (particle Lagrangian frame of reference) could be employed. However experimental measurements based on such a reference frame are not possible and measurement of relative velocity is difficult. Consequently, a consistent over-estimation of St in experimental studies, using the Eulerian reference frame, causes maximum preferential concentration effects to be observed at higher St than the theoretical value of $St \sim 1$ (Longmire and Eaton, 1992).

4.2.2 Numerical calculations of particle - fluid structure interactions

Numerical simulation aims to solve the particle equation of motion directly while modelling accounts for the dominant factors in particle motion. Neither is attempted here due to the complexity of PJ flows. Additional complexity is introduced by the interaction of the annular conveying fluid with the PJ fluid. Nevertheless a review is provided because of the insights which numerical calculations can provide.

"Lagrangian particle tracking" uses either an experimental or numerically generated time dependent Eulerian turbulent flow field and then solves the Lagrangian form of the equation of particle motion. To model more complex flows non-homogeneous eddies can be added to the turbulence formulation. For example, using the k-ε turbulence model, the fluctuating velocity component, u', can be assumed to affect particles traversing an eddy for a period equal to the eddy lifetime, $\tau \sim 0.16k/\varepsilon$ (Weber *et al.*, 1984). Models such as this and others (e.g. Abbas *et al.*, 1981) which use random or time averaged turbulence are useful for predicting particle dispersion relative to characteristic time mean mixing zones. However, they cannot account for the effects of transient structures on particles and so cannot predict instantaneous preferential concentration effects (Eaton and Fessler, 1994). Lagrangian particle tracking also becomes prohibitively complex if modelling particles emanating from a range of positions or with a range of particle sizes (Stock, 1996).

Another approach is Direct Numerical Simulation, DNS, of particle interactions with fluid structures (Eaton and Fessler, 1994). However the complexity involved in solving 3-D Navier Stokes equations to model large structures limits the use of DNS to modelling turbulent structure in simple low Re flows. For example, an Eulerian formulation can be used for both the gas and solid phases, with a k-ε turbulence model for isotropic turbulence. Using such a model in isotropic turbulence, Squires and Eaton (1990) verified that particles can be caused to form clusters in regions of low vorticity and high strain, with the effect strongest for $St = 1$, with τ_f based on the Kolmogorov length scale.

A more realistic approach for complex flows is discrete vortex modelling. Vortex models simplify the turbulence field by modelling only the large-scale dominant vortical motion. Chein and Chung (1987) showed that the pairing of two discrete vortices entrains particles with $0.5 < St < 5$ into the mixing layer and subsequently flings them out, causing increased dispersion. Extending this to the plane mixing layer but still using discrete vortices, Chein and Chung (1988), showed that particles with $0.5 < St < 5$, concentrate around vortex

boundaries. Wen *et al.* (1992) showed 'stretching' apart of particles when they enter high velocity regions and folding together of clusters when vortices merge.

The discrete vortex method has been used effectively in the near field of simple round jets where large coherent ring like structures exist. Chung and Troutt (1988) modelled this region using axisymmetric vortex rings. In agreement with experimental data they found that particles with $St \sim 1$ which enter the shear layer, move to the outside of vortices and show greatest dispersion by being flung outwards by vortices. Less dispersion was observed for particles near the centre-line of the flow. Hansell *et al.* (1992) modelled droplets in turbulent oil sprays by simulating jet structures with rings and using 3-D vortex tracking, solving the vorticity form of the Navier-Stokes equations. In that case particle velocities and Lagrangian particle trajectories were calculated by including an "acceleration number" correction to Stokes drag for $Re_p > 0.1$ (ie. beyond the Stokes regime). Allowances for alteration in drag due to vaporisation were also made. Plots of particle location indicate that particles "stranded" or left behind by vortices are dispersed radially by following vortices as described by Chung and Troutt (1988), and again that this maximum dispersion occurs at $St \sim 1$. However, Hansell *et al.* (1992) also show that outside the Stokes regime, e.g. as d_p increases to 150 μm, other forces, in particular the Basset History force, become important in dispersion. None-the-less, St remains a useful parameter for determining the preferential concentration effects of coal particles, the bulk of which are much smaller than 150 μm. The vortex tracking results described above highlight the controlling influence of St in preferential concentration.

4.2.3 Experimental measurements of particle concentration effects

Flow visualisation has been widely used to investigate interactions between particles and turbulent structures and to measure the extent of zones with characteristic mean flow conditions, such as reverse flow zones. The extension of these flow visualisation techniques to planar concentration measurements and particle image velocimetry (PIV) has increased current understanding of particle laden flows. Kulick *et al.* (1993) used single laser pulses to capture images of particles on photographic media in a fully developed channel air flow. The extent of preferential particle concentration was shown to depend on St, with τ_f based on the Kolmogorov length scale. Particles with $St < 10$, demonstrated less random concentration distributions than heavier particles, since they are more significantly affected by fluid eddies. Longmire and Eaton (1992) studied free and acoustically forced round jets. They defined the fluid velocity scale as $U_o/2$, where U_o is the jet exit velocity, and the length scale as the distance between vortex ring cores, producing experimental Stokes numbers in the range $3 < St < 29$. They measured large increases in the number density of the particle clusters formed between ring structures as St was reduced towards 3, confirming the significance of preferential concentration by the action of turbulent structures. Vortex pairing was shown to be important for dispersion, as found in the modelling study of Chung and Troutt (1988). Sakakibara *et al.* (1996) used PIV to measure the velocities of fluid tracer particles and larger particles in a co-axial jet simultaneously. This enabled particle - fluid velocity correlations to be measured directly. Allowance was made for the "halo effect" of extra light scattering from large particles. Preferential particle concentration effects were shown to be correlated to the instantaneous fluid and particle velocity fields.

Laser Doppler anemometry can be used in non-reacting cold flows to obtain preferential concentration data. Particle and fluid properties can be distinguished by the use of different sized particles and fluid tracers. Longmire and Eaton (1992) used LDA to show that phase-averaged particle velocities in forced round jets correlate with the location of flow structures, thereby confirming that local fluid velocity variations caused by structures are responsible for the formation of clusters. Rogers and Eaton (1989) used LDA to investigate particle motion in air in a flat plate boundary layer. They found that particles respond to the fluid fluctuations in the stream-wise direction, but not to the higher frequency fluctuations in the spanwise direction. Hishida *et al.* (1992) used LDA with modifications to also allow particle counting, and demonstrated that maximum dispersion of particles in a turbulent shear layer occurs when $St \sim 1$ (with τ_f based on the length scale of large structures).

In PF flames where mass loadings are high and other techniques are ineffective, LDA can potentially be used to measure preferential concentration effects. However, to date LDA has generally been used to map the spatial extent of zones with characteristic mean fluid properties, eg. reverse flow zones, and the residence time of particles in them (Weber *et al.* (1992b), Schnell *et al.* (1993), Jensen *et al.* (1994). For these purposes it is commonly assumed that the mean velocities are sufficiently representative of the gas phase due to the high number fraction of smaller particles in PF size distributions. Jensen *et al.* (1994) provided evidence for this assumption in a cold non-reacting flow, operating under the same conditions as a 1.3 MW swirl stabilised coal flame. They showed almost identical mean velocity profiles for coal particles and 5 μm Al_2O_3 tracer particles in the near burner zone. However, it should be noted that due to the small time-scale of structures in the NBZ of a swirled flow, even 5 μm particles may have $St \sim 1$, and in fact be too large to be faithful flow tracers.

An indication of the influence of turbulent structures on particles in swirled PF flames can be found in previous measurements of fluctuating velocity data. Jensen *et al.* (1994) found a maximum axial r.m.s. velocity of approximately 10 ms^{-1} compared to a maximum mean velocity of 30 ms^{-1} at 114 mm downstream from the quarl exit (390 mm diameter). Weber *et al.* (1992b) investigated the region immediately downstream from a burner ($0 < x/D_q < 0.11$) and measured r.m.s. values of 25% of peak mean axial velocity. In both cases the r.m.s. velocities drop dramatically to $\sim$ 2 ms^{-1} in the external recirculation zone (ERZ) where turbulence effects are less significant. The data demonstrates that particles do respond to turbulent fluctuations rather than simply to the mean flow field. Although the mechanism of the response can not be determined from these measurements, it is evident that large-scale structures are important in determining particle motion.

4.2.4 Summary

The two most dominant forces on PF sized particles in jet flows are particle inertia and fluid drag. The drag force on particles is commonly calculated by assuming Stokes drag applies, even when the particle Reynolds number is outside the creeping flow regime (ie. for $Re_p > 0.1$). The Stokes number, St, is defined as the ratio of the particle and fluid time-scales. The particle time-scale, $\tau_p = \rho_p d_p^2 / 18\mu$, is a measure of the response time of particles to the drag produced by the fluid. The time-scale of fluid structures, τ_f, is defined as the ratio of fluid structure length and velocity scales.

Numerical and experimental studies reviewed above allow classification of the effects of structures on particles. Assuming that an accurate estimate of the fluid time-scale, τ_f is used, particles with $St \gg 1$ are unaffected by the fluid structures. In contrast, those with $St \sim 1$ are affected, but can not follow the curved stream-lines of large vortical structures and are preferentially concentrated or "clustered" in regions between structures where vorticity is low and fluid strain rate is high (Eaton and Fessler, 1994). Particles with $St \ll 1$ follow the vortical motion and remain within the structure. Uthuppan and Aggarwal (1994) classify these three interaction mechanisms as 'inertial', 'centrifugal' and 'vortical' respectively.

4.3 Experimental Equipment and Procedures

4.3.1 Experimental Equipment

Two experimental rigs were used for flow visualisation. (A third experiment employed laser Doppler annemometry to determine the mean and fluctuating particle velocities in a PJ-annular flow. The results of this third experiment are supplementary to those reported here and are presented in Appendix 3). The experimental arrangement illustrated schematically in Figure 4.1 was used for the majority of the visualisations. Glass beads with a nominal size of 50 μm, and a size distribution shown in Figure 4.2, were fed from a vibrating pan feeder at 0.085 gs^{-1} to a funnel on the suction side of an ejector. The ejector provides motive air that conveys particles to the nozzle. The pressure of the motive air was measured with a Bourdon tube pressure gauge and the flow-rate was determined from a calibration detailed in Appendix 1. Additional transport air was also entrained with the particles at the ejector. The flow-rate of entrained air was measured using a vane anemometer placed on top of the funnel. For combined fluid - particle visualisation sub-micron (0.1 to 1 μm) TiO_2 particles were added with the glass beads to act as a flow tracer. Particles were fed to the annular channel of the 19PJ-annular nozzle described in Chapter 3. The pressure of air supplied to the 19PJ nozzle was measured with a Bourdon tube gauge. The 19PJ flow-rate was determined from the flow / pressure calibration detailed in Appendix 1. The particles were removed through an extraction hood above the imaging plane. Verification that particles did not fall back into the imaging region was obtained from video-tape recorded after turning off the PJ and annular flows.

The experimental arrangement, shown in Figure 4.3, was used to further investigate the effects of precession on particle motion by observing the motion of particles injected from a single location, in contrast to the annular injection described above. A 10PJ nozzle with a throat diameter, d_t, of 2 mm and a wall thickness is 3.6 mm was horizontally mounted in a 400 mm diameter perspex cylinder. Particles were injected from a 1.5mm I.D. injector located on the underside of a 10mm FPJ nozzle. In this way, entrainment of particles into the FPJ flow acted in the opposite direction to gravity and any entrainment is therefore unambiguous. The small injector was used to create a point source of particles to enable the trajectories of individual particles to be traced using video tape. By varying particle size and transport velocity independently, at a constant 10PJ flow rate, the relative effects of fluid drag and particle inertia could be isolated. The containing cylinder was open at the nozzle end to allow ambient air to be entrained into the jet. A low pressure drop air-conditioning filter pad covered the exit, trapping particles or forcing them to drop to the bottom of the perspex cylinder, from which they were removed following each experiment.

For the experiment depicted in Figure 4.3, glass beads were sieved into two size ranges with mean particle sizes of 80 and 46 μm respectively, using (a) 76 and 84 μm sieves and (b) 44 and 48 μm sieves. Beads were fed through a 10mm diameter, vibrating mini-hopper, to the inlet of a miniature ejector. The beads were subsequently conveyed to the 1.5 mm diameter injector. The flow-rate of motive primary transport air introduced into the ejector was metered by a Fischer and Porter FP-1/8-25-G-5 Tri-flat meter and corrected for pressure, which was up to 30 kPa(g). The quantity of air entrained by the ejector with the particles was negligible, being estimated by measurements of the suction pressure to be less than 1% of the minimum primary flow. The flow-rate of precessing jet air was metered with a Fischer and Porter FP-1/2-27-G-10 rotameter with ½-GNSVT-45 float, and corrected for pressure.

4.3.2 Light Sources and recording media

Planar laser sheet lighting was used in the rig depicted in Figure 4.1, to illuminate the particles. A light sheet was created either by using a continuous Coherent Innova 70 Series 5W Ar-ion laser or a pulsed CU10-A 15W copper vapour laser operating at 510.6 nm (Oxford Lasers). The copper vapour laser was operated a frequency of 10 kHz, at a nominal 1.5 mJ/pulse (Fick *et al.*, 1996). Beams were spread by a cylindrical lens before passing through two spherical lenses to produce a sheet of approximately 2 mm thickness and 200 mm width.

Particle positions were recorded on photographic and high-speed cine media. Photographs were taken on Konica 3200 ASA and Fuji 1600 ASA 35 mm film using a Nikon-F-801s SLR camera. When using the Ar-ion laser, shutter speeds of 1/4000s to 1/1000s were required to provide reasonable exposure. This speed is insufficient to freeze particle motions so that particles are seen as streaks in the photographs. When the pulsed copper vapour laser was used, good exposure was achieved and particles were frozen. Shutter speeds of around 1/1000s provided multiple exposures and allowed particle tracking to be achieved. Exposures of 1/8000 s provided single images of particles and were used for concentration measurements.

A Photec high speed cine camera with a 45 mm Mamiya F4 lens operated with a focal length of 770 mm was used to visualise particle motion under conditions (a) and (c) in Table 4.1 (see below). Ilford HP5 Plus 16 mm film was used. The nominal framing rate was 4000 frames per second, but the mechanical drive mechanism results in a non-uniform framing rate with the initial part of a film being recorded at slower framing rates while the drive mechanism accelerates. The Photec camera was used in conjunction with the copper vapour laser pulsing at 10 kHz.

For imaging particles emanating from the 1.5 mm injector (Figure 4.3) a thick light sheet (about 15 mm) was used to ensure that most particles stayed within the light sheet. It was created by the use of a slit located on the top of a high intensity overhead projector aligned vertically to pass through the nozzle centre-line. Particles were imaged by a VHS video camera operated at 1/25 s and 1/1000 s exposure settings, to vary the length of particle tracks. The mean maximum particle spread, y_p, at $\frac{x}{D} = 1,2,3,4$ and 5 was determined from 50 frames exposed at 1/25 s. The maximum particle spread was measured between the two

edges of the particle stream, ie. it would be twice the jet concentration half width ($2 \cdot r_{1/2}$) if the particles followed the flow perfectly.

The field of view chosen for each of the various techniques was different to highlight specific features of the flows and to account for different film resolution capabilities. The single image photographs taken using the pulsed laser technique, visualise the gross particle flow patterns and preferential concentration effects over the region $0 \leq \frac{x}{D} \leq 10$. The field of view when using the high-speed movie film was reduced to $0 \leq \frac{x}{D} \leq 7.7$ to maximise the image quality. For photographs intended for particle concentration measurements, a smaller region, $0 < x/D < 6.1$, was chosen. This allowed individual particles to be more clearly imaged. A large field of view, $0 \leq \frac{x}{D} \leq 10$, was used to capture the gross particle tracks of particles emanating from the point source.

4.4 Flow visualisation experimental conditions and results

4.4.1 PJ – annular flows

The conditions under which laser sheet visualisations of 19PJ – annular flows were performed are summarised in Table 4.1. The 19PJ exit velocity and annular "primary" velocity are calculated from the respective flow rates. (PJ exit velocities are estimated using the method given in Chapter 3). The mass flow of particles ($0.085gs^{-1}$) is ignored in the calculation of the momentum ratio, G_{PJe}/G_1, since it contributes only 1.5% of the total mass. In conditions (a) to (d) the primary air flow-rate is the same as that also used in 130 kW combustion experiments (Chapter 5), while in conditions (e) - (h) a lower primary air flow-rate is used to allow a greater range of momentum ratios to be investigated.

Table 4.1 Input conditions used in flow visualisation and concentration measurements.

Condition	*19PJ pressure (kPa,g)*	*19PJ Flow (g/s)*	*19PJ exit Velocity(ms^{-1}) (estimated)*	*Annular Velocity (ms^{-1})*	G_{PJe}/G_1
(a)	0	0	0	9.8	0
(b)	20	1.445	33.7	9.8	1.12
(c)	60	2.699	63.0	9.8	3.91
(d)	100	3.667	85.6	9.8	7.22
(e)	0	0	0	2.4	0
(f)	20	1.445	33.7	2.4	18.6
(g)	60	2.699	63.0	2.4	64.7
(h)	100	3.667	85.6	2.4	119.0

The influence of the enhanced large scale mixing produced by the PJ flow on preferential concentration of particles, can be seen in Figure 4.4. Figure 4.4(a) shows a 1/1000 s exposure photograph of the annular air flow alone, condition (a) in Table 4.1, illuminated by an Ar-ion light sheet, and seeded with glass beads only. The relatively parallel directions of the glass bead streaks suggest that the scale and intensity of the large sale turbulent motions, is insufficient to greatly affect particle trajectories. Figure 4.4(b) shows a 1/4000s exposure photograph of the 19PJ flow with $G_{PJe}/G_1 = 3.91$, with the annular stream seeded with flow tracer particles and glass beads. Some beads are concentrated on the boundaries of the large structures. This effect appears to be related to the "centrifugal" mechanism defined by Uthuppan and Aggarwal (1994). Other larger beads punch through these structures. Figure 4.4(b) also shows a 1/1000s exposure photograph of the annular flow alone seeded with the same concentration of glass beads and flow tracer particles. The two photographs shown in Figure 4.4(b) demonstrate the dramatic increase in the scale of large structures, and in the clustering of glass beads, produced by the precessing jet.

Preferential concentration effects in the 19PJ flow with $G_{PJe}/G_1 = 3.91$ can be observed in Figure 4.5 which is a 1/1000 s exposure photograph of glass bead tracks without flow tracer particles. The beads are illuminated by the copper vapour laser pulsed at 10 kHz. Consequently, particles that stay within the light sheet are imaged about 10 times. It is apparent that, in the NBZ, despite the over-exposure, a wide dispersion of particle trajectories occurs, indicating an influence of the deflected PJ flow in the exit plane. The larger particles are "spread" rather than formed in clusters, since their momentum appears to be high enough to punch through the NBZ. In contrast, what appear to be small particles concentrate in clusters off the centre-line in the region $1 \leq \frac{x}{D} \leq 3$, where large-scale flow structures were first observed in water flow experiments (Chapter 3). This clustering of smaller particles is deduced to be due to particles acting as flow tracers, ie. corresponding to the "vortical" mechanism ($St < 1$) defined by Uthuppan and Aggarwal (1994). The deduction is based on the observation that the shapes of clusters are similar to that of large-scale structures (observed in Chapter 3).

Figure 4.6 is another image of the $G_{PJe}/G_1 = 3.91$ condition taken with a shorter shutter time corresponding to two laser pulses. Here the clouds of smaller particles near the nozzle are not as clearly defined, instead evidence of some clustering of the larger particles can be observed. The bulk forms of the clusters appear to be related to the large structures observed in water flow modelling in Chapter 3, providing evidence that they are generated by these structures. However, the clusters are more angular and elongated than the fluid structures, which may result from them being influenced by the fluid structures without conforming to them ($St \geq 1$).

The dynamics of the particle clustering effects can be observed in the cine film. Figure 4.7 is a digitised version of a 16 mm movie sequence showing 10 successive frames, of the flow with $G_{PJe}/G_1 = 3.91$, illuminated by the Cu vapour laser sheet pulsing at 10 kHz. The nominal framing rate of these images was 1000 frames per second, so that particle traces with up to 10 pulses per image can be seen in some cases. Clustering effects (preferential concentration) can be seen throughout the region, $\frac{x}{D} \leq 3$. The clusters appear to retain some coherence as they are convected downstream, despite being folded, compressed and stretched by large structures. In contrast some, presumably large, particles punch through the imaged region.

4.4.2 Flow visualisation of particles from a "point source"

Figure 4.8 shows eleven digitised, 1/25s images of particles emanating from the 1.5 mm "point source" particle injector using the experimental technique depicted in Figure 4.3. Each image shows particle tracks and "spread" for a different momentum ratio, G_{PJe}/G_J, achieved by varying the particle injection velocity at a constant 10PJ mass flow of 0.0012 kgs^{-1} and exit velocity of 101 ms^{-1}. The particle injection velocity (given in the caption) reduces from 25 ms^{-1} in frame (a) to 3.3 ms^{-1} in frame (f), which were collected using 46 μm particles, and from 21 ms^{-1} in frame (g) to 4.3 ms^{-1} in frame (k), which were collected using 80 μm particles. The precession frequency, f_p, of a 10 mm FPJ at the experimental flow-rate is calculated to be of the order of 330 Hz, using equation 1-14. A single video image, at 1/25 s, therefore is averaged over about 13 precession cycles. For low particle injection velocities, $U_J < 10$ ms^{-1}, ie. cases (d) to (f) and (i) to (k) in Figure 4.8, particles are strongly deflected in the NBZ towards and across the centre line by the PJ flow. Clearly, the unsteady PJ flow in the region $\frac{x}{D} \sim 1$ is very effective at spreading particles. For higher injection velocities the deflection of particles in the NBZ is less substantial, and the influence of large structures on particle spreading is reduced.

Figure 4.9 shows an image taken with a shutter speed of 1/1000s, so that only 1/3 of a precession cycle was captured. It shows that 80 μm particles, injected with a velocity of 4.5ms^{-1}, are deflected in the NBZ. Only minor variations in the deflection angle were observed over many such images. Downstream from the NBZ, particles are clustered dramatically by the large-scale structures, also shown in Figure 4.9. This observation suggests that the extent of particle spreading can be used to provide an indication of the strength of subsequent clustering effects.

When Saffman lift forces dominate particle motion, particles move to regions of highest fluid velocity as is observed in "roping" of particles along the centre-line in pipe flow (Beer *et al.*, 1984). Ward (1986) showed that 80μm glass beads were entrained from the low speed side to the high speed side of a plane mixing layer by Saffman lift forces. Particles in the NBZ of an FPJ flow could also be expected to migrate to the centre-line of the exiting precessing jet if lift forces dominate. From close observation of numerous images such as that in Figure 4.9 it is deduced that particles, on leaving the 1.5mm injector, do in fact always move towards the centre-line of the PJ nozzle.

Figure 4.10 shows estimations of axial acceleration of 46 μm glass beads injected at 3.3ms^{-1} into the NBZ of the 10PJ flow, with PJ exit velocity of 101ms^{-1}. Particle acceleration due to drag, Saffman lift, and pressure gradients are estimated using Equation 4-2 and shown as a function of the axial slip velocity, (U_i - V_i). The maximum axial slip velocity, 68 ms^{-1}, occurs at the exit plane, and is calculated by assuming that the exiting precessing jet is directed at 45° from the nozzle axis. Lower values of (U_i - V_i) model interactions between the fluid and particles downstream from the exit plane. For the range of slip velocities, (U_i - V_i), shown in the figure, the particle Reynolds numbers vary between 5 and 210, so that Stokes drag does not apply. Accordingly, the drag force is calculated using the relationship of Ossen (cited by Kulick *et al*, 1993),

$$Drag\ Force = C_D\left(\frac{\pi}{8} d_p^{\,2} \rho_f (U-V)^2\right), \text{ where } C_D = \frac{24}{\mathrm{Re}_p}\left(1+0.15\,\mathrm{Re}_p^{\,0.687}\right) \qquad 4\text{-}8$$

Particle acceleration due to Saffman lift and pressure forces are obtained using Equation 4-2. The axial fluid velocity gradient, $\frac{\partial U_i}{\partial x_i}$, and deceleration, $\frac{\partial U_i}{\partial t}$, (required for calculation of lift and pressure forces, as per Equation 4-2) are estimated by assuming that the PJ velocity decays to half of its initial value in an axial distance, $x/D = 1$. This decay rate is taken from measurements made at the equivalent axial position in a mechanically precessed jet, ie. $x/d = 3$ (Schneider *et al*, 1997).

Figure 4.10 demonstrates that under all conditions, the influence of drag forces dominates over that of lift and pressure forces. Furthermore, the magnitude of Saffman lift forces illustrated in Figure 4.10 are overestimated when $Re_p > 10$ (McLaughlin, 1991) which is the case for all conditions in Figure 4.10, except that corresponding to the lowest slip velocity. From the estimates above, it can be deduced that the initial deflection of particles towards the nozzle centre-line in the NBZ is primarily due to the drag forces exerted by the ambient and primary air, as they are entrained towards the nozzle centre line by the PJ.

4.4.3 Summary of flow visualisation results

The key findings of the visualisations are:

- The initial unsteady flow and the large-scale structures generated by the combined FPJ - annular flows produce clustering effects on particles of a range of sizes, possibly by the "vortical" and "centrifugal" mechanisms.
- The clusters of small particles are formed contiguously with the large-scale structures, i.e. in the region broadly corresponding to $1 < \frac{x}{D} < 2$. In contrast, larger particles take longer to respond to the large-scale structures so that the clusters formed by the centrifugal mechanism are first observed further downstream at $\frac{x}{D} \sim 3$.
- The effect of clustering is evident throughout the viewing plane, which extends to *x/D* >10 in some images. The clustering effects are far more significant in the combined PJ – annular flow than in the annular flow alone.
- It can be deduced that deflection of particles towards the nozzle centre-line in the NBZ is primarily due to entrainment of ambient and primary air towards the nozzle centre line by the PJ. The particles are dragged towards the centre-line by the entrained fluid.
- The extent of clustering by large structures downstream from the NBZ increases with the angle of deflection of the particle stream in the NBZ. Both effects are related to the momentum of the PJ flow relative to the transport flow.

4.5 Measurements of particle concentration and trajectories

4.5.1 Particle counting methodology: PJ – annular flows

Indicative measurements of particle concentration were performed to quantify the extent of clustering, and the mechanisms responsible for it, in the various PJ-annular flows. A photograph of particles for each of the eight conditions tested (see Table 4.1) was digitised and used for particle concentration measurements. Photographs were taken of flows in which the particle seeding density was low enough to allow resolution of individual particles. A shutter speed 1/8000s and laser pulse frequency of 10,000Hz were used to obtain single images of each particle. (The photographs were later inspected to verify this). To allow indicative results to be obtained within a realistic time frame, only a small section of one photograph was examined for each condition. A grid with 2.5mm square cells was overlaid on each photograph in the manner illustrated in Figure 4.11. Particle counting was performed in a single column of cells extending axially from the middle of the annular slot to the end of the image (Figure 4.11). The photographs used for each condition are shown in Figure 4.12 at 1.19 times actual size. For each photograph, 52 or 53 cells were counted, so that an axial slice corresponding to actual dimensions of 2.1 mm wide and 110 mm long was examined. In this way the variation in particle concentration with axial position could be investigated.

Particle counting using commercial software was also attempted. However a number of difficulties were experienced which precluded the use of the software. Firstly, variation in particle size and intensity of the light sheet across its thickness led to variation in intensity of reflected light. Secondly, the particle loading used was too high to allow accurate discrimination of individual particles. Despite attempts to enhance images, the software could not detect particle edges and tended to group particles together. When images were adjusted so that only the brighter particles were recognised, many particles were excluded. Unfortunately, the experiments could not be repeated with graded particle sizes and lower seeding densities, so the manual counting method described above was adopted.

4.5.2 Factors which influence particle clustering in PJ - annular flows

In the present section, the dependence of clustering on G_{PJe}/G_1, St and jet half width, $r_{1/2}$, is investigated. Histograms of particle number density are plotted in Appendix 2 for each photograph presented in Figures 4.11 and 4.12. These histograms show that increasing G_{PJe}/G_1 causes an increase in the frequency of cells containing high or low numbers of particles, ie. it enhances preferential concentration of particles (see Appendix 2). A collation of the particle concentration data presented in Appendix 2, to show the effect of G_{PJe}/G_1 on clustering is presented in Figure 4.13. Here the ratio of standard deviation to mean particle number density (σ/μ) is presented as a function of G_{PJe}/G_1. For the cases with annular velocity equal to 9.8ms^{-1} the effect of increased G_{PJe}/G_1 is to increase the standard deviation in particle number per cell by a factor of 2. For the cases with an annular velocity equal to 2.4ms^{-1}, even the lowest PJ momentum (above zero) dramatically increases the variability in particle number per cell. Further increases in PJ momentum do not alter the variability significantly. The data demonstrates that $G_{PJe}/G_1 > 4$ produces significant clustering. The cell size used for the above analysis is considerably smaller than the size of the largest fluid structures observed, and so is useful for determining statistical effects generated by the large structures.

In addition to providing an insight into the influence of G_{PJe}/G_1, the particle concentration data also provides a means of estimating the effect of the characteristic local Stokes number on clustering, since fluid structure time-scales are also affected by variation in G_{PJe}/G_1. The particle time-scale (Equation 4-6) is constant for the PJ-annular flows since the particle size distribution was not altered, and can be characterised as that for glass beads with diameter, d_p = 50 μm and ρ_p = 2500 kg/m^3. (In the next section, experiments in which the particle time-scale is varied to provide a more comprehensive test of the effect of St on clustering are reported.) At least two methods can be used to calculate the fluid time-scale, τ_f, and hence St, in the PJ-annular flows. Firstly, τ_f can be scaled from the inverse of the measured characteristic local strain rates obtained in the 19PJ-annular water flow experiments (Figure 3.20) for corresponding values of G_{PJe}/G_1. This method assumes that the fluid length scale, taken to be the jet half width, $r_{1/2}$, is identical in water and air flows for a given G_{PJe}/G_1. The assumption that PJ flows have identical half-widths in water and air flows is based on the findings of Nobes (1998) and Newbold (1997) who investigated PJ flows in air and water respectively. A correction factor, equal to the ratio of PJ exit velocities in the air and water cases can be applied to estimate τ_f in air (since the PJ flow controls the mean convection velocity). In the case of primary "annular" flows alone, the correction factor is based on the

ratio of primary velocities. Use of this method produced poor correlation between *St* and clustering effects, and an alternative method of estimating τ_f was attempted.

A second estimate of τ_f can be made by assuming that the characteristic velocity scales with the mean jet concentration field. In this case the local fluid axial velocity component is assumed to decay linearly with axial distance, $U \alpha U_e(1+x/d_e)^{-1}$, whilst the local length scale of large structures, l, is assumed to grow in proportion to the jet half width or axial distance, ie. $l \alpha\ r_{1/2} \alpha\ x$. The assumptions are illustrated in Figure 4.14. The fluid time-scale in air is thus given by:

$$\tau_f = l/U = r_{1/2}\frac{(1+r_{1/2}/d_e)}{U_e} \qquad 4\text{-}9$$

The value of U_e is given by the total flow-rate divided by the sum of exit areas and, the equivalent exit diameter is given by:

$$d_e = [\text{sum of exit areas}/(\pi/4)]^{1/2} \qquad 4\text{-}10$$

Figure 4.15 shows the relationship between clustering effects and characteristic *St* numbers calculated using Equation 4-9. For $U_1 = 2.4$ ms^{-1} the expected trend of increased σ/μ as *St* tends to 1 is observed, although the variation in *St* is small. The annular flow alone has the highest value of *St* and also shows the weakest clustering effects. The trend of increasing σ/μ is also associated with increasing G_{PJe}/G_1 as noted above. The trend for $U_1 = 9.8$ ms^{-1} is less obvious. While it is clear that the flow with the lowest G_{PJe}/G_1 exhibits the weakest clustering, and conversely that with the flow with highest G_{PJe}/G_1 exhibits the greatest effect, the limitations of the present estimates of *St* become apparent, since a correlation of *St* and clustering is poor.

The relatively poor correlation between *St* and clustering contrasts with findings of other studies (eg. Longmire and Eaton, 1992). A possible reason for the poorer correlation in the current study is that the particles are introduced in a separate stream from the PJ flow. Mixing between the PJ and annular streams is controlled by the momentum ratio, G_{PJe}/G_1, which also controls the jet half width. Accordingly there is a good correlation between G_{PJe}/G_1 and clustering (Figure 4.13), and between $r_{1/2}$ and clustering (Figure 4.16). It can be deduced from these data that the extent to which the structure of the annular flow is affected by the momentum of the PJ flow has a dominant effect on the drag forces that are responsible for the preferential concentration effects. In contrast, other studies (such as

Longmire and Eaton, 1992) have been performed in simple jets where interaction with a second jet is not required to generate the structures of interest.

Another reason for the lack of correlation between *St* and clustering shown in Figure 4.15 may be an overestimation of the effect of velocity on *St*, by Equation 4-9. Data taken in water (Figure 3.18) showed that for $G_{PJe}/G_1 \geq 1$, the convection velocities of fluid structures in 19PJ-annular flows are relatively constant in the measurement region, ie. $2 < \frac{x}{D_{A,2}} < 5$. If this is also the case in the PJ-annular air flows with $G_{PJe}/G_1 \geq 1$, then *St* is inversely proportional to $r_{1/2}$ (Equation 4-9). Figure 4.16 shows that there is a general trend of increasing clustering effects with increasing values of $r_{1/2}$, i.e. with decreasing values of St, as would be expected for $St > 1$.

A further reason for the lack of correlation between *St* and clustering shown in Figure 4.15 may be that the use of the particle size distribution shown in Figure 4.2 results in a range of clustering mechanisms. It is likely, for example, that smaller particles may act as flow tracers, while larger particles may partially punch through flow structures. Furthermore, the calculated range of *St* is underestimated by the assumption of a single particle size.

An alternative means of calculating the fluid time scale, defined by Equation 4-9, is to use a "momentum weighted" mean velocity. The momentum weighted mean velocity, U_e, is defined as:

$$U_e = \frac{(u_1.G_1 + u_{PJe}.G_{PJe})}{(G_1 + G_{PJe})} \qquad 4\text{-}11$$

This value of the mean exit velocity is biased in favour of the streams that have greatest influence on particle motion in the near nozzle region. Consequently, it can be expected to be useful in scaling the influence of the PJ exit velocity on clustering. Figure 4.17 shows the clustering data of Figure 4.15 re-plotted with U_e calculated using Equation 4-11. A general trend, opposite that expected, of increasing clustering with increasing *St* is observed. This trend is deduced to be due to an increase in slip velocity with increasing *St* in the near nozzle region, which causes increased drag on particles and hence increased deflection of particles. The deflection of particles in the near nozzle region is also associated with increased preferential concentration effects as can be observed from the photographs in Figure 4.12. Consequently, the use of the momentum weighted mean velocity to calculate *St* highlights the effect of the PJ in the near field, rather than the commonly observed mechanism of preferential concentration by large structures, which is more relevant in the region $x/D \geq 2$.

In Chapter 6, flame scaling using Stokes numbers calculated from momentum weighted mean exit velocities, is presented. In this way near burner zone effects are taken into account.

Further work in this area may fruitfully explore the influence of two regions of the PJ flow on particle clustering. In the near nozzle region, $x/D < 2$, where particles are deflected by the precessing jet as it exits the nozzle, the fluid time-scale may be more effectively characterised by the time taken for a particle to traverse the region, i.e., $\tau_f = U_1/2D$, than that given by Equation 4-9. Alternatively, the fluid time-scale may be characterised as the ratio of the initial slip velocity and the length of the near nozzle region, i.e., $\tau_f = (U_e - U_1)/2D$. Conversely, in the region downstream from the near nozzle region, where the PJ velocity has decayed and clustering is controlled by the action of large structures, a relationship such as Equation 4-9 may be more applicable. Alternatively, experimental measurements of local velocities may be used in this region. Using the rationale above, separate Stokes numbers can be defined for each region.

Further work may also investigate the motion of particles with known size ranges, injected directly through a PJ nozzle with no surrounding flow. Clustering data can be compared with that of particles introduced through an annulus that surrounds a PJ flow, to assess the relative importance of the precessing jet velocity and the initial slip velocity. Analysis of this type awaits more comprehensive data collection.

In conclusion, despite the strong influence of G_{PJe}/G_1 on clustering in PJ-annular flows, there is some ambiguity regarding the effect of St on clustering. The clustering data was obtained by varying G_{PJ}, so that variables that influence both St and particle motion, ie. fluid velocities, $r_{1/2}$ and the strength of PJ-annular mixing, were all co-varied. The next section details results that allow the effects of St on particle motion to be isolated.

4.5.3 Factors which influence particle dispersion from the 1.5 mm injector

Figure 4.18 compares the mean total particle spread, y_p, as a function of axial position and "primary" (particle exit) velocity for the 80 μm and 46 μm diameter particles introduced through the 1.5 mm injector located adjacent to a 10PJ air flow as illustrated in Figure 4.3. While both the particle diameter and the particle exit velocity have a significant effect on particle spread, the effect of particle exit velocity is more significant for the conditions shown. Figure 4.19 compares the total particle spread at $\frac{x}{D}=3$ as a function of particle exit velocity for the two particle sizes. The significance of the primary air velocity is again evident.

For the present series of experiments the momentum ratio, G_{PJe}/G_1, depends only on the primary air velocity (ie. primary air mass flow rate) since nozzle dimensions and PJ flow-rate are not varied. Hence the effect of varying particle exit (transport) velocity can be observed by plotting particle spread at $\frac{x}{D}=3$ as a function of G_{PJe}/G_1, as shown in Figure 4.20. The effect of variation in particle size can be represented as a Stokes number. This is possible because in all cases investigated, $G_{PJe}/G_1 >> 1$, so that the fluid length and velocity scales are controlled by the PJ rather than the primary flow. The PJ flow-rate is constant, implying that τ_f is constant at a given axial position, and that St depends only on τ_p. Consequently, the effects of particle exit velocity and particle size on spreading can be represented by a single parameter that is a function of G_{PJe}/G_1 and Stokes number.

Figures 4.21 and 4.22 show that the parameters $(G_{PJe}/G_1)St^{-0.5}$ and $(G_{PJe}/G_1)St^{-1}$ both provide reasonable collapse of the spread data at $\frac{x}{D}=3$ for the two different sized particles. In these figures, the constant fluid time-scale is calculated using Equation 4-9, where the jet half-width at $x/D = 3$, $r_{1/2} = 14.8$ mm, is measured directly from Figure 3.13a for the 10 mm PJ water flow case with the maximum PJ to annular momentum ratio investigated, ie. $G_{PJe}/G_1 = 18.4$. The jet air exit velocity, U_e, and equivalent diameter, d_e, are calculated for the PJ air flow alone, and are constant. Using these data, the Stokes number of 80μm particles is calculated to be 59, whilst that of 46μm particles is 19. Consequently both sizes of particles are within the range of St of interest, being too large to be flow tracers, but not so large that they are unaffected by fluid structures.

The collapse of the data in Figures 4.21 and 4.22 demonstrates that, within the level of accuracy of the data, both the momentum ratio and the Stokes number are important in determining the response of particles to fluid structures. It can be deduced that the momentum ratio, $G_{PJe}/G_{1,}$ largely determines the nature of the structures generated by interactions between PJ and annular fluids, whilst the Stokes number determines the response of particles to such structures. In contrast to the data obtained using the 1.5 mm injector, there is a lack of evidence for a strong relationship between St and clustering in PJ-annular flows (Figures 4.15 and 4.17). Nevertheless, it can be deduced from the above results, that a relationship between the parameter, $(G_{PJe}/G_1)/St^n$, and clustering exists, and that further work using discrete particle size ranges, and more accurate determination of fluid time-scales and particle concentrations should be undertaken in PJ-annular flows.

4.5.4 Key findings – Measurements of particle concentration and trajectories

Indicative measurements of concentrations of unclassified glass beads in PJ-annular flows were obtained from photographs. Particles were counted in a single column of square cells extending axially from the middle of the annular slot to the end of the image. Key findings are:

- Preferential concentration (increased clustering) is measured as a two-fold increase in the ratio of standard deviation to mean particle number per cell (σ/μ).
- Clustering effects in PJ-annular air flows scale with the momentum ratio, G_{PJe}/G_1, and jet half width, $r_{1/2}$. For $G_{PJe}/G_1 > 4$, σ/μ is increased dramatically from ~ 0.4 to ~ 0.8.
- Poor correlation between preferential concentration and *St* in PJ-annular flows is found because variation in the PJ flow-rate causes simultaneous variation in a number of variables which influence *St*. These include: jet half widths, fluid velocity and length scales, and the relative strength of the large structures in the jet.

Glass beads, closely sieved into diameter ranges, 76 μm< d_p< 84 μm, and 44 μm< d_p< 48 μm were introduced through a 1.5 mm injector adjacent to a 10 mm PJ air flow. The fluid time-scale, τ_f, was held constant by fixing the PJ flow-rate. Consequently, *St* could be determined unambiguously from the particle time-scale, which depended only on d_p. The primary (particle exit) velocity was varied to investigate the effect of G_{PJe}/G_1 on particle spreading, but in all cases, $G_{PJe}/G_1 >> 1$, so that constancy of τ_f was retained. Key findings are:

- Increases in particle diameter and particle exit velocity were both shown to significantly reduce particle spread.
- The parameter $(G_{PJe}/G_1)/St^n$, where $0.5 \leq n \leq 1$, provides good collapse of the particle spread data for $St > 1$.
- It is deduced that the momentum ratio, G_{PJe}/G_1, largely determines the nature of the structures generated by interactions between PJ and annular fluids, whilst the Stokes number determines the response of particles to such structures.

4.6 Conclusions

Evidence is provided in support of the second hypothesis, "that clustering of pulverised coal particles within jet flows can be significantly increased by enhanced large scale turbulence and reduced small scale turbulence, here generated by precession".

- Preferential particle concentration (clustering) effects have been found to occur when particles are injected into FPJ - annular flows. Particles are deduced to be entrained towards the centre of the flow in the NBZ by drag forces and then to form clusters in the region $1 < \frac{x}{D} < 5$ due to the action of large-scale turbulent motions.

- Small particles are able to follow the large-scale motions and display preferential concentration even in the near field. Larger particles, while not precisely following the flow, are sufficiently influenced to display increased clustering effects further downstream, presumably in the regions between structures.

- Precessing flows are deduced to increase preferential concentration effects by increasing the size and time-scale of the large fluid structures, which increases the significance of drag on particles relative to lift forces and particle inertia.

- Preferential concentration effects were measured in 19 mm PJ-annular flows by dividing photographic images of particles into cells and counting particles in individual cells. Glass beads with a size distribution similar to industrial PF distributions were used. When an annular velocity of 9.8 ms^{-1} was used, an increase in the momentum ratio, across the range $0 < G_{PJe}/G_1 < 7.2$, caused an increase in the ratio of standard deviation / mean number of particles per cell, from 0.4 to 0.8. Higher momentum ratios, achieved by the use of a lower annular velocity of 2.4 ms^{-1}, did not increase the variation in particle concentration further. The correlation between St and clustering in PJ-annular flows was poor. It is postulated that the use of a wide particle size distribution and inaccuracies in estimation of fluid time-scales prevented accurate determination of St in these flows.

- A 1.5 mm diameter injector located adjacent to a 10 mm PJ nozzle was used to study the effect of St on clustering. In these flows the fluid time-scale was held constant, and particle time-scale, τ_p, was determined unambiguously. The parameter $(G_{PJe}/G_1)St^{-n}$, where $0 \leq n \leq 1$, collapsed the particle spread data for 46 and 80 μm diameter particles.

Increased radial particle spread is expected to correlate with increased clustering effects, which consequently can also be expected to vary with $(G_{PJe}/G_1)St^{-n}$.

- LDA data (Appendix 3) also supports the second hypothesis. The r.m.s. axial and azimuthal velocities of particles in a PJ-annular flow with $G_{PJe}/G_1 = 14.3$ were shown to be higher than those in the annular flow alone by a factor of 2. The large scale structures present in FPJ flows are deduced to cause this change and to be responsible for increased clustering effect following the arguments of Longmire and Eaton (1992).

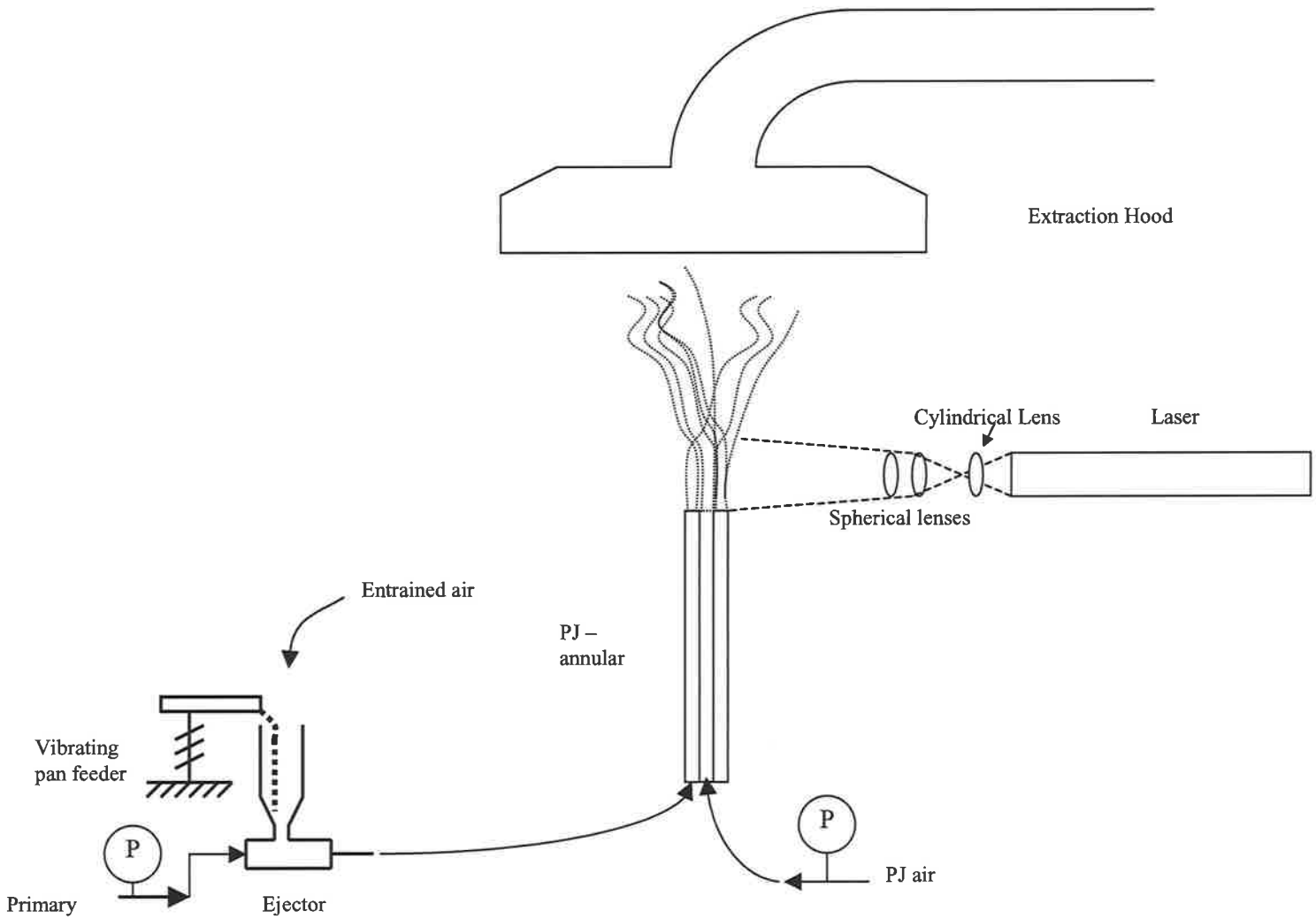

Figure 4.1 A schematic diagram of planar laser sheet – particle visualisation experiments

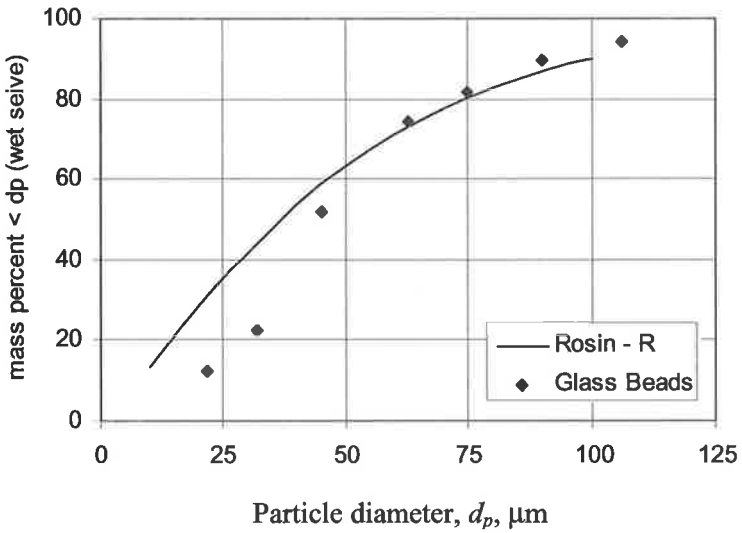

Figure 4.2 Glass bead particle size distribution of 50 μm (nominal) particles used in the experimental arrangement illustrated schematically in Figure 4.1 (Rosin-Rammler distribution for 50 μm particles also shown)

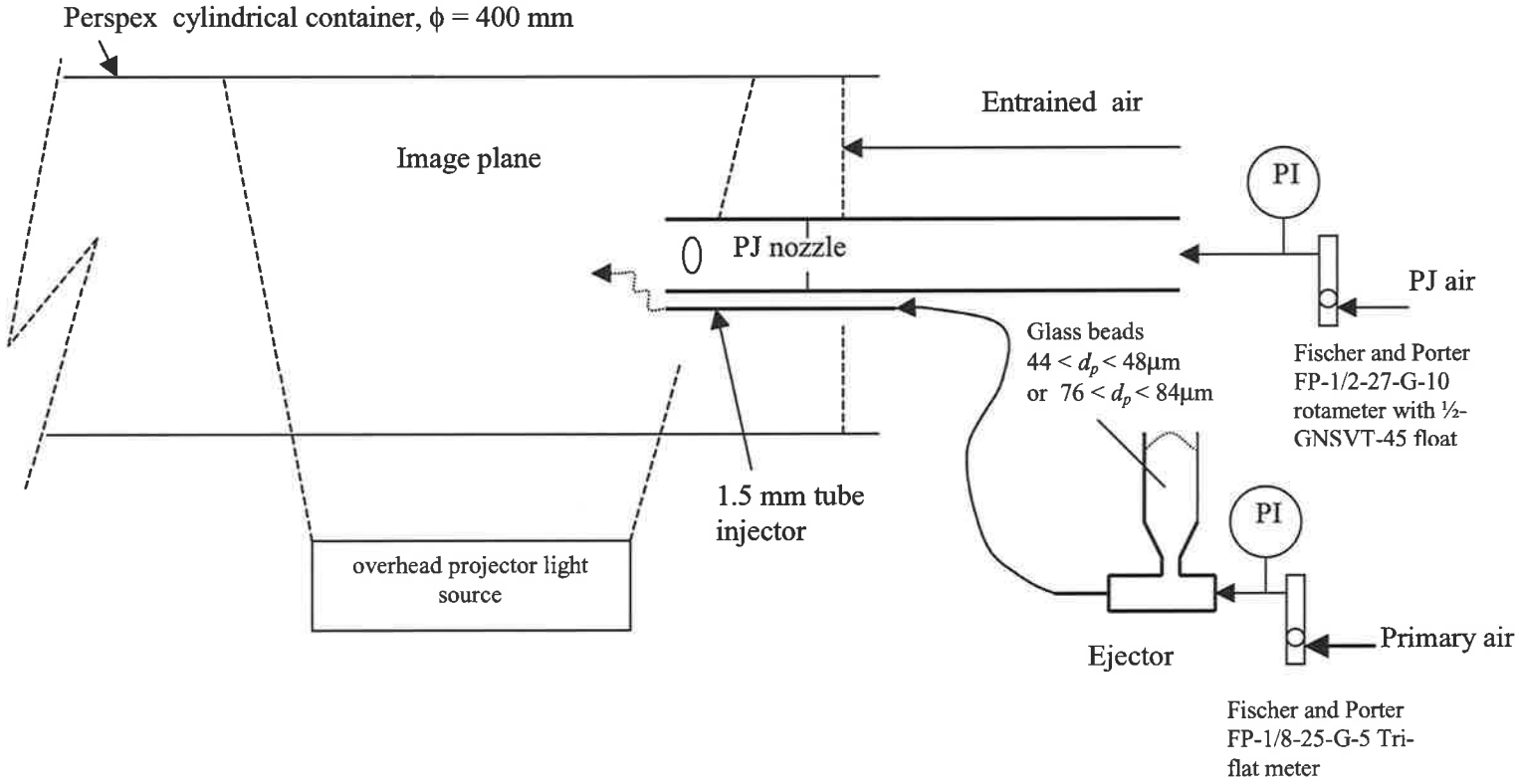

Figure 4.3 A schematic diagram of the experimental equipment used to perform visualisation of particles emanating from a "point" source

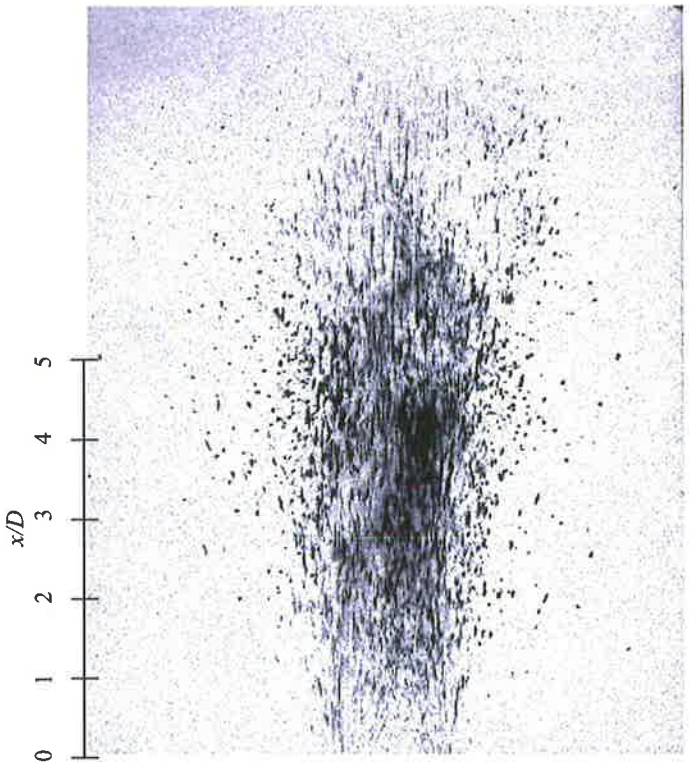

Figure 4.4a. A photograph (1/1000 s exposure) of an annular air flow alone with an exit velocity of 9.8 ms^{-1}, seeded with glass beads only and illuminated by an Ar-ion light sheet.

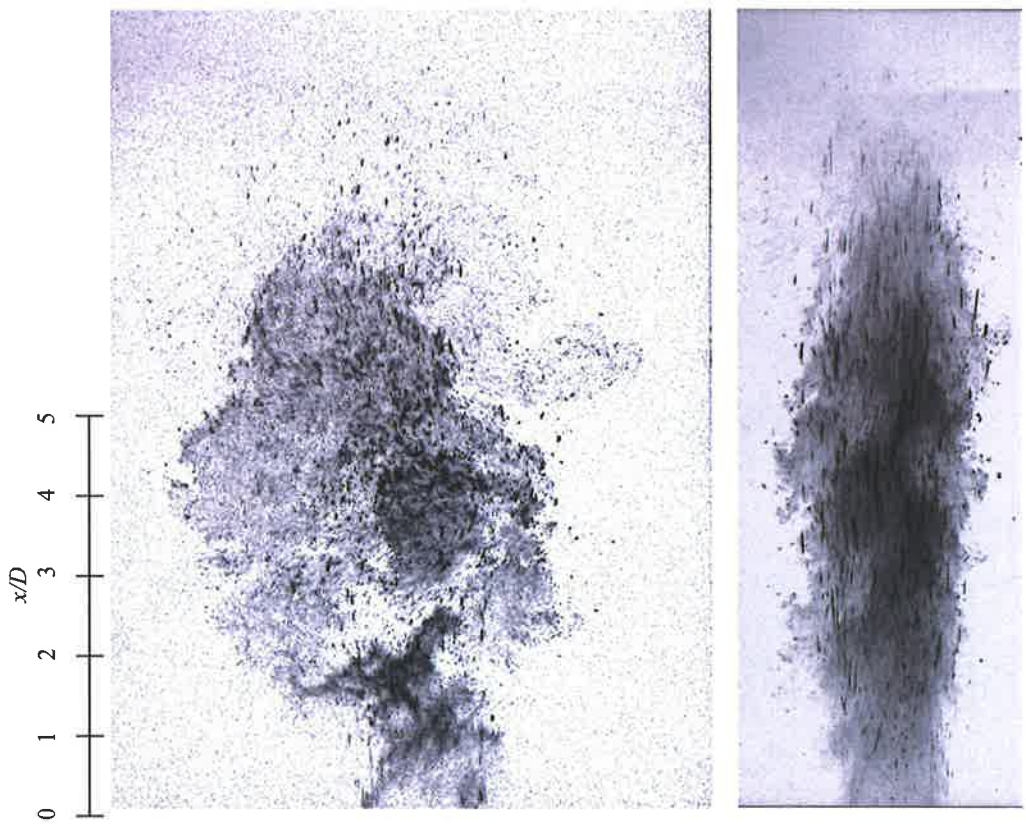

Figure 4.4b. A 1/4000 s photograph of the 19PJ flow with G_{PJe}/G_1 = 3.91 (at left) compared with a 1/1000 s photograph of the annular flow alone (at right). In both cases the annular stream was seeded with flow tracer particles and glass beads.

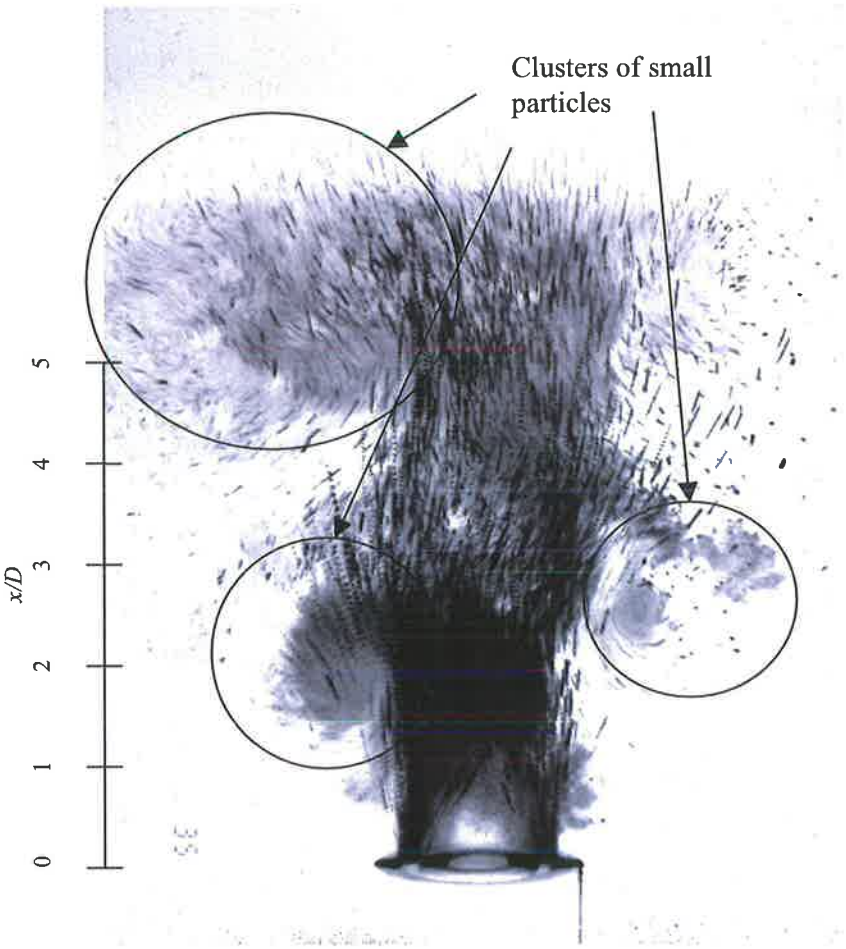

Figure 4.5 A 0.001 s photograph of glass bead tracks without flow tracer particles, $G_{PJe}/G_J = 3.91$. Beads are imaged up to 10 times each by the copper vapour laser pulsed at 10 kHz. Small particles concentrate in clusters off the centre-line in the region $1 \leq \frac{x}{D} \leq 3$.

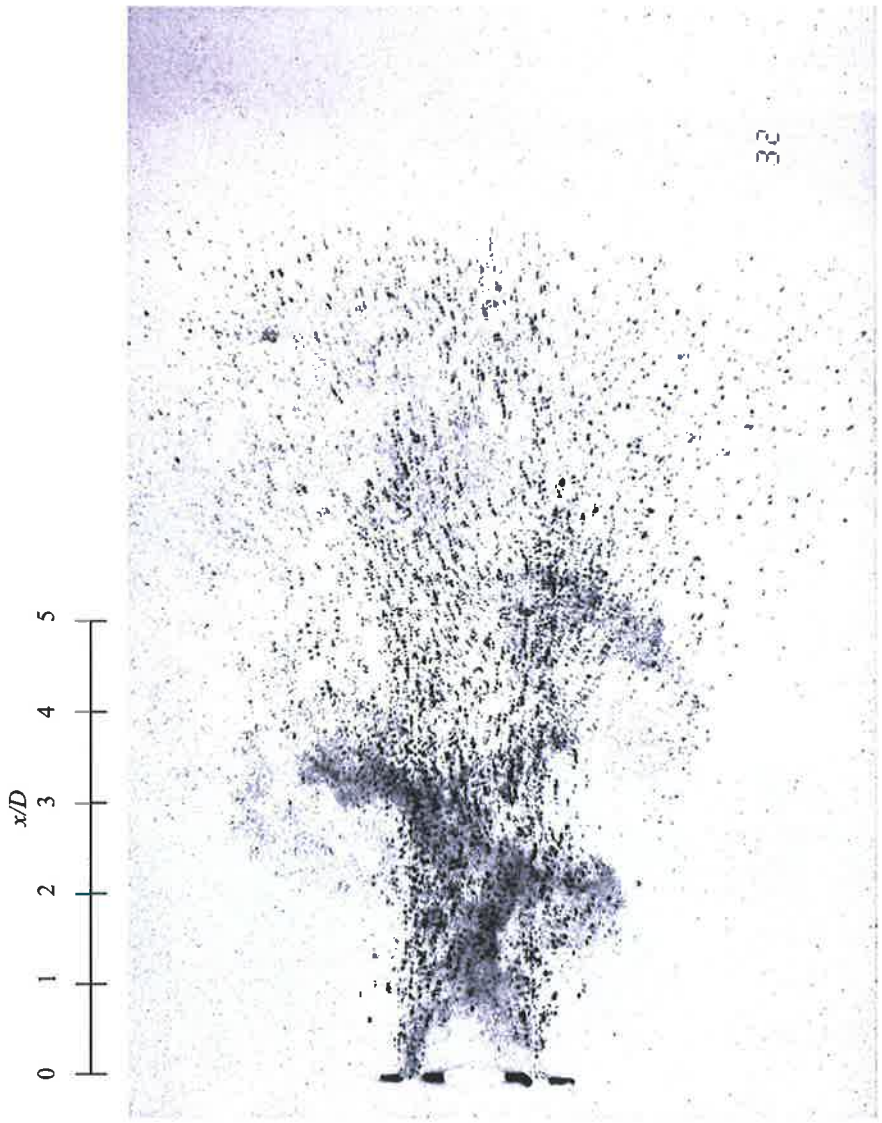

Figure 4.6 A 1/1000 s photograph of glass bead tracks without flow tracer particles, $G_{PJe}/G_J = 3.91$. Beads are imaged 2 times each by the copper vapour laser pulsed at 10 kHz. The bulk forms of the clusters appear to be related to the large structures observed in Chapter 3.

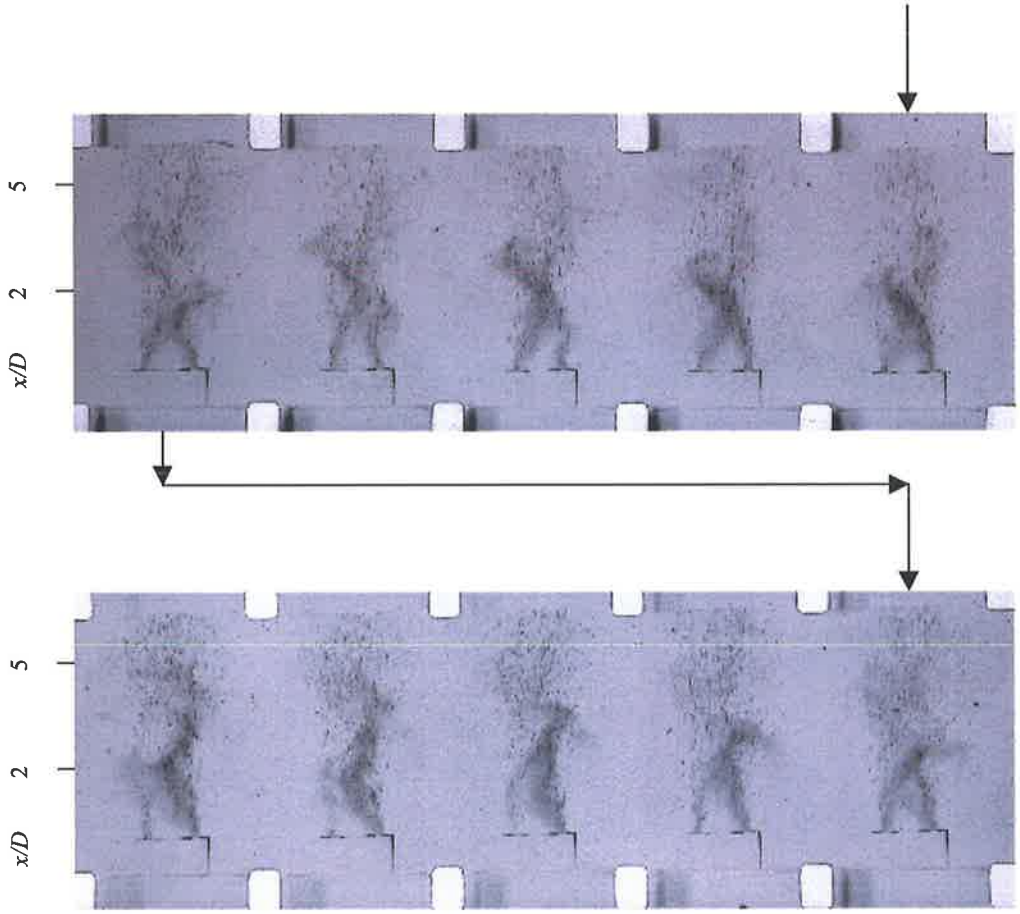

Figure 4.7 Digitised version of a 16 mm cine film sequence, illuminated by the Cu vapour laser sheet pulsing at 10 kHz. The framing rate is nominally 1000 frames per second. Flow conditions are as per Figure 4.4b. Clustering effects (preferential concentration) can be seen throughout the region, $\frac{x}{D} \leq 3$.

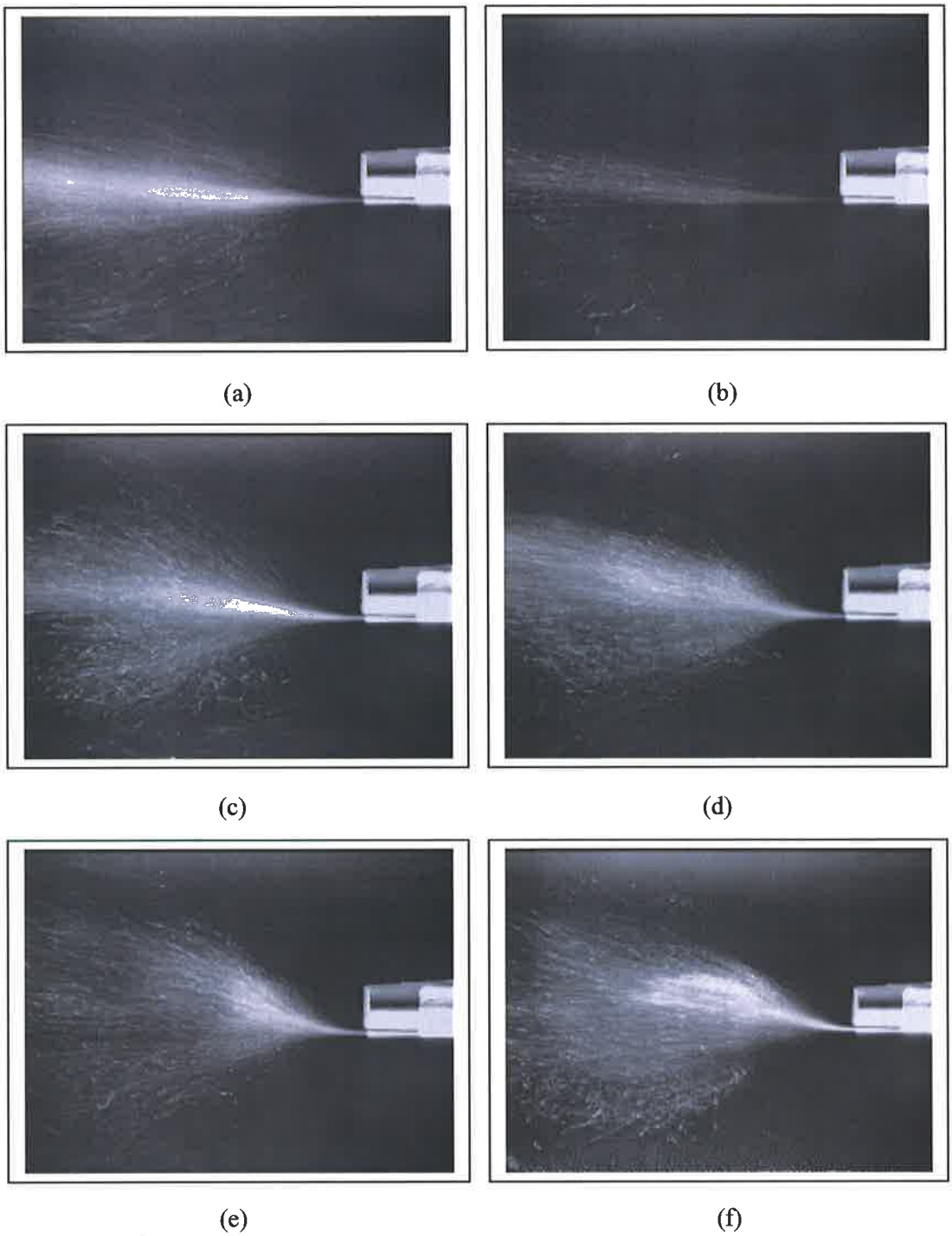

Figure 4.8 Digitised, 1/25s images showing the effect of varying particle injection velocity at a constant 10PJ exit velocity of 101 ms^{-1}, on particle tracks and spread of 46 μm particles.
(a) $G_{PJe}/G_1 = 36$, $U_1 = 25.3$ ms^{-1}, (b) $G_{PJe}/G_1 = 75$, $U_1 = 17.5$ ms^{-1}, (c) $G_{PJe}/G_1 = 160$, $U_1 = 12$ ms^{-1}, (d) $G_{PJe}/G_1 = 240$, $U_1 = 9.7$ ms^{-1}, (e) $G_{PJe}/G_1 = 390$, $U_1 = 7.7$ ms^{-1}, (f) $G_{PJe}/G_1 = 2100$, $U_1 = 3.3$ ms^{-1}

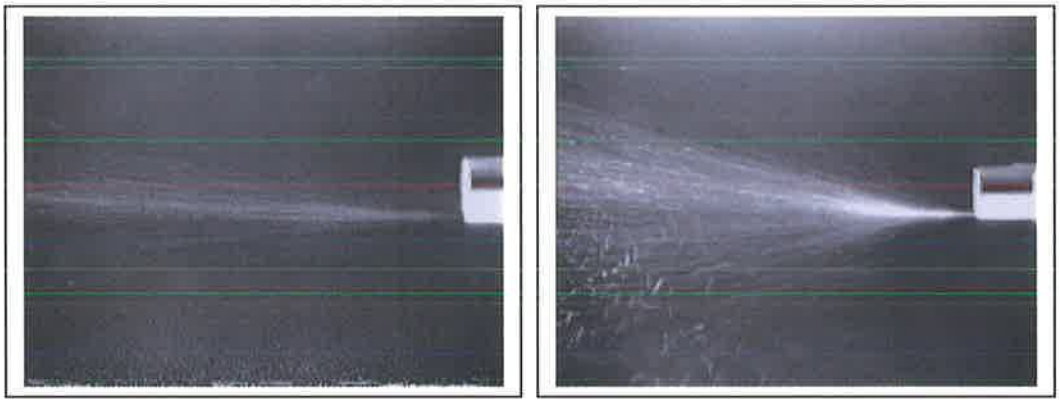

(g) (h)

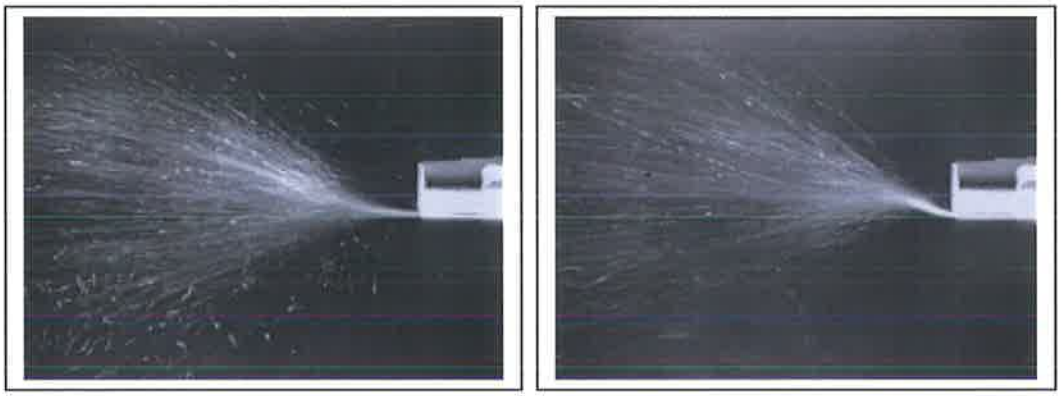

(i) (j)

(k)

Figure 4.8 (continued) Digitised, 1/25s images showing the effect of varying particle injection velocity at a constant 10PJ exit velocity of 101 ms^{-1}, on particle tracks and spread of 80 μm particles.
(g) $G_{PJe}/G_J = 51$, $U_J = 21.3$ ms^{-1}, (h) $G_{PJe}/G_J = 95$, $U_J = 15.6$ ms^{-1}, (i) $G_{PJe}/G_J = 216$, $U_J = 10.3$ ms^{-1}, (j) $G_{PJe}/G_J = 410$, $U_J = 7.5$ ms^{-1}, (k) $G_{PJe}/G_J = 1260$, $U_J = 4.3$ ms^{-1}.

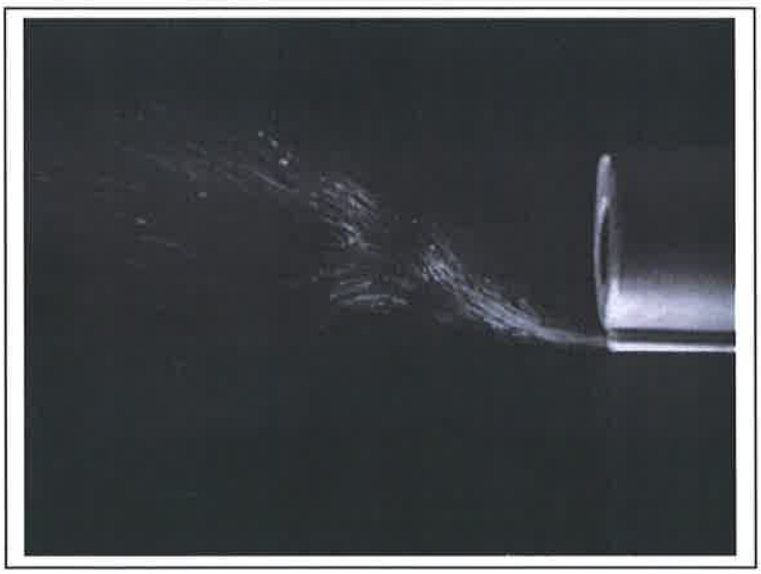

Figure 4.9 A photograph (1/1000 s exposure ~ 1/3 of a precession cycle) of 80 μm particles injected through the 1.5 mm injector at 4.5 ms^{-1} (G_{PJe}/G_1 = 1260). Particles are deflected in the NBZ and subsequently clustered by the large-scale structures.

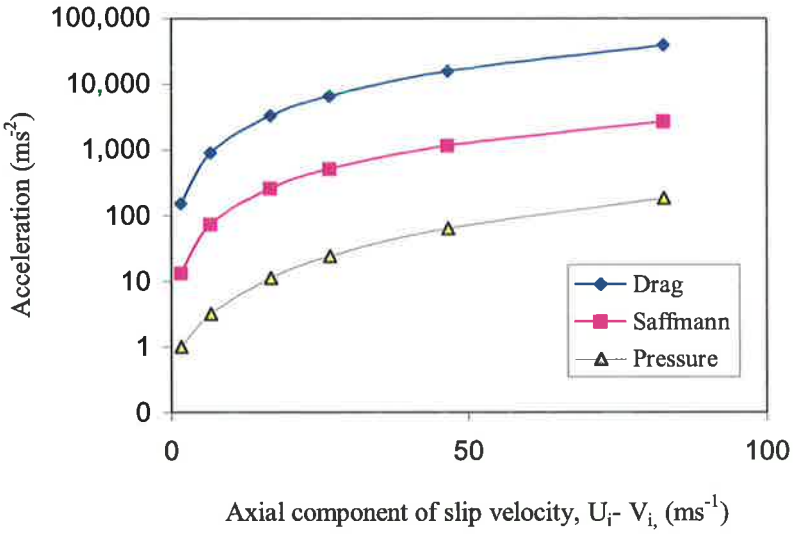

Figure 4.10 Estimates of axial acceleration of 46 μm glass beads introduced through the 1.5 mm injector at 3.3ms^{-1} into the NBZ of the 10PJ air flow, with PJ exit velocity of 101ms^{-1}. Since particle acceleration due to drag forces dominates over the acceleration due to Saffmann lift and pressure gradients, it can be deduced that the initial deflection of particles towards the nozzle centre-line in the NBZ is primarily due to drag forces.

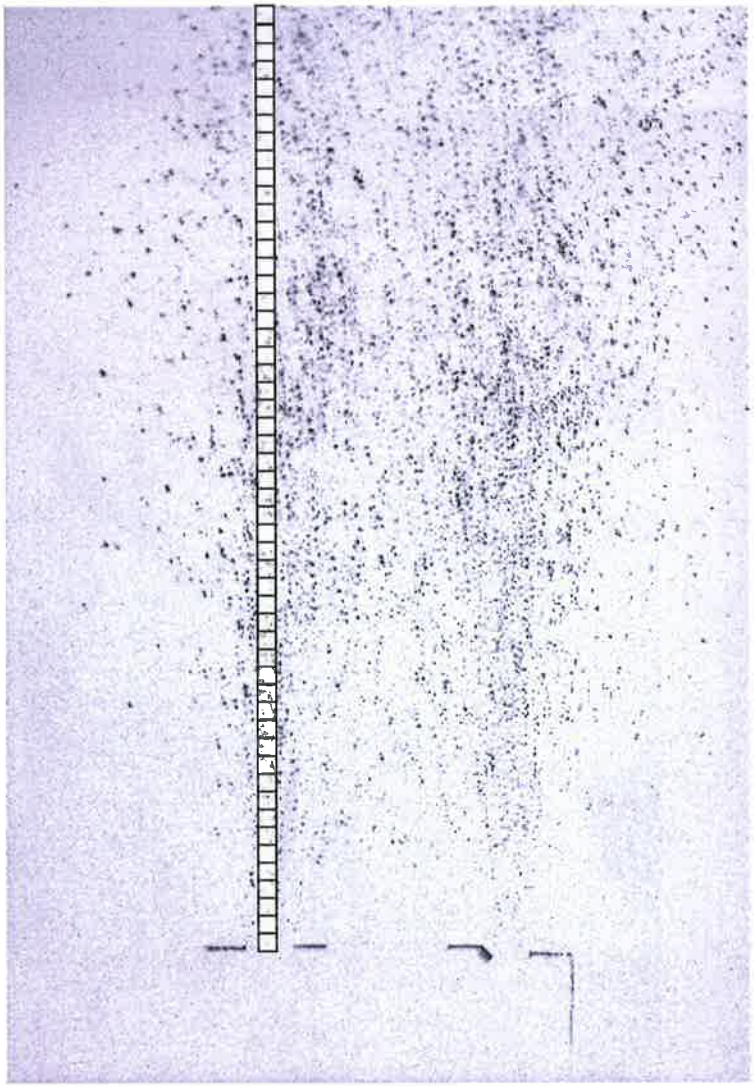

Figure 4.11 The particle concentration measurement grid overlaid on a photograph of glass beads in an annular air flow with velocity 9.8 ms^{-1}, $G_{PJe}/G_J = 0$. Shutter speed = 1/8000 s, Cu-vapour laser frequency = 10 kHz.

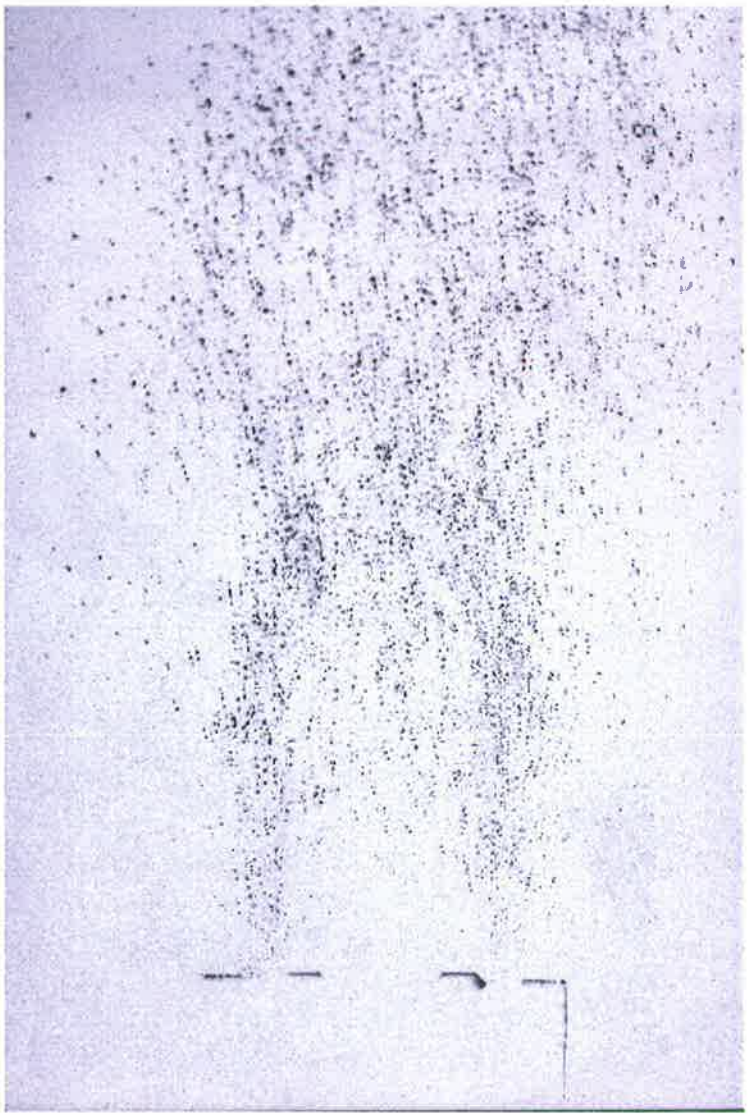

(a)

Figure 4.12 Photographs used for particle concentration measurements, of glass beads in 19PJ-annular flows:
(a) annular velocity = 9.8ms^{-1}, G_{PJe}/G_l = 1.12 (b) annular velocity = 9.8ms^{-1}, G_{PJe}/G_l = 3.91
(c) annular velocity = 9.8ms^{-1}, G_{PJe}/G_l = 7.22 (d) annular velocity = 2.4ms^{-1}, G_{PJe}/G_l = 0
(e) annular velocity = 2.4ms^{-1}, G_{PJe}/G_l = 18.6 (f) annular velocity = 2.4ms^{-1}, G_{PJe}/G_l = 64.7
(g) annular velocity = 2.4ms^{-1}, G_{PJe}/G_l = 119

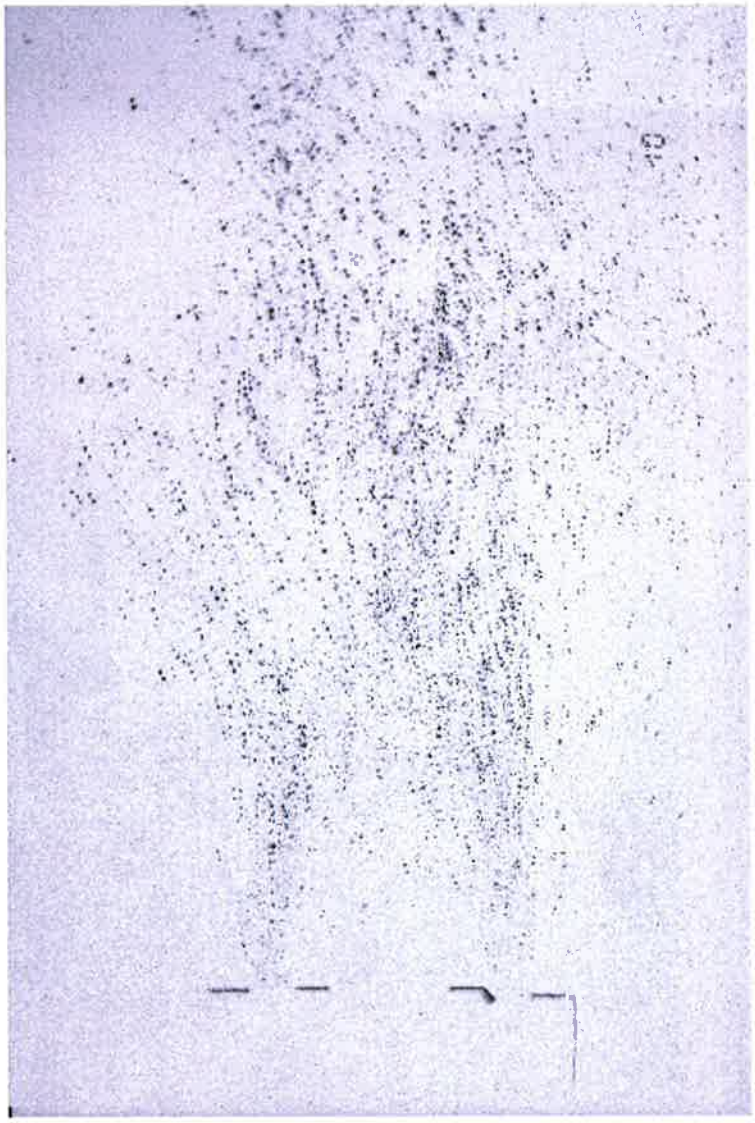

(b)

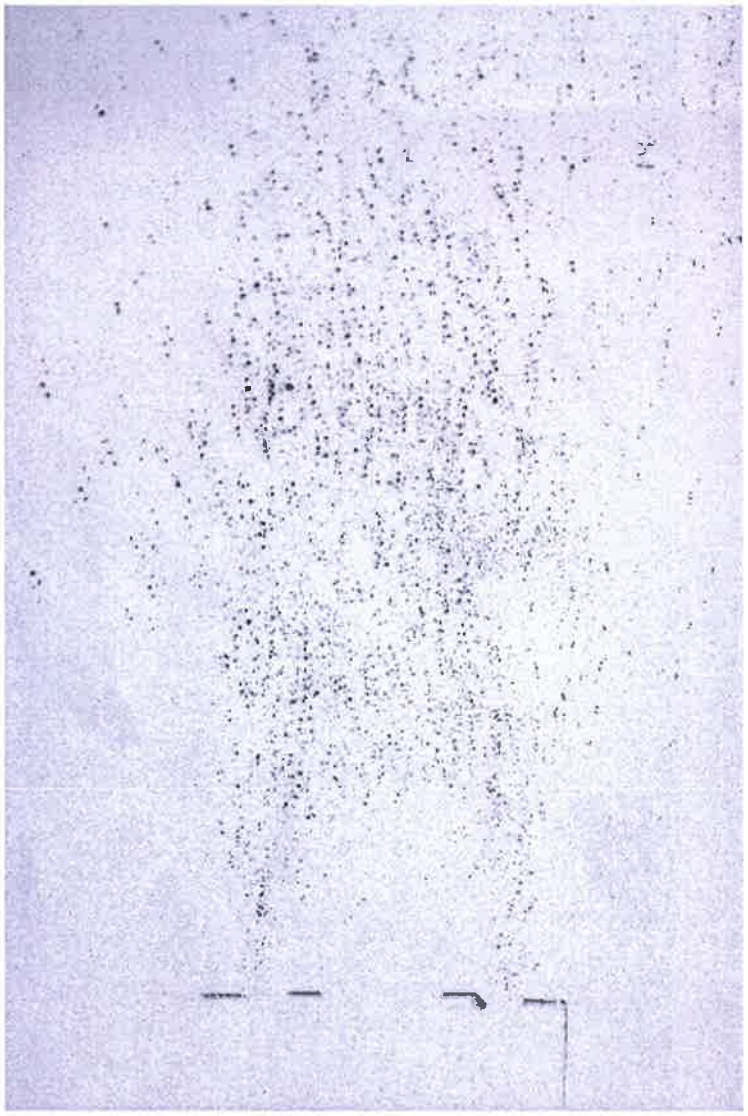

(c)

(d)

(e)

(f)

(g)

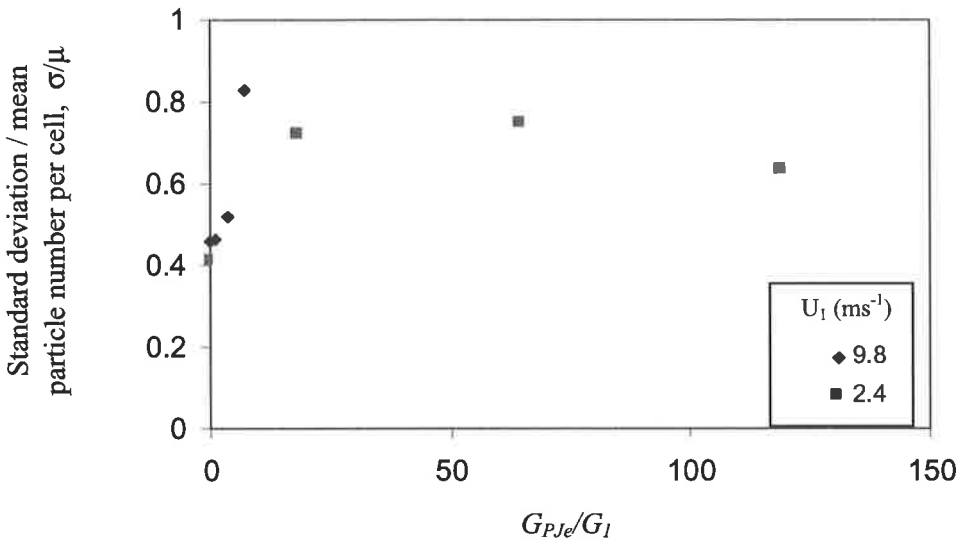

Figure 4.13 The influence of G_{PJe}/G_1 on the ratio of standard deviation to mean particle number per cell (σ/μ) of glass beads in PJ-annular flows.

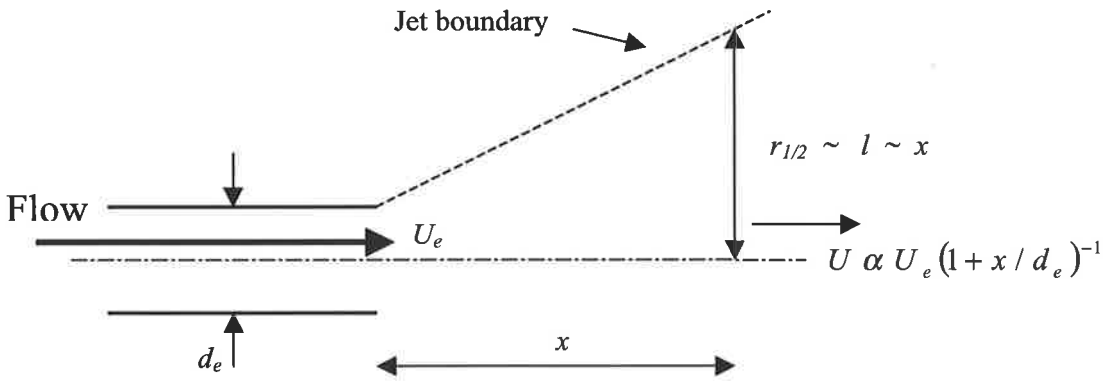

Figure 4.14 A schematic diagram of a jet showing the assumptions used to estimate the fluid time-scale, given by equation 4-9.

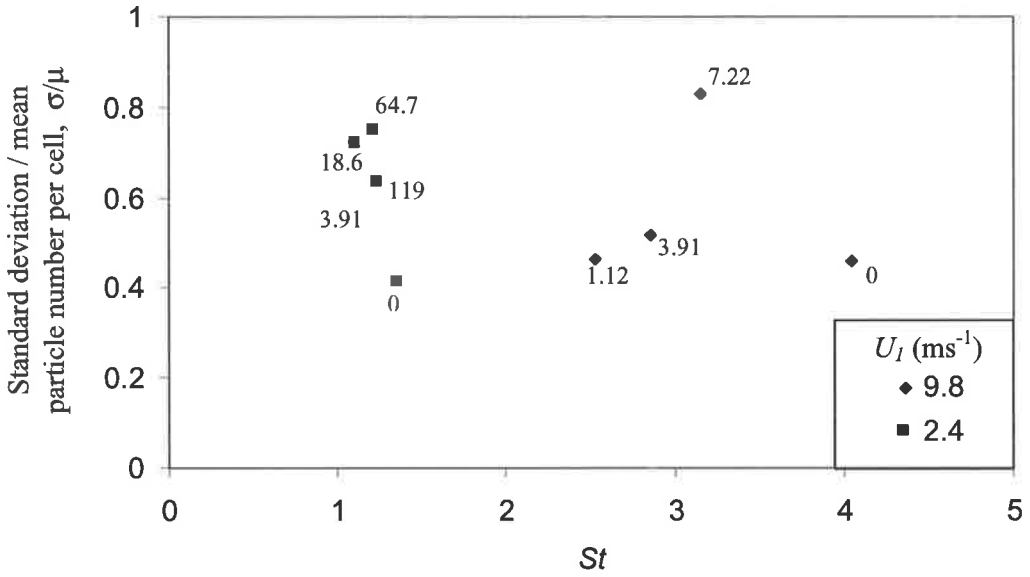

Figure 4.15 Relationship between the ratio of standard deviation to mean number of particles per cell, σ/μ and *St* in PJ- annular flows (G_{PJe}/G_1 values shown adjacent to data points). Fluid time-scale calculated according to assumptions illustrated in Figure 4.14.

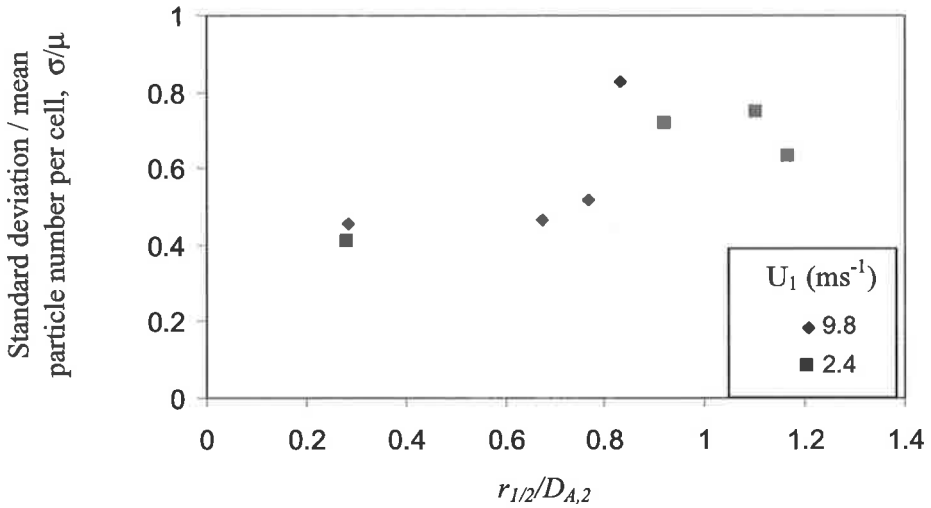

Figure 4.16 Relationship between the ratio of standard deviation to mean number of particles per cell, σ/μ, and jet half angle, $r_{1/2}$, in PJ-annular flows.

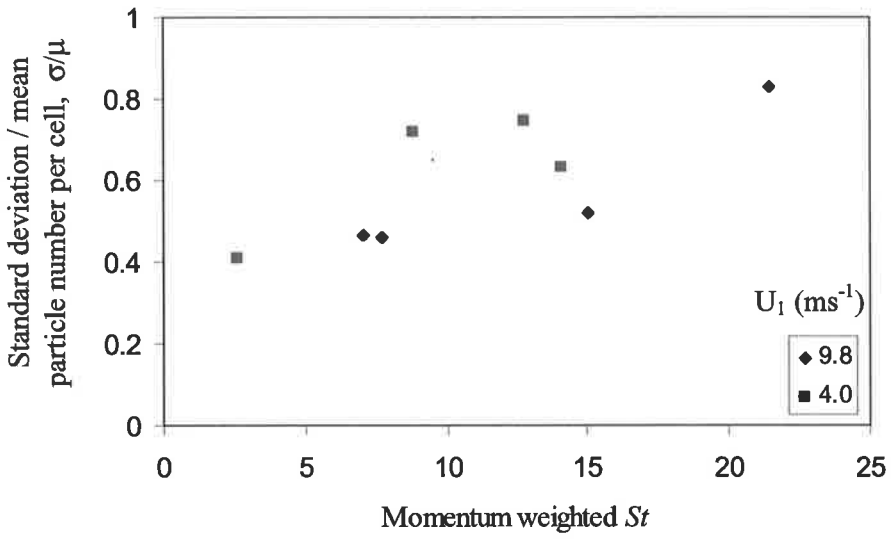

Figure 4.17 Relationship between the ratio of standard deviation to mean number of particles per cell, σ/μ and *St* in PJ- annular flows. The fluid time-scale is calculated according to assumptions illustrated in Figure 4.14. The exit velocity is a momentum weighted value, calculated from Equation 4-11.

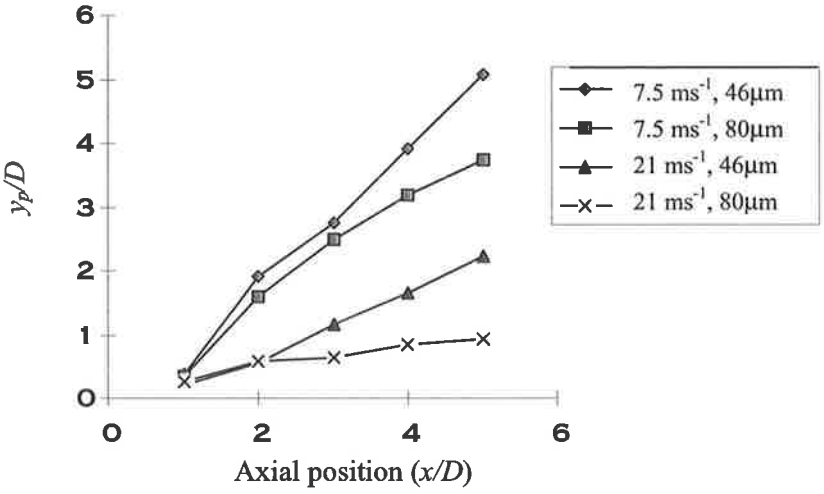

Figure 4.18 Mean total spread, y_p/D, of 80 μm and 46 μm particles emanating from the 1.5 mm injector as a function of axial position and particle exit velocity.

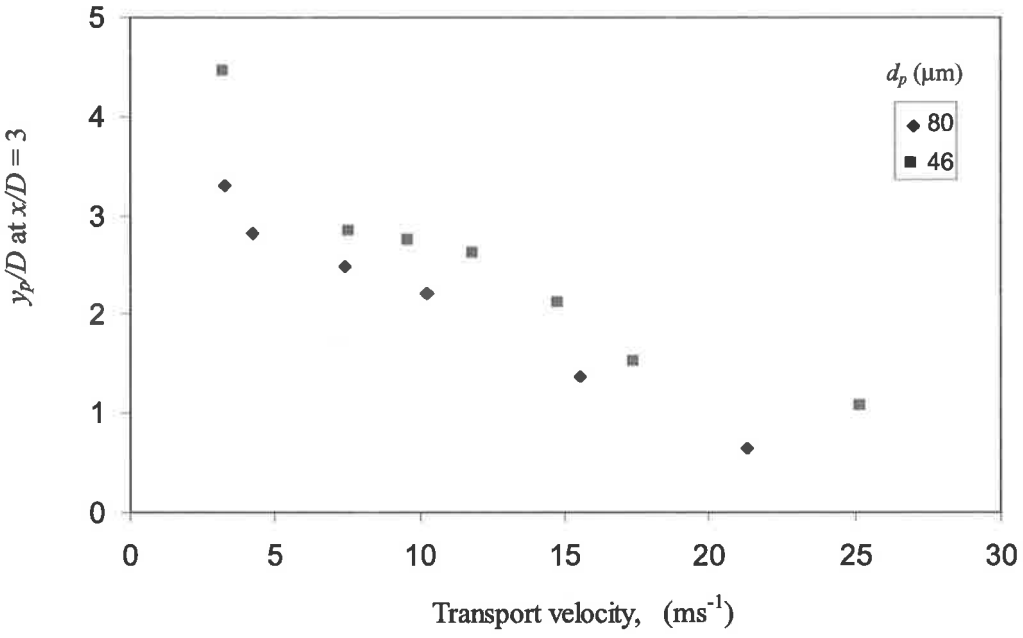

Figure 4.19 Mean total spread, y_p/D, of 80 μm and 46 μm particles emanating from the 1.5 mm injector as a function of particle exit velocity, at $x/D = 3$.

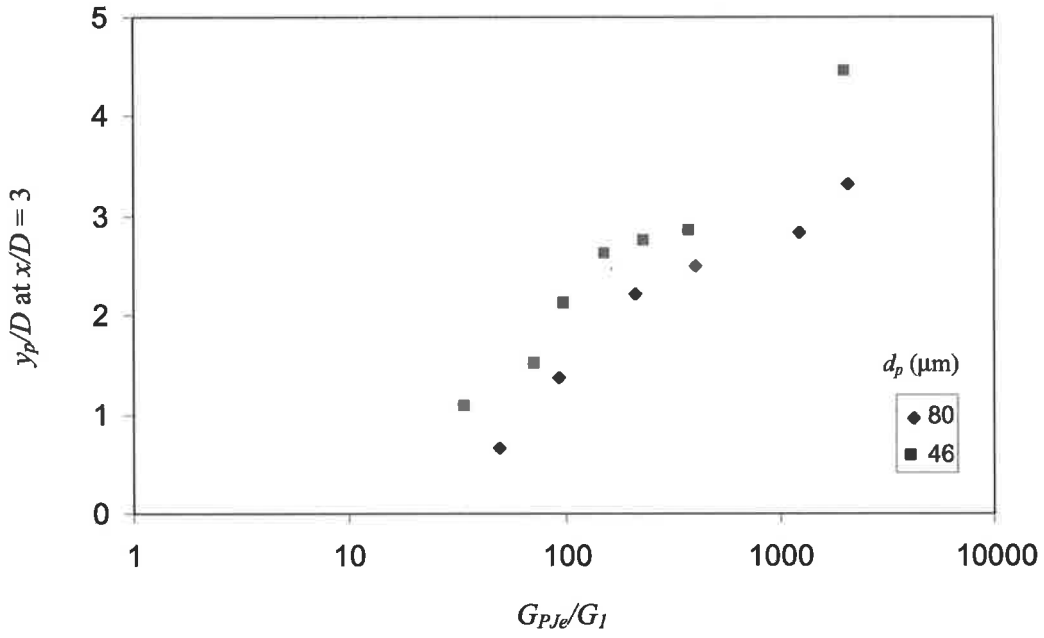

Figure 4.20 Influence of (G_{PJe}/G_1) on the maximum spread of particles emanating from the 1.5 mm injector, $x/D = 3$

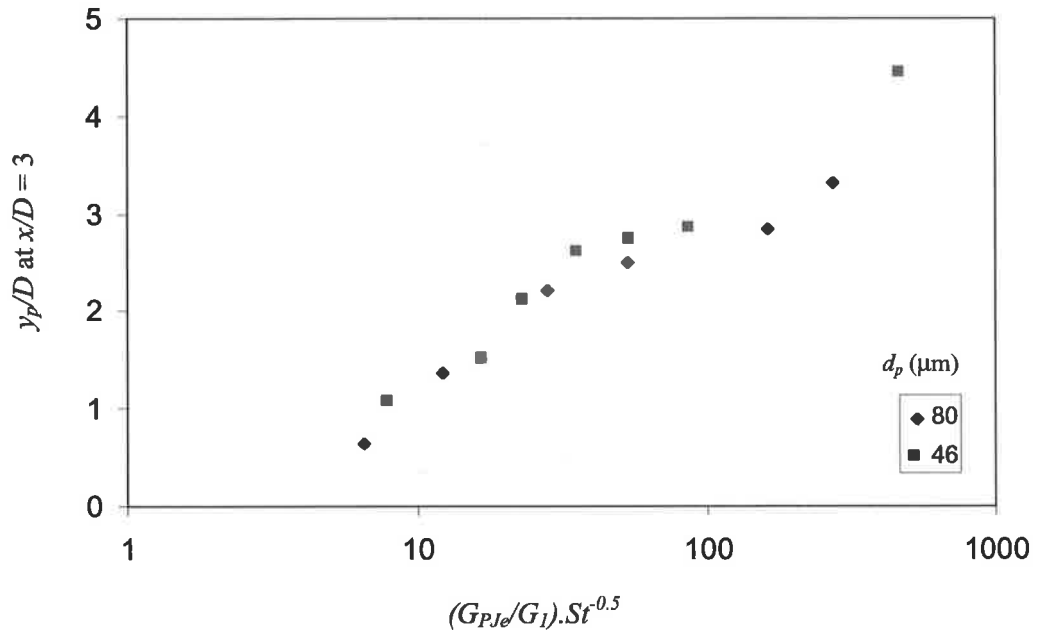

Figure 4.21 Influence of $(G_{PJe}/G_1).St^{-0.5}$ on the maximum spread of particles emanating from the 1.5 mm injector, $x/D = 3$

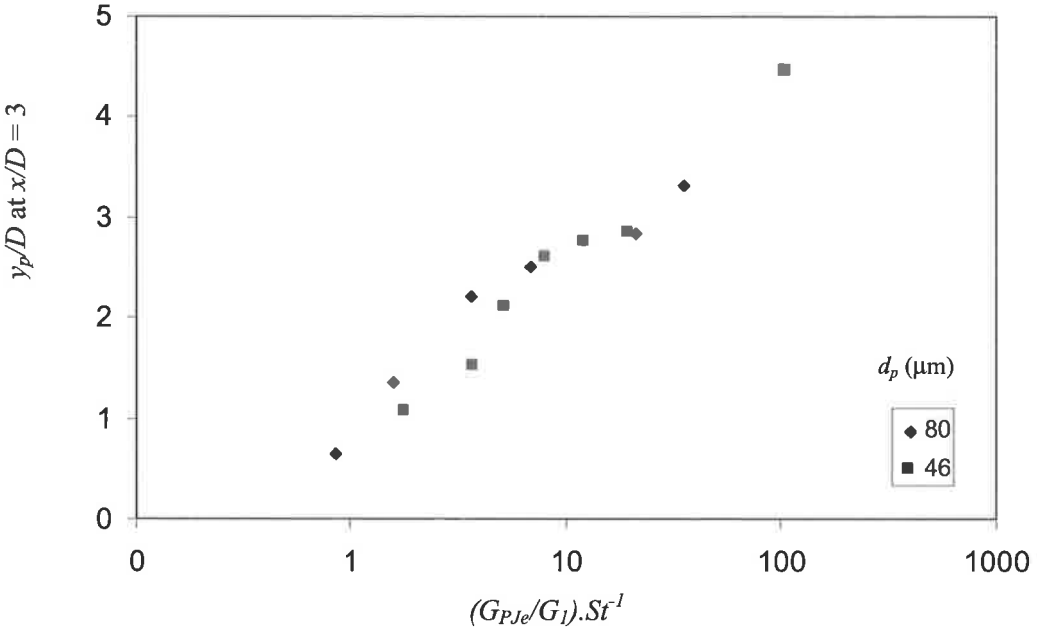

Figure 4.22 Influence of $(G_{PJe}/G_1).St^{-1}$ on the maximum spread of particles emanating from the 1.5 mm injector, $x/D = 3$

Chapter 5 The influence of precession on small-scale PF flames

5.1 Introduction

Previous chapters have demonstrated the effects of a central precessing flow on the structure of a surrounding annular flow and on the clustering of particles transported in the annular flow. The third and fourth hypotheses, detailed in section 1.8, can be summarised as follows: *that the control of the structure of jet turbulence, and hence particle clustering, can be used to beneficially influence flame stability, heat release rates and/or NO_x emissions*. In the current chapter and in Chapter 6 these hypotheses are investigated experimentally at 130 kW scale and 2.5 MW scale respectively.

The following literature review of flame performance expands on that provided in Chapter 1. The review provides a background for the design of the combustion experiments detailed in Chapters 5 and 6. It also provides information that is subsequently used in sensitivity analyses in Chapter 7, which are performed to clarify the mechanisms by which enhanced large scale mixing and large scale unsteady motion in the near field influence flame characteristics.

5.2 A review of factors that influence flame combustion characteristics

5.2.1 Introduction

The combustion of PF in flames occurs in a number of stages. Particles are heated, liberating combustible gases that ignite upon reaching a temperature in the region of 500°C (Zhang and Wall, 1994). Flames are stabilised at the axial position where all the physical and chemical requirements outlined in section 1.3.1. are met (ie. liberation of volatile matter, oxygen availability, and sufficiently low local velocities). The current work concentrates on medium to high volatile matter coals as they are applied to rotary kiln type PF flames.

In a study of the effect of fuel type on cement kiln flames, van de Kamp and Daimon (1996) found that "*heat release patterns are a function of volatile matter content, particle size distribution, burner type and operation*". When low volatile matter PF, such as coke is used, stabilisation and the position of peak heat release occur further downstream than when medium to high volatile PF is used (van de Kamp and Smart, 1992). When medium to high volatile matter bituminous coal is used, the highest flame temperatures, which correspond to the highest rates of heat release to the kiln walls, occur relatively near the burner due to the combined effects of volatile and partial char combustion (van de Kamp and Smart, 1992). The bulk of thermal and fuel NO_x formation also occurs close to the burner due to high local temperatures. Combustion of char occurs over a larger time-scale than volatile matter and consequently is completed beyond the position of peak flame temperature, and as such usually contributes little to total NO_x emissions.

The effect of temperature is significant in determining NO_x emissions from medium to high volatile matter coal flames. This is clear from measured peak wall temperatures, which are higher than those of coke flames under most conditions (van de Kamp and Smart, 1992). However pulverised coke flames can also generate high thermal NO_x emissions due to long ignition distances, which allows entrainment of large quantities of air into the flame prior to ignition. Due to the focus on medium to high volatile matter PF flames in the current work, the following literature review deals primarily with processes related to volatile matter rather than char reactions. Processes occurring in the pre-ignition and ignition region of flames, and the potential influence of particle clustering on these processes, are considered.

5.2.2 Particle heating rate in the pre-ignition region

Coal particle ignition and flame stabilisation are influenced by devolatilisation kinetics, particle heating rates and mixing. The heating rate determines the transient particle temperature and so influences devolatilisation rates. The significance of heating rate is illustrated by the fact that some experimental techniques utilise the time required to heat particles to a nominal "ignition temperature" (typically 500°C) as one criterion to determine ignition (Zhang and Wall, 1994). For PF sized particles, particle heating rates are limited by the heat transfer rate to the surface of particles rather than internal heat conduction within particles. (This can be verified by calculation of the Biot number, ie. $Bi = \frac{hd_p}{k_p} << 1$ for PF particles, assuming no slip, ie. $Nu = \frac{hd_p}{k_g} = 2$).

The particle heating rate also influences ignition via its effect on volatile flammability limits and flame speeds. For example, a theoretical analysis (Glassman, 1987) showed that the laminar flame speed of a gas/air mixture depends on the thermal diffusivity of the gas mixture, $\alpha = \frac{\lambda}{\rho C_p}$, and reaction rate, RR, ie.

$$S_L \sim (\alpha \cdot RR)^{0.5} \qquad 5\text{-}1$$

where the reaction rate is typically given by an Arrhenius type relationship. According to Equation 5-1 the laminar flame speed increases with flame temperature. If the particle heating rate in the pre-ignition region of a flame is increased, it will cause an increase in the local temperature of evolved volatile matter, as well as an increase in the devolatilisation rate. It can be argued that such an increase in temperature can allow stabilisation to occur in regions closer to the burner, that is, with smaller *x/D*, despite higher local velocities. An increase in local temperature will also slightly broaden the flammability limits (Glassman, 1987), an effect that also aids stability.

The heating rate of single particles is given by the energy balance:

$$m_p C_p \frac{dT_p}{dt} = (Q_c + Q_r) \qquad 5\text{-}2$$

where the convective term is given by:

$$Q_c = \pi d_p Nu k_g (T_g - T_p) \qquad \text{(W)} \qquad 5\text{-}3$$

If the particles are assumed to have minimal slip with surrounding gases, the equation can be simplified by setting Nu = 2. This assumption is commonly made for PF particles in the literature (Wall, 1987). In section 7.4 the influence of high fluctuating slip velocities on particle combustion rates is investigated.

The characteristic time-scale for convective heating of single particles, τ_{hc}, can be obtained from Equation 5-3 with Nu = 2. It is equivalent to the time required to heat the particle through 63.2 % of the temperature difference, (T_g -T_p), and is given by Wall (1987) as:

$$\tau_{hc} = \frac{\rho_p C_p d_p^{\,2}}{12 k_g} \qquad \text{(s)} \qquad 5\text{-}4$$

Using this relationship, the convective heating time-scale of a 50 μm particle is of the order of 4ms. The effects of the temperature and entrainment rates of secondary air and externally recirculated gases on convective particle heating rates are discussed in Chapter 7, with reference to the combustion experiments reported in Chapters 5 and 6.

The radiant heat transfer to a single particle from surrounding hot walls is given by Wall (1987):

$$Q_r = \varepsilon_p \sigma A_p \left(T_w^{\,4} - T_p^{\,4}\right) \qquad \text{(W)} \qquad 5\text{-}5$$

A comparison of radiant and convective heating rates, using Equations 5-5 and 5-3 respectively, shows that radiant heating only becomes significant for relatively larger particles (> 50 μm) and if the wall temperatures are high (>1300°C), and similar to gas temperatures (Wall, 1987). In practice wall temperatures are significantly lower than gas temperatures, although in cement kilns wall temperatures are of the order of 1300°C, so that radiant heating is not normally considered to be significant. However, Wall's analysis does not take into account additional radiant heating of particles from the flame itself. Direct radiant heating of particles by the flame, and the influence of enhanced large scale mixing on flame to particle radiant heating, are considered later.

Although Equation 5-5 can be used to calculate the heating rate of individual particles, in practice the presence of surrounding particles modifies the heating rate of individual particles, so that it is more useful to consider "particle clouds" than individual particles. Clouds of PF particles can be assumed to have zero reflectance since individual particles have high absorptivity and significantly larger diameters than the wavelength of radiation. Consequently the radiant absorptivity of a particle cloud, α_{cl}, can be assumed to be equal to

its emissivity, and is given by a relationship developed by analogy to gases. The cloud emissivity is given by Hottel and Sarofim, (1967):

$$\varepsilon_{cl} = 1 - \exp(-caL_b / 4), \qquad 5\text{-}6$$

where c is the number of particles per unit volume, a is the particle surface area, πd_p^2, L_b (m) is the mean radiation beam length, which in the case of particle clouds can be taken as the cloud diameter. Alternatively, the cloud emissivity can be expressed in terms of mass concentration, C ($kg.m^{-3}$) and particle density ($kg.m^{-3}$), as:

$$\varepsilon_{cl} = 1 - \exp(-1.5CL_b / \rho_p d_p) \qquad 5\text{-}7$$

Equations 5-6 and 5-7 can be applied to the entire particle stream or to individual particle clusters. Experiments and calculations to follow will investigate whether the observed increases in cluster diameters and particle concentration within clusters (Chapter 3), alter particle cluster heating rates, especially those not obscured from direct flame radiation by other clusters. Experiments reported in the current chapter and Chapter 6 investigate this premise, and relevant calculations are presented in Chapter 7.

The mean radiative flux from hot furnace walls to the entire particle stream in the pre-ignition region can be obtained from Equation 5-9, given below. This equation is developed from radiation heat transfer theory as follows. The net radiative heat flux between two black bodies, in terms of areas, A_1 and A_2, and view factors, F_{12} and F_{21}, is given by Holman (1981) as:

$$Q_{1-2} = A_1 F_{12} E_1 - A_2 F_{21} E_2 \qquad 5\text{-}8$$

where the emissive power, E_i, at a temperature T_i is given by, $\sigma(T_i^4 - T_o^4)$, T_o is the datum temperature. If the particle stream (body 2) and furnace walls (body 1) are gray, and the particle stream is much smaller than, and totally enclosed by, the furnace so that $A_2/A_1 \rightarrow 0$, Equation 5-8 can be simplified to give the approximate net radiative heat exchange, ignoring absorption of radiation by gases, (Holman, 1981):

$$Q_{1-2} = A_2 \varepsilon_2 \sigma (T_1^4 - T_2^4) \qquad 5\text{-}9$$

Radiative transfer from the furnace walls to the entire particle cloud in the pre-ignition region is estimated in Chapter 7 by use of Equation 5-9, which accounts for multiple reflections from the furnace walls. The area A_2 is equal to A_{cl}, the cross-sectional area of the coal stream seen by the walls.

In contrast to the treatment above, some radiative particle heating processes occur as the result of a single pass of radiation. The energy exchanged between two bodies in a single pass of radiation is given Holman (1981) as:

$$Q_{1-2} = \left[\frac{\sigma F_{12} A_1 \left(T_1^4 - T_2^4 \right)}{1/\varepsilon_2 + 1/\varepsilon_1} \right] \qquad 5\text{-}10$$

where F_{12} is the view factor for a single pass of radiation. Equation 5-10 can be applied to the heating of individual particle clusters, rather than the entire particle stream, by direct radiation from either the flame or the furnace walls. A single pass of radiation is considered because any radiation that is transmitted through the cluster is dispersed or absorbed by other clusters. The view factor, F_{12}, varies with the distance between the cluster and the heat source, and may be reduced by partial obscuration by other clusters. Consequently the maximum flame to cluster view factor occurs when the cluster reaches the flame front where there is no obscuration by other clusters. At this location, the view factor is one and A_2 is cross-sectional area of the cluster. Equation 5-10 can also be used to calculate the mean radiative heat transfer from the flame to the entire particle stream or cloud in the pre-ignition region. In this case A_2 is equal to the cross-sectional area of the particle stream seen by the flame. Equation 5 – 9 can not be applied in this case because the flame does not enclose the particle stream.

Equation 5-10 can be used to calculate the heating rate of an individual cluster by radiation from the furnace walls. The maximum view factor of 1 only applies when the cluster is located on the outer boundary of the flame where there is no obscuration by other clusters. The emissivity of refractory walls is conservatively estimated at 0.7 in Chapter 7, where calculations are presented. This estimate of wall emissivity is based on the data provided by Perry *et al.* (Table 10-17) for refractories in the temperature range 600°C to 1000°C.

In summary, the key points in the above review are:

- Heating rates determine the transient temperature of PF particles in the pre-ignition region of flames, and thereby have a strong influence on devolatilisation rates.
- Particle temperature affects local gas phase temperature and so flame speed and flammability limits.

- PF particle heating rates are limited by heat transfer to the surface of the particle.
- Convective heating of PF particle surfaces is generally considered to be of greater importance than radiant heating.
- Equations for radiative heat transfer from the flame and furnace walls to particles are presented. These equations allow the effects of characteristics of PJ flows, such as large jet half widths, and enhanced clustering, to be calculated. Calculations are presented in Chapter 7.

5.2.3 Moisture evaporation, devolatilisation rates and yields, and soot formation

Coal is a complex organic matrix, consisting of macromolecules made up of aromatic ring structures, bridges and side chain groups (Watt, *et al.* 1996). The combustion experiments reported in Chapters 5 and 6 make extensive use of bituminous coals. Upon initial heating, the moisture in bituminous pulverized coal evaporates rapidly at low temperatures, so that it has an insignificant effect on coal devolatilisation rates. Nevertheless, the energy required to evaporate the moisture contained in pulverised coals accounts for approximately 20% of the energy absorbed in heating to the nominal ignition temperature.

Investigations over recent decades have shown that coal rank, structure, heating rate, final temperature and particle size all influence the nature, yield and rate of devolatilisation (Lau and Niksa, 1992, Solomon and Fletcher, 1994). During primary devolatilisation, high molecular weight tars originating from coal matrix fragments are evolved, followed by non-condensable gases (Lau and Niksa, 1992). The rate of tar formation, evolution (mass transfer to the gas phase) and destruction are influenced by the rate at which chemical bridges are broken and formed (Solomon and Fletcher, 1994). These processes are dependent on the heating rate and final temperature. Secondary pyrolysis is dominated by the conversion of tars to soot. Combustion of soot can increase devolatilisation rates by radiating heat back to particles, whereas in contrast, blowing (out-flowing volatiles moving away from particles) reduces energy feedback to the particle from which they were liberated (Lau and Niksa, 1992). However, Heidenreich and Zhang (1999) showed that blowing is insignificant during the pyrolysis of coal particles in the PF size range.

Devolatilisation kinetics can be modelled by first order kinetics (Jones, 1993):

$$\frac{dV}{dt} = k(V^* - V) \qquad 5\text{-}11$$

where V^* is the ultimate volatile yield, and V is the volatile yield at a given time. The first order rate constant (Jones, 1993) is given by:

$$k = Ae^{\frac{-E}{RT}} \qquad 5\text{-}12$$

Integrating 5-12 yields,

$$\ln(V/V^*) = -kt \qquad 5\text{-}13$$

If the time-scale, $t_{1/2}$, is given as the half life of reaction, $V/V^* = 0.5$, ie:

$$t_{1/2} = \frac{1}{k}\ln 2 \qquad 5\text{-}14$$

Such first order expressions do not fit experimental devolatilisation data well. The apparent activation energy changes with temperature due to the range of chemical bond strengths of the many decomposition reactions occurring at different temperatures (Wall, 1987). Wall (1987) recommends a simple two competing reaction model, using kinetic data obtained at fast heating rates in laminar flow reactors (Badzoich and Hawksely, 1970 and Kimber and Gray, 1967). This data and approach is widely used in flame modelling studies (eg. Costa *et al.* 1990b). The scheme of two competing reactions can be written as:

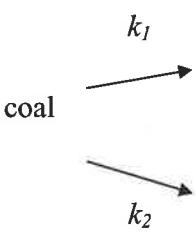

5-15

where k_1 and k_2 are the rate constants, α_1 and α_2 are fractions of coal converted to volatiles (V_1 and V_2), leaving the remaining solids (S_1 and S_2). Reaction 1 dominates at particle temperatures below 950°C, while reaction 2 dominates above 1100°C (Morgan and Roberts, 1987). The kinetic parameters are shown in the table below.

Table 5.1 Kinetic parameters for the two-competing reaction scheme.

	Reaction 1	Reaction 2
E ($kJgmol^{-1}$)	74	251
A (s^{-1})	$1.34x10^5$	$1.46x10^{13}$

The more powerful "Distributed Activation Energy" model (DAEM) was proposed by Anthony *et al.* (1975). It models devolatilisation by a set of independent first order parallel reactions with a Gaussian distribution of activation energies. Some recently developed models for devolatilisation rates and yields based on coal structure, also make use of the DAEM to model the dependence of devolatilisation rate on rank, temperature and heating rate (Niksa and Lau, 1993). Fletcher (1989) proposes that the wide variation in previous kinetic data was due to the use of wall or gas temperatures, which relate differently to particle temperature depending on experimental conditions. Fletcher (1989) used an optical technique to measure the temperature of individual bituminous coal particles in conjunction with weight loss. The particles were transported in a nitrogen stream at 1050 – 1250 K in an entrained flow reactor. Heating rates were nearly 10^4 Ks^{-1}. The resulting devolatilisation kinetics are based on particle temperatures which were 100 –150 K lower than gas

temperatures in these experiments. Fletcher's pseudo – first order Arrhenius parameters, in the temperature range studied are, $A = 2.3x10^{14}$ s^{-1} and $E = 55{,}000$ $calmol^{-1}$ (230 $kJmol^{-1}$).

Recent work (Sampath *et al.* 1998) has suggested that, at fast heating rates, a finite time is required for the coal structure to relax after being heated to the devolatilisation temperature. Subsequent evolution of heavy compounds extends volatile matter liberation time. The additional enthalpy required to relax the structure is of the same order as that required to heat the coal to devolatilisation temperature. Sampath *et al.* (1998) modelled the volatile enthalpy term by assigning a higher specific heat capacity to volatiles than to the solid. They demonstrated good agreement between model and experimental particle temperatures by including the volatile enthalpy term and particle mass loss in particle energy balance. The devolatilisation delay pushes volatile evolution to higher temperatures. This finding demonstrates that the kinetics of devolatilisation need to be applied under the same heating conditions to that at which they were obtained. For this reason the kinetics of Badzioch and Hawksley (1970), taken at $> 2.5x10^4$ Ks^{-1}, are more appropriate for PF flame modelling than those of Fletcher (1989), taken at heating rates of $<10^4$ Ks^{-1}, despite the greater errors in temperature measurements.

The time required for the coal structure to relax may partly explain the extended ignition delays observed in experimental swirled boiler type flames, where quarl zone (IRZ) volatile matter combustion rates are lower than predicted by most models. For example, Weber *et al.* (1992b) investigating this phenomenon predicted higher temperatures by 150 – 200 K than measured in the IRZ. This was despite reducing the mixing rate by adjusting the Magnussen and Hjertager (1977) mixing model constant, A, from 4 to 0.6 (Visser *et al.* 1990). Costa *et al.* (1990b) also found an ignition delay in the IRZ, not predicted by models. They checked the validity of their volatile matter combustion model, also based on Magnussen and Hjertager's (1977) eddy dissipation model, in a natural gas flame. They suggested that the kinetics of secondary pyrolysis might be slow enough to account for the ignition delay, discounting potential errors in combustion and radiation models. The devolatilisation kinetics used by all groups were those of Badzoich and Hawksely (1970) – which deal only with primary pyrolysis. Experimental secondary pyrolysis kinetic data, which support the points made by Sampath *et al.* (1998) in modelling studies, is limited, but some recent experimental results are outlined below.

Ma *et al.* (1996) measured soot yields in conditions designed to simulate the fuel rich near-burner region of large scale coal boiler furnaces. They injected coal particles into the post flame region of a CH_4/H_2/air flat flame, ie. into a region with zero oxygen. Soot yields (from secondary pyrolysis) correlated with tar yields reaching approximately 20 % of the original mass of coal (d.a.f. basis) for a high volatile bituminous coal. Soot yields peaked at approximately 1650 K, with a slight reduction at 1900 K explained by a reduction in tar molecular stability at high temperatures, which in turn was attributed to increased concentrations of oxygen containing radicals. Submicron (~ 25 nm) soot formed within 15 ms of injection. Results such as these provide the most relevant empirical time-scales available for secondary pyrolysis under flame conditions. Agglomeration of soot particles was also observed by Ma *et al.* (1996) and was attributed to the low oxygen concentration and lack of convection of soot away from particle surfaces.

A modified Damköhler number, *Da*, which is the ratio of devolatilisation kinetic rate, r' (s^{-1}), to particle surface heating rate is (Heidenreich and Zhang, 1999, Ross *et al.* 1999):

$$Da = \frac{r' \rho_s C_{ps} d_{p_s}}{h} \qquad 5\text{-}16$$

This fomulation is equaivalent to the traditional definition of *Da* as the ratio of mixing time to reaction time, since the surface heating rate is a convective, ie. mixing controlled, rate. Using this relationship, Ross *et al.* (1999) showed that, at a given temperature in the range typical of ignition (500 – 900 K), the devolatilisation rate of PF sized particles is limited by kinetics rather than heating. However, in practice, kinetics are highly temperature dependent in this range and the particle heating rate controls the transient particle temperature and hence the kinetic rate of devolatilisation. Particle heating rates may in fact be substantially higher than that determined by the surface convection, due to radiation from burning volatile matter and soot. At combustion temperatures, both heating and kinetic devolatilisation rates are rapid as demonstrated by numerous experiments (eg, Anthony, *et al.* 1975) and combustion is generally limited by mixing rates.

The influence of turbulence on devolatilisation rates has not been widely considered in the literature. Almost all devolatilisation experiments have been performed under laminar flow conditions, either on electrically heated grids, in entrained flow reactors, or in flat flames. Nevertheless, some data does exist. Costa *et al.* (1994) found that the devolatilization rates in turbulent, high heating-rate flat flame experiments is greater than those in laminar flow

environments. The particles were transported through a 5mm pipe into a flat flame. Short residence times of up to 10 ms were possible, in which time, weight losses were recorded to be more than twice those of Kobayashi *et al.* (1977), who used a bituminous coal and similar heating rates, but in a laminar entrained flow furnace.

The yield of volatile matter under fast heating rates such as that experienced in PF flames ($>10^4$ Ks^{-1}) is much greater than that produced by standard ASTM proximate analyses. High temperature yields up to 1.6 – 1.8 times the proximate analysis value for most coals (excluding lignites) were measured using an isothermal plug flow reactor with gas temperatures in the region of 1500°C (Knill *et al.* 1988). Numerous studies have shown similar results (Wall, 1987). Total volatile yield has little dependence on particle size for particle diameters less than 200 μm, depending more on coal type, temperature, and heating rate (Solomon and Fletcher, 1994). Final volatile yields from high volatile bituminous coals contain large quantities of tars (Niksa and Lau, 1993). One typical pyrolysis experiment produced a volatile-tar/gas ratio of 2.3 for Pittsburgh #8 high volatile bituminous coal compared to 0.43 for a lignite. Total tar yields were 37.7 % and 15.4 % (d.a.f. basis) respectively (Lau and Niksa, 1992).

Knill *et al.* (1988) proposed an empirical formula for volatile matter yield, in which no volatiles are released until the particle temperature reaches 500°C, beyond which devolatilisation increases linearly with temperature until all is released at T_p = 1000°C. In the formulation that follows, the volatile matter yield at a given temperature, is denoted by Y_{vol}, and $Y_{vol,ht}$ is the high temperature yield, ie. for $T_p > 1000$°C.

$$
\begin{aligned}
Y_{vol} &= 0 && \text{for } T_p < 500^{\circ}\text{C} \\
&= \frac{1}{2}\left(1+\frac{T_p-500}{500}\right)Y_{vol,ht} && \text{for } 500^{\circ}\text{C} < T_p < 1000^{\circ}\text{C} \\
&= Y_{vol,ht} && \text{for } T_p > 1000^{\circ}\text{C}
\end{aligned}
\qquad 5\text{-}17
$$

A model which predicts volatile yields, based on the physical and chemical processes occurring during devolatilisation, and makes use of the distributed activation energy concept is the "functional group, -depolymerisation, vaporisation, cross-linking" (FG-DVC) model. It predicts thermal decomposition progressively into light gases, tars and char as the size of parent polymer clusters in the coal matrix increase (Zhao *et al.* 1994). The FG sub-model accounts for thermal evolution by a distributed activation energy formulation. The DVC

sub-model accounts for the effects of temperature on cross-linking and breaking of the connections between polymer clusters. The model confirms that coals with the same rank (same %C) have similar yields, and that the devolatilisation yield of any given coal at a given heating rate can be interpolated from known coals on the basis of elemental composition (Zhao *et al.* 1994).

The key points of the above review can be summarised as follows:

- Moisture evaporation from bituminous PF pulverized coal is rapid and has an insignificant effect on devolatilisation rates.
- Primary devolatilisation, in which gases and tars are formed, can be modelled by the two competing reaction model, using kinetic data obtained at fast heating rates in laminar flow reactors (Badzoich and Hawksely, 1970 and Kimber and Gray, 1967), or by the Distributed Activation Energy Model.
- To be accurate, kinetic data needs to be applied under the same heating conditions to that at which they were obtained.
- Turbulence has been shown to increase devolatilisation rates relative to those obtained in a laminar entrained flow furnace.
- Bituminous coals yield large quantities of tar which pyrolyses to soot.
- The yield of volatile matter under fast heating rates is much greater than that produced by standard ASTM proximate analyses.

5.2.4 Ignition

Historically, experimental investigations of ignition characteristics of clouds of coal particles were conducted to gain an understanding of the conditions that could lead to dust explosions (Essenhigh *et al.* 1989). The two main mechanisms proposed for the onset of ignition are homogeneous ignition of evolved volatile matter, and heterogenous ignition on the particle surface and within pores. Experimental techniques used to investigate these proposals have involved heating a single particle or a mass of particles in a hot gas or flame, or by laser irradiation (Zhang and Wall, 1994). The ignition temperature is normally taken as the gas temperature at which a visible flash is observed or at which mass loss is first detected (Zhang and Wall, 1994). The differences in technique influence the results, so that meaningful comparisons can only be made from trends obtained using the same technique (Zhang and Wall, 1994).

It is generally thought that heterogenous ignition only occurs when particles are isolated and of small size (< 100 μm) so that heating time is small (Essenhigh *et al.* 1989). Recent imaging studies of particles in a flat flame, using a digital camera, have confirmed that heterogenous ignition does occur under these conditions (Kharbat *et al.* 1995). However, in flames where particle concentrations are high, ignition is homogeneous. Cassell and Liebman (1959) reported a reduction in the ignition temperature of clouds of metal particles as the particle concentration was increased. Similar effects have been observed in both coke and coal particle clouds using both pulse and continuous flow experiments in a drop tube furnace (Zhang and Wall, 1994). The pulse experiments used 0.2 to 10 mg of coal/pulse, whilst the continuous experiments employed 1.5 to 12 grams coal /hour. Ignition temperatures ranged from 600 to 900 K and reductions in ignition temperature of the order of 100 K were observed. The researchers concluded that the experimental variations in particle concentration were not significant enough to influence cloud radiant absorptivity. Consequently heating rates of particles by radiation from furnace walls did not vary significantly. They concluded that the co-operative effect is due to an increase in the concentration of volatile matter. Lucas and Wall (1994) found, further, that the cloud ignition event was reliant on the evolution of sufficient volatile tars to produce a flammable mixture. While ignition occurred in a fuel lean environment in the experiments of Zhang and Wall (1994), due to the oxygen present in the primary transport air, the stoichiometry of the gas phase of particle clouds in flames may rapidly become fuel rich as devolatilisation proceeds. Enhanced large scale mixing may influence local cloud stoichiometry and so play a role in flame stabilisation. This point will be discussed further in section 5.2.5.

Theoretical analyses have been developed which explain some of the observations outlined above. Ryan and Annamali (1991) developed a transient group ignition model for spherical particle clouds, from which they were able to determine the cloud particle number density above which homogeneous ignition occurred. They also obtained good agreement with ignition times measured in a laminar flow reactor. A similar model was developed for coal particle streams, modelled as a cylindrical cloud (Du *et al.* 1995).

Krishna and Berlad (1980) developed steady-state energy balance equations for particles and the gas phase in a spherical particle cloud. Using these equations Zhang (1993) showed that, while the heterogeneous ignition temperature varies with particle size due to the changing particle area/volume ratio, the homogeneous ignition temperature is independent of particle size, decreasing with increases in cloud size and density. In Chapter 7 energy balance equations, similar to those used by Zhang (1993) but with the additional consideration of radiant effects, are used to assess the affects of particle concentration and cluster size on cluster heating rates.

The key points of the above review can be summarised as follows:

- In flames, where particle concentrations are high, ignition is homogeneous.
- A reduction in the ignition temperature of clouds of particles occurs as the particle concentration is increased due to an increase in the concentration of volatile matter.
- The homogeneous ignition temperature of a cloud of particles is independent of particle size, and decreases with increasing cloud size and density.

5.2.5 Effects of large scale mixing on gas flame stability

In section 1.3.1. the physical and chemical requirements for flame stability were outlined. Stabilisation in simple jet methane flames has been attributed to the propagation of the flame front through stoichiometric premixed zones generated by large structures (Chen and Roquemore, 1986, Chen *et al.* 1988). Stability is also only achieved in regions with sufficiently low velocity and quenching rates (Vervisch and Poinsot, 1998). "Edge flame" regions where vortex stretching causes high scalar dissipation rates can provide the intense mixing required for production of premixed conditions, and in the extreme can also cause quenching where local heat losses exceed heat production (Vervisch and Poinsot, 1998).

Newbold (1997) investigated the stabilisation region of methane FPJ flames using planar OH-LIF imaging techniques, and found that stabilisation occurs in regions around the edges of large structures as in simple jet flames. He also used non-reacting instantaneous concentration imaging techniques to show that these reaction zones correspond to regions within the flammability limits and with generally low velocity well downstream from regions of high scalar dissipation. Newbold (1997) concluded that the stabilisation regions in methane PJ flames are large enough to discount the influence of small scale mixing, indicating that large scale mixing upstream from the stabilisation point provides the velocity field and stoichiometric conditions required for stability.

The experimental sections of the current chapter and Chapter 6 investigate whether the enhanced large scale mixing affects the stabilisation of PF flames, similarly to gas flames. The combined PJ-annular nozzle design described in Chapters 3 and 4 will be used because it provides a means to vary the extent of enhanced large scale mixing and particle clustering, and consequently is also likely to affect devolatilisation rates and local stoichiometry.

5.2.6 Factors affecting the profile of heat release to walls and particle burnout

The heating value of volatile matter can account for up to a half of the total heating value of bituminous coals (Wall, 1987). Consequently combustion of volatiles plays a significant role in determining flame heat-release profiles. As outlined in section 1.2.3. cement kilns operate most efficiently and produce best quality product when the peak heat release occurs near the burner. The IFRF Cemflame I study (van de Kamp and Smart, 1992) showed that heat release near the burner was increased by the use of medium to high volatile coals and swirled mixing air, both of which acted to increase volatile matter combustion rates. Char combustion rates were considered to make an insignificant contribution to near-burner zone heat release (but were considered important for overall fuel efficiency).

It is hypothesised that enhanced large scale mixing may influence the heat release profile by affecting flame convection velocity (residence time), mixing and combustion rates, flame emissivity and temperature. Particle clustering and the subsequent soot formation may also influence flame emissivity. Each of these factors is considered briefly below.

Volatile combustion rates in flames are generally controlled by either the rate of devolatilisation or mixing rates. In contrast, the kinetics of volatile matter combustion are rapid. Shaw *et al.* (1990) isolated volatile combustion kinetics in an investigation of a wide range of coals. Coals were pyrolysed at 1000°C and the volatiles released through a burner pipe and combusted immediately to prevent tar condensation. Combustion occurred in an intensely mixed region at the burner exit, designed to ensure that mixing did not limit combustion. Kinetic data did not vary widely for the different coals studied, with mean values of ln k = 12.7 and E = 12.3 kcal.mol^{-1}, comparable with those for CO and hydrocarbon combustion, which have typically been used to simulate volatile combustion. The kinetic half-life time-scale was thus rapid and of the order of $2\text{x}10^{-6}$ s, confirming that mixing generally controls volatile matter combustion rates.

A number of models have been proposed for mixing controlled rates of gas phase and soot reactions. Spalding's (1971) eddy break-up model and Magnussen and Hjertager's (1977) eddy dissipation model are widely used. Both assume that the mixing rate is proportional to the ratio of the fluctuating velocity and the mixing length scale, u'/l, or inversely proportional to the large scale structure time-scale. If applied to flames in which precession enhances of the largest scales of mixing, these models would suggest that local mixing and combustion rates are reduced. However precession may also act to increase mixing rates in

the regions between structures by creating large layered regions with high concentration gradients. These possibilities will be discussed in more detail in Chapter 7.

Secondary pyrolysis of primary devolatilisation products forms soot, which can increase flame radiation. Wornat (reported by Solomon and Fletcher, 1994) found, that under pyrolysis conditions, soot yields increased with both increasing temperature and residence time. For example, soot yields increased from 13% to 16% at 1375 K as residence time was increased from 0.3 to 0.75 seconds, and from 12% to 21 % as temperature rose from 1130 to 1470 K for 0.75 s residence time. These data, together with that of Ma *et al.* (1996) reported earlier, allow the influence of soot volume fractions and particle size on flame radiation to be estimated. The influences of particle clustering and increased large scale structure time-scales generated by precession, on sooting and flame radiation are explored experimentally in the current chapter and Chapter 6, and calculated in Chapter 7.

The profile of heat release to furnace walls is a function of the combustion rate, and radiation and convective heat transfer processes. Radiation dominates the heat transfer in furnaces. Radiation modelling can be performed by solving the radiation intensity transport equation numerically (eg Lockwood and Shah, 1981). However in the present study modelling is not attempted, rather fundamental radiation equations are employed in the sensitivity calculations presented in Chapter 7. The net radiant energy transferred from the flame to the furnace walls, ignoring that absorbed by furnace gases, is given according to the "zone method" of Hottel and Sarofim (1967) in terms of the wall area, A_w, and flame and wall emissivities as,

$$Q_{f-w} = \overline{S_f S_w}\sigma(T_f{}^4 - T_w{}^4) \qquad 5\text{-}18$$

where the total interchange area, $\overline{S_f S_w} = \dfrac{A_w}{1/\varepsilon_f + 1/\varepsilon_w - 1}$ 5-18(a)

Soot emissivity is a component of flame emissivity and can be estimated using Equation 2-4 in combination with typical soot concentration data reviewed in section 5.2.3. The mean beam length required in Equation 2-4 can be approximated as that of a flame completely filling the furnace, ie. $L_b = 3.5V/A$ where V is the furnace volume and A is the furnace surface area. Calculation of soot emissivity should account for the agglomeration of soot into irregular shapes and sizes. Farias and Carvalho (1998) calculated the effects of soot aggregation using the radiation transport equation. They used a fractal dimension to model

the shape of the aggregate, and varied the number of primary particles in an aggregate. For uniform clouds of particles containing aggregates of up to 256 primary particles, the emissivity was increased by a maximum of only 23 % at temperatures up to 2000K and with soot volume fractions, f_{vL} of 10^{-8} to 10^{-6}. Hence, Equation 2-4 may be used to calculate soot emissivity with sufficient accuracy to establish trends. Soot emissivity is often taken to be 0.1 (Hottel and Sarofim, 1967), but enhanced particle clustering and the production of fuel rich zones may increase soot emissivity. These effects will be estimated in Chapter 7. Flame emissivity can be estimated from the combined particle cloud, soot and gas emissivities using Equation 2-3.

Other researchers have investigated the effect of increasing the fluctuating slip velocity between particles and gas on combustion rates. These investigations are reviewed because of the potential for precession to likewise increase fluctuating slip velocities. Hanby (1967) estimated the effect of acoustic oscillations with frequencies of 100 – 300 Hz, in pulsating combustors. The additional convective heat transfer between the gas and particles due to oscillations was responsible for a 75% reduction in particle burning time in a small experimental combustor (Hanby, 1967).

More recently, Yavuzkurt *et al.* (1991a) have investigated the effects of acoustic oscillations on combustion rates of coal particles with diameters of 20-70 μm, when entrained with the fuel in a methane flat flame. They inferred increased combustion rates from increased luminosity, which was observed at acoustic frequencies in the region of 600 Hz. The effects of increased slip created by the oscillations were estimated using a formula for the "entrainment factor", so called because it is a measure of the extent to which particles are "entrained" by the local flow structures. The entrainment factor is given by:

$$\eta = \frac{1}{1+\omega^2 \tau_p^{\ 2}}, \quad 0 < \eta < 1 \qquad 5\text{-}19$$

where ω is the frequency of oscillation, and τ_p is the particle time constant. It can be seen from Equation 5-19 that the entrainment factor is a form of the Stokes number, incorporating the ratio of particle time constant to the time-scale of oscillation, 1/ω. When $\eta \sim 1$, particles are "entrained" by the local flow fluctuations, whereas when $\eta \sim 0$, particles cannot follow the flow and experience an extra slip velocity due to the fluctuations. Yavuzkurt *et al.* (1991b) used a relationship to calculate the time and space averaged Nusselt number due to

oscillations, Nu_t, based on the Nusselt number for a steady slip velocity, Nu, and the ratio of oscillating slip velocity to steady slip velocity (ξ):

$$Nu_t = 2 + F(\xi)(Nu - 2) \qquad 5\text{-}20$$

where, for $\xi > 1$,

$$F(\xi) = 0.7628\xi^{0.5} + 0.1372 \qquad 5\text{-}21$$

The burning time of coal particles can be influenced by diffusion of oxygen to the particle surface, intra-particle diffusion, kinetics or a mixture of these mechanisms (Wall, 1987). Field *et al.* (1967) gives the burning time under diffusion controlled conditions at constant particle density:

$$t_b = \frac{\rho_{po} R T_m}{96 \phi D p_g} d_o^{\,2} \qquad 5\text{-}22$$

This relationship demonstrates that mixing can influence burnout by affecting the maximum temperature, T_m, local gas – surface diffusion coefficient, D, and the local partial pressure of oxygen, p_g. If the combustion is kinetically controlled, the burning time still shows a dependence on oxygen partial pressure (Field *et al.* 1967):

$$t_b = \frac{\rho_{po}}{2 k_c p_g} d_o \qquad 5\text{-}23$$

Fractional char burnout also increases with the ultimate volatile yield (Niksa and Lau, 1993) which, as discussed earlier, is influenced by the heating rate and final temperature. In summary, char combustion has little influence on NBZ heat release profiles, but rapid volatile matter release and combustion can improve carbon burnout and the overall efficiency.

The key points of the above review can be summarised as follows:

- Heat release rates near the burner increase with the rate of volatile matter combustion.
- The kinetics of volatile matter combustion are rapid, confirming that, under turbulent conditions, mixing generally controls volatile matter combustion rates after devolatilisation has occurred.
- Eddy dissipation concepts are widely used to model volatile matter combustion rates.
- Char combustion has little influence on heat release profiles near the burner, but rapid volatile matter release and combustion can improve carbon burnout.

- Equations are presented for calculation of the radiant heat transfer from flames to furnace walls. The influences of enhanced particle clustering and increased large scale structure time-scales on sooting and flame radiation is deduced to be potentially significant and will be explored further in the present study.
- An increase in heat and mass transfer and combustion rates resulting from increased slip velocity between particles and gas has been observed by some researchers.

5.2.7 Nitrogen release rates and NO_x formation

The following review deals with volatile-N release rates and volatile NO_x formation, which is deduced to be the dominant mechanism in the experiments to be reported in Chapters 5 and 6, due to the low temperatures used. Pohl and Sarofim (1977) measured total N release during devolatilisation of dispersed PF particles in attached diffusion flames in a laminar flow electrically heated furnace. High heating rates of $2x10^4$ - $6x10^5$ Ks^{-1} and temperatures up to 2100 K were used to model PF flame conditions. For a bituminous coal, 10 % of the coal weight loss occurred prior to any N loss, followed by N loss, proportional to the volatile yield. N release increases with final temperature and with increasing heating rate, with 80 % of N released above 1000K. The N pyrolysis pseudo-first order N release rate is $9.3x10^3 exp(-22700/RT)$ s^{-1}, where T is the wall temperature (K). Pohl and Sarofim (1977) acknowledged that their rates are much slower than the rates of elementary reactions, which have frequency factors of approximately 10^{15} s^{-1}, demonstrating that the N release process is complicated. The quantity of N retained in char (at T =1500 K) is also dependent on equivalence ratio (fuel/stoichiometric fuel) – increasing from near zero at $\phi = 0.5$, to 46% at $\phi = 2$.

Nitrogen yield also depends on coal rank. A 6 % oxygen post flat flame arrangement with heating rates of $5x10^4$ Ks^{-1}, residence times of 47ms and particle temperatures of ~ 1400 K was used by Mitchell *et al.* (reviewed in Solomon and Fletcher, 1994), to investigate N yields. They found that low rank lignites and high volatile bituminous coals liberate 40-60 % of total N in volatiles, whereas low volatile bituminous coals liberate < 20 % of N in volatiles. The bulk of volatile N from bituminous coals is released in tars due to their higher proportion of aromatic ring structures.

Chen and Niksa (1992) studied the yields of N and the major fuel NO_x precursor, HCN, from coal particles of varying rank in a radiatively heated stream. Rupturing of the aromatic rings in tars produced HCN during secondary pyrolysis reactions at temperatures above 1000K, but simultaneous formation of soot locked some N into ring structures. Chen and Niksa (1992) postulate that this process would leave less N available for NO control by staging. Another species commonly assumed to be a NO_x precursor, NH_3, is only observed in low heating rate experiments such as thermogravimetric analyses (Solomon and Fletcher, 1994).

The volatile NO_x kinetic data provided by de Soete (1975) assumes that the HCN route to fuel NO_x dominates. The formation of NO is modeled by two rate equations. The first describes the formation of NO from HCN and oxygen and the second the reduction of NO to N_2. The net production rate of NO is given by (5-24) – (5-25).

$$\frac{d[X_{NO}]}{dt} = A_1 X_{HCN} X_{O2}^{b} \exp\left[\frac{-67000}{RT}\right] \quad s^{-1} \qquad 5\text{-}24$$

$$\frac{d[X_{N_2}]}{dt} = A_2 X_{HCN} X_{NO} \exp\left[\frac{-60000}{RT}\right] \quad s^{-1} \qquad 5\text{-}25$$

where, X is the mole fraction, $A_1 = 0.35 \times 10^{11}$ s^{-1}, $A_2 = 3.0 \times 10^{12}$ s^{-1}. Lockwood and Romo-Millares (1992) plot the exponent "b" as a function of the oxygen concentration using the original data of de Soete (1975). Experimental in-flame HCN concentrations were obtained in swirl stabilised flames by Abbas *et al.* (1993b) using a high volatile coal and a simple pipe coal injector (known as the "SCO" – single central orifice). HCN concentrations peaked at 200 ppm for small particles (d_p = 25 μm), at locations upstream from the ignition region and reduced to 70 ppm post combustion. The key points of the above review can be summarised as follows:

- Nitrogen release rates are relatively slow, but rapid enough to occur in the region of flames where most of the volatile matter burns.
- High volatile bituminous coals liberate 40-60 % of total N in volatiles.
- The NO_x precursor, HCN, forms during secondary pyrolysis reactions at temperatures above 1000K, whereas NH_3 is not a significant precursor at temperatures typical of PF flames.

5.2.8 Possible effects of enhanced large scale mixing on flames

Based on the above review of literature, it can be hypothesised, that enhanced large-scale mixing and preferential particle concentration can have a range of effects on PF flames. These include changes in:

- flame stability by affecting particle heating rates, devolatilisation rates and local residence times
- flame heat release profiles due to altered volatile combustion rates and the quantity of soot formed
- NO_x emissions due to altered flame temperatures and local or global staging phenomena

The experiments presented in the remainder of Chapter 5 are designed to measure the effects of changes in turbulent structure on flame stability, heat release and NO_x emissions. The experiments conducted at 2.5 MW (nominal) scale, reported in Chapter 6, and the related calculations reported in Chapter 7, are used to further explore the dominant mechanisms.

5.3. Experimental Design

5.3.1. Introduction

The hypotheses presented at the start of this chapter are tested in a series of 130 kW combustion experiments in which the ratio G_{PJ}/G_1 is varied to create a range of turbulent structures. A baseline mono-channel flame is provided by the condition $G_{PJ}/G_1 = 0$. Comparison is also made between PJ flames and others in which alternative types of mixing were used. These comparisons are performed on the basis of similar "mixing jet" momentum. Finally, a range of variables such as secondary air temperature and coal flow rate are used to explore mechanisms that are responsible for the observed changes in flame properties.

5.3.2. Selection of the range of momentum ratios

An additional burner design criteria to those outlined in Chapter 2 can be applied from the results in section 4.5.3. The finding that similarity in the ratio, $(G_{PJ}/G_1)St^{-n}$, where $0.5 < n < 1$, provides similarity in fluid dynamics and particle clustering effects, is used in conjunction with the clustering data presented in Chapter 4, to determine the required range of momentum ratios, G_{PJe}/G_1. Note that the parameter, $(G_{PJ}/G_1)St^{-n}$ does not take into account changes due to temperature, and as such provides no insight into thermal similarity. For example, expansion of gas as it is heated to approximately 500°C in the pre-ignition region of flames will alter the fluid time-scales and fluid properties relative to the isothermal cases reported in Chapter 4. However the scaling parameter can be used to approximately scale clustering effects in flames if it is noted that a large number of relatively small particles, which are formed into clusters in the region $x/D < 2$, are present in PF size distributions. A more complete treatment of the effects of gas expansion and particle size on clustering awaits further work.

In the current work no allowance for gas expansion has been made when scaling from PJ-annular isothermal cases, investigated in Chapter 4, to combusting cases. The particle size distribution is also assumed to be identical. Employing these assumptions, and using $(G_{PJ}/G_1)St^{n}$ (where $n = 0.5$) as the mixing similarity parameter, clustering effects can be produced in 130 kW flames with a reduction of ~ 20% in (G_{PJ}/G_1) relative to the isothermal cases. The difference is due to the change in particle density. For the 2.5 MW scale flames reported in Chapter 6, an increase in length scale by a factor of 5, allows a reduction in (G_{PJ}/G_1) by ~ 60 %, relative to the isothermal cases investigated earlier, to produce comparable clustering effects. On the basis of these estimations, the combustion

investigations can focus on the lower part of the momentum ratio range ($0 \leq G_{PJe}/G_1 \leq 25$) investigated in cold flow, particularly at 2.5 MW scale. However it should also be noted that the parameter $(G_{PJ}/G_1)St^{n}$ can be expected to provide a good comparison between the clustering effects in different flames, since changes in temperature and particle size distribution from the isothermal cases are similar for all flames.

5.4. 130 kW flames - Experimental equipment and procedures

5.4.1. Scope

Three types of experiments were conducted in which the influence of enhanced large scale mixing on PF flames was investigated, namely:

a) Experiments in which PJ flames were compared with mono-channel flames.
b) Experiments in which PJ flames were compared with flames created using a range of burner types.
c) Experiments using PJ burners in which operating conditions were varied.

In the experiments in which PJ flames were compared with flames from other types of burner, the primary air flow-rate was generally held constant. Variation of the ratio of mixing air momentum to primary air and PF momentum was usually performed by varying the mixing air flow-rate. Ignition distances, wall temperatures, and flue gas emissions were measured for the majority of flames. Solid samples for measurement of coal burnout were only taken for selected flames. In-flame measurements of temperature, burnout, gas species and fractional volatile matter evolution were taken in key 19PJ and Mono-channel flames. Smaller data sets were obtained for the other burners illustrated in Figure 5.3. The conditions that were varied in the experiments using PJ burners (item c above) included the secondary air temperature, the coal mass flow-rate, and primary air mass flow-rate.

5.4.2. Furnace and instrumentation

A schematic diagram of the experimental furnace is shown in Figure 5.1. The internal diameter is 0.6 m, and the length is 3.1 m (excluding the inlet shroud and a flue gas section). The refractory lining consists of 0.114 m thickness of refractory bricks backed by 0.38 m thickness of calcium silicate bricks. This combination of refractories was designed to limit furnace heating time to 2-3 hours, whilst also allowing wall temperatures to reach a maximum of 1300 °C (Syed, 1975). An outer casing of rectangular cross section is constructed from mild steel. In the current experiments the nominal heat input was 130 kW and internal wall temperatures reached a maximum of 1200°C. Figures 5.1 and 5.2 show the location of a window through which the dynamic motion of the flames in the near burner zone was recorded on 8 mm videotape. Video-tape images were used to analyse the stabilisation process and measure the mean ignition distance.

The secondary air was supplied by a fan and could be preheated to up to 500 °C by a gas fired, shell and tube heat exchanger, with the secondary air on the shell side. Kiln pressure was maintained at negative 0.01 – 0.02 inches water gauge, to ensure safety while minimising the ingress of ambient air. The flue oxygen concentration was controlled to 2.5%, by adjusting the secondary air fan damper, stack damper, and dilution fan damper. The stack dilution fan was used to cool flue gases to prevent damage to the steel flue. The ports for in-flame sampling and a larger window for visualisation of the ignition region are depicted in Figure 5.1. These ports were closed by means of sliding water-cooled brass doors. The doors were left closed for at least 3 minutes prior to recording flue gas emissions.

Approximately 80% of the total air was supplied in a co-flow around the burner as secondary air. The internal diameter of the mild steel secondary air inlet shroud was 200 mm, so that the secondary air velocities were of the order of 1 ms^{-1} when the air was not preheated. Ceramic fibre blanket insulation was placed over the exterior of the inlet shroud when experiments with preheated air (up to 500°C) were performed. The insulation limited heat losses from the shroud, so that the maximum reduction in secondary air temperature over the length of the shroud was 15 °C.

Uniform feeding of pulverised fuel was achieved by using a screw feeder, from which particles dropped through a sealed flexible tube into a 150mm diameter PVC conduit (with smooth internal surface) which was anchored to a vibrating table. The operation of the screw was unaffected by the vibrations which were damped out by the flexible tube. The PVC

conduit was inclined at approximately 5 degrees from the horizontal. Vibration of the PVC conduit caused the pulverised fuel to flow smoothly downwards along the conduit. Particles then dropped into an ejector from which they were conveyed to the burner through a 15mm internal diameter, semi-rigid hose at a typical velocity of 25 ms^{-1}. Steady coal feeding to the burner was achieved without the need for heating of the primary air. The primary air flow-rate was the sum of the measured ejector motive air flow-rate and the air entrained into the ejector with the coal particles. The latter was measured with a vane anemometer and verified against pitot tube measurements.

Flue emission data were taken for each flame, with mean flue oxygen concentrations of 2.5%, after the kiln came to thermal equilibrium. Flue gas species concentration data are normalised to 0% O_2 for presentation. A Kane and May, Quintox 9006 electrochemical cell gas analyser, capable of measuring CO, NO_2, NO and O_2 emissions was used to measure flue gas concentrations. Total NO_x emissions were obtained by addition of the individually measured NO and NO_2 components. However since the NO_2 concentration was found to be typically only 0 – 5% of total NO_x, only the NO data is presented. The "Quintox 9006" CO cell was designed for flue gas sampling only. The manufacturer advised that the CO cell needed 12 hours to recover if subjected to > 4000 ppm CO. Consequently a Procal Ltd, infra red analyser was used to measure the in-flame CO concentrations. The electrochemical cell analyser was used to measure other in-flame gas concentrations.

A 10 mm stainless steel tube was used as the flue gas sample probe. Rapid quenching of the sample occurred in the part of the probe outside the furnace due to natural convection. A short run of downward sloping Teflon tube conveyed the gas and condensate from the sample probe to a condensate trap that was used to collect condensate and dissolved SO_2. The sample then passed through a particle filter before entering the gas clean-up train installed in the analyser, which consisted of a further water trap, particle filter and SO_2 filter. The configuration of the condensate system was not altered during the trials so that possible small errors in NO due to retention in the condensate would not affect the relative comparison between different flames. A 40 mm water cooled suction probe was used to take gas and solid samples from within the flame, and a 55 mm water cooled suction pyrometer fitted with a Pt/Pt-13% Rd thermocouple was used for in-flame temperature measurements. Coal burnout was determined by the ash trace method which assumes that the ash is inert (Abbas *et al.* 1994). The coal burnout (%) is given by:

$$Burnout = 100\frac{\left(1-\left[\frac{W_k}{W_x}\right]\right)}{(1-W_k)} \qquad 5\text{-}26$$

where W_k = fraction of ash in the raw coal, and W_x = fraction of ash in the partially burnt sample.

Furnace wall temperatures were monitored by K-type thermocouples, which were mounted in slots at the same axial positions as the sampling ports. The thermocouple junctions were flush mounted to, and in physical contact with, the interior refractory wall. They were also exposed to direct radiation from the flame. The readings therefore may differ slightly from actual wall temperatures. More importantly the wall temperature measurements illustrate trends in flame heat release profiles, since the thermal conductive resistance of the walls was constant over the entire furnace. That is, the refractory was of constant thickness over the entire length of the furnace, and the exterior furnace casing temperature was maintained at a relatively constant temperature, slightly above ambient, by natural convection.

5.4.3. Burners

Descriptions of the PJ-annular and mono-channel burners used in the 130 kW experiments, together with their operating ranges, are presented in section 2.4. As discussed in Chapter 2, only partial scaling is possible when designing small scale flames. For example, in the current work standard PF size distributions have been chosen. This typically results in a significantly greater ignition distance, in terms of x/D, in small scale kilns. Consequently, while the absolute values of ignition distance, heat release and emissions will not relate directly between small and large facilities, the trends are informative. On this basis, and employing partial scaling principles, the use of a lower primary velocity (to aid flame stability) than the industry standard of 17-20 ms^{-1} is justified at 130 kW scale. A low primary air velocity, of 9.8 ms^{-1}, was used to prevent "blow-off" of 130 kW mono-channel flames. Despite this low primary air velocity, steady conveying of PF was achieved. To allow comparisons to be made, the PJ flames were also generally operated with primary air velocity of 9.8 ms^{-1}. Since the relative significance of the PJ flow is governed by the momentum ratio, G_{PJ}/G_1, the use of a lower transport velocity also allows a lower PJ flow-rate than would have been necessary otherwise.

The exit plane of the burner was located 300 mm downstream from the secondary air inlet to allow visualisation of the ignition region through the first window as shown in Figure 5.2. The 10PJ and 19PJ burners and annular channel with dimensions given in Table 2.1, were used, along with a number of other burner configurations, illustrated in Figure 5.3. The burners denoted "Diffuser" and "Adjacent" were designed to provide different NBZ mixing between particles and the precessing flow. The burner denoted "Diffuser" was also designed to reduce the transport velocity by 70% by means of a 10^o expansion. The burner denoted "Adjacent" in Figure 5.3, employed a simple 15mm bore pipe for primary air located adjacent to the 19 mm PJ nozzle. This pipe has half the exit area of the annular channel, but the primary air velocity can by manipulated to provide equal momentum to that provided by the annular channel.

Two other burners, also illustrated in Figure 5.3, were designed to model aspects of typical conventional means of enhancing stability, and are denoted the "Multiple-orifice" and "Bluff-body" burners. The "Multiple-orifice" (Figure 5.3c) burner introduces mixing air at a high velocity through six 0.9 mm diameter holes, located outside the annular transport flow on a pitch circle diameter of 46 mm. The holes are angled at 45^o to the burner axis in the

azimuthal direction to produce a swirl. The "Bluff-body" burner (Figure 5.3d) was designed to generate an external recirculation zone between the annular transport channel, and a 98 mm diameter circular plate flush mounted to the outside of the 19mm PJ-annular burner, with a view to providing a stabilisation mechanism. The plate also affected the entrainment of secondary air. The "Conically diverging" and "45° angled jet" nozzles described in Chapter 3 were not used as they were shown to offer no advantage in terms of enhancing the large scales of mixing compared to the annular jet.

The influence of enhanced large scale mixing on PF flames was also investigated by injecting coal through a PJ nozzle, although this is not a practical industrial burner design due to high wear rates. This technique has the advantage of removing the need for the annular channel and hence allowing the influence of enhanced large scale mixing to be studied in isolation. A burner with a 40 mm chamber diameter and an inlet diameter of 7.5 mm was used to provide sufficient primary channel cross-section for transport of coal without back pressuring the ejector. Coal was transported to the PJ nozzle through the usual 15 mm conveying line.

5.4.4. Fuels

Bituminous coals were selected because of their wide usage in the cement industry. Unfortunately a sufficient quantity of a single coal was not available to conduct all of the trials. Consequently, three bituminous coals were selected because they had relatively consistent lower heating value (29 – 31.6 MJ kg^{-1}), volatile matter content (30 - 33 % air dried basis), and equal ash content (3.5% d.b.), fixed carbon content (64.0% d.b.) and nitrogen content (1.8%, d.a.f). Pulverised petroleum coke with volatile matter content of 4.31 % was also used for comparison in some cases. The fuels were pulverised to a typical size distribution of 70% < 75 μm.

5.4.5. Determination of ignition distance

Ignition distances were measured directly from the video screen using the annular channel outer diameter as a reference length. The video camera was mounted on a tripod and was aligned perpendicular to the kiln centre-line. Reference marks on the floor were used to ensure that the tripod and camera were located in the same position for each flame. The reference marks were positioned so that the camera lens was 100 mm away from the combustor, in order to minimise exposure to heat from the flame.

5.5. Results - Comparison of mono-channel annular flames with PJ flames

5.5.1. Stabilisation in flames influenced by enhanced large scale mixing

Mono-channel, 10PJ and 19PJ flames were operated without pre-heating of the secondary air to highlight the effect of the burner aerodynamics on flame stabilisation. The mono-channel burner was operated with a particle exit velocity of 9.8 ms^{-1} and was found to require a continuous gas pilot flame (9 kW), located adjacent to the annular channel, to establish ignition and prevent blow-off. Any further increase in the primary air velocity resulted in worsening stability and blow-off problems, whilst reductions in the primary air velocity resulted in poorer combustion and higher CO emissions due to reduced air entrainment. By contrast, the use of precessing air through either PJ nozzle achieved stabilisation without the need for a gas pilot.

The central precessing jet air-flow produced stable flames over a range of conditions with greatly reduced ignition distances in comparison with the mono-channel flame. Figure 5.4 shows that the otherwise unstable mono-channel flame (primary velocity = 9.8ms^{-1}) is stabilised by supplying in excess of 1% of the total combustion air through the 10PJ nozzle. A further increase in the PJ air flow to 3% of the total combustion air reduced the mean ignition distance by a factor of three. A similar trend was noted with the 19PJ nozzle, although video tape was only taken for a single condition. However, ignition distances were recorded for a range of 19PJ momenta with preheated secondary air, and these showed a similar trend. More details are provided in section 5.7.

The mechanism by which the precessing air stabilised pulverised bituminous coal flames was ineffective when firing the petroleum coke, highlighting the important role played by volatile matter, as described by Wolanski and Wojcicki (1974) and Abbas *et al.* (1993a). Specifically, ignition distances, $\frac{x_{ign}}{D} < 13$ were observed when firing bituminous coal using the 10PJ burner compared to $\frac{x_{ign}}{D} \sim 100$, with petroleum coke, at which point stabilization was not related to NBZ mixing.

The stabilisation mechanism in the bituminous coal PJ flames appears to be similar over the entire range of flows investigated. The mechanism is illustrated in Figure 5.5, which shows 9 consecutive images of the ignition region of the 10PJ flame with a PJ inlet pressure of 108 kPa(g) corresponding to 2.0% of the total air flow. The primary air velocity was 9.8ms^{-1}, so

that G_{PJt}/G_1 = 3.9. Figure 5.5 shows that considerable fluctuation in the stabilisation position, both radially and axially, can be observed in consecutive frames. This movement in the stabilisation position is deduced to be directly influenced by the precession frequency (f_p = 380 Hz for this flame), since it can not be easily tracked at the camera framing rate (25 Hz). However once ignition has occurred large burning clusters can be easily tracked propagating downstream in consecutive frames. For example see the large cluster on the centre-line in the three images in the bottom row of Figure 5.5. The motion of these clusters is deduced to be associated with the large scale motions of PJ flows, downstream from the precessing region (x/D <2).

Figure 5.6 is a video image taken with a shutter opening time of 1/1000s. It shows the ignition region of the 19PJ flame with a PJ inlet pressure of 60 kPa(g) and primary air velocity of 9.8ms^{-1}, G_{PJt}/G_1 = 8.5. The image demonstrates wide spread of the flow and a tendency for ignition to occur in a manner strongly influenced by the local fluid structures. In Figures 5.5 and 5.6, volatile matter can be observed burning in large structures at the point of ignition. This suggests that the PJ flow causes rapid deceleration of the PF stream. The slow moving burning structures are deduced to then provide an ignition source for other particles.

The reduction in ignition distance with increasing G_{PJt}/G_1 reported in Figure 5.4 follows the trend of increased clustering observed in cold flow conditions (Chapter 4). An increase in flame spread was also observed with increasing G_{PJt}/G_1, but was not quantified. This is consistent with the trends in water flow visualisation experiments (Chapter 3), namely, that the convection velocity of the large structures decreases with increasing G_{PJ}/G_1. No evidence of in-flame recirculation was observed, rather the stabilisation mechanism appears to be related to radial fluctuations in particle trajectories, and the creation of large clusters of low velocity particles. Appendix 4 provides further evidence for this stabilisation mechanism. It details an experiment in which PF particles were injected at low seeding densities into open gas flames. In these open flame experiments the affect of precession on clustering can be clearly visualised, due to the low particle seeding density.

5.5.2. The influence of enhanced large scale mixing on heat flux profiles

The influence of G_{PJ}/G_1 on wall temperature profiles is presented in Figure 5.7 for the 10PJ burner and Figure 5.8 for the 19PJ burner. A general trend of increasing wall temperature near to the burner with increasing G_{PJ}/G_1 is observed for both burners. For the 10PJ burner the greatest affect of G_{PJ}/G_1 is observed at $x/D = 75$, whereas for the 19PJ, the influence of precession is most significant at $x/D = 16$. (The data for the 19PJ burner at x/D = 40 is not presented, due to an error arising from incorrect placement of the thermocouple).

5.5.3. The influence of enhanced large scale mixing on flue gas emissions

Table 5.1 summarises mean ignition distances, flue gas NO and CO emissions and burnout for typical flames from the 10PJ, 19PJ and mono-channel burners. The 10 PJ flame was operated with a PJ inlet pressure of 108 kPa(g), G_{PJt}/G_J = 3.9, and the 19PJ flame at 60 kPa(g), G_{PJt}/G_J = 8.5. The mono-channel flame, with primary velocity = 9.8ms^{-1}, was very poor, with 84% burnout and high CO levels. Improvements in CO emissions and burnout of mono-channel flames could not be achieved by increasing transport air momentum, due to blow-off problems. Research in larger rotary kilns suggests that increasing primary air flow-rate would be undesirable since dramatic increases in NO_x occur with the increased momentum required for good burnout and low CO levels (van de Kamp and Smart, 1992). A 4 - 5 fold reduction in CO and a reduction in NO emissions were observed in the PJ flames relative to the mono-channel flame.

Table 5.1. Flame outputs: Mono-channel and PJ burners

	Ignition Distance (mm)	NO (ppm)	CO (ppm)	Burnout (%)
Mono	270	190	826	84
10 PJ, G_{PJt}/G_J = 3.9	151	82	310	87
19 PJ, G_{PJt}/G_J = 8.5	134	85	192	92

Figure 5.9 shows that, for the 10PJ and 19PJ burners, an increase in the quantity of precessing air beyond the minimum required for flame stabilisation, results in a reduction in CO emissions, denoted in parenthesis. Initially the reduction in CO occurs without significantly increasing NO emissions, but NO rises at higher precessing air levels. The "optimal" quantity of precessing air, taken to be that which reduces CO emissions to [CO] < 200 ppm is about 3% of total air for the 10 mm PJ burner and 5% for the 19 mm PJ burner. While this "optimal" value is unlikely to translate directly to full scale plant, the quantities are in the range that is acceptable to industry.

As the precessing air flow-rate through the 10PJ and 19PJ nozzles is increased beyond the optimum value, NO emissions from both burners increase. Since the ignition distance does not change significantly over this range, the additional precessing air and associated additional entrainment of secondary air can be deduced to increase the oxygen availability at the point of ignition (van de Kamp and Smart, 1992). Figure 5.9 shows that, with the same mass flow of precessing air, the 19 mm PJ nozzle produces less NO than the 10 mm nozzle. However the two PJ burners produce similar NO emissions for the same momentum up to

$G_{PJ\theta}/G_1 < 7$ (Figure 5.10). This indicates that momentum is a primary control parameter relating the "strength" of the local mixing patterns produced by the precessing jet flow in dominating particle motion and NO production. However the diameter ratio of PJ nozzle to annular channel also has an influence, which is especially noticeable for $G_{PJ\theta}/G_1 > 7$. These findings provides a key for optimisation of the PJ flow-rate and momentum.

5.5.4. The influence of enhanced large scale mixing on in-flame measurements

Centre-line measurements in the 19PJ flame with G_{PJ}/G_1 = 8.5 and the mono-channel annular flame are shown in Figures 5.11 - 5.16. The mono-channel flame was operated with an 8 kW gas pilot to aid stability, producing an ignition distance similar to that of the 19PJ flame, thereby allowing meaningful comparisons of in-flame temperatures, gas concentrations and solids composition to be made. The mean ignition distance of the mono-channel flame was reduced from $\frac{x}{D_{A,2}} = 8.3$ to 3.4 by the application of the gas pilot flame.

The 19PJ flame was operated without a pilot flame. Figure 5.11 demonstrates that a more rapid temperature rise occurs in the 19PJ flame than the mono-channel, which correlates with the increase in wall temperature observed near the burner with increasing G_{PJ}/G_1 (Figure 5.8). Likewise the consumption of oxygen is more rapid in the 19PJ flame than in the mono-channel flame and the oxygen concentration reaches a lower initial minimum near the burner (Figure 5.12). The 19PJ flame also demonstrates more rapid burnout at the position, $\frac{x}{D} = 26$, and more complete burnout in the flue (Figure 5.13).

Figure 5.14 suggests at first sight that the 19PJ flame has slower initial volatile matter release, despite more rapid burnout at $\frac{x}{D} = 26$. This apparent anomaly can be explained by the radial traverses, measured for the 19PJ flame at $\frac{x}{D} = 10$ and 26 and presented in Figures 5.15 to 5.20. (Radial traverses were not taken in the mono-channel flame due to time constraints). The first radial traverse at, $\frac{x}{D} = 10$ (Figures 5.15 to 5.17), was taken immediately downstream from the mean ignition distance, ie. $\frac{x_{ign}}{D} \sim 7$, while the second traverse (Figures 5.18 to 5.20) was located within the bulk of the flame. Figure 5.15 shows that $[O_2] > 11\%$ throughout the 19PJ flame cross-section at $\frac{x}{D} = 10$, however the burnout is greater at the edge of the flame than on the axis. Figure 5.16 shows that the solids volatile matter content on and near the centre-line was that of the raw coal, at $\frac{x}{D} = 10$, and that devolatilisation occurs towards the edge of the flame at larger $\frac{r}{D}$. The centre-line ash content is also the same as the raw coal, consistent with the low burnout there (Figure 5.13).

These data demonstrate that little combustion occurs at the centre-line by $\frac{x}{D} = 10$. That the highest temperature was measured on the centre-line (Figure 5.17), shows that heat is radiated both inwards (toward the centre-line) and outward (to the walls) from the flame zone at the edge of the flame, resulting in a high temperature, but non-reacting, flame core.

At $\frac{x}{D} = 26$, the peak mean temperature again occurs at the centre-line (Figure 5.18). Figure 5.19 shows that substantial burnout, in the range 60 – 75%, has occurred throughout the flame. The lowest O_2 concentration occurs at the centre-line, indicating that the majority of the entrained oxygen is consumed before it reaches the centre-line. That the volatile matter content peaks at the centre-line (Figure 5.20) suggests that at least some parts of the centre-line flow have not been exposed to the high mean temperature there, and that the mean conditions are not representative of instantaneous conditions. This would also suggest that the peak temperatures are significantly higher than the mean. The mean residence time within the flame at $\frac{x}{D} = 26$ is estimated to be 0.1s, based on a mean convection velocity of $5ms^{-1}$, which is sufficient to allow complete devolatilisation even at mean flame temperatures, according to the kinetic information reviewed in section 5.2.2. The data taken at $\frac{x}{D} = 26$ suggests that combustion on the outside of clusters occurs simultaneously with lower temperatures and higher volatile content at the cluster cores.

Figures 5.21 and 5.22 show the centre-line NO and CO measurements for $\frac{x}{D} \geq 26$ in the 19 PJ flame, with G_{PJ}/G_J = 8.5, and the mono-channel flame, respectively. The 19PJ flame shows higher initial NO concentration than the mono-channel flame, which correlates with higher mean temperatures and entrainment rates. A subsequent rapid reduction in NO lags the reduction in oxygen concentration (Figure 5.12). NO concentrations in the mono-channel flame also follow the in-flame oxygen concentration, but do not reduce as rapidly or to the extent observed in the 19PJ flame. The maximum mean in-flame temperature of 1160°C is too low for any significant thermal NO_x formation, which is typically the major factor in cement kilns (van de Kamp and Smart, 1992). Thus, NO emissions are deduced to be dominated by the fuel-N route in these flames.

A reduction in NO concentration with axial distance occurs in the region, $50 \leq \frac{x}{D} \leq 75$, for the 19PJ flame. The majority of the volatile matter remaining in the solids at $\frac{x}{D} = 26$ has been released prior to the start of this region and at least some of it can be assumed to be combusted in a manner which contributes to the NO reduction. The possibility of a mean fuel staging effect for the reduction of volatile NO can be precluded due to the relatively high centre-line oxygen concentrations of approximately 6 – 8 % in both flames in the region $50 \leq \frac{x}{D} \leq 75$ (Figure 5.12). The alternative is a local fuel staging effect within particle clusters in the PJ flame. A rapid reduction in CO concentration, and lower flue CO is also observed in the 19PJ flame (Figure 5.22) despite generally lower oxygen concentrations and lower NO. The CO data indicates that more complete mixing with the secondary air occurs in the 19PJ flame.

5.6. Comparison of flames from different burner types

The burners illustrated in Figure 5.3 were designed to allow the generation of a range of scales of turbulent structures and clustering effects. Flames were compared to determine the effects on stability, heat release and emissions. The burner types and input conditions of thirteen 130 kW flames are listed in Table 5.2. The conditions used for the first 6 burners listed in Table 5.2 were chosen to provide the closest possible match in momentum ratios to the conditions used in the standard 10PJ and 19PJ flames listed. To facilitate these comparisons the mixing air momentum, G_{MIXe}, (ie. PJ momentum or multiple-orifice momentum) was calculated at the nozzle exit in each case. Four additional flames from the 19 and 10 mm burners under altered conditions are also listed as the last four flames in Table 5.2. The NO and CO emissions and the ignition distances measured for the thirteen flames are summarised in Fig 5.23.

Table 5.2 Input conditions – 130 kW PF flames

Burner/ Flame Type	Name in Figures 5.23- 5.25	Mixing air flow (% of total)	G_{MIXe}/G_1
Mono-channel annular	Mono	0	0
Adjacent	Adjacent	5.2	0.92
Diffuser	Diffuser	5.2	4.26
Multiple-orifices	Multi	2.3	2.30
Bluff-body (19 mm PJ)	Bluff body	5.2	1.96
40 mm PJ (coal through PJ)	40 CPJ	15.5	N/a
10 mm PJ	10 PJ	2.1	1.10
19 mm PJ	19 PJ	5.2	1.96
High transport (19 mm PJ)	Hi trans	5.2	1.14
19mmPJ with preheat	Preheat	5.2	1.96
High flow 19mm PJ	Hi 19 PJ	7.1	3.61
High flow 10mm PJ	Hi 10 PJ	4.1	4.30

NB. The primary air velocity was 9.8 ms^{-1} in all cases (7% of the total air flow) except for the "High transport" flame in which case it was 13.5 ms^{-1} (10% of total air), and the 40 mm PJ flame in which case the primary air (15.5% of total air) is directed through the PJ nozzle.

Figure 5.23 shows that introducing air through the 10PJ and 19PJ nozzles dramatically reduces ignition distance (ie. increases stability) in comparison to the Mono-channel annular and Adjacent PJ designs. Even though the Adjacent PJ burner flame was operated with a slightly higher primary velocity (17.6 ms^{-1}) it is evident that it is less effective than the annular arrangement. This can be deduced to be attributed to particles "punching through" the NBZ of the PJ flow from the cold flow experiments. Figure 5.23 shows that the Adjacent PJ flame has both increased ignition distance and higher CO emissions than the central PJ

configurations. The long ignition distance of the Bluff-body flame (in comparison to the 19PJ flame) may be due to a delay in entrainment of secondary air and hot ERZ gases.

The increased ignition distance of the High-transport flow design relative to the 19PJ, and the slightly reduced ignition distances of the flames with higher PJ momentum ("Hi 19PJ" and "Hi 10PJ") are consistent with a direct relationship between G_{PJe}/G_I and reduced ignition distance. To reinforce this trend, the 40CPJ flame, which has no separate primary air stream, demonstrates a significantly shorter ignition distance than the mono-channel flame.

Figure 5.23 also demonstrates that there is an optimum fraction of PJ air for both low NO_x and CO emissions. The 10PJ and 19PJ flames were found to produce low NO emissions relative to the other flames and that CO emissions that are significantly lower than the Mono-channel and Adjacent flames. A possible explanation for the combination of low NO and CO emissions, given the presence of clusters which ignite on the outside, is that the momentum of the PJ flow causes sufficient air to be entrained into the flame to allow diffusion of oxygen into fuel rich particle clusters after NO_x precursors are converted to N_2. This explanation is supported by the further reductions in CO emissions, and increases in NO emissions measured for the Hi 19PJ and Hi 10PJ flames.

Figure 5.24 shows the wall temperature profiles for the different burner types. The data at x = 300 mm (T_1) was chosen as indicative of the heat released in the near burner zone. The 19PJ flame has the highest wall temperature at T_1 and indeed for the first 1500 mm. The data shows that the 19 PJ flame produces more rapid heat release than all the other flames. Note that the data for the Multiple-orifice burner has been offset because the burner was located in a physically different axial location due to physical constraints on burner position. In this way all data is referenced to the burner exit plane. It is deduced that rapid entrainment by the small jets in the Multiple-orifice flame causes rapid heat release, but not as great as for the 19PJ.

The influence of altered G_{PJe}/G_I and secondary air temperature on the wall temperature profiles produced by the PJ flames is shown in Figure 5.25. The data shows that increasing G_{PJe}/G_I in 19PJ flames increases T_1, which corresponds to improved stability, as evidenced by a reduction in ignition distance (Figure 5.23). The increased NO emissions of the "Hi transport" flame relative to the 19PJ flame (Figure 5.23) may be due to the combined effect

of increased mass of air entrained at ignition and a reduction in the strength of particle clustering effects. In contrast, the "Hi 19PJ" and "Hi 10PJ" flames have higher NO emissions than the standard 19PJ and 10PJ flames, despite a slightly reduced ignition distances (Figure 5.23). This effect is deduced to be due to increased entrainment rates with increasing PJ momentum, which in turn increases oxygen availability.

The conclusion to be drawn from these results is that PJ burners can be used to provide a means of modifying jet turbulence to increase unsteady effects and provide a stabilisation mechanism which promotes rapid heat release, whilst also reducing NO_x and CO emissions. It can also be deduced that the mechanism is one of "local staging" in which the core of clusters of particles burn under fuel rich conditions.

5.7. Experiments to explore the mechanisms by which enhanced large scale mixing affects flame properties

The effect of enhanced large scale mixing, and the accompanying enhanced particle clustering, on the relative significance of convective and radiant particle heating, and on the mechanism of NO formation, was further investigated by varying the secondary air temperature. Figure 5.26 demonstrates that increasing the secondary air temperature from ambient to 300 °C reduces the ignition distances of 19PJ flames (G_{PJ}/G_1 = 8.5) from $\frac{x}{D} = 7.1$ to $\frac{x}{D} = 6.5$. Figure 5.27 demonstrates that an increase in the peak wall temperature, from 1040°C to 1075°C, accompanies the increase in secondary air temperature. Similar increases were found for two 10PJ flames. Both convective and radiant particle heating rates can be expected to be increased by increasing the secondary air temperature, and to contribute to the shorter ignition distances. Their relative contributions are calculated in Chapter 7.

Figure 5.28 shows a general trend of increasing flue NO emissions with increased secondary air temperature, from approximately 100 ppm, without any secondary air pre-heating, to 200 - 300 ppm with preheating to 300 - 500°C. The increased NO emissions occur despite a deduced reduction in the mass of air in the flame at ignition due both to reduced ignition distance the reduced density of entrained gases. These data indicate that when enhanced clustering effects are held relatively constant an increase in temperature increases fuel-NO emissions, as expected. (The peak in-flame temperatures of approximately 1200°C dictate that little thermal NO_x is produced).

Figure 5.29 shows the effects of varying coal mass flow-rate, and hence the heat input, on 19PJ flames. The secondary air flow rate was varied with the coal flow to maintain a constant flue oxygen concentration of 2.5%. The PJ pressure was held constant at 60 kPa(g), and a constant primary air velocity of 9.8ms^{-1} was used (corresponding to G_{PJ}/G_1 = 8.5 when a coal flow of 4.5 g/s was used). The secondary air temperature was held constant at 430°C. Figure 5.29 shows that the peak wall temperature and the T_1 both increased dramatically by approximately 200°C with increasing heat input. A corresponding reduction in ignition distance from 225mm (x/D = 12) to 86mm (x/D = 4.5) was observed as the heat input was increased. It follows that, precession creates conditions under which particle heating rates can be dramatically increased even at the highest experimental ratio of coal to PJ air flow-

rate, which favours the application of PJ nozzles in industrial kilns. Figure 5.29 also shows the expected dependence of fuel NO emissions on temperature.

At the lowest heat input of 50 kW thermal (with an additional 7 kW due to the elevated secondary air temperature, 430°C), the peak wall temperature was comparable with that reported for the nominal heat input (130 kW) with ambient secondary air (Figure 5.27). Consequently, the radiative heat transfer from the walls to the particles in the pre-ignition region would also be comparable. However, despite this, and the higher secondary air temperature employed, the 50 kW flame has a much longer ignition distance of x/D = 12.2. It is hypothesised that the increased ignition distance of the 50 kW flame arises from two effects related to the lower particle density. The first is a reduction in radiant absorptivity. The second is a reduction in the volumetric rate of evolution of volatile matter, so that the mean lower flammability limit is achieved further downstream. The significance of these two mechanisms, and the effects of cluster concentration and size, are investigated further in Chapter 7.

The NO emissions generated by Diffuser burner flames are compared with those of 19PJ flames employing the standard annulus in Figure 5.30. Here the primary air flow-rate was varied at constant PJ pressure of 60 kPa(g) (5.2% of the total air flow). The larger annulus caused an increase in NO emissions by 70 ppm at the same primary air flow rate (Figure 5.30). Increasing the primary air flow-rate reduced CO emissions in Diffuser flames, but increased CO emissions in 19PJ flames (Figure 5.31). Only one Diffuser flame, employing the standard primary air flow-rate of 277 $lmin^{-1}$, (G_{PJe}/G_1 = 4.26 – see Table 5.2 for details of conditions) was video-taped. The flame had an ignition distance of 115 mm (x/D = 6.1) compared to 134 mm (x/D = 7.1) for the standard 19PJ flame.

Three consecutive video images of the Diffuser flame with G_{PJe}/G_1 = 4.26 (Figure 5.32) are shown in grey-scale rather than colour, which in this case provides better resolution of particles in the pre-ignition region. Despite the fact that particles are poorly imaged due to the high flame luminosity, Figure 5.32 shows that a significant fraction of those particles injected near the outer rim of the Diffuser are not significantly influenced by the PJ near burner zone field in pre-ignition region. This is deduced to be due to their remote proximity to the PJ nozzle and shows that the diameter of the PJ nozzle relative to the diameter of the annular flow is an important dimensionless parameter. The combination of results reported in the previous paragraph can be explained by this observation. The higher NO emissions

from "Diffuser" flames can not be attributed to temperature effects since peak wall temperatures were typically 30 °C lower than those of corresponding 19 PJ flames. Rather, they are deduced to result from the reaction of volatiles evolved from the particles originating from the outer rim of the Diffuser, where oxygen availability is high due to the larger surface area on the outside of the annular flow. Increasing the primary air flow-rate further increases mixing rates in this region, increasing NO emissions (Figure 5.30) and reducing CO emissions (Figure 5.31) from the Diffuser flames. In contrast, increasing the primary air flow-rate when using the standard annulus reduces the dominance of PJ mixing and hence increases CO emissions towards those produced by the mono-channel flame (Figure 5.23). The shorter ignition distance of the "Diffuser" flame (Figure 5.23) compared to the 19PJ flame is deduced to be due to the reduced primary air velocity (and momentum), which allows a stronger influence of the PJ flow on the centre-line.

The influence of PJ momentum on ignition distances of flames generated by introducing PF directly through the 40 mm PJ nozzle is presented in Figure 5.33, where it is compared with 10PJ and 19PJ flames. The secondary air was provided at ambient temperature for the 10PJ and 40PJ flames, whereas it was preheated to 500°C for the 19PJ flames. The minimum ignition distance of any 40PJ flame (x/D = 2.85) is considerably shorter (in terms of x/D) than the smaller burners, and approaches the location of the highly fluctuating NBZ. Increasing ignition distances observed with increasing mass flow of air through the 40PJ nozzle demonstrates the importance of velocity decay in stabilisation. The flame sequence illustrated in Figure 5.34, of the 40PJ flame with a PJ air flow-rate equivalent to 15% of the total air, suggests that particles emerge at a high velocity, and after being formed into clusters, rapidly decelerate once the exiting jet is directed away from the cluster. A similar mechanism is also observed in the 19PJ and 10PJ flames with annular injection (eg. see Figure 5.5), but is not as clearly demonstrated as in these 40PJ flames. Emissions of NO and CO are illustrated in Figure 5.35 for the 40PJ burner. The NO emissions (165 – 187 ppm) are lower than those of the mono-channel burner (195 ppm, see Figure 5.23) despite the higher primary momentum. The trend of increasing NO emissions from the 40PJ burner with increasing PJ momentum follows that established earlier for the 10 and 19PJ flames (Figure 5.10). In particular, Figure 5.36 shows that the trend is similar to that of the 19PJ flames, despite the lack of an annular channel in the 40 PJ flames. It is hypothesised that the same mechanism as described in Section 5.5.4, ie. combustion under fuel rich conditions within individual clusters, is responsible for the relatively low NO_x emissions in 40 PJ flames. It is proposed that combustion commences on the outer boundary of clusters and

proceeds inwards consuming the oxygen that is initially present. If combustion is then limited by the rate of addition of oxygen from outside the cluster, it will proceed fuel rich. This mechanism is deduced to dominate NO formation in the 19 and 40 PJ flames, whereas in the 10 PJ flames, the highest PJ momenta can increase the oxygen availability to a significant fraction of particles, which may not be enveloped into large clusters, owing to the large ratio of annular channel to PJ nozzle diameter.

5.8. Conclusions

Stabilisation

The 130kW combustion experiments show that the unsteady mixing characteristics of precessing jet nozzles are conducive to the stabilisation of pulverised fuel flames for rotary kilns. The specific conclusions are:

- A dramatic reduction in ignition distances of 10PJ and 19PJ flames (x/D <10) compared to mono-channel flames.
- The amount of precessing air required to produce a dramatic reduction in ignition distance, is about 2% - 5% of the total air which is acceptably low for application in industrial rotary kilns.
- The reductions in ignition distance are deduced to result from the augmentation of particle and volatile matter clusters, which dominate the flow and provide an ignition source for other particles. Combustion of volatile matter is deduced to commence on the cluster boundaries and to proceed towards the cores of clusters.
- A reduction in the coal flow-rate from 160 to 50 kW in 19PJ flames with $G_{PJt}/G_1 \sim 8.5$ increased ignition distances from $\frac{x}{D} = 4.5$ to $\frac{x}{D} = 12.2$, demonstrating that stabilisation in PJ flames is strongly dependent on direct radiative heating of particle clusters in the pre-ignition region from the flame.
- The findings in 130 kW PF flames are supported by visualisation of coal particles in open gas flames (Appendix 4), where the clustering effects can be clearly seen to be associated with the production of dense clusters of burning volatile matter. The use of high speed photography in these open gas flames also showed that clusters in PJ flames move with low convection velocities, which is also deduced to aid stabilisation.

Emissions and burnout

- Flames from the 10PJ and 19PJ burners with $G_{PJt}/G_1 = 3.9$ and 8.5 respectively produced lower NO emissions (82 and 85 ppm respectively) than any of the other burners and CO emissions which were significantly below those of the mono-channel flame. The PJ flames also demonstrated improved burnout compared to the mono-channel flame.
- Increasing the quantity of precessing air beyond the minimum required for flame stabilisation reduces CO emissions. Further increases in PJ air flow-rate increases NO emissions to in excess of 200ppm for $G_{PJt}/G_1 > 7$. Since the 10PJ and 19PJ burners produce similar NO emissions for the same PJ momentum in the range $G_{PJt}/G_1 < 7$, despite different PJ flow-rates, it can be concluded that the momentum ratio is the

dominant parameter.

- The relative diameter of PJ nozzle to annular channel is also important in influencing combustion and in particular NO emissions. Low NO_x emissions were shown to occur only if primary and PJ geometries are arranged so that the PJ flow affects the entire primary flow and influences all particles. This fact is further demonstrated by the fact that NO emissions from 40PJ flames, in which particles were injected directly through the PJ nozzle so that no annular primary flow was required, were more comparable with those of the 19PJ-annular flames than the 10PJ-annular flames. (The relative diameter of 19PJ nozzle to the annular channel is 1.9 times that of the 10PJ nozzle.) Further evidence was supplied by a 19PJ flame employing a large diameter PF annulus, which caused an increase in NO emissions by 70 ppm compared to the standard 19PJ flame at the same primary air flow-rate. A significant fraction of the particles, injected near to the outer rim of the annulus, were not influenced by the PJ flow. In contrast, visualisation of coal particles in open gas flames (Appendix 4) under conditions simulating the PJ flames with the standard annular channel, shows dense volatile matter clusters immediately downstream from the NBZ. For this reason it is hypothesised that the formation of clusters and subsequent combustion of volatile matter in a localised fuel rich regime is crucial to the production of low NO_x emissions in PJ flames.
- By considering in-flame gas concentration, temperature and solids composition data of a 19PJ flame, it was deduced that combustion of volatiles is initiated on the outside of clusters, and propagates inwards. It is hypothesised that the low NO emission exhibited by the 19PJ flame is due to the subsequent fuel-rich combustion of evolved volatile matter in the cores of clusters. It is also suggested that the low CO emissions occur because the PJ flow produces more complete, albeit large-scale, mixing between the secondary air and the PF.

Heat release profile

- PJ burners can provide a means of utilising jet momentum and modifying jet turbulence to provide a stabilisation mechanism which promotes rapid heat release, whilst also minimising NO_x and CO emissions.
- PJ flames demonstrated high and early heat release with wall temperatures near to the burner in excess of 100°C higher than most other burners tested, and slightly higher than that generated by a multi-channel burner. Increases in G_{PJ}/G_1 caused both the ignition position and the heat release profile to move closer to the burner due to increased entrainment rates.

- Visualisation of coal particles in open gas flames (Appendix 4) indicates that enhanced clustering may increase sooting and hence flame emissivity and heat release in the NBZ.
- PJ mixing has a significant effect on flame heat flux profiles, a fact which can be observed by comparison with steady mono-channel flames and by varying the PJ momentum. This is consistent with cold flow visualisations of the scale of the dominant large structures and calculations of strain rates.

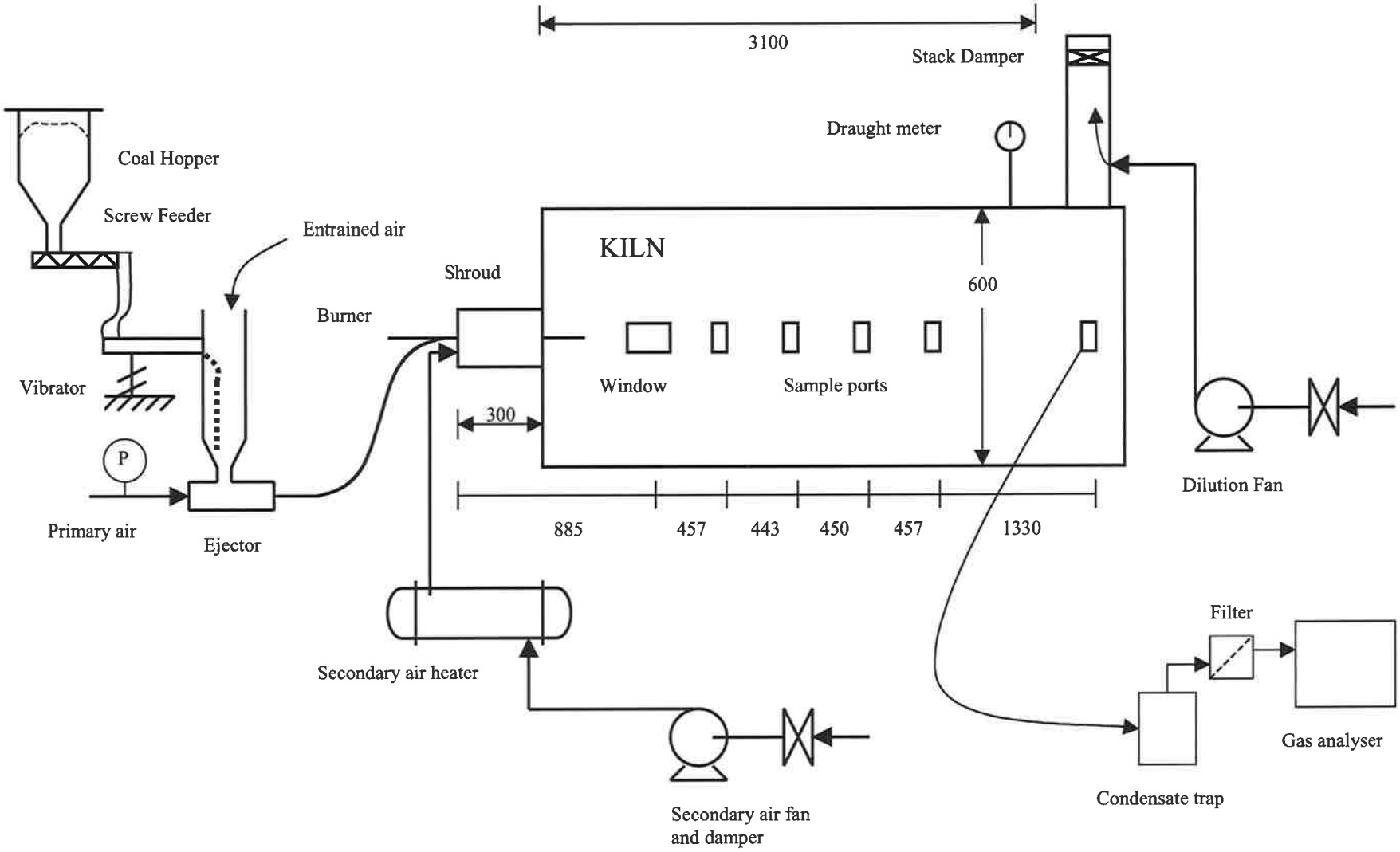

Figure 5.1 A schematic diagram of the 130 kW furnace

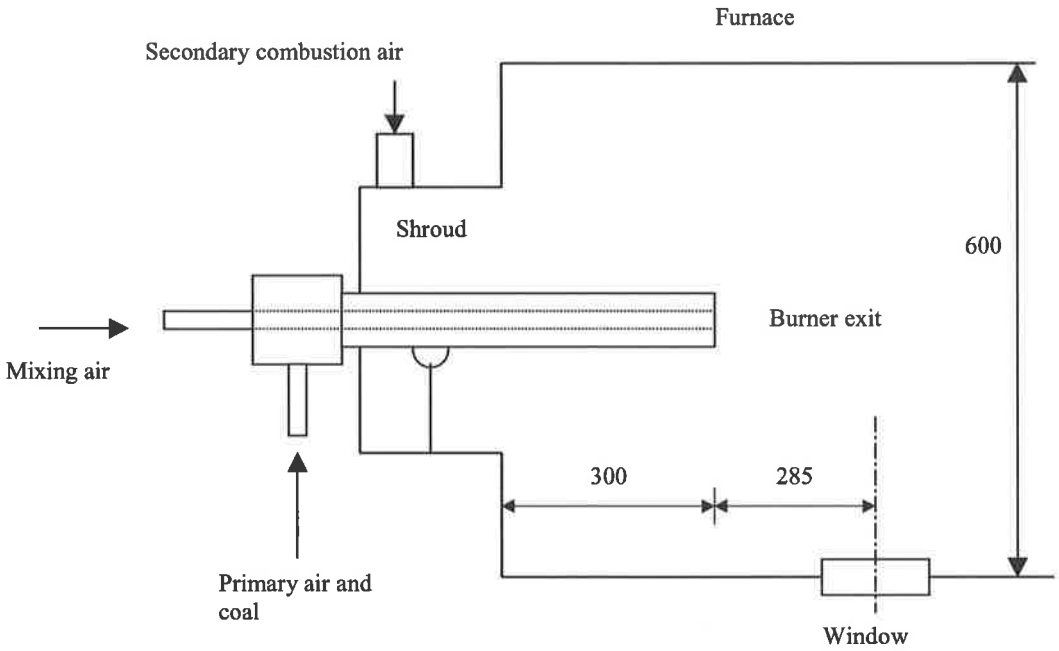

Figure 5.2. A schematic diagram of the standard burner arrangement used in the 130 kW furnace

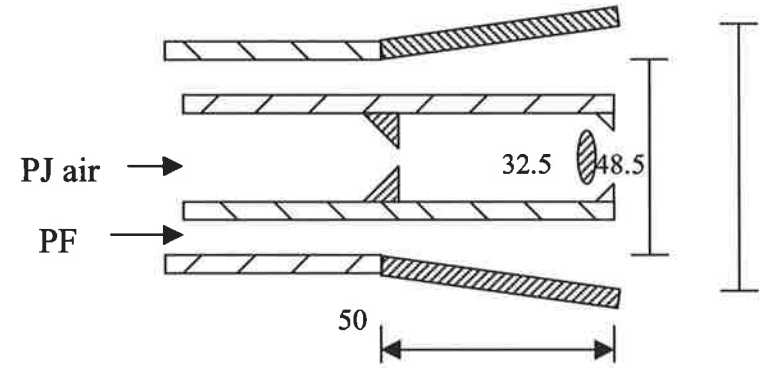

(a)

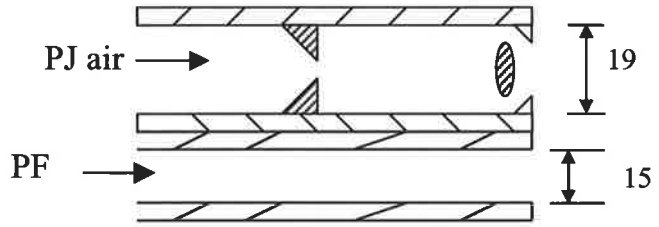

(b)

Figure 5.3. Schematic diagrams of supplementary burners
(a) Diffuser, (b) Adjacent

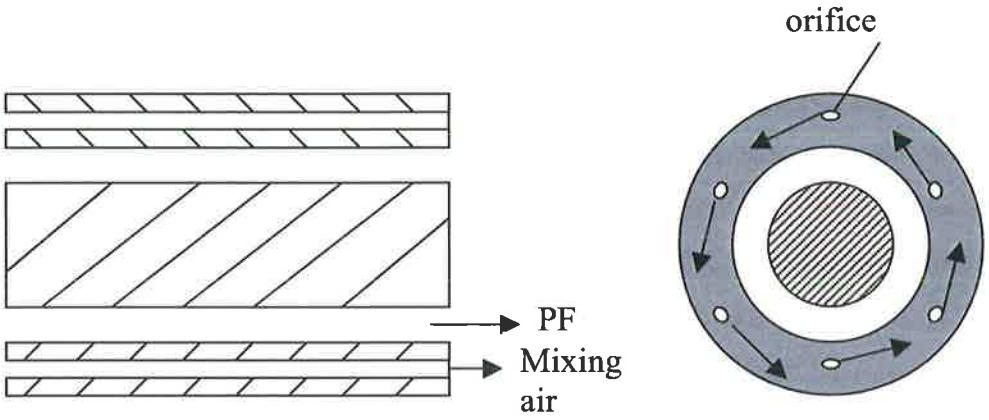

(c)

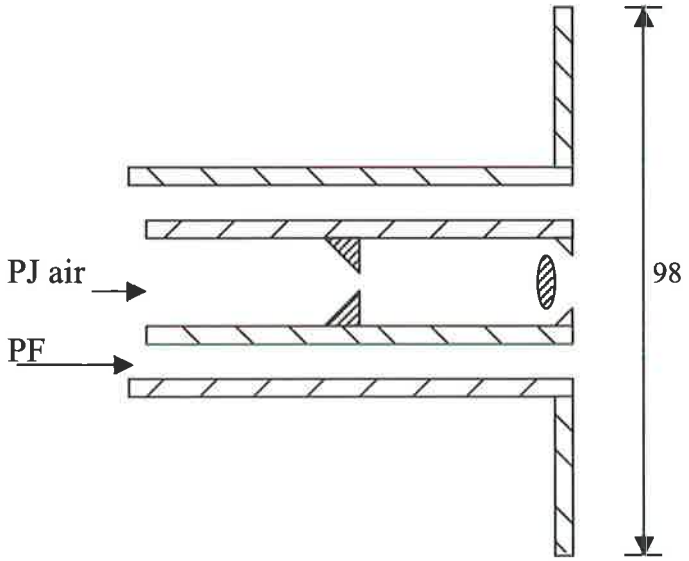

(d)

Figure 5.3. (continued)
(c) Multiple - orifice, (d) Bluff – body.

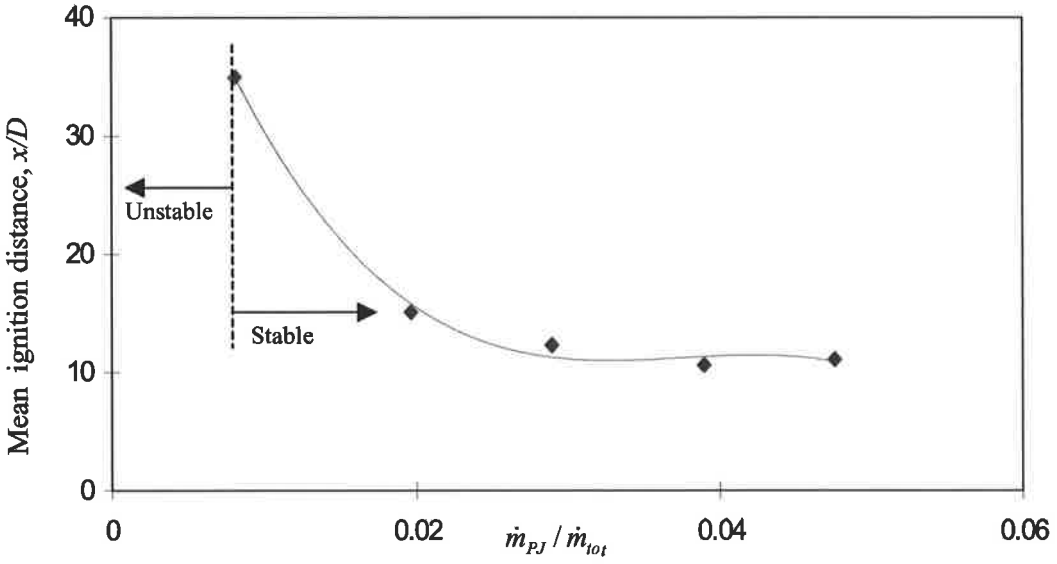

Figure 5.4. Normalised mean axial ignition distance - 10PJ confined 130kW PF flames with no pilot - as a function of PJ mass flow fraction

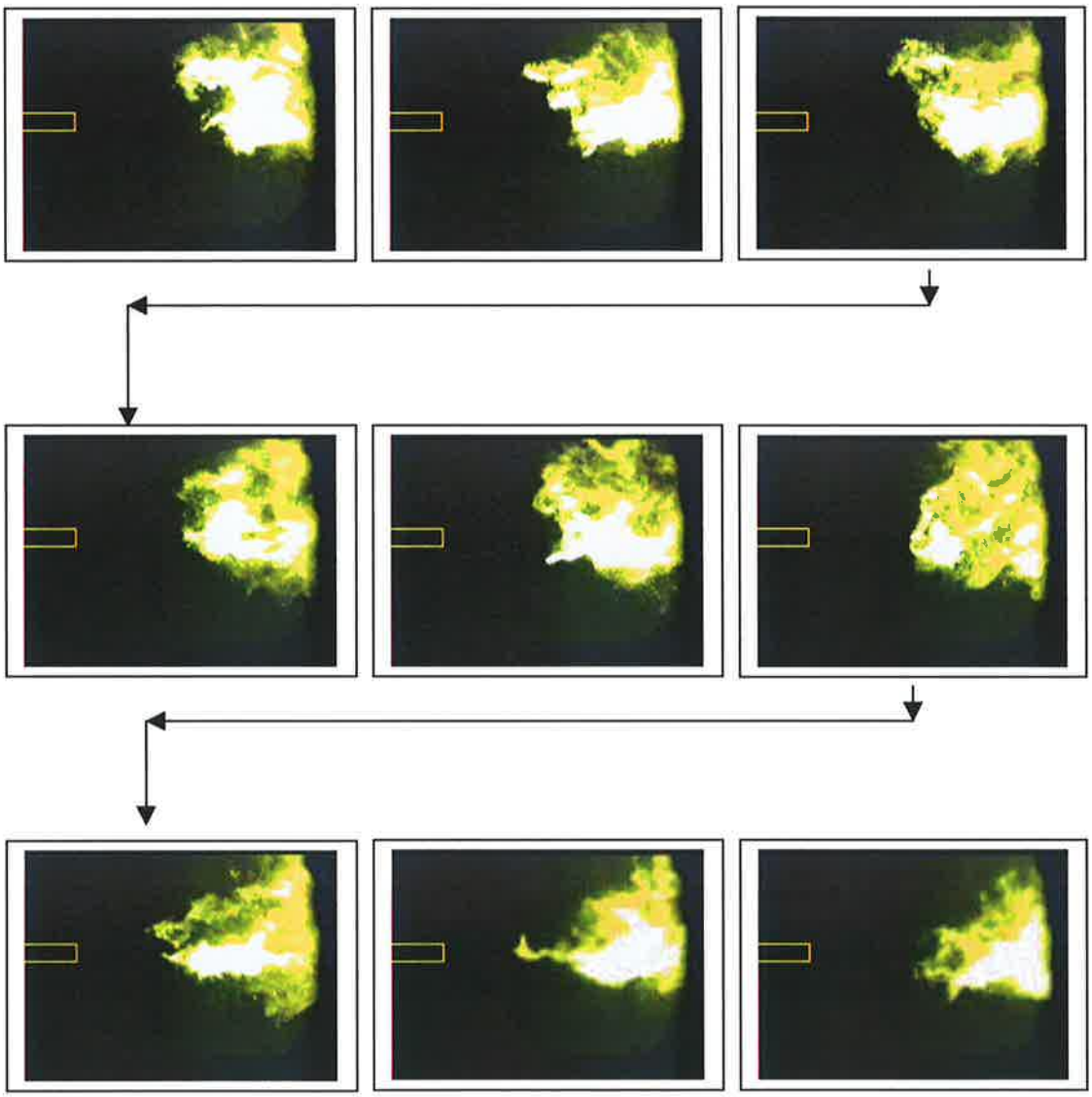

Figure 5.5 Consecutive video images (framing rate = 25 frames per second) of the ignition region of the 10PJ flame with a PJ inlet pressure of 108 kPa(g) corresponding to 2.1% of the total air flow. The primary air velocity was 9.8ms^{-1}, so that $G_{PJ}/G_1 = 3.9$. Images are in rows starting at top left. The burner position is shown at the left of each image.

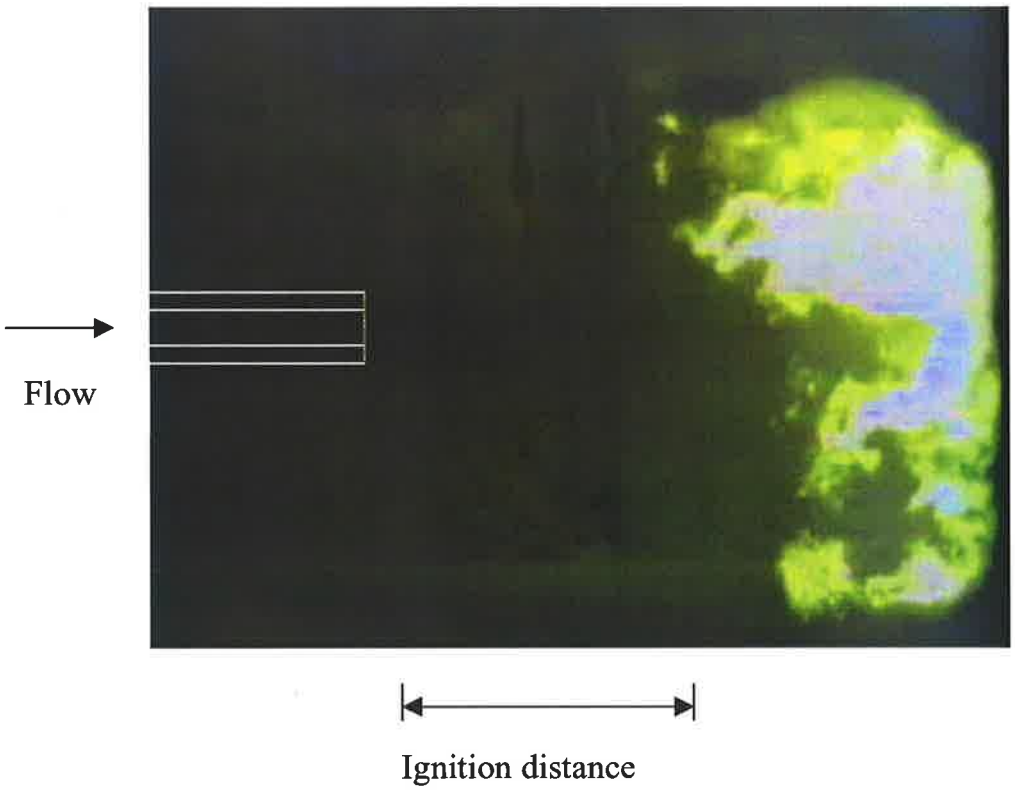

Figure 5.6. 1/1000s video image of 19PJ flame with a PJ inlet pressure of 60 kPa(g) and primary air velocity of 9.8ms^{-1}, G_{PJ}/G_1 = 8.5.

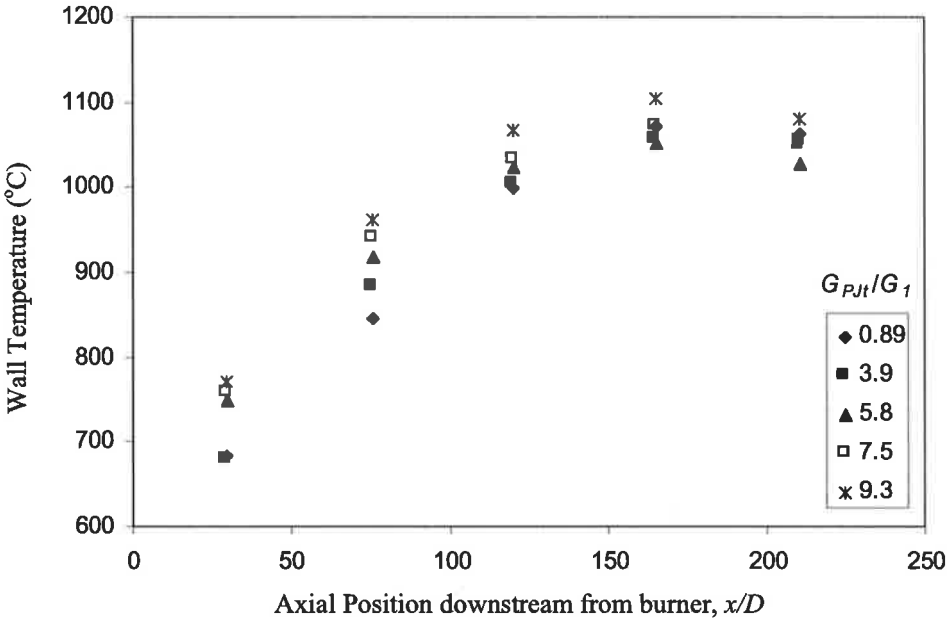

Figure 5.7 Effect of G_{PJt}/G_1 on wall temperatures for 10PJ flames

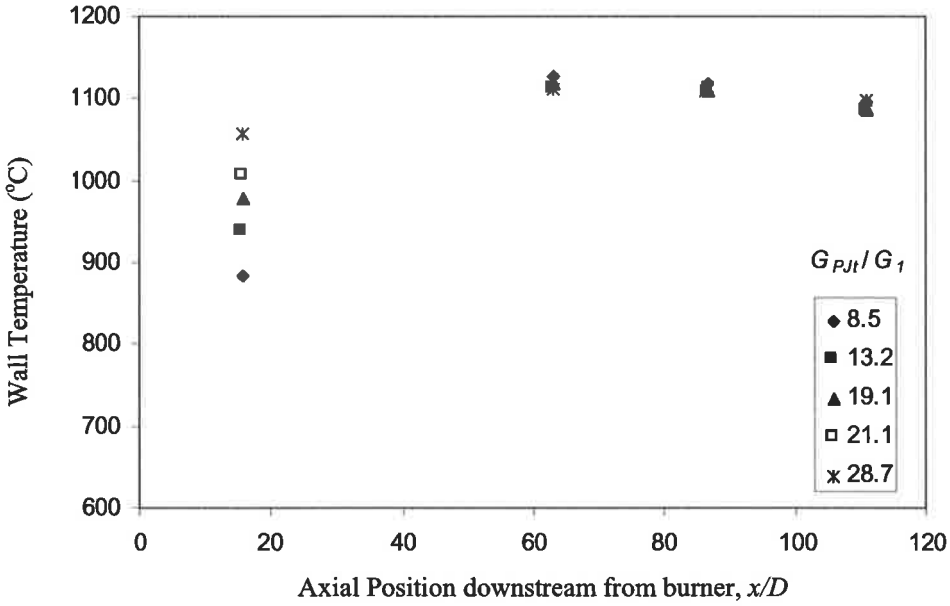

Figure 5.8 Effect of G_{PJt}/G_1 on wall temperatures for 19PJ flames

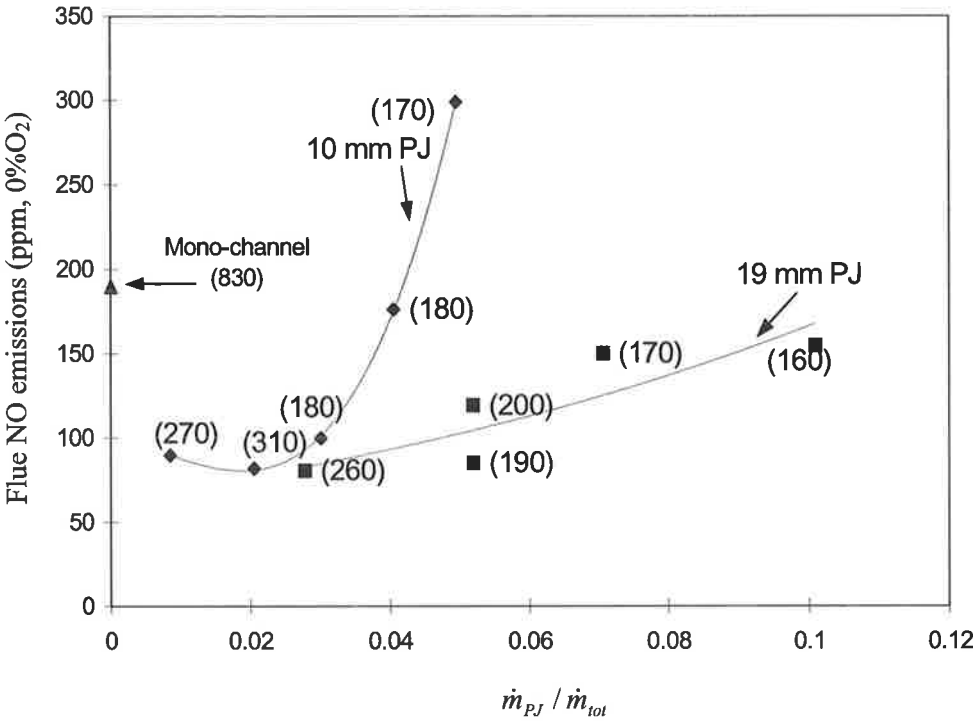

Figure 5.9 Effect of PJ flow-rate on flue NO and CO emissions (CO emissions in ppm in brackets)

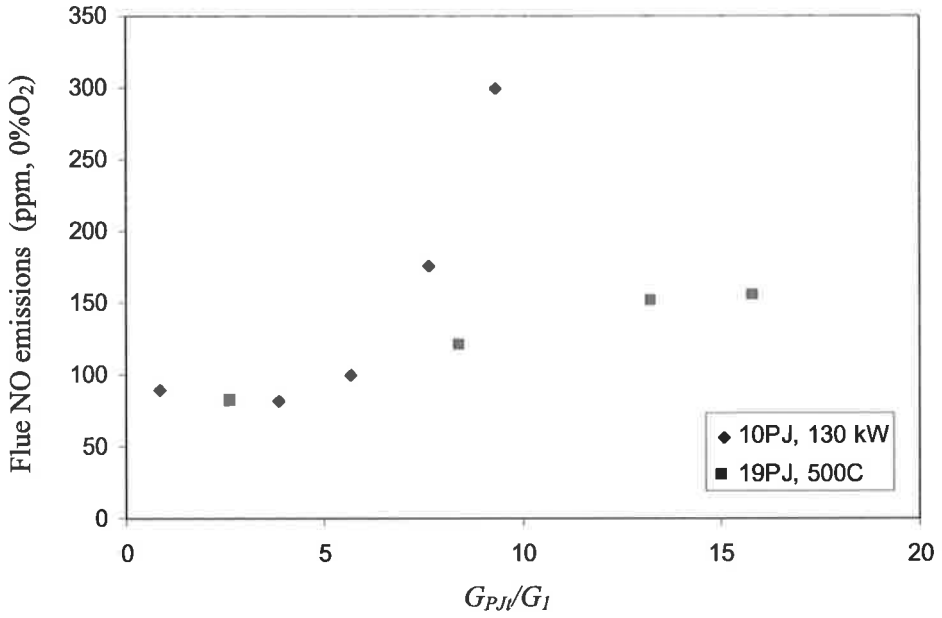

Figure 5.10 Comparison of NO emissions from 10PJ and 19PJ flames as a function of PJ momentum

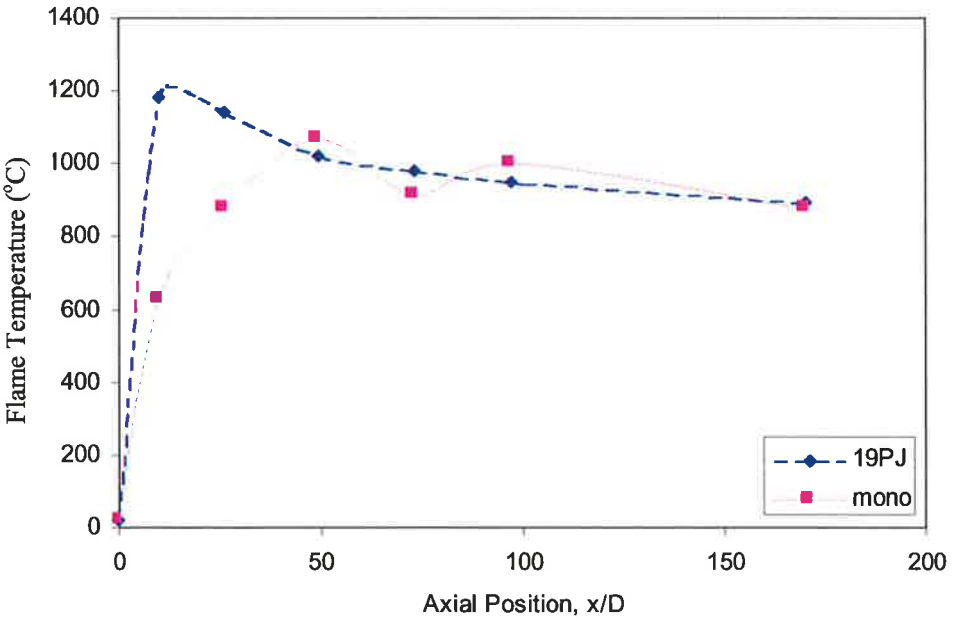

Figure 5.11 Centre-line in-flame temperature profiles – 19PJ flame with PJ pressure of 60 kPa(g), primary velocity of 9.8 ms^{-1}, G_{PJt}/G_1 = 8.5, and mono-channel flame, primary velocity = 9.8 ms^{-1}.

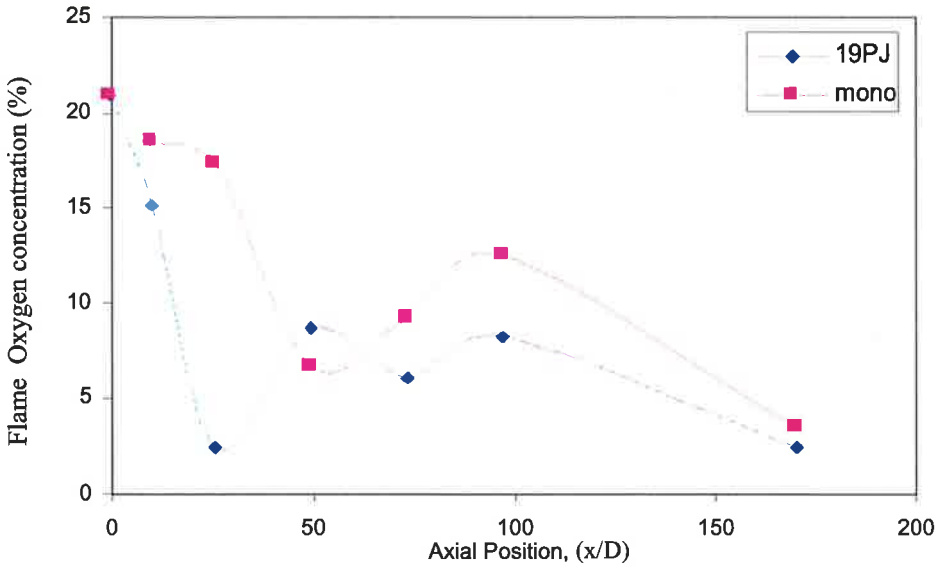

Figure 5.12 Centre-line in-flame oxygen concentration profiles – 19PJ flame with PJ pressure of 60 kPa(g), primary velocity of 9.8 ms^{-1}, G_{PJt}/G_1 = 8.5, and mono-channel flame, primary velocity = 9.8 ms^{-1}.

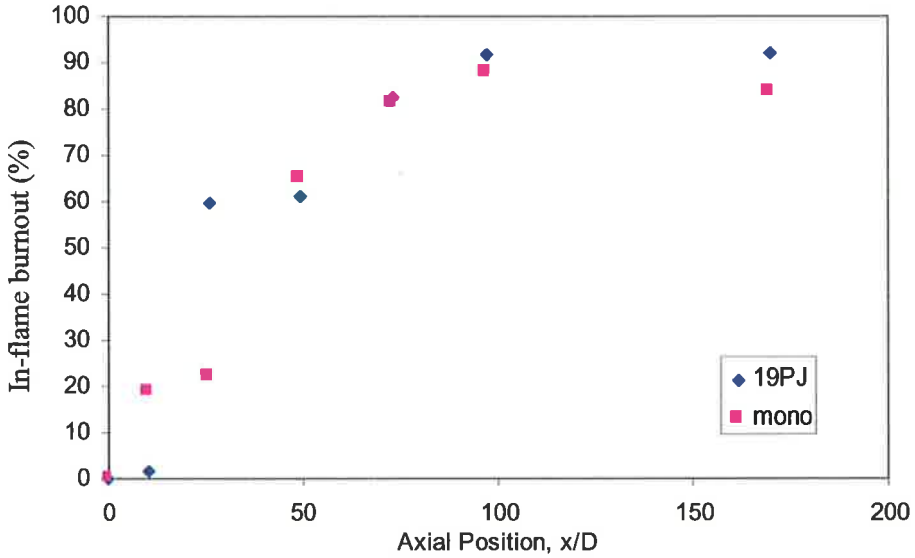

Figure 5.13 Centre-line in-flame burnout profiles – 19PJ flame with PJ pressure of 60 kPa(g), primary velocity of 9.8 ms^{-1}, G_{PJ}/G_1 = 8.5, and mono-channel flame, primary velocity = 9.8 ms^{-1}.

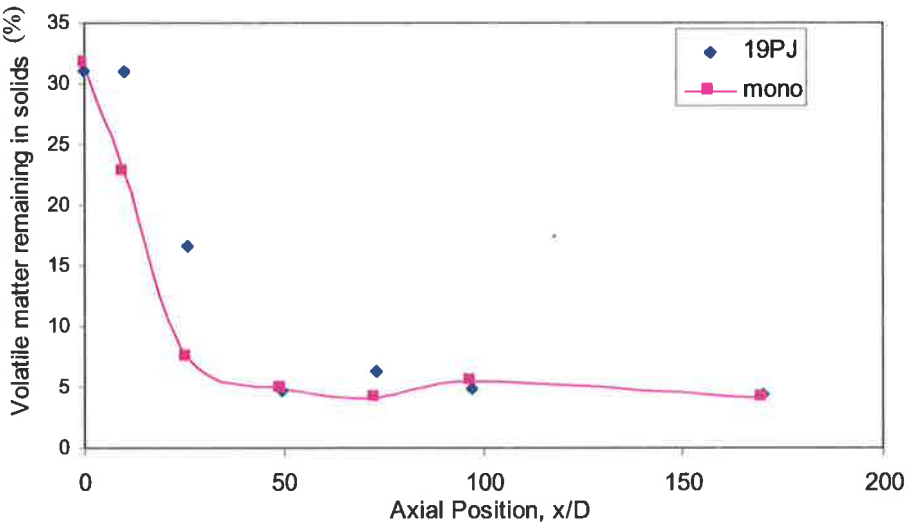

Figure 5.14 Centre-line in-flame particle volatile matter content profiles – 19PJ flame with PJ pressure of 60 kPa(g), primary velocity of 9.8 ms^{-1}, G_{PJ}/G_1 = 8.5, and mono-channel flame, primary velocity = 9.8 ms^{-1}.

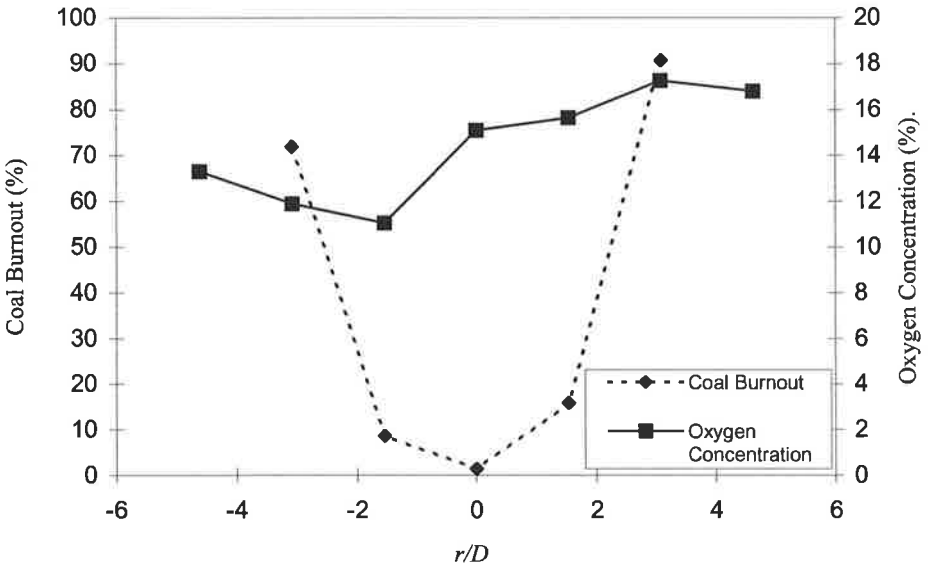

Figure 5.15 Radial coal burnout distribution and oxygen concentration profiles for the 19PJ flame with $G_{PJt}/G_J = 8.5$, at $x/D = 10$

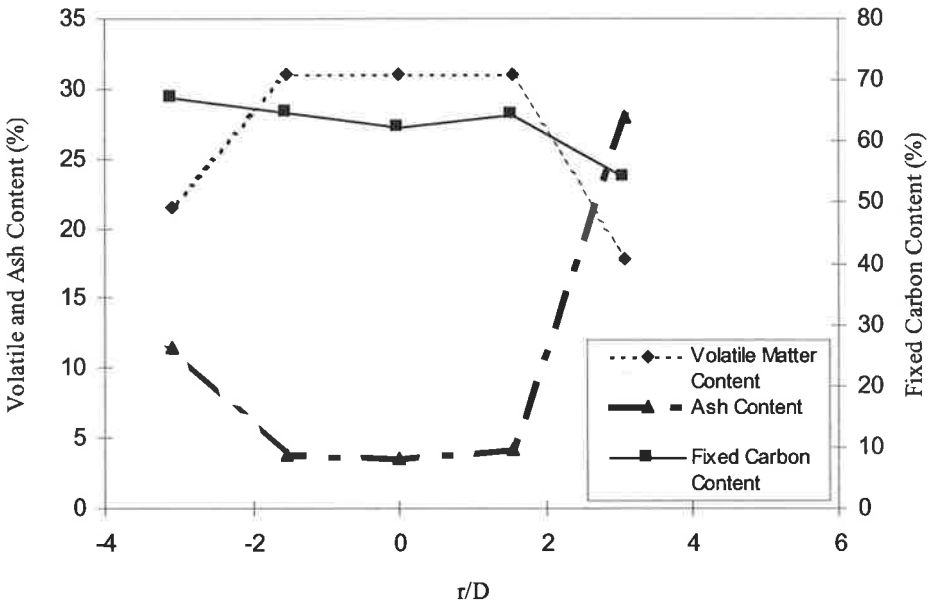

Figure 5.16 Radial volatile matter, fixed carbon and ash content profiles for the 19PJ flame with $G_{PJt}/G_J = 8.5$, at $x/D = 10$

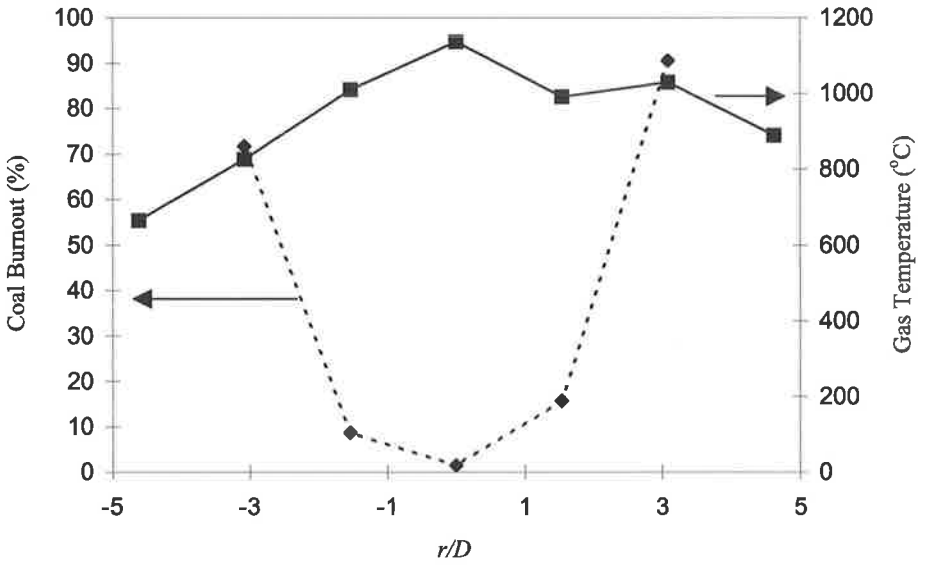

Figure 5.17 Radial coal burnout distribution and gas temperature profile for the 19PJ flame with $G_{PJt}/G_1 = 8.5$, at

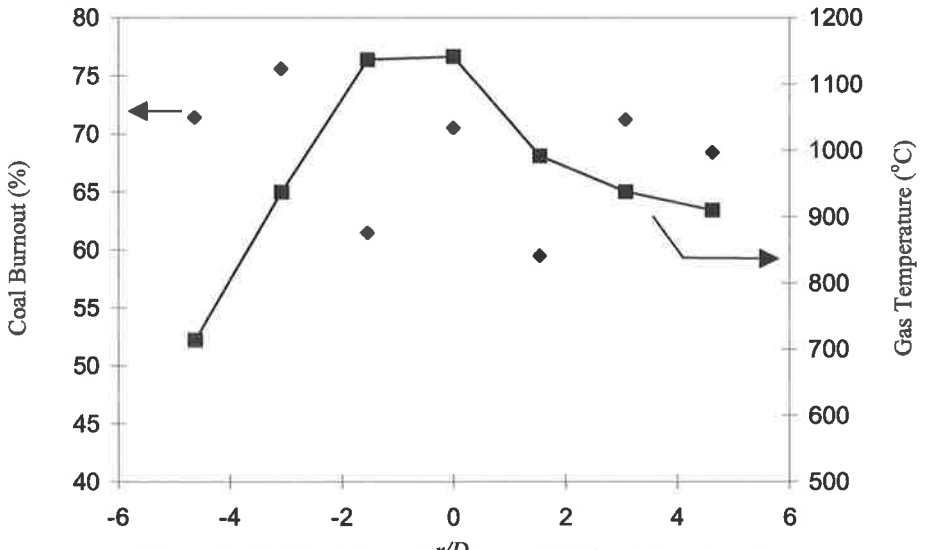

Figure 5.18 Radial coal burnout distribution and gas temperature profiles for the 19PJ flame, $G_{PJt}/G_1 = 8.5$, at $x/D = 26$

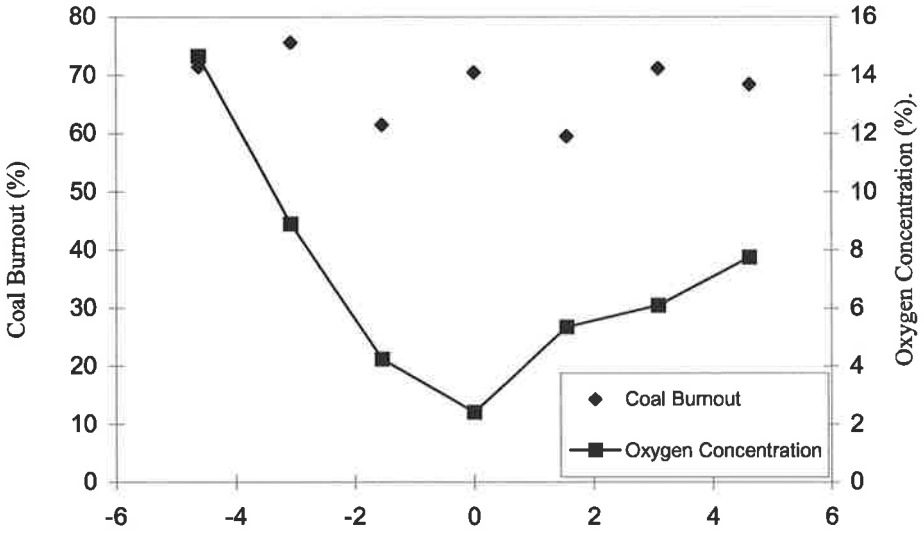

Figure 5.19 Coal burnout distribution and oxygen concentration profile for 19PJ flame, with $G_{PJt}/G_1 = 8.5$, at $x/D = 26$

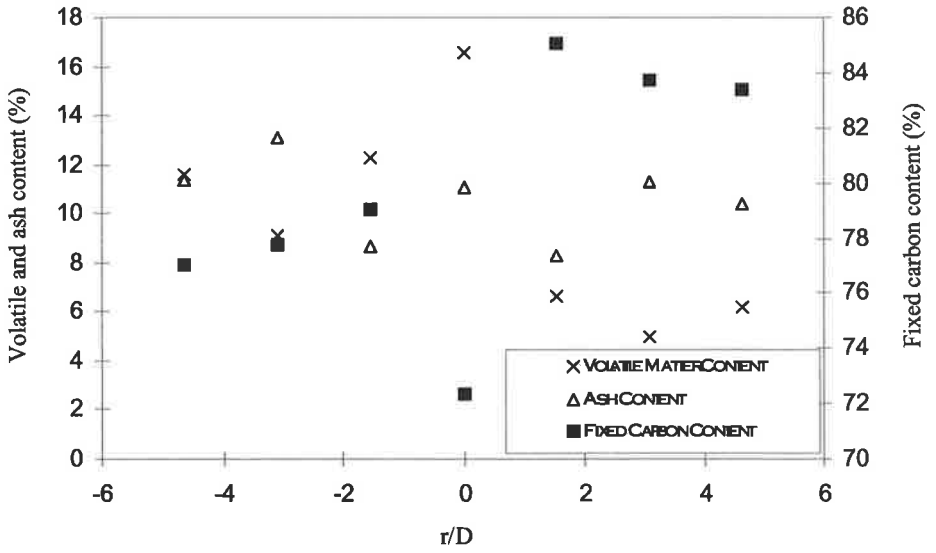

Figure 5.20 Radial volatile, fixed carbon and ash profiles for 19PJ flame, with $G_{PJt}/G_1 = 8.5$, at x/D = 26

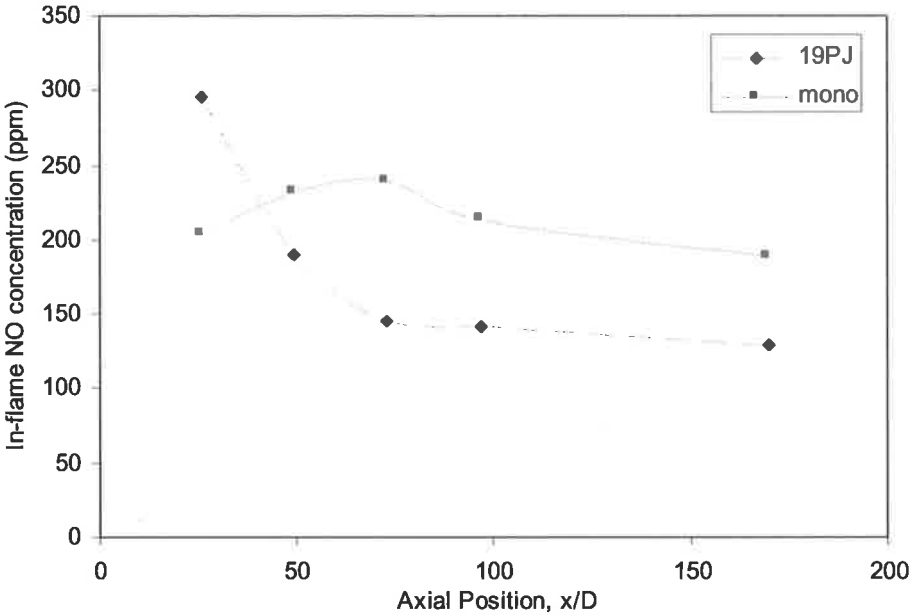

Figure 5.21 Centre-line in-flame NO concentration profiles – 19PJ flame with PJ pressure of 60 kPa(g), primary velocity of 9.8 ms^{-1}, $G_{PJf}/G_1 = 8.5$, and mono-channel flame, primary velocity = 9.8 ms^{-1}.

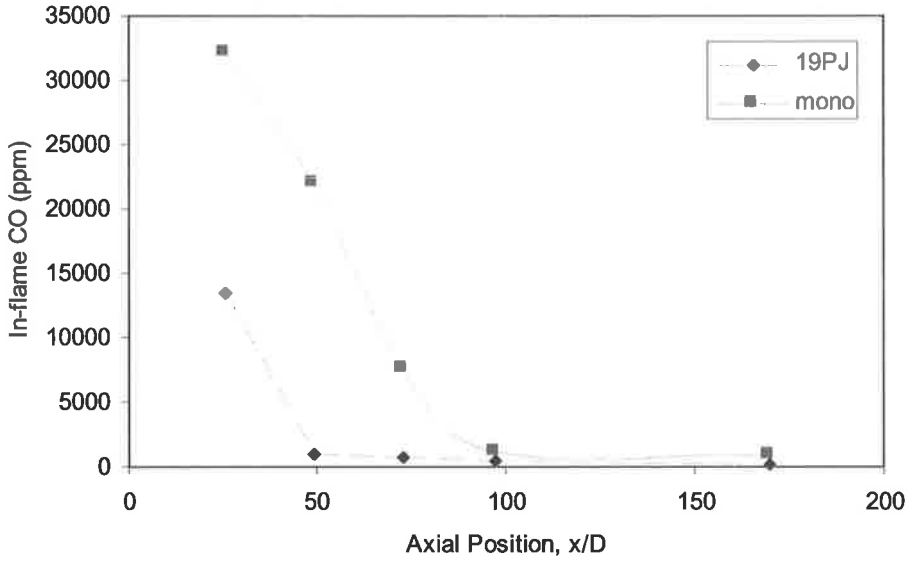

Figure 5.22 Centre-line in-flame CO concentration profiles – 19PJ flame with PJ pressure of 60 kPa(g), primary velocity of 9.8 ms^{-1}, $G_{PJf}/G_1 = 8.5$, and mono-channel flame, primary velocity = 9.8 ms^{-1}.

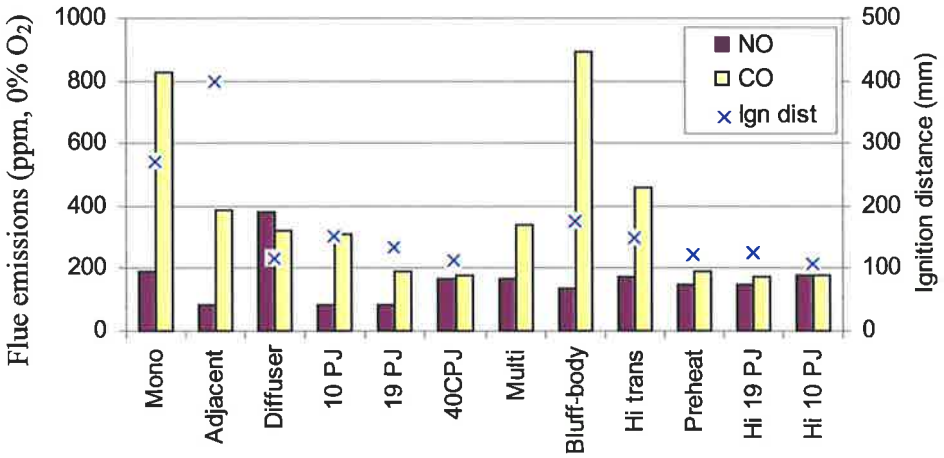

Figure 5.23 Flue emissions and ignition distances for the 130 kW flames. Refer to Table 5.2 for conditions.

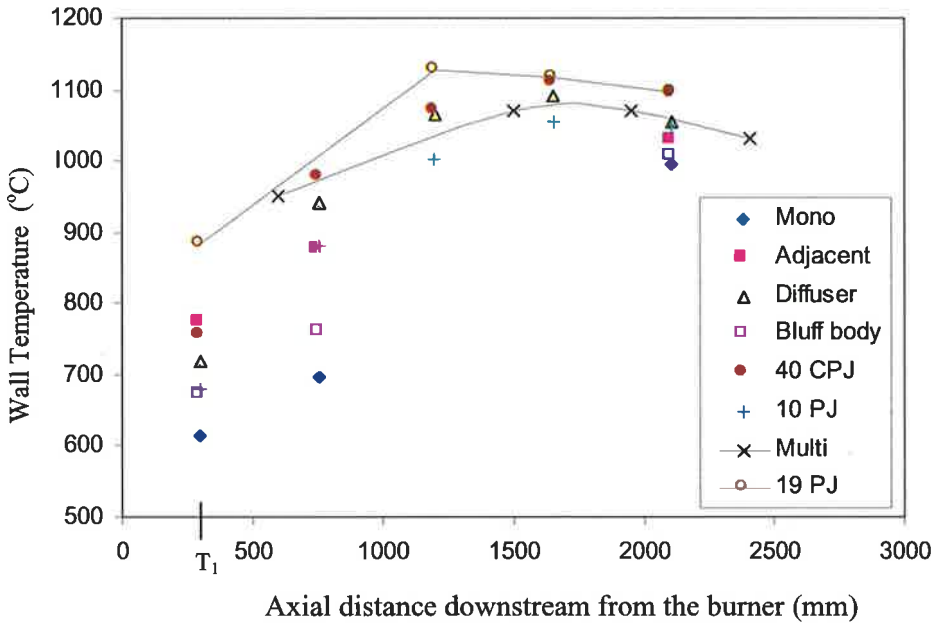

Figure 5.24 Comparison of wall temperatures for the 130 kW flames. Refer to Table 5.2 for conditions.

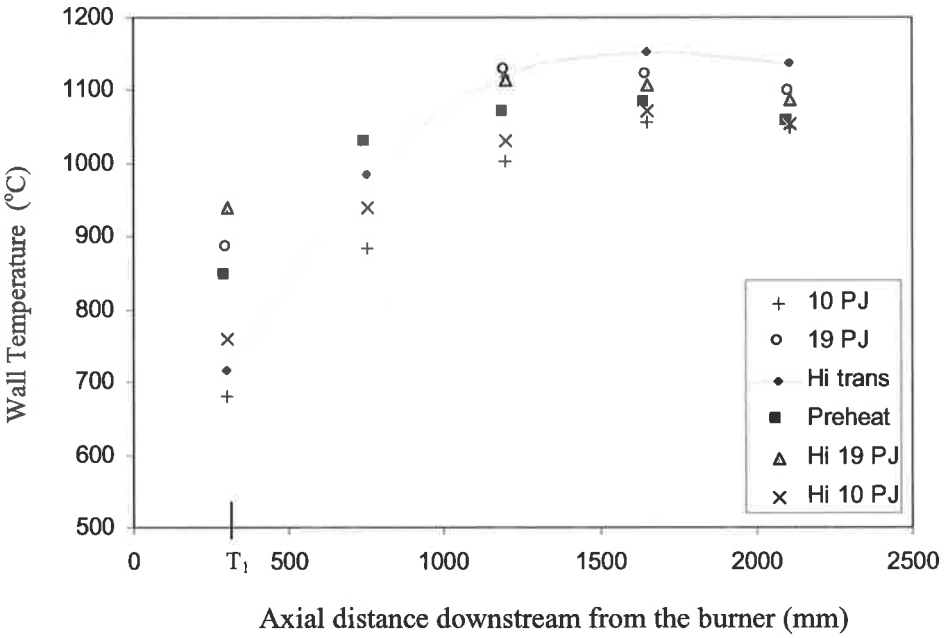

Figure 5.25 Comparison of wall temperatures profiles of various 130 kW PJ flames. Refer to Table 5.2 for conditions.

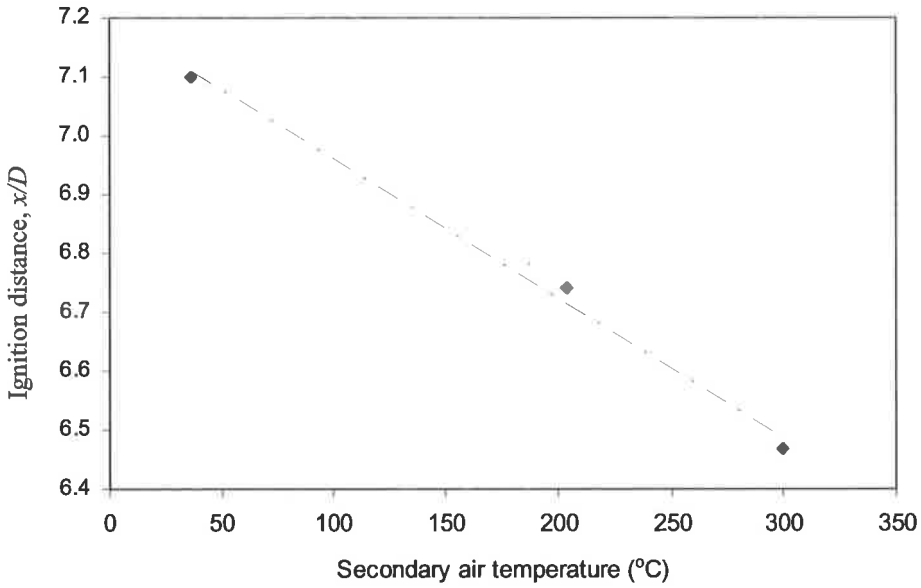

Figure 5.26. Effect of secondary air temperature on ignition distance of 19PJ flames with a PJ inlet pressure of 60 kPa(g) and primary air velocity of 9.8ms^{-1}, $G_{PJ}/G_1 = 8.5$.

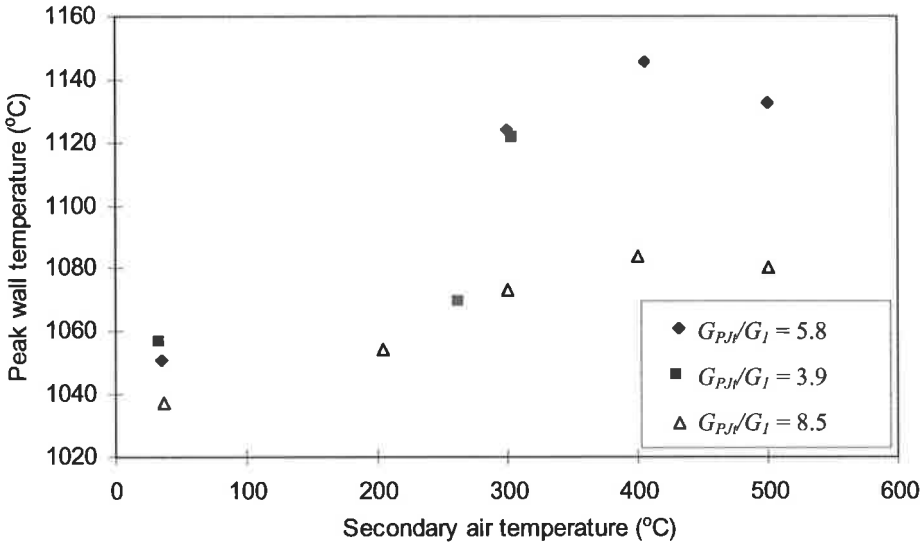

Figure 5.27. Correlation between peak wall temperature and secondary air temperature for:
(a) 10PJ flame with a PJ inlet pressure of 200 kPa(g), $G_{PJt}/G_1 = 5.8$,
(b) 10PJ flame with a PJ inlet pressure of 100 kPa(g), $G_{PJt}/G_1 = 3.9$,
(c) 19PJ flame with a PJ inlet pressure of 60 kPa(g), $G_{PJt}/G_1 = 8.5$.

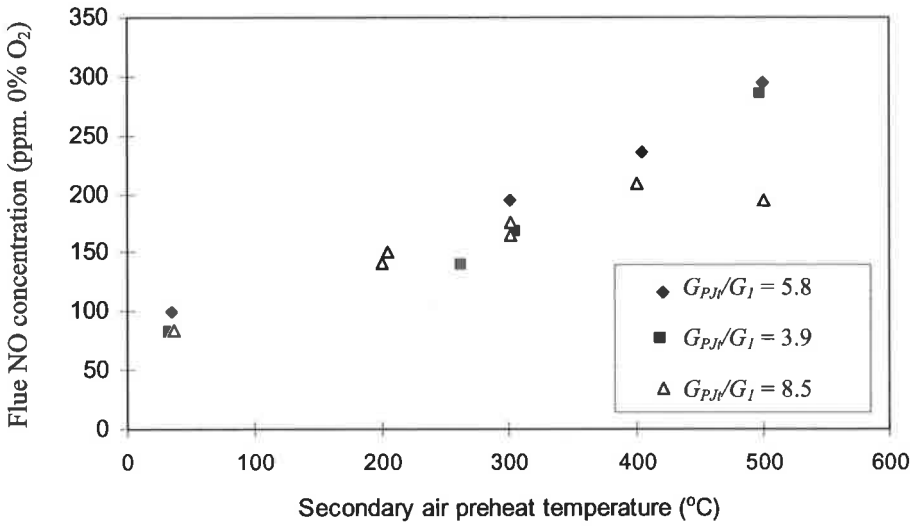

Figure 5.28. Effect of secondary air temperature on NO emissions:
(a) 10PJ flame with a PJ inlet pressure of 200 kPa(g), $G_{PJt}/G_1 = 5.8$,
(b) 10PJ flame with a PJ inlet pressure of 100 kPa(g), $G_{PJt}/G_1 = 3.9$,
(c) 19PJ flame with a PJ inlet pressure of 60 kPa(g), $G_{PJt}/G_1 = 8.5$.

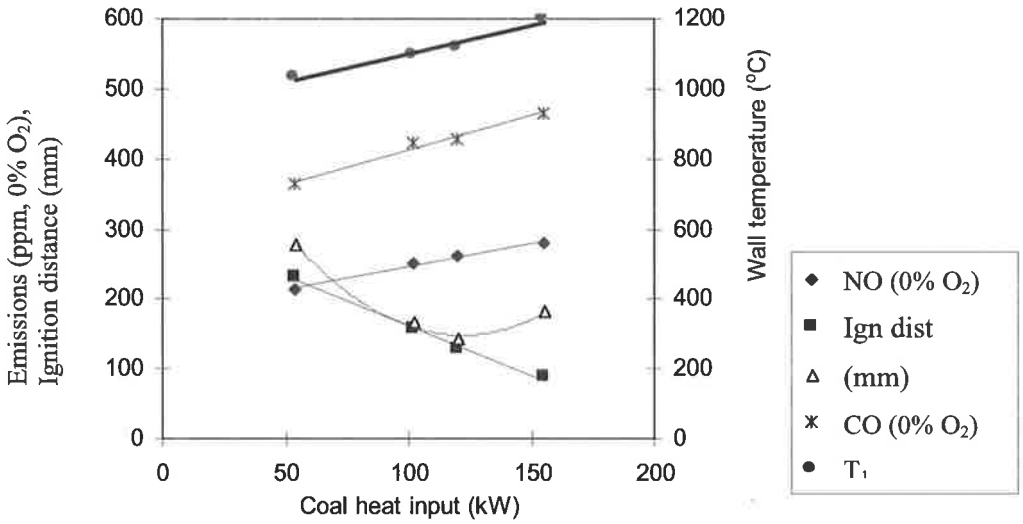

Figure 5.29 Effect of coal flow (energy input) on 19PJ flames at constant excess air. PJ pressure = 60 kPa(g), primary air velocity = 9.8ms^{-1} (G_{PJ}/G_1 = 8.5 when coal flow = 4.5 gs^{-1}). The secondary air temperature was held constant at 430°C

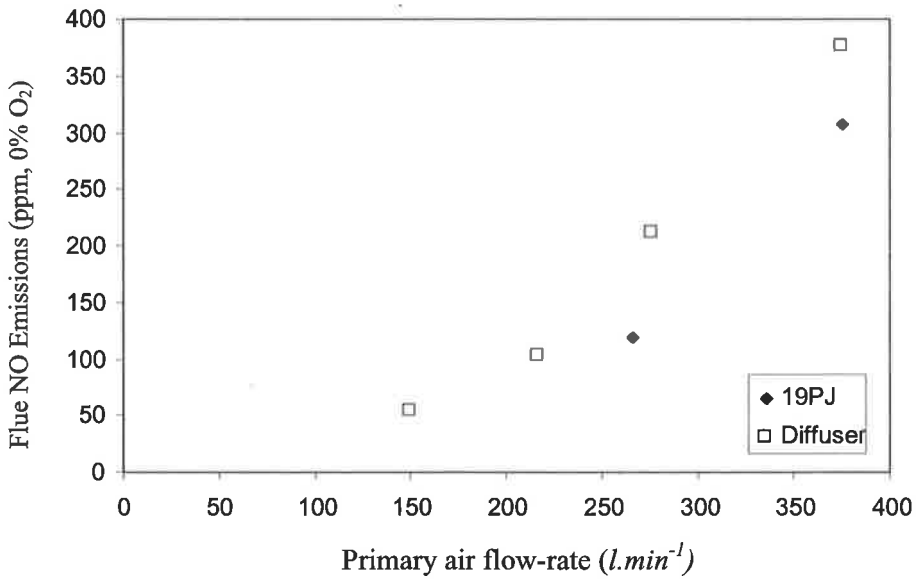

Figure 5.30 Effect of primary air channel diameter and flow-rate on NO emissions. The Diffuser burner shown in Figure 5.3(a) has a larger primary channel cross-section than the standard 19PJ burner. PJ pressure is held constant at 60 kPa(g), equivalent to 5.2% of the total air flow.

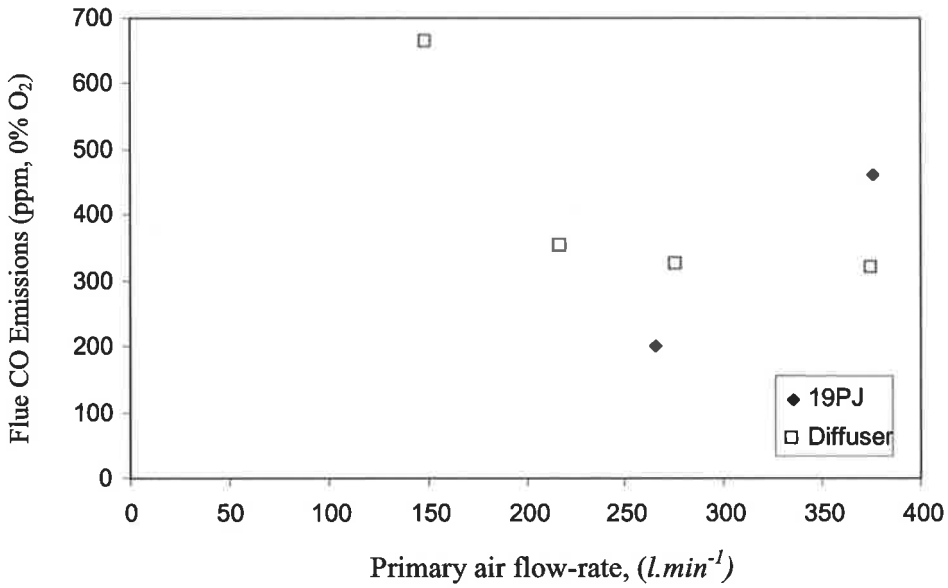

Figure 5.31 Effect of primary air channel diameter and flow-rate on CO emissions. The Diffuser burner shown in Figure 5.3(a) has a larger primary channel cross-section than the standard 19PJ burner. PJ pressure is held constant at 60 kPa(g), equivalent to 5.2% of the total air flow.

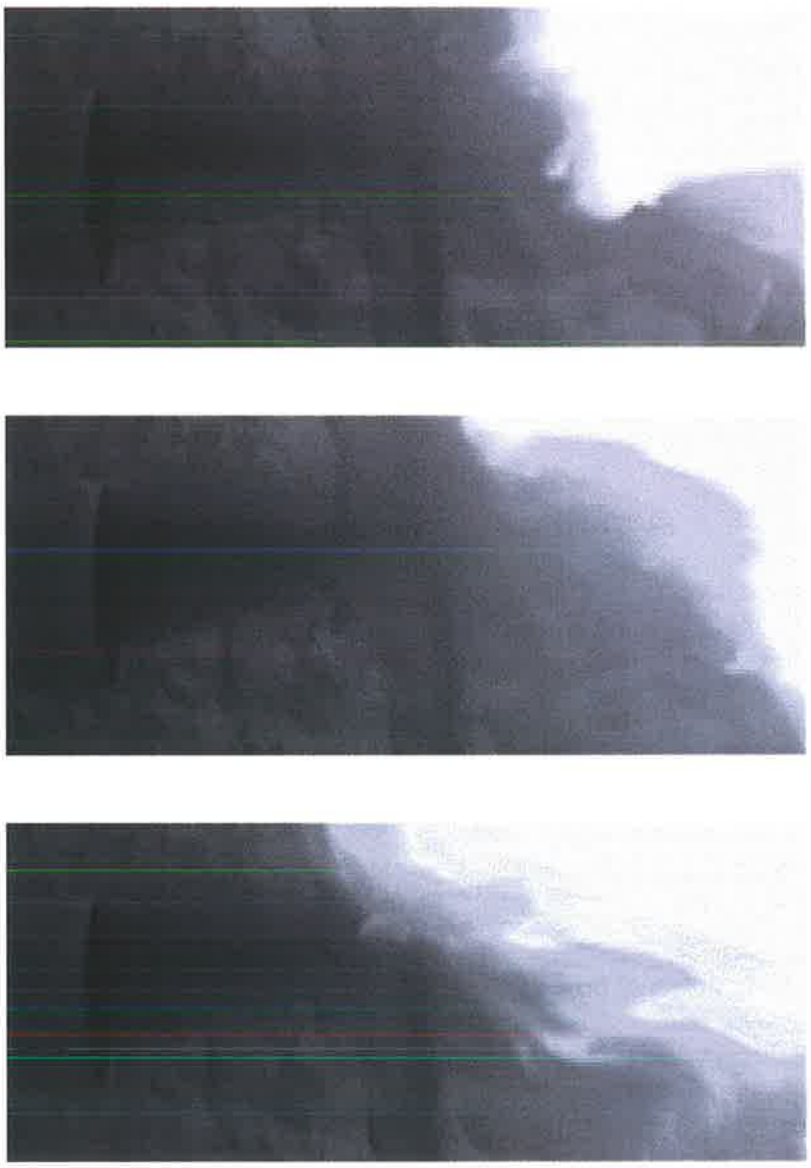

Figure 5.32 Three consecutive images of the ignition region of the Diffuser flame, with a primary air flow-rate of 277 $l.min^{-1}$, and PJ pressure = 60 kPa(g), G_{PJe}/G_1 = 4.26, showing that precession has little effect on the motion of particles emanating from the outer rim of the Diffuser.

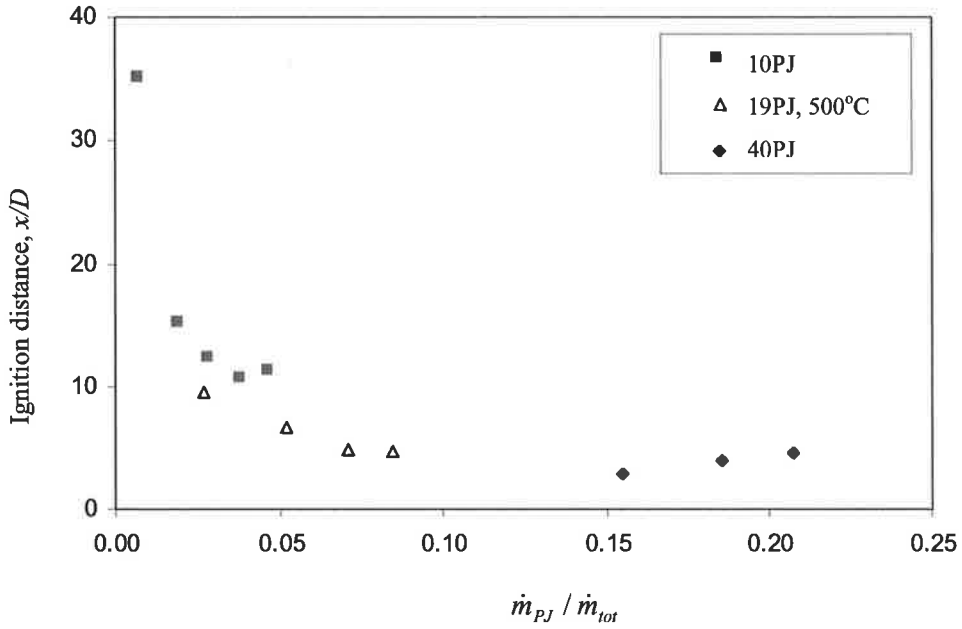

Figure 5.33 The effect of PJ air mass fraction on the ignition distance of 10PJ, 19PJ and 40PJ flames. The secondary air was supplied at ambient temperature for the 10PJ and 40PJ flames, whereas it was preheated to 500°C for the 19PJ flames. Coal was introduced directly through the 40PJ nozzle rather than through an annular injector.

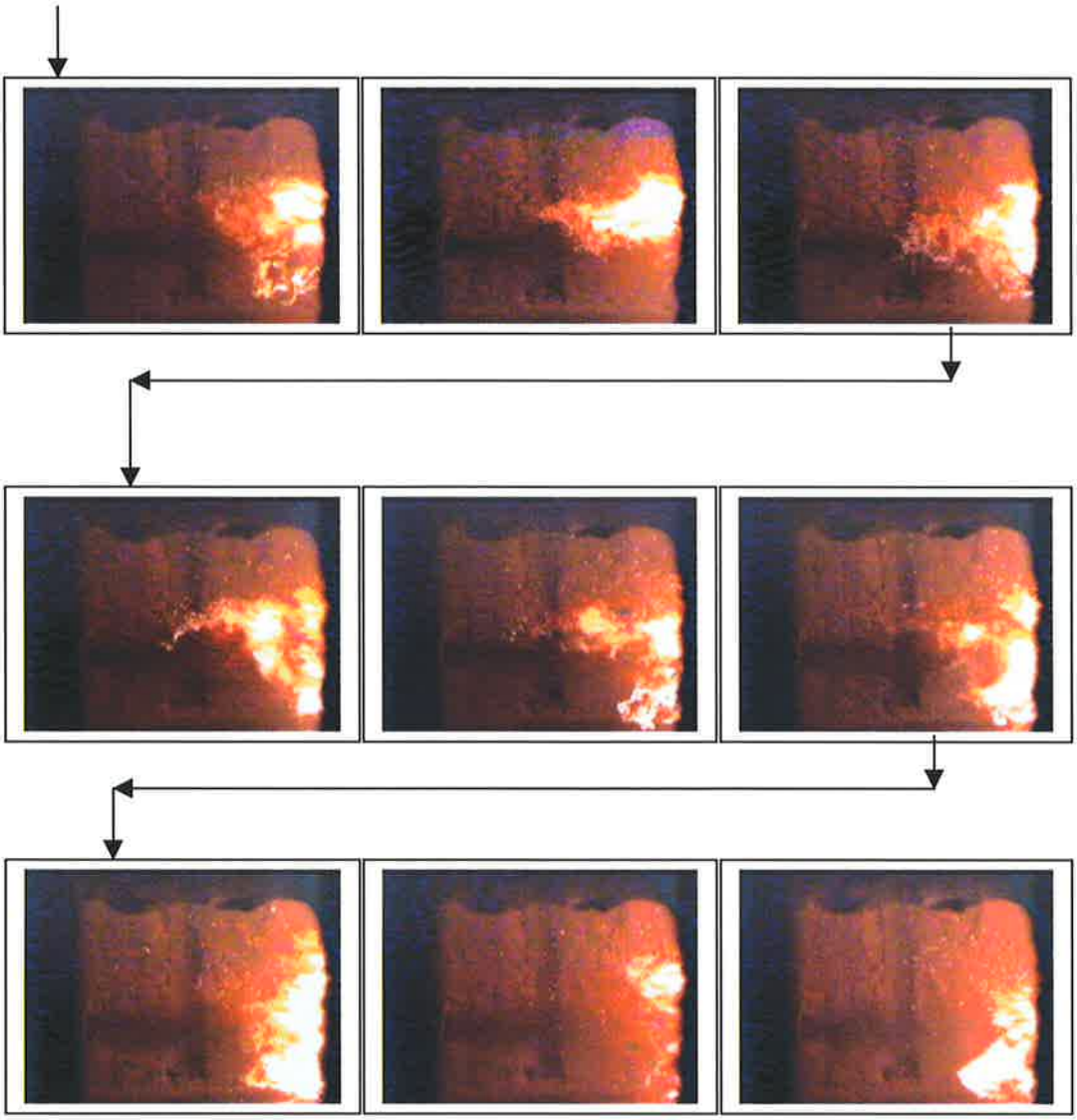

Figure 5.34 Nine consecutive images of the flame created by introducing the primary air (15% of the total air) and particles directly through a 40 mm PJ nozzle. The nozzle tip can be observed at the left of each image.

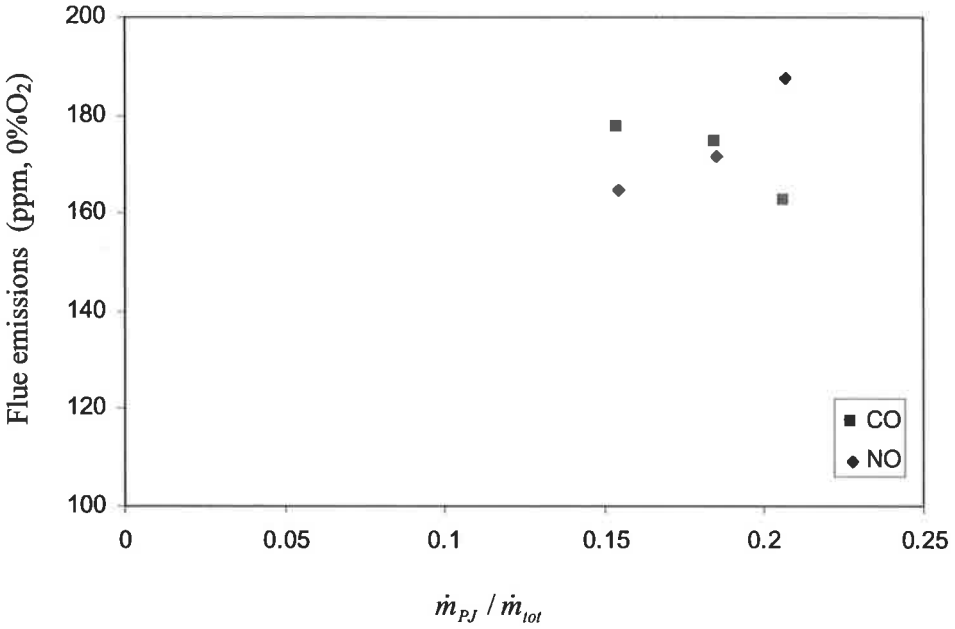

Figure 5.35 The effect of PJ air mass fraction, introduced with PF directly through the 40 mm PJ nozzle, on NO and CO emissions.

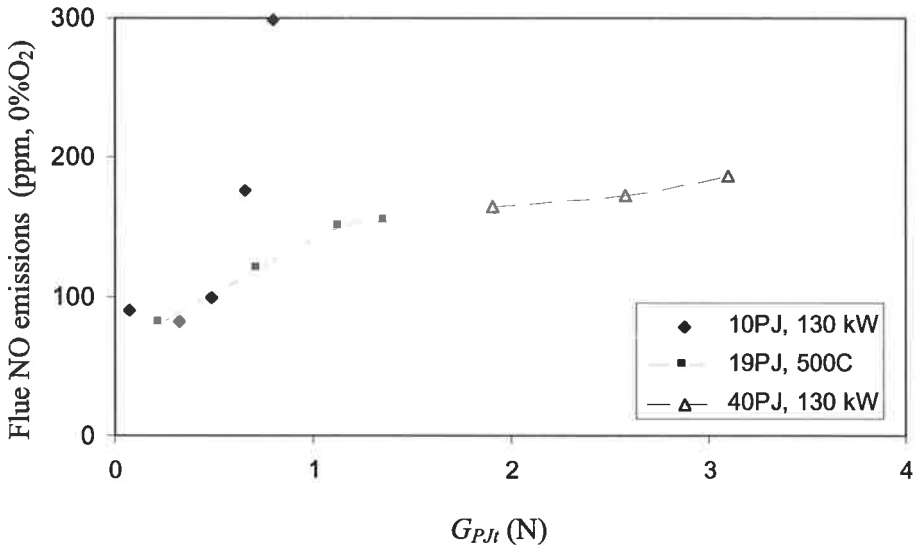

Figure 5.36 The effect of PJ air momentum flux (N), through the 10, 19 and 40 mm PJ nozzles on NO emissions. The 10PJ and 19PJ data are for PJ-annular arrangements, whilst the 40PJ data is for coal and primary air introduced through the PJ nozzle.

Chapter 6 2.5 MW Combustion Experiments

6.1. Introduction

Chapter 5 explored the effects of enhanced large scale mixing on particle motion, particle clustering, flame ignition and stabilisation, heat extraction and NO_x emissions at 130 kW scale under flow conditions modelled in the non-reacting water and air experiments (Chapters 3 and 4 respectively). The combustion results support the key hypotheses presented in Chapter 1. It has been shown that enhanced large scale mixing and consequent particle clustering have strong influences on flame characteristics. The visualisation of coal particles in unconfined gas flames (Appendix 4) suggests that enhanced particle clustering has the potential to generate local regions with fuel-rich conditions and increased emissivity and sooting.

The present chapter builds on the results of Chapter 5, presenting data from larger scale combustion experiments, where particle-turbulence interactions are more representative of those in full scale industrial operations. The experiments were performed in No. 1 furnace at The International Flame Research Foundation, "IFRF" (The Netherlands). The furnace was nominally operated at 2.5 MW (2.2 MW thermal, and approximately 0.3 MW from preheated air). The aims were to investigate the key aspects of the hypotheses, namely to:

(a) Perform experiments at a large enough scale for particle-turbulence interactions and mixing time-scales to be representative of those in full scale flames.

(b) Determine the influence of enhanced large scale mixing on coal particle clustering in the pre-ignition region of semi-industrial scale lifted turbulent diffusion flames.

(c) Measure more accurately than was possible at 130 kW scale, the effects of enhanced large scale mixing on heat release profiles.

(e) Use the data so obtained, in combination with that obtained at 130 kW scale, to explore scaling relations, based on dominant physical mechanisms, which describe results at both scales. If a scaling parameter can be developed, a further aim is to use it to predict the influence of enhanced large scale mixing at industrial scales.

6.2. Experimental Equipment

6.2.1. IFRF Furnace No.1 and Instrumentation

The furnace is configured as a boiler simulator, with the burner located inside a quarl, and provides the capability to swirl the secondary air using moveable block swirlers. A schematic diagram of the furnace is shown in Figure 6.1. The furnace is 2x2m in cross section and 6.25 m in length and consists of a water-cooled outer shell lined with refractory. Six steel pipe loops, each with surface area exposed to the flame of area 1 m^2, are installed inside the furnace near the walls. The temperature rise (measured using PT100 thermo-resistors) and water flow rates (measured using Promag 30 electromagnetic inductive flow meters) were used to calculate heat extraction. Heat removal through the refractory walls to exterior water-cooled jackets (segments) is measured by the temperature rise of the water in the same way as for the steel pipe loops. The heat release profile of the flame and total heat removed can be calculated from the water loop and segment flow-rate and temperature measurements. The refractory walls are extensively instrumented with Type B (Pt6%Rh/Pt30%Rh), thermocouples, which also provide an indication of the heat extraction through the walls.

The primary, secondary and PJ air flow rates were controlled with Protronic PS controllers and measured with orifice flow-meters. Coal was fed using a K-Tron T-35 twin screw, loss-in-weight feeder. Coal feed rate was adjusted by controlling the speed of rotation of the screws. Gas analysis was performed using a paramagnetic analyser for O_2, an infrared analyser for CO_2 and CO, and a chemiluminescent analyser for NO_x (Visser *et al.*, 1990). On one side of the furnace a 2m long horizontal slot in the wall allows flame photographs and videos to be taken. Probe access is provided at a number of ports at the positions illustrated in Figure 6.1. These ports were used for detailed in-flame measurements of gas composition and for solid sampling using a suction probe, temperature measurement using a suction pyrometer fitted with a type B thermocouple (capable of measurement up to 1830°C, Weber *et al,* 1992b), and for laser Doppler velocity measurements. The LDA equipment and the technique used are the same as those used previously at the IFRF in coal flames (Weber *et al.,* 1992b). Flue gas temperatures were measured with a suction pyrometer fitted with a Type B thermocouple. Provision was also made for laser sheet visualisation using a laser sheet through the slot and a camera mounted to an endoscope inserted through the furnace roof.

The primary transport air mass fraction is of the order of 0.2. Despite the fact that the furnace does not simulate cement kiln conditions its use was justified on the grounds that the mechanisms proposed from 130 kW scale experiments could be tested at a larger scale, by operating with no swirl on the secondary air.

6.2.2. Burners

Burner design was constrained by the dimensions of the quarl and annular primary air pipe and the need to cover a similar range of momentum ratios to those investigated at the 130 kW scale. The quarl, primary air channel and burners are illustrated in Figure 6.2. The relevant dimensions are given in Table 6.1 using the notation introduced in Figures 1.3 and 2.1. The quarl has a length to diameter ratio of 1.0 and expansion ratio of 2.0. The characteristic dimension of the quarl is its throat diameter, D_q. The quarl profile is designed to reduce flow separation in swirling flames by conforming to a third order polynomial (Smart, 1992). The diameter ratio of the primary to secondary air channels is 0.6, and the primary channel is sized to provide typical boiler primary air mass flow of 20% of the total air at a velocity of 20 ms^{-1}. PJ nozzles with chamber diameters of 80 and 55 mm and with dimensional ratios conforming to those used in commercial gas burners, as established by Hill (2000), were selected, according to the criteria outlined below, and denoted as "80PJ" and "55 PJ" respectively.

Table 6.1. Burner, air channel and quarl dimensions

Nozzle or channel	Nozzle throat (mm)	Inside diameter (mm)	Outside diameter (mm)
80PJ	$d_1 = 14.9$	$D = 80$	$D_{A,1} = 88.5$
55PJ	$d_1 = 10.5$	$D = 55$	$D_{A,1} = 88.5$
Primary air channel		$D_{A,1} = 88.5$	$D_{A,2} = 135.8$
Secondary air channel		141.3	$D_q = 234$
Quarl throat		$D_q = 234$	
Quarl exit		468	

Burner sizing was based on scaling up from the 130 kW flames. However it was considered more important to use the industry standard primary air velocity of 20 ms^{-1}, to allow better scale-up of results to conditions in full-scale kilns, than to apply constant velocity scaling from the 130 kW trials. In the 2.5 MW flames the secondary air velocities were of the order of 35 ms^{-1} at the burner exit plane (quarl throat), much higher than those used at 130 kW scale. The secondary air momentum was also significantly higher than the primary momentum at 2.5 MW scale. Consequently constant velocity and constant momentum ratio scaling criteria were not strictly applied when scaling from 130 kW to 2.5 MW scale. Rather, the PJ nozzle sizes at 2.5 MW scale were chosen to provide a range of momentum ratios comparable to those investigated at 130 kW scale. In addition, the momentum ratio used to scale from 130 kW to 2.5 MW incorporates the secondary air momentum in order to assess the significance of the PJ flow relative to the total flow, i.e. the momentum ratio used

is $G_{PJ}/(G_1+G_2)$. This momentum ratio is assumed to provide a measure of the strength of large scale mixing. Following the rationale developed in Section 5.3, the parameter $[G_{PJ}/(G_1+G_2)].St^{-0.5}$ can also be used to scale the effect of enhanced large sale mixing on particle clustering.

Figure 6.3 shows the effect of PJ nozzle pressure on the strength of large scale mixing, assumed to scale with the momentum ratio $G_{PJ}/(G_1+G_2)$. It can be seen that much higher pressures are required at 2.5 MW scale to achieve the same mixing effect as that produced by the 19PJ at 130 kW scale. However, the momentum ratios obtained with the 10PJ nozzle can be replicated at similar pressures. Figure 6.4 shows the effect of PJ nozzle pressure on particle clustering, which is assumed to scale with the parameter $[G_{PJ}/(G_1+G_2)].St^{-0.5}$. It shows that clustering effects obtained with the 10PJ nozzle can be replicated at similar pressures in the 2.5 MW flames, whereas it is only feasible to replicate clustering effects generated using low 19PJ pressures.

The calculated values of St, used to evaluate the parameter $[G_{PJ}/(G_1+G_2)].St^{-0.5}$ in Figure 6.4., are calculated as follows. The particle time-scale is calculated for a nominal PF particle density of 1600 kg.m^{-3} and particle diameter of 50 μm (following Wall, 1987). For consistency, the fluid viscosity, used in calculation of the particle time-scale, is evaluated at 320°C in each case. This is the temperature of the secondary air in the 2.5 MW experiments. The fluid time- scale is estimated from equation 4-9, which is restated here,

$$\tau_f = l/U = r_{1/2}\frac{(1+r_{1/2}/d_e)}{U_e} \qquad 4-9$$

The nominal jet half widths, $r_{1/2}$, of 10PJ and 19PJ flames with varying G_{PJ}/G_1 are taken from the water flow data provided in Figure 3.14. The nominal half widths of the 2.5 MW flames are also estimated from the Figure 3.14 in the following manner. The diameter ratio of PJ nozzle, to that of the dominant annular co-flowing stream is calculated. In the case of the 2.5 MW flames, the dominant flow is the secondary air stream. For the 80PJ nozzle, D/D_2 = 0.34, whilst for the 55PJ, D/D_2 = 0.24. In the water flow modeling reported in Chapter 3, the diameter ratios of PJ to annular stream were 0.58 for the 19PJ and 0.31 for the 10PJ. Hence the 10PJ data models the PJ to annular channel diameter ratios used in 2.5 MW flames more accurately than the 19PJ data. Consequently values of $r_{1/2}/D_2$ for the 2.5 MW flames are estimated from the 10PJ data in Figure 3.14. The momentum ratio $G_{PJ}/(G_1+G_2)$ is used for the 2.5 MW flames, instead of G_{PJ}/G_1, as shown in Figure 3.14 to account for the secondary air momentum. Figure 3.14, shows that the values of $r_{1/2}/D_2$ are of the order of

0.75 for all the 2.5 MW flames studied. The velocity, U_e, is characterised by a "momentum-weighted mean" value, shown in Section 4.5.2. to highlight the significance of NBZ effects on particle motion. Here the calculation of U_e incorporates the secondary air stream, because the secondary air is introduced through the burner, i.e.

$$U_e = \frac{(u_1.G_1 + u_2.G_2 + u_{PJe}.G_{PJe})}{(G_1 + G_2 + G_{PJe})} \qquad 6\text{-}1$$

The 80 PJ nozzle supplies the closest similarity in terms of pressure, and hence PJ exit velocity, to the nozzles used at 130 kW scale, and consequently the majority of 2.5 MW experiments are performed using it in preference to the 55PJ nozzle. Note that in this Chapter the PJ momentum is calculated at the nozzle throat where it can be accurately determined, rather than at the exit plane, where it is more relevant but less accurately known.

6.2.3. Fuel Characteristics

A single high volatile bituminous, low ash, washed coal was used throughout the trials so that the influence of variation in coal properties is eliminated, and the experiments could focus on mixing effects. A coal with low ash content was chosen so that fouling of heat transfer surfaces could be minimised. Fuel properties are given in Table 6.2. Coal was milled to a particle size distribution of 75 % < 75 μm using the IFRF solid fuel preparation facility.

Table 6.2. Coal Properties

	Units	Guasare Coal
Ultimate		
C	Wt% dry	78.30
H	Wt% dry	5.21
N	Wt% dry	1.49
O	Wt% dry	10.88
S	Wt% dry	0.82
Ash	Wt% dry	3.30
Sum		100.00
Proximate		
Ash	Wt% dry	3.4
C-fix	Wt% dry	58.5
Volatiles	Wt% dry	38.1
Sum		100.0
LCV measured	MJ/kg ıel(dry)	31.74
Fineness	%<90 μm	80%
	%<75 μm	75%

6.3 Experimental program

The effect of the strength and scale of enhanced large scale mixing, and Stokes number, on particle clustering and flame performance were investigated by varying the primary and PJ flow-rates. Most data was obtained by varying precessing jet air flow-rate from the minimum practical value, 25kg.hr^{-1} (0.88% of the total air mass flow), which was chosen as a precaution to prevent the nozzle from over-heating, to 500kg.hr^{-1} (17.7% of the total air). In these cases a constant primary air flow rate of 600kg.hr^{-1} (21.3% of the total air) was used. The secondary air flow-rate was adjusted in all cases to maintain flue oxygen concentration at 3%. The use of the two different sized precessing jet nozzles, 55 mm and 80 mm, allowed the dominant mixing scale, and hence Stokes number, to be varied independently of PJ momentum. A baseline flame, which employed the minimum precessing jet flow (0.88% of the total air), was also tested.

The primary transport air temperature was maintained at 70°C, whilst the PJ air was at ambient temperature. The secondary combustion air temperature was 320°C for all flames reported here, except those in which in-flame sampling and laser sheet visualisation were performed, in which case it was 450°C. This was the maximum achievable secondary air temperature, and was used to provide temperatures closest to the higher temperatures used in industrial cement kilns. The tests were performed using a coal rate of 254 kg.hr^{-1}.

For each flame, a minimum of 20 minutes was allowed for furnace temperatures to approach equilibrium. Water temperatures in the interior loops responded to changes in flame conditions rapidly, typically reaching 80% of the final temperature change within three minutes of the alteration to flame conditions. After 20 minutes, fluctuations in water temperature rise (ΔT) were of the order of ± 0.25°C. However, wall temperatures and the calculated heat removed from the external water jackets showed cycles resulting from flame changes made 2-3 hours previously. Consequently, data from the internal loops were used for heat extraction measurements, while wall temperatures were only used as a gauge to trends in heat extraction and flame temperature. The total heat extracted through loops and walls was not used for an overall mass and energy balance due to the errors in heat extraction through the walls associated with the non-steady state conditions. Instead an energy balance based on flue gas temperature and burnout measurements is developed in Chapter 7.

Photographs and videotape of the flames were taken through the horizontal slot in the side of the furnace, to establish ignition distances and provide qualitative visualisation. A planar

Mie scattering technique, similar to those used in the experiments described in Chapters 2 and 3, was used to visualise and qualitatively assess the extent of coal particle clustering, with a focus on the pre-ignition region of selected flames. A schematic diagram of the experimental arrangement is shown in Figure 6.5. The technique has been employed previously at the IFRF in gas flames (Dugue *et al.* 1994,1995) and in gas PJ flames (Nathan *et al.* 1992). Previous attempts to use the technique to image the dense coal particle concentrations in 2MW flames at IFRF have met with limited success due to the introduction of the laser sheet through the outlet end of the furnace. This technique results in heavy attenuation of the laser light since the optical path takes the beam through dense particle clouds along the entire length of the furnace. At the same time imaging within the flame zone results in poor signal to noise ratios because of the background flame radiation. Introduction of the laser transversely to the flame in the current work (Figure 6.5) alleviated both of these problems sufficiently to obtain good qualitative images. A horizontal laser sheet was introduced through the slot at the side of the furnace to allow imaging of the first 800 mm downstream from the quarl exit plane. In this way, predominantly the pre-ignition regions of flames were imaged so that background flame radiation was minimal.

Other aspects of the technique and apparatus were the same as those used previously at the IFRF (Dugue *et al.* 1994,1995). A Nd:YAG laser (532nm) was pulsed at 25 Hz, producing 190 mJ per pulse. The beam was spread with a cylindrical lens to form the sheet. Scattered light passed though an endoscope, installed at a viewing position on top of the furnace, to a black and white, image intensified, CCD camera that was triggered by the laser pulses. The image intensifier allowed the camera to be gated to 1 μs, minimising the effects of background radiation. Images were collected on VHS videotape, and individual frames were captured at random and digitised for presentation.

6.4. Results

6.4.1. Laser sheet visualisation

Figure 6.6 (a) shows a random selection of images from the pre-ignition region of flames with negligible PJ air flow-rate of 25 kg.hr^{-1} (0.88% of the total air) from the 80PJ nozzle, $G_{PJf}/G_I = 0.034$. Figures 6.6 (b) and (c) show images from flames using 125 and 250 kg.hr^{-1} respectively from the 55PJ nozzle, $G_{PJf}/G_I = 1.46$ and 3.30 respectively. The secondary air temperature in all these cases was 320°C. Similar images to those presented in Figure 6.6 were also observed in flames employing air flows of 250 and 500 kg.hr^{-1}, through the 80PJ nozzle.

It is evident that some preferential concentration (clustering) occurs in all flows presented in Figure 6.6. However clustering is weaker in the flame with $G_{PJf}/G_I = 0.034$ (Figure 6.6.a), which is dominated by the turbulence generated by the secondary and primary flows, together with oscillations and recirculation generated by the rapid expansion within and downstream from the quarl. Large scale flow structures and particle clustering effects that are broadly comparable with those shown to occur in simple particle laden jets (Longmire and Eaton, 1992) are evident in Figure 6.6(a). However it is very clear from Figures 6.6(b) and (c) that the size and significance of such large-scale particle clusters increases as the PJ momentum is increased. Local particle concentrations in some regions appear to also increase, although quantitative information is not possible from the current technique due to saturation of some pixel regions. The enhanced clustering generated by precession correlates with reduced ignition distance.

6.4.2. Effects of enhanced large scale mixing on ignition distance and heat extraction

The ignition distances of eight flames were calculated using the technique detailed below and illustrated in Figure 6.7. The camera was positioned at a distance, "a", from the external furnace wall. The doors on the horizontal slot were video-taped in the closed position for each camera position as depicted in Figure 6.7(b), as a length reference. The width of the video-taped image of each door as it appears on a 50 cm television screen, x_{door}, is given in Table 6.3, which also provides a summary of the complete calculation procedure. The variation in x_{door} is due to differences in camera position and zoom. The actual width of each of the doors is 285 mm. To record images of flames, the doors were opened and the camera was positioned at a = 2.06 m for flames with $G_{PJ}/G_1 \geq 1.49$. A larger field of view was required to record the longer ignition distances of flames with $G_{PJ}/G_1 < 1.49$, and the camera was positioned at a = 3.88 m in these cases. The distance from the furnace centre-line to the exterior of the furnace wall, "b" is 1.425m.

Table 6.3. Ignition Distance Calculations

Nozzle	G_{PJ}/G_1	Door width on video screen, x_{door} (mm)	Measured ign. dist. on screen $x_{ign,s}$ (mm)	(a+b)/a	Ign. dist. from quarl exit plane $x_{ign,q}$ (mm)	Actual ignition dist. x_{ign} (mm)
80PJ	4.52	305	170 ± 20	1.692	269 ± 32	503 ± 32
80PJ	6.09	305	105 ± 20	1.692	166 ± 32	400 ± 32
80PJ	2.90	305	320 ± 30	1.692	506 ± 48	740 ± 48
80PJ	0.72	101	240 ± 20	1.367	926 ± 77	1160 ± 77
80PJ	0.03	101	340 ± 20	1.367	1311 ± 77	1545 ± 77
80PJ, 450°C	2.90	289	215 ± 30	1.692	359 ± 50	593 ± 50
55PJ	1.49	283	400 ± 50	1.692	682 ± 85	916 ± 85
55PJ	3.23	283	285 ± 30	1.692	486 ± 51	720 ± 51

The fourth column in Table 6.3 shows the mean ignition distances, $x_{ign,s}$, downstream from the quarl exit plane, as measured from images displayed on the screen. The errors listed are the maximum extent of fluctuation of ignition distance observed in 100 frames. The actual ignition distances from the quarl exit plane, $x_{ign,q}$, are shown in the last column of Table 6.3, being derived, by similar triangles, from the expression:

$$x_{ign,q} = \left(\frac{285}{x_{door}}\right)\left(\frac{a+b}{a}\right)\left(x_{ign,s}\right) \qquad 6\text{-}1$$

The ignition distance from the burner exit plane is then given by:

$$x_{ign} = \left(x_{ign,q}\right) + L_q \qquad 6\text{-}2$$

where L_q is the length of the quarl.

Figure 6.8 presents typical examples of the video-taped images of the flames, demonstrating a dramatic reduction in ignition distance with increasing G_{PJ}/G_1. The reduction in ignition distance with increasing G_{PJ}/G_1 confirms the influence of enhanced large scale mixing in the near burner zone, as demonstrated in Chapter 5. Figure 6.9 presents the actual measured ignition distances from the burner exit plane, x_{ign}, normalised against the PJ chamber diameter, D, as a function of G_{PJ}/G_1. The single data point, for the only flame with ignition distance measured at the higher secondary air preheat of 450°C, shows a further reduction in ignition distance due to the increased particle heating rate.

Figure 6.10 shows the effect of G_{PJ}/G_1 on the profile of heat extracted by the internal water loops for the 80PJ nozzle. Increasing G_{PJ}/G_1 results in a dramatic increase in both the heat extraction close to the burner and the overall heat released. In Figure 6.11 the heat extraction data is replotted against the axial distance downstream from the ignition point. Comparing the two figures shows that the movement of the position of peak heat extraction closer to the burner is largely due to the changes in ignition distance associated with the effect of enhanced large scale mixing on ignition distance. The additional influence of mixing on combustion accounts for a movement in the position of peak heat extraction by approximately 500 mm towards the burner. In addition, the magnitude of the peak heat extraction increases from 195 to 230kW with G_{PJ}/G_1, indicating an increase in combustion rates caused by the mixing. That this is associated with the increased particle clustering effects with increased G_{PJ}/G_1 is demonstrated in the laser sheet visualisation shown in Figure 6.6. One plausible contribution to the correlation between enhanced clustering and increased heat release is an increase in the quantity of soot formed due to the promotion of fuel rich clusters, resulting in increased flame emissivity. Figure 6.12 shows similar heat extraction data to that in Figure 6.10 but for the 55PJ burner. Again as G_{PJ}/G_1 is increased the magnitude of peak heat extraction is increased. The above trends in heat extraction are significant, as demonstrated by an estimate of the maximum experimental error in heat extraction at each measurement point of ±1% (see Appendix 5 for details).

6.4.3. The effect of enhanced large scale mixing on NO_x emissions and coal burnout

The effect of increasing G_{PJf}/G_1 on NO_x emissions is demonstrated in Figure 6.13. The results show the same trend as that found at 130 kW scale, where NO_x emissions were shown to increase with G_{PJ}/G_1. As was also the case at 130 kW scale, increases in NO_x emissions correlated with decreasing ignition distances (Figure 6.9). The reverse trend was shown in 2MW flames in a rotary kiln simulator (van de Kamp and Smart, 1992) where ignition distance also correlated with the mass of air in-flame at ignition. One possible reason for the reverse trend in the PJ flames is that the mass of air at the point of ignition may increase with decreasing ignition distance due to rapidly increasing initial entrainment rates with increasing G_{PJ}/G_1. The trends of increasing coal burnout (Figures 6.14 and 6.15) and increasing heat extraction near to the burner (Figures 6.10 and 6.12) with increasing G_{PJf}/G_1 lend support to this suggestion.

The influence of flame temperature on NO_x emissions is difficult to ascertain from the heat extraction and coal burnout data, whereas the flue gas temperature provides more insight since it is a single value measure of the total heat absorbed by the heat sinks. Figures 6.13 and 6.16 show that the trend of increasing NO_x emissions with increasing G_{PJf}/G_1 is accompanied by a reduction in flue gas temperature from 1044 °C to 945°C. This shows that the total quantity of heat removed by the heat sinks is increased dramatically as G_{PJf}/G_1 increases, consistent with the results of Figure 6.11, and with increased wall temperatures, and by deduction, increased flame temperatures. For example, the peak wall temperature increased from 1029 to 1090 °C when G_{PJf}/G_1 was increased from 0.03 to 6.1. The reason for the increase in wall temperature with increasing heat extraction is that the cooling tubes and external water cooled jacket only remove a relatively small fraction of the total heat released by the flame. In contrast, in the NBZ of a cement kiln, wall temperature profiles are held relatively constant due to the endothermic clinkering reaction. Thus, the observed trends of increasing NO_x and burnout with G_{PJf}/G_1 can be partially attributed to an increase in flame temperature, which may not apply in industrial cement kilns. More detailed measurements of in-flame temperatures and the effects on NO_x emissions are reported in Section 6.4.5. The additional effects of the high secondary air velocities used at 2.5 MW on NO_x emissions are considered in the next section. In Chapter 7 calculations are performed to estimate the influence of air entrainment and the external recirculation of furnace gases on heat extraction profiles and NO_x emissions.

6.4.4. The effects of secondary air momentum on flame characteristics

Figure 6.17 compares the heat extraction profiles for two 80PJ flames, G_{PJt}/G_1 = 5.19 and 2.90 respectively, with a constant PJ flow-rate of 250 kg.hr^{-1} (8.8% of the total air) and primary (transport) air flow-rates of 400 kg.hr^{-1} and 600 kg.hr^{-1} respectively. The secondary air flow-rate was adjusted to balance the flue oxygen concentration to 3% in each flame. Consequently the comparison includes the effects of varying both the secondary and primary air momenta. A slight trend of increased NBZ heat extraction with increasing G_{PJt}/G_1, which also represents an increase in secondary air momentum, is observed.

Figure 6.18 compares the heat extraction profiles for two 80 PJ flames with the same two primary air flow-rates as those used in Figure 6.17, but with a PJ flow-rate of 375 kg.hr^{-1} (13.2 % of the total air). The momentum ratios of these two flames are G_{PJt}/G_1 = 8.09 and 4.53, for primary air flow rates of 400 kg.hr^{-1} and 600 kg.hr^{-1} respectively. In Figure 6.19 data is shown for flames with the same two primary air flow rates and a PJ flow-rate of 500 kg.hr^{-1} (G_{PJt}/G_1 = 10.89 and 6.08 respectively). Figures 6.18 and 6.19 show that there is an increase in the heat extracted in the loop closest to the burner exit plane relative to the cases shown in Figure 6.17, due to the increase in G_{PJ}. However, Figures 6.18 and 6.19 also show that, for each constant PJ flow-rate, there is a reduction, by 20 kW, in the heat extracted in the loop closest to the burner exit plane, as the primary air flow-rate is reduced and the secondary air flow-rate is increased (shown as an increase in G_{PJt}/G_1). The trend is the opposite of that observed earlier, in terms of G_{PJt}/G_1, and can be explained by the increase in the secondary air momentum. For example, for the cases in Figure 6.19, the reduction in primary air flow-rate from 600 to 400 kg.hr^{-1} caused an increase in the combined momentum of the primary and secondary air flows from 19.5 N to 20.3 N, with a corresponding increase in mean velocity. The secondary air velocity also increased from 31.6 to 34.0 ms^{-1}. The increased secondary and total momentum is deduced to have caused an acceleration in particles and a reduction in the influence of precession, and hence a reduction in NBZ heat release.

Figure 6.20 illustrates that increasing secondary air momentum, and reducing primary air as above, also caused increases in NO_x emissions for the flames considered above. Increases in secondary air momentum are again displayed as increases in G_{PJt}/G_1. The observed trend of increasing NO_x correlates more strongly with increasing secondary momentum than with any variation in PJ flow-rate and momentum. Increased secondary air momentum can be deduced to increase NO_x emissions by increasing the oxygen concentration in the region

where volatiles are released. Possible mechanisms are (a) entrainment of a greater fraction of particles into the shear layer between the primary and secondary flows where high mixing rates and high oxygen concentrations occur, (b) an increase in the mean entrainment rate and ignition distance, or (c) a reduction in preferential particle concentration, generated by precession.

6.4.5. In-flame measurements

In-flame sampling was performed in two 80PJ flames with PJ air flow-rates of 25 and 250 kg.hr^{-1} (G_{PJ}/G_J = 0.03 and 2.9 respectively). The secondary air temperature employed, 450°C, was the maximum achievable using the electric air pre-heater and was selected to provide the highest flame temperatures, and hence to best simulate cement kiln temperatures. However if should be noted that the higher secondary air temperature, relative to the flames discussed earlier, also increases the secondary air velocity and so moves mixing similarity further from cement kilns. Flame temperature, gas, and coal burnout data were taken to investigate the mechanisms underlying the stabilisation, flue NO_x and heat extraction findings reported above. Velocity data were used to determine the mass of externally recirculated gases, and to investigate clustering effects.

The flame temperature data are shown in Figures 6.21 and 6.22. Coal burnout data are shown in Figure 6.23. The peak centre-line temperature occurs closer to the nozzle with G_{PJ}/G_J = 2.9 than with G_{PJ}/G_J = 0.03, correlating with the trends of decreasing ignition distance and early heat release with increasing G_{PJ}/G_J, reported in Figures 6.9 to 6.11. Significantly the peak temperature in the flame with G_{PJ}/G_J = 2.9 is 50°C lower than that of the baseline flame. The lower peak temperature may be due to increased radial spread of the flame, which may reduce volumetric mean combustion rates, or to low temperatures in cluster cores, as proposed in section 5.5.4. The reasonably flat radial flame temperature distribution supports both of these propositions. However it is also possible that a flame cooling effect occurs due to the increased heat flux to the walls. If the trend of decreasing peak flame temperature with increasing G_{PJ}/G_J also occurs in higher temperature environments, such as industrial rotary kilns, where thermal NO_x is more significant, they may result in significant NO_x reductions.

In-flame gas species concentrations for the flame with G_{PJ}/G_J = 2.9 are shown in Figures 6.24 – 6.26. These figures show that combustion is well advanced by an axial distance of 730 mm downstream from the quarl exit plane (x/D = 12.1), with high levels of oxygen consumption, and the attainment of peak NO levels. Centre-line NO levels reduce slightly from 690 ppm at an axial distance of 730 mm to near flue gas levels of 575 ppm at an axial position of 2640 mm. The CO data indicates that the early stages of combustion are fuel-rich on the centre-line, which may limit the peak of NO formation, although the data provides no direct evidence of whether a mean or local staging effect within clusters occurs. On the basis of the above results, the measured increase in flue NO_x emissions found to occur with

increasing G_{PJf}/G_1 (Figure 6.13), is hypothesised to be due to increased entrainment rates of air. Despite the increases in entrainment rates, the mixing limits increases in NO_x emissions by promoting fuel-rich conditions on the flame centre-line. Increased NO_x emissions are exacerbated by limitations in the control of furnace cooling, which dictate that it is not possible to operate flames with different heat flux at the same wall temperature.

Figures 6.27 - 6.29 show velocity data, determined by laser Doppler anemometry, at four axial positions in the 80PJ flame with $G_{PJf}/G_1 = 2.9$. Figure 6.27 shows that natural seeding provided by coal particles is adequate for LDA measurements. It compares the mean axial velocity data, 150 mm downstream from the quarl exit plane (x/D = 4.8) measured using natural seeding provided by coal particles alone, with those obtained with natural seeding and the additional seeding of < 5 μm TiO_2 flow tracer particles into the secondary air. Seeding of the secondary air was performed using a pressurised cyclonic feeder. Figure 6.27 shows that seeded and unseeded flames produce substantially the same axial velocity profiles. It is evident that sufficient fine coal particles are present to provide unbiased natural seeding in both the primary and secondary streams. Consequently all other axial planes were measured using only the natural seeding provided by the coal particles.

The magnitude of peak axial velocities in the first 500 mm downstream from the quarl exit (Figure 6.28) are comparable with those produced by a baseline 2.5 MW Type II swirled flame in the same furnace (Weber *et al.,* 1992b). Figure 6.28 also demonstrates the absence of any mean internal recirculation zone, and also shows the presence of an external recirculation zone, at radial distances $r/D > 3$. The external recirculation zone extends back towards the quarl exit plane, with reverse flow velocities up to 1.5 ms^{-1} at x/D = 4.8. Consequently large quantities of recirculated gases may be entrained into the jet flow near the quarl exit plane, contributing to particle heat up and ignition.

The mean mass flow-rate of externally recirculated gases at each axial plane can be calculated from the relation, $\dot{m}_r = \int_{r1}^{r2} 2\pi\rho urdr$. Since the axial velocity profile shows good symmetry, the mean velocity is used, $\dot{m}_r = \pi\rho\bar{u}\left(r_2^2 - r_1^2\right)$. The flame temperatures given in Figure 6.22 are used to determine the sensible enthalpy. Table 6.4 shows the recirculated mass flow-rates and the rate of transfer of sensible enthalpy (kW) at each axial plane. The recirculated mass fractions are lower than those observed for the previously investigated swirl flame, which peaked at 157% of the inlet flow (Weber *et al.* 1992b).

Table 6.4. Characteristics of the external recirculation zone

Axial Position , x/D	Mass fraction recirculated, (% of total inlet air flow)	Sensible enthalpy recirculation rate, (kW)
4.8	68	247
8.3	51	250
12.1	89	367
19.6	49	281

The calculated temperature rise of the combined inlet flows, assuming complete mixing with the externally recirculated flow, is 269°C at $x/D = 4.8$. This demonstrates the significance of the ERZ for particle heating. Estimations of the magnitude of particle temperature increases due to entrainment of hot gases are presented in Chapter 7. Note that $x/D = 4.8$ is the only plane sampled in the pre-ignition region - the ignition distance of the flame was $x_{ign}/D = 7.4$.

Figure 6.29 shows that, for the flow with $G_{PJ}/G_1 = 2.9$, the fluctuations in axial velocity are approximately half the centre-line mean value in the region near the centre-line, $-2.5 \leq r/D \leq 2.5$. These values are similar to those in the PJ dominated cold flow investigated in Appendix 3, and also similar to those obtained in a swirl stabilised flame in the same furnace (Weber et al, 1992b). These high local r.m.s. axial velocities, relative to the mean values, demonstrate that particles respond to the turbulent fluctuations in both the pre-ignition region and the flame, and together with the laser sheet visualisations reported in section 6.4.1, provide evidence that enhanced particle clustering effects persist within the flame.

6.5. Scaling the influence of precession on flames

Trends observed with increasing G_{PJt}/G_1 at both 130 kW and 2.5 MW scales include decreasing ignition distances, increasing heat release and increasing NO_x emissions. Here, an attempt is made to determine the dominant scaling parameters based on ignition distance data obtained at both scales, in order to provide a deeper insight into the controlling mixing mechanisms, and to assess whether those mechanisms are likely to persist at full scale. Ignition distance, rather than heat flux, is chosen as the scaling parameter because ignition distance is a single-valued parameter and therefore easier to handle. It nevertheless can be expected to relate to heat flux trends since the two parameters are strongly correlated (Figures 6.10 and 6.11). Scaling of NO_x emissions is not attempted due to the variation in flame temperature and residence time at the two experimental scales, the lack of control of furnace temperatures, and the absence of flame temperature measurements in a sufficient number of flames. In contrast, the processes that control ignition - convective and radiant particle heating rates and mixing between volatile matter and air – are all influenced by large-scale turbulence. Consequently, ignition distance is less sensitive than NO emissions to temperature, so that the influences of furnace, air and flame temperatures can be ignored in order to investigate scaling parameters based solely on large scale mixing considerations.

The influence of PJ momentum on the ignition distance of flames from the 10PJ, 19PJ, 55PJ and 80PJ burners is presented in Figure 6.30. The momentum ratio is expressed as $G_{PJt}/(G_1+G_2)$ to ensure that the differences in secondary air momentum at the two experimental scales are taken into account. The parameter, $G_{PJt}/(G_1+G_2)$ provides good collapse of the ignition distance data, apart from that of the 10PJ flames. However, it does not take into account differences in the ratio of particle and fluid time-scales (Stokes number), which occur due to changes in burner dimensions (and hence fluid length scale) and fluid velocity scales.

In Figure 6.31 ignition distances are plotted as a function of the aerodynamic scaling parameter, $[G_{PJ}/(G_1+G_2)].St^{-0.5}$, which was shown in Section 4.5.3 to influence the mean spread of particles injected into PJ flows. A comparison with Figure 6.30 shows that incorporation of the parameter $St^{-0.5}$ results in improved collapse of the data. It is also worth noting that the flame that shows the worst fit to the general trend in Figure 6.31 is the 10PJ flame with the lowest PJ momentum. It is effectively a mono-channel flame, in which precession does not dominate. The relative success of the simple aerodynamic parameter, $[G_{PJ}/(G_1+G_2)].St^{-0.5}$, in characterising the ignition distance of flames from 4 burners and two

different scales, with varying air pre-heat temperatures and furnace temperatures, clearly demonstrates the dominating influence of precession.

Other scaling parameters that aim to model the effect of precession more accurately have also been assessed. One of these parameters employed G_{PJe} in preference to G_{PJt}, another employed the relative velocity between the jet exiting the PJ nozzle and the primary stream, in an attempt to more accurately account for the drag on coal particles. The mass fractions of primary and precessing air were also incorporated in scaling parameters to model the effect of oxygen availability. However none of these changes provided a significant improvement on the scaling parameter, $[G_{PJ}/(G_1+G_2)].St^{-0.5}$, and consequently they are not presented here. Moreover, the thermal and kinematic differences between the two experimental scales render any further sophistication quite speculative. Nevertheless it may be possible to account for other factors (eg thermal) in the future with additional data.

Having selected a scaling parameter, $[G_{PJ}/(G_1+G_2)].St^{-0.5}$, it is possible to assess the likely practical requirements to achieve a substantial influence of enhanced large scale mixing at full scale. Figure 6.32 presents predicted PJ nozzle pressure requirements as a function of the scaling parameter, $[G_{PJ}/(G_1+G_2)].St^{-0.5}$, for burners in two hypothetical full-scale kilns. The dimensions of the hypothetical full-scale kilns are selected to be typical of "small" and "large" kilns, having internal diameters and thermal capacities of (a) 3m and 35MW and (b) 5m and 105 MW respectively. The secondary velocity corresponding to these conditions is close to $8ms^{-1}$ at $900^{o}C$ (the temperature also assumed in the momentum calculations), which is also typical of industrial kilns. The primary air momentum is based on a primary air mass fraction of 3% of the total air, simulating indirect fired kilns. Calculations are presented for PJ mass flows corresponding to 3% and 5% of the total combustion air. These mass fractions are typical of those used in various mixing devices in currently available commercial cement kiln burners.

By way of reference, a value $G_{PJ}/(G_1+G_2)/St^{0.5} \sim 1$ was found to provide a significant influence on experimental flames, based on an almost 3-fold reduction in flame ignition distance (Figure 6.31). The same value of the scaling parameter can by achieved at full scale using $\leq 3\%$ of the combustion air as PJ air at pressures that can be supplied by fans operating at < 20 kPa(g) (Figure 6.32). It is interesting to note that the required pressures are lower than those used in the small-scale experiments. Likewise the full-scale burner diameter, at around 10% of the kiln diameter using 3% PJ air, is not unrealistic (Figure 6.33). It can be

expected that minimising the mass flow of PJ air would assist in keeping NO_x emissions to a minimum. Hence the scaling criteria suggests that the PJ-annular design is realistic for full-scale plant.

6.6. Conclusion

At 2.5MW scale, particle-turbulence interactions and mixing time-scales are sufficiently representative of full scale to enable confidence in scaling up of experimental trends. The effects of enhanced large scale mixing, as provided by PJ flows, on the absolute errors in heat released to individual cooling tubes were determined to within an accuracy of ±1% (Appendix 5). This value includes the effects of errors in flow-rate measurements of fuel and air.

Laser sheet visualisation in the pre-ignition and ignition regions of flames showed that particle spreading rates and clustering effects are enhanced in large PJ flames with high particle loadings, compared to a baseline flame with minimal PJ flow. Increasing PJ momentum in the range, $0 < G_{PJt} / G_1 < 6$, with a secondary air temperature of 320°C, caused a four-fold reduction in ignition distance, from $\frac{x}{D} = 20$ to $\frac{x}{D} = 5$ and caused the position of peak heat flux to move closer to the burner by a similar distance. It also caused the magnitude of the peak heat flux to increase from 195 to 230kW. The flue gas temperature reduced by 100°C, demonstrating a substantial increase in the total heat transferred through the furnace walls and cooling tubes. A reduction in the peak flame temperature from 1501°C to 1450°C was found to occur as G_{PJt}/G_1 was in increased from 0 to 2.9, showing that the additional heat release was not due to higher flame temperatures. It is hypothesised that the generation of increased quantities of soot in fuel-rich particle clusters, and hence increased flame emissivity, is responsible for the increased heat flux. NO_x emissions increased from 400 to 580 ppm (0% O_2), and burnout increased from 94.4 to 97.8% as the PJ momentum was increased in the range $0 < G_{PJt} / G_1 < 6$. These NO_x and burnout results may be due to the combination of increasing air entrainment rates with increasing G_{PJt}/G_1, and the fact that it is not possible to control wall temperatures of the furnace to a fixed value. Thus the wall temperatures increased with G_{PJt}/G_1, providing increased radiant feedback to the flame.

Fluctuations in axial velocity are approximately a half of the mean maximum axial velocity in the flame with $G_{PJt}/G_1 = 2.9$. These values are similar to those in the PJ dominated cold flow investigated in Appendix 3, and in a swirl flame previously investigated in the same

furnace. The fluctuating velocity data provides evidence that turbulent structures produce a significant influence on particles, not just in the pre-ignition of PJ flames, but in the flame region also. Laser Doppler velocity and flame temperature measurements were used to calculate the sensible enthalpy recirculated in the external recirculation zone. The ERZ was found to contribute up to 269°C to particle temperature rise in the pre-ignition region.

The scaling parameter, $[G_{PJ}/(G_1+G_2)].St^{-0.5}$, provides reasonable collapse of the ignition distance data from the 130 kW and 2.5 MW experiments, despite the lack of thermal and kinematic similarity between scales. The scaling parameter models the large scale clustering and fluid mixing effects which control ignition distances. On this basis, reductions in ignition distance are predicted at full scale using lower PJ nozzle pressures than necessary at experimental scales.

In contrast to the effect of increasing PJ momentum, an increase in secondary air momentum caused an increase in NO_x emissions coincident with a reduction, by 20 kW, in the heat extracted in the water loop nearest to the burner. This finding suggests that the high secondary air velocity used in the 2.5 MW flames (~ $35ms^{-1}$) contributes significantly to the observed NO_x emissions.

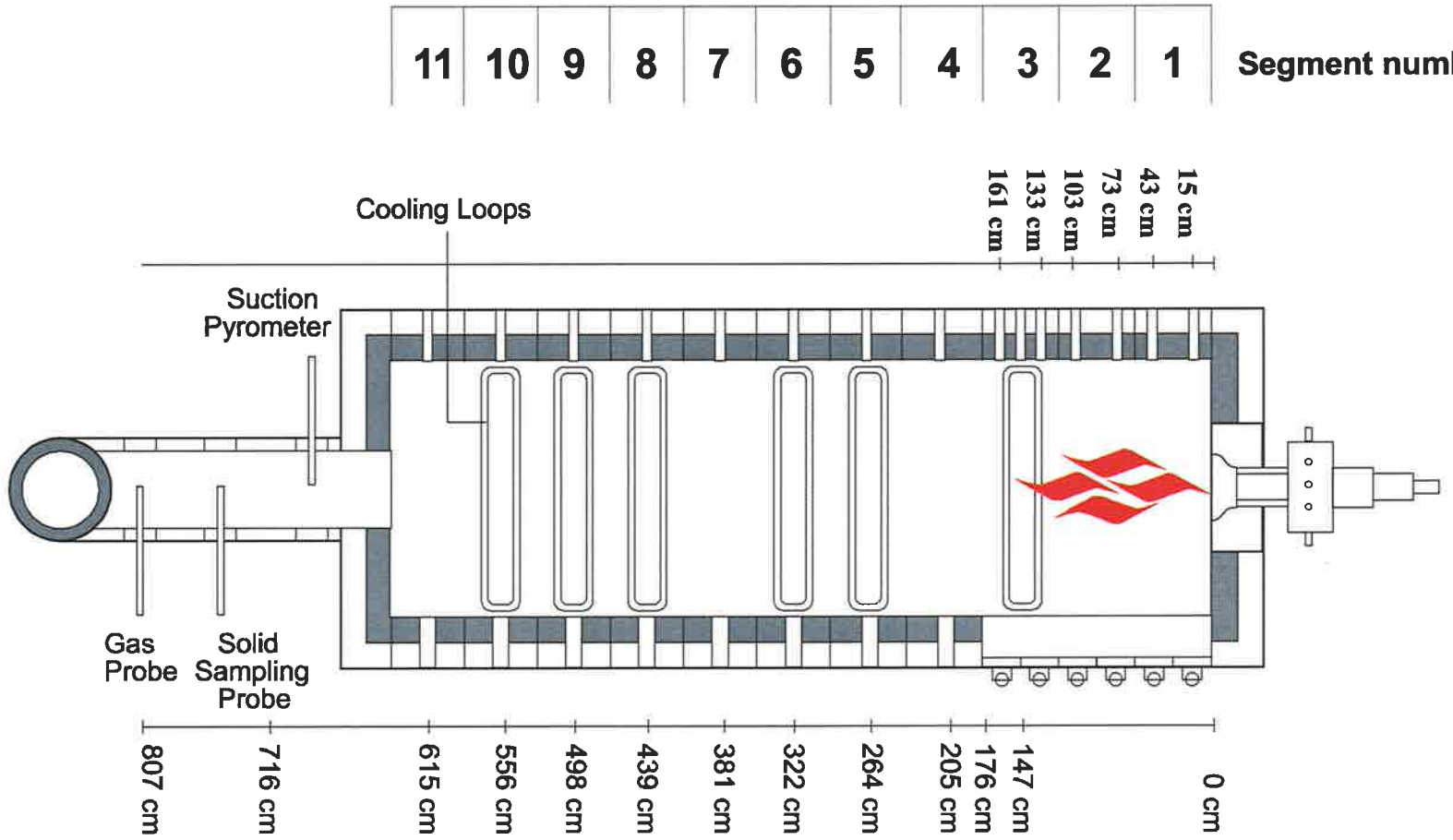

Figure 6.1 A schematic diagram of the IFRF Furnace No.1., operated here at 2.5 MW (from IFRF trial documentation, Dacombe, 1998)

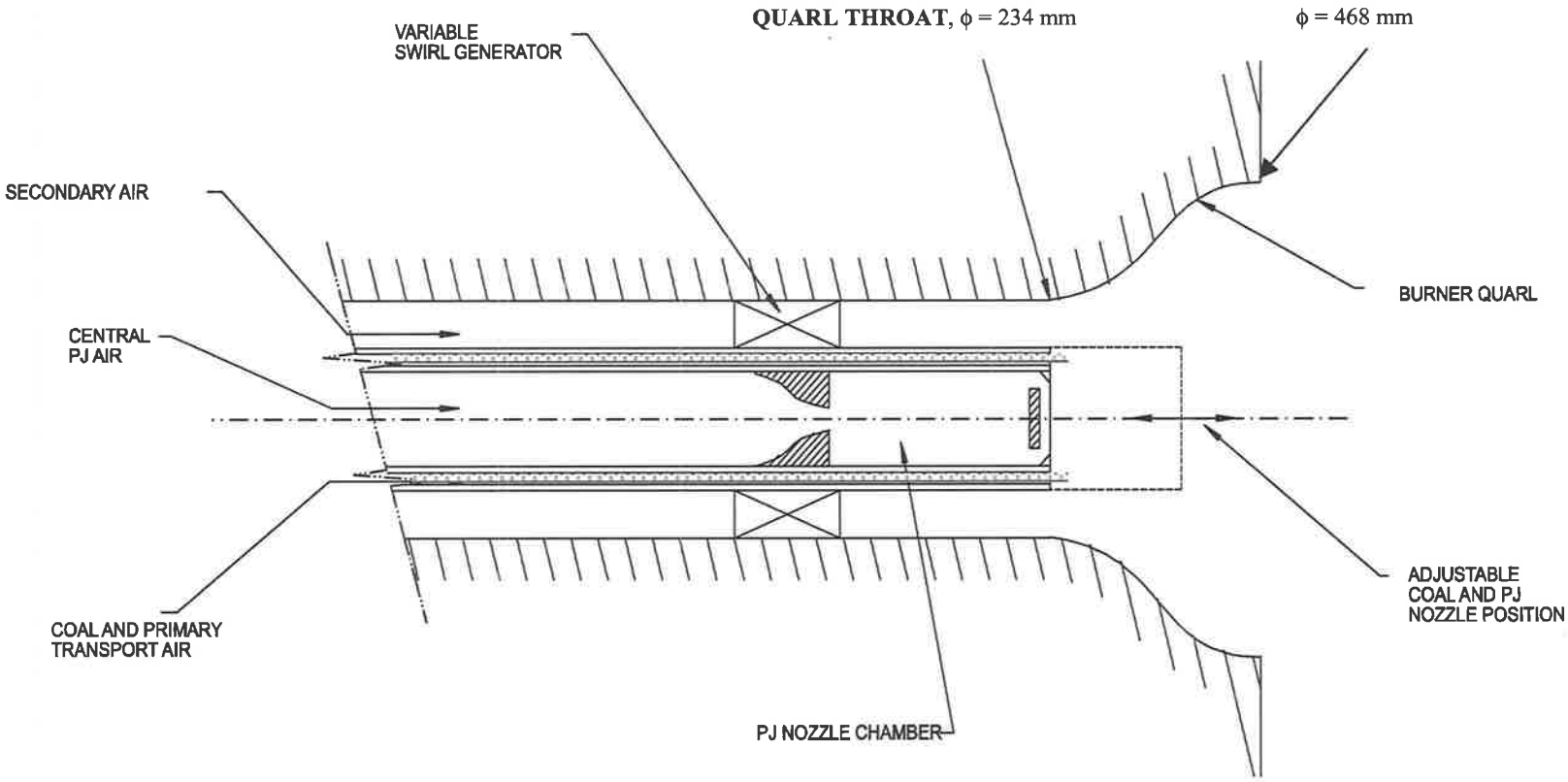

Figure 6.2 A schematic diagram of the burner and quarl arrangement, showing the primary and secondary air channels. PJ nozzles with internal chamber diameters of 80 and 55 mm were used. In the Single Central Orifice (SCO) burner, the PJ nozzle was replaced with a pipe of 82 mm (I.D.). (adapted from the drawing in Smart *et al.*, 1999)

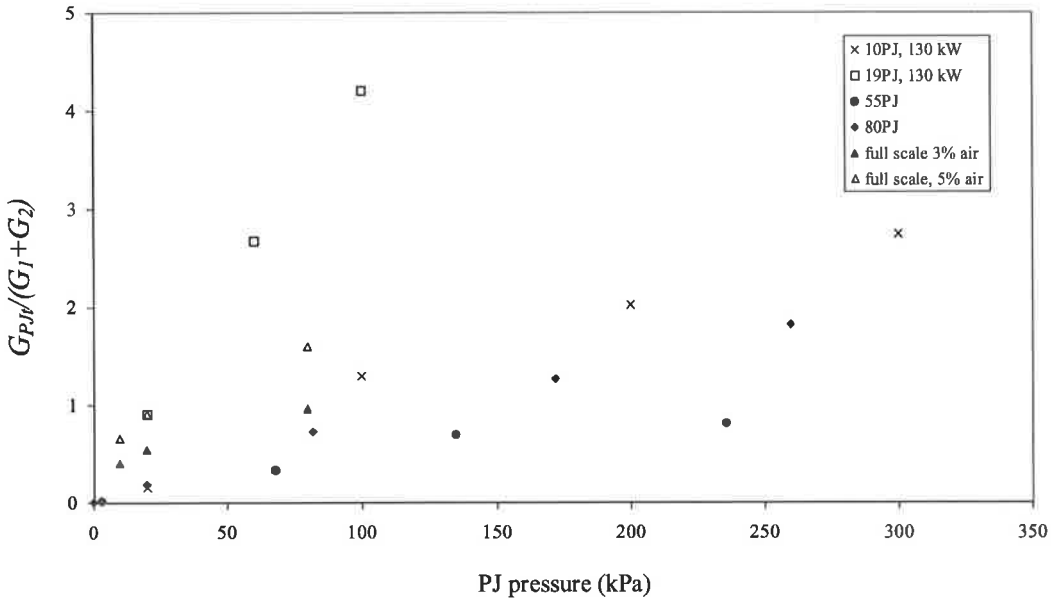

Figure 6.3 Effect of PJ throat pressure on $G_{PJt}/(G_1+G_2)$. Measured values are given for the 10, 19, 55 and 80 mm PJ nozzles. Calculated values are given for full-scale nozzles, in which the primary air velocity is 20 ms^{-1}, and the primary air flow rate is either 3% or 5% of the total air flow. The secondary air velocity at full scale (at 900°C) is calculated for a 35 MW flame in a 3 m internal diameter cylindrical kiln.

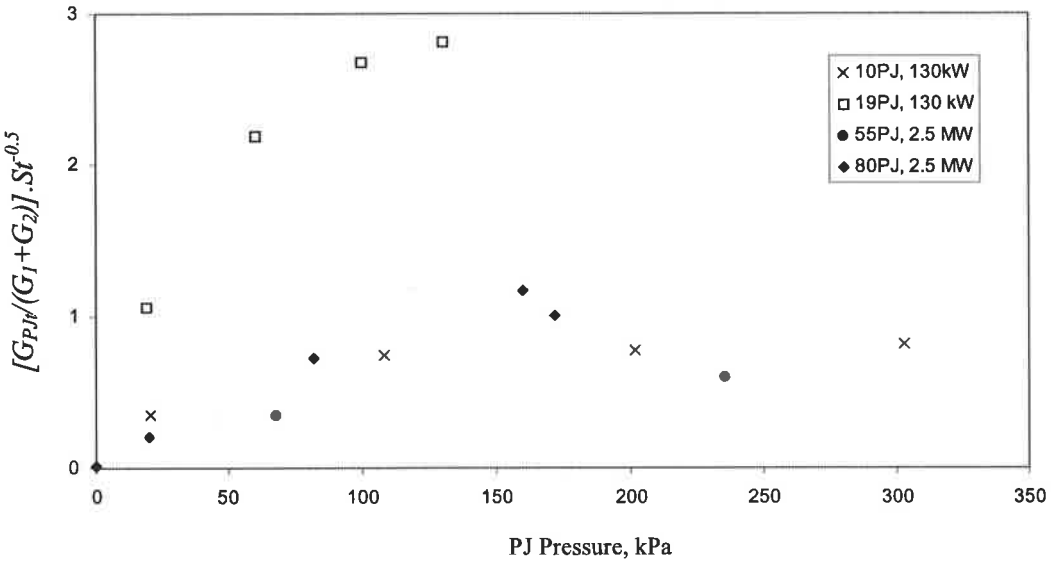

Figure 6.4 Effect of PJ throat pressure on calculated values of $[G_{PJt}/(G_1+G_2)].St^{-0.5}$ at the experimental scales.

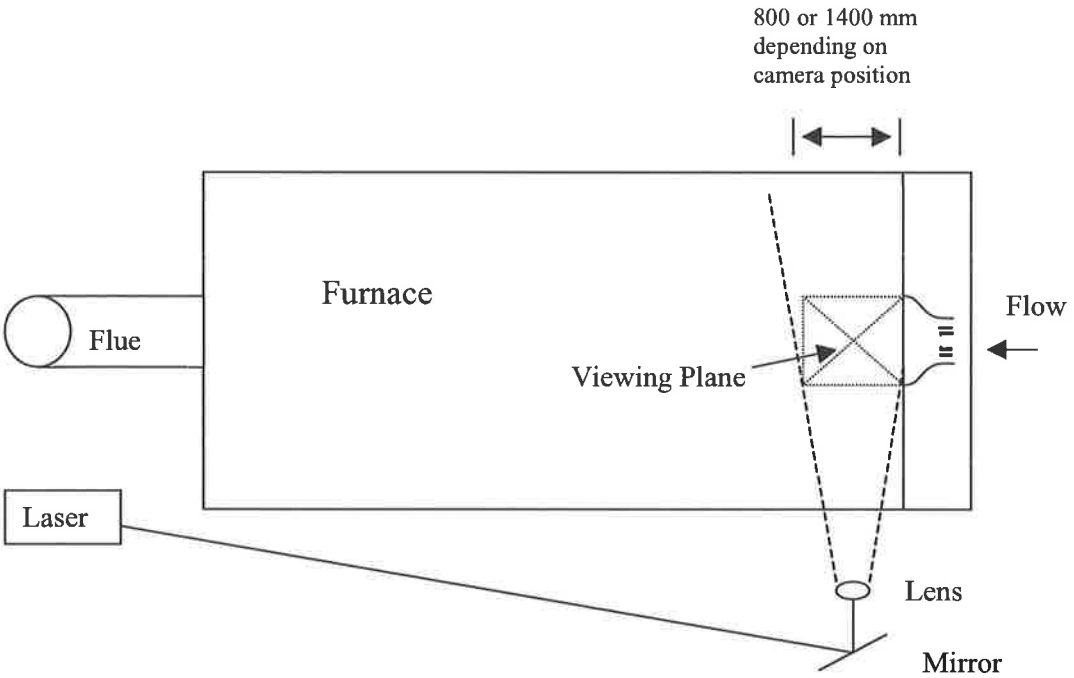

Figure 6.5 A schematic diagram of the laser sheet visualisation technique – plan view.

A horizontal pulsed Nd:YAG laser sheet was introduced through the slot at the side of the furnace to allow imaging of the first 800 mm downstream from the quarl exit plane. Scattered light passed though an endoscope, installed at a viewing position on top of the furnace, to a black and white, image intensified CCD camera that was triggered by the laser pulses. The image intensifier allowed the camera to be gated to 1 μs, minimising the effects of background radiation. Images were collected on VHS videotape, and individual frames were captured at random and digitised for presentation.

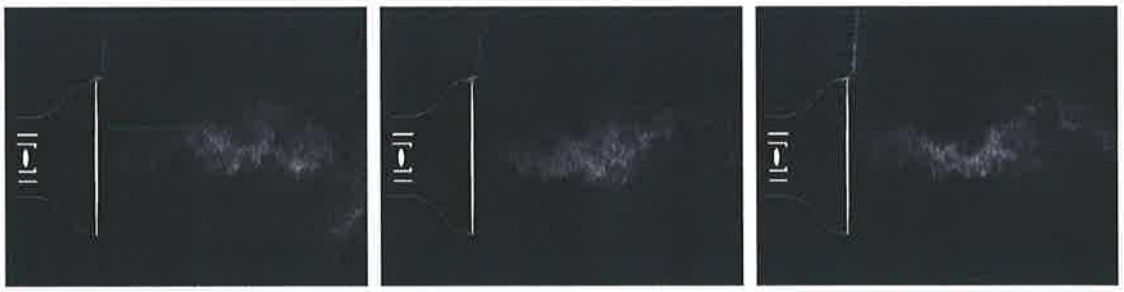

Figure 6.6(a)

Figure 6.6(b)

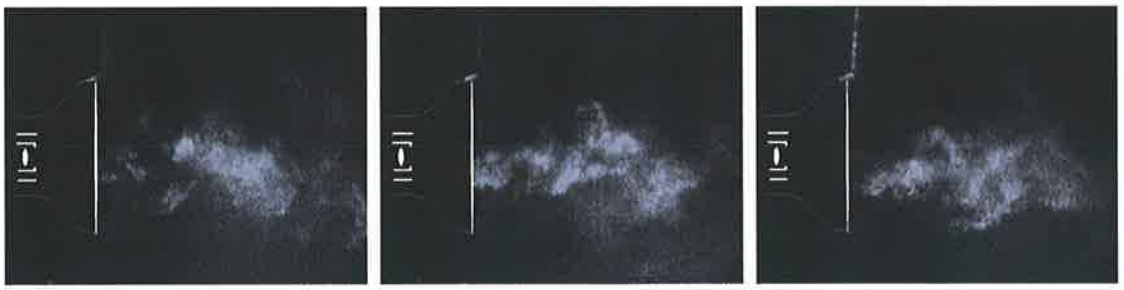

Figure 6.6(c)

Figure 6.6 Typical laser sheet visualisation images from the pre-ignition region of flames showing the influence of PJ momentum on particle clustering effects. The quarl and PJ nozzle are represented schematically at left and the flow is from left to right. The tests were performed using a coal rate of 254 kg.hr^{-1} transported by primary air supplied at 70°C and a constant velocity of 20 ms^{-1}. Secondary air temperature was 320°C. The PJ air was supplied at ambient temperature. Three images are shown for each condition, having PJ air flow-rates, mass fractions and momentum ratios as follows;

(a) 25 kg.hr^{-1} from the 80PJ nozzle, $\dot{m}_{PJ}$ = 0.9% of total air, G_{PJt}/G_1 = 0.034

(b) 125 kg.hr^{-1} from the 55PJ nozzle, $\dot{m}_{PJ}$ = 4.3% of total air, G_{PJt}/G_1 = 1.46

(c) 250 kg.hr^{-1} from the 55PJ nozzle, $\dot{m}_{PJ}$ = 8.6% of total air, G_{PJt}/G_1 = 3.30

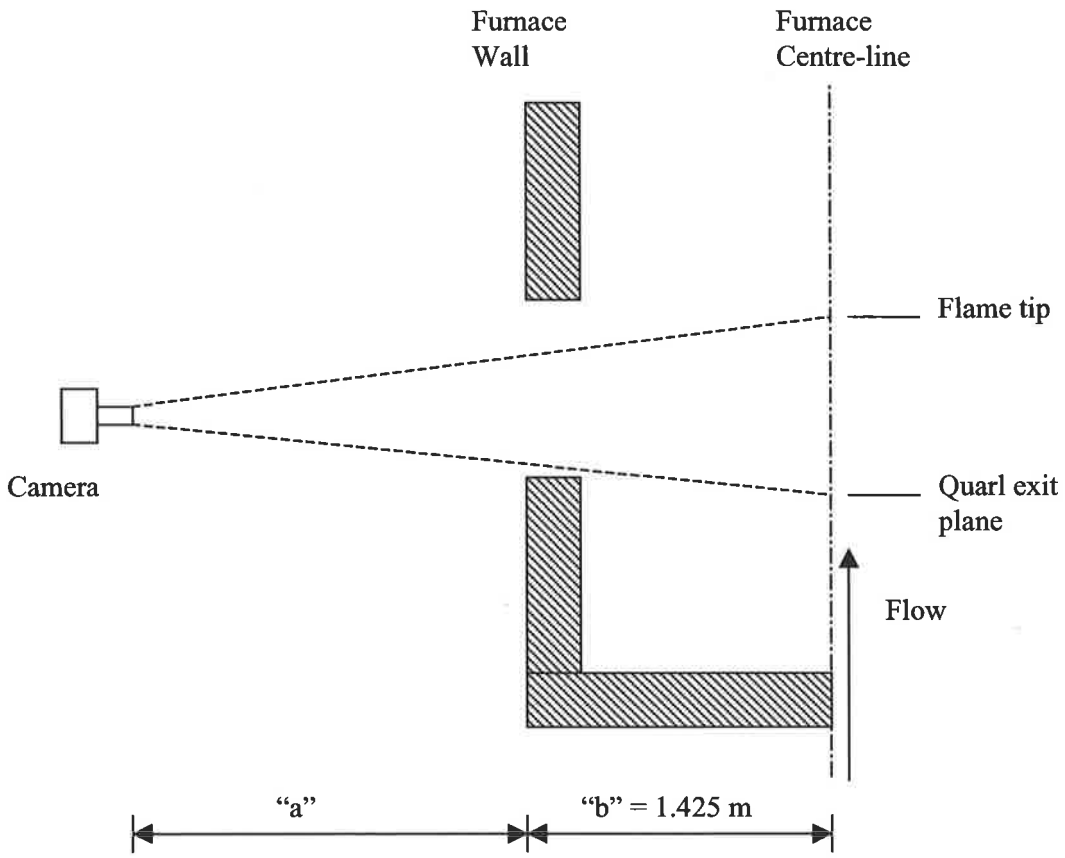

(a)

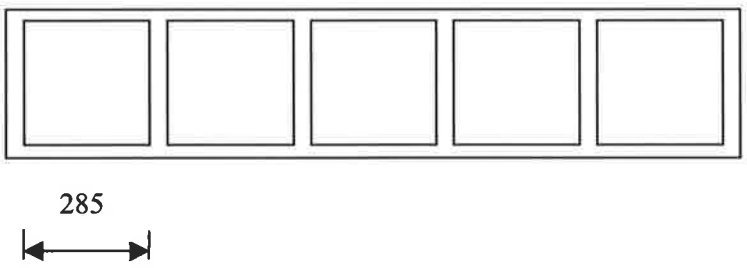

(b)

Figure 6.7. Schematic diagrams of the video recording arrangements.
(a) Plan view of experimental arrangement for measurement of ignition distance
(b) A schematic diagram of door locations on the horizontal slot (side elevation)

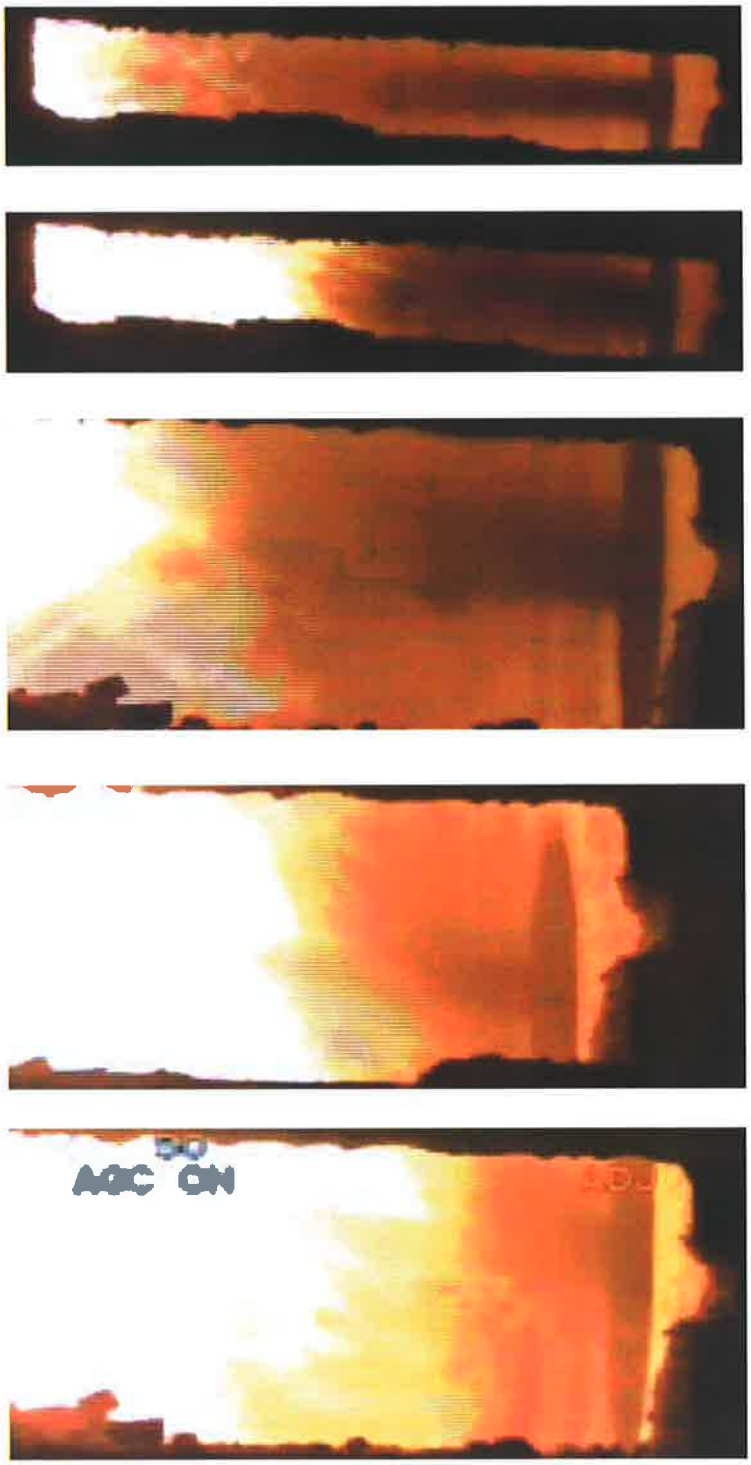

Figure 6.8 Typical video images of 80PJ-annular flames with momentum ratios, G_{PJ}/G_1, of: (a) 0.03, (b) 0.72, (c) 2.90, (d) 4.52 and (e) 6.09.
The images in (a) and (b) have longer ignition distances than the others, and required a larger field of view. Mean ignition distances were calculated from a hundred such images of each flame.

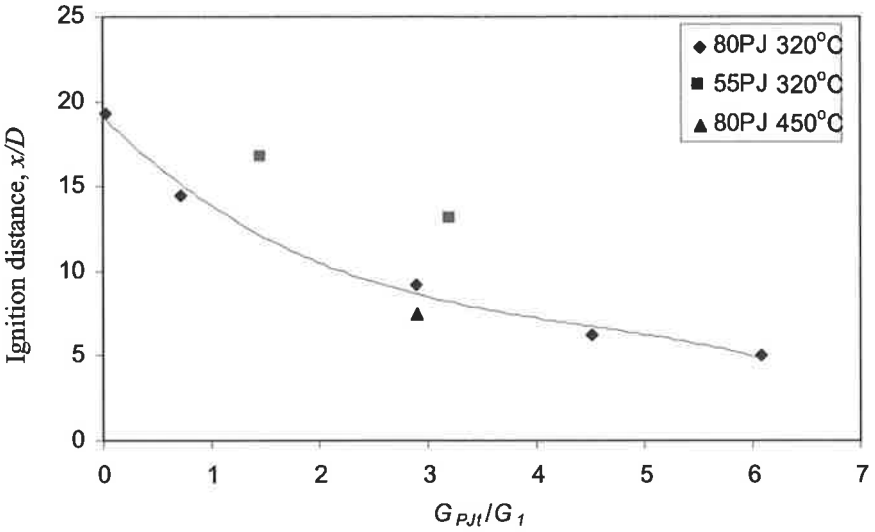

Figure 6.9 Effect of G_{PJt}/G_1 on ignition distance, 2.5 MW flames. Secondary air temperatures are shown in the legend.

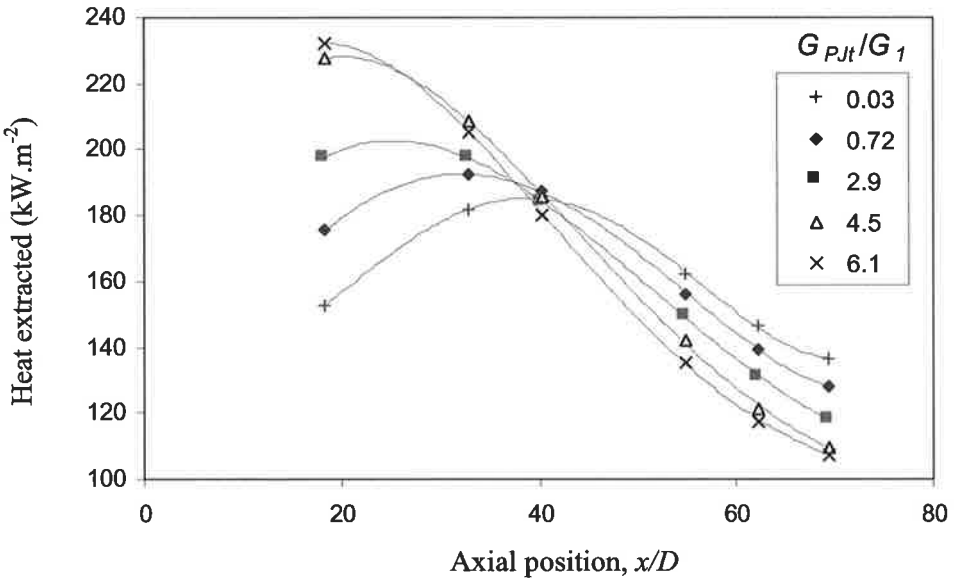

Figure 6.10 The effect of G_{PJt}/G_1 on the profile of heat extracted by individual water cooled loops located along the furnace length, from 80PJ, 2.5 MW flames. (Each loop has a projected surface area of 1 m^2 for radiative heat transfer from the flame)

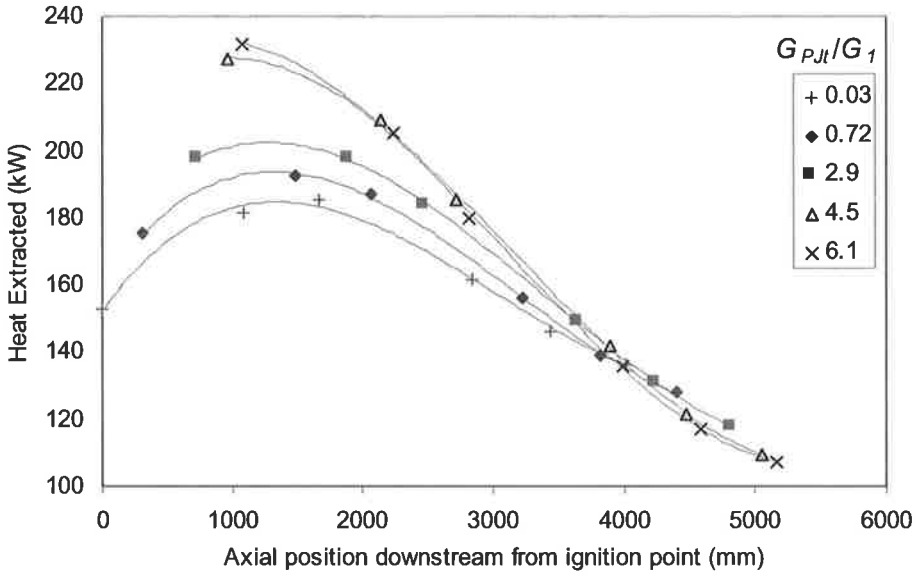

Figure 6.11 The effect of G_{PJt}/G_1 on the profile of heat extraction from 80PJ, 2.5 MW flames as a function of axial distance downstream from ignition. (Each loop has a surface area of 1 m^2)

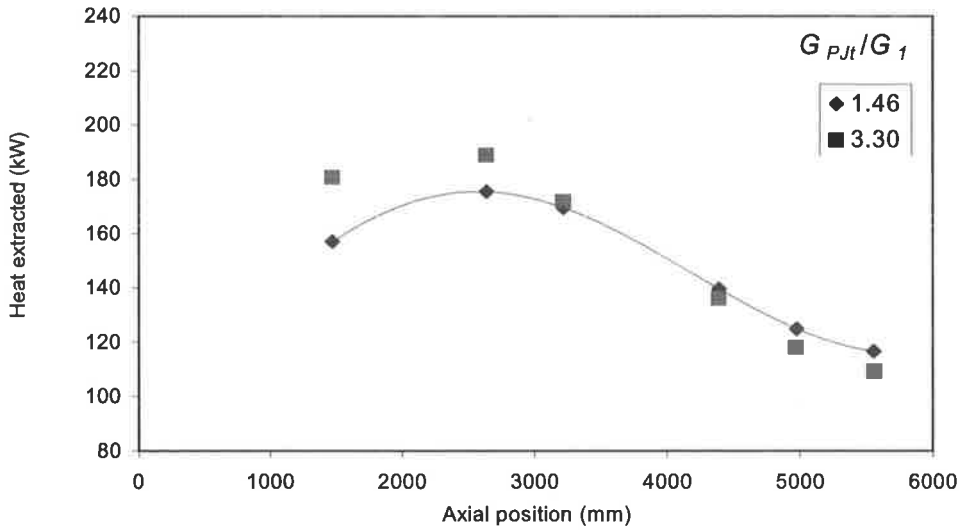

Figure 6.12 The effect of G_{PJt}/G_1 on the profile of heat extraction along the furnace length, from 55PJ, 2.5 MW flames.
(Each loop has a surface area of 1 m^2)

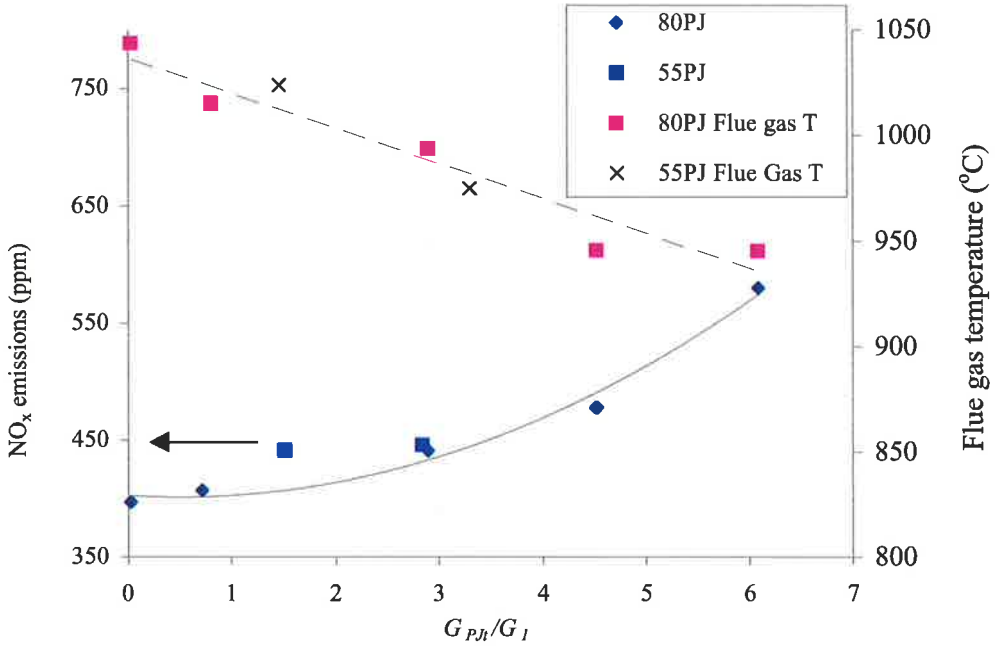

Figure 6.13 Effect of precessing jet momentum on NO_x emissions and flue gas temperatures, 80PJ and 55PJ, 2.5 MW flames.

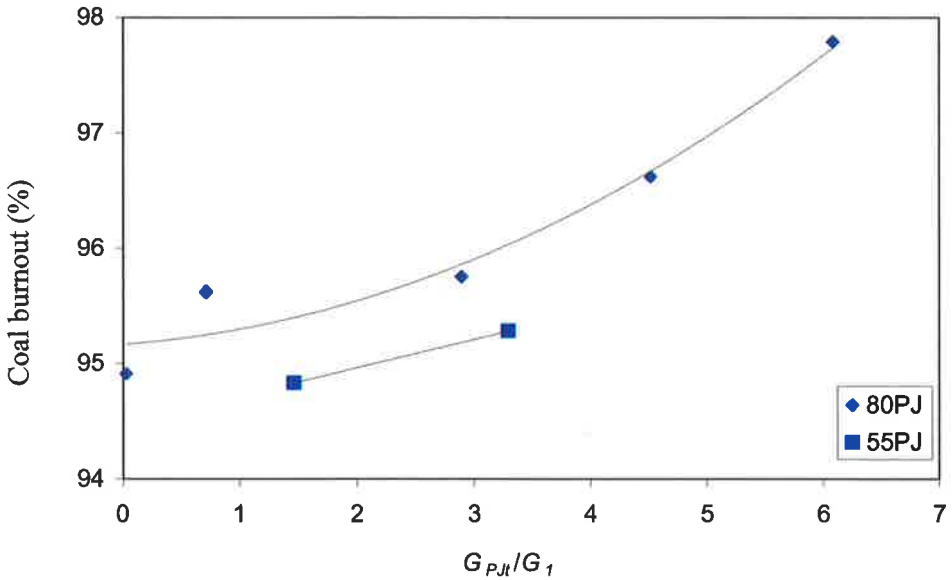

Figure 6.14 Effect of PJ momentum on coal burnout, as defined by Equation 5-26

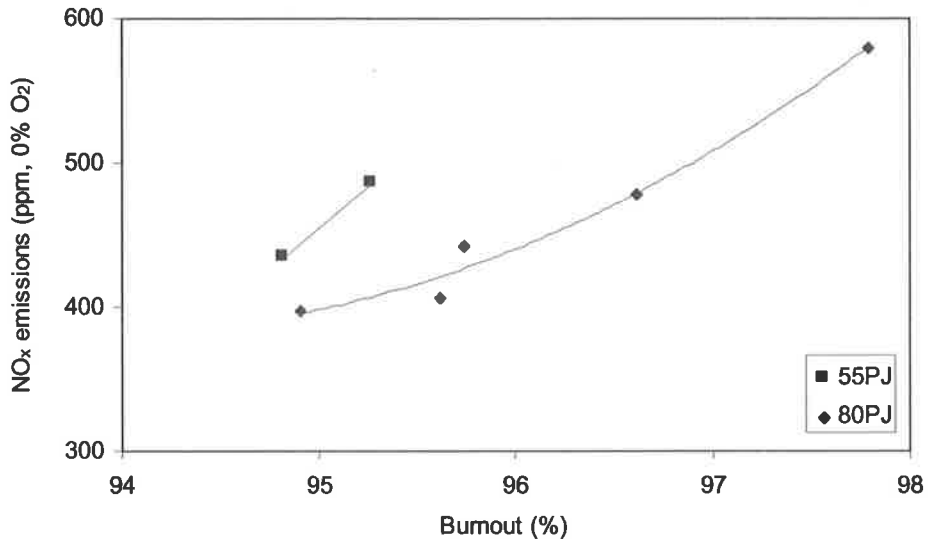

Figure 6.15 Relationship between NO_x emissions and coal burnout (Burnout defined by Equation 5-26)

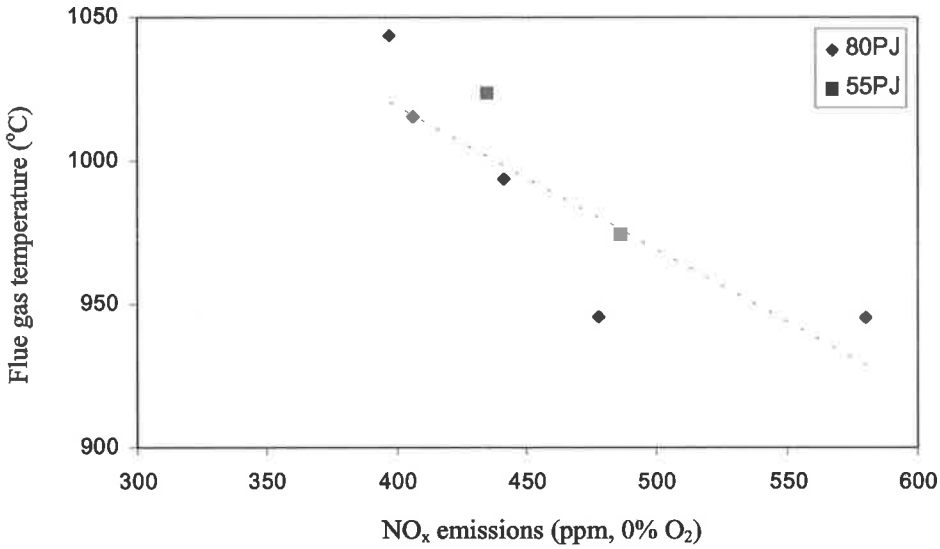

Figure 6.16 Relationship between flue gas temperature and NO_x emissions.

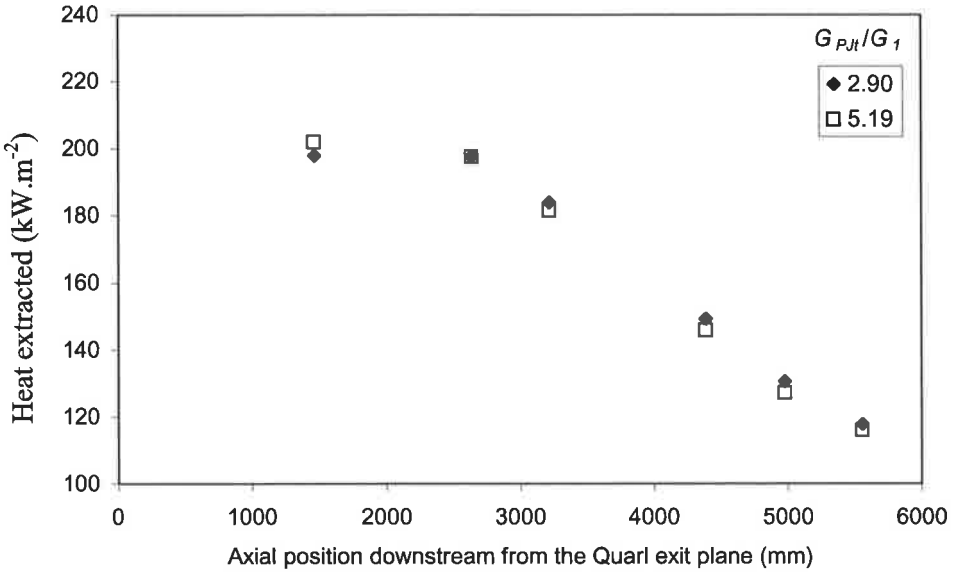

Figure 6.17 The effect of secondary momentum on the heat extraction profiles of 80PJ flames with a constant PJ flow-rate of 250 kg.hr^{-1}. The primary (transport) air flow-rate was varied (400 kg.hr^{-1} and 600 kg.hr^{-1}) and the secondary air flow rate was also adjusted to balance the flue oxygen concentration to 3% in each flame. Consequently secondary air momentum varies with G_{PJt}/G_1.

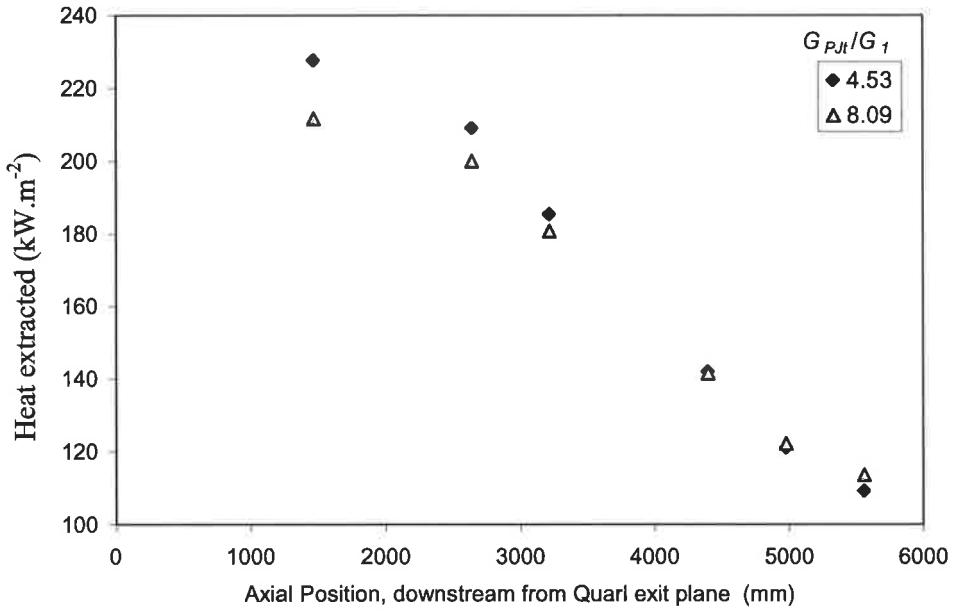

Figure 6.18 The effect of secondary momentum on the heat extraction profiles of 80PJ flames with a constant PJ flow-rate of 375 kg.hr^{-1}. The primary (transport) air flow-rate was varied (400 kg.hr^{-1} and 600 kg.hr^{-1}) and the secondary air flow rate was also adjusted to balance the flue oxygen concentration to 3% in each flame. Consequently secondary air momentum varies with G_{PJt}/G_1.

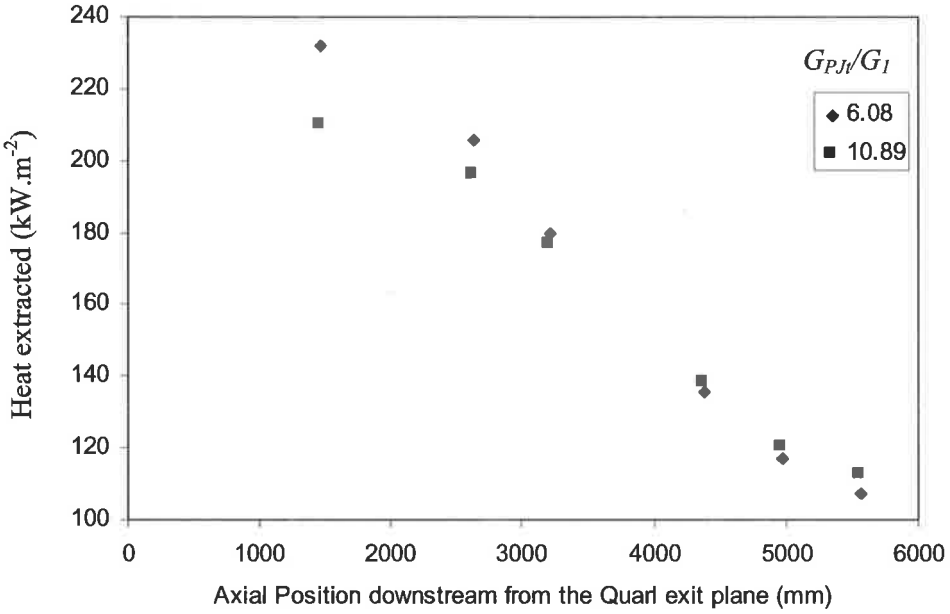

Figure 6.19 The effect of secondary momentum on the heat extraction profiles of 80PJ flames with a constant PJ flow-rate of 500 kg.hr^{-1}. The primary (transport) air flow-rate was varied (400 kg.hr^{-1} and 600 kg.hr^{-1}) and the secondary air flow rate was also adjusted to balance the flue oxygen concentration to 3% in each flame. Hence the secondary momentum varies with G_{PJt}/G_1.

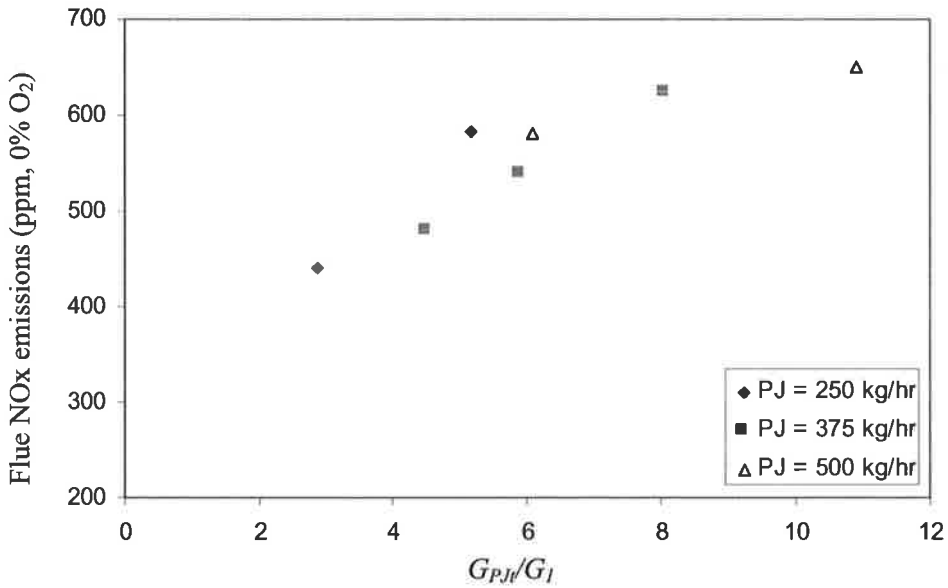

Figure 6.20 The effect of secondary momentum on NO_x emissions from 80PJ flames. For each PJ flow, the primary (transport) air flow-rate was varied, and the secondary air flow rate was also adjusted to balance the flue oxygen concentration to 3%. Hence the secondary momentum varies with G_{PJt}/G_1. The observed trend of increasing NO_x correlates more strongly with increasing secondary momentum than variation in PJ momentum.

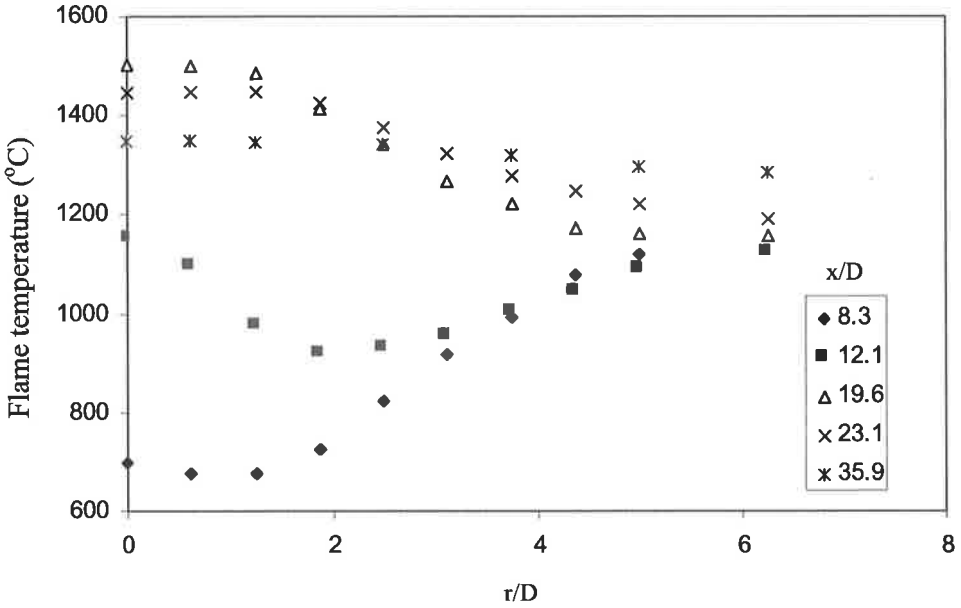

Figure 6.21 In-flame temperature measurements as a function of radial and axial position, for the 80PJ flame with G_{PJt}/G_1 = 0.03, secondary air temperature = 450°C

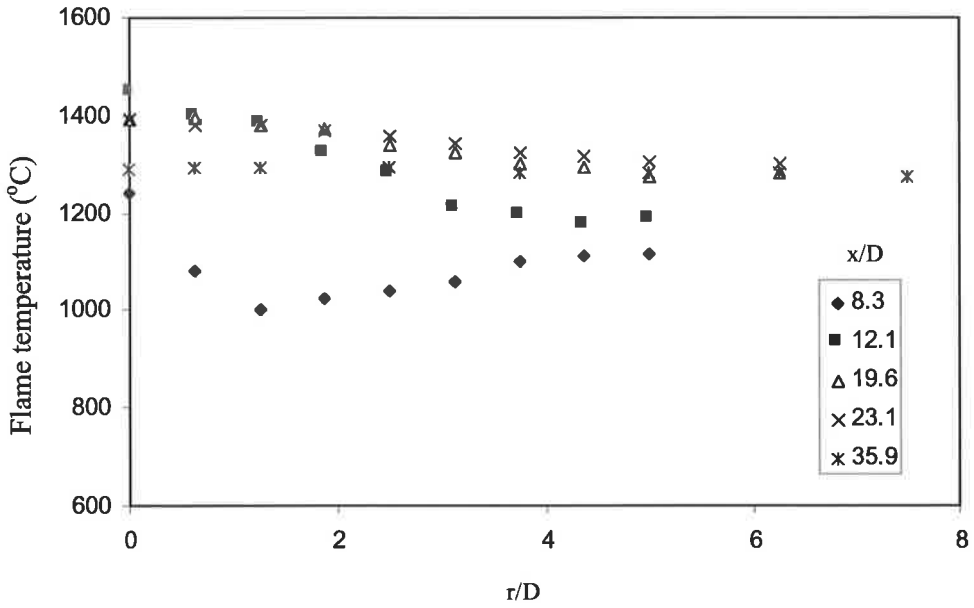

Figure 6.22 Temperature distribution in the 80PJ flame with G_{PJt}/G_1 = 2.90, secondary air temperature = 450°C

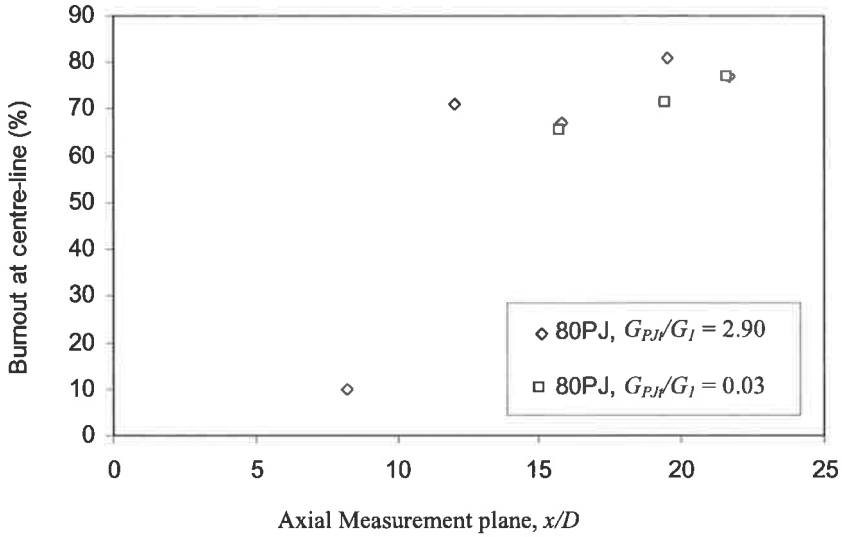

Figure 6.23 Dependence of centre-line coal burnout on axial position for 80PJ flames, with secondary air temperature = 450°C

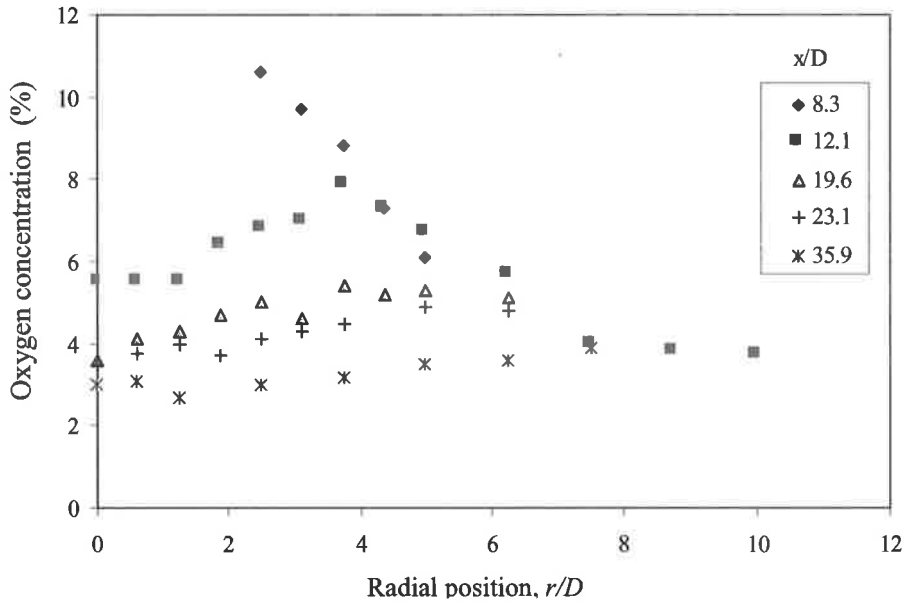

Figure 6.24 In-flame oxygen concentration for the 80PJ flame with G_{PJ}/G_1 = 2.90 and secondary air temperature = 450°C

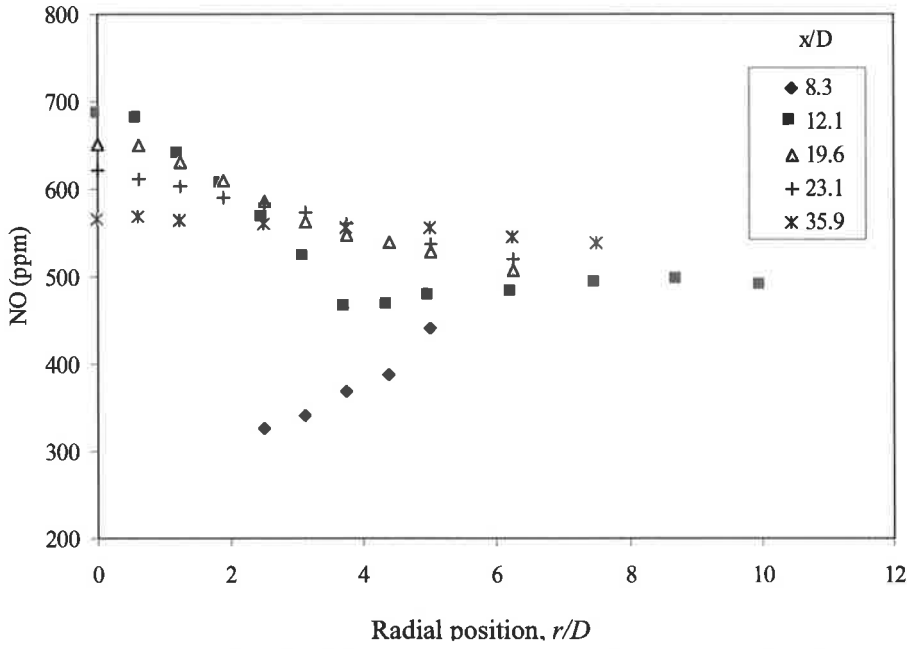

Figure 6.25 Radial NO concentration profiles in the 80PJ flame with $G_{PJ}/G_1 = 2.90$ and secondary air temperature = 450°C

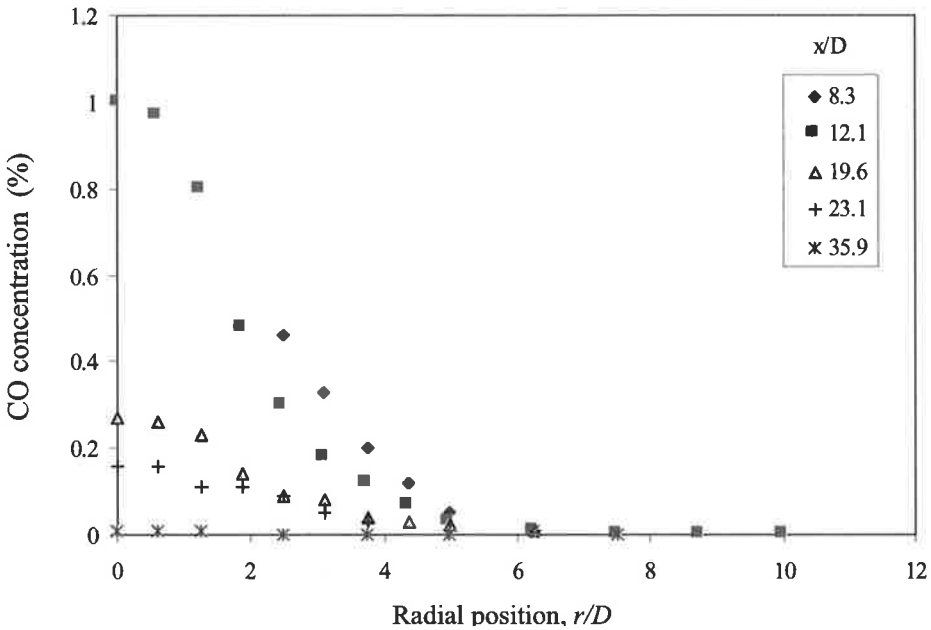

Figure 6.26 Radial CO concentration profiles in the 80PJ flame with $G_{PJ}/G_1 = 2.90$ and secondary air temperature = 450°C

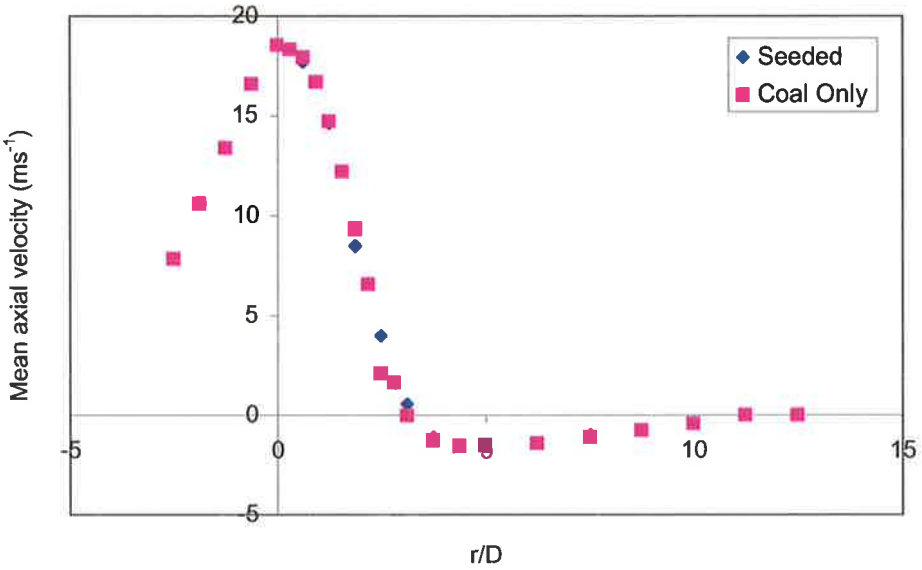

Figure 6.27 Mean axial velocity at x/D = 4.8, for the 80PJ flame with G_{PJf}/G_1 = 2.90, and secondary air temperature = 450°C, showing that coal particles provide adequate natural seeding for LDA measurements

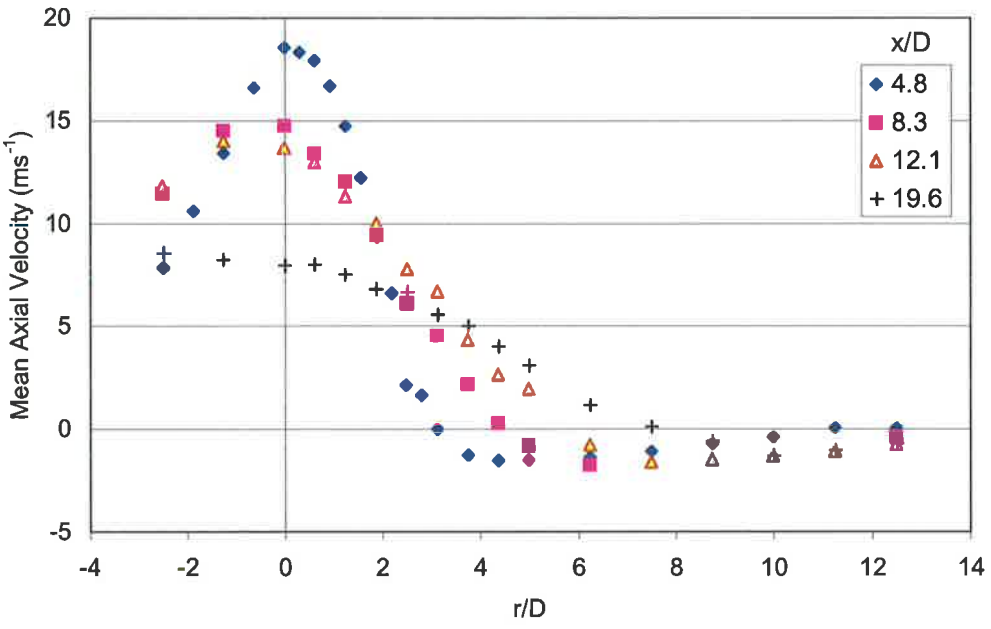

Figure 6.28 Mean axial velocity as a function of position in the 80PJ flame with G_{PJf}/G_1 = 2.90 and secondary air temperature = 450°C

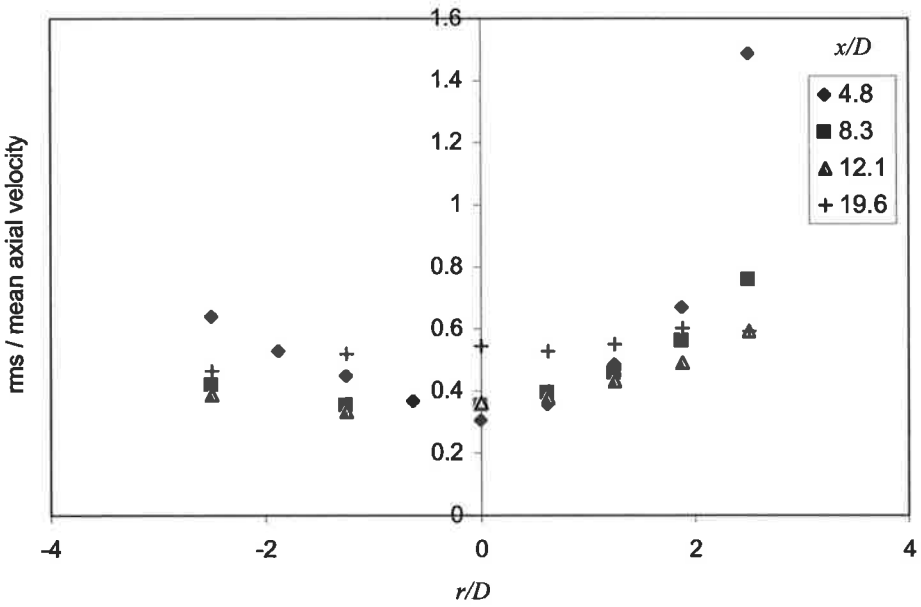

Figure 6.29 Distribution of rms/mean axial velocity for the 80PJ with G_{PJ}/G_1 = 2.90 and secondary air temperature = 450°C

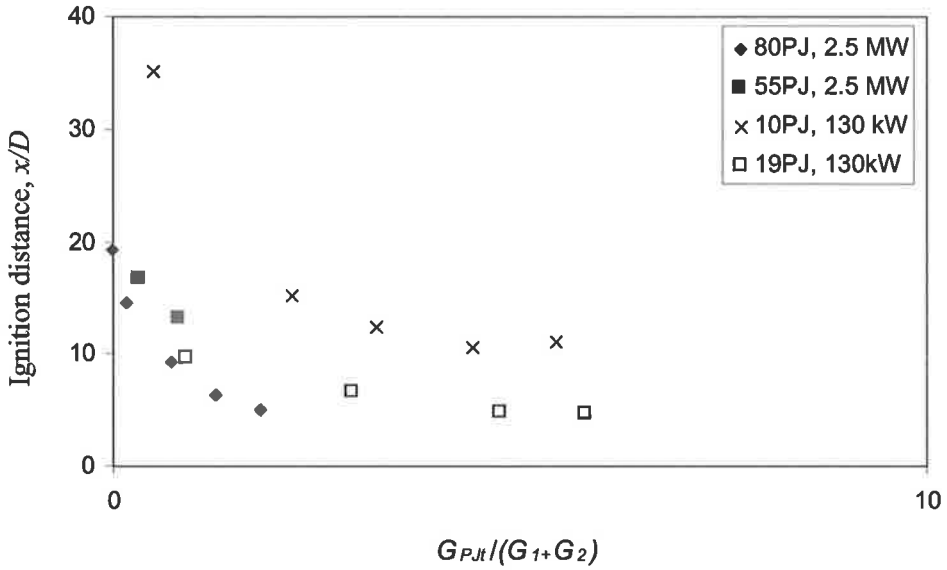

Figure 6.30 The influence of PJ momentum on the ignition distance of flames from the 10PJ, 19PJ 55PJ and 80 PJ burners. The momentum ratio is expressed as $G_{PJt}/(G_1+G_2)$ to take into account the differences in secondary air momentum.

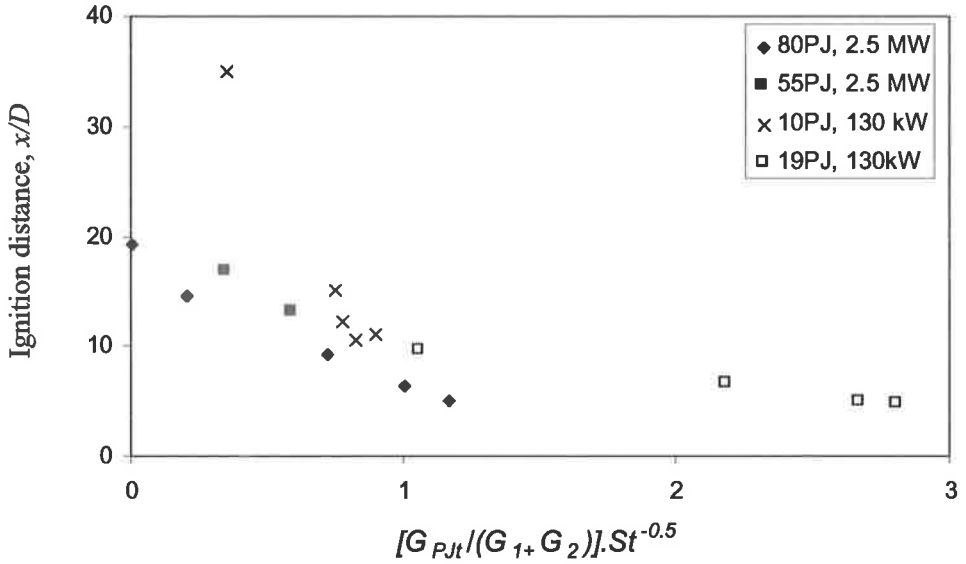

Figure 6.31 Experimental ignition distances plotted as a function of the aerodynamic scaling parameter, $[G_{PJ}/(G_1+G_2)].St^{-0.5}$

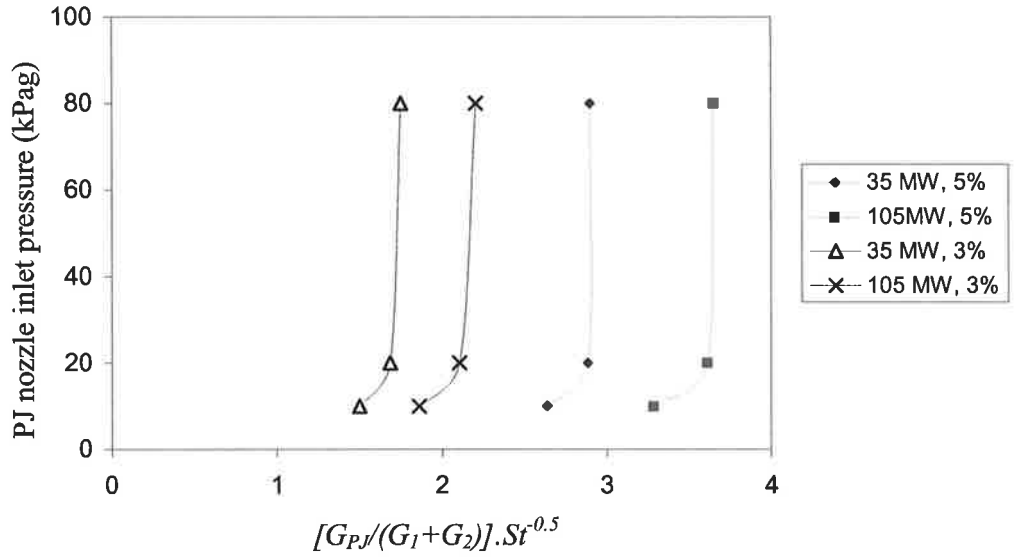

Figure 6.32 Predicted PJ nozzle pressure requirements as a function of the scaling parameter, $[G_{PJ}/(G_1+G_2)].St^{-0.5}$ for burners in two hypothetical full-scale kilns with internal diameters and thermal capacities of (a) 3m and 35MW, and (b) 5m and 105 MW respectively. The primary air mass fraction is assumed to be 3% of the total air, and the secondary air velocities are all approximately 8 ms^{-1} at 900°C. The PJ pressures are predicted for PJ mass flows corresponding to 3% and 5% of the total combustion air.

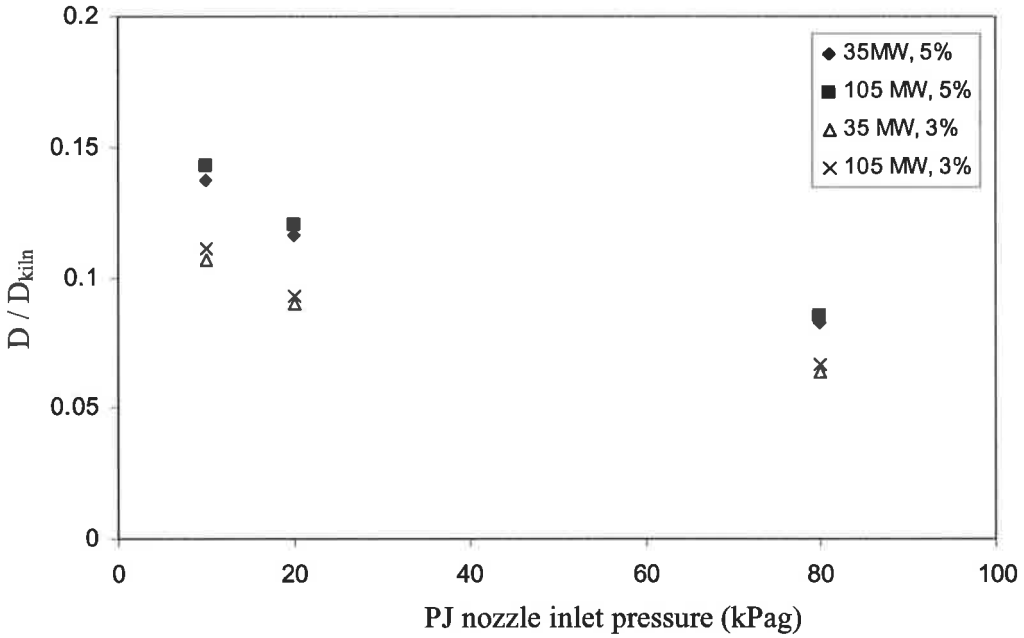

Figure 6.33 Predicted PJ nozzle diameters for burners in two hypothetical full-scale kilns with internal diameters and thermal capacities of (a) 3m and 35MW, and (b) 5m and 105 MW respectively. PJ nozzle diameters are predicted for PJ mass flows corresponding to 3% and 5% of the total combustion air.

Chapter 7 Assessment of the dominant mechanisms by which precession influences ignition and combustion using sensitivity analyses.

7.1 Introduction

The aim of the analysis presented in Chapter 7 is to determine the dominant mechanisms by which precessing jets affect PF flames. Relative to annular mono-channel PF flames, precessing jets have been shown to reduce ignition distances, increase peak heat fluxes, move the heat release profile towards the burner, and under certain conditions, reduce NO_x emissions. The dominant mechanisms by which precessing jets produce these effects are deduced by using experimental data in conjunction with sensitivity analyses. The analyses may also provide a basis for the development of future mathematical models of the effects of enhanced large scale mixing in PF flames.

7.2 Scope

7.2.1 Ignition distance

Ignition occurs at locations where a flammable mixture of volatile matter and air, with sufficiently low velocity, is heated to a temperature of typically 500°C (see Sections 1.3.2 and 5.2). A sensitivity analysis is performed to determine which of these factors (heating, stoichiometry or local velocities) controls stabilisation in PJ PF flames. Equations detailed in Section 5.2.2. are used to determine the influence of convective and radiant heating rates on mean ignition distances. The influence of jet entrainment rates and the enthalpy of externally recirculated gases on ignition is also evaluated.

7.2.2 Heat release and NO_x emissions

The primary means by which enhanced large scale mixing causes heat release profiles to move closer to the burner is deduced to be associated with a reduction in ignition distance relative to the base-line annular mono-channel flame (Figures 6.9 - 6.11). The further influences of the enthalpy of externally recirculated gases, volatile matter reaction rates, and sooting on the heat flux profile and NO_x emissions are also estimated. The potential influences of any mean or local staging effects on NO_x emissions are also assessed.

7.2.3 The influence of PJ mixing

The near field of PJ flames, $\frac{x}{D} \leq 2$, is defined to be the region where the precessional motion dominates the flow (see section 1.7). It is a complex, intensely sheared and stirred, three dimensional, time-dependent region. It is well upstream of the ignition region in PF flames, and so has predominantly indirect, but not necessarily insignificant, affects on PF flames. These affects include rapid entrainment of secondary air and ERZ gases, and the generation of large scale structures and particle clusters that dominate the flow in the region, $\frac{x}{D} > 2$. Section 7.4 investigates one potential direct affect of precession, in the region $x/D < 2$, on ignition, namely its potential to alter the convective heating rates of particles due to rapid entrainment of gases and the imposition of widely fluctuating slip velocities on particles. The nature of large structures generated by FPJ flows mixing in the region, $\frac{x}{D} > 2$, can be observed in Figure 7.1, which shows PLIF images, taken in water, of 19PJ-annular flows with $G_{PJe}/G_I = 0$, 2.9 and 5.6. The extent to which the characteristics of precession, ie. rapid entrainment and enhancement of large structures and particle clusters,

influence ignition, heat release and NO_x emissions is investigated in Sections 7.3 and 7.5 – 7.7.

In addition to the promotion of large structures, increased "layering" of fluids of different concentrations, as reported by Newbold (1997), can be observed in Figure 7.1 as G_{PJe}/G_J is increased. Images taken in water and shown in Figures 3.3, 3.4 and 3.7 also illustrate this point. The fraction of nozzle fluid in these "layered structures" has been estimated to increase from 5 to 30 % as G_{PJe}/G_J increases from 0 to 5.6. The persistence of the layered structures, even at large x/D, demonstrates that mixing between them is slow. Consequently, molecular diffusion may become a significant means of heating "layered particle clusters" and of mixing volatile matter with entrained gases, especially if the layers are thin. However it should be noted that laminar diffusion is much less significant in air than in water, ie. Sc ~ 1000 in water compared to Sc ~ 1 in air, so that in flames, pure laminar diffusion is likely to be augmented by fine scale turbulent diffusion. In contrast to the layered structures, the roughly spherical large structures evident in Figures 7.1, 3.3, 3.4 and 3.7 contain predominantly nozzle fluid. The influence of the observed increase in "layering" on particle heating rates in the pre-ignition region, and on volatile matter combustion rates (further downstream) is also investigated in the sections to follow.

7.3 Interactions between entrainment, external recirculation, heat extraction and NO_x emissions.

7.3.1 Theoretical considerations

Jet entrainment rates and the position and mass flow of external recirculation zones impact significantly on ignition distances, heat release rates and NO_x emissions by their influence on particle heating rates, flame temperatures and oxygen availability. In semi-industrial rotary kiln flames (van de Kamp and Smart, 1992) flue NO_x emissions (chiefly thermal) were shown to increase with the mass of secondary air entrained into the flame at ignition, despite the fact that the maximum in-flame NO_x concentrations and temperatures both occurred downstream from the ignition region.

A widely used formula for the entrainment of surrounding fluid into the fully developed region of an unconfined jet is that of Ricou and Spalding (Beer and Chigier, 1972):

$$\frac{\dot{m}_o + \dot{m}_e}{\dot{m}_o} = 0.32\left(\frac{\rho_e}{\rho_o}\right)^{0.5} \frac{x}{d_{eq}} \qquad 7\text{-}1$$

where $\dot{m}_o$ is the nozzle mass flow, and $\dot{m}_e$ is the entrained fluid mass flow, d_{eq} is the equivalent diameter based on the total mass, $\dot{m}_o$, and momentum of air and coal exiting the burner, G, that is,

$$d_{eq} = 2\,\dot{m}_o/(\pi \rho_e G)^{0.5} \qquad 7\text{-}2$$

A later formulation obtained by pressure probe determination of velocity and the edge of unconfined, concentric particle laden jets (Wall *et al.* 1982) is used in calculations performed later in this chapter. The volumetric ratio of entrained air to burner air, E, in the jet at the axial distance, x, is:

$$E = \left(\frac{Q - Q_o}{Q_o}\right) = 0.128(x/d_{eq}) + 0.004(x/d_{eq})^2 \qquad 7\text{-}3$$

The relation holds for Re > 23,000 and for the first ten nozzle diameters downstream from the jet exit plane.

Particles alter the entrainment of jets slightly. Small particles, which conform to the eddies (St < 0.5), act to increase the momentum and hence entrainment of the jet, whilst larger particles, which partially respond to the flow (0.5 < St < 100), damp turbulence and reduce entrainment by up to 20% (Wall *et al.* 1982). For industrial scale burners, most particles have St < 0.5, and so act to increase jet entrainment. Under these conditions, d_{eq} can be

calculated by increasing the density of the particle laden air stream in proportion to the mass fraction of particles (Wall, 1987). In contrast, in the initial region of smaller burners, many particles will have $St \sim 1$ and so have negligible effect on entrainment. Consequently, for current purposes, it is sufficient to assume that the mean effect of particles on entrainment is negligible. Equation 7-3 was derived for isothermal jets, but it can be expanded, using a mass based formulation, to account for non-isothermal conditions, ie:

$$E = \left(\frac{\dot{m} - \dot{m}_o}{\dot{m}_o} \right) = \left(0.128(x/d_{eq}) + 0.004(x/d_{eq})^2\right)(\rho_e / \rho_o)^{0.5} \qquad 7\text{-}4$$

External recirculation in confined (enclosed) jets occurs when the jet momentum is greater than that required to entrain all of the secondary air (Thring and Newby, 1953). In boiler type furnaces, the temperature and mass of the external recirculation zone (ERZ) gases can have a greater influence on ignition and flame properties than that of the secondary air. For example, Sayre *et al.* (1994) compared two 300 kW unstaged non-sooty swirling natural gas flames, both with flue gas recirculation, but one with water cooled walls (T_{max} = 100°C), and the other with hot refractory walls. The flame with water cooled walls demonstrated lower temperature and mass flow of the ERZ gases, causing a reduction in peak flame temperatures, combustion rates, and NO_x emissions (Sayre *et al.* 1994). In contrast, standard flue gas recirculation techniques reduce NO_x emissions by vitiation of the combustion air, which reduces flame temperatures.

The mass flow and position of the ERZ of confined jets can be estimated by assuming that the jet spreads at a constant angle until it reaches the wall (Beer and Chigier, 1972). Mean flow patterns in a rotary kiln are illustrated in Figure 7.2. The recirculation eddy is located between positions, X_N, where all secondary air is entrained into the jet, and X_P where the jet meets the wall. The core of the recirculation eddy, where entrainment ceases, occurs at *Xc*. The total mass of ERZ gases entrained at *Xc* can then be calculated. For a jet half angle of 9.7° and using the Ricou and Spalding entrainment relationship, the recirculated flow $\dot{m}_r$, in terms of the Thring –Newby parameter, θ, (Beer and Chigier, 1972) is:

$$\frac{\dot{m}_r}{\dot{m}_o} = \frac{0.47}{\theta} - 0.5 \qquad 7\text{-}5$$

If all the secondary air is introduced as a co-annular stream around the nozzle:

$$\theta = \frac{d_{eq}(\rho_o / \rho_e)^{0.5}}{2L} \qquad 7\text{-}6$$

For a jet entraining a low velocity co-flow, typically secondary air in a rotary kiln, d_{eq} is calculated from the burner jet mass and momentum alone, and θ becomes:

$$\theta = \frac{\dot{m}_o + \dot{m}_e}{\dot{m}_o} \cdot \frac{d_{eq}(\rho_o / \rho_e)^{0.5}}{2L} \qquad 7\text{-}7$$

The Thring -Newby parameter, θ, for constant density systems, is generally applicable for ratios of nozzle and duct radii, $r/L < 0.1$, and assumes the nozzle fluid concentration in the far field is $(\dot{m}_o + \dot{m}_e)/\dot{m}_o$ (Beer and Chigier, 1972). For combustion modelling the Thring-Newby parameter is often preferred to the Craya - Curtet parameter, the latter being based on solution of the equations of motion, since it provides similar results, is simpler to calculate and readily applicable to combusting systems in which density varies (Beer and Chigier, 1972).

7.3.2 Estimation of entrainment and recirculation in PJ flows

The types of external recirculation zone patterns deduced to occur in the 2.5 MW and 130 kW experiments are shown in Figure 7.3. These patterns are dependent on the geometric arrangements used, as well as the momenta of the primary and secondary streams. The deduced patterns indicate that in the 130 kW flames, mixing of ERZ gases with secondary air is possible prior to entrainment of the mixture into the PJ-annular jet, whereas this is less likely in the 2.5 MW flames. Flame images taken at both experimental scales (eg. Figures 5.5, 5.6, 6.6) demonstrate the rapid spread rate and enhancement of the large scales in flames influenced by precession. Nathan and Luxton (1991) found that isothermal precessing jets, in quiescent surroundings, entrain up to 7 times their own mass by x/D = 3 after which entrainment rates are much reduced. This data is used in preference to the entrainment correlations described in section 7.3.1, which apply for steady jets. In all PJ flames investigated in the present study, ignition occurs downstream from the region of rapid entrainment, so that in each case the contribution of the PJ to the total entrainment up to the point of ignition is estimated to be seven times the PJ mass flow in the calculations to follow.

The entrainment of the primary and secondary jets, are calculated independently from that of the precessing jet using the correlation of Wall *et al.* (1982) written in terms of mass (Equation 7-4). At 2.5 MW a combined equivalent diameter, d_{eq}, defined by Equation 7-2, is used for the primary and secondary streams and the entrainment of ERZ gases is assumed to commence at the burner exit plane. The entrainment rates of all three streams can then be summed, assuming that the total momentum of the jets is available for entrainment of the relatively quiescent ERZ gases. The total entrainment adjusted for non-isothermal conditions is thus:

$$\dot{m}_e = \left[7 * \dot{m}_{PJ} + (\dot{m}_1 + \dot{m}_2) \cdot \left(0.128(x/d_{eq}) + 0.004(x/d_{eq})^2\right)\right] \cdot (\rho_e / \rho_o)^{0.5} \qquad 7\text{-}8$$

In the 130 kW flames entrainment of ERZ gases by the secondary air commences at the exit plane of the secondary air shroud. Entrainment by the primary and PJ streams commences 400 mm further downstream due to axial positioning of burner (Figure 7.3a). Accordingly, at 130 kW scale, the entrainment rates of the primary and secondary jets are calculated separately, commencing at their respective origins.

An alternative means of estimating entrainment by combined PJ-annular flows, to that given by Equation 7-8, is to include the PJ mass flow rate and momentum in the calculation of d_{eq},

and to use the entrainment formulation of Wall *et al.* (1982), Equation 7-4. This method assumes that the PJ operates as a steady jet, and the calculated entrainment rate is significantly lower than that calculated by Equation 7-8. To demonstrate this, Figure 7.4 shows the calculated entrainment rates for PJ air flow rates of 25 and 500 $kghr^{-1}$ from the 80PJ nozzle, $(G_{PJ}/(G_1+G_2)$ = 0.007 and 1.82 respectively, using the two techniques. It demonstrates the rapid entrainment at high PJ flow-rates calculated by Equation 7-8 compared to that calculated by assuming that the PJ acts as a steady jet. In the absence of experimental validation of the calculated entrainment rates of combined flows, the values calculated using equation 7-8 are used in the next section. However the issue of validation should be addressed in future work.

7.3.3 Mean effects of externally recirculated gases

To estimate the enthalpy of ERZ gases, their temperature is assumed to be equal to that of flue gas. Due to the lack of complete flue gas temperature data from the 130 kW flames, the mean flue gas temperature from those flames in which it was measured, namely 1000°C, was used for all 130 kW flames for the purposes of this analysis. However, at 2.5 MW, measured flue gas temperatures for each individual flame are available. Figure 7.5 presents the calculated mass of ERZ gas, $\dot{m}_e$, entrained into 2.5 MW flames by the combined PJ, primary and secondary flows at the mean ignition distances. Equation 7-8 was used for calculation of $\dot{m}_e$. The flames are the first five listed in Table 6.3, having 80PJ flow-rates of 25, 125, 250, 275 and 500 kg.hr^{-1} respectively. The ERZ enthalpy (above that at standard conditions) is calculated from the ERZ temperature (assumed to be equal to the flue gas temperature) and $\dot{m}_e$, and is shown in Figure 7.6. Figures 7.5 and 7.6 show that by increasing the 80PJ flow-rate from 25 to 500 kghr^{-1}, the mass flow of ERZ gases is increased significantly, so that an additional enthalpy of 260kW is recirculated at the point of ignition, despite a measured reduction in ERZ (flue gas) temperature of 99°C. A consequent mean temperature rise of the combined PJ, primary, secondary air, ERZ gas and coal mixture, of over 60°C, due to the change in sensible enthalpy of entrained gas is also shown in Figure 7.5. This calculation assumes that ERZ gases lose negligible enthalpy by convection to the walls and cooling loops.

Note that for the only flame in which velocity data was obtained, ie. the flame with $G_{PJf}/(G_1+G_2)$ = 0.73 (80PJ flow rate = 250 kg.hr^{-1}) the measured total ERZ enthalpy was 367 kW, which is within 20% of the value calculated at the point of ignition by the above method, ie. 457 kW, constituting reasonable agreement. The higher value of the calculated ERZ enthalpy, may be due to an over-estimation of the entrainment rate of ERZ gases by the PJ, since it doubtless also entrains some secondary air. However the purpose of the calculations is to provide a sensitivity analysis. The calculated ERZ flow rates and enthalpies shown in Figures 7.5 and 7.6 are used for this purpose.

Figure 7.6 shows that a strong correlation exists between the calculated ERZ enthalpy and the measured NO_x emissions for the five 80PJ, 2.5 MW flames considered above. Also shown in Figure 7.6, are the calculated values of total heat extracted through the walls and by the cooling loops, in excess of that extracted under the baseline condition, ie. with $G_{PJf}/(G_1+G_2)$ = 0.007. The additional heat extracted by cooling loops and through furnace

walls was calculated from flue gas temperature and coal burnout data. For example as $G_{PJf}/(G_1+G_2)$ was increased from 0.007 to 1.82 the sensible heat of flue gases reduced by 110kW (calculated from flue gas temperatures and CO_2, N_2, and water vapour enthalpies). It is assumed that heat extraction through the walls and by cooling tubes increased by an equivalent amount to maintain the energy balance. Over the same increase in momentum ratio, coal burnout also increased by 2.88% (Figure 6.14), contributing another 52 kW (based on the enthalpy of complete oxidation of carbon, 32.8 MJ/kg) to the heat extracted through the cooling loops and walls. Thus a total of 160 kW of additional heat was extracted through water tubes and walls as $G_{PJf}/(G_1+G_2)$ was increased from 0.007 to 1.82.

In comparison to the above calculated values, the measured increase in heat extraction by the six water-cooled loops and 13 segments as $G_{PJf}/(G_1+G_2)$ was increased from 0.007 to 1.82, was 52 kW. This value has at least 38 potential sources of experimental error, one temperature and flow-rate for each of 19 loops or segments. If the average error in the heat flux measured for each cooling flow is ± 2 kW (see Appendix 5), the total error can amount ± 38 kW. Additional errors of approximately ±1% can be expected in each of the three inlet air flows, measured using orifice flow meters, whilst the error in coal feed rate is claimed to be ± 0.25% by the manufacturer of the screw feeder. (Occasional major upsets in coal feed-rate occurred. On these occasions data was discarded until at least 20 minutes after the problem was overcome.) An additional error in the measured values of heat transfer through the walls occurs due to the heat capacity of the refractory, which imposes a considerable time lag for the furnace to come to complete thermal equilibrium. Given the limited length of campaign, data was taken before the furnace came to complete thermal equilibrium. The consequence of all the above sources of error is that the value of total heat transfer obtained by summing the calculated values for each heat sink is considered to be less accurate than the value obtained by use of the flue gas temperature and burnout data.

Figure 7.6 shows that an increase in $G_{PJf}/(G_1+G_2)$ in 80PJ-annular flames causes a greater increase in the calculated enthalpy of recirculated gases than in heat extraction. (The reverse situation may occur in a furnace with greater heat extraction capability.) Consequently, the trend of increasing NO_x emissions with increasing PJ momentum in the 2.5 MW flames (also shown in Figure 7.6), is deduced to be at least partly the result of increasing flame temperatures arising from limitations in furnace heat extraction capacity. In further work, manipulation of heat extraction profiles to produce equal flue gas temperatures may provide a more meaningful comparison between flames (Weber, 1996). However, as observed in

Chapter 6, water-cooled heat sinks, located outside of the refractory, provide little control of wall temperature. An alternative experimental technique, which may be explored, is to adjust fuel and air inputs over a small range to maintain constant flue gas temperature and oxygen concentration.

At 130 kW, the combined primary and 19PJ flows have a greater entrainment appetite than the secondary air (Figure 7.7). Entrainment is calculated using Equation 7-8 for flames with a secondary air temperature of 500°C. Due to the positioning of the burner within the kiln, entrainment of ERZ gas by the secondary air stream occurs upstream of the burner exit plane (see Figures 5.2 and 7.3a). Consequently, to calculate the mean temperature rise of the combined PJ-primary air and coal flows due to entrainment, the mass of ERZ gas entrained by the secondary air, was first calculated using Equation 7-4. Then the entrainment of mixed secondary air and ERZ gases by the PJ-primary streams was calculated using Equation 7-8. Figure 7.8 shows that the mean temperature of the combined PJ air, primary air and coal at the ignition distance, increases by more than 300K due to entrainment of secondary air and ERZ gas.

For the 130 kW flames obtained using the 10PJ nozzle (operated without secondary air preheat) the ERZ mass entrained by the secondary air peaks at 0.003 kgs^{-1}, or only 6% of the secondary air flow (Figure 7.9). Consequently, the temperature rise of the combined 10PJ-primary flow upstream from the ignition location, due to entrainment of secondary air and ERZ gases, is insignificant (Figure 7.10). The data in Figure 7.10 demonstrates that the trend of increasing NO_x emissions with increasing $G_{PJ}/(G_1+G_2)$ cannot be attributed to entrainment of ERZ enthalpy. Instead it can be deduced that in the 10PJ flames with $G_{PJ}/(G_1+G_2) > 2.5$, corresponding to inlet pressures beyond 200 kPa (g), increased local oxygen concentration caused by increased entrainment rates of secondary air, and possibly an increase in small scale turbulence as the precession frequency is increased, are responsible for the increased NO_x emissions. The precession frequency of a choked 10 mm PJ nozzle is 380 Hz, which can be expected to contribute to an increase in small scale mixing, relative to a 19 mm PJ nozzle, for which the choked f_p = 230 Hz, and a 80PJ nozzle, for which the choked f_p = 48 Hz. (These values are calculated using Equation 1-14.) The high NO_x emissions at high 10PJ nozzle pressures are deduced to be exacerbated by the effect of the small ratio of PJ nozzle diameter to annular channel diameter. This promotes a mechanism whereby particles are mixed rapidly with air in regions with high oxygen concentrations at the outer boundaries of the flow, rather than being enveloped in large clusters (Chapter 5). It

also causes a reduction in the mean size of fluid structures, and hence particle clusters, relative to those generated by larger PJ nozzles (see Chapter 3).

In the calculations performed above, no effort has been made to use a geometric argument, such as that of Thring-Newby, to estimate the total mean mass flow rate of ERZ gases. This is because calculations based, for example, on the Thring-Newby parameter, require accurate knowledge of the location of *Xp* and *Xc*. In PJ flows, which spread rapidly initially but then at more modest rates, such data is not available. Measurements of jet spread from water flow visualisation studies are not a reliable source of this data because combustion can be expected to alter the spread rate, and mean spreading angles of the flames are difficult to ascertain from flame video-tape due to the limited field of view. In-flame sampling was not performed on a sufficient number of flames for determination of a mean spread angle from CO concentration contours (as has been done, for example, by Sayre *et al.* 1994). These difficulties reflect the nature of PJ flows, in which large structures control local entrainment rates, producing widely varying local stoichiometry and instantaneous spread rates. The influence of these local mixing effects will be considered in the following sections.

7.3.4 Summary

The analysis of the sensitivity of flame characteristics to changes in PJ momentum and ERZ mass flow and enthalpy shows that:

- An increase in $G_{PJ}/(G_1+G_2)$ at 2.5 MW scale increases the enthalpy of externally recirculated gases by 260 kW, while also increasing the heat extracted in the cooling loops by of 160 kW. This is deduced to increase mean flame temperatures by 60°C and hence may contribute to increased thermal and fuel NO_x. (Measured NO_x emissions increased from 400 ppm to 580 ppm as $G_{PJ}/(G_1+G_2)$ was increased from 0 to 1.8.). The enthalpy of the ERZ flow is strongly dependent on the furnace geometry and confinement, and is expected to be less significant in rotary kilns.
- Increases in NO_x emissions with $G_{PJ}/(G_1+G_2)$ were most significant at very high PJ momenta in 2.5 MW flames. For example a flame with intermediate PJ momentum, $G_{PJ}/(G_1+G_2) \sim 0.7$, produces substantial increases in heat release (80kW) relative to the baseline flame, corresponding to an increase in ERZ enthalpy of 55 kW, but with minimal increases in NO_x emissions (40 ppm above the baseline flame).
- In 130 kW flames, a trend of increasing NO_x emissions with increasing $G_{PJ}/(G_1+G_2)$ correlates with increased entrainment rates of secondary air, rather than increased enthalpy of ERZ gases. Consequently it is clear that in general both the quantity of oxygen entrained and the enthalpy of entrained gases influence heat release and NO_x emissions.

7.4 Effect of precession in the NBZ on convective heating of particles

In this section, the potential for the flow characteristics in the NBZ of PJ flows to increase convective particle heating rates, relative to steady flows, is assessed. The NBZ of PJ flows, ie. $\frac{x}{D} \leq 2$, is where the precessional motion dominates. In this region, particles which do not follow the flow are likely to be exposed to widely fluctuating slip velocities. Any increase in particle heating rate therefore relies on the extent to which particles follow the flow as well as the entrainment rates of hot gases. The extent to which particles follow the precessing flow is estimated using the entrainment factor, η, of Yavuzkurt *et al.* (1991a), defined by Equation 5-19. Yavuzkurt *et al.* (1991a) used the entrainment factor to assess the effect of fluctuating velocities on particle combustion rates, (Section 5.2.6). Here it is used to assess the influence of fluctuating slip velocities on particle heating rates in the pre-ignition region of flames.

Precession frequencies of typical PJ flows in 130 kW and 2.5 MW flames are as follows (calculated from Equation 1-14). The 19PJ nozzle operated at 100 kPa(g), generates a flow that precesses at 230 Hz, while the 10PJ nozzle operated at 200 kPa(g) generates a flow that precesses at 380 Hz. These frequencies are approaching those found by Yavuzkurt *et al.* (1991a), who used acoustic oscillations at 600 Hz, to increase combustion rates of coal particles with diameters of 20-70 μm in a methane flat flame. At 2.5 MW, the 80PJ was operated at flow rates of 250 and 500 kg.hr^{-1}, ie. $G_{PJ}/(G_1+G_2)$ = 0.73 and 1.8, equating to precession at frequencies of 46 and 48 Hz respectively. Figure 7.11 shows the effect of particle size on the entrainment factor, η, for choked flows through the 10PJ, 19PJ and 80PJ nozzles. Data calculated for a "small" full scale burner, ie. a 350 mm nozzle, operated at 20 kPa(g) is also included in Figure 7.11. The precession frequency of this PJ flow is 22 Hz. Figure 7.11 shows that significant fluctuating slip velocities, U_{rel}, (which occur when $\eta <$ 0.5) are achieved only for the larger sized particles in typical pf size distributions and in flows with higher precession frequencies, ie. especially the 130 kW flames. Figure 7.11 also shows that at full scale (350 mm PJ nozzle) no particles are expected to experience significant slip velocities, and consequently no enhancement of convective heating rates occurs. However the mechanism of cluster formation which relies on entrainment of particles into the exiting precessing jet may be enhanced relative to small scale, as the particles follow the flow more faithfully.

The entrainment factor can be used to calculate a fluctuating Nusselt number due to precession in the NBZ, Nu_t (defined in Equation 5-20). The fluctuating Nusselt number can be used to estimate any enhancement of convective heating rates in those flows in which significant slip velocities occur, ie. in the 130 kW flames. Figure 7.12 shows the effect of the estimated fluctuating slip velocity, U_{rel}, on Nu_t for the particle sizes $d_p \geq 40$ μm, in the NBZ of a 19PJ flow with f_p = 230 Hz. The no slip case, (Nu = 2) is also shown for comparison. Calculations are made for three fluctuating slip velocities, 100 ms^{-1}, which is representative of PJ exit velocities, and 30 and 10 ms^{-1}, which are more representative of velocities in the NBZ after entrainment of hot gases. The greatest value of Nu_t, calculated for realistic slip velocities of 30 ms^{-1}, is a factor of two higher than that of the no slip case. However it occurs for large particles (d_p = 100 μm). As particle size is reduced, Nu_t tends towards 2. Consequently any increase in the heating rate of large particles due to increased Nu_t does not compensate for the reduction in heating rate due to increased particle mass, as can be deduced from the Equations 5-2 and 5-3 for convective particle heating rate with no slip, i.e. the heating rate is inversely proportional to d_p^2:

Particle heating rate by convection , $\frac{dT_p}{dt} = \frac{Q_c}{m_p C_{pp}} = \frac{6Nuk_g \Delta T_{gs}}{C_{pp} \rho_p d_p^2}$ (Ks^{-1}) 7-9

In summary, significant fluctuating slip velocities between particles and fluid in the NBZ of PJ flows only occur at small scale, such as the 130 kW experimental scale, but even at this scale do not contribute significantly to convective particle heating rates. In the following section the influence of large scale clustering on convective and radiant particle heating, and hence on ignition, is considered.

7.5 The influence of clustering on the heating of particles in the pre-ignition region

7.5.1 Introduction

In Chapters 5 and 6 a trend of decreasing ignition distance with increasing PJ momentum was observed in both 130 kW and 2.5 MW flames. Section 6.5 shows that the scaling parameter $[G_{PJt}/(G_1+G_2)].St^{-0.5}$ provides reasonable collapse of the ignition distance data across scales, demonstrating the dominating effect of enhanced large scale mixing and clustering on ignition. It was proposed that increases in $[G_{PJt}/(G_1+G_2)].St^{-0.5}$ correlate with the enhancement of large scale mixing and particle clustering and increased deflection of particles in the NBZ. Two possible mechanisms by which these large scale mixing effects may reduce ignition distances are:

(a) movement closer to the nozzle, of regions in which velocities suitable for stabilisation occur

(b) an increase in the heating rate of particles

Data presented earlier in the thesis demonstrates the significance of mechanism (a) i.e. "velocity effects". For example, enhancement of large scale mixing was shown to reduce mean structure convection velocities (Chapter 4), and increase the fraction of fluid with low axial velocities (Appendix 3). Evidence also suggests that mechanism (b), i.e. particle heating rate effects, is significant at these experimental scales. For example, in Section 5.7, the ignition distances of 19PJ, 130 kW flames, with PJ inlet pressures of 60 kPa(g), were shown to decrease with increasing coal heat input and furnace temperature. Since the velocity fields of these flames are almost identical, the variation in ignition distance was deduced to be due to either altered local stoichiometry or altered heating rates and hence volatile matter evolution rates.

The influence of enhanced large-scale mixing and particle clustering on particle heating rates in the pre-ignition region of flames is estimated by sensitivity analysis in the following sections. The analysis provides a means of testing the hypothesis outlined in Chapter 5, that ignition commences on cluster boundaries, and that combustion subsequently propagates into structures, resulting in fuel rich-combustion inside the clusters.

7.5.2 Cluster energy balances

Energy balances for a large spherical particle cluster in the pre-ignition region of a PF flame are developed here to enable the influence of enhanced large scale mixing to be estimated. For spherical clusters the equations are based on those of Zhang and Wall (1993), with additional consideration of a radiation term. Heating of particles in a large spherical structure by a single pass of radiation is estimated using Equation 5-10. Layered clusters are approximated as a mono-layer of small spherical clusters in some of the arguments to follow.

The major energy exchange routes for the most general case of a large spherical cluster are illustrated in Figure 7.13, with heat addition to the cluster denoted as positive. Nomenclature is also given in Figure 7.13. Note that convective heating of particles within the cluster is assumed to be a two-step process, with initial convective heating of cluster gas, followed by convective transfer between cluster gas and particles. "Blowing" or convection of gas out of the cluster (Ryan and Annamali, 1991) is ignored.

The transient energy balance equations for particles and cluster gas are, respectively:

$$NM_pC_p\,dT_p/dt = Qr_{wp} + Qr_{fp} - Q_d - Q_p - Q_{pg} - Qr_{ep} \qquad 7\text{-}10$$

$$M_gC_g\,dT_g/dt = Q_v + Qc_{cg} + Qr_{wg} + Qr_{cg} + Q_{pg} \qquad 7\text{-}11$$

In the pre-ignition region it is assumed that particles are heated to the ignition temperature, but with no reaction. During this phase, Q_d, Q_p and Q_v are all zero and there is minimal radiant exchange between the cluster and upstream (incoming) flow. It can also be assumed that all incident radiation is absorbed by particles (with no scattering losses) rather than cluster gas, so the energy balance for single clusters reduces to:

$$NM_pC_p\,dT_p/dt = Qr_{wp} + Qr_{fp} - Q_{pg} \qquad 7\text{-}12$$

$$M_gC_g\,dT_g/dt = Qc_{cg} + Q_{pg} \qquad 7\text{-}13$$

Where Qc_{cg} and Q_{pg} are given by,

$$Qc_{cg} = h_cS_c\left(T_s - T_g\right) \qquad 7\text{-}14$$

$$Q_{pg} = 2Nk_g\pi d_p\left(T_p - T_g\right)) \qquad 7\text{-}15$$

k_g = thermal conductivity of cluster gas at 300°C

T_s = temperature of hot entrained air or externally recirculated combustion gases.

The remainder of the symbols are listed in the notation section.

Note that to calculate Qc_{cg} it is assumed that the cluster gas has negligible motion relative to the surrounding gas, so that, Nu_{cl} = 2. Rather than solving the energy balances, the contributions of the different heating mechanisms to the overall particle and gas heating rates, dT_p/dt and dT_g/dt, are estimated. The influence of char reactions on heat release and NO_x formation are ignored in this analysis since the main interest is in the initial region of the flame where peak heat release rates are achieved. If it is assumed that the particle clusters correlate with flow structures observed in water flow visualisation, video images of water flow analogies of each of the flames can be used to estimate convection velocities of clusters, mean cluster sizes and residence time. Photographs of glass beads in air flows (Chapter 4) are used to estimate the influence of enhanced large scale mixing on cluster number densities.

7.5.3 Particle heating rate sensitivity analysis

In the current section the energy balances developed in Section 7.5.2. are used to evaluate the dominant effects on particle heating rate, dT_p/dt, and gas heating rate, dT_g/dt, in the pre-ignition region. Figure 7.14 shows the contributions of wall and flame radiation to hypothetical mean particle heating rates of the entire particle stream, $Qr_{wp}/(NM_pC_p)$ and $Qr_{fp}/(NM_pC_p)$ respectively, as a function of coal jet half angle. The entire particle stream in the pre-ignition region, i.e. the coal jet extending from the burner exit to the flame front, is referred to as a particle "cloud" to distinguish it from particle "clusters", which are correlated with large fluid structures. The particle cloud is assumed to be conical in shape and to consist of a uniform distribution of particles (Figure 7.15). The assumed cloud properties are given in Table 7.1. Equation 5-9 describes radiation between two bodies when one encloses the other, and so is used to calculate mean particle heating due to wall radiation. Equation 5-10 is used to calculate the contribution of a single pass of radiation to the mean particle heating rate, and can be used to calculate cloud heating rate due flame radiation, since the flame does not enclose the particle cloud. Equation 5-10 requires a view factor, which is assumed to be 1. The cloud absorptivity (assumed equal to the emissivity) was estimated, using Equation 5-7, by approximating the entire particle stream in the pre-ignition region as a spherical cloud with diameter equal to the typical ignition distance of the 130 kW flames (100 mm), and assuming a mean particle concentration given in Table 7.1. Under these assumptions the cloud emissivity has a value of 0.847.

Table 7.1. Assumed mean particle cloud properties in the pre-ignition region

	Assumed value
Ignition Distance	100 mm
Mean particle concentration	0.2 kgm^{-3}
Mean particle diameter on a number basis	10μm
Flame temperature	1500 K
Mean particle temperature	300 K
Flame emissivity	0.8

Calculations were made to test the sensitivity of particle cloud heating rate to flame half angle. The range of half angles tested include those measured for the PJ-annular water jets in Chapter 3. Note that in considering the effect of jet half angle alone, this analysis ignores any effects of enhanced large scale mixing on local particle clustering. It also ignores the trend of decreasing ignition distance that is observed with increasing jet spread angle. Figure 7.14 demonstrates that, under the assumptions made, the mean particle heating rate in the cloud, due to flame radiation, is constant with increasing spreading angle. This is because

the increase in jet spread does not alter the ratio of particle cloud cross-sectional area, as viewed from the flame, to cloud mass. The heating rate due to wall radiation decreases with increasing spreading angle, due to a decrease in the ratio of particle cloud cross-sectional area, as viewed by the walls, to cloud mass. These effects are independent of the chosen ignition distance and depend only on the jet half angle. The sum of mean particle heating rates due to wall and flame radiation is shown to reduce with increasing jet half angle. Consequently the observed experimental trend of decreasing ignition distance with increasing spread angle is not due to the effect of mean radiative heating on the particle cloud, considered as a whole. However the effect of preferential concentration of particles on local radiative heating rates may be significant, and is considered below.

The heating rates of particles in individual clusters by direct flame radiation, are illustrated in Figures 7.16 and 7.17. The data in these figures is calculated using Equation 5-10 for a single pass of radiation through a cluster. Clusters are assumed to be located near to the flame front so that attenuation of radiant heating by other clusters is ignored and the view factor is one. The area for heat exchange is projected area of the cluster seen by the flame, i.e. the cluster cross-sectional area. The flame emissivity and temperature were taken from Table 7.1. The cluster is assumed to be heated uniformly and to have a uniform temperature. Figure 7.16 presents the heating rates of particles in clusters, as a function of four cluster diameters (10, 20, 40 mm) and particle diameters in the range, 5 – 100 μm, assuming a constant particle concentration of 0.2 kgm^{-3}. The calculations show that heating rates are greatest for small particles in small clusters. Figure 7.17 demonstrates that the heating rate of 10 μm particles, in 20 mm clusters, decreases as particle concentration is increased. The reduction in heating rate is due to increased particle mass, which dominates over the effect of increased radiant absorptivity. However it should be noted that in the pre-ignition region, where entrainment is incomplete, particle concentrations are of the order of 0.2 to 1 $kg.m^{-3}$, so that the highest practical heating rate under the assumptions made is ~ 20,000 Ks^{-1}.

Figures 7.16 and 7.17 demonstrate that if ignition is controlled by radiative heating rates of clusters with uniform particle temperature, then it is most likely to occur in small clusters. The assumption of uniform particle temperature requires that heat transfer rates within the cluster are very rapid. If, on the other hand, the assumption of uniform particle temperature is relaxed, then particles on the outside of clusters, where little attenuation of radiation by other particles occurs, are able to be heated more rapidly than those in the cores of clusters. The issue of how convective heat transfer occurs within clusters is dealt with later. The

mechanism of preferential heating of the outer layer of a large cluster can be appreciated from Figure 7.16 by considering the outer layer to be composed of a number of smaller spherical clusters, each of which has its own uniform temperature. Preferential heating of the outer layer of large clusters would encourage ignition to occur in these locations.

Figure 7.18 shows the effect of cluster diameter on cluster emissivity and particle heating rate by both convection and radiation. The data in Figure 7.18 implies that small clusters or the outer layers of large clusters are heated more rapidly than the cores of large clusters, by both radiation and convection. Again for the purposes of analysis, heat transfer within the cluster is assumed to be very rapid so that particle temperatures within a cluster are assumed to be uniform. The emissivity (assumed equal to the absorptivity) of clusters of 10 μm particles with a particle concentration of 0.2 $kg.m^{-3}$ (determined by Equation 5-7) is shown to increase from 0.09 to 0.61 as the cluster diameter is increased from 5 mm to 50 mm. However the radiant heating rate shows the reverse trend, reducing with increasing cluster size, because the effect of the increase in total particle mass dominates over that of the combined increases in emissivity and cluster cross-sectional area. The trend of reduced radiative heating rate with increasing cluster size implies that, for real large clusters in which uniform temperature will not occur, the outer-most "layer", which has a heating rate analogous to a small cluster, will be heated more rapidly than the inner regions.

Figure 7.18 shows that for clusters with diameters smaller than 7 mm, particle heating rates due to convection, $Qc_{cg}/(M_gC_g)$, are higher than those due to flame radiation. The convective heating rates at the outer edge of clusters, given in Figure 7.18, are calculated from equation 7-14, where it is assumed that the cluster gas has negligible motion relative to the surrounding gas, so that $Nu_{cl} = 2$. It is also assumed that the gas in contact with the cluster is 1000 °C hotter than the cluster, and that no mass transfer occurs between hot gas and the cluster. Figure 7.18, thus demonstrates that the combined effects of convective and radiant heating results in both rapid heating of small clusters, and/or the thin outer layers of large clusters, and reduced heating rates of the cores of clusters. This is consistent with ignition commencing at the edge of clusters and then propagating inwards.

An alternative means of estimating convective heating rates of the gas within clusters is to use a "mixing length" approach, if the large-scale structure mixing length l, is assumed to control the cluster size. The mixing time-scale of a large structure is given by

$$\tau_l = \frac{l}{u} \qquad 7\text{-}16$$

where the length scale can be assumed to be equal to the cluster diameter, and the velocity scale, u, can be assumed to be the structure convection velocity measured in water (Chapter 3), corrected for the change in inlet velocity that occurs in air flows. A mean value for PJ air flows of $u = 2$ m.s^{-1} is used in the calculations. Heating of particles is assumed to occur due to complete mixing with entrained gases within the mixing time-scale.

For the purposes of this analysis the temperature of the cluster is assumed to increase by 200°C due to transfer of sensible heat, which is typical of the values calculated earlier for heating due to entrainment of ERZ gas and secondary air (Figure 7.5). Figure 7.19 shows the effect of cluster diameter on the ratio of radiative heating rate of particles to convective heating rate of gas within the clusters (due to transfer of sensible heat). These clusters are assumed to consist of 10 μm particles with a particle concentration of 0.2 kg.m^{-3}. The heating rate due to flame radiation $Qr_{fp}/(NM_pC_p)$ is calculated using Equation 5-10. The calculation method may under-estimate the fluid time-scale due to the use of convection velocities rather than relative velocities of structures, and consequently over-estimate sensible heat transfer rates. Accordingly Figure 7.19 provides a slightly higher estimate for the convective heating rate of gas in clusters than is provided in Figure 7.18. However the trend is the same, ie. convective heating becomes increasingly significant as the cluster size is reduced and so contributes significantly to the heating of the outer regions of clusters, which have a mixing length smaller than the scale of the entire cluster.

In the analysis to date, jet precession has been assumed to cause an increase in the diameter of spherical clusters, and the heating rates of the outer layers of clusters have been analysed by analogy with a layer of small clusters. This analysis can be developed further by noting from section 7.2.3 that precession also increases the "layering" of fluid within structures. In section 7.2.3 it is also suggested that laminar diffusion mixing is likely to occur between these layered structures. Here the critical thickness of these "layered" structures at which the laminar diffusion mixing time-scale is sufficiently small to significantly influence heating rates is calculated. The maximum rate of laminar diffusion through a layer on the boundary of a structure, is given by Fick's law:

$$\frac{N_a}{A} = -D\frac{dC_a}{dx} \qquad 7\text{-}17$$

where N_a = the molar flow rate of species, a, through a region with cross-sectional area A, C_a is the local concentration of species a, and D = laminar diffusivity (m^2s^{-1}). The time-scale for laminar diffusion, τ_{lam}, across a layer of thickness, Δx, with concentration gradient, Δc, is given by,

$$\tau_{lam} = \frac{(\Delta x)^2}{D}. \qquad 7\text{-}18$$

Figure 7.20 presents calculated heating rates, obtained using Equation 7-18, due to laminar diffusion of hot gas, with a composition similar to that of air, through a layer of volatile matter. These calculations assume that a temperature difference of 200°C is associated with the concentration gradient across a layered structure, and that diffusion of temperature occurs in the same time-scale as that of mass (Equation 7-18). Such a situation may occur when hot ERZ gases and secondary air are entrained into the PF stream. Hence the heating rate of the cloud due to laminar diffusion is given by,

$$\frac{dT_{g,lam}}{dt} = \frac{200}{\tau_{lam}} \qquad (K.s^{-1}) \qquad 7\text{-}19$$

The laminar diffusivity, D, is assumed to be that of air at 500°C, ie, 0.002 m^2s^{-1}. The data shown in Figure 7.20 were calculated for layer thicknesses of 2 to 50 mm and are compared (on a log scale) to the radiant and convective heating rates presented in Figure 7.18. Although laminar diffusion is much less significant in gas than in water and is likely to be augmented by turbulent diffusion, Figure 7.20 demonstrates that the pure laminar diffusion heating rate of layers with thickness < 5 mm can be more rapid than the radiant heating rate of spherical clusters of the same characteristic dimension, under the assumptions made. The laminar diffusion heating rate follows a similar trend to that of the convective heating rate of spherical clusters. The calculations of heating due to both laminar and turbulent mixing confirm the earlier findings that mixing and heating rates at the edges of large structures are much greater than those within the large structures, commensurate with the shift in the energy spectrum.

The findings presented above assume that particle concentrations and hence volatile matter concentrations in the outer regions of large structures are sufficient to promote ignition, and that the heating rate of individual particles, by convection from the heated fluid, is high. The latter point is demonstrated by Figure 7.21 which shows that particles with $d_p \leq 25\mu m$ are heated at rates of $\geq 100{,}000\ Ks^{-1}$, when exposed directly to a gas 200 K hotter than the

particle (using Equation 7.15 to evaluate Q_{pg}). The results presented in Figures 7.20 and 7.18 show that, under the assumptions made, devolatilisation can proceed in the interior of spherical clusters with diameters ≥ 7mm, chiefly due to radiative heating, more rapidly than oxygen is mixed into the cluster. This would result in a rapid reduction in local oxygen concentration as combustion proceeds and so provide a plausible explanation for the relatively low NO_x emissions recorded in PJ PF flames. The quantity of soot formed may also increase due to the fuel-rich conditions and contribute to the recorded increases in heat flux from PJ, PF flames to walls. This possibility is investigated further in Section 7.7.

7.5.4 Summary

The preceding sensitivity analysis of the effects of precession on particle and gas heating rate shows that:

- The increase in spreading angle of PJ-annular flows with increasing $G_{PJ}/(G_1+G_2)$ increases the relative contribution of flame radiation to the mean particle heating rate in the pre-ignition region, but cannot explain the observed decrease in ignition distance with increasing $G_{PJ}/(G_1+G_2)$.
- By assuming that clusters are of a uniform temperature, the mean radiative heating rate of particles in clusters increases dramatically with reduced particle size, and also with reduced cluster size. Consequently, if particle segregation on the basis of differing St is promoted by enhanced large scale mixing, it can provide a plausible explanation for promotion of ignition in clusters which contain a high concentration of small particles.
- If clusters are assumed to be spherical, then the convective heating rate of the outer-most layer of a cluster by entrained hot gases, assuming no slip (Nu_{cl} = 2) and no mass transfer, increases with reduced cluster diameter. The transfer of heat from cluster gas to particles occurs rapidly for particles with $d_p < 40$ μm.
- The mean heating rate of particles of fixed diameter in clusters of uniform temperature was shown to decrease as particle concentration is increased, due to increased particle mass. Nevertheless ignition is likely to be favoured by clusters that contain high particle concentrations due to higher volatile matter concentration and the effects of non-uniform temperature in the cluster.
- The corollary of the finding that the mean radiative and convective heating rates of smaller clusters is greater than that of large clusters, is that the outer layers of clusters are heated preferentially to the cluster interior by both radiation and convection. In particular convective heating rates of the outer layer of clusters are shown to be highly significant.
- Convective heating of the outer layer of a cluster (< 5mm) can be significant even when laminar diffusion is significant. This mechanism, together with those above, provide strong support for the hypothesis that ignition occurs in the outer layers of structures and propagates into the fuel-rich interior, a mechanism which may increase the quantity of soot formed in large clusters. This hypothesis provides a plausible explanation for both the relatively low experimental NO_x emissions and the high levels of heat transfer to furnace walls.

7.6. The influence of enhanced large scale mixing on gas phase combustion rates

7.6.1. Theoretical considerations - The use of turbulence scales in combustion models

Spalding (1971) developed an "eddy break-up" model for the rate of spread of turbulent premixed propane - air flames after noting the existence of "isolated pockets of hot and cold gas" in flames. The eddy break-up model assumes that the rate of energy decay from the large scales of turbulence determines the mixing rate. Prandtl's mixing length hypothesis is used to calculate the mass rate of consumption of fuel per unit time and volume, $\dot{m}'''_{fu}$, by the expression,

$$\dot{m}'''_{fu} = C(1-\tau)\rho\frac{\partial u}{\partial y} \qquad 7\text{-}20$$

where C is a constant and τ is the *reactedness*. Spalding (1971) showed that Equation 7-20 provided good agreement between calculated and experimental oxygen and velocity profiles.

The eddy dissipation model of Magnussen and Hjertager (1977) assumes that fuel and oxygen exist in separate eddies, and that the rate of dissipation of eddies determines mixing on molecular scale and hence reaction rate. The dependence of the rate of dissipation on fluctuations in concentration is simplified by relating it to mean concentrations. The reaction rate is given by,

$$R_f = A.\overline{c_f}(\varepsilon/k) \qquad 7\text{-}21$$

where, A is a constant depending on flame structure, $\overline{c_f}$ is the mean fuel concentration, and ε is the dissipation rate of kinetic energy (k). Two similar expressions are presented by Magnussen and Hjertager (1977) for oxygen and combustion products. The overall reaction rate is controlled by whichever of the three rates is the slowest.

Magnussen and Hjertager (1977) used A = 4 in equation 7-21 for turbulent diffusion flames, but Visser *et al.* (1990), found it necessary to use A = 0.5 for volatile matter combustion and 0.7 for CO combustion in the IRZ of swirled PF flames. As noted in Chapter 5, Costa *et al.* (1990b) attribute the over-predictions of volatile reaction rates in the IRZ of swirl flames to the neglect of the time required for tar cracking.

In numerical computations, values of ε and k are obtained from their transport equations (Launder and Sharma, 1974). The values of ε and k are also used to calculate the turbulent

viscosity, and used in transport equations for mass and momentum (Magnussen and Hjertager, 1977, Truelove, 1984). Calculation of ε relies on the specification of a length scale as an initial condition. An initial length scale of one tenth of the jet diameter, *d*, is commonly used, so that the initial value for ε, is:

$$\varepsilon = \frac{C_\mu^{0.75} k^{1.5}}{0.007(d/2)} \qquad 7\text{-}22$$

where C_μ = 0.09 (Weber *et al.* 1990). Similar estimations of the initial length scale are required, whether used in the k-ε model, or in more sophisticated turbulence models (see examples in, Weber *et al.* 1990, Wilcox, 1998). The initial conditions for solving the transport equations for kinetic energy can be obtained from velocity fluctuation measurements.

Magnussen *et al.* (1978) refined their original model to take into account the influence of Reynolds number on fluid structure, and hence soot combustion rates, in round jet acetylene diffusion flames. By measuring scattered light from an Ar-ion laser, they showed that a reduction in *Re* increased peak soot concentrations and caused broader soot concentration probability density functions. Soot was found to form in eddy-like structures, which burn from the outside of eddies and propagate inwards. For modelling purposes, the mass fraction in fine structures, γ, was assumed to be related to the energy in fine structures by the relation:

$$\gamma \sim (u^*/u')^3 \qquad 7\text{-}23$$

where u^* is the characteristic velocity of fine structures, and u' is the fluctuating velocity component. The fraction of fine structures which are heated sufficiently to react, χ, is given by the ratio of local product concentration to initial fuel concentration. The rate of combustion was assumed to be proportional to γ, χ, and whichever of the normalised local mean concentrations of fuel or oxygen limits the reaction, ie. the reaction rate was given by the expression:

$$R = K.(\nu\varepsilon/k)^{0.25}.\frac{\varepsilon}{k}.\chi.\overline{c_{min}} \quad \text{kg.m}^{-3}\text{s}^{-1}, \qquad 7\text{-}24$$

where *K* is a constant, and ν is the kinematic viscosity. This model provided good agreement with measured mean soot concentration data, when used in combination with a soot formation model.

A further development of the Magnussen *et al.* (1978) model, by Magel *et al.* (1996) argued that a better representation of the similarity between the mass fraction in fine structures and energy decay should be given by the relation,

$$\gamma \sim (u^*/u')^2 \qquad 7\text{-}25$$

and used the concentration gradient, Δc, rather than concentration. Hence the mean reaction rate is:

$$R = K.\frac{\varepsilon}{k}.\chi.\overline{\Delta c} \qquad \text{kgm}^{-3}\text{s}^{-1} \qquad 7\text{-}26$$

which has similarities to the original formulation of Magnussen and Hjertager (1977) given by Equation 7-21.

Eddy dissipation models are widely used to calculate volatile matter and CO oxidation rates in mathematical models. However NO_x reactions contribute little to the overall mass and energy balances, and so can be ignored in the main program calculations. Consequently, the computationally more demanding probability density function approach can be used for post processor calculations of NO_x emissions (Peters and Weber, 1995).

As described in Chapter 1, Newbold (1997) presented a concentration probability density function, pdf, on the axis of an ambient FPJ air jet and compared it to a simple jet. The FPJ demonstrated a less dominant peak at $\xi = 1$ (pure jet fluid) close to the nozzle, increased unmixedness and intermittency, and a much broader spread of concentrations at all axial locations. Similar results were obtained in 2 MW gas PJ flames, Nathan *et al.* (1992). The findings were summarised thus, *"precession acts to reduce the uniformity of the mixed fluid relative to a simple jet"* (Newbold, 1997, p 93). Newbold's measurements also show the presence of ambient fluid on the centre-line in the near nozzle region (x/D <2). Similar distortions of the volatile matter concentration field, with additional effects due to preferential particle concentration and altered devolatilisation rates, can be expected in PF flames influenced by jet precession.

For thermal NO_x prediction Peters and Weber (1995) use the Zeldovich mechanism, with the oxygen radical concentration 2-4 times larger than the equilibrium concentration given by Westenberg (1971). A Beta function pdf for temperature is used, due to the dominant effect of temperature on NO_x emissions. Similarly for volatile NO_x, Peters and Weber (1997) use unstaged rate equations for HCN reactions (here given as Equations 5-24 and 5-25) in combination with a Beta function pdf for temperature. The standard deviation of the Beta

pdf can be adjusted, with larger values producing larger fluctuations in temperature and hence higher peak temperature and mean NO_x emissions. Peak temperatures occur on the oxygen-rich side of stoichiometric.

7.6.2. Estimation of the dominant effects of precession on volatile matter and NO_x reaction rates.

The influence of enhanced large scale mixing on volatile matter reaction rates and consequent effects on NO_x emissions and heat release are considered. Using the eddy dissipation model to predict the trends in reaction rate of volatile matter in PJ flames, the mean strain rate, $\frac{u}{l}$ (or $\frac{S}{r_{1/2}}$), is substituted for $\frac{\varepsilon}{k}$ in Equation 7–26, to give:

$$R = K\frac{\varepsilon}{k}\chi.\Delta c = K\frac{u}{l}\chi.\Delta c \qquad 7\text{-}27$$

In Figure 3.11 the mean strain rate, $\frac{S}{r_{1/2}}$, of water flows with G_{PJe}/G_1 = 0 and 2.56 were presented as 10.2 and 5.2 s^{-1}, respectively. If a similar reduction in strain rate with increasing G_{PJ}/G_1 also occurs in PJ flames, an increase in χ or Δc would be necessary to maintain similar reaction rates to those that occur in non-PJ flames, according to Equation 7-27. Further increases in χ or Δc, relative to mono-channel flames, may occur as $G_{PJ}/(G_1+G_2)$ is increased, as demonstrated by the associated increases in NO_x formation, and the possibly of increased volatile matter reaction rates at higher $G_{PJ}/(G_1+G_2)$.

A possible explanation for the increase in volatile matter reaction rates and NO_x formation rates with $G_{PJ}/(G_1+G_2)$ can be made by considering Equation 7-27, assuming that it can be applied to the small scale turbulence. The images in Figure 7.1 show that fine scale turbulence, and the associated high local small-scale strain rate, is concentrated at the "edges" of large clusters. In these regions high concentration gradients also exist (Newbold, 1997). Figure 7.1 also shows an increase in the fraction of fluid in layers at the edge of large structures, which may be available for reaction, ie. an increase in χ with G_{PJ}. The combination of these factors allow high gas-phase reaction rates to occur locally, while lower reaction rates occur within large clusters. NO_x emissions from pulverised coal PJ flames may be curtailed by local staging within clusters. Other explanations for increased volatile matter reaction and NO_x formation rates with increased $G_{PJ}/(G_1+G_2)$ are increased entrainment rates of air (resulting in higher mean oxygen concentration and flame temperatures) and limitations in furnace heat removal capacity (resulting in higher flame temperatures). Further work in which these factors are better assessed and quantified is required.

7.7. The sensitivity of heat release to soot concentration

The flame emissivity, being a composite of the gas, soot and particle emissivity is given by Equation 2-3. Figures 7.22 and 7.23 show the sensitivity of total flame emissivity, calculated by Equations 2-3 and 2-4, to soot concentration for conditions that apply in the 2.5 MW and 130 kW flames, respectively. Mean beam lengths of 1.76 m for the 2.5 MW furnace and 0.53 m for the 130 kW furnace are used to calculate emissivities. In the sensitivity analysis, soot concentrations are varied from a typical value of 7.1×10^{-5} kgm^{-3} to a maximum of 20% of the total solid mass. The latter value is the maximum reported by Solomon and Fletcher (1994) for combustion under fuel-rich conditions at 1470K. Figures 7.22 and 7.23 also show the contributions of gas and particles to flame emissivity. For a combined CO_2 and H_2O partial pressure of 0.7 atm, the combined gas emissivity is approximated by use of the Hadvig plot (Sarofim and Wall, 1980). At 1500 K the combined gas emissivity is 0.4 at 2.5 MW and 0.2 at 130 kW. Particle emissivity is given by Equation 5-7. The particle mass concentration is assumed to be 4% of that of the original coal, made up of 1% unburnt carbonaceous particles, and 3% ash particles. Both types of particles are assumed to have a particle diameter of 10 μm. Figures 7.22 and 7.23 demonstrate that sooting can have a major influence on the total emissivity of the experimental flames.

Figure 7.24 shows the calculated net radiant energy transferred from 2.5 MW flames to a single metal cooling loop. The net energy transferred was calculated using Equation 5-18, as a function of total flame emissivity, assuming that the metal surface is blackened and has an emissivity of 0.7. The metal tube surface area is 1 m^2. The calculation was performed for flame temperatures of 1500K and 1600K providing heat extraction values in good agreement with experimental values (see also Figures 6.10 and 6.11). Figure 7.24 demonstrates that soot can contribute up to 50% of flame emissivity and up to 35% of heat transfer. Hence changes in flame emissivity due to the presence of soot can provide a plausible explanation for the observed experimental trends in heat transfer.

7.8. Conclusions

The preceding sensitivity analysis of the influence of PJ momentum on ERZ mass flow and enthalpy shows that:

- An increase in $G_{PJt}/(G_1+G_2)$ at 2.5 MW scale increases the enthalpy of externally recirculated gases by 260 kW, while also increasing the heat extracted in the cooling loops by of 160 kW. This is deduced to increase mean flame temperatures by 60°C and hence may contribute to increased thermal and fuel NO_x. (Measured NO_x emissions increased from 400 ppm to 580 ppm as $G_{PJt}/(G_1+G_2)$ was increased from 0 to 1.8.). The enthalpy of the ERZ flow is strongly dependent on the furnace geometry and confinement, and is expected to be less significant in rotary kilns.
- Increases in NO_x emissions with $G_{PJt}/(G_1+G_2)$ were found to be most significant at very high PJ momenta. For example a flame with intermediate PJ momentum, $G_{PJt}/(G_1+G_2) \sim$ 0.7, was found to produce a substantial increase in heat release (80kW), corresponding to an increase in ERZ enthalpy of 55 kW, but with a minimal increase in NO_x emissions (40 ppm above the baseline flame).
- A similar trend of increasing NO_x emissions with increasing $G_{PJt}/(G_1+G_2)$ in 130 kW flames correlated with increased entrainment rates of secondary air rather than increased enthalpy of ERZ gases. Consequently it is clear that both the quantity of oxygen entrained and the enthalpy of entrained gases influence heat release and NO_x emissions.

The preceding sensitivity analysis of the effect of precession on particle and gas heating rate shows that:

- Flow fluctuations associated directly with the near field precessional motion increase convective particle heating rates by a factor of 2 compared to the no slip case for $d_p >$ 30μm at 130 kW scale. However the effect is negligible at 2.5 MW scale and full scale since only the largest particles are affected.
- The spreading angle of PJ-annular flows increase with increasing $G_{PJ}/(G_1+G_2)$. The increase in spreading angle increases the relative contribution of flame radiation to the mean particle heating rate in the pre-ignition region, but cannot explain the observed decrease in ignition distance with increasing $G_{PJ}/(G_1+G_2)$.
- By assuming that clusters are of a uniform temperature, the mean radiative heating rate of particles in clusters increases dramatically with reduced particle size, and also with reduced cluster size. Consequently, if particle segregation on the basis of differing *St* is promoted by enhanced large scale mixing, it can provide a plausible explanation for promotion of ignition in clusters that contain a high concentration of small particles.

- If clusters are assumed to be spherical, then the convective heating rate of the outer-most layer of a cluster by entrained hot gases, assuming no slip (Nu_{cl} = 2) and no mass transfer, increases with reduced cluster diameter. The transfer of heat from cluster gas to particles occurs rapidly for particles with $d_p < 40$ μm.
- The mean heating rate of particles of fixed diameter in clusters of uniform temperature was shown to decrease as particle concentration is increased, due to increased particle mass. Nevertheless ignition is likely to be favoured by clusters that contain high particle concentrations due to higher volatile matter concentration and the effects of non-uniform temperature in a cluster.
- The corollary of the finding that the mean radiative and convective heating rates of smaller clusters is greater than that of large clusters is that the outer layers of clusters are heated preferentially to the cluster interior by both radiation and convection. In particular convective heating rate of the outer layer of clusters is shown to be highly significant.
- Convective heating of the outer layer of a cluster (< 5mm) can be significant even when laminar diffusion is significant. This mechanism, together with those above, provide strong support for the hypothesis that ignition occurs in the outer layers of structures and propagates into the fuel-rich interior, a mechanism which may increase the quantity of soot formed in large clusters. This hypothesis provides a plausible explanation for both the relatively low experimental NO_x emissions and the high levels of heat transfer to furnace walls.

The preceding sensitivity analysis of the effect of precession on soot emissivity shows that:

- The formation of additional soot in fuel-rich clusters can realistically increase total emissivity of 130 kW experimental flames from 0.25 to 0.9 and of 2.5 MW flames from 0.55 to 1.0.
- The mean heat extraction by a single water tube in the 2.5 MW furnace can increase by 35% due to the increase in emissivity.

The reduction in strain rate produced by precession acts to reduce volatile matter reaction rates. However insight provided by the eddy dissipation model showed that precession can also increase volatile matter reaction and NO_x formation rates in the regions of small-scale structures and "layered" structures at the edges of large clusters. Concurrently, combustion can also propagate at a slower rate through large clusters. These effects explain why mean combustion rates in PJ flames can be higher than those in mono-channel flames. A local staging effect within large clusters is believed to limit flame NO_x emissions.

(a)

(b)

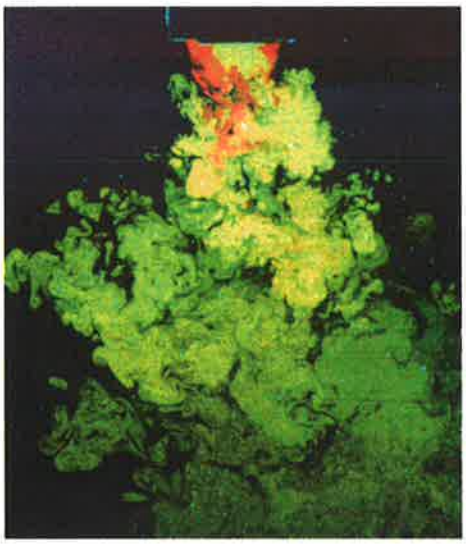

(c)

Figure 7.1 PLIF photographs (1/1000 s exposure) of 19PJ-annular water flows: G_{PJe}/G_l = (a) 0 (b) 2.9, (c) 5.6.

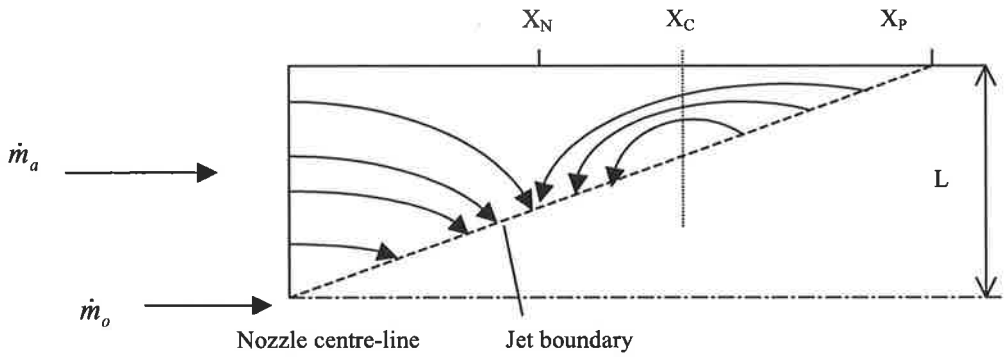

Figure 7.2 A schematic diagram of recirculation in confined jets. (after Barchilon and Curtet, 1964).

Where:

$\dot{m}_o$ = nozzle mass flow rate

$\dot{m}_a$ = secondary air mass flow rate

X_C = Axial position of the core of external recirculation eddy (m)

X_N = Axial position where all secondary air is entrained into an enclosed jet (m)

X_P = Axial position where an enclosed jet meets the wall (m)

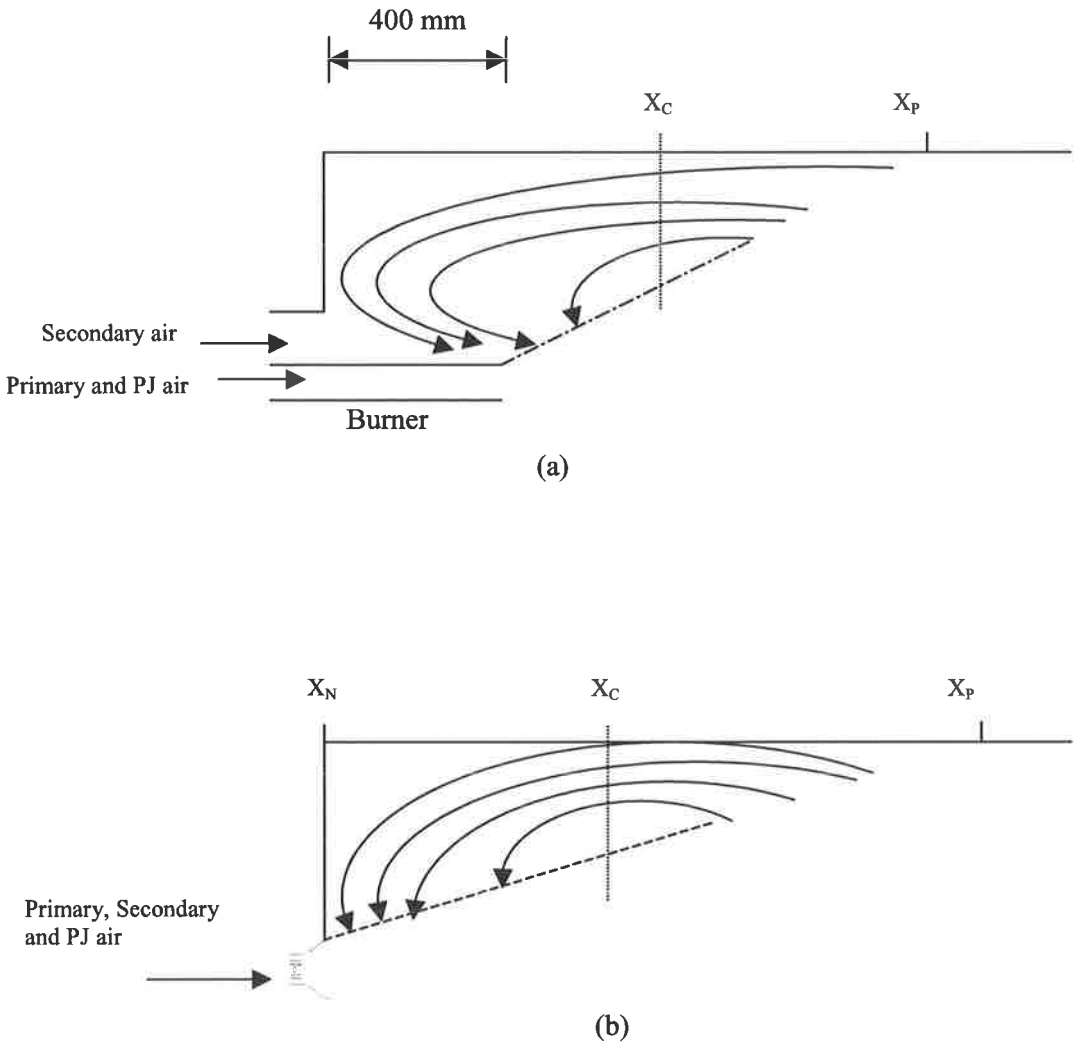

Figure 7.3 Schematic diagrams of external recirculation patterns deduced to occur in (a) the 130 kW furnace configuration
(b) the 2.5 MW furnace

Refer to Figure 7.2 for notation.

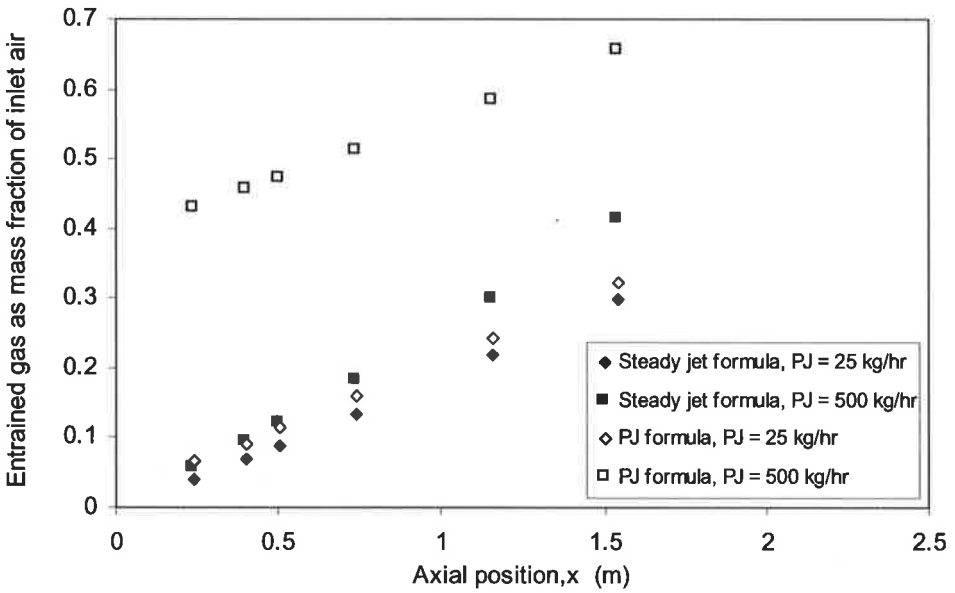

Figure 7.4 Calculated entrainment of ERZ gases by the combined PJ, primary and secondary jets for two 80PJ, 2.5 MW flames with 80PJ air flow rates of 25 and 500 kghr^{-1}, ie. $G_{PJ}/(G_1+G_2)$ = 0.007 and 1.82 respectively. Two techniques are used to calculate entrainment. The steady jet formula uses Equation 7-4 and treats all jets as steady jets. The PJ formula (Equation 7-8) assumes that the PJ entrains 7 times its own mass, and treats the primary and secondary jets as steady jets. The graph demonstrates the rapid entrainment at high PJ flow-rates calculated by equation 7-8 compared to that calculated assuming the PJ acts as a steady jet.

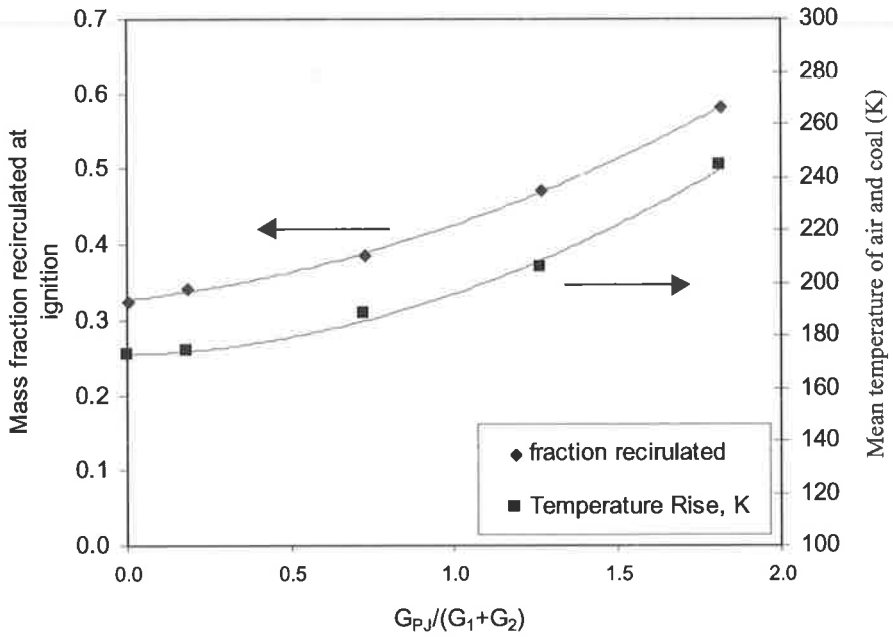

Figure 7.5 Effect of the mass of entrained ERZ gases at ignition (calculated by Equation 7-8) on the mean temperature rise of the combined PJ, primary, secondary air, ERZ gas and coal mixture in 2.5 MW flames. The flames are the first five listed in Table 6.3, which have 80PJ flow-rates of 25, 125, 250, 275 and 500 kg.hr^{-1}, respectively.

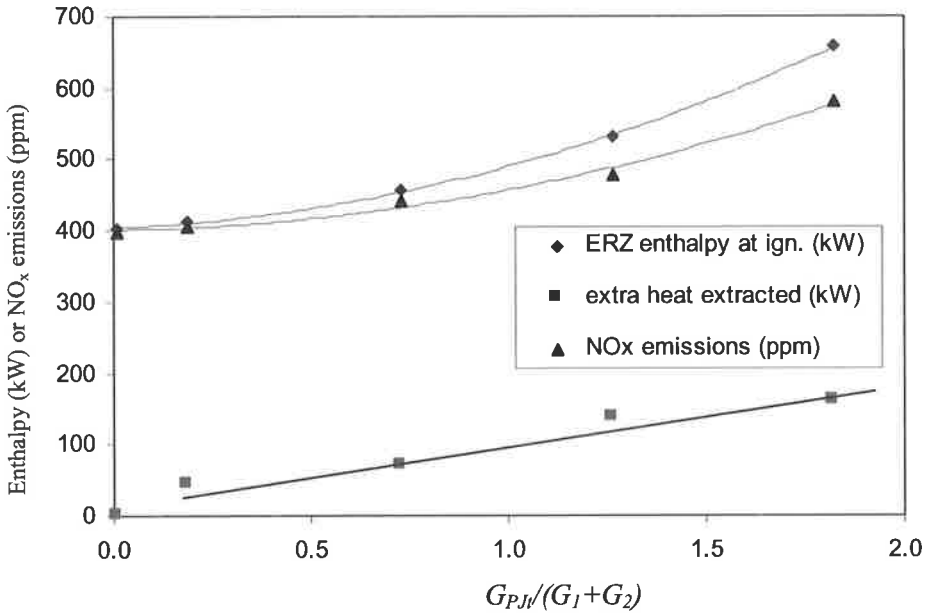

Figure 7.6. Correlation between the calculated enthalpy of ERZ gases and measured NO_x emissions from 2.5 MW flames with 80PJ flow-rates of 25, 125, 250, 275 and 500 kg.hr^{-1}. The mass of ERZ gases and flue gas temperature were used to calculate the ERZ enthalpy. Also shown is the additional heat extracted, in excess of that extracted by the flame with $G_{PJ}/(G_1+G_2)$ = 0.007, through furnace walls and by cooling loops. The additional heat extracted was calculated from the flue gas sensible heat and flue solids burnout data.

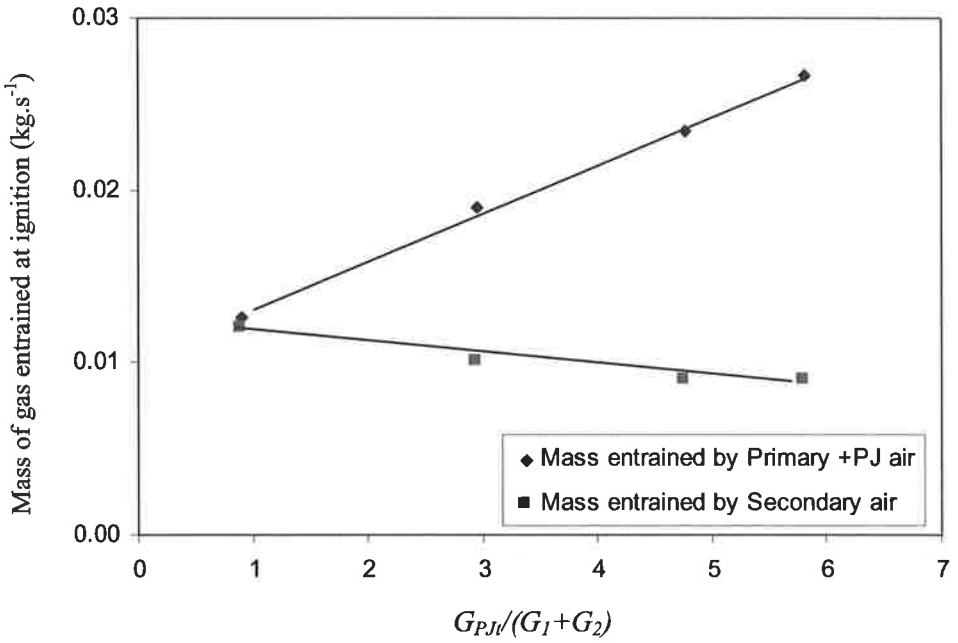

Figure 7.7 The effect of 19PJ momentum on the calculated mass of gas entrained by the combined 19PJ-primary flows and the secondary flow (at 500°C) in 130 kW flames. Entrainment is calculated using Equation 7-8.

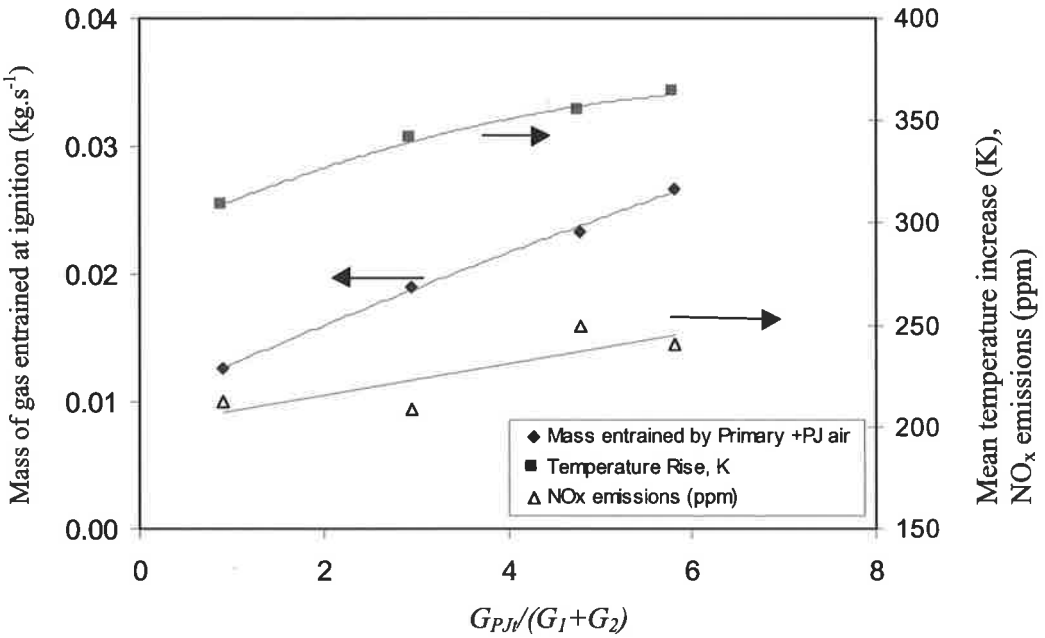

Figure 7.8 Correlation between the mass of ERZ gas and secondary air, entrained by the combined 19PJ-primary stream (calculated using Equation 7-8), measured NO_x emissions, and the calculated increase in the mean temperature, due to entrainment of hot gases, of the combined 19PJ-primary stream at the ignition distance. Data is for 130 kW flames with secondary air preheated to 500°C.

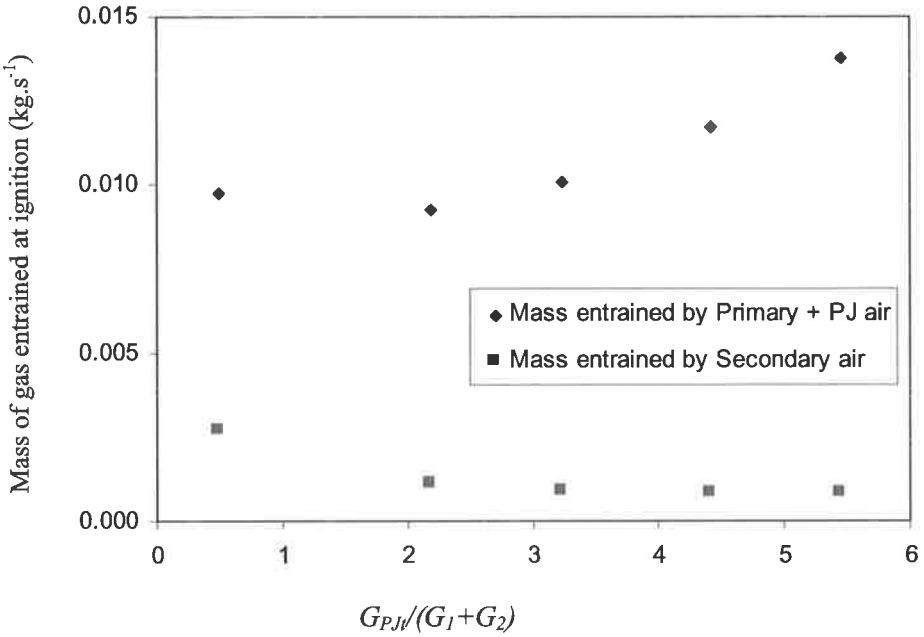

Figure 7.9 The effect of 10PJ momentum on the mass of ERZ gas entrained by the secondary flow, and the mass of mixed ERZ gas and secondary air entrained by the combined 10PJ-primary flows. Entrainment is calculated using Equation 7-8. Data is for 130 kW flames with secondary air at 15 °C.

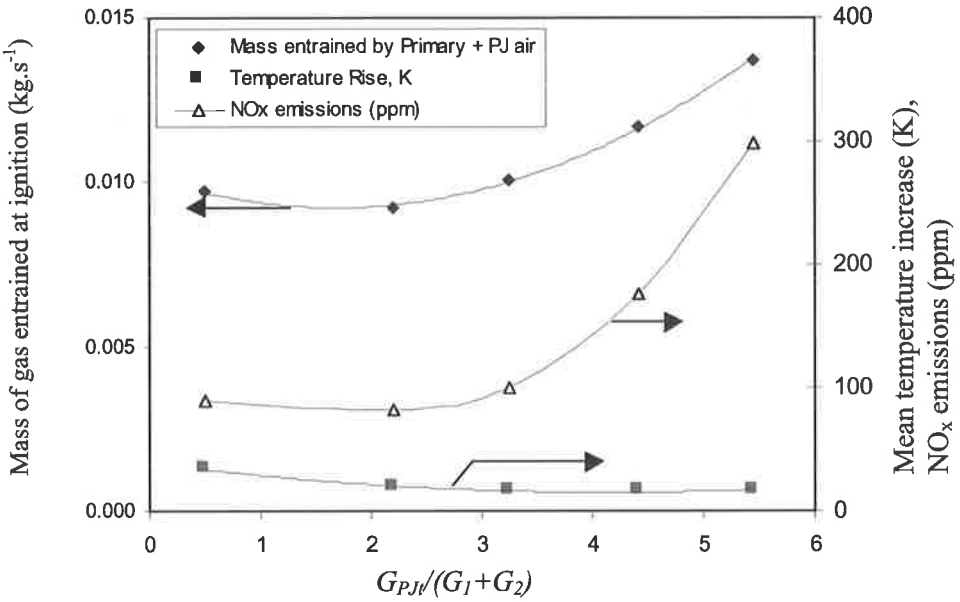

Figure 7.10 Data for 130 kW flames with secondary air at 15°C.
(a) the mass of ERZ gas and secondary air, which is entrained by the combined 10PJ-primary stream (calculated using Equation 7-8)
(b) NO_x emissions
(c) the increase in the mean temperature of the combined 10PJ-primary stream at the ignition distance (due to entrainment of pre-heated gases)

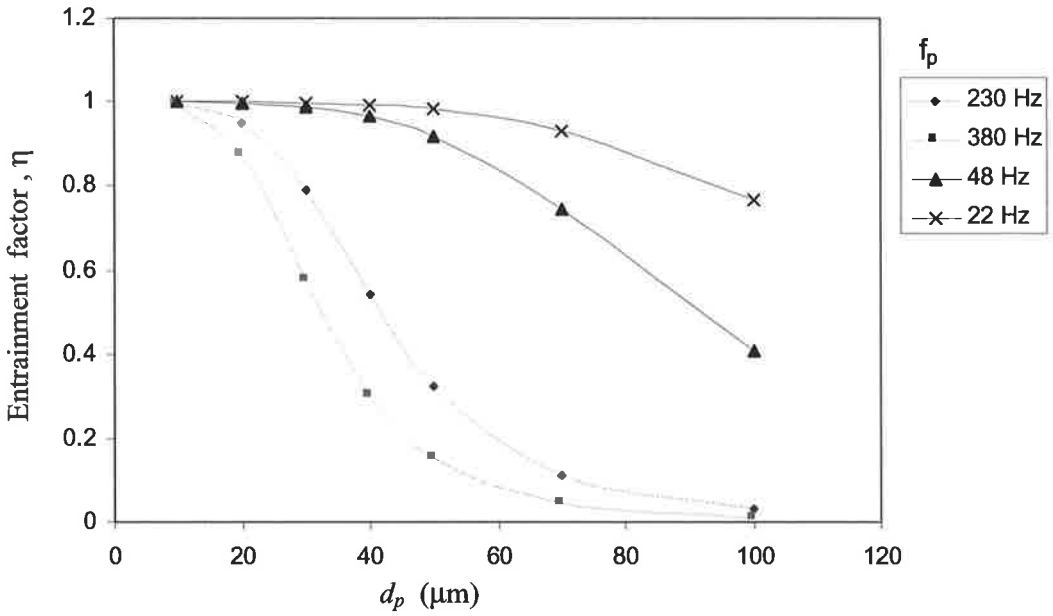

Figure 7.11 Effect of precession frequency and particle size on the entrainment factor (defined by Equation 5-19). The precession frequencies are for choked flows through PJ nozzles with chamber diameters, D, of 10 mm (380 Hz), 19 mm (230 Hz), 80 mm (48 Hz) and 350 mm (22 Hz)

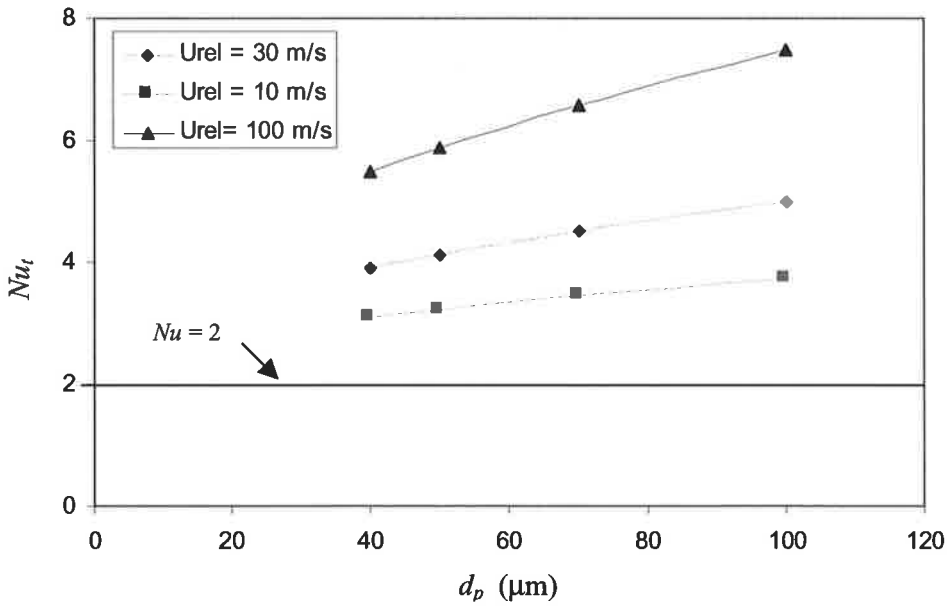

Figure 7.12 Effect of fluctuating slip velocity, U_{rel}, and particle size, d_p, on the fluctuating Nusselt number due to precession, Nu_t.

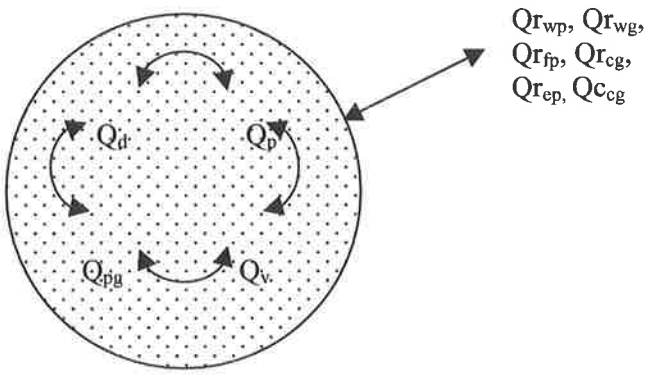

Qc_{cg} = Convective heat transfer between surface of cluster and surrounding gases (W)
Qr_{cg} = Radiative transfer between the cluster gas and surrounding gases (W)
Qr_{wp} = Radiative transfer between the furnace walls and particles in the cluster (W)
Qr_{wg} = Radiative transfer between the furnace walls and cluster gas (W)
Qr_{fp} = Radiative transfer between the flame and particles in the cluster (W)
Qr_{ep} = Radiative transfer between the cluster particles and the entrained flow (W)
Q_d = Heat of devolatilisation (W)
Q_v = Rate of heat release by volatile matter combustion (W)
Q_p = Rate of heat release by solid particle combustion (W)
Q_{pg} = Rate of convective heat transfer between particles and gas within a cluster (W)

Figure 7.13 A schematic representation of energy exchange within a large spherical particle cluster.

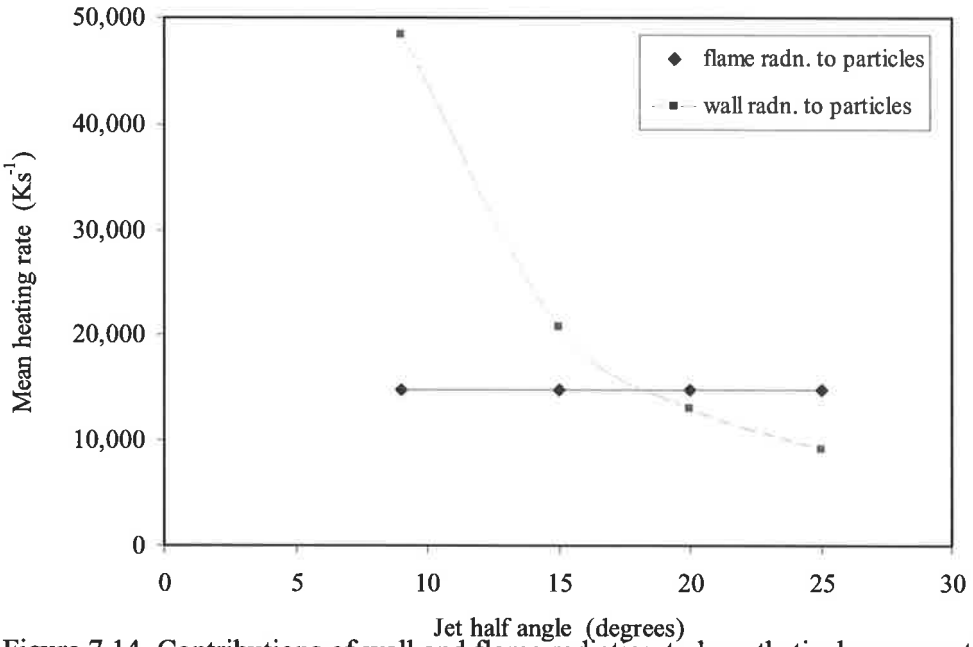

Figure 7.14 Contributions of wall and flame radiation to hypothetical mean particle heating rates of the entire particle cloud in the pre-ignition region, $Qr_{wp}/(NM_pC_p)$ and $Qr_{fp}/(NM_pC_p)$, as a function of jet half angle.

The calculations were made using Equations 5-9 and 5-10 to calculate wall and flame radiative heating, respectively. The pre-ignition region is assumed to be a single uniform conical particle cloud extending from the burner exit to the flame front (see Figure 7.15). Particles are assumed to have a number mean diameter of 10μm. The cloud is assumed to have a mean particle concentration of 0.2 kgm^{-3}. The radiation view factor from the flame front to the cloud is assumed to be 1. The cloud absorptivity was estimated, using Equation 5-7, as that of a spherical cloud with diameter equal to the typical ignition distance of the 130 kW flames (100 mm), ie. the ignition distance is fixed, independent of jet half angle. Other assumptions were; flame temperature, 1500 K, mean particle temperature, 300 K, and flame emissivity, 0.8. The particle cloud is assumed to have a uniform temperature and to be heated uniformly.

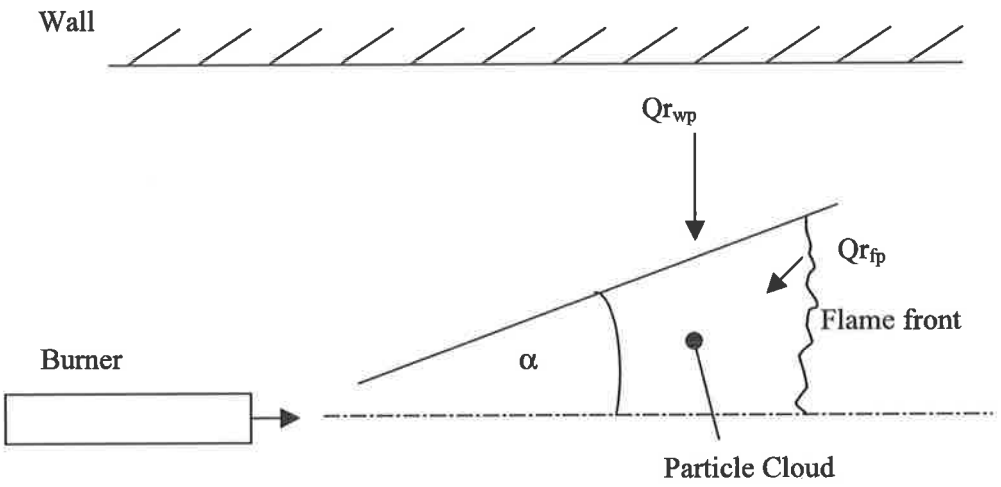

Figure 7.15 Conical particle cloud and flame front, showing radiant heating mechanisms. The terms, Qr_{wp} and Qr_{fp} (W), represent the radiant heat transfer rate from the wall and flame to the particle cloud, respectively.

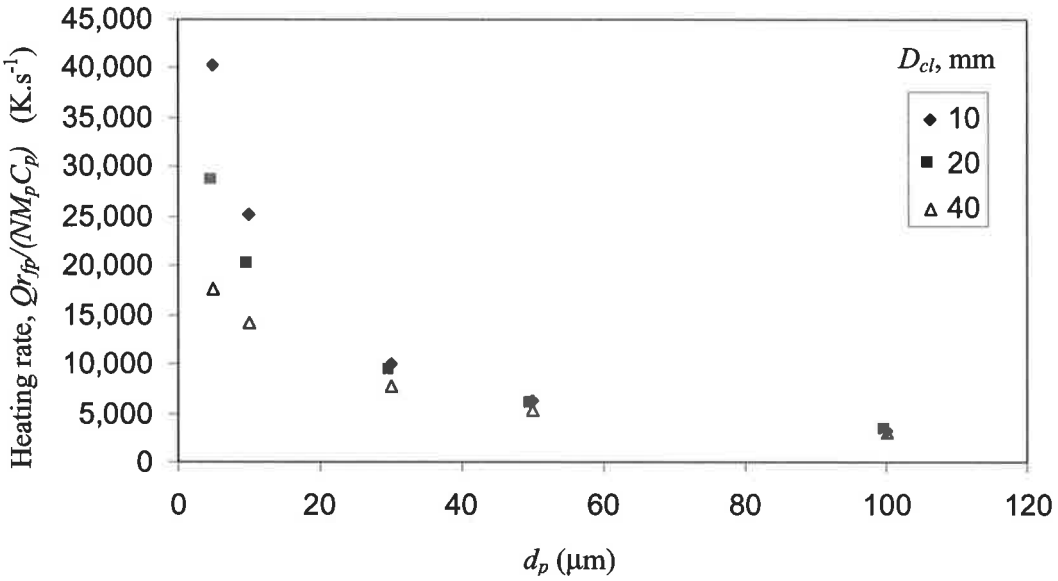

Figure 7.16 Calculated effect of particle size and diameter of particle clusters on the heating rates of particles, due to flame radiation. Clusters are assumed to be spherical. Particle temperatures are assumed to be uniform throughout the cluster. Clusters are assumed to be located near to the flame front so that attenuation of radiant heating by other clusters is ignored. A constant particle concentration of 0.2 kgm^{-3} is assumed.

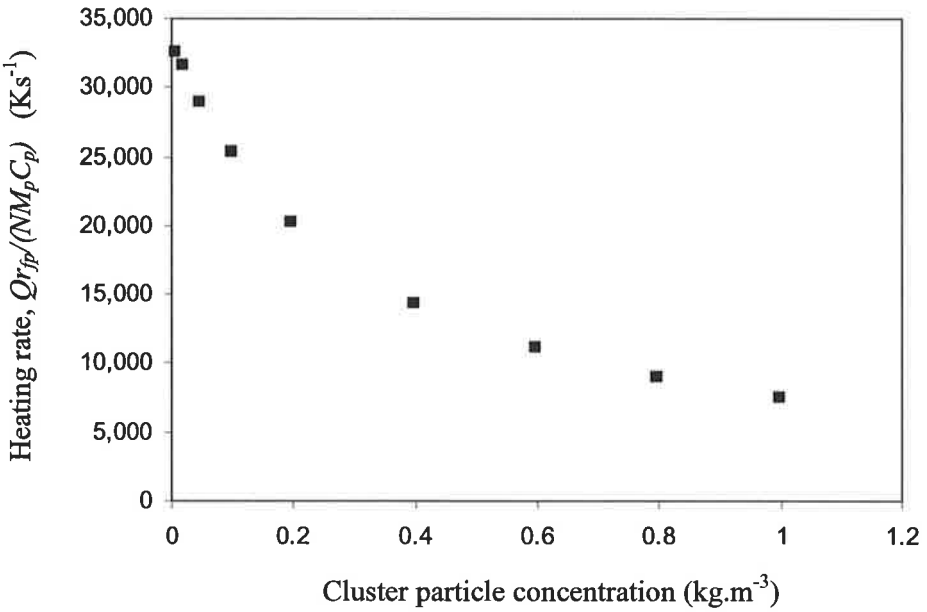

Figure 7.17 Calculated effect of particle concentration on the heating rates of 10 μm particles, due to flame radiation. Clusters are assumed to be spherical and 20 mm diameter. Particle temperatures are assumed to be uniform throughout the cluster. Clusters are assumed to be located near to the flame front so that attenuation of radiant heating by other clusters is ignored.

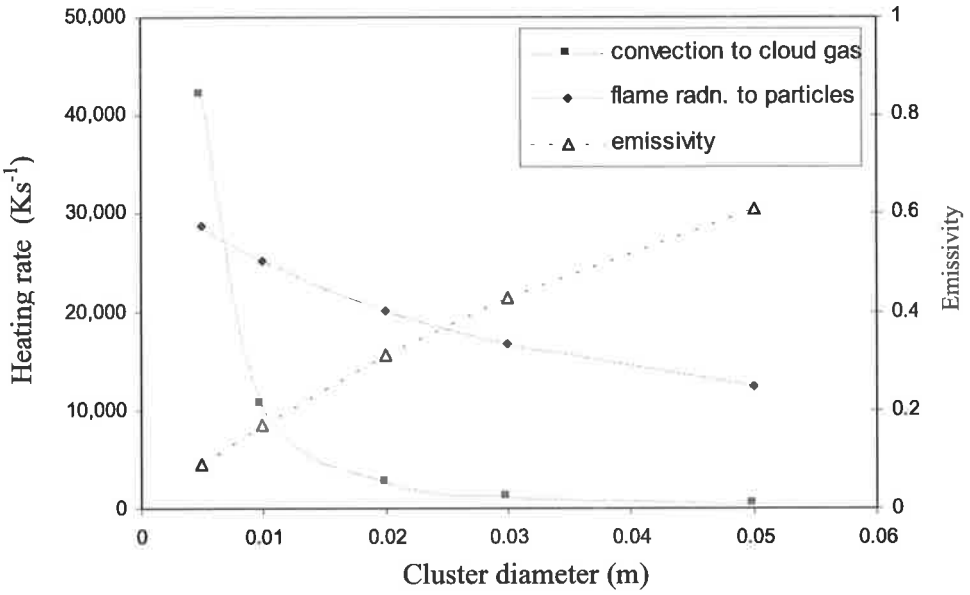

Figure 7.18 Calculated effect of cluster diameter on cluster emissivity and heating rates. Particle temperatures are assumed to be uniform throughout a cluster. Clusters are assumed to consist of 10 μm particles with a particle concentration of 0.2 kgm^{-3}. The emissivity is given by Equation 5-7. The heating rate due to flame radiation $Qr_{fp}/(NM_pC_p)$ is given by Equation 5-10. The heating rate due to convection from hot gases, $Qc_{cg}/(M_gC_g)$, is given by Equation 7-14. It is assumed that the gas in contact with the cluster has a temperature 1000K higher than the cluster, that the cluster gas has negligible motion relative to the surrounding gas, so that, $Nu_{cl} = 2$, and that no mass transfer occurs between hot gas and the cluster.

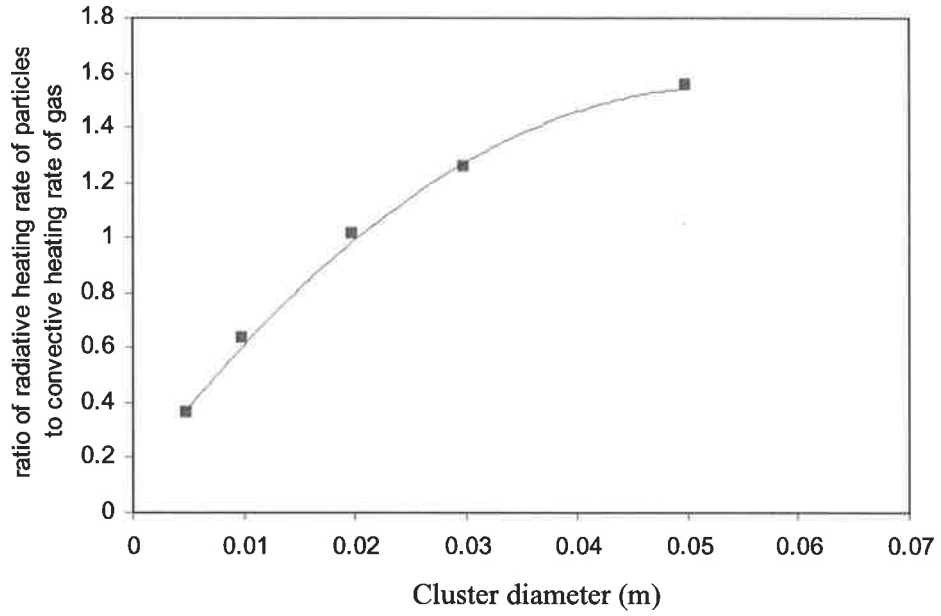

Figure 7.19 Calculated effect of cluster diameter on the ratio of radiative heating rate of particles to convective heating rate of gas within clusters. Clusters are assumed to consist of 10 μm particles with a particle concentration of 0.2 kgm^{-3}. Cluster temperature is assumed to be uniform. The heating rate due to flame radiation $Qr_{fp}/(NM_pC_p)$ is given by Equation 5-10. A temperature increase of 200°C is assumed to occur due to convective heating in a time controlled by the large-scale mixing rate.

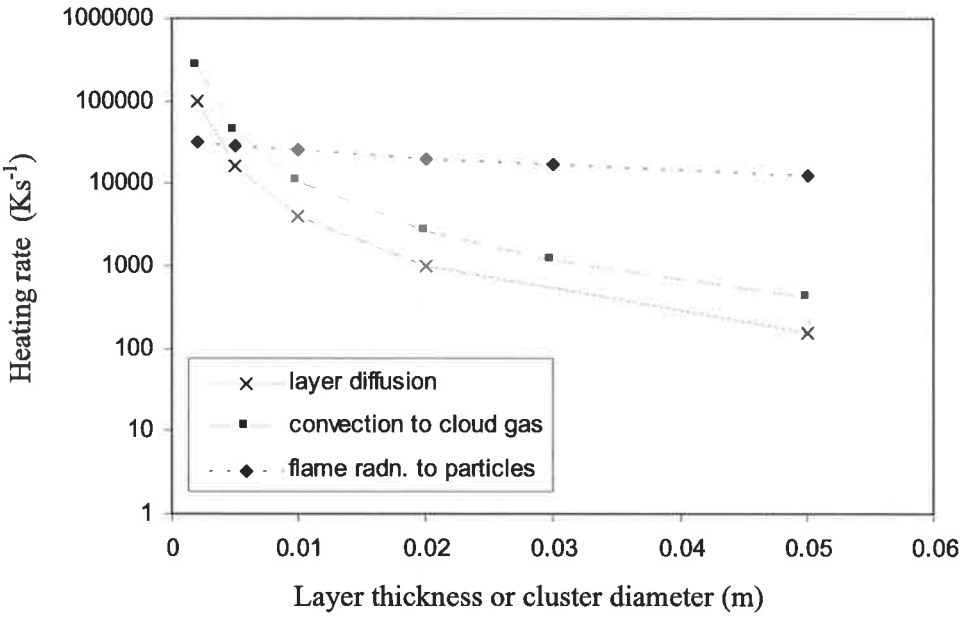

Figure 7.20 Calculated heating rate of layers of fluid by laminar diffusion, assuming a temperature gradient of 200°C across the layer, using Equation 7-19. Data is calculated using Equation 7.18. The laminar diffusivity, D, is assumed to be that of air at 500°C. Also shown, for comparison, are the heating rates of particles in spherical clusters by radiation and of gas in spherical clusters by convection (from Figure 7.18).

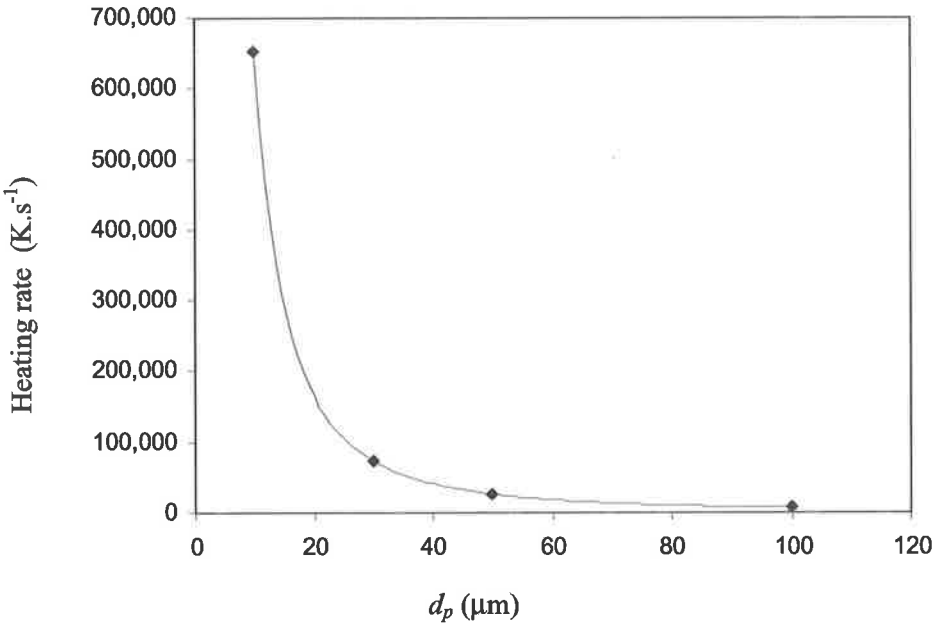

Figure 7.21 Calculated heating rate of individual particles exposed to gas 200°C hotter than the particles. This calculation was performed using Equation 7.15 to evaluate Q_{pg}. Particles with $d_p \leq 25\mu m$ are heated at rates of $\geq 100{,}000\ Ks^{-1}$, which is greater than the heating rate of 2mm layers by laminar diffusion (Figure 7.20).

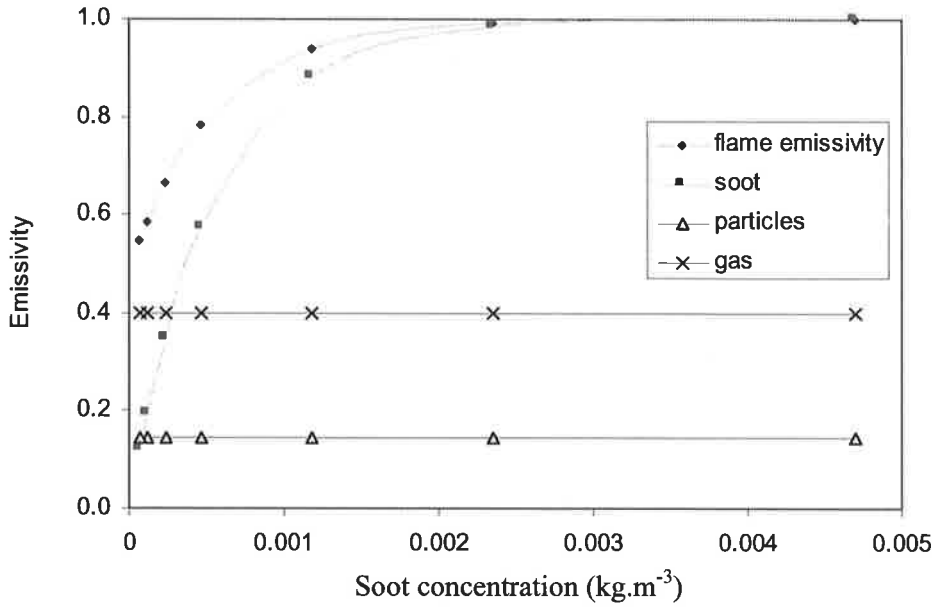

Figure 7.22 Calculated total flame emissivity based on conditions that apply in the 2.5 MW flames, as a function of soot concentration. Flame radiation is calculated by Equation 2-3, ie. $\varepsilon_f = 1-(1-\varepsilon_g)(1-\varepsilon_s)(1-\varepsilon_p)$, where $\varepsilon_{soot} = 1-\exp\left(-1.24x10^{-3}(C/\rho)TL\right)$, $\varepsilon_p = 1-\exp\left(-1.5CL_b/\rho_p d_p\right)$, and the combined gas emissivity at 1500 K is approximated at 0.4 by use of the Hadvig plot (Sarofim and Wall, 1980).

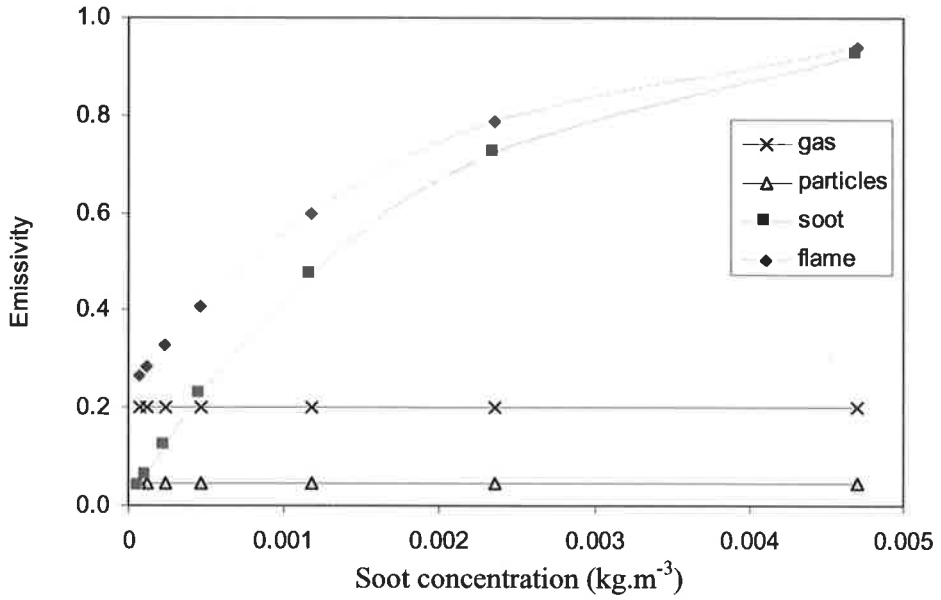

Figure 7.23 Calculated total flame emissivity based on conditions that apply in the 130 kW flames, as a function of soot concentration. Values calculated as for Figure 7.22, but the combined gas emissivity (at 1500 K) is reduced to 0.2 due to the shorter beam length at 130 kW scale.

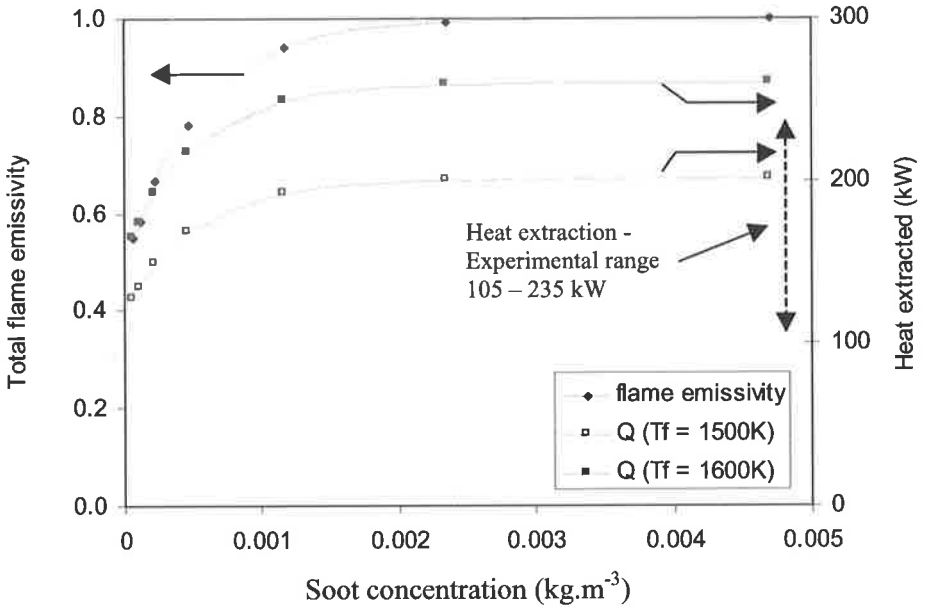

Figure 7.24 Calculated effect of soot concentration on flame emissivity and the calculated net radiant energy transferred from 2.5MW flames to a single metal cooling loop. The net energy transferred was calculated using Equation 5-18, assuming that the metal surface is blackened and has an emissivity of 0.7. The metal tube surface area is 1 m^2. The calculation was performed for flame temperatures of 1500K and 1600K.

Chapter 8 Conclusions and Future Work

8.1 Conclusions

8.1.1 Introduction

The key question tested in the present work is *whether enhancement of large-scale turbulent motions within a two-phase jet can beneficially influence pulverised fuel combustion, and in particular, whether it can improve flame stability, heat release and/or reduce NO_x emissions.* A range of experimental techniques, each addressing a specific hypothesis by modelling a particular aspect of the dominant physics or chemistry of full-scale flames, was used to explore this question. FPJ flows were used as the means of promoting the large scales of turbulence in both reacting and non-reacting experiments. Here, conclusions are presented in the context of each hypothesis proposed in Section 1.8.

8.1.2 The influence of precession on the structure of annular flows

The first hypothesis, introduced in Section 1.8, stated *"that the structure of the turbulence in an annular jet used to transport coal particles can be altered, here by a centrally located precessing jet flow, to enhance large scale turbulence at the expense of small scale turbulence"*. The hypothesis was formulated in this way because annular primary air channels are common in industrial burners, and because it was considered that introducing a PJ flow on the centre-line of a surrounding annular primary flow would provide the greatest effect on the primary flow.

Experiments conducted in water, using planar laser induced fluorescence visualisation, provided support for the above hypothesis. The effects of a range of alternative central mixing jets, all with equal exit cross-sectional areas, on the structure of a surrounding annular jet were assessed. The alternative central mixing nozzles were designed as steady analogues of a 19mm PJ nozzle. Each central jet, including the 19PJ, was operated with a ratio of exit velocity to annular velocity = 4.5, and a momentum flux ratio, $G_{MIX}/G_1 = 2.56$. The 19mm FPJ flow produced the largest "coherent" structures of any of the central mixing jets, and increased the half width, $r_{1/2}$, of the annular flow by 66%. In contrast the other central mixing jets decreased the half width of the annular jet by 7 – 32 %. Note that qualitative images show that large motions span the entire jet, and hence half width measurements quantify structure size. The inability of the steady jets to enlarge the structure of turbulence in the annular jet illustrates that it is the precession of the PJ flow, and not just the large initial spread of the PJ flow, that is responsible for enlarging the structure of turbulence.

A reduction in mean strain rate is indicative of an increase in the fraction of energy associated with large-scale motions. The characteristic strain rate of the 19PJ-annular water flow with $G_{PJe}/G_1 = 2.56$, was 5 s^{-1}, a significant reduction from the characteristic strain rate of the annular flow alone, which was 10 s^{-1}. In contrast, the steady jets all increased the strain rate of the annular flow from 10 s^{-1} to values in the range 17 to 32 s^{-1}.

The influence of the strength of PJ mixing was investigated by varying the momentum ratio, G_{PJe}/G_1. Significant enhancement of the large-scale structure in 19mm PJ - annular flows, measured as an increase in jet half width by up 66% as described above, was observed for momentum ratios $G_{PJe}/G_1 > 0.8$. However 10mm PJ-annular flows produced mean half widths similar to those of the annular jet for $G_{PJe}/G_1 < 18$, increasing by only 26% above that of the annular flow for momentum ratios, $G_{PJe}/G_1 > 18$. Likewise, strain rates of the 10mm

PJ-annular flows were similar to those of annular jets for $G_{PJe}/G_1 < 2$. The reason for these differences is that the measurements are indicative of the combined effects of PJ and annular jets. The ratio of PJ nozzle diameter to annular channel outside diameter is 0.31 for the 10mm PJ-annular arrangement, meaning that the effect of the 10mm PJ is largely confined to the region taken up by the annular flow. In contrast the ratio of PJ nozzle diameter to annular channel outside diameter is 0.58 for the 19mm PJ-annular arrangement, making it easier for large structures generated by the 19mm PJ to penetrate through the surrounding annular flow.

8.1.3 Particle response to turbulence

The second hypothesis introduced in Section 1.8 stated *"that clustering of pulverised coal particles within jet flows can be significantly increased by enhanced large-scale turbulence and reduced small-scale turbulence, here generated by precession"*. The hypothesis was investigated in ambient temperature, non-reacting, air jets, and in flames.

Flow visualisation techniques were used to determine the mechanisms of preferential concentration, or clustering, and to quantify its extent. Particles in ambient temperature FPJ-annular flows are deduced to be entrained towards the centre-line of the flow in the NBZ ($\frac{x}{D} < 2$) by drag forces and then to form clusters in the region $1 < \frac{x}{D} < 5$ due to the action of large-scale turbulent motions. Small particles (d_p < 30 μm) are deduced to be able to follow the large-scale motions generated by a 19mm FPJ flow and display preferential concentration within the large-scale motions in the near field. Larger particles, while not precisely following the flow, can be "clustered" into regions on the boundaries of large fluid structures downstream from the NBZ. Laser sheet visualisation in the pre-ignition and ignition regions of 2.5 MW flames showed qualitatively, that particle spreading rates and clustering effects persist in large PJ flames (using 55mm and 80mm FPJ nozzles) with high particle loadings, and are enhanced by increasing PJ momentum in the range $0 < G_{PJt} / G_1 < 6$. Video images of a 19mm PJ, 130 kW flame, in which an annulus with outer diameter of 48.5 mm, as opposed to the usual 32.5 mm was used, suggested that a significant fraction of particles injected remotely from the PJ flow were not subject to clustering forces. This finding implies that maximising the ratio of PJ nozzle to annular channel diameter enhances clustering effects.

Particle clustering effects were quantified in non-reacting 19mm PJ-annular air jets by dividing photographic images of particles into cells and counting particles in individual cells. Glass beads with a size distribution similar to industrial PF distributions were used. When an annular velocity of 9.8 ms^{-1} was used, an increase in the momentum ratio, across the range $0 < G_{PJe}/G_1 < 7.2$, caused an increase in the ratio of standard deviation / mean number of particles per cell, from 0.4 to 0.8. Higher momentum ratios, achieved by use of a lower annular velocity of 2.4 ms^{-1}, did not increase the variation in particle concentration further. The use of a wide particle size distribution and inaccuracies in estimation of fluid time-scales prevented accurate determination of Stokes numbers in these flows.

The extent of variation in particle velocities, due to the influence of large structures, is an indirect measure of preferential concentration effects, and can provide evidence of

preferential concentration effects under conditions such as high particle loading, or in flames, where quantitative visualisation techniques have not been developed. Investigations (reported in Appendix 3) were conducted under ambient conditions in a non-reacting 19mm PJ-annular flow with $G_{PJe}/G_1 = 14.3$, and particle size distribution and mass loading typical of that of a PF flame. The r.m.s. axial and azimuthal particle velocities, determined by laser Doppler anemometry, were shown to be a factor of 2 higher than those in the annular flow alone. Similarly, in an 80mm, PJ-annular 2.5 MW PF flame with $G_{PJ}/G_1 = 2.9$, fluctuations in axial velocity were high, being approximately half the mean maximum axial velocity. These data provide evidence that precession enhances clustering effects under high particle mass loading conditions, and that these effects persist in flames.

A 1.5 mm diameter injector located adjacent to a 10 mm PJ nozzle was used to study the effect of St on particle spreading and clustering. In these flows the fluid time-scale was held constant, and particle time-scale, τ_p, was varied. The particle time-scale was determined unambiguously by using discrete particle size ranges, so that Stokes numbers could also be determined unambiguously. A parameter, which incorporates both the effects of the strength of PJ mixing and the Stokes number, was found to collapse the particle spread data for 46 and 80 μm diameter particles. The parameter is $(G_{PJe}/G_1)St^{-n}$, where $0.5 \leq n \leq 1$. Increased clustering effects can be expected to correlate with radial particle spread and consequently can also be expected to vary with $(G_{PJe}/G_1)St^{-n}$.

8.1.4 The influence of enhanced large scale mixing on PF flame stability and heat release

The third hypothesis introduced in Section 1.8 stated *"that control of the structure of jet turbulence, and hence particle clustering, can be used to improve flame stability and increase early heat release rates.* The hypothesis links flame stability and heat release because, in practice, flame ignition distances have a strong influence on the profile of heat transfer to furnace walls.

Flame Stability (Ignition)

The ignition distances of 130kW flames were reduced from $x_{ign}/D_{A,2} \sim 8$ to $x_{ign}/D_{A,2} \sim 4$, as PJ momentum was increased over the range $0 < G_{PJe}/G_1 < 2$, by application of up to 2% (for 10 mm PJ flames) or 5% (for 19 mm PJ flames) of the total air. In 2.5 MW, 80mm PJ flames particle-turbulence interactions and mixing time-scales are more representative of those that occur at full scale. Increasing 80PJ momentum in the range, $0 < G_{PJt} / G_1 < 6$, caused a four-fold reduction in ignition distance, from $\frac{x_{ign}}{D} = 20$ to $\frac{x_{ign}}{D} = 5$, or from $x_{ign}/D_{A,2} = 6.8$ to $x_{ign}/D_{A,2} = 1.7$.

The augmentation of particle and volatile matter clusters in PJ flames is deduced to be partly responsible for the observed reductions in ignition distance. These clusters dominate the flow and provide an ignition source for other particles. Combustion of volatile matter is deduced to commence on the cluster boundaries and to proceed towards the cores of clusters. These deductions are supported by visualisation of coal particles in open gas flames (Appendix 4), where the particle clustering effects is seen to be associated with the production of dense clusters of burning volatile matter. The use of high speed photography in these open gas flames also showed that clusters in PJ flames have convection velocities that are typically a factor of 3 slower than those of particles in the core of a base-line mono-channel flame. This reduction in convection velocity in PJ flames is also deduced to aid stabilisation.

The action of precession in reducing local axial velocities of fluid structures and clusters was further demonstrated in non-reacting studies. In water flow investigations, the mean convection velocity of structures in a 19mm PJ - annular flow with $G_{PJe}/G_1 = 2.56$, were 12% lower than those in the annular flow alone, despite an increase in total flow-rate. In contrast, the jets used as steady analogues of the PJ, all caused increases the mean convection velocity of the annular flow, in the range of 40 – 225 %. In addition to the mean

effects, the 19mm PJ also caused some large structures to penetrated through the annular flow and became "isolated" from the bulk flow. These structures proceeded downstream with lower velocity than the mean flow. These "isolated" large structures were deduced to result from the large cycle to cycle variability in precession motion and are partly responsible for the greater variability in structure convection velocities observed in PJ flows than in steady jet flows. It is hypothesised that the "isolated" structures may contribute to the measured reduction in the ignition distance by increasing the residence time available for particle heating. Similarly, greater variability in axial particle velocities was found in the non-reacting PJ-annular air flow with G_{PJe}/G_1 = 14.3, than in the annular flow alone (Appendix 3). The implication of these findings is that the fraction of fluid and particles with low instantaneous axial velocity, conducive to stabilisation of flames, is increased by the action of precession.

Sensitivity analyses were performed to determine the most significant influences on particle heating rate in the pre-ignition region, and by implication ignition distance. The analyses showed that, if the gas temperature in a cluster is assumed to be uniform, increased heating rates by radiation, convection and laminar diffusion mechanisms occur with decreasing cluster size. The corollary of this finding is that, if the assumption of uniform cluster temperature is relaxed, the outer layers of large clusters are heated preferentially to the cluster cores. Since precession increases the size of clusters, this corollary supports the hypothesis that ignition occurs in the outer layers of structures and combustion then propagates into the fuel-rich interior. In this way heating of particles can be concentrated in the outer layers of large clusters, which can therefore reach the ignition temperature more rapidly than would be possible if the entire flow was heated uniformly.

Laser Doppler velocity and in-flame temperature measurements were used to show that an increase in the sensible enthalpy recirculated in the external recirculation zone of 2.5 MW flames as G_{PJt}/G_1 was increased from 0 to 2.9, contributed to particle heating in the pre-ignition region. The scaling parameter, $[G_{PJt}/(G_1+G_2)].St^{-0.5}$, provides reasonable collapse of the ignition distance data from the 130 kW and 2.5 MW experiments, despite departures from thermal and kinematic similarity between scales. The scaling parameter models the large scale clustering and fluid mixing effects which control ignition distances. It is used to predict that the reductions in ignition distance observed at the experimental scales will occur using lower PJ nozzle pressures at full scale.

Flame Heat Release

130 kW PJ flames demonstrated high early heat release with wall temperatures near the burner in excess of 100°C higher than most other burners tested, and slightly higher than that generated by a multi-channel burner. Increases in G_{PJ}/G_1 caused both the ignition position and the heat release profile to move closer to the burner. In 2.5 MW flames, increases in G_{PJ}/G_1 from 0 to 2.9 caused the position of peak heat flux to move closer to the burner by a similar distance to the reduction in ignition distance. Increased PJ momentum also caused the magnitude of the peak heat flux to increase from 195 to 230 kWm^{-2}. A corresponding reduction in flue gas temperature, by 100°C, demonstrated a substantial increase in total heat transmitted through the furnace walls and cooling tubes. A reduction in peak in-flame temperature from 1501°C to 1450°C also occurred as G_{PJ}/G_1 was increased from 0 to 2.9, showing that the additional heat release was not due to the higher flame temperatures.

Visualisation of coal particles in open gas flames (Appendix 4) supports the hypothesis that enhanced clustering may increase sooting within fuel-rich particle clusters and hence flame emissivity. A sensitivity analysis shows that the formation of additional soot in fuel-rich clusters can increase the total emissivity of 130 kW flames from 0.25 to 0.9, and of 2.5 MW flames from 0.55 to 1.0. These increases in emissivity can explain the majority of the increase in mean heat extraction observed experimentally. For example the heat extracted by a single water tube in the 2.5 MW furnace can increase by 35% due to increased emissivity associated with fuel-rich combustion in large clusters. Consideration of the eddy-dissipation model shows that increased heat transfer may also be associated with increased volatile matter combustion rates, relative to mono-channel flames.

8.1.5 The influence of enhanced large scale mixing on NO_x emissions

The fourth hypothesis introduced in Section 1.8 stated *"that control of the structure of jet turbulence, and hence particle clustering, can be used to control NO_X emissions"*. Although NO_x emissions are influenced by stability and heat release characteristics of flames, they are also influenced by other factors and as such are considered separately. In the conclusions to follow, CO emissions and coal burnout data are considered alongside NO_x emissions.

Flames from the 10PJ and 19PJ burners, with G_{PJf}/G_1 = 3.9 and 8.5 respectively, produced lower NO emissions (82 and 85 ppm respectively) than any of the other 130 kW flames, which produced NO emissions in the range 150 – 190 ppm. Flue gas NO emissions from a base-line mono-channel annular flame, with lower total momentum than the PJ flames, was 190 ppm. CO emissions from the 10PJ and 19PJ flames were 310 and 190 ppm respectively, significantly below those of the mono-channel flame (830 ppm). The PJ flames also demonstrated improved coal burnout compared to the mono-channel flame. A flame employing six angled, steady jets, with similar total momentum to that of the PJ flames, produced NO emissions of 164 ppm and CO emissions of 340 ppm. From these findings, it can be seen that PJ flames utilise momentum to alter mixing in a manner conducive to the simultaneous reduction of NO and CO emissions. Increasing the quantity of precessing air beyond the minimum required for flame stabilisation, decreases CO emissions from 10PJ flames. Further increases in 10PJ air flow-rate increases NO emissions to in excess of 200ppm for $G_{PJf}/G_1 > 7$. The 10PJ and 19PJ burners produce similar NO emissions for the same PJ momentum in the range $G_{PJf}/G_1 < 7$, despite different PJ flow-rates. Consequently it can be concluded that the momentum ratio is the dominant parameter in determining NO emissions of PJ flames.

In 2.5 MW PF flames, NO_x emissions increased from 400 to 580 ppm (0% O_2), and coal burnout increased from 94.4 to 97.8% as the PJ momentum was increased in the range $0 < G_{PJf} / G_1 < 6$. These NO_x and burnout results are partly due to the combination of increasing air entrainment rates with increasing G_{PJf}/G_1 and the fact that it is not possible to control wall temperatures of the furnace to a fixed value with changes in flame heat flux. Calculations show that increasing G_{PJf}/G_1 also increases the ERZ gas enthalpy, a factor that is strongly dependent on the furnace geometry and confinement, and is expected to be less significant in rotary kilns. Another experiment in which the PJ flow rate was held constant and the primary and secondary air flow-rates were varied, showed that NO_x emissions increased strongly with increases in secondary air momentum. This finding suggests that the

high secondary air velocity used in the 2.5 MW flames (~ 35ms^{-1}) contributes significantly to the observed NO_x emissions in all the 2.5 MW flames.

The relative diameter of the PJ nozzle to the annular channel is also important in determining NO emissions. A 19PJ, 130 kW flame employing a large annulus, which reduces the influence of the precessing flow on a significant fraction of outlying particles, caused an increase in NO emissions by 70 ppm compared to the standard 19PJ flame, at equal primary air flow-rate. For this reason it is hypothesised that the formation of clusters and subsequent combustion of volatile matter in a localised fuel-rich regime is crucial to the production of low NO_x emissions in PJ flames.

It is hypothesised that the generally low NO emissions exhibited by PJ flames are due to fuel-rich combustion of evolved volatile matter in the cores of clusters. It is also suggested that the low CO emissions occur because the PJ flow produces more complete, albeit large-scale, mixing between secondary air and PF. These hypotheses were formed after considering the conclusions detailed above, together with in-flame gas concentration, temperature and solids composition data. By considering all the data it was deduced that combustion of volatiles is initiated on the outside of clusters, and propagates inwards. Further insight was provided by the eddy dissipation model showed that precession can increase volatile matter reaction and NO_x formation rates in the regions of small-scale structures and "layered" structures at the edges of large clusters. Concurrently, combustion can propagate at a slower rate through large clusters. These effects amount to a local staging effect within large clusters.

8.2 Further work

The current work has provided support for the hypotheses introduced in section 1.8. and has shown that enhanced large scale mixing has potential for application in the design of PF burners for rotary kilns. Suggestions for further work, which may extend the understanding established by the present work, are detailed in the sections to follow. Further work should focus on improving the quantification of the mechanisms identified in the current work, and on providing additional data, which may improve the understanding of these mechanisms. Ideally, the data so obtained will be useful for the design of full-scale rotary kiln burners. The relevance of precessing jet mixing in other applications, such as swirled boiler flames where the aerodynamics are vastly different to rotary kiln flames, should also be investigated using quantitative techniques. Section 8.2.1 details specific objectives for future work, and Section 8.2.2 outlines suggested methods of investigation.

8.2.1 Specific objectives of further work arising from the present work

A. Particle – fluid interactions

- Gain a greater understanding of the mechanisms responsible for enhanced clustering in a range of flows, in particular, in the momentum driven region of PJ flows, $x/D \leq 2$, and in the region of large structures in PJ flows, $x/D > 2$.
- Further quantify preferential concentration effects produced by precession in a range of flows. Quantify the extent to which the preferential concentration effects, measured in cold flow, persist in flames.
- Determine the most appropriate characteristic velocity scale to be used in the calculation of Stokes number for the two regions $x/D \leq 2$ and $x/D > 2$. Refine the measurement technique for the characteristic velocities.
- Quantify the convection velocities and significance of "isolated" large structures in FPJ flows. Investigate the hypothesis that these "isolated" structures result from variations in cycle-to-cycle precessional motion. Investigate whether "isolated" structures trap particles and so increase their residence times relative to the mean flow. Determine the influence of "isolated" structures on flame ignition distance.
- Better assess the validity of the parameter $[G_{PJ}/(G_1+G_2)]St^{-0.5}$ as a means of predicting the effects of momentum, velocity, particle size and scale on preferential concentration, spanning conditions representative of a rotary kiln environment.

B. Flames

- Measure ignition distance, NO_x and CO emissions and heat release profiles under conditions representative of rotary kilns. Assess the influence of clustering effects and/or large scale mixing on these flame properties. Assess the validity of the parameter $[G_{PJ}/(G_1+G_2)]St^{-0.5}$ as a means of scaling flame ignition distance. Adapt the parameter to allow scaling of heat flux and emissions data by taking into account chemical reaction and temperature effects.
- Determine the entrainment rates of secondary air and ERZ gases by unconfined PJ-annular flows as a function of x/D and modify Equation 7-8 as necessary. Determine the effect of confinement on entrainment rates and ERZ patterns of PJ-annular flows.
- Visualise the ignition process in PJ-annular PF flames to further explore the proposed ignition and combustion propagation mechanism, ie. ignition on the boundaries of large clusters and flame propagation inwards.

8.2.2 Suggested methods for future investigations

- To assess particle-fluid mixing issues, laser sheet flow visualisation and quantitative measurements of preferential concentration may be performed. The dependence of the extent and nature of clustering on the following variables should be quantified:
    - PJ-annular geometry eg. varying ratios of $D/D_{A,1}$, $D/D_{A,2}$, D/D_2.
    - Geometries other than the PJ-annular arrangement, e.g. direct injection of particles through a PJ nozzle.
    - Momentum ratios of, PJ air, primary air, secondary air and external recirculation.
    - Particle size.
    - Particle mass loading.
    - The region of the PJ flow under investigation, i.e. two regions of particular interest (a) the region where the PJ deflects particles, $x/D < 2$, and (b) the region further downstream where the initial PJ velocity has decayed and the large structures formed have the greatest influence on particle motion.
- Differences in clustering effects produced by FPJ and MPJ flows should also be assessed to determine whether the MPJ can be used for further quantitative measurements. An MPJ can be used provide phase averaged velocity data (eg. by Particle Image Velocimetry, or Laser Doppler Velocimetry). The respective velocities of particles and structures can be measured as a function of structure position by alternately seeding the flow with tracer particles and larger particles, under the same phase averaged conditions. The same technique, using flow tracer particles, can be used to measure relative velocities between structures, or the convection velocities of structures, either of which may be the most representative characteristic velocity scale when PF sizes particles follow the flow reasonably well as is expected to occur at full-scale.
- Entrainment rates of combined PJ-annular flows can be measured in ambient conditions using the shroud technique of Ricou and Spalding (1961), or by velocity measurements. To determine the effect of confinement on entrainment rates and ERZ patterns, entrainment measurements and flow visualisation can be performed in ducts with varying D/D_{duct}.
- Experimental nozzles and burners may designed by scaling down from the 35 and 105 MW burners described in Chapter 6, taking into account the findings of the experiments suggested in section 8.2.1.
- A rotary kiln simulator can be used to assess the influence of known cluster parameters, such as particle concentration and cluster size, on flames. Flame tests should be

performed under conditions that maintain geometric, thermal and kinematic similarity with conditions in a typical real kiln. The NO_x emissions, heat extraction profiles and wall temperature profiles of flames with equal heat inputs can be compared by maintaining a constant flue gas temperature between flames. In principle, such conditions can be obtained by variable heat sinks (eg. using varying cooling water flow-rates) to produce equal total heat removal through walls. Concurrently, wall temperatures simulating those dictated by the endothermic clinkering reaction in real kilns can be maintained. However, as observed in Chapter 6, water-cooled heat sinks, located outside of the refractory, may provide little control of wall temperature. An alternative technique, which may be explored, is to adjust fuel and air inputs over a small range to maintain constant flue gas temperature and oxygen concentration.

Appendix 1. Measurement of PJ and annular air flow rates

A1.1 Pressure / flow calibration of 10PJ and 19PJ nozzles.

Figure A1.1(a) presents the measured pressure / flow characteristic of the 10 PJ nozzle (with 1.75mm diameter throat) used in the 130 kW combustion experiments reported in Chapter 5. Figure A1.1(b) presents the pressure / flow characteristics of the 19 mm PJ nozzle (inlet diameter 3.5 mm) used in the isothermal PJ-annular air flows reported in Chapter 4, and in the 130kW combustion experiments (Chapter 5). The calibrations in Figure A1.1 were obtained with a Fischer and Porter, 1-35-G-10 rotameter tube, fitted with a 1-GUSVT-611 float, which has a stated accuracy of ± 2% of full scale. Nozzle inlet pressures were measured using calibrated Bourdon tube pressure gauges, with a range of 0 -160 kPa (for the lower pressures) and 0-400 kPa (for pressures above 160 kPag).

Calculated characteristics for nozzles with ideal smooth contraction inlets are also shown in Figure A1.1. These characteristics were obtained by assuming (a) compressible flow through a truncated nozzle with an ideal smooth inlet, and (b) that the pressure inside the PJ nozzle chamber is atmospheric. The following equations (Roberson and Crow, 1980) are used.

The Mach number is given by:

$$M = \left(2/k - 1\right)^{0.5}\left[\left(P_t/P\right)^{(k-1)/k} - 1\right]^{0.5} \qquad \text{A1-1}$$

For M<1 the total temperature is given by:

$$T_t = T(1 + \frac{k-1}{2}M^2) \qquad \text{A1-2}$$

Equations A1-1 and A1-2 are used to calculate the restriction exit temperature, T, which is used to calculate the velocity at the restriction:

$$u = cM = \sqrt{kRT}.M \qquad \text{A1-3}$$

The mass flow rate is determined from the continuity equation, with the density at the restriction exit is given by:

$$\rho = \frac{P}{RT} \qquad \text{A1-4}$$

For M > 1, the mass flow rate is determined from;

$$\dot{m} = \frac{P_t A}{\sqrt{RT_t}} k 0.5 \left(2/k+1\right)^{(k+1)/2(k-1)} \qquad \text{A1-5}$$

Figure A1.1(a) shows that the calibrated flow-rates from the 10PJ nozzle are similar to, but slightly lower, than the calculated values. This is to be expected since the 10PJ nozzle has a conical inlet, which approximates an ideal smooth contraction. The 19PJ nozzle has an inlet that is only slightly tapered, and is similar to a square edged orifice, so that the actual flow-rates are significantly below calculated values (Figure A1.1b).

A1.2. Error analysis – 10PJ-annular and 19PJ-annular flow-rates and G_{PJ}/G_1

Fischer and Porter rotameters have a specified accuracy of ±2% of full scale. For the meter used to measure 10 and 19 mm PJ flow-rates this corresponds to 8.1×10^{-5} kgs^{-1}, or 8.0% and 5.6% of the minimum experimental 10PJ and 19PJ flow-rates respectively. (The minimum experimental 10PJ flow used in Chapter 5 is 1.016×10^{-3} kgs^{-1} - corresponding to a pressure of 100kPa(g), whilst that for the 19PJ is 1.445×10^{-3} kgs^{-1} - see Table 4.1). The pressure / flow calibration curves for the 10 and 19 PJ nozzles (Figure A1.1) can be used to assess whether such errors exists, or at least whether or not they are likely to be systematic or random. Figure A1.1 shows that the majority of data points, including the actual values used in the experiments in Chapters 4 – 6, fall on a smooth line of best fit. The maximum random error in PJ mass flow rate can be taken as the difference between individual values of $\dot{m}_{PJ}$ and that of the line of best fit shown in Figure A1.1. Given that the spacing of grid lines is 0.0001 kgs^{-1}, the maximum random error can be estimated conservatively to be $\pm 2 \times 10^{-5}$ kgs^{-1}, significantly lower than the specified value. Consequently, the specified value of ± 2% of full scale can be considered to be either overly conservative, or a systematic error, which the graphical technique followed above, can't detect. Random errors are of greater significance in the current work, because it is the trends in data rather than the absolute values that are of most significance. Using the estimate of $\pm 2 \times 10^{-5}$ kgs^{-1}, the maximum random errors in 10 PJ and 19PJ flow-rates are 2.0% and 1.4% respectively.

A calibration curve was also obtained for the annular flow and is shown in Figure A1.2. In this case the ejector flow and the entrained flow were metered separately. Data was measured with the PJ-annular burner arrangement in place, so that the actual experimental system pressure – flow characteristic was measured. As was the case for the PJ flows, the data points fit on a smooth line of best fit within a tolerance of $\pm 2 \times 10^{-5}$ kgs^{-1}. For the

annular flow with velocity of 9.8 ms^{-1}, this corresponds to a random error of 0.6%, whilst for the annular flow with a velocity of 2.4 ms^{-1}, it corresponds to 1.8%.

The maximum fractional random error in G_{PJe} is 2 times that of the PJ flow, since $G_{PJe} \alpha \dot{m}_{PJ}^{2}$, and likewise that of G_1 is 2 times that of the annular flow-rate. Consequently the maximum random error in G_{PJe}/G_1 for the 10PJ nozzle (for which only the higher annular flow-rate was investigated) is 2x2+2x0.6 = 5.2%, whilst that for the 19PJ is 6.4% (for the lower annular flow-rate). The majority of the flows investigated have insignificant random errors in G_{PJe}/G_1 of the order of ~ 1%. Consequently error bars for G_{PJe}/G_1 are not shown in the body of the text.

A1.3 Pressure / flow calibration of 55PJ and 80PJ nozzles.

The measured pressure / flow-rate characteristics for the 55 and 80 mm PJ nozzles used in the 2.5 MW combustion experiments (Chapter 6) are shown in Figure A1-3. Also shown are calculated values for ideal inlets using Equations A1-1 to A1-5. The 55mm and 80 mm PJ nozzles have smooth contraction inlets with throat diameters of 10.5 and 14.9 mm respectively. The smooth contraction in the 80 mm nozzle terminates with a small square edged lip of width 0.5 mm, which may explain why the measured flows are slightly lower than calculated (Figure A1.1). With this caveat, excellent agreement is demonstrated between the measured and calculated values. Consequently, measured values were used to calculate the precessing jet momentum, G_{PJ} for the 55 and 80 mm PJ nozzles, and errors can be assumed to be of a similar order of magnitude to those estimated above.

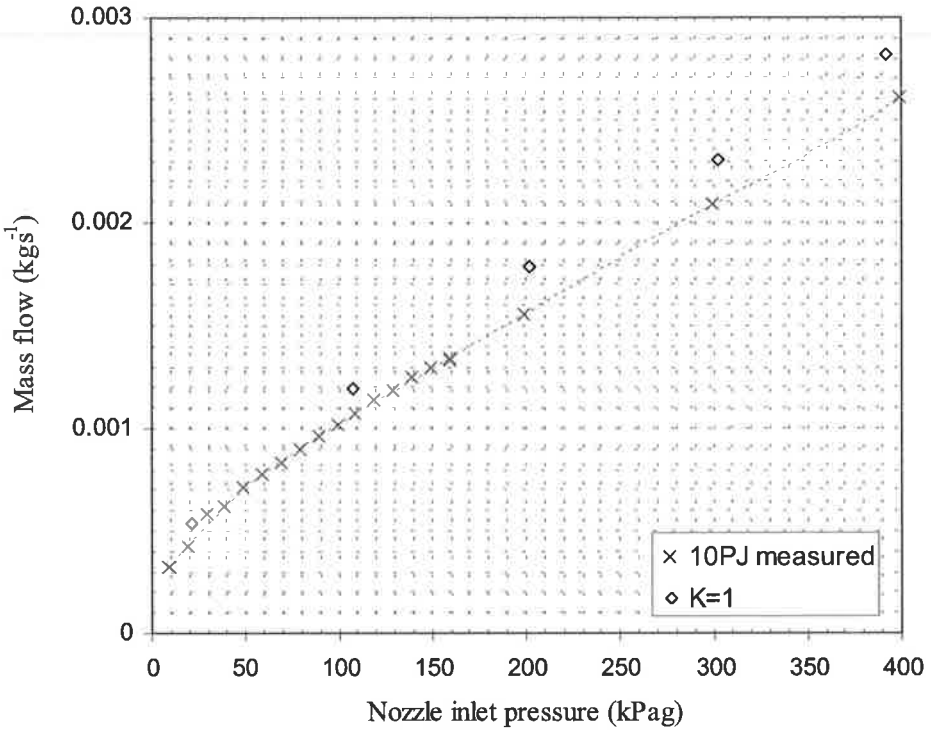

(a)

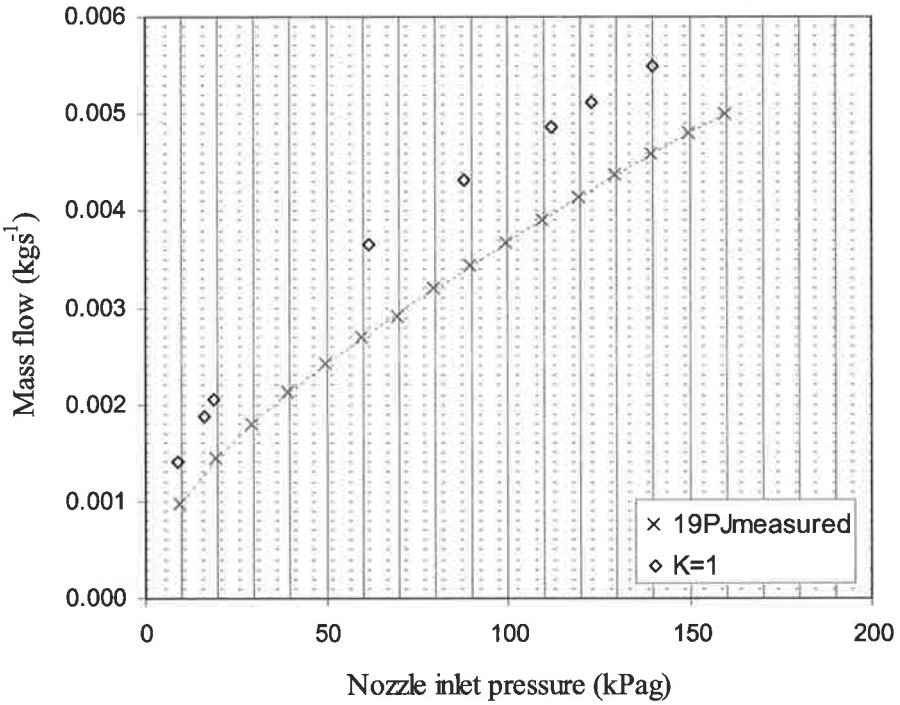

(b)

Figure A1.1 Measured mass flow rate through the PJ nozzles (a) 10PJ with a 1.75 mm throat and conical inlet. (b) 19 PJ nozzle with a 3.5 mm throat. In each case the calculated flow through an ideal smooth contraction with an equal throat diameter is also shown.

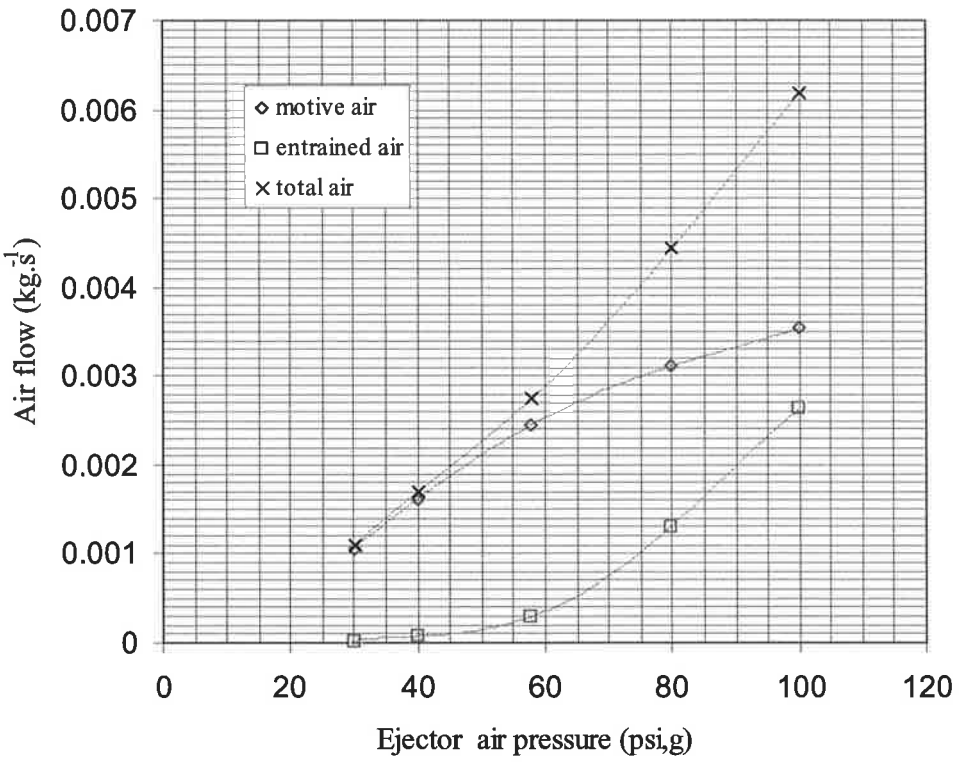

Figure A1.2 Measured mass flow rate of ejector and entrained air. The total of these two flows is the primary annular air flow-rate used in the 10PJ-annular and 19PJ-annular nozzles.

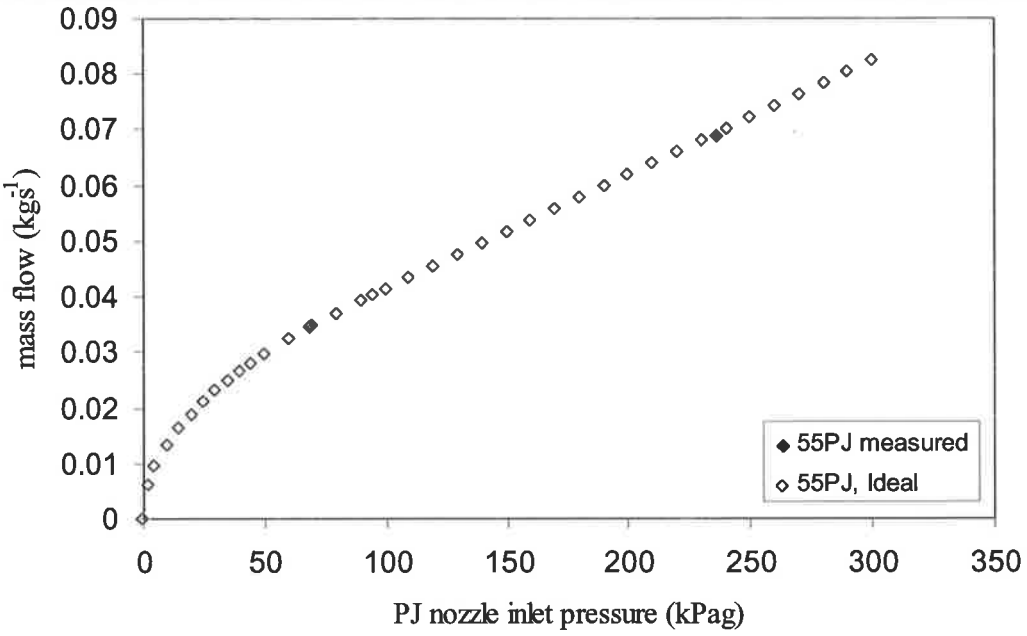

(a)

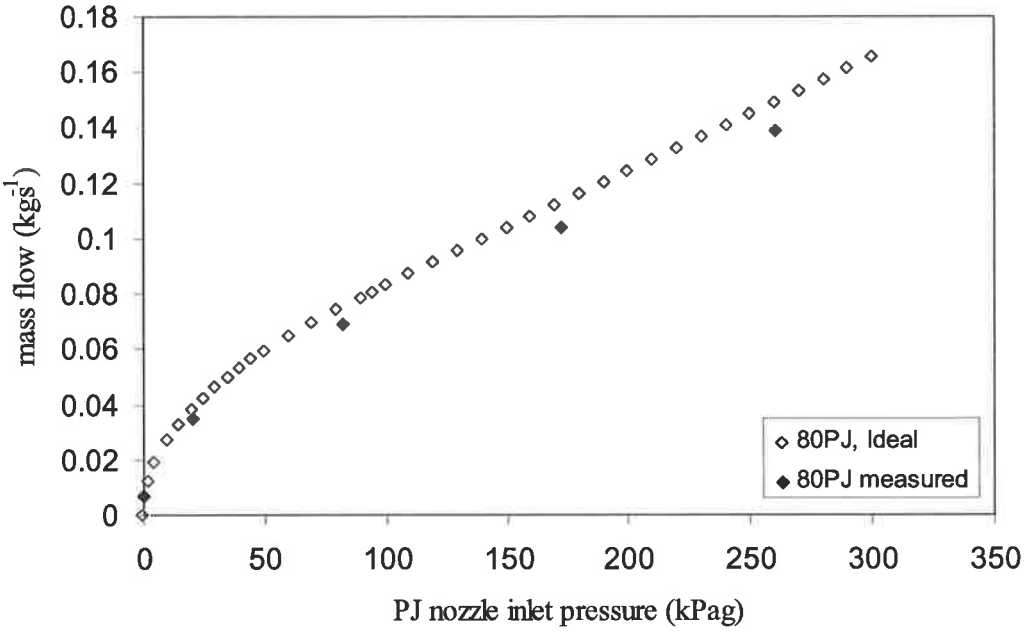

(b)

Figure A1.3 Measured air mass flow-rates, (a) 55PJ (10.5 mm throat) and (b) 80PJ (14.9 mm throat). In each case the calculated flow through an ideal smooth contraction of equal throat diameter is shown.

Appendix 2 Histograms of particle number density

Histograms of the number of particles in individual 2.5 mm square cells, overlaid on the eight photographs shown in Figures 4.11 and 4.12, are plotted below. In each case the Poisson distribution is included for comparison. The Poisson distribution represents a random distribution and is given by:

$$p_k = \frac{e^{-\mu}\mu^k}{k!} \qquad \text{A2 -1}$$

where k = the number of particles in a given cell, μ = the mean number of particles per cell, and p_k = the fraction of cells containing k particles (Kulick *et al,* 1993). The measurements span both the NBZ and the region of large-scale structures immediately downstream. No attempt is made to separate clustering effects between these two regions; that is, the distribution is averaged across all measurement locations.

Figures A2.1(a) to (d) show the distributions for the cases with annular air velocity of 9.8 ms^{-1}, with increasing PJ flow-rate from (a) to (d). Although the limited data set makes interpretation difficult, it is nonetheless apparent that the addition of PJ air (cases b and c) causes a greater departure from the random Poisson distribution than the annular flow alone (case a). Increased momentum ratio, G_{PJe}/G_1, also increases the frequency of cells containing a high or low number of particles. At higher PJ flow rates (case d) an increasing frequency of cells with very low particle concentrations was also detected. These results show that, despite the limitations of the technique, clustering effects are detectable at the scale of grid chosen. In comparison to Figures A2.1(a) – (d), Figures A2.1(e) – (h) show that the distributions are broadened to a greater extent when the annular velocity is reduced from 9.8 ms^{-1} to 2.4 ms^{-1} due to the increased influence of the PJ flow.

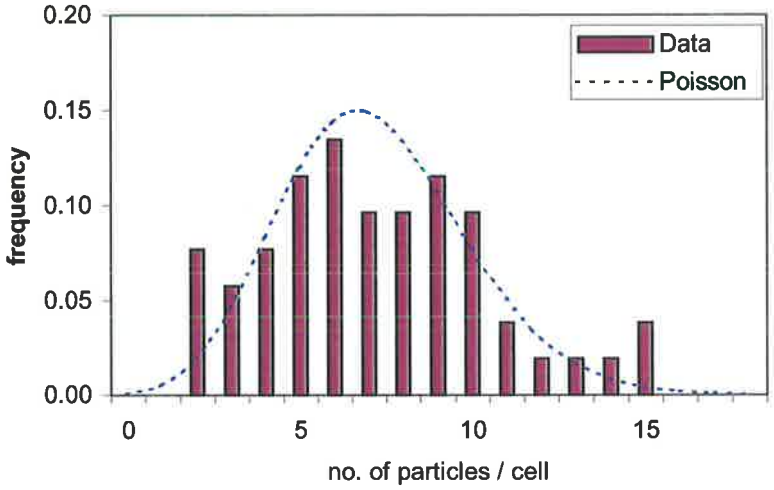

Figure A2.1(a) Measured particle distribution, and the Poisson distribution for the annular air flow alone, with velocity = 9.8 ms^{-1}, $G_{PJe}/G_1 = 0$.

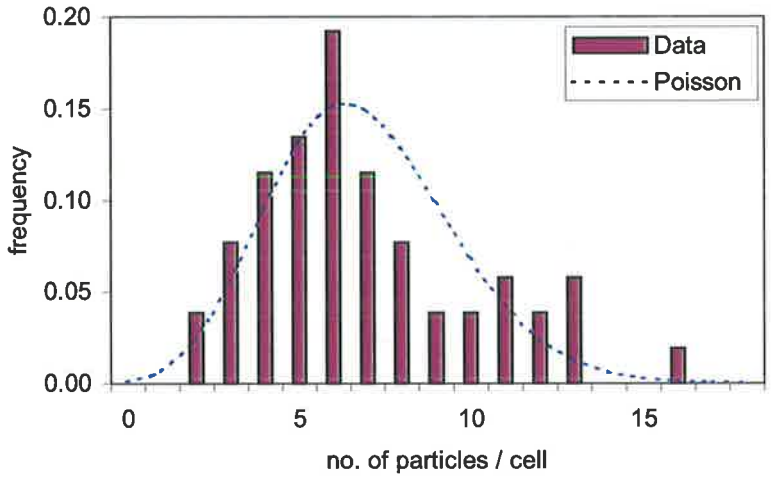

Figure A2.1(b) Measured particle distribution, and the Poission distribution for annular air with velocity = 9.8ms^{-1}, and $G_{PJe}/G_1 = 1.12$.

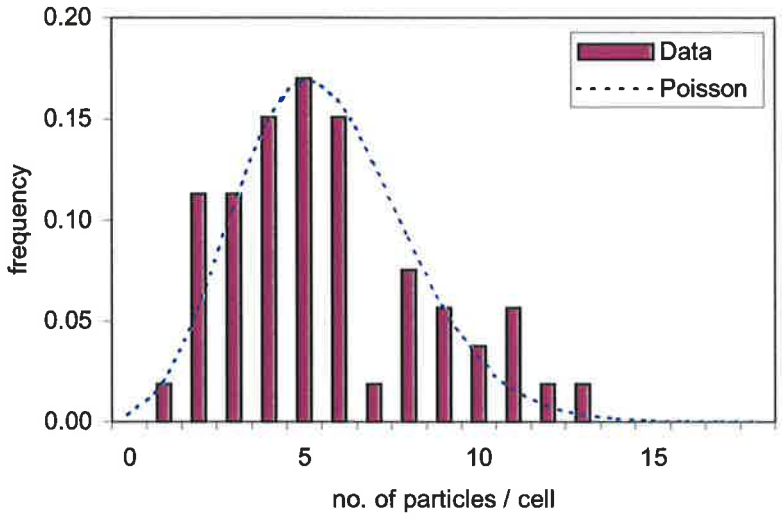

Figure A2.1(c) Measured particle distribution, and the Poission distribution for annular air with velocity = 9.8ms^{-1}, and $G_{PJ}/G_1 = 3.91$.

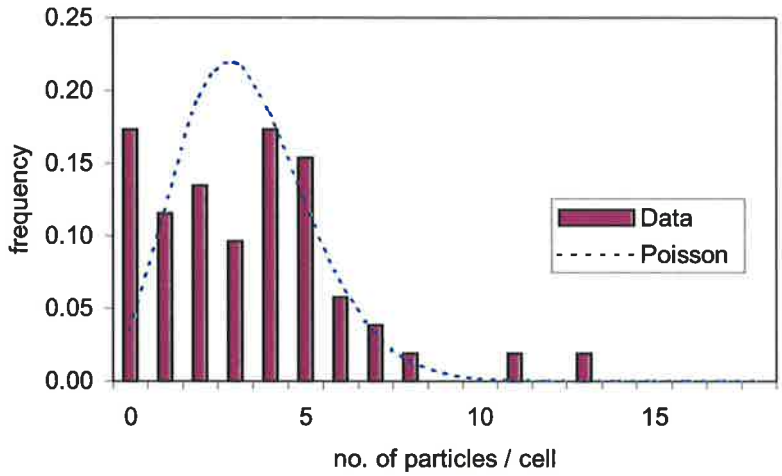

Figure A2.1(d) Measured particle distribution, and the Poission distribution for annular air flow with velocity = 9.8 ms^{-1} and $G_{PJe}/G_1 = 7.22$

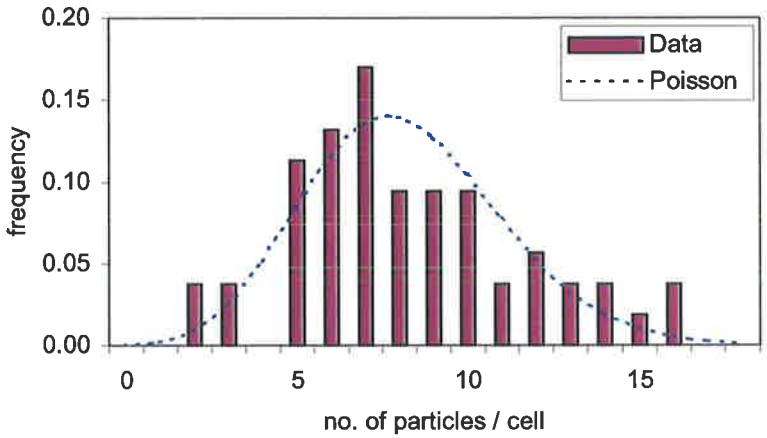

Figure A2.1(e) Measured particle distribution, and the Poission distribution for annular air flow with velocity = 2.4 ms^{-1}, and no PJ air, ie. $G_{PJe}/G_1 = 0$

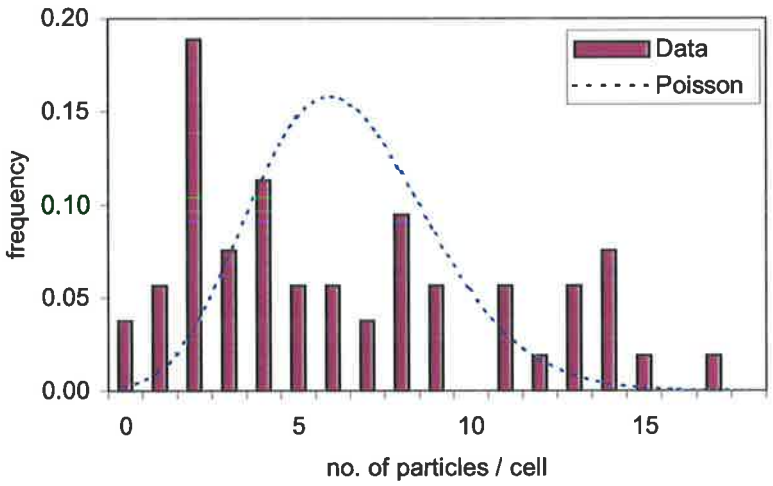

Figure A2.1(f) Measured particle distribution, and the Poission distribution for annular air flow with velocity = 2.4 ms^{-1} and $G_{PJe}/G_1 = 18.6$

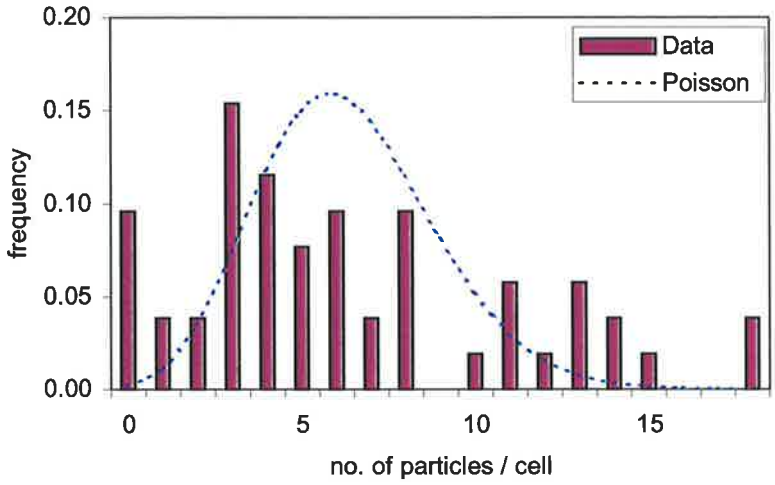

Figure A2.1(g) Measured particle distribution, and the Poission distribution for annular air flow with velocity 2.4 ms^{-1} and $G_{PJe}/G_l = 64.7$

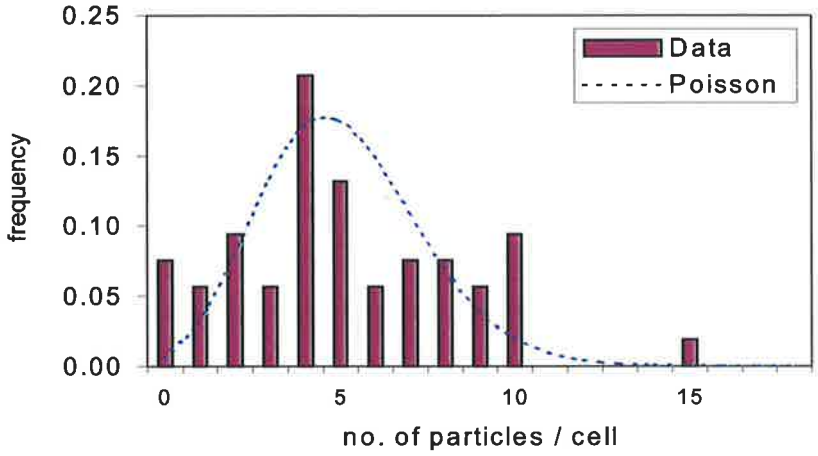

Figure A2.1(h) Measured particle distribution, and the Poission distribution for annular air flow with velocity = 2.4 ms^{-1} and $G_{PJe}/G_l = 119$

Appendix 3 Clustering in non-reacting flows with high particle loading

A3.1 Introduction

Laser Doppler annemometry (LDA) was used to assess the influence of particle loading on clustering in PJ – annular flows. The experimental conditions simulate the particle loading typically found in the NBZ of rotary kiln PF flames. The data supplements that provided in Chapter 4, where visualisation techniques were used to investigate flows with lower seeding densities.

A3.2 Experimental apparatus

Experiments were conducted at ambient temperature in a cylindrical, refractory lined, kiln with an internal diameter of 420 mm, operated in vertical down flow as shown in Figure A3.1. The nozzle is of the PJ - annular configuration, with D = 19mm, $D_{A,1}$ = 24.0 mm and $D_{A,2}$ = 41.5 mm. It was located centrally in the kiln as shown in Figure A3.1. A secondary air flow was used to simulate the conditions in rotary kilns. The secondary air enters the kiln at right angles near to the top.

The annular flow was seeded with silica flour with particle size distribution, determined by wet sieving and Malvern laser sizing, shown in Figure A3.2. Also shown for comparison is a typical theoretical Rosin-Rammler PF size distribution. The Rosin-Rammler distribution is given by,

$$R = 100\exp\left(-(d/\bar{d})n\right) \qquad \text{A3 -1}$$

where R is the mass percent of coal greater than size d, and $\bar{d}$ is the size for which $R = 100/e$. A typical PF distribution has n = 1.2 and $\bar{d}$ = 50 (Wall, 1987). The size distribution of silica flour is broadly comparable with that of PF.

A TSI laser Doppler velocimeter with a 25 mm TSI fibre, optically coupled to a 195.8 mm focal length lens, was used to obtain two – dimensional (axial and azimuthal) simultaneous velocity data. The lens was kept clean by purging with nitrogen. The laser is a 5W Spectra Physics 165 Ar-ion laser, with green and blue beams frequency shifted by means of a Bragg cell. The probe was traversed in a single horizontal plane. The mechanical traverse mechanism was mounted to an access port on the kiln, located 1.05 m below the bottom of the secondary air inlet.

The measurement volume created by crossing of the beams was 3.5 mm long and 1.33 μm in diameter. The fringe spacing, d_f, was 6.85 μm (based on the green wavelength of 514.5 nm). Counters in the TSI 1990C LDV signal processor were used to provide data for the velocity calculation. High and low pass filters in the signal processor removed background noise. On-line data analysis by TSI software provided a velocity amplitude pdf, and calculated mean, r.m.s., and turbulence intensity.

A3.3 Experimental method

The two conditions tested were, (a) an annular flow alone, ie $G_{PJe}/G_1 = 0$, and (b) $G_{PJe}/G_1 = 14.3$. The latter of the two momentum ratios, at the high end of the range investigated in Chapter 3 and 4, was selected to highlight the influence of the PJ flow on particle motion. In both cases the primary (annular) air was supplied at 4.05 ms^{-1}, (0.005195 kgs^{-1}, equivalent to 8.7% of the total air flow). Despite this low primary air velocity, the vertical down-flow arrangement prevented particle slugging in the annular channel. In case (b) the 19PJ nozzle was supplied with air at 0.003475 kgs^{-1} (5.8% of the total air flow, at an exit velocity of 81.5 ms^{-1}). Secondary air was supplied with a velocity of 0.31ms^{-1} (85% of the total air flow). The silica particle flow rate was 0.005 kgs^{-1}, which simulates the PF flow rate used in a 150 kW flame assuming a heating value of 30$MJkg^{-1}$ of the coal.

Laser Doppler annemometry was used to quantify mean and r.m.s. axial and azimuthal velocities at 4 horizontal planes downstream from the burner exit plane. The planes were located 50, 77, 119 and 203 mm downstream from the nozzle exit plane, corresponding to the region immediately downstream from the NBZ, ie, $2.6 \leq \frac{x}{D} \leq 10.7$, where large structures are generated in FPJ flows. The burner was moved axially, to position it in each of these four measurement planes. At each position 4096 samples were collected, which provides an error of < 3% in r.m.s. at the 95% confidence interval.

A3.4 Results

The distribution of the secondary air velocity without the burner installed is shown in Figure A3.3. For this measurement the secondary air was seeded with calcium carbonate flow tracer particles (nominally 2 μm in diameter) prior to entry into the kiln. Figure A3.3 shows that the secondary air distribution was non-uniform, with a small recirculation zone on the right, despite the use of an inlet flow correction baffle. To minimise the influence of the poor co-flow distribution on the results, the co-flow velocity was kept at $0.31 ms^{-1}$ (8% of the annular velocity). In this way the effect to the PJ flow could still be determined. It should also be noted that the co-flow in most real kilns is likewise highly non-uniform.

Comparisons were made between the annular flow alone and the PJ – annular flow, with the secondary air unseeded to ensure that only particle velocities were measured. Figure A3.4 compares the mean axial velocities of the simulated PF for the two flows. The annular data is shown at left and the combined flow data at the right. The radial position, $r = 0$ mm corresponds to the kiln centre-line. High data rates in the annular flow were generally restricted to the region near the centre-line, ie. $0 < r < 60$ mm, due to the narrow spreading angle of the jet. The PJ - annular flow demonstrates a broader spread of data (except for $x/D = 6.3$ where only centre-line data was taken due to experimental difficulties). The PJ – annular flow shows an absence of any reverse flow zones, in agreement with observations in the FPJ flow field (Newbold *et al.* 1995). There is a noticeable reduction in the mean axial velocity at $r/D_{kiln} \sim 0.2$, as would be expected at the edge of the jet flow. However, increased mean axial velocity closer to the wall at $r/D_{kiln} > 0.2$, is also observed. It appears that this latter effect is an artefact of the non-uniform secondary air flow. The artefact is not observed in the annular flow because of the reduced jet spread and hence weak signal at $r/D_{kiln} \sim 0.2$. The mean azimuthal velocities are all approximately zero and are not shown.

Of greater interest than the mean velocity data for the current argument are the rms. values. The magnitude of fluctuations in measured velocity is primarily a measure of the variation in response of particles to fluid structures. The rms values also incorporate a contribution from any systematic experimental errors that occur. This contribution can be assumed to be similar for both flows. Additional variation caused by variation in particle and fluid history, and variation in particle size and roughness, is generally insignificant (Rogers and Eaton, 1989). Figure A3.5 shows that the ratio of r.m.s./mean axial velocity of the PJ – annular flow has a peak value of 1 and is consistently double that of the annular flow alone in the near field, $x/D \leq 6$. Figure A3.6 shows that the magnitude of r.m.s. azimuthal velocities are also increased in the PJ flow by a factor of 2 in the region, $x/D \leq 6$. The larger variation in

velocities can be expected to result from particles responding to low frequency turbulence, ie. larger structures, which themselves have a greater range of velocities than those in the annular flow. The result shows that the enhanced large scale structures present in FPJ flows can increase the intensity of local fluid velocity fluctuations and lead to the formation of clusters as observed by Longmire and Eaton (1992).

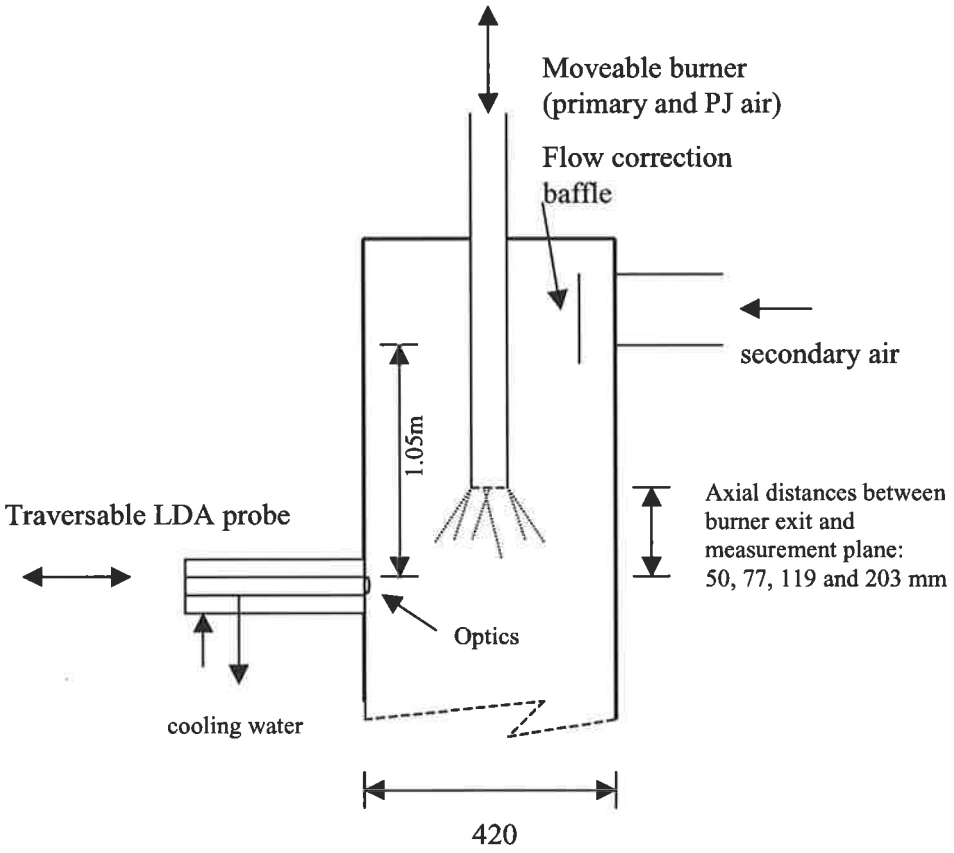

Figure A3.1 A schematic diagram of the experimental apparatus used for LDA measurements in ambient air flows in a cylindrical refractory lined kiln.

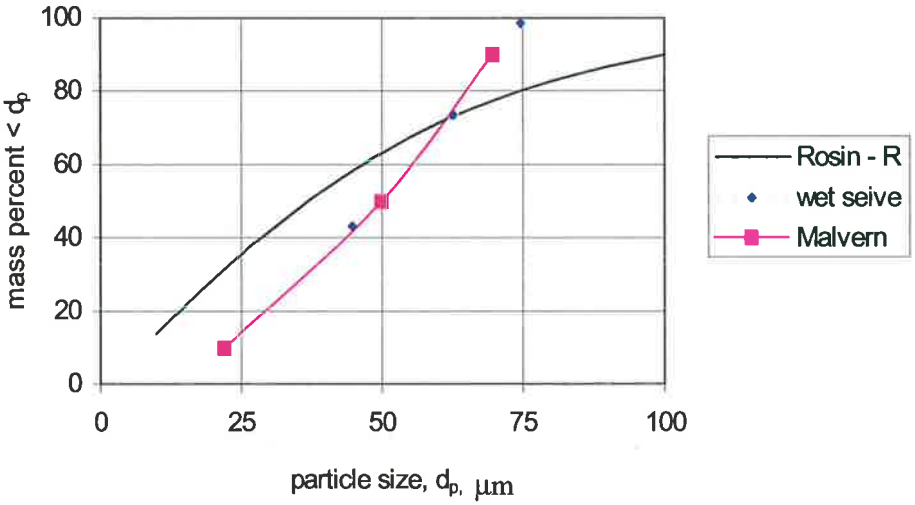

Figure A3.2 Silica flour size distribution, as determined by both wet sieving and laser sizing, with Rosin – Rammler distribution for 50 µm particles

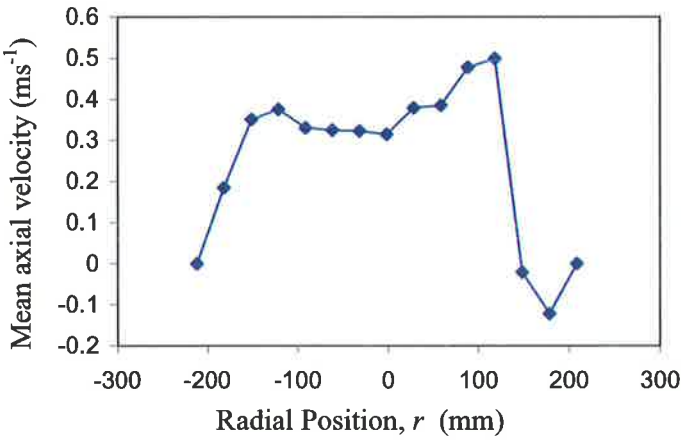

Figure A3.3 The distribution of secondary air velocity without the burner installed, at the measurement plane, located 1.05 m below the bottom of the secondary air inlet. The flow was seeded with 2 µm calcium carbonate particles. The kiln centre-line is at $r = 0$ mm .

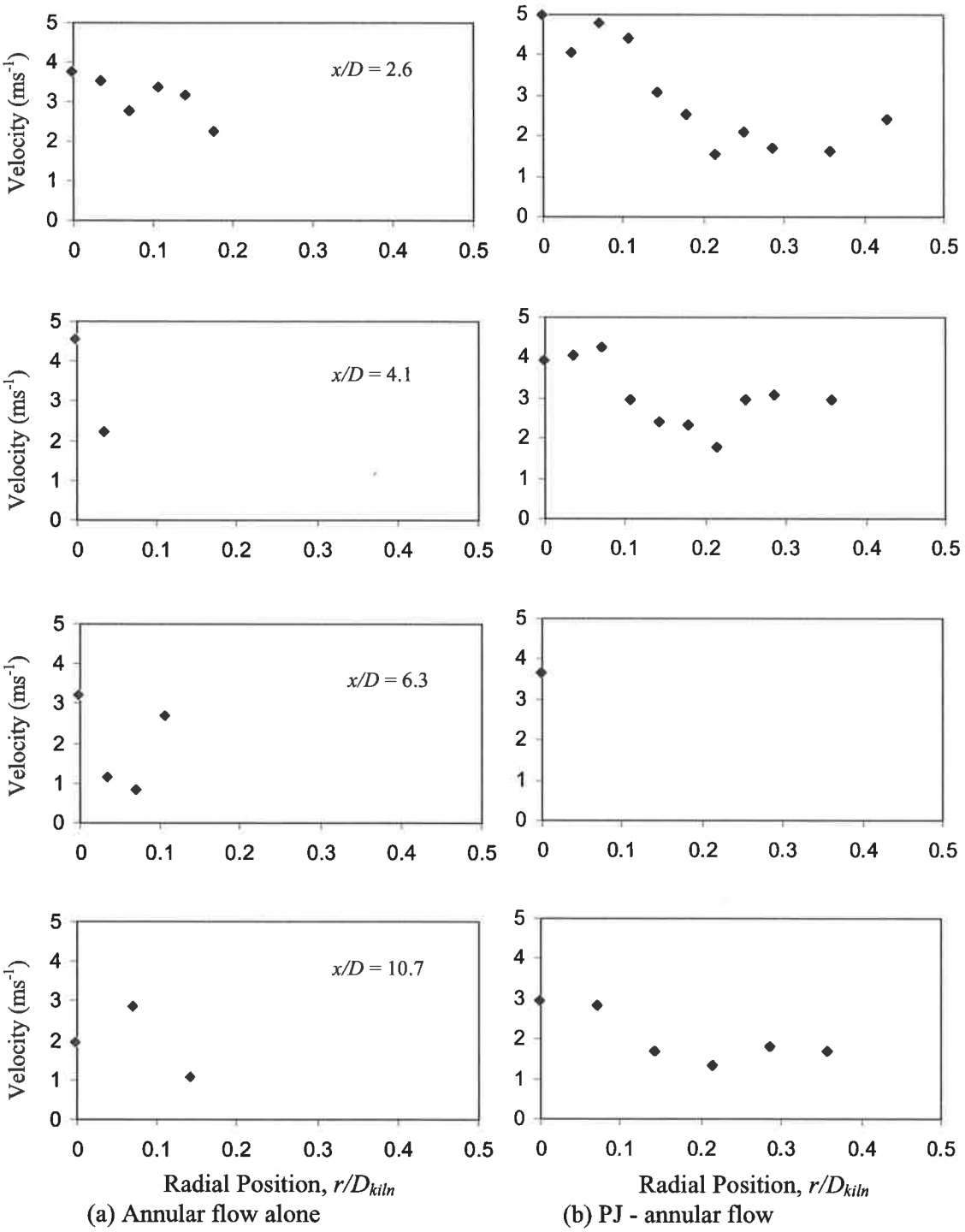

Figure A3.4 Comparison of mean axial particle velocities as a function of axial and radial position. Radial position, r/D_{kiln} = 0 corresponds the kiln centre-line, where the kiln diameter D_{kiln} = 420 mm. Data was only taken on one side of the kiln, nearest the optics. Axial measurement locations are x/D = 2.6, 4.1, 6.3, 10.7 from the nozzle exit plane, where D is the PJ nozzle diameter (19 mm).
(a) Annular flow alone – data shown on left
(b) 19PJ-annular flow with G_{PJe}/G_1 = 14.3 - data shown on right.

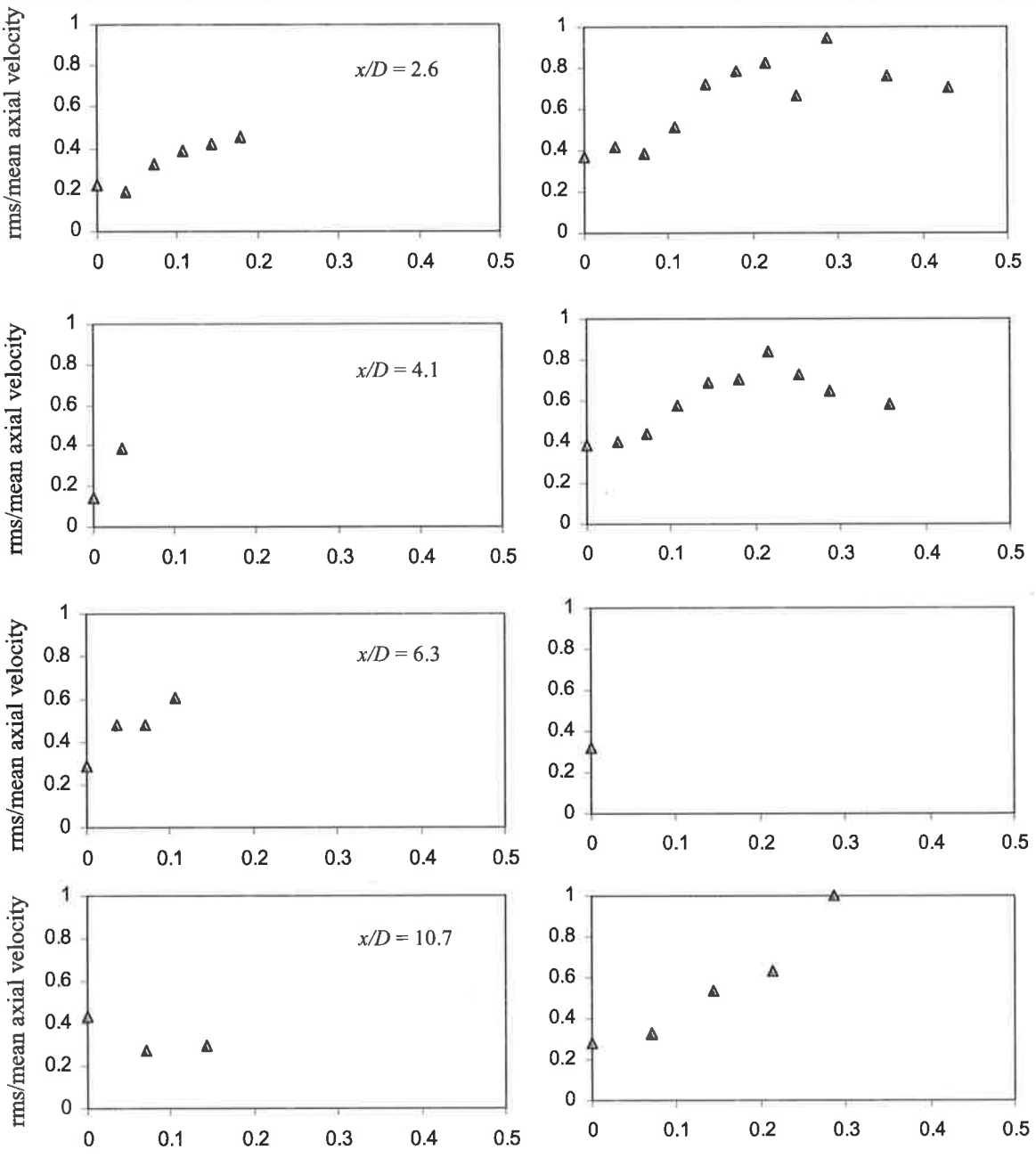

Radial position, r/D_{kiln} (a) annular flow alone

Radial position, r/D_{kiln} (b) PJ-annular flow

Figure 3A.5 Comparison of rms/mean axial particle velocities (a) annular flow alone at axial locations x/D = 2.6, 4.1, 6.3, 10.7 downstream from the nozzle exit plane (b) PJ – annular flow with G_{PJe}/G_J = 14.3, at the same axial locations. (Radial position, r/D_{kiln} = 0 corresponds to the kiln centre-line.)

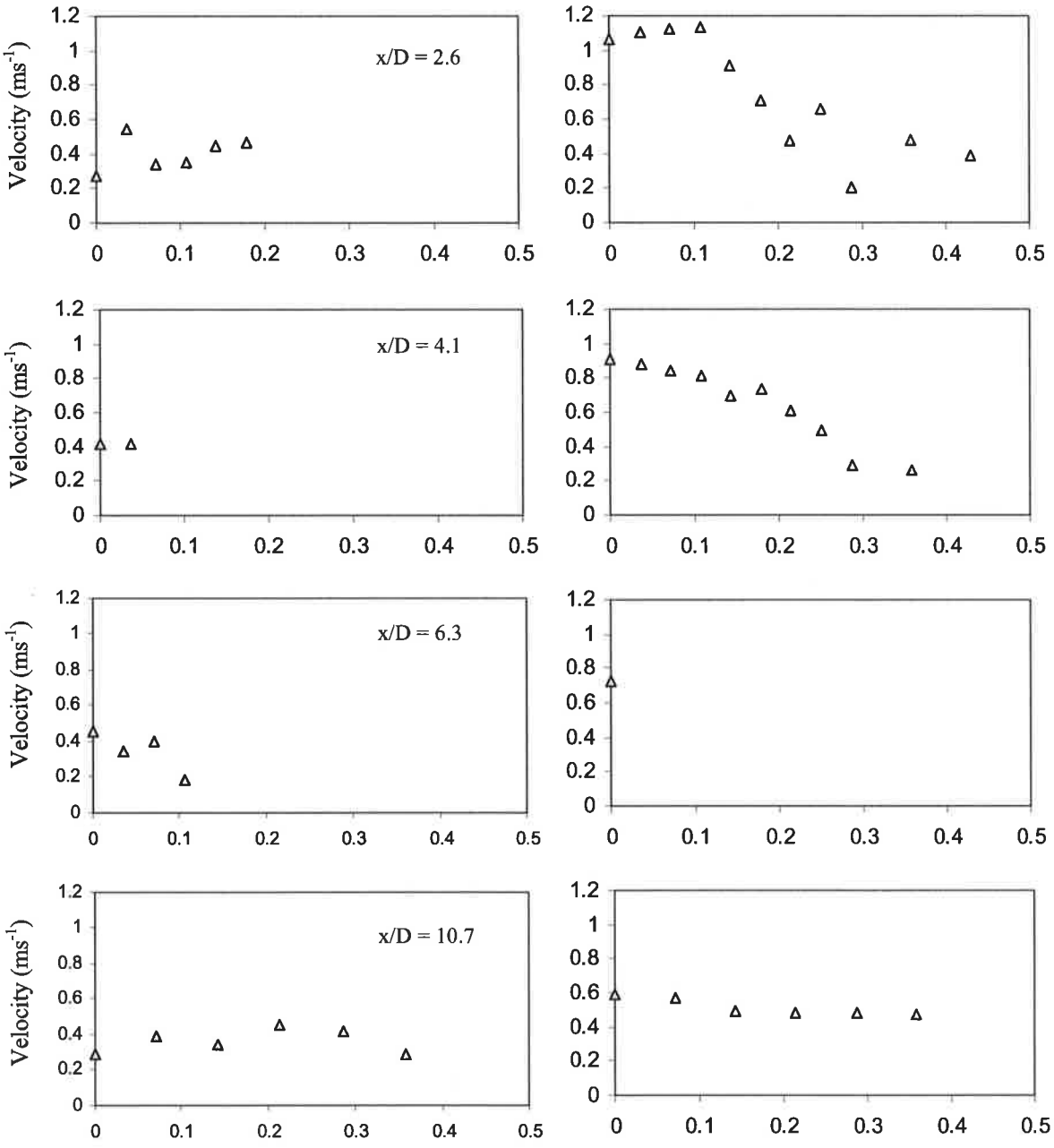

(a) annular flow alone

(b) PJ-annular flow

Figure A3.6 Comparison of rms azimuthal particle velocities velocities (a) annular flow alone at axial locations x/D = 2.6, 4.1, 6.3, 10.7 downstream from the nozzle exit plane (b) PJ – annular flow with G_{PJe}/G_1 = 14.3, at the same axial locations. (Radial position, r/D_{kiln} = 0 corresponds to the kiln centre-line.)

Appendix 4 Visualisation of burning coal particles in open gas flames

The influence of enhanced large scale mixing on particle trajectories, volatile matter liberation and combustion was investigated qualitatively in open gas flames, using a much lower particle loading than occurs in PF flames to assist in visualisation. The experimental arrangement is the same as that illustrated in Figure 4.1, except that natural gas is used as the annular transport fluid. The gas flow rate was limited to 120 $l.min^{-1}$ (76 kW) to minimise suction, and hence entrainment, of air through the ejector. The gas transport velocity in the annular injector, 5.3 ms^{-1}, was considerably lower than that used in the coal flame studies. The 19 PJ burner was selected and air was supplied through the PJ nozzle at the standard flow rate of 0.0027 kgs^{-1} (at 60 kPa). The momentum ratio, G_{PJe}/G_1 = 24.2, (G_{PJt}/G_1 = 105) was higher than that used in coal flames, to ensure that the PJ flow dominates so that any influence of enhanced large scale mixing on particle trajectories and devolatilisation can be clearly evident. For comparison the mono-channel annular flow (with no PJ air flow) was also used.

Tests were conducted both with unclassified particles (70% < 70μm) and with a classified sample range: 150 < *dp* < 300μm. The latter sample was used to provide a case with high *St* so that particles do not follow the flow. The PF particle feed rate was selected to be 0.51 $g.min^{-1}$, so that not only was the seeding density relatively low, but also the ratio of PF to gas heating values was small, ie. 0.0033. The Photec high-speed 16-mm cine camera, described in section 4.2.1, was used with a framing rate of 4000 s^{-1}. After volatile matter ignited, its luminosity was found to dominate the images. Consequently, illumination using the pulsed Cu vapour laser was only effective in the pre-ignition region.

Images of particles and burning volatile matter in open gas flames, taken on high-speed 16 mm cine-film, are shown in Figure A4.1. Figure A4.1(a) and (b) show unclassified PF particles (70% < 70μm) in the mono-channel annular flow and the 19PJ flow with G_{PJe}/G_1 = 24.2, respectively. Figure A4.1(c) shows the 19PJ flow with particles classified into the range 150 < d_p < 300 μm. Burning volatile matter and soot appear as streaks or "tails" in all of these images. Note that the length of the burning tails does not relate to particle velocity as has been deduced from tracking the location and length of several such streaks in consecutive frames. Comparing Figures A4.1(a) and (b) clearly demonstrates that precession acts to increase the spread of the particles and to greatly increase the number of ignited particles in the NBZ relative to the annular flow, an effect which is deduced to be attributed to increased heating rates by back radiation from the flame, and increased residence times (see below). There is also evidence of much stronger clustering effects in

the PJ flows. The particle clusters generate highly dense volatile matter clusters immediately downstream from the NBZ. The chosen gas heat input (76 kW) is similar to that of volatile matter in the 130 kW flames. Consequently, similar volatile matter clustering can be expected in the 130 kW PF flames when the PJ momentum dominates over that of the primary and secondary streams.

The length of volatile matter tails is deduced to be a function of residence time and particle heating rate (and hence devolatilisation rate). The rate of entrainment of surrounding air into the mono-channel flow is low owing to its low momentum. The resulting mono-channel gas flame is orange and luminous indicative of fuel rich conditions. Fuel rich conditions can be expected to result in flame temperatures and devolatilisation rates that are lower than in the PJ flame, which was blue in the region, x/D < 10. However, reduced residence times also contribute to short tail lengths in the mono-channel flame. In the mono-channel flame the annular flow maintains a well defined core and a large fraction of particles remain in the core and were observed to pass through the imaged flame region ($1.2 < x/D_{A,2} < 4.2$) within 30 consecutive frames, which equates to a mean convection velocity of 13 ms^{-1}. The convection velocities of other particles, which were not confined to the annular core, were lower. In contrast, particles in the PJ flame were observed to form into clusters that were convected downstream with a mean velocity of 4 ms^{-1}.

Despite the complications introduced by modelling coal flames with open gas flames, ie. slightly altered stoichiometry and buoyancy effects, the method provides evidence for high volatile yields close to the nozzle in PJ flames, and the presence of large fuel-rich clusters of volatile matter.

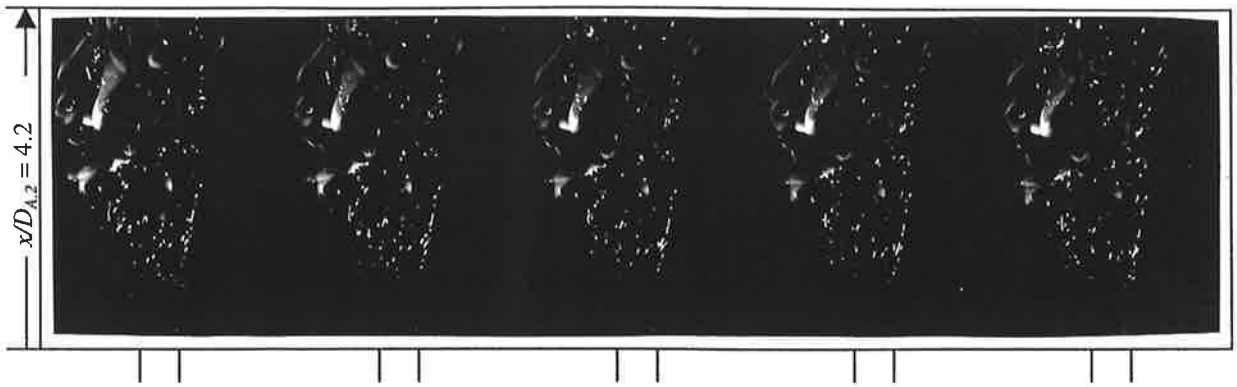

(a) ← time sequence proceeds right to left ←

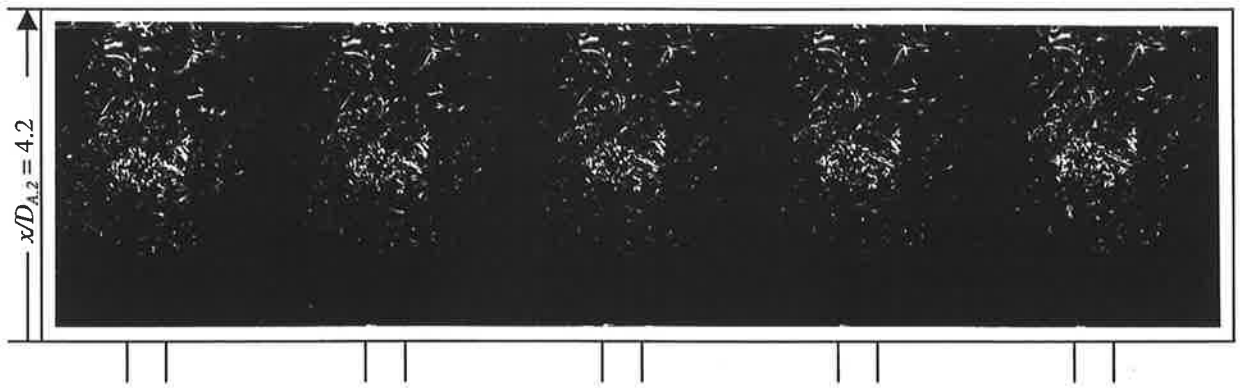

(b) → time sequence proceeds left to right →

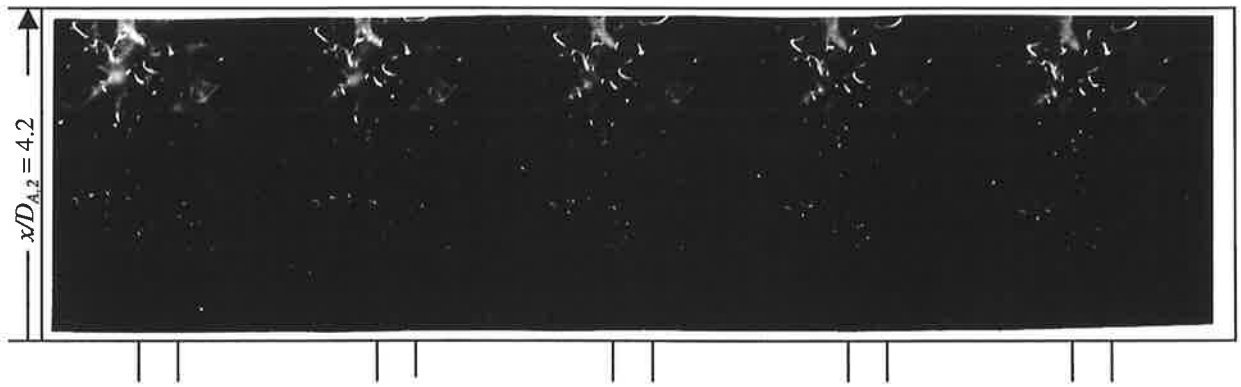

(c) ← time sequence proceeds right to left ←

Figure A4.1. Consecutive images of PF particles and burning volatile matter "tails" in open gas flames (framing rate 4 kHz). (a) Mono-channel annular flow of natural gas at 2 litres.s^{-1} (5.3 ms^{-1}) transporting 0.0085 g.s^{-1} unclassified PF (70% < 70 μm), sequence proceeds right to left (b) 19PJ-annular flow with air supplied at 60 kPa(g) to the PJ nozzle, and the same annular flow conditions as in the mono-channel case (G_{PJe}/G_1 = 24.2), sequence proceeds left to right (c) the same 19PJ-annular flow, but with particles in the size range 150 < d_p < 300 μm introduced with annular gas, sequence proceeds right to left. Burner locations are illustrated at the base of each frame.

Appendix 5 Errors in heat flux measurements in 2.5 MW flames

As noted in Section 6.3, the heat removed by cooling loops from the 2.5MW flames was measured after a period of 20 minutes was allowed for the furnace to approach thermal equilibrium. After 20 minutes, fluctuations in the water temperature rise ($\Delta T = T_{in} - T_{out}$) were of the order of ± 0.25 °C. Fluctuations in the water flow rate were ± 0.5% of the measured mean values, which is similar to the manufacturer's claims of ± 0.25% accuracy. An example of the trends in water flow rates through a cooling loop and the measured ΔT is given in Figure A5.1. It presents data for the loop nearest the burner, over a 20 minute period from the time when the burner flows were altered to produce an 80 PJ flame with $G_{PJ}/G_1 = 4.5$. Figure A5.2. shows that the corresponding variation in absolute values of heat flux near the end of the 20 minute period, was of the order of ±2 kW or < ±1% of the heat removed by the loop (~ 220kW). This value includes the effects of errors in flow-rate measurements of fuel and air, which are not considered in the above analysis.

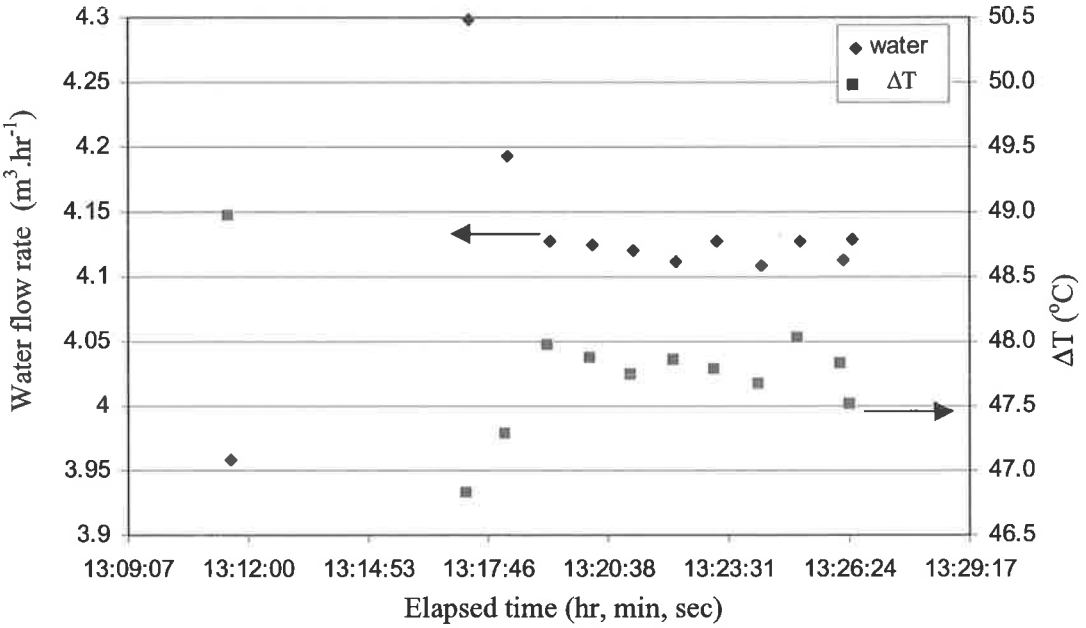

Figure A5.1 Water flow rates through the cooling loop closest to the burner and measured ΔT, as a function of time for the 80 PJ flame with $G_{PJ}/G_J = 4.5$. Near the end of the twenty minute period fluctuations in ΔT are of the order of ± 0.25 °C, while those in water flow rate are ± 0.5% of the measured values.

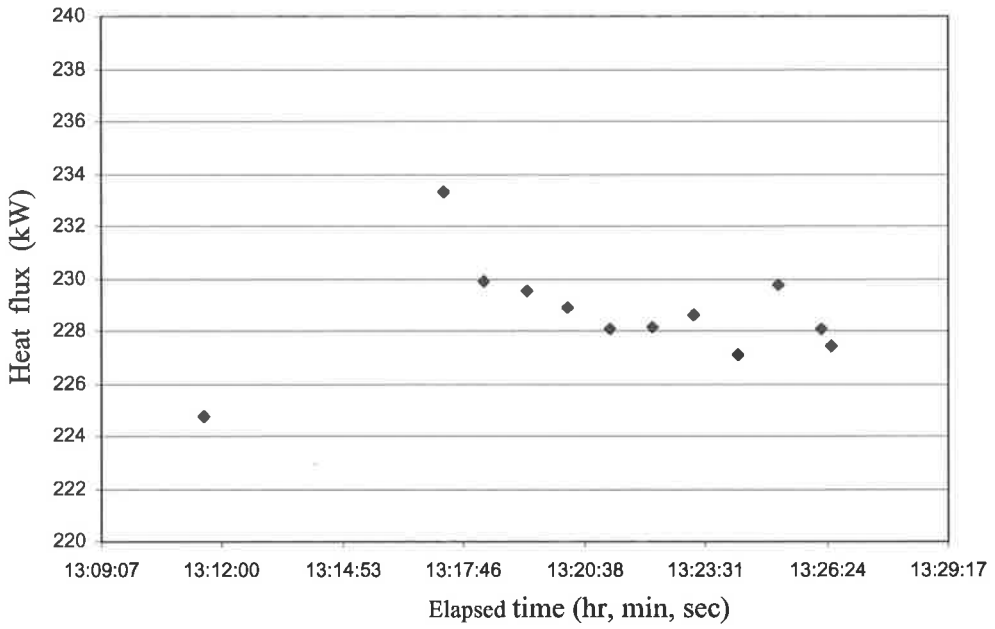

Figure A5.2. The variation in heat flux through the cooling loop closest to the burner over a 20 minute period for the 80 PJ flame with $G_{PJ}/G_J = 4.5$. Near the end of the period the variation was of the order of ± 2 kW or < ± 1%.

References

Abbas, T., Costa, M., Costen, P., Godoy, S., Lockwood, F.C., Ou, J.J., Romo-Millares, C. and Zhou, J. (1994) NO_x formation and reduction mechanisms in pulverised coal flames, *Fuel*, 73,1423-1436.

Abbas, T., Costen, P., Hassan, M.A. and Lockwood, F.C. (1993a) The effect of the near burner aerodynamics on pollution, stability and combustion in a pf fired furnace. *Combustion Science and Technology*, 93, 73-90.

Abbas, T., Costen, P., Lockwood, F.C. and Romo-Millares, C.A. (1993b). The effect of particle size on NO formation in a large-scale pulverized coal-fired laboratory furnace: Measurements and modeling. *Combustion and Flame*, 93, 316-326.

Abbas, T., Koussa, S.S. and Lockwood, F.C. (1981) The Prediction of the particle laden gas flows. *18th Symposium (International) on Combustion*, The Combustion Institute, Pittsburgh, 1427-1437.

Abramovich, G.N. (1963). *The theory of turbulent jets*. MIT Press, Cambridge, Massachusetts.

Achenbach, E. (1974) Vortex shedding from spheres. *Journal of Fluid Mechanics*, 62, 209 – 221.

Aggarwal, S.K. (1994) Relationship between Stokes number and intrinsic frequencies in particle laden flows. *AIAA Journal*, 32, 1322 – 1324.

Anthony, D. B., Howard, J. B., Hottel, H. C., and Meissner, H. P. (1975) Rapid devolatilization of pulverized coal. *15th Symposium (International) on Combustion*, The Combustion Institute, 1303-1317.

Arcoumanis, C., McGuirk, J.J. and Palma, J.M.L.M. (1990) On the use of fluorescent dyes for concentration measurements in water flows. *Experiments in Fluids*, 10, 177-180.

Atreya, A., Zhang, C., Kim, H.K., Shamim, T. and Suh, J. (1996) *26th Symposium (International) on Combustion*, The Combustion Institute, Pittsburgh, 2181-2189.

Badzioch, S., and Hawksley, P. G. W. (1970) Kinetics of thermal decomposition of pulverized coal particles. *Ind. Eng. Chem. Process Des. Develop.*, 9, 521-530.

Ballal, D.R. and Lefebvre, A.H. (1974) Turbulence effects on enclosed flames. *Acta Astronautica*, 1, 471-483.

Ballal, D.R. and Lefebvre, A.H. (1975) The structure and propagation of turbulent flames. *Proceedings of the Royal Society. London*, A, 344, 217-234.

Barchilon, M. and Curtet, R. (1964) Some details of the structure of an axisymmetric confined jet with backflow. *Transactions of the ASME, Journal of Basic Engineering*, 777-787.

Bauer, C. (1990) Pyro-jet Burners to Reduce NOx Emissions - Current Developments and Practical Experience. *World Cement*, April, 118 - 124.

Becker, H.A., Hottel, H.C. and Williams, G.C. (1967) The nozzle fluid concentration of the round, turbulent, free jet. *Journal of Fluid Mechanics*, 30,2, 285-303.

Beer, J.M. (1962) in Thring, M.W. *The science of flames and furnaces*. Wiley, 2nd edition, p210ff.

Beer, J.M. (1964) The Effect of Fineness and recirculation on the combustion of low volatile pulverized coal. *Journal of the Institute of Fuel*, 37, 287-313.

Beer, J.M. and Chigier, N.A. (1972) *Combustion Aerodynamics* Applied Science, London.

Beer, J.M. and Chigier, N.A. (1969) Stability and combustion intensity of pulverized-coal flames – effect of swirl and impingement. *Journal of the Institute of Fuel*, Dec 1969, 443-450.

Beer, J.M., Chomiak, J. and Smoot, L.D. (1984) Fluid dynamics of coal combustion. *Progress in Energy and Combustion Science*, 10, 177-208

Bellan, J. and Harstad, K. (1988) Turbulence effects during evaporation of drops in clusters. *International Journal of Heat and Mass Transfer*, 31,8, 1655 – 1668.

Berger, E., Scholz, D. and Schumm, M. (1990) Coherent vortex structure in the wake of a shpere and a circular disk at rest and under forced vibrations. *Journal of Fluid Structures*, 4, 231 – 257.

Blair, D.W., Wendt, J.O.L. and Bartok, W. (1977) Evolution of Nitrogen and Other Species During Controlled Pyrolysis of Coal. *16th Symposium (International) on Combustion*, The Combustion Institute, 475 - 489.

Bolin, B., Houghton, J. and Filho, L.C.M. (eds.) (1995) *The Science of Climate Change*, Working Group 1 2nd Assessment Report of the Intergovernmental panel on Climate Change.

Bose, A.C., Dannecker, K.M. and Wendt, J.O.L. (1988) Coal composition effects on mechanisms governing the destruction of NO and other nitrogenous species. *Journal of Energy and Fuels*, 2, 301.

Bowman, C.T. (1992) Control of Combustion Generated Nitrogen Oxide Emissions: Technology Driven by Regulation. *24th Symposium (International) on Combustion*, The Combustion Institute, Pittsburgh, 859-878.

Brown, G.L. and Roshko, A. (1974) On the density effects and large structure in turbulent mixing layers, *Journal of Fluid Mechanics*, 64, 693-704.

Cassel and Liebman (1959) The cooperative mechanism in the ignition of dust dispersions, *Combustion and Flame,* 3, 467-475.

Chein, R. and Chung, J.N. (1987) Effects of vortex pairing on particle dispersion in turbulent shear flows. *International Journal of Multiphase Flow*, 13, 785-802.

Chein, R. and Chung, J.N. (1988) Particle dynamics in a gas-particle flow over normal and inclined plates. *Chemical Engineering Science*, 43, 1621-1636.

Chen, J.C. and Niksa, S. (1992) Suppressed Nitrogen Evolution from Coal-Derived Soot and Low-Volatility Coal Chars. *24th Symposium (International) on Combustion*. The Combustion Institute, 1269-1276.

Chen, L.-D. and Roquemore, W.M. (1986) Visualisation of jet flames. *Combustion and Flame*, 66: 81-86.

Chen, L.-D., Seaba, J.P. and Roquemore, W.M. and Goss, L.P. (1988) Buoyant diffusion flames. *22nd Symposium (International) on Combustion*, The Combustion Institute, 677-684.

Cho, S., Marlow, D. and Niksa, S. (1995) Burning velocities of multicomponent organic fuel mixtures derived from various coals. *Combustion and Flame*, 101, 399-410.

Chung, J.N. and Troutt, T.R. (1988) Simulation of particle dispersion in an axisymmetric jet. *Journal of Fluid Mechanics*, 186, 199 – 222.

Claypole, T.C. and Syred, N. (1982) The stabilisation of flames in swirl combustors. *Journal of the Institute of Energy*, 55, 14-19.

Costa, M., Costen, P. and Lockwood, F.C. (1990a) Burner stability limits and gas species measurement for lignite pulverized fuel in a cylindrical furnace. *Fuel*, 69,403-406.

Costa, M., Costen, P., Lockwood, F.C. and Mahmud, T. (1990b) Detailed mesaurements in and modelling of an industry type pulverized coal flame. *23rd Symposium (International) on Combustion*, The Combustion Institute, 973-980.

Costa, M., Godoy, S., Lockwood, F.C., Zhou, J. (1994) Initial stages of the devolatilisation of pulverised-coal in a turbulent jet. *Combustion and Flame*, 96,1-2, 150-162.

Crow, S.C. and Champagne, F.H. (1971) Orderly structure in jet turbulence. *Journal of Fluid Mechanics*, 48, 547 – 591.

Crowe, C.T. Gore, R. and Troutt, T.R. (1985) Particle dispersion by coherent structures in free shear flows. *Particulate Science and Technology*, 3, 149 - 158.

Dacombe, P. (1998) IFRF trial documentation notes, for trials run from 22/11/98 to 4/12/98.

Dahm, W.J.A., and Dimotakis, P.E. (1987). Measurements of entrainment and mixing in turbulent jets. *AIAA Journal*, 25(9), 1216-1223.

Dahm, W.J.A., Frieler, C.E. and Tryggvason, G. (1992) Vortex steructure and dynamics in the near field of a coaxial jet. *Journal of Fluid Mechanics*, 241, 371-402.

De Soete, G.G. (1975) Overall reaction rates of NO and N_2 formation from nitrogen. *15th Symposium (International) on Combustion*, The Combustion Institute, 1093-1102.

Du, X., Chengappalli, G. and Annamalai, K. (1995) Ignition and combustion of coal particle streams. *Fuel*, 74, 487-494.

Dugué, J., Horsman, H., Mbiock, A. and Weber, R. (1995) Flow visualisation and mixing characterisation in industrial natural gas flames. *International Gas Research Conference*, Cannes, 6-9 Nov, also published by *The International Flame Research Foundation*, IJmuiden, The Netherlands, IFRF Doc. No. K 70/y/94.

Dugué, J., Mbiock, A and Weber, R. (1994) Mixing characterisation in semi-industrial natural gas flames using Mie scattering visualisation. *7th International Symposium on Applications of Laser Techniques to Fluid Mechanics*, Lisbon, Portugal.

Eaton, J.K. and Fessler, J.R. (1994) Preferential concentration of particles by turbulence. *International Journal of Multiphase Flow*, 20, Suppl, 169 –209.

Essenhigh, R.H. (1962) in Thring, M.W. *The science of flames and furnaces*. Wiley, 2nd edition, 192ff.

Essenhigh, R.H., Mahendra, M.K. and Shaw, D.W. (1989). Ignition of Coal particles: A review. *Combustion and Flame*, 77, 3-30.

Farias, T.L. and Carvalho (1998) Radiative heat transfer in soot-containing combustion systems with aggregation. *International Journal of Heat and Mass Transfer*, 41,17, 2581-2587.

Fenimore, C.P. (1971) Formation of Nitric Oxide in Premixed Hydocarbon Flames. *13th Syposium (International) on Combustion*, The Combustion Institute, 373-380.

Fick, W., Griffiths, A.J. and O'Doherty (1996) Visualisation of coherent structures in a highly turbulent swirling flame. *Eigth International Symposium on the applications of laser techniques to fluid mechanics*. Lisbon, July 8-11.

Field, M.A., Gill, D.W., Morgan, B.B. and Hawksley, P.G.W. (1967) *Combustion of pulverised coal.* The Institute of Energy.

Fletcher, T. H. (1989) Time-resolved particle temperature and mass loss measurements of a bituminous coal during devolatilization. *Combustion and Flame*, 78, 223-236.

Foust, A.S., Wenzel, L.A., Clump, CW., Maus, L. and Andersen, L.B. (1980) *Principles of unit operations*, 2nd Edition, Wiley, New York.

Fulkerston, W, Judkins, R.R. and Sanghvi, M.K. (1990) Energy from fossil fuels. *Scientific American*, Sept, 83 - 89.

Glass, J.W. and Wendt, J.O.L. (1983) Mechanisms governing the destruction of nitrogenous species during the fuel rich combustion of pulverized coal. *19th Symposium (International) on Combustion*, The Combustion Institute, Pittsburgh, 1243-1251.

Glassman, I. (1987) *Combustion*, Academic Press, London.

Godoy, S., Hirji, K., Ismail, M. and Lockwood, F.C. (1986) Stability limits of pulverized coal firing. *Journal of the Institute of Energy*, March 1986, 38-44.

Guilbault, G. (1973) *Practical Fluorescence: Theory, Methods and Techniques*. Marcel Dekker Inc., New York.

Hanby, V.I. (1967) The effect of gaseous oscillations on the combustion rate of solid fuel particles. *Journal of the Fuel Society*,18, 44-49.

Hansell, D, Kennedy, I.M. and Kollmann, W. (1992) A simulation of particle dispersion in a turbulent jet. *International Journal of Multiphase Flow*, 18, 559-576.

Heidenreich, C.A. and Zhang, D.K. (1999) Measuring the temperature response of large wet coal particles during heating. *Fuel*, 78, 8, 991-994.

Hill, S.J. (2000). *Precession in flows through axisymmetric sudden expansions*. Ph.D. Thesis, The University of Adelaide, Australia.

Hill, S.J., Nathan, G.J., and Luxton, R.E. (1995). Precession in axisymmetric confined jets. *12th Australasian Fluid Mechanics Conference*, The University of Sydney, Australia, December 10-15, 135-138.

Hishida, K., Ando, A. and Maeda, M. (1992) Experiments on particle dispersion in turbulent mixing layer. *International Journal of Multiphase Flow*, 18, 181-194.

Holman, J.P. *Heat Transfer* , 5th edition, 1981, McGraw-Hill

Hottel, H.C. and Sarofim, A.F. (1967) *Radiative Transfer* McGraw-Hill, New York.

Husain, Z.D. and Hussain, A.K. M.F. (1979) Axisymmetric mixing layer: influence of the initial and boundary conditions. *AIAA Journal*, 17,1,48-55.

Hussain, A.K.M.F. (1986) Coherent structures and turbulence. *Journal of Fluid Mechanics*, 173, 303 - 356.

Jensen, P.A., Ereaut, P.R., Clausen, S. and Rathmann, O. (1994) Local measurements of velocity, temperature and gas composition in a pulverised-coal flame. *Journal of the Institute of Energy*, 67, 37-46.

Jones, J.C. (1993) *Combustion Science: principles and practice* Millennium Books

Kent, J.H. and Bastin, S.J. (1984) Parametric effects on sooting in turbulent acetylene diffusion flames. *Combustion and Flame*, 56, 29-42.

Kharbat, E., Annamalai, K. and Gopalakrishnan, C. (1995) Ignition and combustion of isolated and binary array of coal particles. *Combustion and Flame*, 100, 413 – 421.

Kimber, G.M. and Gray, M.O. (1967) Rapid devolatilisation of small coal particles. *Combustion and Flame*, 11, 360-362.

Knill, K.J. Maalman, F.J. and Morgan, M.E. (1988) Development of a combustion characterisation technique for high volatile bituminous coals. *IFRF Doc. F88/a/10.*

Kobayashi, H., Howard, J.B. and Sarofim, A.F. (1977) Coal devolatilisation at high temperatures. *16th Symposium on Combustion (International)*, The Combustion Institute, 411-425.

Koochesfahani, M.M. and Dimotakis, P.E. (1985) Laser-induced fluorescence measurements of mixed fluid in a liquid plane shear layer, *AIAA Journal*, 23, 11, 1700 – 1707.

Krishna, C.R. and Berlad, A.L. (1980) A Model for Dust Cloud Autoignition *Combustion and Flame*, 37, 207-210.

Kulick, J.D., Fessler, J.R. and Eaton, J.K. (1993) *On the interactions between particles and turbulence in a fully-developed channel flow in air.* Department of Mechanical Engineering, Stanford University, Report No. MD-66.

Lau, C.W. and Niksa, S. (1992) The combustion of individual particles of various coal types. *Combustion and Flame* 90, 45-70.

Launder, B.E. and Sharma, B.I. (1974) Application of the Energy Dissipation Model of Turbulence to the Calculation of Flow Near a Spinning Disc. *Letters in Heat and Mass Transfer*, 1, 2, 131-138.

Lazaro, B.J. and Lasheras, J.C. (1992) Particle dispersion in the developing free shear layer. Part 2. Forced Flow. *Journal of Fluid Mechanics*, 235, 179 – 221.

Leweke, T. and Provansal, M. (1995) The flow behind rings: bluff body wakes without end effects. *Journal of Fluid Mechanics*, 288, 265 – 310.

Lockwood, F. C.; Shah, N. G. (1981) New radiation solution method for incorporation in general combustion prediction procedures. *18th Symposium (International) on Combustion, The Combustion Institute*, 1405-1414.

Lockwood, F.C. and Romo-Millares, C.A. (1992) Mathematical modelling of fuel-NO emissions from PF burners, *Journal of the Institute of Energy*, 65, 144-152.

Longmire, E.K. and Eaton, J.K. (1992) Structure of a particle-laden round jet. *Journal of Fluid Mechanics*, 236, 217 - 257.

Longmire, E.K. and Eaton, J.K. (1994) Active open loop control of praticle dispersion in round jets. *AIAA Journal*, 32, 555-563.

Longmire, E.K., Eaton, J.K. and Elkins, C.J. (1992) Control of jet structure by crown-shaped nozzles. *AIAA Journal*, 30, 505 –512.

Lowes, T. M. and Evans, L.P. (1989) Optimisation of the Design and Operation of Coal Flames in Cement Kilns. *Journal of the Institute of Energy*, 62, 220-228.

Luxton, R.E. (1993) On mixing, cement and the hot end of aerodynamics. *Advances in aerodynamics and astronautics*, Prof. Roddam Narashima FRS FESTSCHRIFT, Ed. Preblise, S. and Visheramasth, M. Bangalore, Dec.

Luxton, R.E., Nathan, G.J. and Luminis Pty. Ltd. (1988) *Australian Patent Office*, Patent Application No.16235/88, International Patent Application No. PCT/AU88/00114

Ma, J. and Fletcher, T.H. (1996) Conversion of coal tar to soot during coal pyrolysis in a post-flame environment. *26th Symposium on Combustion (International)* The Combustion Institute, 3161-3167.

Magel, H.C., Schnell, U. and Hein, R.G. (1996) Simulation of detailed chemistry in a turbulent combustor flow. *26th Symposium on Combustion (International)*, The Combustion Institute, 67-74.

Magnussen, B.F. and Hjertager, B.H. (1977) On mathematical modelling of turbulent combustion with emphasis on soot formation and combustion. *16th Symposium on Combustion (International)*, The Combustion Institute, 719-729.

Magnussen, B.F., Hjertager, B.H., Olsen, J.G. and Bhaduri, D. (1978) Effects of turbulent structure and local concentrations on soot formation and combustion in C_2H_2 diffusion

flames. *17th Symposium on Combustion (International)*, The Combustion Institute, 1383-1393.

Manias, C.G. and Nathan, G.J. (1994). Low NO_x Clinker Production., *World Cement*, May 1994.

Maxey, M.R. (1993) The equatoin of motion for a small rigid sphere in nonuniform flow. *ASME/FED Gas-solid flows*, 166, 57-62.

McCreath, C.G. and Makepeace, R. (1971) Report on the investigation into the interaction of both an isothermal and a burning oil spray with their aerodynamic environments behind a bluff body. *Fuel and Combustion Technology Ltd. interim report.*

McLaughlin, J.B. (1991) Inertial migration of a small sphere in linear shear flows. *Journal of Fluid Mechanics*, 224, 261-274.

Mi, J.C., (1997) "Control of Jet Oscillations for Enhanced Combustion Performance" *SPIRT Grant Application*, University of Adelaide.

Monin, A.S. and Yaglom, A.M. (1975) *Statistical fluid mechanics*. MIT Press.

Morgan, M. E., and Roberts, P. A. (1987) Coal combustion characterisation studies at the international flame research foundation. *Fuel Process. Technol.*, 15, 173-187.

Mullinger, P.J. and Jenkins, B.G. (1994) NO_x reduction techniques for rotary kilns, *Joint AFRC/JFRC Conference*, Hawaii

Mullinger, P.J. (1994a) Cement Kiln Firing and Clear Air Requirements. *World Cement*, December, 27 – 31.

Mullinger, P.J. (1994b) Personal communication to G.J. Nathan, 20/7/94.

Muniz, L. and Mungal, M.G. (1997) Instantnaeous flame-stabilisation velocities in lifted-jet diffusion flames. *Combustion and Flame*, 111, 16-31.

Nathan, G.J. (1988) *The Enhanced Mixing Burner.* PhD. Thesis, The University of Adelaide.

Nathan, G.J. and Luxton, R.E. (1991). The Entrainment and Combustion Characteristics of an Axi-symmetric, Self-exciting Enhanced Mixing Nozzle., *Proceedings of the ASME/JSME Thermal Engineering Joint Conference*, Reno, Nevada, 5, 145-152.

Nathan, G.J. and Luxton, R.E. (1989). The combustion characteristics of an enhanced mixing nozzle. *Joint International Conference, The Combustion Institute*, Sydney, 248-251.

Nathan, G.J., Hill, S.J. and Luxton, R.E. (1998) An axisymmetric "Fludic" nozzle to generate jet precession. *Journal of Fluid Mechanics*, 370:347-380

Nathan, G.J., Luxton, R.E. and Smart, J.P. (1992). Reduced NO_x Emissions and Enhanced Large Scale Turbulence from a Precessing Jet Burner., *24th Symposium (International) on Combustion*, The Combustion Institute, 1399-1405.

Nathan, G.J., Nobes, D.S. Mi J., Schneider, G.M., Newbold, G.J.R., Alwahabi, Z.T., Luxton., R.E. and King, K.D. (1997) Exploring the relationship between mixing, radiation, and NO_x emissions from natural gas flames. In *'Combustion and Emissions Control III'*, The Institute of Energy, London, 49-69.

Nathan, G.J., Smart, J.P. and Jenkins, B.G. (1995) Criterion for modelling gyrotherm burners. *FCT Ltd. and Department of Mechanical Engineering Internal Report.*

Nathan, G.J., Turns, S.R. and Bandaru, R.V. (1996) The influence of fuel jet precession on the global properties and emissions of unconfined turbulent flames. *Combustion Science and Technology*, 112, 211-230.

Nelson, P.F., Buckley, A. N., and Kelly, M.D. (1992) Functional Forms of Nitrogen in Coals and the Release of Coal Nitrogen as NOx Precursors. *24th Symposium (International) on Combustion*, The Combustion Institute, 1259-1267.

Newbold, G.J.R (1997) *Mixing and combustion in precessing jet flows.* PhD. Thesis, The University of Adelaide.

Newbold, G.J.R., Nathan, G.J. and Luxton, R.E. (1997) Large Scale Dynamics of an Unconfined Precessing Jet Flame, *Combustion Science and Technology*, 126, 71-95.

Newbold, G.J.R., Nobes, D.S. Alwahabi, Z.T. Nathan, G.J. and Luxton, R.E. (1995) The application of PIV to the precessing jet nozzle. *12th Australasian Fluid Mecahanics Conference*, Sydney, 395 -398.

Niksa, S. and Lau, C.W. (1993) Global rates of devolatilisation for various coals. *Combustion and Flame*, 94, 293-307.

Nobes, D.S (1998) *The generation of large-scale structures by jet precession.* PhD. Thesis, The University of Adelaide.

Nobis, R.H. (1991) Latest Rotary Kiln Burner Technology: Possibilities and experiences. *IEEE Trans on Industry Applic*, 27, 5, 798 – 806.

Offen, G.R. Eskinazi, D., Mcelroy,M.W. and Maulbetsch, J.S. (1987) Stationary Combustion NO_x control. *Journal of the Air Pollution Control Association*, 37, (7), 864-871.

Ono, Y (1980) Microscopical Estimation of Burning Condition and Quality of Clinker. *7th International Congress Chemistry Cement*, 7, 206-211.

Parham, J. (1998) *Prediction and control of heat flux and NO_x emissions in gas fired rotary kilns.* Departmental Report, The University of Adelaide.

Perry, R.H., Green, D.W. and Maloney, J.O. (eds.) (1984) *Perry's Chemical engineers' handbook* 6th edition, McGraw-Hill, New York.

Pershing, D.W. and Wendt, J.O.L. (1977) Relative Contributions of Volatile Nitrogen and Char Nitrogen to NO_x Emissions from Pulverised Coal Flames. *16th Symposium (International) on Combustion*, The Combustion Institute, 389-399.

Peters, A.A.F. and Weber, R. (1995) Mathematical Modeling of a 2.25 MW_t Swirling Natural Gas Flame. Part 1: Eddy Break-up Concept for Turbulent Combustion; Probability Density Function Approach for Nitric Oxide Formation. *Combustion Science and Technology*, 110, 67-101.

Peters, A.A.F. and Weber, R. (1997) Mathematical Modeling of a 2.4 MW_t Swirling Pulvised Coal Flame. *Combustion Science and Technology*, 122, 131-182.

Pohl, J.H. and Sarofim, A.F. (1977). Devolatilization and oxidation of coal nitrogen. *16th Symposium (International) on Combustion*, The Combustion Institute, 491-501.

Rehab, H., Villermaux, E. and Hopfinger, E.J. (1997) Flow regimes of large-velocity-ratio coaxial jets. *Journal of Fluid Mechanics*, 345, 357 – 381.

Ricou, P.F. and Spalding, D.B. (1961) Measurement of entrainment by axisymmetrical turbulent jets, *Journal of Fluid Mechanics*, 11, 21-32.

Roberson, J.A. and Crowe, C.T. (1980) *Engineering Fluid Mechanics*, 2nd edition, Houghton Mifflin , Boston.

Robinson, S.K. (1991) Coherent motions in the turbulent boundary layer. *Annual Review of Fluid Mechanics*, 23, 601- 639.

Rogers, C.B. and Eaton, J.K. (1989) *The interaction between dispersed particles and fluid turbulence in a flat-plate turbulent boudary layer in air.* Department of Mechanical Engineering, Stanford University, Report No. MD-52.

Rosemann, H. and Kunne, P. (1990) Operating Experience with a new type of Burner for Rotary Kilns. *Translation of ZKG*, 9, 421-424.

Ross, D.P., Heidenreich, C.A. and Zhang, D-K. (1999) Devolatilisation Times of Large Coal Particles in a Fluidised-bed. Submitted to *Fuel*

Ryan, W. and Annamalai, K. (1991) Group ignition of a cloud of coal particles. *Journal of Heat Transfer*, 113, 677-687.

Sakakibara, R.B., Wicker, R.B. and Eaton, J.K. (1996) Measurements of the particle-fluid velocity correlation and the extra dissipation in a round jet. *International Journal of Multiphase Flow*, 22, 863-881.

Sampath, R. Maloney, D.J. and Zondlo, J.W. (1998) Evaluation of Thermophysical and themochemical heat requirements for coals at combustion level heat fluxes. *27th Symposium (International) on Combustion*, The Combustion Institute, Pittsburgh, 2915-2923.

Sarofim, A.F. and Wall, T.F. (1980) *Notes on raditive heat transfer*, Department of Chemical Engineering, University of Newcastle.

Sayre, A., Lallemant, N., Dugue, J. and Weber, R. (1994) Effect of radiation on nitrogen oxide emissions from nonsooty swirling flames of natural gas, *25th Symposium (International) on Combustion*, The Combustion Institute, Pittsburgh, 235-242.

Schefer, R. W. and Goix, P.J. (1998) Mechanism of flame stabilisation in turbulent lifted jet flames. *Combustion and Flame*, 112, 559-574.

Schefer, R.W., Kerstein, A.R. Namazian, M. and Kelly, J. (1994). Role of large-scale structure in a nonreacting turbulent CH_4 jet. *Physics of Fluids*, 6, 2, 652 – 661.

Schneider, G.M. (1996) *Structure and turbulence characteristics in a precessing jet flow*. PhD. Thesis, The University of Adelaide.

Schneider, G.M., Froud, D., Syred, N., Nathan, G. J., and Luxton, R.E. (1997) Velocity measurements in a precessing jet flow using a three dimensional LDA system. *Experiments in Fluids*, 23, 89 –98.

Schneider, G.M., Vidakovic, S.S., Hooper, J.D., Musgrove, A.R.,Nathan, G.J., and Luxton, R.E. (1993) Theoretical and Experimental Pressure Field Evaluation Downstream of a Mechanically Precessing Jet. *Australian Heat and Mass Transfer Conference*, 43-1 - 43 -6.

Schnell, U. (1993) Flow Characterisation in Particle-Laden Coal Burner Systems. An *International Journal of Physical Chemistry*, 97,12, 1582-1589.

Schnell, U., Kaess, H., Brodbek, H. (1993) Experimental and Numerical Investigation of NO_x Formation and its Basic Interdependencies on Pulverized Coal Flame Characteristics. *Combustion Science and Technology*, 93, 91-109.

Shaw, D.W., Zhu, X., Mahendra, M.K. and Essenhigh, R.H. (1990) Determination of Global kinetics of coal volatiles combustion. *23rd Symposium (International) on Combustion*, The Combustion Institute, 1155-1162.

Smart, J.P. (1992) *On the Effect of Burner Scale and Coal Quality on Low NO_x Burner Performance*. Ph.D. Thesis University of London.

Smart, J.P. and Weber, R. (1989) Reduction of NO_x and optimisation of burnout with an aerodynamically air-staged burner and an air staged pre-combustor burner. *Journal of the Institute of Energy*, 62, 237-245.

Smart, J.P., Woycenco, D. M., Morgan, D.J. and van de Kamp, W.L. (1996) Studies on scale-up of swirl-stabilised pulverised-coal burners in the thermal input range 2.5 - 12 MW. *Journal of the Institute of Energy*, 69, 13-143.

Smart, J.P., Nathan G.J., Smith, N.L., Newbold, G.J.R., Nobes, D.S. and Morgan, D.J. (1999) Further Developments in Precessing Jet Burner Technology, *5th International Conference on Technologies and Combustion for a Clean Environment*, Lisbon, Portugal, July 12 - 15.

Smoot, L.D. and Smith P.J. (1985) *Coal Combustion and Gasification*, The Plenum Chemical Engineering Series, Plenum Press, NY.

Solomon, P.R. and Fletcher, T.H. (1994) The impact of coal pyrolysis on combustion. *25th Symposium (International) on Combustion*, The Combustion Institute, Pittsburgh, 463-474.

Spalding, D.B. (1963) The art of partial modelling. *9th Symposium (International) on Combustion*, The Combustion Institute, Pittsburgh, 833.

Spalding, D.B. (1971) Mixing and chemical reaction in steady confined turbulent flames. *13th Symposium (International) on Combustion*, The Combustion Institute, Pittsburgh, 649-657.

Squires, K.D and Eaton, J.K. (1990) Particle response and turbulence modification in isotropic turbulence. *Physics of Fluids A*, 2, 1191 – 1203.

Stock, D.E. (1996) Particle dispersion in flowing gases – 1994 Freeman Scholar Lecture. *Journal of Fluids Engineering*, 118, 5 – 17.

Subbarao, E.R. and Cantwell, B.J. (1992) Investigation of a co-flowing buoyant jet: experiments on the effect of Reyolds number and Richardson number. *Journal of Fluid Mechanics*, 245, 69-90.

Syed, Z.A. (1975) *The performance of a low pressure air atomised oil burner*. Ph.D. Thesis. The University of Surrey.

Tegart, W.J.M., Sheldon, G.W. and Griffiths ,D.C. (eds.) (1990) *Intergovernmental Panel on Climate Change Impacts Assessment*, Australian Government Publishing Service.

Tennekes, H. (1968) Simple model for the small-scale structure of turbulence. *Physics of Fluids*, 11, 3, 669 –671.

Tennekes, H. and Lumley, J.L.A. (1972) *A First Course in Turbulence*, MIT Press

Thring, M.W. (1962) *The science of flames and furnaces*. Wiley, 2nd edition, p 225.

Thring, M.W. and Newby, M.P. (1953) Combustion length of enclosed turbulent jet flames, *4th Symposium (International) on Combustion*, The Combustion Institute, Pittsburgh, 789-796.

Truelove, J.S. (1984) The modelling of flow and combustion in swirled, pulverized-coal burners, *20th Symposium (International) on Combustion*, The Combustion Institute, Pittsburgh, 523-530.

Truelove, J.S. and Holcombe, D. (1990) Measurement and modelling of coal flame stability in a pilot-scale combustor. *23rd Symposium (International) on Combustion*, The Combustion Institute, Pittsburgh, 963 - 971.

Turns, S.R. and Myhr, F.H. (1991) Oxides of nitrogen emissions from turbulent jet flames: Part 1 – Fuel effects and flame radiation. *Combustion and Flame*, 87, 319-335.

Uthuppan, J. and Aggarwal, S.K. (1994) Particle dispersion in a transitional axisymmetric jet: a numercial simulation. *AIAA Journal*, 32, 2004 -2014.

van de Kamp, W. L. and Daimon, J. (1996). *Further studies on the effect of burner design variables and fuel properties on the characteristics of cement kiln flames*. The International Flame Research Foundation, IJmuiden, The Netherlands, IFRF Doc. No. F 97/y/3.

van de Kamp, W. L. and Smart, J.P. (1992). *The Effect of Burner Design and Operation and Fuel Type on the Properties of Cement Kiln Flames.*, The International Flame Research Foundation, IJmuiden, The Netherlands, IFRF Doc. No. F 97/y/1.

Vervisch, L. and Poinsot, T. (1998) Direct Numerical Simulation of Non-Premixed Turbulent Flames. *Annual Review of Fluid Mechanics*, 30, 655-691.

Visser, B.M., Smart, J.P., van de Kamp, W.L. and Weber, R. (1990) Measurement and predictions of quarl zone properties of swirling pulverized coal flames. *23rd Symposium (International) on Combustion*, The Combustion Institute, Pittsburgh, 949-955.

Wall, T.F. (1987) "The Combustion of Coal as Pulverised Fuel through Swirl Burners." In '*Principles of Combustion Engineering for Boilers'* (Ed. C.J. Lawn), Academic Press, London, pp 197 - 335.

Wall, T.F., Subramanian, V. and Howley, P. (1982) An experimental study of the geometry, mixing and entrainment of particle-laden jets up to ten diameters from the nozzle. *Transactions of the Institute of Chemical Engineers*, 60: 231-239.

Ward, D.E. (1986) *The two phase plane turbulent mixing layer* PhD. Thesis, The University of Adelaide.

Wark, C., Eickmann, K., Richards, C. (2000) Structure of an acoustically force, reacting two-phase jet, *Combustion and Flame*, 120, 4, 539-548.

Watt, M., Fletcher, T.H., Baui, S. and Solum,M.S., and Pugmire, R.J. (1996) Chemical structure of coal tar during devolatilization. *26th Symposium on Combustion (International)*, The Combustion Institute, 3153-3160.

Weber, R. (1996) Scaling characteristics of aerodynamics, heat transfer, and pollutant emissions in industrial flames. *26th Symposium on Combustion (International)*, The Combustion Institute, 3343-3354.

Weber, R., Boysan, F., Ayres, W.H. and Swithenbbank, J. (1984) Simulation of dispersion of heavy particles in confined turbulent flows. *AICHE Journal*, 30, 490 – 492.

Weber, R., Dugue, J., and Roberts, P.A. (1992a) in Roberts, P.A. (ed) *Research at IJmuiden during the Triennial 1989-1991*, International Flame Research Foundation, IJmuiden, The Netherlands., p 18.

Weber, R., Dugue, J., Sayre, A., and Visser, B.M. (1992b) Quarl Zone Flow Field and Chemistry of Swirling Pulverized Coal Flames: Measurements and Computations. *24th Symposium (International) on Combustion*, The Combustion Institute, 1373-1380.

Weber, R., Visser, B.M. and Boysan, F. (1990) Assessment of turbulence modeling for engineering prediction of swirling vortices in the near burner zone. *International Journal of Heat and Fluid Flow*, 11, 3, 225-235.

Wen, F., Kamalu, N., Chung, J.N., Crowe, C.T. and Troutt, T.R. (1992) Particle dispersion by vortex structures in plane mixing layers. *Journal of Fluids Engineering*, 114, 657-671.

Westenberg, A.A. (1971) Kinetics of NO and CO in Lean, Premixed Hydocarbon-Air Flames. *Combustion Science and Technology*, 4, 59.

Wilcox, D.C. (1998) Turbulence *Modelling for CFD*, 2nd Edition, DCW Industries, inc. La Cañada, California

Winnant, C.D. and Brownand, F.K. (1974) Vortex pairing: mechanisms of mixing layer growth at moderate Reynolds number. *Journal of Fluid Mechanics*, 63, 237-255.

Wolanski, P. and Wojcicki,S. (1974) Stabilisation of coal dust – air mixture by bluff bodies. *15th Symposium (International) on Combustion*, The Combustion Institute, Pittsburgh, 1295-1302.

Yavuzkurt, S. Ha, M.Y., Koopman, G. and Scaroni, A.W. (1991b) A model of the enhancement of coal combustion using high intensity acoustic fields. *Journal of Energy Resources Technology*, 113, 277-285.

Yavuzkurt, S. Ha, M.Y., Reethof, G., Koopman, G. and Scaroni, A.W. (1991a) Effect of an acoustic field on the combustion of coal particles in a flat flame burner. *Journal of Energy Resources Technology*, 113, 286-293.

Zhang, D.K., and Wall, T.F. (1993) An analysis of the ignition of coal dust clouds. *Combustion and Flame*, 92, 475-480.

Zhang, D.K., and Wall, T.F. (1994) Ignition of coal particles: the influence of experimental technique. *Fuel*, 73, 1114-1119.

Zhang, D.K., Wall, T.F. and Lucas, J.A. (1993) The co-operative mechanisms of p.f. cloud ignition. *The Australian Symposium of Combustion and Third Australian Flame Days*, Newcastle, Australia.

Zhao,Y., Serio, M.A., Bassilakis, R. and Solomon, P.R. (1994) A method of predicting coal devolatilisation behaviour based on the elemental composition. *25th Symposium (International) on Combustion*, The Combustion Institute, 553-560.

Publications arising from this thesis

Smith, N.L., Nathan, G.J., Megalos, N.P. and Zhang, D.K. (1995) The influence of a precessing jet flow field on coal flame ignition patterns. *The Australian Symposium on Combustion*, The Combustion Institute, Gawler, Nov 9-10

Smith, N.L., Zhang, D.K. and Nathan, G.J. (1997) Pre-ignition particle heating mechanisms in precessing jet pulverised coal flames. *The Australian Symposium on Combustion*, The Combustion Institute, 148 – 152, Sydney, A.R. Masri and J.C. Mackie (eds).

Smith, N.L., Megalos, N.P., Nathan, G.J., Zhang, D.K., and Smart, J.P. (1998) Precessing jet burners for stable and low NO_x pulverised fuel flames - Preliminary results from small-scale trials. *Fuel*, 77, 9/10,1013-1016.

Smith, N.L., Megalos, N.P., Nathan, G.J., Zhang, D.K., and Smart, J.P. (1998) The role of fuel rich clusters in flame stabilisation and NO_x emission reduction with precessing jet PF flames. *27th Symposium (International) on Combustion*, The Combustion Institute, Pittsburgh, August 2 –7.

Megalos, N.P., Smith, N.L. and Zhang, D.K. (1997) "Pilot Scale Coal Combustion Trials with Precessing Jet Nozzles", *First Asia Pacific Conference on Combustion, ASPACC 97*, Osaka, Japan, May 12-15, 523-526.

Megalos, N.P., Smith, N.L., Nathan, G.J. and Zhang, D.K. (1996) "Burning Profiles of Pulverised Coal in Precessing Jet Flames", *24th Australian and New Zealand Chemical Engineering Conference and Exhibition, CHEMECA 96*, Sydney, Australia, September, 107-112.

Nathan, G.J., Smith, N.L., Mullinger, P.J. and Smart, J.P. (2000) Performance characteristics of, and an aerodynamic scaling parameter for, a practical PF burner design employing jet excitation to promote particle clustering. *5th International Conference on Industrial Furnaces and Boilers (INFUB)*, 2000, Porto, Portugal. April, 11-14.

Smart, J.P., Nathan G.J., Smith, N.L., Newbold, G.J.R., Nobes, D.S. and Morgan, D.J. (1999) Further Developments in Precessing Jet Burner Technology, *5th International Conference on Technologies and Combustion for a Clean Environment*, Lisbon, Portugal, July 12 - 15.